

**New Helmholtz-Energy Equations of State for  
Pure Fluids and CCS-Relevant Mixtures**

Dissertation  
zur  
Erlangung des Grades  
Doktor-Ingenieur

der  
Fakultät für Maschinenbau  
der Ruhr-Universität Bochum

von

Stefan Herrig  
aus Essen

Bochum 2018

Dissertation eingereicht am: 13. November 2018  
Tag der mündlichen Prüfung: 17. Dezember 2018  
Erster Referent: Prof. Dr.-Ing. Roland Span  
Zweiter Referent: Prof. Dr.-Ing. Markus Richter

*“I’ve crossed the ocean  
I’ve traveled the seas  
Getting a bit closer  
To where I should be  
I know I’m supposed to  
Let my mind ease, please...”*

— Pete Philly, *Ocean*



## Danksagung | Acknowledgments

Diese Arbeit entstand während meiner Tätigkeit als wissenschaftlicher Mitarbeiter am Lehrstuhl für Thermodynamik an der Ruhr-Universität Bochum unter der Leitung von Prof. Dr. Roland Span.

An dieser Stelle möchte ich mich herzlich bei all denen bedanken, die mich während meiner Doktorandenzeit unterstützt und damit die Ausarbeitung dieser Dissertation ermöglicht haben.

An erster Stelle danke ich meinem Doktorvater Prof. Dr. Roland Span, der mir meine Promotion ermöglicht hat und sie über die Jahre begleitet hat. Roland, vielen Dank für das große Vertrauen, das Du stets in mich gesetzt hast, für meine Förderung und Forderung, die viel zu meiner persönlichen und fachlichen Entwicklung beigetragen haben, sowie Deine wissenschaftlichen Anregungen und kritischen Fragen.

Weiterhin gilt mein Dank Prof. Dr. Markus Richter, der nicht nur das zweite Gutachten der vorliegenden Dissertation übernommen hat, sondern auch die ihr zugrundeliegenden Forschungsarbeiten von Beginn an mit großem Interesse und Anteilnahme begleitet hat. Vielen Dank, Markus, für Deine vielen motivierenden Worte, Deine kritischen fachlichen Beiträge und nicht zuletzt auch Deine wichtige Einschätzung bezüglich vieler experimenteller Daten aus der Literatur. Darüber hinaus danke ich Dir besonders, dass du meine Aufenthalte am NIST in Boulder ermöglicht hast, die für das Gelingen dieser Arbeit unverzichtbar waren.

The present work would simply have been impossible without the incredible help of Dr. Eric Lemmon and Dr. Ian Bell of NIST. Eric, thank you so much for teaching me almost everything I know about equations of state. Thank you for the enthusiasm you have always shown about this research and for all the wonderful times we had in Colorado. Ian, I cannot thank you enough for all the input you gave to this work and especially for constantly motivating me during its preparation. I am very grateful for your friendship!

The description of the thermodynamic properties of heavy water, which represents an essential part of this thesis, results from almost six years of fruitful collaboration with Dr. Allan Harvey of NIST. Allan, your thorough style of working and your incredible scientific knowledge has been a huge inspiration. Thanks a lot, also for all your “little English lessons” that did not only improve our D<sub>2</sub>O publication but also the writing of this thesis.

I am furthermore very grateful for the collaboration with Dr. Lorena Souza of Imperial College, London, which led to the mixture model for CO<sub>2</sub> + CO included in this work. Thank you, Lorena, for developing together this excellent model, and especially for being a wonderful “fellow sufferer”, while we both completed our theses.

Allen aktuellen und ehemaligen Mitarbeiterinnen und Mitarbeitern des Lehrstuhls für Thermodynamik danke ich herzlichst für die wunderbare gemeinsame Zeit. Ein solch kollegiales, freundschaftliches Umfeld ist wohl kaum anderswo zu finden. Ihr werdet mir immer in guter Erinnerung bleiben! Ganz besonders möchte ich dabei aber meiner Arbeitsgruppe „Team Z“ und im Speziellen den langjährigen Kolleginnen und Kollegen Dr. Theresa Eckermann, Sebastian Hielscher, Dr. Andreas Jäger und Dr. Monika Thol danken. Aus der Zusammenarbeit mit euch sind wichtige Freundschaften gewachsen. Eure fachlichen aber vor allem auch persönlichen Beiträge lassen sich nicht in einer Danksagung zusammenfassen... Vielen, vielen Dank!

Mein besonderer Dank gebührt außerdem Prof. (em) Dr. Wolfgang Wagner, der meine wissenschaftliche Arbeit stets mit großem Interesse verfolgt und mit guten Ratschlägen, motivierenden Worten und der richtigen Literatur unterschützt hat. Vielen Dank, Wolfgang!

Darüber hinaus danke ich meinen langjährigen studentischen Hilfskräften Tobias Neumann und Matthias Körber für ihre große Unterstützung. Die von Euch gesammelten und vorbereiteten Daten, entwickelten Modelle und Eure vielen anderen Beiträge haben diese Arbeit mit ermöglicht. Vielen Dank auch für die große Geduld, mit der Ihr immer wieder auch weniger wichtige Dinge bearbeitet habt (dicke Linien in dünne Linien, kursiv in nichtkursiv, blaue Symbole in magentafarbene Symbole...). Ich danke außerdem Mirco Kortmann, Kira Oberbossel, Judith Rohde, Christopher Tietz und Vira Zosimenko für ihre wichtigen studentischen Arbeiten sowie Sven Pohl für die Unmengen an gesammelter Literatur.

Mein ganz besonderer Dank geht an Alexander Maurer, Dr. Nico Schneider, Dr. Robin Wegge sowie meinen Schulfreund und weltbesten Bürokollegen Dr. Rafael Lentner. Tausend Dank für die unvergessliche und abenteuerliche Zeit, die Motivation und nicht zuletzt auch für Eure fachlichen Beiträge!!!

Over the last years, I had the great privilege to interact with many exceptional scientists. For many essential scientific contributions, inspiring talks and personally valuable moments, I would like to thank: Prof. (em) Dr. Hans-Joachim Kretzschmar, Dr. Matthias Kunick, Dr. Olaf Hellmuth, Prof. Dr. Jan Hrubý, Dr. Václav Vinš, and the complete working group TPWS of IAPWS; furthermore, I am grateful to Dr. Johannes Gernert, Dr. Tara Fortin, Dr. Arno Laesecke, Dr. Mark McLinden, Prof. Dr. Martin Trusler, Camelia Vasile, Dr. Sigurd Løvseth, Dr. Andreas Köster, and Prof. Dr. Jadran Vrabec. Für viele motivierende Gespräche und freundschaftliche Ratschläge danke ich außerdem meinen drei ehemaligen Chefs Dr. Florian Dauber, Dr. Stefan Schimpf-Willenbrink und Dr. Reza Seif.

Zu guter Letzt danke ich meiner Familie und meinen Freundinnen und Freunden für die große Unterstützung sowie die Geduld, mit der sie mein Verschwinden zum Ende dieser Dissertation toleriert haben. Tausend Dank, Alessa, dass du diese Arbeit mitgetragen und ertragen hast: „Wenn ich Dich nicht hätte, müsste ich Dich erfinden!“

## Table of Contents

<b>1</b>	<b>Introduction.....</b>	<b>1</b>
<b>2</b>	<b>Motivation .....</b>	<b>3</b>
2.1	Development of a New IAPWS Formulation for Heavy Water .....	3
2.2	Development of an Extended Equation of State for CCS-Relevant Mixtures.....	6
<b>3</b>	<b>Equations of State - A Brief Introduction .....</b>	<b>9</b>
3.1	Cubic Equations of State .....	10
3.2	Lee-Kesler-Plöcker Equation of State .....	12
3.3	Multi-Parameter Helmholtz-Energy Equations of State .....	16
3.4	“Predictive” Equations of State .....	22
<b>4</b>	<b>Fitting Helmholtz-Energy Equations of State .....</b>	<b>25</b>
<b>5</b>	<b>Equations of State for Pure Fluids .....</b>	<b>35</b>
5.1	New Reference Equation of State for Heavy Water .....	36
5.1.1	Physical Constants and Characteristic Properties .....	37
5.1.2	Melting- and Sublimation-Pressure Equations .....	40
5.1.3	Ideal-Gas State .....	45
5.1.4	Thermal Saturation Data .....	47
5.1.5	Homogeneous Density and Virial Coefficient Data .....	55
5.1.6	Caloric Property Data .....	69
5.1.7	Data at Metastable States .....	81
5.1.8	Representation of Physical Behavior and Extrapolation .....	87
5.2	Equation of State for Chlorine .....	91
5.3	Equation of State for Monoethanolamine.....	102
<b>6</b>	<b>Extended Equation of State for CCS-Mixtures .....</b>	<b>113</b>
6.1	Overview of the Mixture Model .....	114
6.2	Binary Mixtures Described with Specific Departure Functions.....	116
6.2.1	Carbon Dioxide + Argon .....	117
6.2.2	Carbon Dioxide + Carbon Monoxide .....	132
6.2.3	Water + Methane .....	141
6.2.4	Water + Hydrogen Sulfide .....	149
6.3	Binary Mixtures Described with Adjusted Reducing Parameters .....	154
6.3.1	Binary Mixtures with Sulfur Dioxide .....	154
6.3.2	Binary Mixtures with Amines.....	186
6.3.3	Chlorine + Hydrogen Chloride .....	194
6.4	Binary Mixtures Described with Simple Combining Rules .....	197

---

6.5	Additional Information on the Multi-Component Mixture EOS.....	200
6.5.1	Range of Validity and Estimated Uncertainties .....	200
6.5.2	Chemically Reactive Mixtures .....	202
<b>7</b>	<b>Impact of Impurities on Thermodynamic Properties of CCS-Mixtures.....</b>	<b>205</b>
<b>8</b>	<b>Conclusions and Recommendations .....</b>	<b>211</b>
	<b>References .....</b>	<b>215</b>
	<b>Appendix A - Supplement to the Lee-Kesler-Plöcker Equation of State.....</b>	<b>237</b>
A.1	Parameters used for Calculations with the LKP EOS .....	237
A.2	Derivatives of the Helmholtz-Energy Transformation of the LKP EOS .....	237
	<b>Appendix B - Supplement to the EOS for Heavy Water .....</b>	<b>239</b>
B.1	Equation-of-State Parameters .....	239
B.2	Data Sets for Heavy Water and Statistical Analysis .....	240
	<b>Appendix C - Supplement to the EOS for Chlorine.....</b>	<b>244</b>
C.1	Equation-of-State Parameters .....	244
C.2	Data Sets for Chlorine and Statistical Analysis.....	245
	<b>Appendix D - Supplement to the EOS for MEA .....</b>	<b>247</b>
D.1	Equation-of-State Parameters .....	247
D.2	Data Sets for MEA and Statistical Analysis.....	248
	<b>Appendix E - Supplement to the CCS-Mixture Model.....</b>	<b>252</b>
E.1	Parameters of the Mixture Model.....	252
E.2	Data Sets for the CCS-Mixture Model and Statistical Analysis .....	254



## Table of Symbols

### Latin Symbols

$A$	Equation-of-state parameter
$AAD$	Average absolute (relative) deviation
$a$	Equation-of-state parameter Interaction parameter in cubic equations of state Integration constants in the ideal-gas Helmholtz-energy function Molar Helmholtz energy Parameter
$B$	Molar second virial coefficient Parameter
$b$	Co-volume in cubic equations of state Equation-of-state parameter
$C$	Molar third virial coefficient
$c$	Constant Equation-of-state parameter
$c_p$	Molar isobaric heat capacity
$c_v$	Molar isochoric heat capacity
$D$	Molar fourth virial coefficient
$d$	Total differential
$d$	Density exponent Equation-of-state parameter Parameter
$F$	Weighting factor for binary generalized departure functions Deviation of a point or constraint from the equation of state
$g$	Molar Gibbs energy
$h$	Molar enthalpy
$i$	Index of summation
$j$	Index of summation
$K$	Number of terms
$k$	Binary interaction parameter Index of summation
$l$	Density exponent
$M$	Molar mass
$m$	Parameter in the SRK equation of state
$N$	Number of components Number of data points Number of terms

---

$n$	Coefficient Parameter
$p$	Pressure
$R$	Universal gas constant
$SSQ$	Sum of squares
$s$	Molar entropy
$T$	Temperature
$t$	Temperature exponent
$U$	Uncertainty
$u$	Exponent in the ideal-gas function Molar internal energy Relative uncertainty
$v$	Coefficient in the ideal-gas function Molar volume
$W$	Weight of a data point or constraint
$w$	Speed of sound
$X$	Arbitrary property
$x$	Mole fraction
$\mathbf{x}, \bar{x}$	Vector of mole fractions
$Z$	Compressibility factor

### Greek Symbols

$\alpha$	Reduced Helmholtz energy Temperature correction parameter in the SRK equations of state
$\beta$	Binary reducing parameter Equation-of-state parameter
$\gamma$	Binary reducing parameter Equation-of-state parameter
$\delta$	Reduced density
$\Delta$	Parameter
$\Delta$	Difference
$\varepsilon$	Equation-of-state parameter
$\eta$	Equation-of-state parameter
$\vartheta$	Reduced temperature
$\mu_{\text{T}}$	Joule-Thomson coefficient
$\pi$	Reduced pressure
$\theta$	Reduced temperature in melting and sublimation-pressure correlations Parameter
$\rho$	Molar density
$\tau$	Reciprocal reduced temperature

$\psi$	Parameter Reduced volume
$\omega$	Acentric factor

### Subscripts

0	Reference state
Ih	Hexagonal ice structure I
III	Ice structure III
V	Ice structure V
VI	Ice structure VI
VII	Ice structure VII
atm	Property at atmospheric pressure (1 atm = 0.101 325 MPa)
c	Property at critical point
calc	Calculated property
con	Physical or mathematical constraint
$\delta$	Partial derivative with respect to the reduced density
exp	Experimentally determined property Exponential term
GBS	Gaussian bell-shaped term
liq	Liquid
m, melt	Property in the melting region
max	Maximum
min	Minimum
mix	Mixture
n	Scaling value
NA	Non-analytic term
nbp	Normal boiling point
PE	Planck-Einstein term
$p$	Constant pressure
pol	Polynomial(-like) term
$r$	Reducing parameter
sat	Property at saturation
sub	Property in the sublimation region
$T$	Constant temperature
tp	Triple point
$\tau$	Partial derivative with respect to the inverse reduced temperature
$v$	Constant volume
vap	Vapor

**Superscripts**

'	Property of the saturated liquid
“	Property of the saturated vapor
o	Property of the ideal gas Simple fluid in the LKP equation of state
E	Excess property
r	Property of the residual part
ref	Reference fluid

**Abbreviations**

CAS	Chemical Abstracts Service
CCS	Carbon capture and storage
DEA	Diethanolamine
EOS	Equation of state
EOS-CG	Equation of State for Combustion Gases and Combustion Gas like Mixtures
GERG	“Groupe Européen de Recherches Gazières” (The European Gas Research Group)
GERG-2008	Reference Equation of State for Natural Gas Mixtures
ITS-90	International Temperature Scale of 1990
IAPS	International Association for the Properties of Steam
IAPWS	International Association for the Properties of Water and Steam
IAPWS-95	Reference equation of state for water of IAPWS
INRiM	“Istituto Nazionale di Ricerca Metrologica” (National Metrology Institute of Italy)
IPCC	Intergovernmental Panel on Climate Change
IUPAC	International Union of Pure and Applied Chemistry
L	Liquid
LKP	Lee-Kesler-Plöcker equation of state
LLE	Liquid-liquid equilibrium
MEA	Monoethanolamine
NIST	National Institute of Standards and Technology
NTNU	Norwegian University of Science and Technology
PC(P)-SAFT	Perturbed-Chain (Polar) Statistical Associating Fluid Theory
PSRK	Predictive Soave-Redlich-Kwong equation of state
PTB	“Physikalisch-Technische Bundesanstalt” (National Metrology Institute of Germany)
ppm	parts-per-million
RUB	“Ruhr-Universität Bochum” (Ruhr-University Bochum)

S	Solid
SINTEF	„Stiftelsen for industriell og teknisk forskning“ (Independent Norwegian research institute)
SLE	Solid-liquid equilibrium
SRK	Soave-Redlich-Kwong equation of state
UNIFAC	Universal Quasichemical Functional Group Activity Coefficients
UWA	The University of Western Australia
V	Vapor
VLE	Vapor-liquid equilibrium
VLLE	Vapor-liquid-liquid equilibrium

### Chemical formulas

$^1\text{H}$	Hydrogen isotope protium
$^2\text{H}$	Hydrogen isotope deuterium
$^3\text{H}$	Hydrogen isotope tritium
$^{16}\text{O}$	Ordinary oxygen isotope
$^{17}\text{O}$	Heavy oxygen isotope
$^{18}\text{O}$	Heavy oxygen isotope
Ar	Argon
$\text{CH}_4$	Methane
$\text{C}_2\text{H}_6$	Ethane
$\text{C}_2\text{H}_7\text{NO}$	Monoethanolamine
$\text{C}_6\text{H}_6$	Benzene
$\text{C}_{11}\text{H}_{24}$	Undecane
$\text{Cl}_2$	Chlorine
CO	Carbon monoxide
$\text{CO}_2$	Carbon dioxide
COS	Carbon oxide sulfide
D	Atomic deuterium
$\text{D}_2\text{O}$	Deuterium oxide, heavy water
H	Atomic hydrogen
$\text{H}_2$	Hydrogen
$\text{H}_2\text{O}$	Ordinary (light) water
$\text{H}_2\text{S}$	Hydrogen sulfide
HDO	Deuterium hydrogen oxide, semi-heavy water
HCl	Hydrogen chloride
i- $\text{C}_5\text{H}_{12}$	Isopentane
$\text{N}_2$	Nitrogen
NaCl	Sodium chloride
$\text{NH}_3$	Ammonia

NO <sub>x</sub>	Nitrogen oxides
O <sub>2</sub>	Oxygen
SO <sub>2</sub>	Sulfur dioxide
SO <sub>x</sub>	Sulfur oxides
T	Atomic tritium
T <sub>2</sub> O	Tritium oxide, super-heavy water

## 1 Introduction

Thermodynamic properties of fluids are essential for many technical applications, in particular for energy and chemical process engineering. A classic example is the design, control, and evaluation of power plants that requires knowledge about the properties of the circulating working fluid, which is mostly water, or sometimes an organic fluid. Properties obviously relevant to this example are the thermal properties temperature, saturation vapor pressure, and specific volume or density; but other properties such as enthalpy, entropy, heat capacity, or speed of sound are also important. Another typical example for the significance of thermodynamic properties is the pipeline transport of natural gas, hydrogen or CO<sub>2</sub>-rich mixtures. For this purpose, knowledge of, for example, the phase boundaries of the gas, liquid, or solid states is essential to apply the appropriate pipeline pressure. In both examples, the accuracy of the used thermodynamic properties is not only relevant to economic targets but also to safety and sustainability.

The most obvious way of providing thermodynamic property data is by carrying out accurate measurements of a property at defined conditions of, for example, temperature and pressure. The results of such experiments are traditionally listed in property tables, which no longer fulfill the requirements of industrial and technical applications. Instead, accurate correlations are needed, which provide thermodynamic properties at given input variables and which can be implemented into process-simulation software. The most accurate approach for such thermodynamic correlations is by means of Helmholtz-energy explicit equations of state. The functional form of these empirical models allows for the calculation of all thermodynamic properties. Conversely, all types of data can be used for correlating, which leads to an exceptionally consistent description of the physical behavior of a fluid.

Within the scope of the present doctoral thesis, Helmholtz-energy explicit equations of state for pure fluids and mixtures were developed with two main targets: (1) the development of a new reference equation of state for heavy water and (2) of an extended equation of state for multi-component CO<sub>2</sub>-rich mixtures.

The new reference equation of state for the thermodynamic properties of heavy water was developed within a project of the International Association for the Properties of Water and Steam (IAPWS) as a collaboration between Ruhr-Universität Bochum (RUB) and the National Institute of Standards and Technology (NIST) in Boulder, Colorado. The equation replaces the previous standard formulation of Hill *et al.*<sup>1</sup> published in 1982. During the more than 35 years since the publication of that equation, new and accurate experimental data became available that are not described within their experimental uncertainties. Compared to modern formulations for other fluids, the equation of Hill *et al.* is also based on a quite

complex mathematical structure that frequently causes numerical problems. The development of a numerically stable and highly accurate new reference equation of state for this fluid of significant technological and scientific importance has been a research need for many years. This need is now satisfied by the equation developed in this work.

The new equation of state for CO<sub>2</sub>-rich mixtures is developed for the application in carbon-capture-and-storage (CCS) processes. CCS denotes the concept of removing the most abundant greenhouse gas, CO<sub>2</sub>, from combustion gases and of storing it as long as technically possible. Different than often thought, the working fluid handled is not pure CO<sub>2</sub> but a CO<sub>2</sub>-rich mixture with various impurities. A first reference equation of state for the thermodynamic properties of such mixtures was presented by Gernert and Span in 2016.<sup>2</sup> This model known as “EOS-CG” enables an accurate description of mixtures containing the major components typically found in CCS processes (carbon dioxide, water, nitrogen, oxygen, argon, and carbon monoxide). The aim of the present work was an improvement of that model as well as an expansion to additional minor impurities such as methane, hydrogen, hydrogen sulfide, sulfur dioxide, hydrogen chloride, chlorine, monoethanolamine, and diethanolamine. In order to implement the components chlorine and monoethanolamine (MEA) into the multi-component mixture model, new Helmholtz-explicit equations of state for these fluids were developed in a similar manner to that for heavy water.

This doctoral thesis is structured into eight chapters. A more detailed discussion of the motivation for both projects is given in Sec. 2. Subsequently, in Sec. 3, a brief introduction into equations of state as developed in this work but also as used for comparative calculations is given. An explanation of the fitting process that led to the new equations of state is provided in Sec. 4. The results of the fitting process for pure fluids (heavy water, chlorine, and MEA) are presented in Sec. 5, whereas the equation of state for CO<sub>2</sub>-rich mixtures is presented in Sec. 6. The results are discussed through detailed comparisons between properties calculated with the new equations and the available experimental and molecular-simulation data. Furthermore, a critical assessment of the representation of the physical behavior of the fluids is provided. Sec. 7 presents exemplary property plots calculated from the equation for CO<sub>2</sub>-rich mixtures that give an impression of the impact of impurities on the thermodynamic properties of the working fluid in CCS processes. The thesis concludes with a summary of the results and recommendations for future work given in Sec. 8.



## 2 Motivation

The importance of high-quality thermodynamic properties was pointed out in the introduction of this thesis; furthermore, it was explained that state-of-the-art equations of state (EOS) for both pure fluids and mixture represent the most suitable source of these properties. The focus of the present doctoral thesis is on such highly accurate EOS. Two main objectives were pursued in its elaboration: (1) the development of a new reference EOS for pure heavy water and (2) of an extended EOS for CO<sub>2</sub>-rich mixtures relevant to Carbon Capture and Storage.

Although the thermodynamic properties of heavy water are of no direct relevance for the description of CO<sub>2</sub>-rich mixtures, the development of the mixture model benefited from experiences made during the work on the formulation for pure heavy water. First of all, fitting an EOS for a fluid with such complex physical characteristics (maximum in density and speed of sound, various anomalies in the subcooled liquid) provided useful insights for the development of other pure fluid EOS that were needed for the description of CO<sub>2</sub>-rich mixtures. Besides, it helped to understand some challenges of describing binary mixtures containing ordinary water resulting from the structure of the corresponding reference EOS. The EOS for heavy water can be considered as an excellent starting point for a potential future development of a new and less complex EOS for ordinary water that would be more suitable for application in mixture models.

The relevance of the development of a new reference EOS for heavy water is discussed in detail in Sec. 2.1, and the motivation for the work on an extended EOS for CO<sub>2</sub>-rich mixtures is pointed out in Sec. 2.2.

### 2.1 Development of a New IAPWS Formulation for Heavy Water

In order to explain the need for a new reference EOS for heavy water, it should first be explained what this special form of water is and why it is relevant. Heavy water or deuterium oxide (D<sub>2</sub>O, CAS no. 7789-20-0) is a liquid at ambient conditions. Although it is often thought to be, it is not radioactive and, if not taken in unreasonably large amounts, nontoxic. It differs from ordinary, light water in its hydrogen isotopes. The heavy water molecule contains two deuterium atoms instead of two ordinary hydrogen atoms. The nucleus of ordinary hydrogen, also called “protium” (<sup>1</sup>H), consists of only one proton. The isotope deuterium (<sup>2</sup>H, D) has one additional neutron. As a result, the molecular mass of heavy water is higher than that of ordinary water by a factor of roughly 20/18. The resulting higher density is vividly presented in Figure 2.1. It shows a photograph of heavy-water ice cubes

that due to their higher density sink in ordinary water, whereas the ordinary-water ice cubes float due to the well-known water anomaly.



**Figure 2.1** Heavy- and ordinary-water ice cubes in an ordinary water sample. The photograph was taken by Tietz<sup>3</sup> in the laboratories of Ruhr-Universität Bochum.

Heavy water should not be confused with other heavier forms of water such as “super-heavy water” (tritium oxide,  $T_2O$ ) containing the hydrogen isotope tritium ( $^3H$ , T), “semi-heavy water” (deuterium hydrogen oxide, HDO), or “heavy-oxygen water” ( $H_2^{17}O$  or  $H_2^{18}O$ ) enriched in heavier oxygen isotopes. The equation of state presented here is developed for a description of deuterium oxide with the oxygen isotopes  $^{16}O$ ,  $^{17}O$ , and  $^{18}O$  in the standard proportions as defined by “Vienna Standard Mean Ocean Water” (V-SMOW), discussed by Kell,<sup>4</sup> and adopted by the International Association for the Properties of Water and Steam (IAPWS).<sup>5</sup> These standard (molar) proportions are:  $x_{16O} = 0.997\ 620\ 6$ ,  $x_{17O} = 0.000\ 379$ , and  $x_{18O} = 0.002\ 000\ 4$ . However, experimentally investigated samples of heavy water never contain 100 %  $D_2O$ , but are contaminated by a varying amount of  $H_2O$  and HDO. Since the EOS was fitted to experimental data, the  $D_2O$  content of the samples investigated within the corresponding references was considered in order to estimate the experimental uncertainty of the data.

In 1932, Urey and co-workers were the first to prove the existence of deuterium and thus of heavy water.<sup>6</sup> Soon after this discovery, heavy water became a target for many nuclear physicists and played an important role in the first research on nuclear fission. It was therefore regarded as a compound of high commercial and military interest. Consequently, the production of  $D_2O$  increased significantly during World War II. A summary of the interesting history of this almost mystical substance is given within the essay of Waltham.<sup>7</sup>

Over the past decades,  $D_2O$  has mostly been used as a neutron moderator in nuclear reactors. It slows free neutrons down to thermal energies, which is necessary for a self-sustaining

chain reaction. The process of moderation can also be done with light water, but due to the additional neutrons in its hydrogen atoms heavy water adsorbs significantly fewer free neutrons.<sup>8</sup> Nowadays, the interest in heavy water is as much scientific as commercial. In biological and medical research, heavy water is used in the “doubly-labeled water method” to measure the average daily metabolic rate of an organism.<sup>9,10</sup> Another application is the “boron neutron capture therapy” for the treatment of brain tumors, in which the above discussed ability of heavy water to moderate neutrons is useful (see for instance Fairchild *et al.*<sup>11</sup>).

The equilibrium geometry of the D<sub>2</sub>O molecule is almost identical to that of H<sub>2</sub>O.<sup>12</sup> While normally isotopic substitution has little effect on the thermal properties of fluids, this is not the case when hydrogen bonding is important. Quantum delocalization has a net weakening effect on water’s hydrogen bonds,<sup>13</sup> so the heavier deuterium atoms make the hydrogen bonding stronger in D<sub>2</sub>O than in H<sub>2</sub>O. The effect is large enough that the EOS of D<sub>2</sub>O must be developed separately, rather than as a small perturbation to the H<sub>2</sub>O EOS. The differences in thermodynamic behavior between H<sub>2</sub>O and D<sub>2</sub>O as quantified by their equations of state therefore provide useful insights into quantum effects and hydrogen bonding.

The previous reference equation for the thermodynamic properties of D<sub>2</sub>O was published in 1982 by Hill *et al.*<sup>1</sup> and became a standard of the International Association for the Properties of Steam (IAPS, now International Associations for the Properties of Water and Steam, IAPWS) in 1984. This formulation was later adjusted to the International Temperature Scale of 1990 (ITS-90)<sup>14</sup> as discussed in the corresponding Release of IAPWS.<sup>15</sup> It is a fundamental EOS explicit in the specific Helmholtz energy with temperature  $T$  and density  $\rho$  as independent variables. The equation is valid from the triple-point temperature up to 800 K at pressures up to 100 MPa, but it is not recommended for calculations in the critical region. In comparison to modern equations of state for other fluids, this previous standard formulation has a quite long functional form with a total of 50 terms. This relatively complex mathematical structure frequently leads to numerical problems. Due to both the great advances in the development of equations of state and modern computer technology, it is now possible to develop equations with a reduced number of terms without loss of accuracy. Based on these factors, IAPWS initiated the development of a new EOS for heavy water in 2013, although at that point new experimental data since the publication of Hill *et al.* were relatively few. Within the scope of this doctoral thesis, a new EOS for the properties of heavy water was developed. During this process, additional accurate data were contributed by various groups associated with IAPWS. Thus, the new formulation is based on the most up-to-date thermodynamic database. The results of the development of the new reference EOS are presented in Sec. 5.1.

## 2.2 Development of an Extended Equation of State for CCS-Relevant Mixtures

Carbon capture and storage, or in short “CCS”, is considered to be a key technology for the reduction of anthropogenic CO<sub>2</sub> emissions that represent the most significant long-lived greenhouse gases in the atmosphere. The basic idea of CCS is simple: CO<sub>2</sub> is captured from exhaust gases of fossil-fuel combustion processes (mostly conventional power plants), transported, and stored in suitable reservoirs.

The design of safe and cost-efficient CCS processes is an interdisciplinary challenge that, among other aspects, requires contributions from process engineering, geological research, material science as well as safety and risk analyses. All these efforts demand high-quality thermodynamic property data. In early studies, such properties were calculated for pure CO<sub>2</sub>. In reality, the working fluids are CO<sub>2</sub>-rich mixtures with some other components on a percentage level and a variety of possible components contained on an impurity level (mole fractions of some parts-per-million). Some of these components have a significant impact on the thermodynamic behavior and especially on phase-equilibrium properties.

The mixture components aside from CO<sub>2</sub> initially vary depending on the technology used for CO<sub>2</sub> separation. The most important types of separation systems are post- and pre-combustion separation, and separation from oxyfuel-combustion processes. A detailed overview and explanation of these options is given by the Intergovernmental Panel on Climate Change (IPCC) in its “Special Report on Carbon Dioxide Capture and Storage”.<sup>16</sup> Post-combustion processes separate the CO<sub>2</sub> from the exhaust gas after the combustion of fossil fuels. The separation can be done by absorption (with amines or chilled ammonia), adsorption (with, for example, zeolites or activated carbon), gas membranes, or cryogenic separation. The separated CO<sub>2</sub>-rich mixture typically contains components of the combustion air (N<sub>2</sub>, O<sub>2</sub>, Ar), water, combustion products (for example NO<sub>x</sub>, SO<sub>x</sub>, H<sub>2</sub>S, CO, COS), fossil-fuel leftovers (such as HCl or Cl<sub>2</sub>), and traces of the solvents used for separation (amines, NH<sub>3</sub>). The post-combustion technology is of particular interest because existing power plants can be retrofitted to add CCS.

Pre-combustion separation requires partial oxidation of the fossil fuels mostly in gasifiers that produce a fluid mixture mainly consisting of CO and H<sub>2</sub> (synthesis gas). In a subsequent water-shift reaction, the synthesis gas is reacted with steam. The products are CO<sub>2</sub>, which is then separated from the fluid stream, and H<sub>2</sub>, which is burned to H<sub>2</sub>O for power generation. The separated CO<sub>2</sub>-rich mixture has very high CO<sub>2</sub> concentrations; however, it typically contains combustion-air components, water, and more significant concentrations of H<sub>2</sub>, CO, H<sub>2</sub>S and CH<sub>4</sub>.

For oxyfuel-combustion processes, the combustion air is separated into O<sub>2</sub> and N<sub>2</sub>. The combustion process is then carried out with almost pure O<sub>2</sub> instead of air. When burning pure alkanes, the resulting exhaust gas only consists of water and CO<sub>2</sub>; however, depending on the fossil fuel, there are always other combustion products. In addition, the exhaust gas

often contains higher fractions of Ar, which are not separated from the O<sub>2</sub> in typical air separation processes, as well as larger fractions of waste O<sub>2</sub>.

Additional impurities become relevant to the CCS chain when discussing transport and storage (or sequestration) processes. To avoid formation of solid structures such as ice, dry ice, or hydrates, the CO<sub>2</sub>-rich stream is often doped with glycols or methanol, which have to be considered in the design of the subsequent process steps. The storage in geological reservoirs requires the consideration of complex aqueous systems such as brines.

It is obvious that providing accurate thermodynamic properties of such highly non-ideal multi-component mixtures is a challenging task. In 2013, the development of a first reference EOS for CCS-relevant mixtures was completed by Gernert,<sup>17</sup> and the model was later on presented by Gernert and Span<sup>2</sup> as the “Equation of State for Combustion Gases and Combustion-Gas-Like Mixtures” (EOS-CG). This Helmholtz-energy explicit EOS already allows for an accurate description of mixtures containing the major components relevant to CCS: CO<sub>2</sub>, H<sub>2</sub>O, N<sub>2</sub>, O<sub>2</sub>, Ar, and CO. The present doctoral thesis presents the results of developing an EOS for CCS-relevant mixtures that extends the EOS-CG mixture model to additional components and also improves some existing models based on new data that recently became available. The new components include Cl<sub>2</sub> and monoethanolamine (MEA) that were so far not described by an accurate pure-fluid EOS. Additional Helmholtz-energy explicit EOS for these pure fluids were therefore developed in this work. The results of these developments and of the complete CCS-mixture model are discussed in Secs. 5.2, 5.3, and 6.



### 3 Equations of State - A Brief Introduction

Because the aim of this work is the development of thermodynamic equations of state (EOS) for pure fluids and fluid mixtures, a brief introduction into this subject is essential for the comprehension of the present doctoral thesis.

EOS are commonly classified into thermal and fundamental formulations. Thermal EOS describe the relation between the three thermal properties pressure  $p$ , molar or specific volume  $v$  (or density  $\rho$ ), and temperature  $T$ . Over the centuries, a variety of different approaches for thermal EOS was developed and published in the literature. Cubic EOS represent the most prominent group of thermal EOS. This type of EOS is briefly discussed in Sec. 3.1 with a focus on the Soave-Redlich-Kwong equation of Soave,<sup>18</sup> which was used to calculate comparative results for various binary mixtures considered in this work. Another thermal EOS relevant to this work is the Lee-Kesler-Plöcker EOS of Plöcker *et al.*,<sup>19</sup> which is introduced in Sec. 3.2. Although they are still widely used, thermal EOS have lost relevance for formulations with reference quality. The main reason for this is that the calculation of caloric (energy related) properties from thermal EOS requires additional correlations for the properties of the ideal-gas state and furthermore potentially complex integrations. This problem significantly increases the computing time in both fitting and employing these formulations. Besides, many thermal (in particular cubic) EOS provide quite reliable results for phase-equilibria but do not represent accurate homogeneous densities or other data for homogeneous state properties within their experimental uncertainties. Especially in the liquid phase, calculated values might deviate considerably from experimental results.

Fundamental EOS are explicitly formulated in a caloric property such as the internal energy  $u$ , enthalpy  $h$ , Helmholtz energy  $a$ , or Gibbs Energy  $g$ . This functional form allows for the calculation of all thermal and caloric properties through combinations of partial derivatives. Conversely, it is also possible to use all types of thermodynamic property data to fit these equations. Most state-of-the-art reference EOS are written in terms of the Helmholtz energy. This approach was also adopted for the EOS developed within this work. The mathematical structure of these equations is explained in detail in Sec. 3.3.

A particular challenge in the development of Helmholtz-energy explicit EOS for mixtures is posed by the poor data situation for many of these systems. Fitting the adjustable parameters of this type of EOS requires a certain amount of reliable experimental or molecular-simulation data. If no or no reliable data are available, combining rules still allow for the calculation of results, but the predictive potential of these rules is limited. Section 3.4

provides a short conceptual introduction into more “predictive” approaches of EOS that were of some interest during the work on the present thesis.

### 3.1 Cubic Equations of State

Due to their large range of validity and their comparably simple mathematical structure, cubic EOS are widely used in technical applications. Over the years, a variety of cubic functions were proposed in order to improve the representation of experimentally obtained thermophysical property data; however, all these approaches are in principle modifications of the well-known functional form introduced by van der Waals in 1873.<sup>20</sup> This functional form reads

$$p = \frac{RT}{v-b} - \frac{a}{v^2}, \quad (3.1)$$

with  $R$  being the universal gas constant. The van der Waals equation itself is a modification of the ideal-gas equation, which is the simplest model for the description of pure gases and gaseous mixtures. The ideal-gas equation is based on the assumption that the gas molecules have no volume and that the thermodynamic behavior is not influenced by interactions between molecules. van der Waals corrected these two assumptions by introducing the parameter  $b$  taking into account the volume of the molecules and the additional parameter  $a$  that considers attractive forces between molecules. For the first time, this modification allowed the whole fluid surface including the gas phase, liquid phase, and supercritical states to be described with one single EOS.

The van der Waals equation was the starting point for the development of many other cubic EOS available in the literature. One of the most famous enhancements is the EOS of Redlich and Kwong<sup>21</sup> that was further modified by Soave.<sup>18</sup> The Soave-Redlich-Kwong, or in short “SRK”, EOS reads:

$$p = \frac{RT}{v-b} - \frac{a(T)}{v(v+b)}. \quad (3.2)$$

Compared to the basic functional form of van der Waals, one of the most significant modifications is the introduction of a temperature dependency in the interaction parameter  $a$ . Considering a mixture of  $N$  fluid components, the full expression for  $a(T)$  is

$$a(T) = \sum_{i=1}^{N-1} \sum_{j=i+1}^N x_i x_j \sqrt{a_i(T) a_j(T)} (1 - k_{ij}), \quad (3.3)$$

which corresponds to a quadratic mixing rule for the arithmetic mean values of the pure-fluid interaction parameters  $a_i$  extended by the binary interaction parameter  $k_{ij}$ . This interaction parameter is fitted to experimental data available for a binary mixture. The most



accurate description of a multi-component mixture is achieved by fitting  $k_{ij}$  values for every possible binary combination of the pure components. The standard value of  $k_{ij}$  without fitting it to experimental data is zero. Of course, the SRK EOS is also valid for pure fluids. In this case,  $k_{ij}$  and the mole fractions are meaningless ( $k_{ij} = 0$  and  $x_i = x_j = 1$ ), which leads to  $a(T) = a_i(T) = a_j(T)$ . The pure-fluid interaction parameters in Eq. (3.3) are calculated from

$$a_i(T) = a_{c,i} \alpha_i(T), \quad (3.4)$$

with the pure-fluid critical parameter  $a_{c,i}$  and the additional temperature-dependent correction term  $\alpha_i(T)$ . The pure-fluid critical parameter is given by:

$$a_{c,i} = 0.42747 \frac{R^2 T_{c,i}^2}{P_{c,i}}. \quad (3.5)$$

This definition is directly derived from the thermodynamic constraint that for every fluid the first and second derivative of the pressure with respect to volume at constant temperature is zero at the critical point defined by  $T_c$  and  $p_c$ . The temperature-dependent correction factor included in Eq. (3.4) enables the description of state points away from the critical point. It can be written as

$$\alpha_i(T) = \left[ 1 + m_i \left( 1 - \sqrt{\mathcal{G}_i} \right) \right]^2, \quad (3.6)$$

with the reduced temperature  $\mathcal{G}_i = T / T_{c,i}$  and the parameter  $m_i$ , which results from a quadratic function of the acentric factor of the pure fluid  $\omega_i$ . The acentric factor considers the deviation of the molecular geometry from a perfect sphere; thus, for noble gases, a good approximation of  $\omega_i$  is obtained by setting it to zero. For other substances,  $\omega_i$  can be derived from the reduced vapor pressure  $\pi_{\text{sat},i} = p_{\text{sat},i} / p_{c,i}$  calculated at  $T = 0.7 T_c$ . The corresponding calculation for the acentric factor reads:

$$\omega_i = -\log \left[ \pi_{\text{sat},i} \left( T = 0.7 T_{c,i} \right) \right] - 1. \quad (3.7)$$

Eqs. (3.3) to (3.7) allow for the calculation of the interaction parameter  $a(T)$ . The initial Eq. (3.2) additionally contains the volume parameter  $b$ . For a mixture of  $N$  components, this parameter is calculated from a linear combination of the pure-fluid volume parameters  $b_i$ :

$$b = \sum_{i=1}^N x_i b_i. \quad (3.8)$$

The pure-fluid volume parameters can be calculated from the critical-point constraints discussed before to yield

$$b_i = 0.08664 \frac{RT_{c,i}}{P_{c,i}}. \quad (3.9)$$

For the calculation of pure-fluid properties, the volume parameter according to Eq. (3.9) can directly be inserted in Eq. (3.2).

Within the scope of the present work, the SRK EOS was frequently used for comparative calculations of thermodynamic properties of CO<sub>2</sub>-rich mixtures as relevant to CCS applications. These calculations were carried out with the thermodynamic property software package TREND, which is continuously developed at RUB.<sup>22</sup> Because TREND was initially developed as a calculation tool for Helmholtz-energy explicit EOS as discussed in Sec. 3.3, the SRK approach was implemented into the framework for Helmholtz-energy explicit EOS. Therefore, the pressure-explicit functional form given in Eq. (3.2) is integrated to the Helmholtz energy. The Helmholtz-energy transformation of the SRK EOS and other common cubic EOS is described in detail by Bell and Jäger.<sup>23</sup> In principle, this approach also allows for a combination of cubic and Helmholtz-energy explicit EOS within calculations of multi-component-mixture properties; however, this procedure has not yet been extensively evaluated and might only partly yield reliable results.

### 3.2 Lee-Kesler-Plöcker Equation of State

Another widely used type of thermal EOS is based on a virial expansion of the compressibility factor  $Z$ . The compressibility factor quantifies the deviation of the real fluid behavior from the hypothetical ideal gas. The simplest form of the virial EOS reads

$$Z = \frac{\rho RT}{p} = 1 + B\rho + C\rho^2 + D\rho^3 + \dots, \quad (3.10)$$

with the molar density  $\rho$ , the second virial coefficient  $B$ , the third virial coefficient  $C$ , and the fourth virial coefficient  $D$ . Adding additional higher order virial coefficients increases the accuracy of the EOS; nevertheless, the expansion is frequently truncated after the third coefficient  $C$ . Various modifications of the virial expansion approach can be found in the literature. One of the most well-known modifications is the Benedict-Webb-Rubin EOS as introduced by Benedict *et al.*<sup>24</sup> It combines the virial expansion with an exponential correction term. That functional form was further modified by Lee and Kesler<sup>25</sup> and finally by Plöcker *et al.*<sup>19</sup> The Lee-Kesler-Plöcker or short “LKP“, EOS describes the compressibility factor by

$$Z = Z^o + \frac{\omega}{\omega_{\text{ref}}} (Z^{\text{ref}} - Z^o), \quad (3.11)$$

with the acentric factor of the investigated fluid  $\omega$  and the compressibility factor  $Z$  defined as

$$Z = \frac{\pi\psi}{\mathcal{G}} \quad (3.12)$$

including the reduced pressure  $\pi$ , the reduced volume  $\psi$ , and the reduced temperature  $\mathcal{G}$  according to

$$\pi = \frac{P}{P_r}, \quad \psi = \frac{P_r V}{RT_r}, \quad \text{and} \quad \mathcal{G} = \frac{T}{T_r}, \quad (3.13)$$

with the reducing temperature  $T_r$  and the reducing pressure  $p_r$ .

Eq. (3.11) includes the special compressibility factors  $Z^o$  and  $Z^{\text{ref}}$ . The first one represents the compressibility factor of a “simple fluid” (such as argon or methane) with an almost spherical molecule (acentric factor  $\omega^o = 0$ ), whereas  $Z^{\text{ref}}$  is the compressibility factor of a “reference fluid” (*n*-octane) with the acentric factor  $\omega^{\text{ref}}$ . Both compressibility factors are calculated at reduced state conditions according to the Benedict-Webb-Rubin EOS:

$$Z = 1 + \frac{B}{\psi} + \frac{C}{\psi^2} + \frac{D}{\psi^5} + \frac{c_4}{\mathcal{G}^3 \psi^2} \left( \beta + \frac{\gamma}{\psi^2} \right) \exp\left( -\frac{\gamma}{\psi^2} \right). \quad (3.14)$$

The virial coefficients are a function of temperature. They are defined as:

$$B = b_1 - \frac{b_2}{\mathcal{G}} - \frac{b_3}{\mathcal{G}^2} - \frac{b_4}{\mathcal{G}^3}, \quad (3.15)$$

$$C = c_1 - \frac{c_2}{\mathcal{G}} + \frac{c_3}{\mathcal{G}^3}, \quad (3.16)$$

$$D = d_1 + \frac{d_2}{\mathcal{G}}. \quad (3.17)$$

The parameters  $\beta$ ,  $\gamma$ ,  $b_1$  to  $b_4$ ,  $c_1$  to  $c_4$ ,  $d_1$  and  $d_2$  used for the “simple fluid“ and the “reference fluid“ are listed in Table A.1 given in Appendix A of the present work. The values were applied for all calculations in this work and correspond to the ones presented in the original publication of Plöcker *et al.*<sup>19</sup>

The calculation of the reduced properties  $\pi$ ,  $\psi$ , and  $\mathcal{G}$  is straightforward for pure fluids because the critical-point parameters  $p_{c,i}$  and  $T_{c,i}$  are used as the reducing temperature  $T_r$  and the reducing pressure  $p_r$ . For mixtures, pseudo-critical parameters are obtained from combining rules for the critical parameters of the pure components. The pseudo-critical temperature of a mixture with  $N$  components is defined as:

$$T_{c,\text{mix}} = \frac{1}{v_{c,\text{mix}}^\eta} \sum_{i=1}^{N-1} \sum_{j=i+1}^N x_i x_j v_{c,ij}^\eta T_{c,ij}. \quad (3.18)$$

The equation contains, among other quantities, the pseudo-critical volume  $v_{c,\text{mix}}$  of the mixtures, which is calculated from the simple quadratic combining rule

$$v_{c,\text{mix}} = \sum_{i=1}^{N-1} \sum_{j=i+1}^N x_i x_j v_{c,ij}, \quad (3.19)$$

with the binary pseudo-critical volume  $v_{c,ij}$  according to:

$$v_{c,ij} = \frac{1}{8} \left( v_{c,i}^{1/3} + v_{c,j}^{1/3} \right)^3. \quad (3.20)$$

Because for many pure fluids the critical molar volume (or density) is not accurately known, it is determined from the critical temperature and pressure and the acentric factor:

$$v_{c,i} = \left( 0.2905 - 0.085\omega_i \right) \frac{RT_{c,i}}{P_{c,i}}. \quad (3.21)$$

The calculation of the pseudo-critical temperature according to Eq. (3.18) also requires the binary pseudo-critical temperature  $T_{c,ij}$ , which is defined as

$$T_{c,ij} = k_{ij} \left( T_{c,i} \cdot T_{c,j} \right)^{1/2}, \quad (3.22)$$

which includes the binary interaction parameter  $k_{ij}$ . As discussed for the SRK EOS in Sec. 3.1, this parameter can be fitted to experimental data in order to improve the accuracy of the EOS. The standard value is applied by setting  $k_{ij}$  to unity.

The last missing quantity in Eq. (3.18) is the exponent  $\eta$ , which is, in principle, an adjustable parameter; however, in this work the standard value  $\eta = 0.25$  as given by *Plöcker et al.*<sup>19</sup> was used.

Following the calculation steps specified in Eqs. (3.18) to (3.22) yields the pseudo-critical temperature of the mixture, which is needed to calculate the reduced temperature  $\vartheta$ . In order to calculate the reduced pressure  $\pi$ , the pseudo-critical pressure of the mixture is needed. This pseudo-critical pressure is calculated analogously to Eq. (3.21)

$$P_{c,\text{mix}} = \left( 0.2905 - 0.085\omega_{\text{mix}} \right) \frac{RT_{c,\text{mix}}}{v_{c,\text{mix}}}, \quad (3.23)$$

with the acentric factor of the mixture  $\omega_{\text{mix}}$  according the simple linear combining rule

$$\omega_{\text{mix}} = \sum_{i=1}^N x_i \omega_i. \quad (3.24)$$

For mixture calculations, this acentric factor  $\omega_{\text{mix}}$  also needs to be used as the acentric factor in Eq. (3.11) ( $\omega = \omega_{\text{mix}}$ ).

Like the SRK EOS (see Sec. 3.1), the LKP EOS was used in this work to calculate comparative results for CO<sub>2</sub>-rich mixtures. The implementation of the LKP into the software package TREND<sup>22</sup> was carried out within the scope of this work. As explained before, it is feasible to implement additional models into the Helmholtz-energy framework of the

TREND algorithms. Transforming the LKP EOS to a Helmholtz-energy explicit functional form requires some mathematical steps, that are briefly described within this section. The residual part of the reduced Helmholtz energy, which is discussed in more detail in Sec. 3.3, can be linked with the compressibility factor described in the LKP approach. According to Span,<sup>26</sup> this link is made through

$$Z = 1 + \delta \frac{\partial \alpha^r}{\partial \delta}, \quad (3.25)$$

with the reduced density

$$\delta = \frac{1}{\psi}. \quad (3.26)$$

Integrating Eq. (3.25) leads to the residual part of the reduced Helmholtz energy:

$$\alpha^r = \int_0^\delta \frac{1}{\delta} (Z-1) d\delta. \quad (3.27)$$

Inserting the compressibility factor according to Eq. (3.14) and solving the integral by substitution and partial integration yields

$$\begin{aligned} \alpha^r = & \frac{B}{Z_c} \delta + \frac{1}{2} \frac{C}{Z_c^2} \delta^2 + \frac{1}{5} \frac{D}{Z_c^5} \delta^5 \\ & - \frac{c_4 \tau^3}{2\gamma} \left( \frac{\gamma}{Z_c^2} \delta^2 + \beta + 1 \right) \exp\left( -\frac{\gamma}{Z_c^2} \delta^2 \right) + \frac{c_4 \tau^3}{2\gamma} (\beta + 1), \end{aligned} \quad (3.28)$$

with the reciprocal reduced temperature

$$\tau = \frac{1}{g} \quad (3.29)$$

and the (pseudo-)critical compressibility factor

$$Z_c = \frac{P_c v_c}{RT_c} \text{ (for pure fluids) or } Z_c = Z_{c,\text{mix}} = \frac{P_{c,\text{mix}} v_{c,\text{mix}}}{RT_{c,\text{mix}}} \text{ (for mixtures)}. \quad (3.30)$$

Following the LKP approach,  $\alpha^r$  needs to be calculated from Eq. (3.28) for the “simple fluid” and the “reference fluid”. The complete residual part of the reduced Helmholtz energy consequently reads:

$$\alpha^r = \left( 1 - \frac{\omega}{\omega_{\text{ref}}} \right) \alpha^{r,o} + \frac{\omega}{\omega_{\text{ref}}} \alpha^{r,\text{ref}}. \quad (3.31)$$

Various thermodynamic properties can be calculated through derivatives of Eq. (3.31). The connections between different properties and the derivatives of the reduced Helmholtz

energy is briefly shown in Sec. 3.3. Relevant derivatives of Eq. (3.31) are given in Appendix A. As also shown in Sec. 3.3, the residual part of the reduced Helmholtz energy only allows calculating thermal properties. In order to calculate caloric properties, additional correlations for the ideal-gas state are needed. In TREND<sup>22</sup> simplified ideal-gas correlations taken from the “VDI Heat Atlas”<sup>27</sup> are combined with the implemented thermal EOS such as LKP or SRK.

### 3.3 Multi-Parameter Helmholtz-Energy Equations of State

The functional form of the EOS developed within this work is written in terms of the Helmholtz energy. It is consequently a fundamental EOS, which allows for the calculation of all thermodynamic properties by combining derivatives of its functional form. This aspect is not only relevant to computing time, but also allows simultaneous fitting of the EOS to all types of experimental thermodynamic property data (see Sec. 4). Within the scope of this work, both pure-fluid EOS and EOS for mixtures (for simplicity’s sake also called “mixture models”) were developed. Explaining the structure of these EOS is easier when starting with the functional form for pure fluids.

In general, EOS explicit in the Helmholtz energy  $a$  can be formulated as:

$$a(T, \rho) = a^o(T, \rho) + a^r(T, \rho). \quad (3.32)$$

The independent variables temperature and molar density enable a clear description of the whole fluid surface, including the vapor-liquid equilibrium region. The function  $a^o$  describes the behavior of the hypothetical ideal gas, whereas  $a^r$  represents the residual Helmholtz energy that results from molecular interactions in the real fluid. Because it is more convenient to work with dimensionless equations, density and temperature are reduced, which leads to the dimensionless function

$$\alpha(\tau, \delta) = \frac{a(T, \rho)}{RT} = \frac{a^o(T, \rho) + a^r(T, \rho)}{RT} = \alpha^o(\tau, \delta) + \alpha^r(\tau, \delta), \quad (3.33)$$

where  $\alpha$  is the reduced Helmholtz energy and  $R$  is the universal gas constant. The reciprocal reduced temperature  $\tau$  and the reduced density  $\delta$  are defined as

$$\delta = \frac{\rho}{\rho_c} \quad \text{and} \quad \tau = \frac{T_c}{T}, \quad (3.34)$$

with the critical-point parameters used as the reducing density and reducing temperature.

The ideal-gas part of the reduced Helmholtz energy can be written as

$$\alpha^{\circ}(\tau, \delta) = \frac{a^{\circ}(T, \rho)}{RT} = \frac{h_0^{\circ}}{RT} - \frac{s_0^{\circ}}{R} - 1 + \ln \frac{\delta \tau_0}{\delta_0 \tau} - \frac{\tau}{R} \int_{\tau_0}^{\tau} \frac{c_p^{\circ}}{\tau^2} d\tau + \frac{1}{R} \int_{\tau_0}^{\tau} \frac{c_p^{\circ}}{\tau} d\tau, \quad (3.35)$$

where  $c_p^{\circ}$  is the isobaric heat capacity of the ideal gas and  $\tau_0$  and  $\delta_0$  are the reduced reciprocal temperature and reduced density at any arbitrary reference state defined by  $T_0$  and  $\rho_0$ . With regard to Eq. (3.35), it is apparent that a correlation for the isobaric ideal-gas heat capacity  $c_p^{\circ}$  is necessary to calculate the ideal-gas part of the reduced Helmholtz energy. The functional form used for the pure-fluid EOS developed in this work is

$$\frac{c_p^{\circ}(T)}{R} = c_0 + \sum_{k=1}^{K_{PE}} v_k \left( \frac{u_k}{T} \right)^2 \frac{\exp(u_k/T)}{[\exp(u_k/T) - 1]^2}, \quad (3.36)$$

with the constant  $c_0$  and an arbitrary number of adjustable coefficients  $v_k$  and exponents  $u_k$ . The value of  $c_0$  is physically meaningful because it corresponds to the internal-energy contributions of translational and rotational motions of the molecule at low temperatures. This aspect can be explained by the example of heavy water ( $D_2O$ ), for which a pure-fluid EOS was developed within this work.  $D_2O$  is a nonlinear triatomic molecule. It has consequently three translational and three rotational degrees of freedom, leading to a total of six degrees of freedom, and thus to the isochoric ideal-gas heat capacity  $c_v^{\circ} = 6/2 R$ . Because Eq. (3.36) is formulated in the isobaric heat capacity, this leads to the constant  $c_0 = (c_v^{\circ} + R)/R = 8/2 = 4$ . Considering the example of pure chlorine ( $Cl_2$ ), the constant is  $c_0 = (5/2 R + R)/R = 3.5$  because  $Cl_2$  is a linear molecular with three translational and two rotational degrees of freedom. As temperature increases, thermal energy additionally contributes to vibrational excitations that yield an increase of  $c_p^{\circ}$ . In Eq. (3.36) this temperature dependency is represented by the so-called ‘‘Planck-Einstein terms’’. Because this approach is empirical and only loosely based on physical considerations, the individual terms do not represent contributions of specific vibrational frequencies. The number of Planck-Einstein terms  $K_{PE}$  used to describe the ideal-gas state is chosen by the correlator. The adjustable coefficients  $v_k$  and exponents  $u_k$  are mainly fitted to ideal-gas heat capacity data obtained by statistical mechanics, extrapolations of heat-capacity or speed-of-sound data, or spectroscopic measurements. However, since the ideal-gas part contributes to all caloric properties calculated from the EOS, it is simultaneously fitted with the residual part to additional data for example for speed of sound and heat capacity of the real fluid. Combining Eq. (3.35) and Eq. (3.36) yields the ideal-gas part of the EOS in a more convenient functional form:

$$\alpha^o(\tau, \delta) = a_1 + a_2 \tau + \ln \delta + (c_0 - 1) \ln \tau + \sum_{k=1}^{K_{PE}} v_k \ln [1 - \exp(-u_k \tau / T_c)]. \quad (3.37)$$

The two integration constants  $a_1$  and  $a_2$  define the values of caloric properties at the chosen reference state of the EOS. For example, the normal boiling point is used as the reference state for many pure-fluid. The constants  $a_1$  and  $a_2$  are then adjusted to yield zero enthalpy and entropy for the saturated liquid at the normal boiling point.

The residual part of the reduced Helmholtz energy included in Eq. (3.33) reads:

$$\begin{aligned} \alpha^r(\delta, \tau) = & \sum_{k=1}^{K_{pol}} n_k \delta^{d_k} \tau^{t_k} + \sum_{k=K_{pol}+1}^{K_{pol}+K_{exp}} n_k \delta^{d_k} \tau^{t_k} \exp(-\delta^{l_k}) \\ & + \sum_{k=K_{pol}+K_{exp}+1}^{K_{pol}+K_{exp}+K_{GBS}} n_k \delta^{d_k} \tau^{t_k} \exp \left[ -\eta_k (\delta - \varepsilon_k)^2 - \beta_k (\tau - \gamma_k)^2 \right] \\ & + \sum_{k=K_{pol}+K_{exp}+K_{GBS}+K_{NA}}^{K_{pol}+K_{exp}+K_{GBS}+K_{NA}} n_k \delta \Delta^{b_k} \psi, \end{aligned} \quad (3.38)$$

with

$$\begin{aligned} \Delta &= \theta^2 + B_k \left[ (\delta - 1)^2 \right]^{a_k}, \\ \theta &= (1 - \tau) + A_k \left[ (\delta - 1)^2 \right]^{1/(2\beta_k)}, \text{ and} \\ \psi &= \exp \left( -C_k (\delta - 1)^2 - D_k (\tau - 1)^2 \right). \end{aligned} \quad (3.39)$$

Eq. (3.38) includes different types of terms, namely polynomial(-like) terms (abbreviated as “pol”), exponential terms (“exp”), “Gaussian bell-shaped” terms (“GBS”), and so-called “non-analytic” terms (“NA”). Non-analytic terms were specifically developed for the description of “non-analytic” effects at the critical point (for example, the isochoric heat capacity approaches infinity and the speed of sound becomes zero). These terms are only used in the functional forms of the reference EOS for CO<sub>2</sub> of Span and Wagner<sup>28</sup> and ordinary water (H<sub>2</sub>O) of Wagner and Pruß.<sup>29</sup> Because they frequently lead to numerical problems, especially when applied in multi-component mixture models, they are not used anymore in the development of new pure-fluid EOS.

Omitting the non-analytic terms,  $\alpha^r$  of the pure fluid still contains quite a number of adjustable parameters, namely the coefficients  $n_k$ , temperature exponents  $t_k$ , density exponents  $d_k$  and  $l_k$ , and the parameters of the Gaussian bell-shaped terms  $\eta_k$ ,  $\varepsilon_k$ ,  $\beta_k$ , and  $\gamma_k$ . The optimal number of each type of terms and thus the total number of terms is chosen by the correlator while fitting the EOS to the available experimental or molecular-simulation data.



Most modern reference EOS for pure-fluids were developed with the same basic mathematical structure as presented in Eqs. (3.33) to (3.38). Excellent examples, which were also developed with a comparably short and thus numerically stable functional form, are the EOS for R-125 of Lemmon and Jacobsen,<sup>30</sup> for propane of Lemmon *et al.*,<sup>31</sup> for R-1234ze(E) of Thol and Lemmon,<sup>32</sup> and for sulfur dioxide of Gao *et al.*<sup>33</sup>

For mixtures, the reduced Helmholtz-energy explicit functional form used in this work was proposed by Lemmon and Tillner-Roth.<sup>34</sup> Its mathematical structure was further modified in the development of the GERG-2008 model for natural gases and similar mixtures introduced by Kunz *et al.* and Kunz and Wagner.<sup>35,36</sup> The general functional form is analogous to Eq. (3.33), but the description of mixtures requires the molar composition  $\bar{x}$  as additional independent variable:

$$\frac{a(\rho, T, \bar{x})}{RT} = \alpha(\delta, \tau, \bar{x}) = \alpha^o(\rho, T, \bar{x}) + \alpha^r(\delta, \tau, \bar{x}). \quad (3.40)$$

For pure fluids, temperature and densities are reduced with the critical-point parameters as shown in Eq. (3.34). For mixtures, this method is not feasible because the critical-point parameters are different for each component. Besides, the critical point of the mixture is, if existing, composition dependent and therefore quite complex to determine (see Bell and Jäger<sup>37</sup>). The reduced density  $\delta$ , and the reciprocal reduced temperature  $\tau$  are therefore calculated with composition-dependent “reducing functions”:

$$\delta = \frac{\rho}{\rho_r(\bar{x})} \quad \text{and} \quad \tau = \frac{T_r(\bar{x})}{T}. \quad (3.41)$$

The reducing functions for density  $\rho_r(\bar{x})$  and temperature  $T_r(\bar{x})$  introduced by Kunz *et al.*<sup>35</sup> span a composition-dependent surface between the critical density and temperature of each pure component in the mixture. The temperature function is given by:

$$T_r(\bar{x}) = \sum_{i=1}^N x_i^2 T_{c,i} + \sum_{i=1}^{N-1} \sum_{j=j+1}^N 2x_i x_j \beta_{T,ij} \gamma_{T,ij} \frac{x_i + x_j}{\beta_{T,ij}^2 x_i + x_j} (T_{c,i} T_{c,j})^{0.5}, \quad (3.42)$$

with  $N$  being the total of components in the mixture. The density function reads:

$$\frac{1}{\rho_r(\bar{x})} = \sum_{i=1}^N x_i^2 \frac{1}{\rho_{c,i}} + \sum_{i=1}^{N-1} \sum_{j=j+1}^N 2x_i x_j \beta_{v,ij} \gamma_{v,ij} \frac{x_i + x_j}{\beta_{v,ij}^2 x_i + x_j} \frac{1}{8} \left( \frac{1}{\rho_{c,i}^{1/3}} + \frac{1}{\rho_{c,j}^{1/3}} \right)^3. \quad (3.43)$$

These two reducing functions contain the binary parameters  $\beta$  and  $\gamma$ , which are adjustable parameters that, if possible, are fitted to experimental or molecular simulation data. They obey the following symmetry rules

$$\beta_{T,ij} = \frac{1}{\beta_{T,ji}}, \quad \beta_{v,ij} = \frac{1}{\beta_{v,ji}} \quad \text{and} \quad \gamma_{T,ij} = \gamma_{T,ji}, \quad \gamma_{v,ij} = \gamma_{v,ji}. \quad (3.44)$$

If scarce or no reliable data are available, the binary parameters can be set to standard values that yield simple combining rules for the reducing functions for temperature and density. This approach is discussed in more detail in Sec. 4. The index “*ij*” indicates the basic concept of the mixture model: the description of multi-component mixtures is enabled by modelling each binary combination of the components.

Analogous to the functional form of pure-fluid EOS, Eq. (3.40) consists of an ideal and a residual part of the reduced Helmholtz energy. The ideal part is given by

$$\alpha^o(\rho, T, \bar{x}) = \sum_{i=1}^N x_i \left[ \alpha_i^o(\delta_i, \tau_i) + \ln x_i \right], \quad (3.45)$$

where  $\alpha_i^o$  is the ideal-gas part of the reduced Helmholtz energy of component *i* with the mole fraction  $x_i$  in the mixture. The reduced ideal-gas Helmholtz energy of each component is calculated from the corresponding pure-fluid EOS according to Eq. (3.37) at the reduced density  $\delta_i$  and reciprocal reduced temperature  $\tau_i$ . In the ideal-gas part, this reduction is done through Eq. (3.34).

The residual part of the Helmholtz energy of the mixture reads

$$\alpha^r(\rho, T, \bar{x}) = \sum_{i=1}^N x_i \alpha_i^r(\delta, \tau) + \Delta\alpha^r(\delta, \tau, \bar{x}), \quad (3.46)$$

where  $\alpha_i^r$  is the reduced residual Helmholtz energy of the component *i* as specified by Eq. (3.38). In this case, the residual part is evaluated at  $\delta$  and  $\tau$  according to Eq. (3.41). Eq. (3.46) additionally contains the function  $\Delta\alpha^r(\delta, \tau, \bar{x})$ , which models the deviation of the real mixing behavior from the simple linear combination of the reduced residual Helmholtz energies of the pure components. This so-called “departure function” can be written as:

$$\Delta\alpha^r(\delta, \tau, \bar{x}) = \sum_{i=1}^{N-1} \sum_{j=i+1}^N x_i x_j F_{ij} \alpha_{ij}^r(\delta, \tau). \quad (3.47)$$

The departure function includes the “binary specific departure function”  $\alpha_{ij}^r(\delta, \tau)$  for the binary mixture of the components *i* and *j* and the weighting factor  $F_{ij}$ . This weighting factor enables the use of “generalized binary departure functions” for a group of chemically similar binary systems.<sup>30</sup> If a departure function specific for a binary mixture is developed,  $F_{ij}$  is set to unity. The mathematical structure of the binary departure function can contain polynomial(-like) terms, exponential terms, so-called “special” exponential terms (abbreviated as “spec”), and Gaussian bell-shaped terms. The functional form including all possible types of terms can be written as:

$$\begin{aligned}
\alpha_{ij}^r(\delta, \tau) = & \sum_{k=1}^{K_{\text{pol},ij}} n_{ij,k} \delta^{d_{ij,k}} \tau^{t_{ij,k}} + \sum_{k=K_{\text{pol},ij}+1}^{K_{\text{pol},ij}+K_{\text{exp},ij}} n_{ij,k} \delta^{d_{ij,k}} \tau^{t_{ij,k}} \exp(-\delta^{t_{ij,k}}) \\
& + \sum_{k=K_{\text{pol},ij}+K_{\text{exp},ij}+1}^{K_{\text{pol},ij}+K_{\text{exp},ij}+K_{\text{spec},ij}} n_{ij,k} \delta^{d_{ij,k}} \tau^{t_{ij,k}} \exp\left[-\eta_{ij,k}(\delta - \varepsilon_{ij,k})^2 - \beta_{ij,k}(\delta - \gamma_{ij,k})\right] \\
& + \sum_{k=K_{\text{pol},ij}+K_{\text{exp},ij}+K_{\text{spec},ij}+K_{\text{GBS},ij}}^{K_{\text{pol},ij}+K_{\text{exp},ij}+K_{\text{spec},ij}+K_{\text{GBS},ij}} n_{ij,k} \delta^{d_{ij,k}} \tau^{t_{ij,k}} \exp\left[-\eta_{ij,k}(\delta - \varepsilon_{ij,k})^2 - \beta_{ij,k}(\tau - \gamma_{ij,k})^2\right].
\end{aligned} \tag{3.48}$$

The selection of term types and of their quantity are chosen by the correlator while fitting the EOS to thermodynamic property data of this specific binary mixture. The “special” exponential terms are widely used in the GERG-2008 model for natural gases and similar mixtures but also for some binary mixtures in the EOS-CG model for CO<sub>2</sub>-rich mixtures of Gernert and Span.<sup>2</sup> Using Gaussian bell-shaped terms not only for pure-fluid EOS but also in mixture models is a comparably new approach, which was recently introduced by Bell *et al.*<sup>38</sup> for the binary mixture of ammonia and water.

With regard to Eqs. (3.40) to (3.48), it should become apparent that the mixture model contains not only three mixture-related terms ( $\rho_r(\bar{x})$ ,  $T_r(\bar{x})$ , and  $\alpha_{ij}^r$ ) but also the quantities  $\alpha_i^o$  and  $\alpha_i^r$  of the pure components. From this it follows that for each component considered in the mixture model, an EOS describing the pure fluid states is mandatory.

The procedure of selecting appropriate terms for EOS for pure fluids and mixtures as well as fitting the adjustable parameters is too complex to be described within this section. A brief introduction into fitting Helmholtz-energy explicit EOS as it was done within the scope of this work is given in Sec. 4.

As mentioned before, the Helmholtz-explicit approach for pure fluids and mixtures allows for the calculation of all thermodynamic properties by combining derivatives of its functional form. Relations between the reduced Helmholtz energy and selected thermodynamic properties relevant to the present work are given in Table 3.1. More details and definitions of additional properties can be found in the works of Span<sup>26</sup> and Kunz *et al.*<sup>35</sup>

With regard to the mathematical complexity of the different types of terms used to describe the reduced Helmholtz energy, it is not surprising that obtaining the required derivatives listed in Table 3.1 is too complex and time consuming to be individually handled by typical users. Besides, a consistent description of the thermodynamic behavior requires various iterations as well as stability-analysis and phase-equilibrium algorithms. Straightforward calculations for less experienced users are enabled in thermodynamic property software packages such as TREND,<sup>22</sup> the REFPROP program developed at NIST,<sup>39</sup> and the open source software CoolProp.<sup>40</sup>

**Table 3.1** Selected thermodynamic properties and their relation to the reduced Helmholtz energy  $\alpha$  and its derivatives. The index  $\delta$  indicates the partial derivative of  $\alpha$  with respect to  $\delta$  at constant  $\tau$  and composition  $\bar{x}$  (as relevant to mixture calculations). The index  $\tau$  indicates the partial derivative of  $\alpha$  with respect to  $\tau$  at constant  $\delta$  and  $\bar{x}$ .

Property	Definition	Relation to the reduced Helmholtz energy $\alpha$ and its derivatives
Pressure	$p = -\left(\frac{\partial \alpha}{\partial v}\right)_{T, \bar{x}}$	$p = \rho RT(1 + \delta\alpha_{\delta}^r)$
Compressibility factor	$Z = p / (\rho RT)$	$Z = (1 + \delta\alpha_{\delta}^r)$
Entropy	$s = -\left(\frac{\partial \alpha}{\partial T}\right)_{v, \bar{x}}$	$s = R(\tau\alpha_{\tau}^o + \tau\alpha_{\tau}^r - \alpha^o - \alpha^r)$
Gibbs energy	$g = h - Ts$	$g = RT(1 + \alpha^o + \alpha^r + \delta\alpha_{\delta}^r)$
Enthalpy	$h = u + pv$	$h = RT(1 + \tau\alpha_{\tau}^o + \tau\alpha_{\tau}^r + \delta\alpha_{\delta}^r)$
Internal energy	$u = a + Ts$	$u = RT(\tau\alpha_{\tau}^o + \tau\alpha_{\tau}^r)$
Isochoric heat capacity	$c_v = \left(\frac{\partial u}{\partial T}\right)_{v, \bar{x}}$	$c_v = -R(\tau^2\alpha_{\tau\tau}^o + \tau^2\alpha_{\tau\tau}^r)$
Isobaric heat capacity	$c_p = \left(\frac{\partial h}{\partial T}\right)_{p, \bar{x}}$	$c_p = -R\left[\left(\tau^2\alpha_{\tau\tau}^o + \tau^2\alpha_{\tau\tau}^r\right) + \frac{\left(1 + \delta\alpha_{\delta}^r - \delta\tau\alpha_{\delta\tau}^r\right)^2}{1 + 2\delta\alpha_{\delta}^r + \delta^2\alpha_{\delta\delta}^r}\right]$
Speed of sound	$w = \sqrt{\frac{1}{M}\left(\frac{\partial p}{\partial \rho}\right)_{s, \bar{x}}}$	$w^2 = \frac{RT}{M}\left[1 + 2\delta\alpha_{\delta}^r + \delta^2\alpha_{\delta\delta}^r - \frac{\left(1 + \delta\alpha_{\delta}^r - \delta\tau\alpha_{\delta\tau}^r\right)^2}{\tau^2\alpha_{\tau\tau}^o + \tau^2\alpha_{\tau\tau}^r}\right]$
Second virial coefficient	$B = \lim_{\rho \rightarrow 0} \left(\frac{\partial Z}{\partial \rho}\right)_{T, \bar{x}}$	$B\rho_r = \lim_{\rho \rightarrow 0} \alpha_{\delta}^r$
Third virial coefficient	$C = \frac{1}{2} \lim_{\rho \rightarrow 0} \left(\frac{\partial^2 Z}{\partial \rho^2}\right)_{T, \bar{x}}$	$C\rho_r^2 = \lim_{\rho \rightarrow 0} \alpha_{\delta\delta}^r$

### 3.4 “Predictive” Equations of State

As mentioned before, the development of Helmholtz-explicit EOS for mixtures as introduced in the previous section is challenging, if scarce or no reliable experimental or molecular-simulation data are available to fit the adjustable parameters. This problem is not only relevant to Helmholtz-explicit EOS; other approaches such as SRK or LKP also yield the most reliable results if a binary interaction parameter was fitted to accurate data. The development of less empirical and more “physically based” EOS is consequently the focus of many scientific works.

A widely used approach is the “Predictive Soave-Redlich-Kwong” EOS of Holderbaum and Gmehling.<sup>41</sup> As evident from its name, this EOS is a modification of the SRK EOS of Soave<sup>18</sup> introduced in Sec. 3.1. The main modification concerns the interaction parameter  $a$ . Instead of calculating  $a$  from combining rules and critical-point constraints (see Eqs. (3.3) to (3.7)), the parameter is obtained from a correlation that includes the excess Gibbs energy

$g^E$  described by the UNIFAC method of Fredenslund *et al.*<sup>42</sup> The basic idea of this method is to split molecules into functional groups that interact with other functional groups present in a mixture; a mixture of groups rather than a mixture of molecules. Following this approach allows for the description of a mixture that is not experimentally investigated as long as the interactions between the present functional groups can be quantified. This restriction highlights that the PSRK EOS is only to a certain extent “physically based”. The accurate description of a mixture still requires UNIFAC interaction parameters to be fitted for every binary combination of the relevant functional groups. Fitting these parameters, again, requires experimental data. Nevertheless, it should be noted that this fitting process is not restricted to experimental information on one binary mixture. Instead, the interaction parameters can be fitted to experimental data for various different mixtures containing the specific binary combination of functional groups.

Another concept of describing the thermodynamic properties of a fluid by modelling intermolecular forces is the “Statistical Associating Fluid Theory”, or in short “SAFT”, originally published by Chapman *et al.*<sup>43</sup> in 1989. Within the SAFT approach, the complex shape of molecules is modelled through a chain of single spherical segments. The EOS is explicit in the Helmholtz energy, containing an ideal part and a residual part that is described through three physical contributions: repulsive dispersion of the spherical segments, the formation of chains, and association interactions such as hydrogen bonding. The SAFT approach was modified by many authors. One of the most well-known modifications is the “Perturbated-Chain Statistical Associating Fluid Theory”, or in short “PC-SAFT”, by Gross and Sadowski<sup>44</sup> that considers dispersive forces as a perturbation to a chain of spherical segments. The concept of adding perturbation terms was further pursued by Gross<sup>45</sup> and Gross and Vrabec,<sup>46</sup> who presented the “PCP-SAFT” EOS that also allows for the description of dipolar or quadrupolar substances. For the description of mixtures, the perturbation theory applied uses an average radial distribution function with van der Waals one-fluid mixing rules. The calculation of thermodynamic properties from PC(P)-SAFT is not described here, but can be found in the original publications as well as in the Ph.D. thesis of Eckermann,<sup>47</sup> who implemented this type of EOS into the software package TREND.<sup>22</sup> With regard to the description of experimentally less investigated mixtures, it should be noted that although PC(P)-SAFT describes the fluid behavior from a molecular perspective, it still includes an interaction parameter that is meant to be fitted to experimental data for a binary mixture. The predictive potential of this approach is consequently limited.



## 4 Fitting Helmholtz-Energy Equations of State

The basic procedure of fitting Helmholtz-energy explicit EOS is the same for pure fluids and mixtures. Nevertheless, there are considerable differences, which is obvious with regard to the different adjustable parameters of the functional form for pure fluids and mixtures (see. 3.3). The following introduction to fitting Helmholtz-energy EOS starts with some general explanations. The procedure is then discussed for pure fluids, before the development of mixture EOS is described.

The essence of the fitting procedure can be described quite simply: The adjustable parameters of the functional form are varied by a fitting algorithm to reach the best agreement between the input data and properties calculated from the EOS. The fitting algorithm used in this work was originally developed by Lemmon and Jacobsen<sup>30</sup> and is continuously improved at NIST, Boulder. It is based on so-called “nonlinear fitting methods” that enable a simultaneous optimization of all parameters to different types of data. Additionally, it is possible to apply thermodynamic constraints to ensure that all properties behave correctly and extrapolate well even in regions beyond the data available. The EOS is fitted to a carefully chosen selection of points from the most accurate and consistent data sets. Each selected data point and constraint is weighted individually depending on type, pressure and temperature region, target accuracy, and, if reliable information is available, experimental uncertainty. Deviations of the calculated properties from the weighted data points and constraints contribute to an overall sum of squares ( $SSQ$ ) that is minimized by varying the adjustable parameters of the EOS. Very simplified, this  $SSQ$  can be written as:

$$SSQ = \sum_i W_{X,i} F_{X,i}^2 + \sum_i W_{con,i} F_{con,i}^2, \quad (4.1)$$

where  $F_X$  is the relative deviation of a data point for an arbitrary property  $X$  from the corresponding value calculated from the EOS multiplied with the applied weight  $W_X$ . This relative deviation is defined as:

$$F_X = \frac{\Delta X}{X} = \left( \frac{X_{exp} - X_{calc}}{X_{exp}} \right). \quad (4.2)$$

The deviation of the EOS from a thermodynamic constraint denoted by  $F_{con}$  is more complex to define. For example, a possible constraint imposes the curvature of a specified isotherm in a  $p, \rho$  diagram to be negative over a given density range. The agreement with this constraint is tested with a specified step size. Every violation (positive curvature) adds an increment to the value of  $F_{con}$ , which is multiplied with the applied weight  $W_{con}$  and then added to the  $SSQ$ . The mathematical calculation of the deviation  $F_{con}$  is not discussed here, but can, for

example, be found in the work of Gernert,<sup>17</sup> which provides some statistical insights into the fitting algorithm.

As explained in Sec. 3.3, developing pure-fluid EOS requires fitting equations for the ideal-gas part and the residual part of the reduced Helmholtz energy. Compared to the residual part, the mathematical structure of the ideal-gas part is relatively simple; thus, the correlation is quite quickly fitted to the available ideal-gas isobaric heat capacity data (see again Sec. 3.3). Because the residual part is much more complex and fitted to the significantly more comprehensive database of the real fluid, most of the time required to fit a pure-fluid EOS is spent on the development of the residual part. The number of each type of term in the residual part according to Eq. (3.38) is not varied by the fitting algorithm. The correlator has to find the optimum number and combination of terms to obtain a good fit. The number of terms should be as small as possible but as large as necessary. Equations with a large number of terms are very flexible and allow the correlator to find special terms to describe particular areas with high accuracy, but the extrapolation behavior of these equations can be unmanageable due to the many mathematical degrees of freedom. In contrast, short equations can be shaped more easily to extrapolate well and to exhibit smooth derivative behavior. It can be difficult to find a solution that covers the whole fluid region and yields a good compromise among the representation of all different types of experimental data.

Among the three pure-fluid EOS developed in this work, the EOS for monoethanolamine is based on the “shortest” functional form. The residual part contains 14 terms with a total of 63 adjustable parameters. The longest functional form was used for the new reference EOS for heavy water, whose residual part consists of 24 terms with a total of 126 adjustable parameters. With regard to these numbers, it is apparent that during the fitting process the number of possible parameter sets is almost unmanageable. For this reason, some guidelines given by Lemmon and Jacobsen<sup>30</sup> were followed. The derivatives of the residual part of the equation must go to zero for small densities, because in that limit the fluid behaves like an ideal gas. Therefore, the density exponents  $d_k$  and  $l_k$  in Eq. (3.38) must be positive integers and are not adjusted in the fitting algorithm, but are defined by the correlator while choosing the optimal set of terms. Special restrictions are defined for the first polynomial(-like) term, which should have a density exponent of  $d_1 = 4$  and a corresponding temperature exponent of  $t_1 = 1$ . This ensures that the isotherms converge for high densities and do not cross or diverge. All other temperature exponents do not have to be integers but should be positive. Negative exponents might result in unreasonable extrapolation behavior at high temperatures. For low temperatures and in the vapor-liquid equilibrium region, the overall behavior of the equation is essentially defined by terms with high temperature exponents. In order to ensure proper behavior in these regions, the exponents  $t_k$  should be as small as possible. For heavy water, this poses a special challenge. As discussed in Sec. 5.1.5.2, at low temperatures, the slope of the second virial coefficient  $B$  with temperature is much steeper



for (heavy) water than for most other fluids. The correct representation of this behavior and of experimental data in the metastable subcooled-liquid region required some higher temperature exponents than are generally needed. Figure 4.1 shows that at low temperatures the derivative of the residual Helmholtz energy with respect to density  $\alpha_\delta^r$ , which in the zero-density limit yields the second virial coefficient  $B$  (see Table 3.1), is basically defined by the second exponential term of the EOS according to Eq. (5.3) (term  $k = 8$ ). The temperature exponent of this term is  $t_{D_2O,8} = 4.6$ . Thus, no unreasonably large exponent was needed to describe the special behavior of  $B$ . The highest temperature exponent is  $t_{D_2O,11} = 5.4644$ , which is still relatively low compared to older reference equations such as those for ordinary water,<sup>29</sup> carbon dioxide,<sup>28</sup> or nitrogen.<sup>48</sup> In those equations, the highest temperature exponents range from 16 up to 50. However, the temperature exponents in the heavy water equation are still relatively high in comparison to those used in the EOS for MEA ( $t_{MEA,9} = 3.0$ ) and chlorine ( $t_{Cl_2,8} = 3.2$ ).

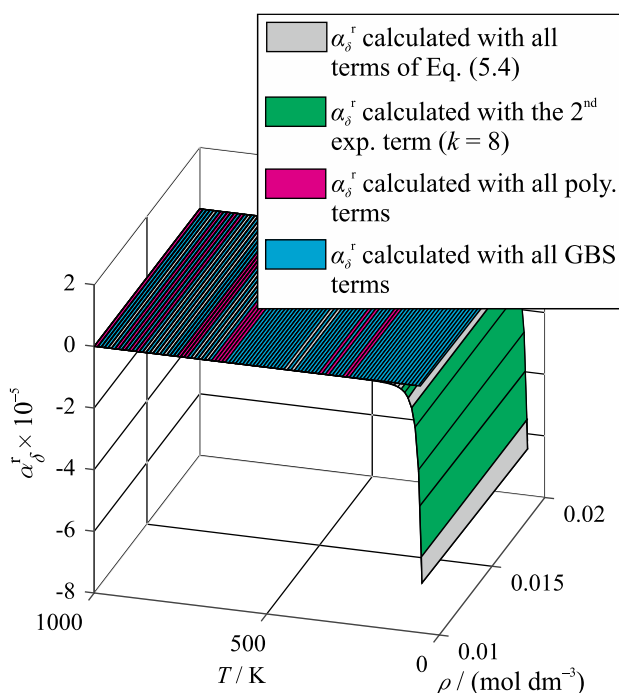


**Figure 4.1** First derivative of the residual Helmholtz energy for heavy water with respect to density as a function of temperature and density. The derivative is calculated with all terms of Eq. (5.3), the sum of all polynomial(-like) terms, the sum of all Gaussian bell-shaped terms, and only by means of the 2<sup>nd</sup> exponential term. The three-dimensional plot was generated with algorithms developed by Neumann.<sup>49</sup>

Another challenge of finding the optimal set of EOS parameters is posed by the description of the critical region. As discussed in Sec. 3.3, the reference equations for ordinary water<sup>29</sup> and carbon dioxide<sup>28</sup> contain so-called “non-analytical” terms that were particularly developed to model the special physical characteristics at the critical point. Since these terms are no longer used for the development of new EOS, the approximate description of the critical point is normally enabled by Gaussian bell-shaped terms. Some EOS contain one particular Gaussian bell-shaped term that has a strong contribution in the critical region, but

which has almost no impact on the description of the rest of the fluid surface. Examples for this functional form are the recently published EOS for hydrogen chloride of Thol *et al.*<sup>50</sup> and the EOS for propane by Lemmon *et al.*<sup>31</sup> For heavy water, two such terms (terms  $k = 23$  and  $k = 24$ ) were set up, with similar parameters but one positive and one negative coefficient. Consequently, these two terms cancel each other out over most of the stable fluid region except in the vicinity of the critical point, where they have a strong contribution. The impact of these terms on properties calculated near the critical point is visualized in Figure 4.2, where the residual part of the isochoric heat capacity is calculated first with all terms of Eq. (5.3) and then with all terms except for the two critical-region terms. Both resulting surfaces are plotted versus temperature and density. The steep increase of the isochoric heat capacity is exclusively modelled by the two Gaussian bell-shaped terms. However, as an analytic EOS, Eq. (5.3) is not capable of reproducing the nonclassical critical exponents that govern fluid behavior in the asymptotic limit of the critical point. The concept of two critical terms with one negative and one positive coefficient was recently successfully adopted in the new EOS for ammonia by Gao *et al.*,<sup>51</sup> which has not yet been published but which is already available in REFPROP.<sup>39</sup> The functional forms of the EOS for chlorine and MEA do not include terms exclusively contributing at the critical point. Both EOS enable the description of the critical region through the overall combination of the Gaussian bell-shaped terms. Besides, for both fluids, data in the critical region are scarce; thus, no strong terms are needed in order to describe the characteristic trends of critical region data.

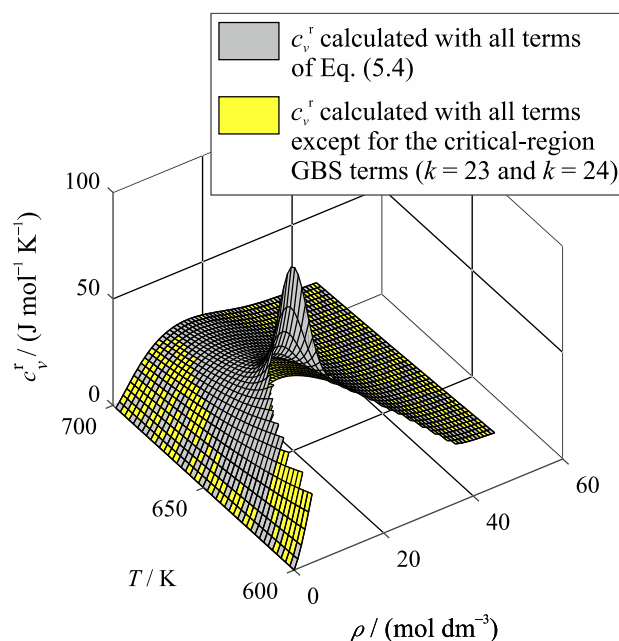


**Figure 4.2** Residual part of the isochoric heat capacity  $c_v^r$  of heavy water versus temperature and density. The heat capacity is first calculated with all terms of Eq. (5.3), and then with all terms except for the two Gaussian bell-shaped terms that specifically contribute in the critical region. For parts of the surface shown with yellow and gray interspersed, the differences between the two surfaces are essentially zero. The three-dimensional plot was generated with algorithms developed by Neumann.<sup>49</sup>

In general, Gaussian bell-shaped terms can be used to describe not only the critical region but any region of the fluid surface. However, they need to be applied carefully, since they might lead to unreasonable results for derivatives of the reduced Helmholtz energy and thus to wrong qualitative behavior of certain properties. For heavy water, Gaussian bell-shaped terms were also important to describe the anomalous behavior of the liquid at low temperatures, especially its density maximum.

While the fitting process for pure-fluid EOS is focused on two mathematical functions, the ideal-gas part and in particular the residual part of the Helmholtz energy, the mathematical structure of the multi-component mixture EOS allows for different types of fitting depending on the quantity and quality of the available data. As briefly mentioned in Sec. 3.3, the functional form of the EOS requires a description for every possible binary combination of the involved components. In the case of the presented model for CO<sub>2</sub>-rich mixtures, this means that it is not sufficient to model all binary mixtures of CO<sub>2</sub> plus the other relevant compounds but also all other binary combinations. For example, a mixture model containing the components CO<sub>2</sub>, N<sub>2</sub>, CO and H<sub>2</sub>O requires descriptions for the binary systems CO<sub>2</sub> + N<sub>2</sub>, CO<sub>2</sub> + CO, CO<sub>2</sub> + H<sub>2</sub>O, N<sub>2</sub> + CO, N<sub>2</sub> + H<sub>2</sub>O, and CO + H<sub>2</sub>O. When developing a comprehensive mixture model, the correlator has to face the challenge that some binary systems are experimentally extremely well investigated, whereas others might be without any data at all.

If very little or even no data for a binary mixture are available, the system can only be described by means of simple combining rules for the critical-parameters of the pure components. These combining rules are realized by special sets for the parameters  $\beta_{T,ij}$ ,  $\gamma_{T,ij}$ ,  $\beta_{v,ij}$ , and  $\gamma_{v,ij}$  of the reducing functions for temperature and density (see Eqs. (3.42) and (3.43)). In this case, no departure function  $\Delta\alpha^r$  is used; therefore, the weighting factor  $F_{ij}$  in Eq. (3.47) is set to zero. The correlator has to choose between linear combinations or the quadratic combinations according to Lorentz and Berthelot.<sup>35</sup> The quadratic combining rules for temperature and density are quite easily realized, since all reducing parameters are set to unity:

$$\beta_{T,ij} = \beta_{v,ij} = \gamma_{T,ij} = \gamma_{v,ij} = 1. \quad (4.3)$$

For the linear combining rules, the parameters are slightly more complex:

$$\beta_{T,ij} = 1, \quad \gamma_{T,ij} = \frac{1}{2} \frac{(T_{c,i} + T_{c,j})}{(T_{c,i} \cdot T_{c,j})^{0.5}}, \quad \text{and} \quad \beta_{v,ij} = 1, \quad \gamma_{v,ij} = 4 \frac{\left( \frac{1}{\rho_{c,i}} + \frac{1}{\rho_{c,j}} \right)}{\left( \frac{1}{\rho_{c,i}^{1/3}} + \frac{1}{\rho_{c,j}^{1/3}} \right)^3}. \quad (4.4)$$

Although both combining rules, linear and Lorentz-Berthelot, are easily implemented into a mixture model, choosing the proper one is demanding without any reliable experimental

information. As shown in Sec. 6.4, the correlator has to be aware that the two parameter sets might lead to qualitatively completely different results.

The real potential of the multi-component EOS is used, when fitting the binary reducing parameters  $\beta_{T,ij}$ ,  $\gamma_{T,ij}$ ,  $\beta_{v,ij}$ , and  $\gamma_{v,ij}$  to experimental (or molecular-simulation) data. The available data must contain at least some vapor-liquid equilibrium (VLE) points to define the phase boundaries of the binary mixture. If only homogeneous data but no VLE data are available, fitting the reducing parameters will not lead to a reliable description of the mixing behavior. Depending on the amount of data one, two, three, or all four parameters can be fitted. Through the use of the reducing functions the “extended corresponding states principle” for mixtures is applied. The basis for this approach was probably laid by Leland *et al.*<sup>52</sup> in 1962; however, there are so many modifications by various groups including many works on transport properties that it is difficult to track down the initial work that lead to this approach. The extended corresponding states principle is illustrated in Figure 4.3.

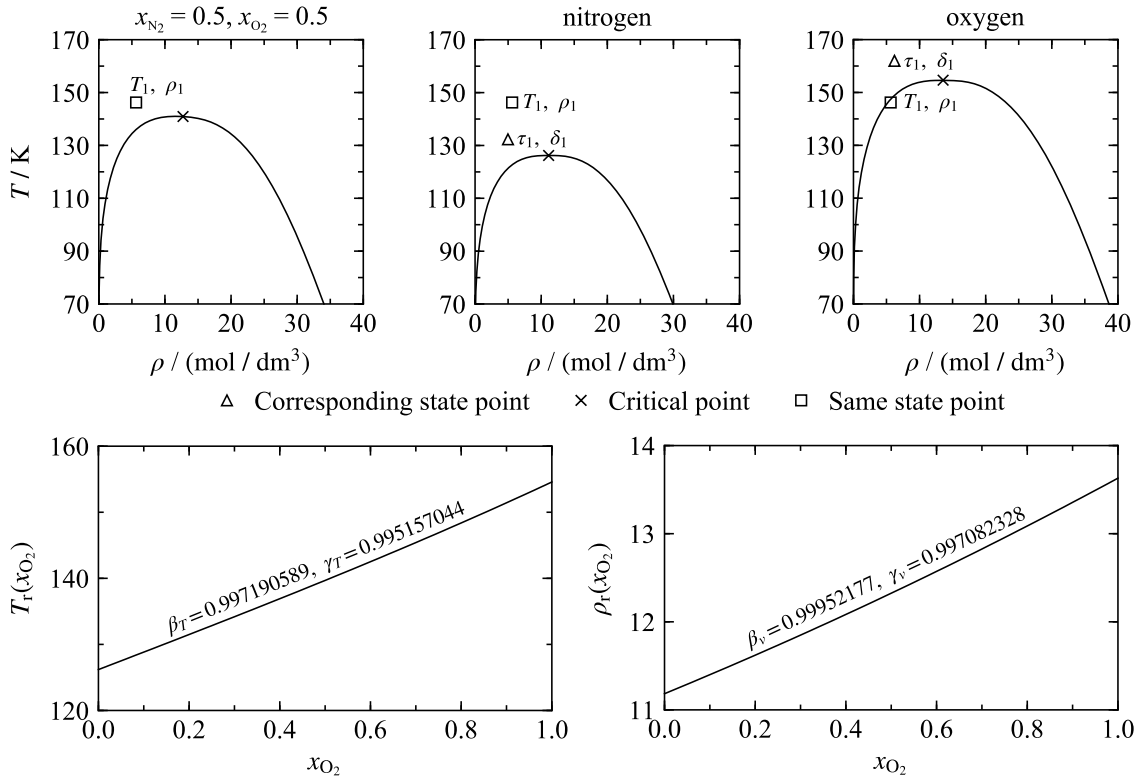
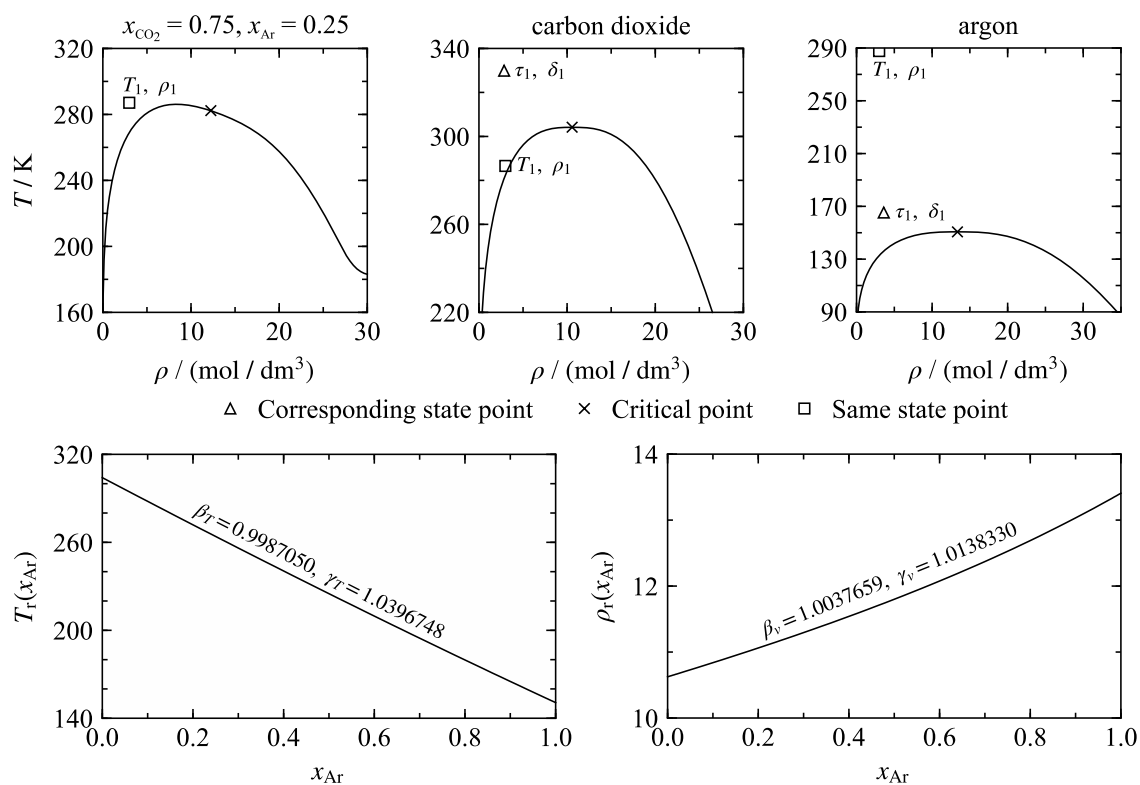


**Figure 4.3** Illustration of the “extended corresponding states principle” by the example of the binary mixture  $\text{N}_2 + \text{O}_2$  at equimolar composition. Top: An arbitrary state point in a  $T, \rho$  diagram of the mixture (left) and the same state point for pure nitrogen (middle) and pure oxygen (right). The  $T, \rho$  diagrams of the pure fluids additionally include points that are at a state corresponding to the one of the mixture. Bottom: The reducing functions for temperature and density, which enable the extended corresponding states principle, as a function of composition.

The top left panel shows an arbitrary state point of the quite “ideal” mixture of  $\text{O}_2$  and  $\text{N}_2$  at equimolar composition in a  $T, \rho$  diagram calculated with the EOS-CG model of Gernert and Span.<sup>2</sup> The point is defined by  $T_1 = 145 \text{ K}$  and  $\rho_1 = 5.5 \text{ mol dm}^{-3}$ ; thus, it is in the supercritical gas-like state region. As explained in Sec. 3.3, the multi-component mixture

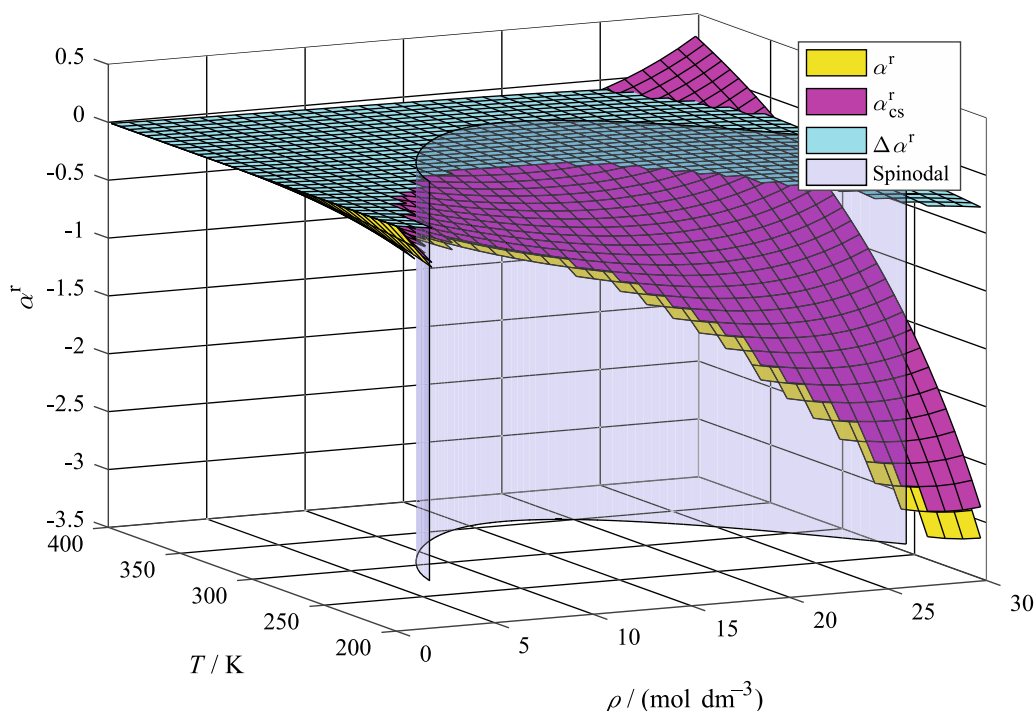
model is to a large extent based on combinations of the pure-fluid EOS. For the pure fluids,  $T_1$  and  $\rho_1$  define state points that are only partly comparable to the mixture state point. For pure nitrogen, the state point is still located in the supercritical gas-like region, but it is in considerable larger distance to the dew line than the mixture state point. For pure oxygen, the point is located in the two-phase region. It is apparent that combining the pure-fluid EOS evaluated at these different conditions does not yield the desired description of the mixture. The temperature and density of the mixture point are therefore reduced with the reducing functions that contain the binary parameters  $\beta_T$ ,  $\gamma_T$ ,  $\beta_v$ , and  $\gamma_v$ . This yields the reduced properties  $\tau_1 = 0.96$  and  $\delta_1 = 0.45$ . For the pure fluids,  $\tau_1$  and  $\delta_1$  correspond to different absolute temperatures ( $T_{O_2} = T_{c,O_2} / \tau_1 = 160.46$  K,  $T_{N_2} = T_{c,N_2} / \tau_1 = 130.99$  K) and densities ( $\rho_{O_2} = \rho_{c,O_2} \times \delta_1 = 6.08$  mol dm<sup>-3</sup>,  $\rho_{N_2} = \rho_{c,N_2} \times \delta_1 = 4.99$  mol dm<sup>-3</sup>) that define state points comparable to the state point of the mixture. At  $\tau_1$  and  $\delta_1$ , the mixture and both pure fluids are at “corresponding states”. The mixture can therefore be reasonably described by combining the pure-fluid EOS evaluated at these corresponding states. The bottom panels of Figure 4.3 illustrate the shape of the reducing functions calculated with the reducing parameters of the EOS-CG model. All parameters are very close to unity and thus very similar to the parameters that yield the quadratic Lorentz-Berthelot combining rules. The reducing functions exhibit an almost linear course, which is typical for relatively “ideal” and symmetric mixtures.

Figure 4.4 illustrates the extended corresponding states principle by the example of the chemically more complex mixture CO<sub>2</sub> + Ar with 75 mol% CO<sub>2</sub>. The calculations were carried out with the binary model developed within the scope of this work (see Sec. 6.2.1). The  $T, \rho$  diagrams show that the extended corresponding states principle also works for this quite asymmetric mixture, but the corresponding state points of the pure fluids seem not entirely equivalent to the state point of the mixture. The large difference in the critical temperatures of both pure fluids ( $T_{c,CO_2} = 304.128$ ,  $T_{c,Ar} = 150.687$ ) makes it difficult to describe the system with the extended corresponding states principle. Normally, this would only be possible with reducing parameters deviating considerably from unity. As depicted in the bottom panels of Figure 4.4, the parameters obtained in this work are still relatively close to unity and the reducing functions do not exhibit considerable asymmetries. The reason for this is that an additional binary specific departure function was developed for this system. The departure function considers deviations of the binary mixture from the predictions of the extended corresponding states principle. This allows for a highly accurate description of the available experimental or molecular-simulation data.



**Figure 4.4** Illustration of the “extended corresponding states principle” by the example of the binary mixture  $\text{CO}_2 + \text{Ar}$  with 75 mol%  $\text{CO}_2$ . Top: An arbitrary state point in a  $T, \rho$  diagram of the mixture (left) and the same state point for pure carbon dioxide (middle) and pure argon (right). The  $T, \rho$  diagrams of the pure fluids additionally include points that are at a state corresponding to the one of the mixture. Bottom: The reducing functions for temperature and density, which enable the extended corresponding states principle, as a function of composition.

The influence of the binary specific departure function is illustrated in Figure 4.5. The residual part of the reduced Helmholtz energy  $\alpha^r$  is shown over temperature and density. Only the homogeneous fluid region is depicted. The border to the two-phase region is represented by the vapor-liquid spinodal as calculated in CoolProp.<sup>40</sup> Calculating the spinodal requires less computing-time than calculations of the dew and bubble line; thus, it is more suitable for three-dimensional evaluations. The complete surface  $\alpha^r$  is plotted as well as the surface  $\alpha_{\text{cs}}^r$  calculated by omitting the departure function; thus, this surface only results from the extended corresponding state principle (abbreviated as “cs”). Finally, the departure function  $\Delta\alpha^r$  itself is plotted. It can be seen that the contribution of the departure function is close to the zero over the whole plotted range of temperature and density; however, its influence is equivalent to the small gap between  $\alpha^r$  and  $\alpha_{\text{cs}}^r$ . Although the contribution of the departure function is seemingly small, it allows the description of most of the highly accurate data available within their experimental uncertainties (see Sec. 6.2.1), which would not be possible without this additional function.



**Figure 4.5** The residual part of the reduced Helmholtz energy  $\alpha^r$  as a function of temperature and density. The complete residual surface is plotted as well as the part only resulting from the “extended corresponding states principle”  $\alpha_{cs}^r$  and the contribution of the departure function  $\Delta\alpha^r$ . The surfaces are limited by the vapor-liquid spinodal as calculated from CoolProp.<sup>40</sup> The three-dimensional plot was generated with algorithms developed by Neumann.<sup>49</sup>

Because of its large influence on the overall description of the binary mixture, the departure function needs to be shaped carefully and should only be developed if a qualitatively and quantitatively sufficient experimental database is available. Developing a departure function based on limited data is challenging and can only be done by fitting many additional thermodynamic constraints. The binary mixture model might otherwise yield small deviations to the data, but physically unreasonable predictions of the mixing behavior. As discussed in Sec. 3.3, the mathematical structure of the multi-component mixture model also allows for the use of generalized departure functions for multiple chemically comparable binary mixtures. In this case, the adjustable parameters of the departure function are not fitted but the weighting factor  $F_{ij}$  is adjusted (see Eq. (3.47)). This approach was used for many systems in the GERG-2008 model of Kunz and Wagner<sup>36</sup> and also for some aqueous systems in the EOS-CG model of Gernert and Span.<sup>2</sup> In this work, only binary specific departure functions were fitted ( $F_{ij} = 1$ ), because the systems discussed in Sec. 6.2 are too different in their mixing behavior.

The process of fitting a binary specific departure function is even more empirical than fitting pure-fluid EOS. Fitting the residual part of a pure-fluid EOS is normally initiated by using the parameters of the EOS for a chemically comparable compound. In contrast, a departure function for a specific binary system is rarely adoptable for another system. Considering the explanations given above, this is unsurprising because the function should be interpreted as a correction term without a physical meaning. In this context, it is worth noting that it is

wrong to interpret the departure function as an excess quantity ( $\Delta\alpha^r \neq \alpha^E$ ) as it is sometimes done in the literature.<sup>53</sup> Since  $\Delta\alpha^r$  is a correction of the extended corresponding states principle, the optimal set of terms and parameters varies widely depending on the binary system to be described. Restrictions to the parameters as discussed for pure-fluids are very few. Density exponents should be positive integers and are not fitted, but defined by the correlator when selecting the type of term. The fitting algorithm sometimes yields negative temperature exponents. Preliminary models including such exponents are mostly characterized by an unreasonable extrapolation behavior; thus, only positive temperature exponents should be applied. Similar to the considerations for pure fluids, the temperature exponents should be as low as possible; nevertheless, for very asymmetric mixtures, higher exponents are needed to describe the characteristics of these systems. In this work, this was especially the case for the system  $\text{H}_2\text{O} + \text{H}_2\text{S}$  (see Sec. 6.2.4). The departure function for this system contains temperature exponents as high as  $t_4 = 8.15$ . Aside from these few considerations, there are essentially no restrictions to the parameters. The same applies for the combination of term types introduced in Eq. (3.48). In principle, all types of terms can be combined. While fitting a binary specific departure function, many different mathematical structures are tested before the final set of parameters is achieved. Most of the departure functions developed over the last years contain between four and eight terms. The GERG-2008 model includes binary formulations with a total of 12 terms;<sup>36</sup> however, such long functions are normally not needed with the modern fitting techniques. For both pure-fluid and mixture EOS, the fitting process is normally completed by carefully rounding all exponents and coefficients. This is done successively while refitting the equation. It guarantees that the rounding of each group of parameters is compensated by the coefficients and exponents that are still included in the fit.

To conclude this brief introduction into fitting EOS, a short outlook to current developments in this field should be given. A new evolutionary optimization algorithm was presented by Bell and Lemmon in 2016.<sup>54</sup> This algorithm allows the automated fitting of the parameters of the temperature-reducing function for mixtures without further input from the correlator. It has already been extended to additionally fit the parameters of the density-reducing functions. For relatively symmetric mixtures, this algorithm leads to reliable binary models; however, for more asymmetric mixtures as considered in this work the non-automatic fitting process is still more suitable. The development of automated fitting algorithms is ongoing at NIST, Boulder, with the aim of extending these algorithms to binary specific departure functions. At RUB, a more automated approach of fitting pure-fluid EOS is currently under development. It is not expected that such algorithms will totally replace the fitting process described in this section, but it might provide better starting values and a reliable pre-selection of the experimental data.



## 5 Equations of State for Pure Fluids

Within this work, three EOS for pure fluids were developed, namely for heavy water, chlorine, and monoethanolamine. The motivation for these works are discussed in detail in Sec. 2. The heavy water EOS was developed to provide a new reference EOS for the International Association for the Properties of Water and Steam (IAPWS) that was needed, for at least, more than 20 years; the EOS for chlorine and monoethanolamine are mandatorily required in order to model the thermodynamic properties of mixtures including these components as relevant to CCS-applications. In the context of this work, an additional EOS for diethanolamine was developed by Kortmann,<sup>55</sup> whose work also includes a preliminary EOS for monoethanolamine that needed to be replaced by the EOS presented in this work. The EOS for diethanolamine is not evaluated in this work, but a detailed discussion can be found in the corresponding Master thesis of Kortmann.<sup>55</sup> In addition to the three EOS presented here and to the work of Kortmann, a first approach of modelling the thermophysical properties of pure nitrogen oxide and nitrogen dioxide was made by Tietz<sup>56</sup> in order to implement these technically relevant components into the new CCS-mixture model. However, this project turned out to be much more complicated than planned, since these compounds never really occur as pure fluids. Both are part of a complex dynamic system that undergoes chemical reactions depending on pressure and temperature. The EOS for these components could consequently not be implemented into the CCS-mixture model. A comprehensive discussion of the outcome of the underlying project is given in the Master thesis of Tietz.<sup>56</sup>

The three EOS presented in this section are based on the Helmholtz-energy explicit functional form introduced in Sec. 3.3 that allows for the most-accurate description of the thermodynamic properties of these fluids. Nevertheless, the accuracies of the new EOS are not comparable, because the underlying experimental databases are extremely different in quality and quantity. The new EOS for heavy water is a reference EOS that was fitted to a large number of multi-property experimental data including some exceptionally high-quality data sets. Therefore, and because this EOS results from a five year-long project additionally including the development of new correlations for the melting- and sublimation pressure curves, the discussion of the new EOS for heavy water is much more comprehensive than for the EOS for monoethanolamine and chlorine. Due to its high toxicity, the experimental database for chlorine is much more limited than for heavy water. These limitations are not only related to the number of experimental studies, but also to the accuracy of the available data that is in many cases significantly lower than achievable by means of state-of-the-art experimental set-ups. Nevertheless, the thermodynamic properties of chlorine are still comparably well investigated, which allowed for the development of an accurate EOS. The new EOS for monoethanolamine enables a very good description of the available

experimental data. However, as discussed in Sec. 5.3, these data are extremely limited and cover only a small part of the fluid surface. Thus, the present EOS for monoethanolamine cannot be considered as a highly accurate formulation, but as shown in Secs. 6.3.1.7 and 6.3.2 it allows for a good description of mixtures containing this component.

In this section, the new pure-fluid EOS are mostly validated through comparisons between calculated values and the available experimental data. Therefore, the relative deviation of every data point from the value determined from the EOS is calculated according to Eq. (4.2). Comparisons of the equations to complete data sets are based on the average absolute relative deviation (*AAD*). This property is defined as the arithmetic average of all percentage absolute deviations of a data set (excluding clear outliers). It reads:

$$AAD = \frac{1}{n} \sum_{i=1}^n \left| 100 \frac{\Delta X_i}{X_i} \right|, \quad (5.1)$$

where  $n$  is the number of data points used in the calculation. In many cases calculating an overall *AAD* for one data set would lead to false conclusions. For example, the *AAD* of a data set including many excellent measurements in the liquid phase can be worsened significantly by a small number of inaccurate data points in the vapor phase. Therefore, it is meaningful to separate the fluid range into parts and calculate the *AAD* for each of them. This separation needs to be different for thermal saturation data than for other types of data and is introduced in Secs. 5.1.4 and 5.1.5, respectively.

## 5.1 New Reference Equation of State for Heavy Water

Within the scope of the present dissertation, the new reference equation of state for heavy water (D<sub>2</sub>O) was published by Herrig *et al.*,<sup>57</sup> and this section is, to a large extent, based on that publication. A preliminary version of the EOS presented in this work was adopted as an IAPWS Release in 2017.<sup>58</sup> A Revised Release based on the final formulation discussed here and published by Herrig *et al.*<sup>57</sup> was recently adopted at the 2018 IAPWS annual meeting in Prague. The Revised Release will soon be available and will replace the 2017 Release.

As introductorily mentioned, the new EOS is based on the functional form presented in Sec. 3.3 (see Eqs. (3.33) to (3.38)) that is explicit in the reduced Helmholtz energy as a function of reduced density and reciprocal reduced temperature. The critical parameters used to reduce density and temperature are given in Table 5.1. As defined by Eq. (3.33), the functional form requires separate formulations for the ideal-gas and for the residual Helmholtz energy. The ideal-gas part of the Helmholtz energy of D<sub>2</sub>O reads:

$$\alpha^o(\tau, \delta) = a_1 + a_2\tau + \ln \delta + (c_0 - 1) \ln \tau + \sum_{k=1}^4 v_k \ln [1 - \exp(-u_k \tau/T_c)]. \quad (5.2)$$

The minimum value of the isobaric ideal-gas heat capacity  $c_0$ , as well as the integration constants  $a_1$ ,  $a_2$ , and the adjustable parameters  $v_1$  to  $v_4$  and  $u_1$  to  $u_4$  are given in Table B.1 in Appendix B of this thesis. The integration constants  $a_1$  and  $a_2$  were adjusted to match the IAPWS criteria for the reference state of the EOS. IAPWS demands that the internal energy  $u'$  and entropy  $s'$  of the real fluid at the saturated liquid state are set to zero at the triple point  $T_{\text{tp}} = 276.969$  K.

The residual part of the EOS consists of six polynomial(-like) terms, six exponential terms, and twelve Gaussian bell-shaped terms. The complete equation reads:

$$\begin{aligned} \alpha^r(\delta, \tau) = & \sum_{k=1}^6 n_k \delta^{d_k} \tau^{t_k} + \sum_{k=7}^{12} n_k \delta^{d_k} \tau^{t_k} \exp(-\delta^{l_k}) \\ & + \sum_{k=13}^{24} n_k \delta^{d_k} \tau^{t_k} \exp\left[-\eta_k (\delta - \varepsilon_k)^2 - \beta_k (\tau - \gamma_k)^2\right]. \end{aligned} \quad (5.3)$$

As discussed in Sec. 2.1, a short and thus numerically stable functional form was one of the main requirements for the new EOS for heavy water. In comparison to the equation of Hill *et al.*,<sup>1</sup> the new formulation has fewer than half the number of terms, 24 instead of 50 (excluding the ideal-gas correlations). All parameters (coefficients  $n_k$ , temperature exponents  $t_k$ , density exponents  $d_k$  and  $l_k$ , and the parameters of the Gaussian bell-shaped terms  $\eta_k$ ,  $\varepsilon_k$ ,  $\beta_k$ , and  $\gamma_k$ ) are listed in Table B.2 in Appendix B. To assist users in verifying the correct computer-implementation of Eqs. (5.2) and (5.3), comprehensive test values are provided in the publication of Herrig *et al.*<sup>57</sup> as well as in the IAPWS Release, which will soon be available.

The new EOS is valid for all stable fluid states from  $T_{\text{min}} = 254.415$  K, which corresponds to the minimum temperature along the melting-pressure curve, to  $T_{\text{max}} = 825$  K at pressures up to  $p_{\text{max}} = 1200$  MPa.

### 5.1.1 Physical Constants and Characteristic Properties

An overview of the most important physical constants and characteristic properties of D<sub>2</sub>O as relevant for the EOS presented here is given in Table 5.1. Aside from information taken from literature references, the table contains values determined from the new equation.

**Table 5.1** Physical constants and characteristic properties of heavy water (D<sub>2</sub>O).

Quantity	Symbol	Value	Reference
Molar gas constant	$R$	8.314 459 8 J mol <sup>-1</sup> K <sup>-1</sup>	Mohr <i>et al.</i> <sup>59</sup>
Molar mass	$M$	20.027 508 g mol <sup>-1</sup>	IAPWS <sup>5</sup>
Critical temperature	$T_c$	643.847 K	IAPWS <sup>60</sup>
Critical pressure	$p_c$	21.6618 MPa	This work

*continued...*

**Table 5.1** ...continued

Quantity	Symbol	Value	Reference
Critical density	$\rho_c$	17.775 55 mol dm <sup>-3</sup>	IAPWS <sup>60</sup>
Triple-point temperature	$T_{tp}$	276.969 K	Markó <i>et al.</i> <sup>61</sup>
Triple-point pressure	$p_{tp}$	0.661 59 kPa	This work
Vapor density at triple point	$\rho_{pv}$	0.000 287 mol dm <sup>-3</sup>	This work
Liquid density at triple point	$\rho_{pl}$	55.188 mol dm <sup>-3</sup>	This work
Normal-boiling-point temperature	$T_{nbp}$	374.549 K	This work
Vapor density at the normal boiling point	$\rho_{nbpv}$	0.033 043 mol dm <sup>-3</sup>	This work
Liquid density at the normal boiling point	$\rho_{nbpl}$	53.039 mol dm <sup>-3</sup>	This work
Maximum density temperature at atmospheric pressure	$T_{\rho_{max,atm}}$	284.748 K	This work
Maximum density at atmospheric pressure	$\rho_{max,atm}$	55.221 mol dm <sup>-3</sup>	This work
Acentric factor	$\omega$	0.364	This work

In the development of equations of state, the critical temperature and density are essential thermodynamic properties. With regard to the structure of modern equations, the reason for this is obvious. Most of these formulations are explicit in the reduced Helmholtz energy with the critical temperature and density as reducing parameters. However, measurements of the critical point are difficult and thus often rare and with wide variation between sources. The experimental determination of the critical density poses a special challenge because of the extreme sensitivity of density to changes in temperature and pressure near the critical point. For heavy water, only four references are available and only two of them include information about the critical density. The available critical parameters are listed in Table 5.2. All temperature values were converted to the International Temperature Scale of 1990 (ITS-90).<sup>14</sup> The critical temperature and density used to develop the new EOS are recommended in the IAPWS Release on the critical values of ordinary and heavy water.<sup>60</sup> The critical temperature given in the IAPWS Release corresponds to the measurement of Blank<sup>62</sup> converted to ITS-90. The critical pressure and density were obtained numerically by Levelt Sengers *et al.*<sup>63</sup> by a scaled analysis of  $p\rho T$  data measured by Rivkin and Akhundov.<sup>64</sup> The recommended critical parameters and their corresponding uncertainties are  $T_{c,IAPWS} / \text{K} = 643.847 + \delta$  with  $\delta = 0.000 \pm 0.200$ ,  $p_{c,IAPWS} / \text{MPa} = 21.671 + 0.27\delta \pm 0.01$ , and  $\rho_{c,IAPWS} / (\text{kg m}^{-3}) = 356 \pm 5$  or  $\rho_{c,IAPWS} / (\text{mol dm}^{-3}) = 17.775 55 \pm 0.25$  on a molar basis. It should be noted that the critical pressure recommended by IAPWS slightly differs (by 0.0092 MPa) from the value obtained from the new EOS as given in Table 5.1. However, this deviation is within the uncertainty of the IAPWS value, which is 0.01 MPa at the chosen critical temperature.

**Table 5.2** Critical and triple-point parameters of D<sub>2</sub>O. See Table 5.1 for values from this work.

Reference	Year	Temperature $T$ / K	Pressure $p$ / MPa	Density $\rho$ / (mol dm <sup>-3</sup> )
Triple-point parameters				
Bartholomé and Clusius <sup>65</sup> <sup>a</sup>	1935	276.967	0.000 6746	-
Jones <sup>66</sup>	1952	276.957	-	-
Markó <i>et al.</i> <sup>61</sup>	1989	276.969	0.000 6593	-
Critical-point parameters				
Riesenfeld and Chang <sup>67</sup>	1935	644.684	22.150	18.125 07
Eck <sup>68</sup>	1939	644.684	21.722	18.223 11
Oliver and Grisard <sup>69</sup>	1956	644.084	21.856	-
Blank <sup>62</sup>	1969	643.847	21.659	-
IAPWS <sup>60</sup> <sup>b</sup>	1992	643.847	21.671	17.775 55

<sup>a</sup>The article presents triple-point parameters without describing a triple-point experiment or giving a reference for these values. Nevertheless, it is included here since no earlier reference for the triple-point parameters was found.

<sup>b</sup>Recommended critical-point parameters: Critical temperature taken from Blank,<sup>62</sup> critical pressure and density determined from  $p\rho T$  measurements of Rivkin and Akhundov.<sup>64</sup>

Equations of state as presented here do not allow calculating properties of solid phases. Thus, knowledge of the melting and sublimation curves is needed to set the lower temperature limit of the range of validity of such thermodynamic formulations. For (heavy) water, the triple point is not the lowest temperature at which the substance remains liquid due to the anomalous shape of its melting curve, which exhibits a negative initial slope ( $dp/dT$ ). Nevertheless, the triple-point parameters of water are important natural constants, which are known extremely accurately for ordinary water<sup>70</sup> but less satisfactorily for heavy water. Although triple-point parameters of D<sub>2</sub>O can be found in a number of publications, almost all of these studies obtained the triple-point pressure by extrapolating vapor-pressure data measured at higher temperatures down to a given triple-point temperature. Furthermore, the triple point is frequently equated with the melting point at atmospheric pressure. Only Jones<sup>66</sup> and Markó *et al.*<sup>61</sup> carried out a “real” triple-point experiment. The data from these studies are given in Table 5.2 with temperatures converted to ITS-90. In addition to these references, the data of Bartholomé and Clusius<sup>65</sup> are included in the table. This reference is given since no earlier work providing triple-point parameters of heavy water was found. However, the authors do not describe a direct experimental investigation of the triple point; thus, the source of the given values is unclear. For the development of the new EOS, the most recent value for the triple-point temperature by Markó *et al.*<sup>61</sup> was adopted. The triple-point pressure given in Table 5.1 was calculated at this temperature from the final EOS, since the pressure reported by Markó *et al.*<sup>61</sup> deviates by about 0.3 % from the most accurate vapor-pressure data at slightly higher temperatures.

### 5.1.2 Melting- and Sublimation-Pressure Equations

As discussed in the previous section, the lower temperature limit of the EOS for heavy water should not be defined by the triple-point temperature, but by the lowest temperature along the melting curve. Thus, additional ancillary equations for the melting pressure of the relevant ice structures of heavy water were developed. The description of phase equilibria (including fluid phases) is completed by an ancillary equation for the sublimation pressure. The correlations for these solid-fluid equilibria were fitted to experimental results available in the literature.

Solid water forms different crystalline structures depending on temperature and pressure. For ordinary water, five ice structures are known that are bordered by the liquid phase (ice structures Ih, III, V, VI, VII). The corresponding melting-pressure curves are limited by triple points, in which two ice structures and the liquid phase are in thermodynamic equilibrium. An exception to this is the lower pressure limit of the melting curve of ice Ih, which is the “normal” solid-vapor-liquid triple point of water. The five ice structures are described by correlation equations that were developed by Wagner *et al.*<sup>71</sup> and also included in the IAPWS-95 publication by Wagner and Pruß.<sup>29</sup> The correlation for ice Ih was later updated by Wagner *et al.*<sup>72</sup> For heavy water, the structures of the original correlations for H<sub>2</sub>O were adopted and refitted to the available experimental melting-pressure data by Bridgman<sup>73</sup> (for ice structures Ih, III, V, VI) and Henderson and Speedy<sup>74</sup> (only for ice structure Ih) in order to develop the correlations given in this section. The triple-point data required to define the range of validity for each ice-structure correlation were taken from Bridgman<sup>73</sup> for the solid-solid-liquid triple points, and from Table 5.1 for the “normal” triple point. All applied triple-point parameters of the different ice structures are listed in Table 5.3.

**Table 5.3** Triple-point parameters limiting the melting-pressure correlations for the different ice structures of heavy water.

Reference	$T_p / \text{K}$	$p_p / \text{MPa}$	Coexisting phases
Table 1	276.969	0.000 661 59	ice Ih-V-L
Bridgman <sup>73 a</sup>	254.415	222.41	ice Ih-ice III-L
Bridgman <sup>73 a</sup>	258.661	352.19	ice III-ice V-L
Bridgman <sup>73 a</sup>	275.748	634.53	ice V-ice VI-L

<sup>a</sup>All pressures of Bridgman<sup>73</sup> were multiplied by 1.0102, since the apparatus used was calibrated by means of an obsolete melting pressure of mercury at 0 °C.

Since no data are available along the ice-VII melting line, it was ensured that the equation for ice VI yields reasonable results up to the upper pressure limit of the new EOS,  $p_{\max} = 1200 \text{ MPa}$ . All experimental values of Bridgman<sup>73</sup> were multiplied by a correction factor of 1.0102. This factor corresponds to the ratio between the melting pressure of mercury at 0 °C obtained by Bridgman<sup>75</sup> (749.2 MPa), which was used to calibrate the apparatus for his light and heavy water melting-pressure measurements, and the reference value reported by Molinar *et al.* (756.84 MPa).<sup>76</sup>

The four melting-pressure equations developed within this work are as follows:

*Melting-pressure equation for ice Ih (temperature range from 276.969 K to 254.415 K):*

$$\frac{P_{\text{m,ice Ih}}}{p_n} = 1 - 0.30153 \times 10^5 (1 - \theta^{5.5}) + 0.692503 \times 10^6 (1 - \theta^{8.2}), \quad (5.4)$$

with reduced temperature  $\theta = T / T_n$ , and the reducing parameters  $T_n = 276.969$  K and  $p_n = 0.00066159$  MPa.

*Melting-pressure equation for ice III (temperature range from 254.415 K to 258.661 K):*

$$\frac{P_{\text{m,ice III}}}{p_n} = 1 - 0.802871 (1 - \theta^{33}), \quad (5.5)$$

with  $\theta = T / T_n$ ,  $T_n = 254.415$  K, and  $p_n = 222.41$  MPa.

*Melting-pressure equation for ice V (temperature range from 258.661 K to 275.748 K):*

$$\frac{P_{\text{m,ice V}}}{p_n} = 1 - 0.1280388 \times 10^1 (1 - \theta^{7.6}), \quad (5.6)$$

with  $\theta = T / T_n$ ,  $T_n = 258.661$  K, and  $p_n = 352.19$  MPa.

*Melting-pressure equation for ice VI (temperature range from 275.748 K to 315 K):*

$$\frac{P_{\text{m,ice VI}}}{p_n} = 1 - 0.1276026 \times 10^1 (1 - \theta^4), \quad (5.7)$$

with  $\theta = T / T_n$ ,  $T_n = 275.748$  K, and  $p_n = 634.53$  MPa.

Comparisons between the melting-pressure curves calculated from the new correlations and the available experimental data are shown in Figure 5.1.

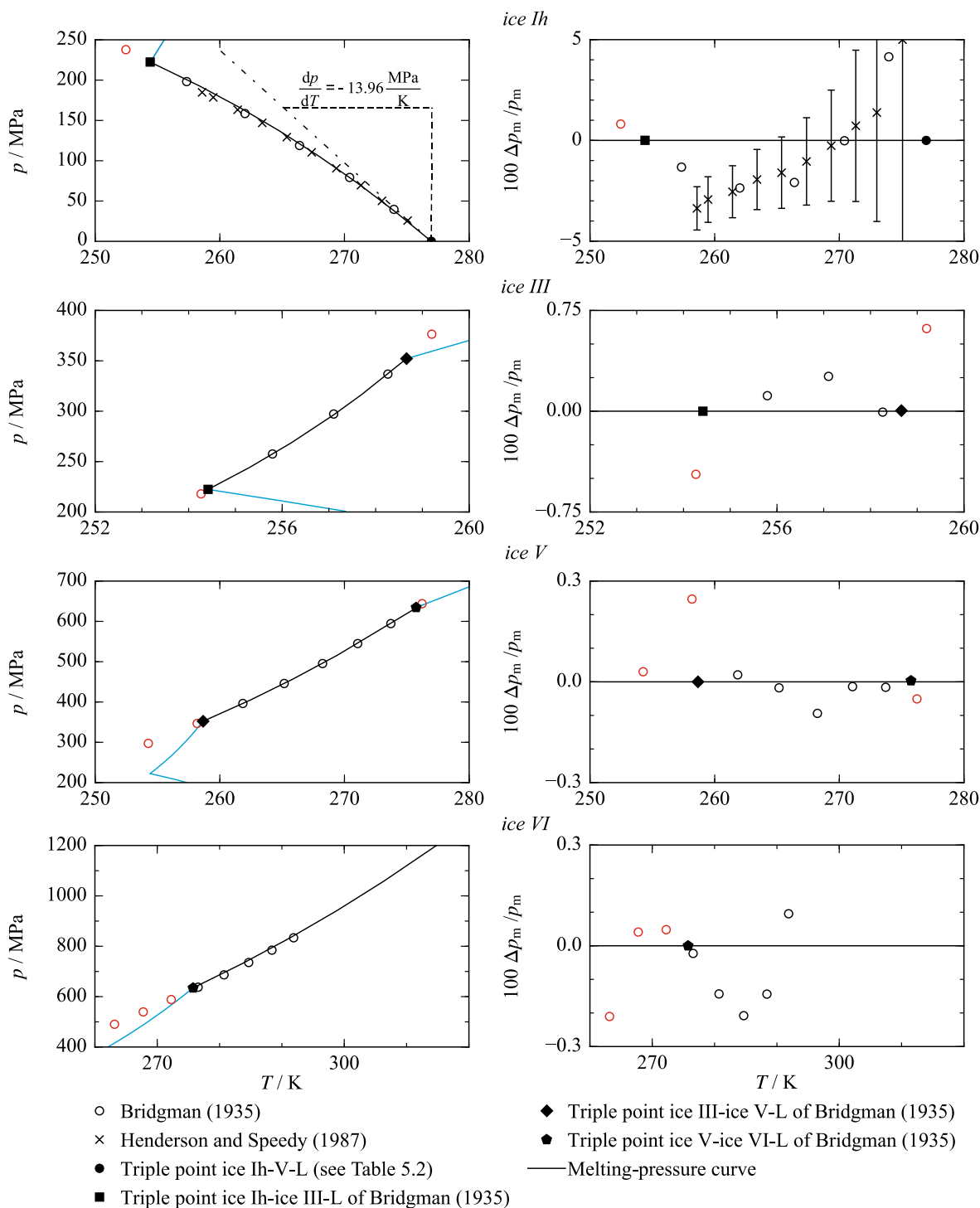


**Figure 5.1** Left: Melting-pressure curves of the different ice structures of heavy water in  $p, T$  diagrams. The curves are calculated by means of Eqs. (5.4) and (5.7). Lines shown in blue represent the melting-pressure curves of adjacent ice structures. The available experimental data including the triple points are shown for comparisons. Right: Relative deviations  $\Delta p_m / p_m = (p_{m, \text{exp}} - p_{m, \text{calc}}) / p_{m, \text{exp}}$  of experimental melting-pressure data from the new correlations versus temperature. Metastable melting points from Bridgman<sup>73</sup> above and/or below the triple points of the corresponding ice structure are shown in red.

As is evident from Figure 5.1, deviations between the experimental data and calculated melting pressures for ice Ih are considerably higher than those for the other ice structures. For ice Ih two data sets are available, namely the already discussed data by Bridgman<sup>73</sup> and additionally the data of Henderson and Speedy.<sup>74</sup> The latter experimentalists state an



uncertainty of 0.1 K in temperature and 0.5 MPa in pressure. Considering these uncertainties, the total combined expanded ( $k = 2$ ) uncertainties in melting pressure range from approximately 1 % at 258.6 K to 11 % at 275.1 K, where uncertainties are higher due to the steep slope of the melting-pressure curve. The correlation describes the data within their uncertainty for temperatures above 265 K. For lower temperatures, the calculated melting line represents a compromise between the best possible description of the data sets by Henderson and Speedy<sup>74</sup> and Bridgman.<sup>73</sup> Although the latter data set is less accurate, it was used to fit the correlation in order to achieve a low deviation from the ice Ih-ice III-L triple point. An accurate description of this state point is necessary to ensure a continuously consistent description along the ice-Ih and ice-III melting curve. Attempts to fit the complete data set of Henderson and Speedy<sup>74</sup> together with the upper triple point led to unreasonable changes in curvature along the saturation curve. Thus, the correlation was fitted to a thorough selection of data points from both references. Additionally, the curvature and third derivative ( $d^3p_m/dT^3$ ) were carefully constrained to avoid any unreasonable shape of the melting-pressure curve. The calculated initial slope of the melting curve at the “normal” solid-vapor-liquid triple point is  $-13.96 \text{ MPa K}^{-1}$ . As a reliability check, this slope is compared to the result of the Clapeyron equation,

$$\frac{dp_m}{dT} = \frac{\Delta h_m}{T(v_L - v_S)}, \quad (5.8)$$

with the enthalpy of fusion  $\Delta h_m$  and the liquid-solid volume change ( $v_L - v_S$ ). Considering the experimental results of Long and Kemp<sup>77</sup> for  $\Delta h_m = 1501 \text{ cal mol}^{-1} = 6280.2 \text{ J mol}^{-1}$  and of Timmermans *et al.*<sup>78</sup> for  $(v_L - v_S) = -1.62 \text{ cm}^3 \text{ mol}^{-1}$ , Eq. (5.8) yields a slope of  $-13.96 \text{ MPa K}^{-1}$  at  $T = T_{tp} = 276.969 \text{ K}$ . Thus, the initial slope calculated from the new melting-pressure equation is in perfect agreement with the result of the Clapeyron equation. With regard to the representation of the data of Henderson and Speedy,<sup>74</sup> the uncertainty of melting pressures of ice Ih calculated from Eq. (5.4) is conservatively estimated to be 4 %.

For a complete description of the phase equilibria of heavy water, an ancillary equation for the sublimation pressure of ice Ih is presented. The equation was set up by adopting the structure of the correlation for ordinary water as given in Wagner *et al.*<sup>71</sup> and Wagner and Pruß.<sup>29</sup> The parameters were fitted to sublimation pressures obtained by Pupezin *et al.*<sup>79</sup> and Bottomley.<sup>80</sup> The data of Pupezin *et al.*<sup>79</sup> range from the triple-point temperature down to about 210 K, whereas Bottomley’s measurements do not cover temperatures below 261 K. Thus, the lower temperature limit of the equation is defined by the data set of Pupezin *et al.*<sup>79</sup> Pressure and temperature are reduced by the “normal” triple-point parameters discussed in Sec. 5.1.1.

*Sublimation-pressure equation for ice Ih (temperature range from 210 K to 276.969 K):*

$$\frac{p_{\text{m,ice III}}}{p_n} = 1 - 0.802871(1 - \theta^{33}), \quad (5.9)$$

with  $\theta = T / T_n$ ,  $T_n = 276.969$  K and  $p_n = 0.00066159$  MPa.

Comparisons between sublimation pressures calculated from Eq. (5.9) and the experimental data are shown in Figure 5.2. For the sake of completeness, the data of Niwa and Shimazaki<sup>81</sup> are shown in addition to the data sets mentioned above, although they comprise only three data points of lower accuracy. Within the deviation plot in the right panel (like in all other deviation plots in this thesis), data points shown at the upper or lower vertical limits of the diagram indicate that the points are off scale.

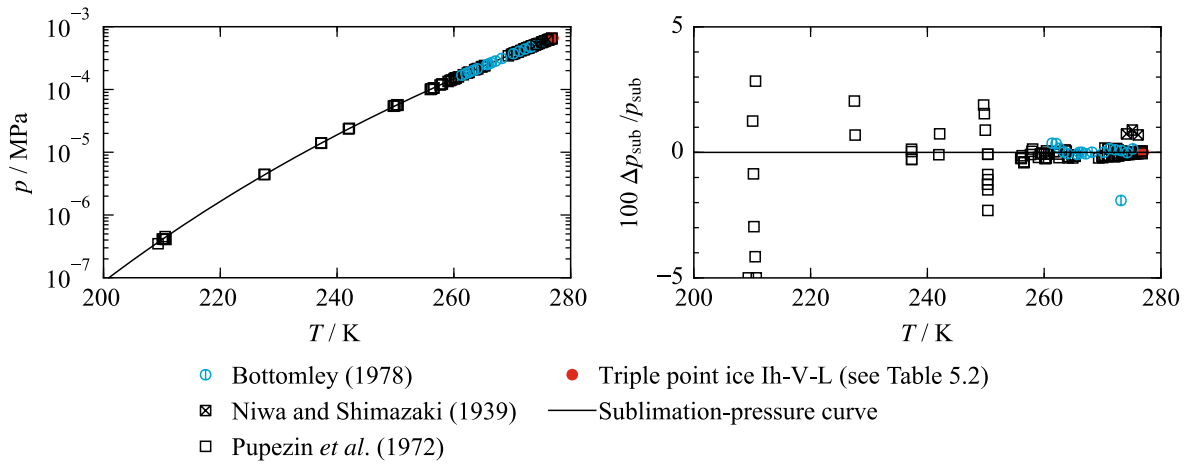


**Figure 5.2** Left: Sublimation-pressure curve of heavy water in a  $p, T$  diagram as calculated from Eq. (5.9). The available experimental data are shown for comparisons. Right: Relative deviations  $\Delta p_{\text{sub}} / p_{\text{sub}} = (p_{\text{sub,exp}} - p_{\text{sub,calc}}) / p_{\text{sub,exp}}$  of experimental sublimation-pressure data from Eq. (5.9) versus temperature.

At temperatures above 255 K, the data of Pupezin *et al.*<sup>79</sup> and Bottomley<sup>80</sup> confirm each other and are represented within 0.5 % in sublimation pressure. At lower temperatures, where the sublimation pressures become quite low ( $p_{\text{sub}} \leq 10^{-4}$  MPa), the data exhibit significantly more scatter. Most of the data between 210 K and 255 K are described within 5 %. The experimental uncertainty of the data of Bottomley<sup>80</sup> is not stated clearly and is difficult to estimate since the publication presents differences between the sublimation pressure and the vapor pressure of the metastable subcooled liquid. The data were calculated by means of vapor pressures obtained from the new EOS extrapolated below the triple-point temperature. The experimental set-up applied to measure the data of Pupezin *et al.*<sup>79</sup> was presented by Jancsó *et al.*<sup>82</sup> together with experimental results for the sublimation pressure of ordinary water. These results deviate from the most accurate sublimation-pressure equation of Wagner *et al.*<sup>72</sup> (IAPWS standard correlation for the sublimation pressure of ordinary water<sup>83</sup>) by up to 0.5 % at temperatures above 250 K. At lower temperatures, the deviations increase significantly to more than 10 % at about 200 K. In this temperature

range, the uncertainty of the sublimation-pressure equation for ordinary water is below 0.5 %.<sup>72,83</sup> Thus, the experimental uncertainty of the data for D<sub>2</sub>O of Pupezin *et al.*<sup>79</sup> can reasonably be estimated based on the deviations between the data for H<sub>2</sub>O of Jancsó *et al.*<sup>82</sup> and the reference correlation by Wagner *et al.*<sup>72</sup> Considering these deviations, the estimated uncertainties of sublimation pressures of D<sub>2</sub>O calculated from Eq. (5.9) are 0.5 % at temperatures above 255 K, 5 % at  $225 \leq T / \text{K} \leq 255$ , and 10 % at  $210 \leq T / \text{K} \leq 225$ . Qualitative comparisons with the equation for H<sub>2</sub>O show that Eq. (5.9) can be reasonably extrapolated down to temperatures of 150 K or lower.

The complete phase diagram as calculated by means of the new EOS and the corresponding ancillary correlations for the melting-pressures of the different ice structures and for the sublimation pressure is shown in Figure 5.3.

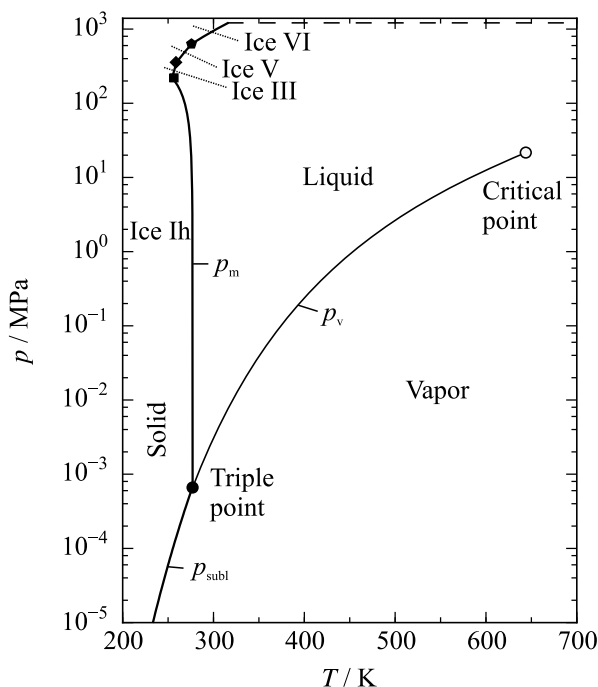


**Figure 5.3** The phase-boundary curves of heavy water in a  $p, T$  diagram. The vapor-pressure curve  $p_v$  is calculated by means of the new EOS. The sublimation- and melting-pressure curves  $p_{\text{subl}}$  and  $p_m$  are obtained from the corresponding ancillary equations. The dashed line indicates the upper pressure limit of the EOS. The sublimation curve and the melting curves correspond to the lower temperature limit of the range of validity.

### 5.1.3 Ideal-Gas State

The ideal-gas part of the new EOS for heavy water, as given in Eq. (5.2), was mainly developed by fitting a correlation for the isobaric ideal-gas heat capacity (see Sec. 5.1.3) to the most recent data of Simkó *et al.*<sup>84</sup> However, since the ideal-gas part contributes to all caloric properties calculated from the new EOS, it was simultaneously fitted with the residual part to additional experimental data for speed of sound and heat capacity ( $c_p$  and  $c_v$ ) of the real fluid. The ideal-gas isobaric heat-capacity data of Simkó *et al.*<sup>84</sup> were obtained from a highly accurate partition function and are part of a comprehensive IAPWS-associated

project in which thermochemical functions for the ideal-gas properties of water and its different isotopologues are developed. The results for  $\text{H}_2^{16}\text{O}$  were published by Furtenbacher *et al.*<sup>85</sup> Because the single-molecule partition functions developed in this study do not account for the dissociation that happens in real water at high temperatures, they produced artificial maxima in the heat capacity. For heavy water this maximum occurs at about 4100 K. Since this is far beyond the upper temperature limit of the new EOS, the correlation given in Eq. (5.2) was only fitted, and is consequently only valid, up to this temperature. Comparisons between the new EOS and the available calculations<sup>84,86,87</sup> for the ideal-gas heat capacity are presented in Figure 5.4. On the absolute  $c_p^\circ, T$ -diagram, the maximum in  $c_p^\circ$  is quite distinct. It is also apparent that the new equation yields reasonable information about the ideal-gas state over a much broader temperature range than the EOS of Hill *et al.*,<sup>1</sup> which was exclusively fitted to the old data of Friedman and Haar<sup>86</sup> up to about 1500 K.

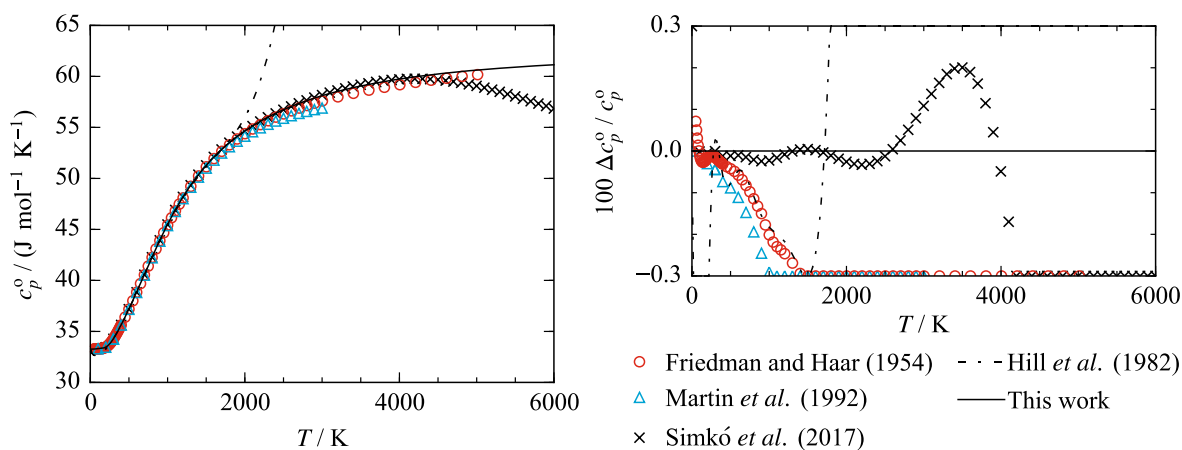


**Figure 5.4** Left: Ideal-gas heat capacity versus temperature as calculated with the new EOS and with the EOS of Hill *et al.*<sup>1</sup> The available data are included for comparison. The complete data set of Simkó *et al.*<sup>84</sup> consists of 6000 points at intervals of 1 K. Thus, only selected points are shown. The ideal-gas correlation was fitted up to 4100 K, where the data of Simkó *et al.*<sup>84</sup> reach a maximum in  $c_p^\circ$ . Right: Relative deviations  $\Delta c_p^\circ / c_p^\circ = (c_{p^\circ, \text{data}} - c_{p^\circ, \text{calc}}) / c_{p^\circ, \text{data}}$  of ideal-gas heat-capacity data from Eq. (5.2) versus temperature. The equation of Hill *et al.*<sup>1</sup> is plotted for comparison.

Based on comparisons to the data of Simkó *et al.*,<sup>84</sup> the uncertainty of calculated ideal-gas heat capacities from the new EOS is estimated to be smaller than 0.01 % at temperatures below 300 K, and within 0.02 % over the whole range of validity of the new EOS (with  $T_{\text{max}} = 825$  K). Since Eq. (5.2) was fitted up to a temperature of 4100 K, the uncertainty of calculated ideal-gas heat capacities from this correlation is still within a maximum uncertainty of 0.25 % up to 4100 K. It should be noted that these uncertainties do not match the standard uncertainties of the data as given by Simkó *et al.*,<sup>84</sup> which are stated to be below 0.01 % up to 1800 K. However, since the present ideal-gas correlation led to the best representation of the real-fluid properties, minor concessions were made in the description of the ideal-gas properties at elevated temperatures.

### 5.1.4 Thermal Saturation Data

In this section, comparisons between the new EOS and the available experimental data for thermal saturation properties, namely for the vapor pressure, the saturated-liquid and saturated-vapor density are discussed. A complete overview of the available data is given in Table B.3 in Appendix B. The table also includes the *AAD* for each data set as defined by Eq. (5.1). Aside from the overall *AAD* that was calculated for the complete data set, separate *AAD* for the low ( $T/T_c < 0.6$ ), medium ( $0.6 \leq T/T_c \leq 0.98$ ), and high ( $T/T_c > 0.98$ ) temperature range are provided.

#### 5.1.4.1 Vapor-Pressure Data

Most of the available saturation data for heavy water are measurements of the vapor pressure. In some cases, the vapor pressure was reported as a difference or ratio relative to that of ordinary water; in these cases, the IAPWS-95 formulation<sup>29,88</sup> was used to calculate the vapor pressure of ordinary water. Comparisons of available data for D<sub>2</sub>O with values calculated from the EOS are shown in Figure 5.5. The figure contains two deviation plots. The first one shows deviations of all available measurements, and thus provides an overview of the entire database. Overall, most of the available data at temperatures higher than the triple-point temperature are represented within deviations of 0.2 %. The database includes vapor pressures of the metastable subcooled liquid at temperatures below the triple-point temperature, published by Kraus and Greer<sup>89</sup> and Bottomley.<sup>80</sup> The description of this scientifically interesting region is discussed in detail in Sec. 5.1.7. For the sake of completeness, deviations of these data are included in the top panel of Figure 5.5. Most of the data of Bottomley<sup>80</sup> deviate from the EOS by less than 0.15 %, although they were not used in the fitting process. Thus, they demonstrate a good extrapolation behavior of the vapor-pressure curve calculated from the new EOS. The triple-point measurement of Markó *et al.*<sup>61</sup> is specifically highlighted in the top panel of Figure 5.5. As noted in Sec. 5.1.1, the corresponding pressure value is obviously less accurate than the available vapor-pressure data at slightly higher temperatures. In fact, the pressure deviates by  $-0.35$  % from the EOS. Therefore, the triple-point pressure provided in Table 5.1 was calculated from the EOS.

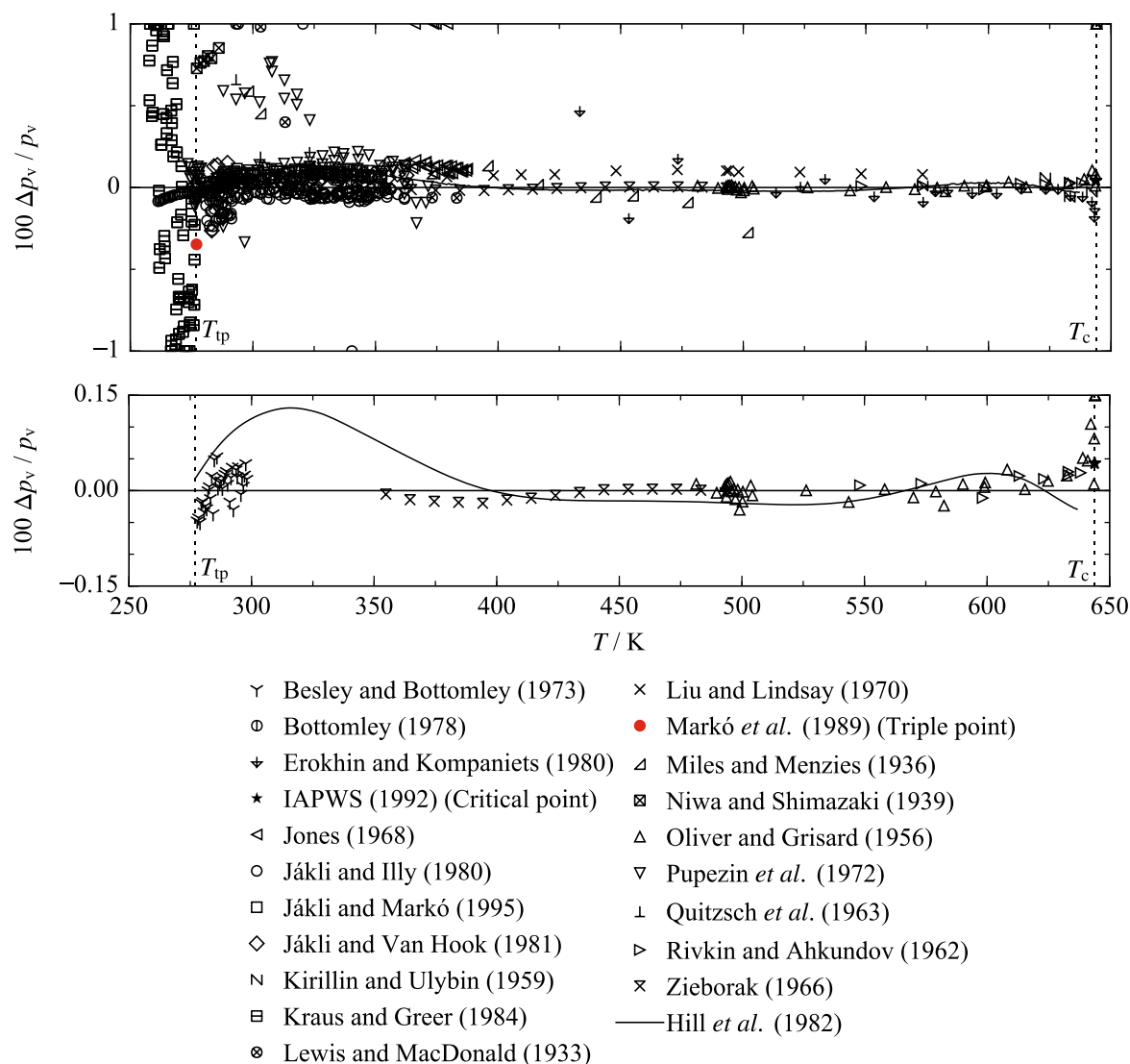


**Figure 5.5** Top: Relative deviations  $\Delta p_v / p_v = (p_{v,\text{exp}} - p_{v,\text{calc}}) / p_{v,\text{exp}}$  of the available experimental vapor-pressure data from the new EOS versus temperature. Bottom: Relative deviations of selected experimental data from the new EOS. The equation of Hill *et al.*<sup>1</sup> is plotted for comparison.

Between the triple-point temperature ( $T_{\text{tp}} = 276.969$  K) and about 300 K, the EOS was fitted to the experimental data of Besley and Bottomley,<sup>90</sup> which are the most accurate data available within this temperature range. The authors provide uncertainties of 3 mK in temperature and 0.02 Torr (about 2.67 Pa) in pressure. Considering this information, relative combined expanded ( $k = 2$ ) uncertainties were calculated for every state point. The results range from 0.02 % to 0.04 %. Except for very few data points, the EOS represents all the data within their estimated experimental uncertainty. The AAD of the data set from the equation is 0.024 %. The relative uncertainty of calculated vapor pressures is conservatively estimated to be within 0.05 % at temperatures up to 300 K. As a further reliability check, the vapor pressures for H<sub>2</sub>O provided by Besley and Bottomley<sup>90</sup> were compared to the reference equation of Wagner and Pruß<sup>29</sup> (IAPWS-95). Although the data were not used in the fitting process of IAPWS-95,<sup>29</sup> they are represented with an AAD of 0.056 %.

In the temperature range between about 300 K and 350 K, the data situation is less satisfactory than for the rest of the vapor-pressure curve, although the amount of data available is relatively large. However, all of the data sets that exhibit an acceptable level of self-consistency come from the same group of experimentalists, namely the Central Research Institute for Physics of the Hungarian Academy of Sciences in cooperation with the Chemistry Department of the University of Tennessee.<sup>79,91–93</sup> Although these data were obtained by means of the same basic experimental set-up, they exhibit considerable differences, indicating that the data are not as accurate as the best measurements at lower and higher temperatures. The earliest study from this group was published in 1972 by Pupezin *et al.*<sup>79</sup> As is apparent from Figure 5.5, these data exhibit considerable scatter. However, the EOS of Hill *et al.*<sup>1</sup> was obviously fitted to this data set, which led to a less reliable description of vapor pressures within this temperature range than with the equation presented here. The later published data sets of Jákli and Illy<sup>91</sup> and Jákli and Van Hook<sup>92</sup> are more consistent, but still exhibit scatter of up to 0.09 % and an offset of about 0.08 % from the very accurate data of Zieborak<sup>94</sup> at higher temperatures. The newest data set was established in 1995 by Jákli and Markó<sup>93</sup> within a study of excess properties of ordinary and heavy water solutions of tetrabutylammonium bromide. The vapor pressures of pure heavy water obtained in this work were not provided in the corresponding publication, but were later provided in a personal communication to Harvey and Lemmon who included them in their article.<sup>95</sup> The reproducibility of these data is roughly within 0.05 %. Considering that the data were published relative to H<sub>2</sub>O and that the uncertainty of vapor pressures calculated from IAPWS-95 is between 0.01 % and 0.02 % within this temperature range,<sup>29,88</sup> the uncertainty of the data is probably not much lower than 0.1 %. Summing up the data situation between 300 K and 350 K, the estimated relative uncertainty of calculated vapor pressures in this temperature range is 0.1 %. However, it should be noted that this estimate is quite conservative. Considering the experimental uncertainty of the data at lower and higher temperatures, the uncertainty of calculated values is expected to be lower than estimated here.

At temperatures between 350 K and 495 K, the vapor-pressure curve calculated from the EOS was mostly defined by fitting the equation to the experimental results of Zieborak.<sup>94</sup> The author states an uncertainty in pressure of 0.02 Torr (about 2.67 Pa), but does not provide comparably clear information about the uncertainty in temperature. Nevertheless, azeotropic temperatures of the H<sub>2</sub>O + D<sub>2</sub>O mixture are reported with an accuracy of 3 mK. Based on this information, combined expanded ( $k = 2$ ) uncertainties were estimated that range from 0.01 % to 0.03 %. The maximum deviation of these data from the EOS is 0.02 % and their overall AAD is 0.008 %. Considering these deviations and the experimental uncertainty of the data, the estimated relative expanded uncertainty of calculated vapor pressures is 0.03 %.

Between about 495 K and the critical temperature ( $T_c = 643.847$  K), the most reliable data were published by Oliver and Grisard.<sup>69</sup> Above 548 K the data overlap with the vapor pressures of Rivkin and Akhundov,<sup>64</sup> who provided no clear information about experimental uncertainties. However, the data confirm the vapor pressures of Oliver and Grisard<sup>69</sup> within about 0.03 %. Oliver and Grisard<sup>69</sup> measured the saturation temperature relative to ordinary water within 0.01 K. The reported pressures were obtained using the H<sub>2</sub>O vapor-pressure correlation of Osborne and Meyers,<sup>96</sup> which is negligibly different from IAPWS-95 in this region. Since the uncertainty of IAPWS-95 in this region is within 0.02 %, <sup>29,88</sup> this can be considered as a good estimate for the uncertainty in saturation pressure of the data by Oliver and Grisard.<sup>69</sup> Thereby, the estimated relative combined expanded ( $k = 2$ ) uncertainties of these data are within 0.06 %. However, at temperatures up to 642 K deviations between these data and the EOS are below 0.05 %, and the data are confirmed by the values of Rivkin and Akhundov.<sup>64</sup> Very close to the critical temperature, the deviations of the data increase up to 0.1 %, but the critical pressure recommended by IAPWS<sup>60</sup> is represented within 0.05 %. As already discussed in Sec. 5.1.1, for a fixed critical temperature, the uncertainty of the IAPWS value is 0.01 MPa, which corresponds to a relative uncertainty of 0.05 %. The EOS consequently represents the critical pressure within its given uncertainty. Therefore, an expanded relative uncertainty in calculated vapor pressures at temperatures between 495 K and the critical temperature of 0.05 % is estimated. A complete overview of the estimated relative uncertainties of calculated vapor pressures as discussed in this section is provided in Figure 5.6.

From Figure 5.5, it is apparent that the new EOS enables a better description of the vapor-pressure curve than the EOS of Hill *et al.*<sup>1</sup> The most significant improvements were obtained at temperatures below 400 K, where the equation of Hill *et al.*<sup>1</sup> was obviously fitted to the less reliable data of Pupezin *et al.*<sup>79</sup> Furthermore, Hill *et al.* did not consider the very accurate data of Besley and Bottomley.<sup>90</sup> Figure 5.5 additionally highlights why IAPWS does not recommend Hill's EOS for calculations in the critical region bordered by  $|T - T_c| \leq 10$  K and  $|\rho / \rho_c - 1| \leq 0.3$ . In fact, numerical issues with this previous standard EOS did not allow including vapor pressures calculated at temperatures higher than approximately 638 K in Figure 5.5.



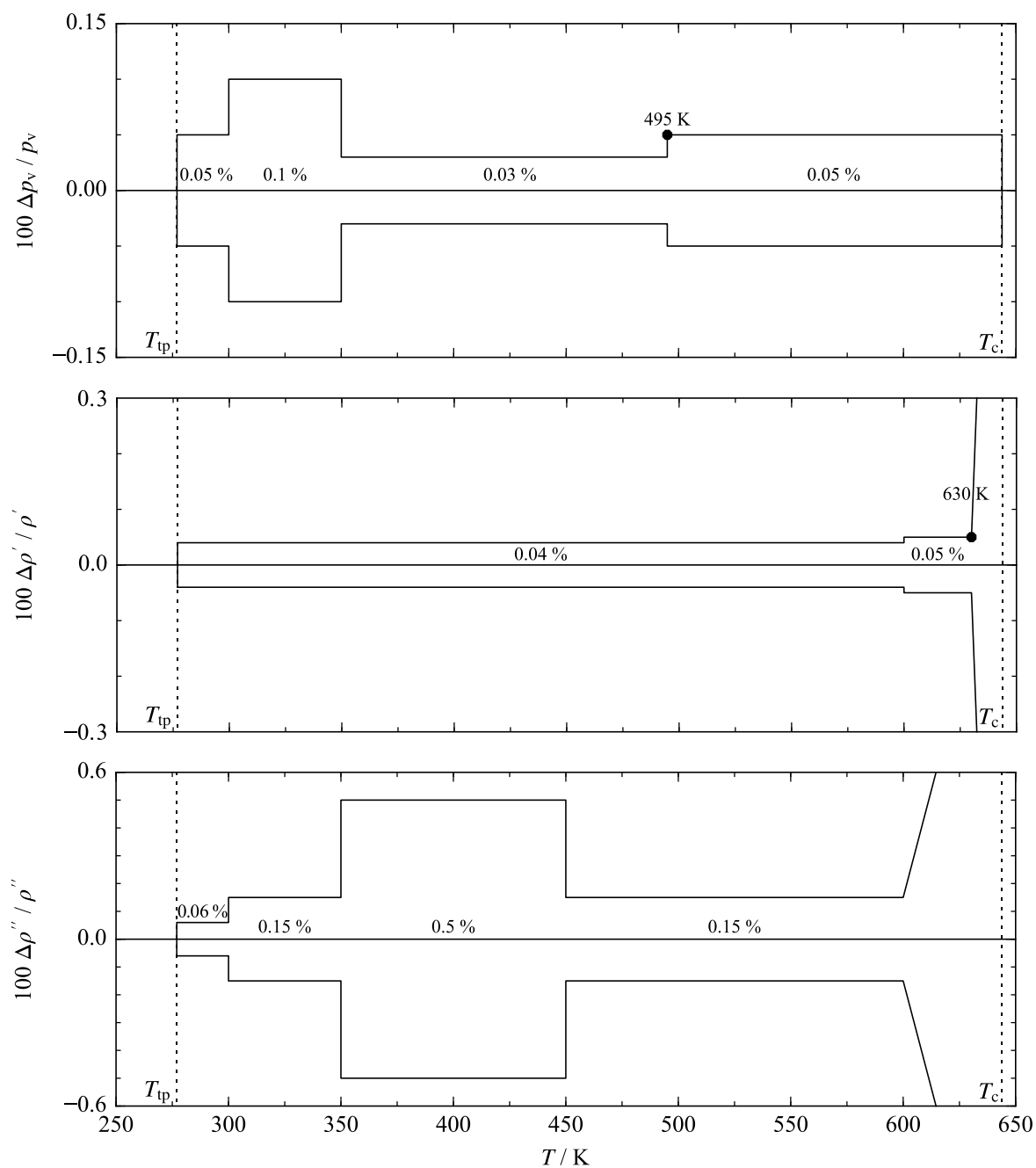


**Figure 5.6** Uncertainties in vapor pressure,  $\Delta p_v / p_v$ , in saturated liquid density,  $\Delta \rho' / \rho'$ , and in saturated vapor density,  $\Delta \rho'' / \rho''$ , estimated for the new EOS. The uncertainties for the saturated densities increase linearly to 1.5 % at the critical temperature.

#### 5.1.4.2 Saturated-Density Data

In comparison to the previously discussed situation for vapor pressures, the data for saturated-liquid and saturated-vapor densities are quantitatively and qualitatively quite limited. Thus, none of the available data sets was used to fit the EOS. Deviations of the data for both properties are shown in Figure 5.7.

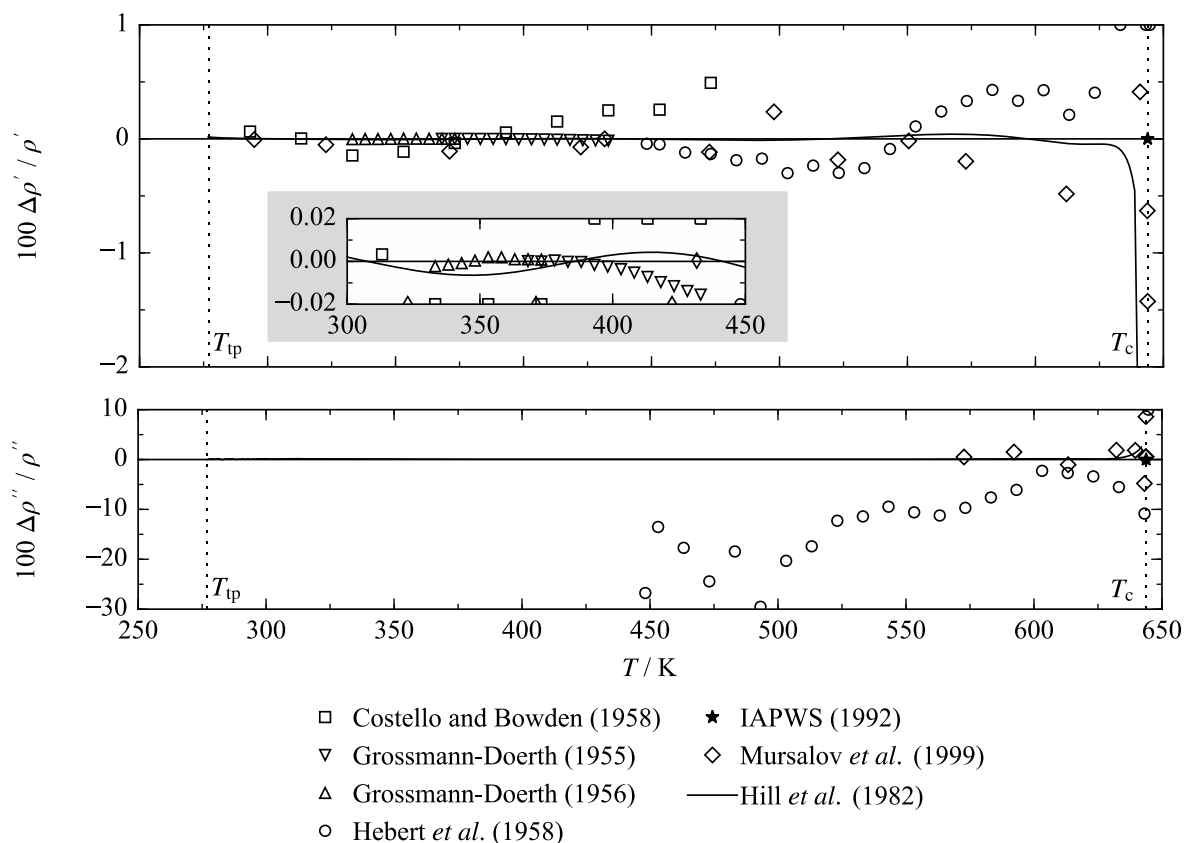


**Figure 5.7** Top: Relative deviations  $\Delta\rho' / \rho' = (\rho'_{\text{exp}} - \rho'_{\text{calc}}) / \rho'_{\text{exp}}$  of experimental saturated-liquid density data from the new EOS versus temperature. The EOS of Hill *et al.*<sup>1</sup> is plotted for comparison. Bottom: Relative deviations  $\Delta\rho'' / \rho'' = (\rho''_{\text{exp}} - \rho''_{\text{calc}}) / \rho''_{\text{exp}}$  of experimental saturated-vapor density data from the new EOS.

The saturated-liquid density data cover almost the entire phase boundary from the triple point up to the critical temperature. The new EOS represents most of these experimental data within 0.5 %, except for some points close to the critical temperature. The newest reference was published by Mursalov *et al.*<sup>97</sup> Their data cover the complete temperature range of vapor-liquid equilibrium. The authors state an uncertainty of 0.05 % in temperature and 0.04 % in volume. Based on this information, the estimated combined uncertainties range from 0.1 % to 0.4 % for temperatures up to 640 K and increase closer to the critical temperature. Except for one point, the new EOS represents this data set within its experimental uncertainty. The most valuable experimental results were measured by Grossmann-Doerth, who published two remarkably accurate data sets in 1955 and 1956.<sup>98,99</sup> The measurements were carried out relative to  $\text{H}_2\text{O}$ . The author states an uncertainty in the ratio between the mass density of  $\text{D}_2\text{O}$  and  $\text{H}_2\text{O}$  of  $3 \times 10^{-5}$ . The saturation temperature is reported with an uncertainty of 0.1 K. Hence, the combined expanded ( $k = 2$ ) uncertainty of the saturated density is estimated to be below 0.03 %. Although the new EOS was not fitted to these data, all points exhibit deviations less than 0.02 %, which underlines the high accuracy of the data and their consistency with the vapor pressures and the homogeneous-density data used to fit the EOS. Hebert *et al.*<sup>100</sup> published their saturated-liquid data with an uncertainty estimate of 1 %, which seems too pessimistic. Although none of the data points was used for fitting the EOS, all deviations are within 0.5 % (except close to the critical

temperature). The publication of Costello and Bowden<sup>101</sup> does not provide any statement on the experimental uncertainty. The maximum deviation of the data is 0.5 %.

Aside from the data of Grossmann-Doerth,<sup>98,99</sup> none of the available data sets is accurate enough to yield appropriate uncertainty estimates for saturated-liquid densities calculated from the new EOS. Therefore, it is important to consider that the density at saturation is not a completely independent property, but a subset of the homogenous density close to the phase boundary  $\rho(T, p)$ . This implies that fitting the EOS to accurate homogenous densities leads to an accurate description of saturated densities, if additional high-quality saturation pressures  $p_v(T)$  are available. Hence, the combined expanded uncertainty in saturated density can be defined reasonably by adding the uncertainty in homogenous density  $u_c(\rho)$  and the uncertainty contribution of the vapor pressure in quadrature. The latter can be determined from the relative uncertainty in vapor pressure estimated in Sec. 5.1.4.1 ( $U_r(p_v) = \Delta p_v / p_v$  in Figure 5.6) multiplied by  $p_v$  and the sensitivity coefficient  $(\partial \rho / \partial p)_{\text{sat}}$  calculated from the EOS. The uncertainty of the homogenous density close to the phase boundary can be reasonably estimated by multiplying the relative uncertainty of the homogenous density by the saturated density. The finally obtained combined uncertainty in saturated density  $u_c(\rho_{\text{sat}})$  is:

$$u_c(\rho_{\text{sat}}) \approx \sqrt{\left[ U_r(p_v) \times p_v \right]^2 \left( \frac{\partial \rho}{\partial p} \right)_{\text{sat}}^2 + \left[ U_r(\rho) \times \rho_{\text{sat}} \right]^2}. \quad (5.10)$$

Over most of the temperature range, the saturated-liquid density is not very sensitive to the pressure and the uncertainty in saturation pressure can be neglected. Thus, the uncertainty in the saturated-liquid density should to a good approximation be no larger than the uncertainty in the homogeneous-liquid density. An uncertainty analysis for this property is discussed in detail in Sec. 5.1.5.1. Between the triple-point temperature and 315 K, the uncertainty in liquid density is 0.04 %, which is adopted as the uncertainty of the saturated-liquid density in this temperature range. The data of Grossmann-Doerth<sup>98,99</sup> cover a temperature range from 333 K up to 434 K. Due to the high quality of these data, the relative uncertainty of calculated saturated-liquid densities in this region is estimated to be 0.04 %. Considering the excellent extrapolation behavior of the new EOS, the uncertainty from the triple-point temperature up to 435 K is defined to be 0.04 %. The 0.04 % uncertainty region can reasonably be extended up to 600 K, corresponding to the uncertainty in liquid density (see Sec. 5.1.5.1). At higher temperatures, the sensitivity coefficient  $(\partial \rho / \partial p)_{\text{sat}}$  becomes larger, which leads to slightly higher combined uncertainties. The estimated uncertainty is therefore increased to 0.05 % between 600 K and 630 K. The phase boundary at temperatures above 630 K is within the critical region (discussed in Sec. 5.1.5.1), where the uncertainty in density increases considerably. The uncertainty of the critical density recommended by IAPWS<sup>60</sup> and given in Sec. 5.1.1 is about 1.5 %. Because the new EOS represents this value with a negligible

deviation, the uncertainties in calculated saturated-liquid densities are estimated to increase linearly from 0.05 % at 630 K to 1.5 % at the critical temperature. The results of the uncertainty analyses for calculated saturated-liquid densities over the entire temperature range of the phase boundary are summarized in Figure 5.6.

The saturated-vapor density was measured by Hebert *et al.*<sup>100</sup> at temperatures above 448 K. At lower temperatures, no experimental data are available. Hebert *et al.*<sup>100</sup> state that between 200 °C and 370 °C their data for light water deviate by about 10 % from the literature values. At higher and lower temperatures, these deviations are even larger. Consequently, comparisons of their data for heavy water do not provide any valuable information on the uncertainty of the new EOS. The above-discussed publication by Mursalov *et al.*<sup>97</sup> contains densities of the saturated vapor at temperatures above 572 K. Considering the given information on their accuracy in temperature and volume, the relative expanded ( $k = 2$ ) uncertainties of their data are within 2 % below 630 K. At higher temperatures, the experimental uncertainties increase significantly. The EOS represents nearly all data points within their uncertainty. Analogous to the experimental saturated-liquid data, the overall data situation for the saturated-vapor density does not allow for reasonable uncertainty estimates for values calculated from the EOS. Therefore, the uncertainty estimates are based on Eq. (5.10). Unlike for the saturated-liquid density, the uncertainty of the saturation pressure is essential for the accuracy of calculated saturated-vapor densities. Thus, the estimated uncertainties in homogeneous vapor density (see Sec. 5.1.5.1) and in vapor pressure (as summarized in Figure 5.6) were considered and the sensitivity coefficient  $(\partial\rho/\partial p)_{\text{sat}}$  was calculated from the EOS. The uncertainties in saturated-vapor densities calculated in this way are: 0.06 % between the triple-point temperature and 300 K (where  $U_r(p_v) = \Delta p / p = 0.05$  % and  $U_r(\rho) = \Delta\rho / \rho = 0.03$  %), 0.15 % between 300 K and 350 K ( $U_r(p_v) = U_r(\rho) = 0.1$  %), 0.5 % between 350 K and 450 K ( $U_r(p_v) = 0.03$  %,  $U_r(\rho) = 0.5$  %), and 0.15 % between 450 K and 600 K ( $U_r(p_v) = 0.05$  %,  $U_r(\rho) = 0.1$  %). At temperatures above 600 K, the sensitivity of the saturated-vapor density to the vapor pressure,  $(\partial\rho/\partial p)_{T_{\text{sat}}}$ , as well as the total uncertainty in density,  $U_r(\rho) \times \rho$ , increase significantly. Therefore, a linear increase of the uncertainties of calculated saturated-vapor densities from 0.15 % at 600 K to 1.5 % at the critical temperature is estimated. All results of the uncertainty analysis for calculated saturated-vapor densities are illustrated in Figure 5.6.

For the EOS of Hill *et al.*,<sup>1</sup> no uncertainty analysis for saturated densities was published. Thus, and due to the poor data situation, a clear statement about the accuracy of that equation with regard to these properties is difficult. However, calculated saturated densities from both EOS agree within the estimated uncertainties. But the new EOS allows for a reliable description of saturated densities in the critical region, where it is not recommended to calculate properties from the previous standard EOS.

### 5.1.5 Homogeneous Density and Virial Coefficient Data

This section presents comparisons between the available experimental data on homogeneous densities and values calculated from the present EOS. Since both properties are strongly correlated, the representation of virial coefficients is presented in the subsequent subsection. In order to provide a complete overview, the available experimental data for homogeneous densities are summarized in Table B.4 in Appendix B. In addition to the overall *AAD*, the table provides separate *AAD* for the vapor, liquid, critical, and supercritical state regions. The supercritical region is subdivided into three areas: the region of low densities ( $\rho / \rho_c < 0.6$ ), of medium densities ( $0.6 \leq \rho / \rho_c \leq 1.5$ ), and of high densities ( $\rho / \rho_c > 1.5$ ). An overview of the available data for the second virial coefficient  $B$  and the third virial coefficient  $C$  is given in Table B.5. The *AAD* are calculated for the complete temperature range. Since percentage deviations are less meaningful for virial coefficients, the *AAD* are given as absolute instead of relative values; these *AAD* are dominated by the values at the lowest temperatures where the magnitude of the virial coefficients is large

#### 5.1.5.1 Density Data

Aside from speed-of-sound measurements, homogeneous density data, also called “ $p\nu T$  data”, are often the most accurate experimental data available. Thus, the majority of the experimental values included in fitting the new EOS are  $p\nu T$  measurements. Therefore, comparisons of the available  $p\nu T$  data and calculated values are important to evaluate the new EOS. Due to the large amount of experimental data, only the most important data sets can be discussed here. An overview of the database and its description by means of the new EOS and the EOS by Hill *et al.*<sup>1</sup> is given in Figure 5.8. The most obvious improvements in accuracy are shown in color, namely the description of the two accurate and comprehensive vapor and liquid-phase data sets of Kell *et al.*<sup>102,103</sup> and the high-pressure data of Bridgman.<sup>73</sup>

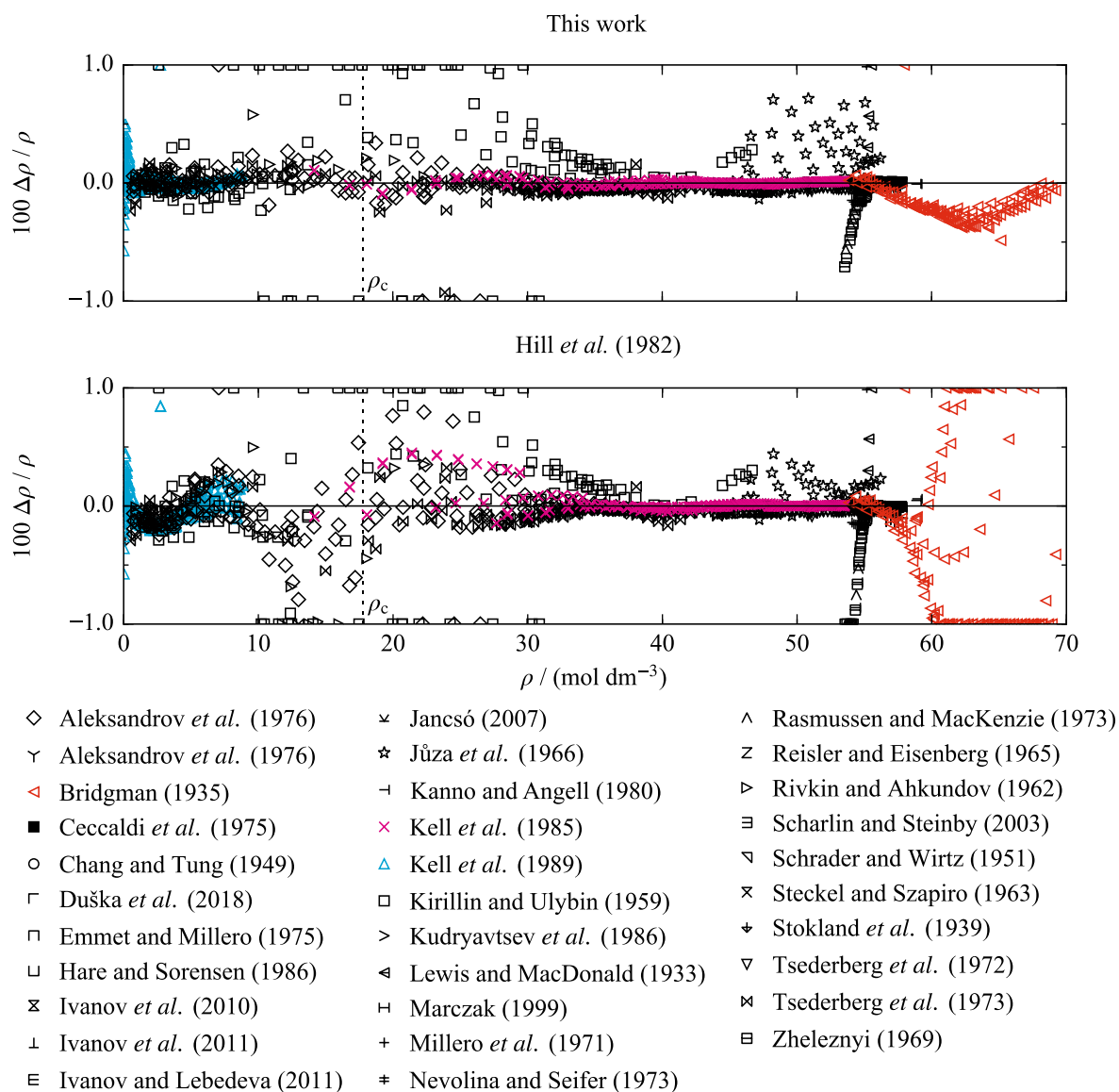


**Figure 5.8** Top: Relative deviations  $\Delta\rho / \rho = (\rho_{\text{exp}} - \rho_{\text{calc}}) / \rho_{\text{exp}}$  of experimental density data from the new EOS versus density. Bottom: Relative deviations of experimental density data from the equation of Hill *et al.*<sup>1</sup>

In the homogeneous vapor phase, the EOS was exclusively fitted to the experimental data of Kell *et al.*<sup>102</sup> This data set comprises the largest number of data points (more than 600) and is within IAPWS considered to be one of the most reliable experimental studies on heavy water. The data range from 423 K to 774 K at pressures up to 37 MPa. Deviations of the data from the new EOS versus temperature and pressure are shown in Figure 5.9. Despite the overall high quality of these data, the corresponding publication is quite brief with regard to information on experimental uncertainties. The authors state their uncertainties in density to be between  $0.1 \text{ mmol dm}^{-3}$  and  $0.3 \text{ mmol dm}^{-3}$ ,<sup>102</sup> which can be interpreted as standard uncertainties in the density measurement, not including any effects of temperature or pressure uncertainty. Earlier papers of Kell and co-workers,<sup>104–106</sup> in which their experimental set-up is discussed in detail, state uncertainties of 2 mK in temperature and 1 mbar in pressure. Considering this information, combined expanded ( $k = 2$ ) uncertainties for every state point were calculated that range from  $0.6 \text{ mmol dm}^{-3}$  to  $1 \text{ mmol dm}^{-3}$ . Except

for a few points, the EOS represents the data within their experimental uncertainties. Since the data cover a wide range of densities ( $0.03 \text{ mol dm}^{-3}$  to  $8.8 \text{ mol dm}^{-3}$ ), their relative uncertainties as well as the deviations from the EOS vary considerably. However, excluding the two lowest isotherms, the EOS represents more than 95 % of the data within 0.1 %, which is adopted as an uncertainty estimate for calculated vapor densities between 450 K and 775 K including the supercritical gas-like fluid at pressures up to 30 MPa. The measurements of the two lowest isotherms (423 K and 448 K) are known to be less accurate, as discussed in detail in the IAPWS-95 publication for ordinary water.<sup>29</sup> Based on the deviations of these data, the estimated uncertainty of calculated vapor densities in this temperature range is 0.5 %.

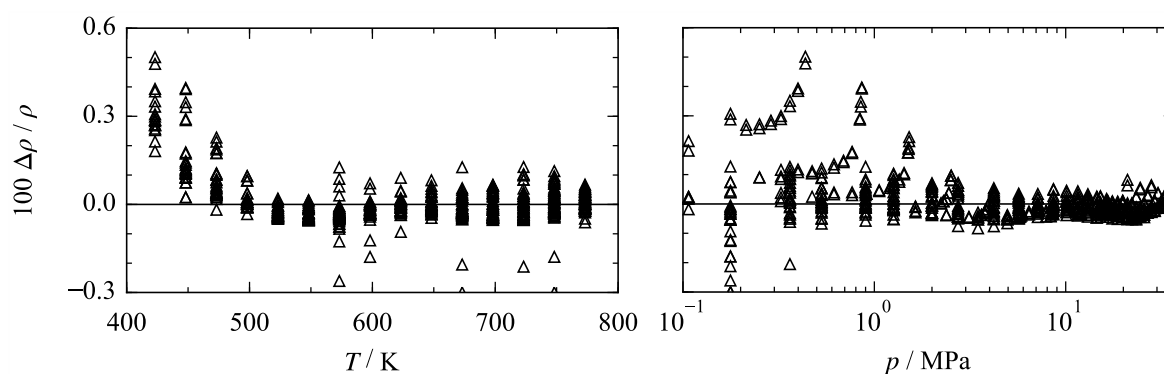


**Figure 5.9** Left: Relative deviations  $\Delta\rho / \rho = (\rho_{\text{exp}} - \rho_{\text{calc}}) / \rho_{\text{exp}}$  of the experimental vapor density data of Kell *et al.*<sup>102</sup> from the new EOS versus temperature. Right: Relative deviations of the experimental data of Kell *et al.*<sup>102</sup> from the new EOS versus pressure.

At temperatures lower than the temperature range investigated by Kell and co-workers, there are no experimental vapor-density data available. However, it is still possible to obtain a reasonable estimate of the uncertainty of the EOS in this region. Because the pressure in this region does not exceed 0.5 MPa ( $p_v(423 \text{ K}) = 0.46 \text{ MPa}$ ), the vapor density can be described by a virial equation truncated after the second virial coefficient. The EOS accurately reproduces values of the second virial coefficient  $B(T)$  obtained from first principles (see Sec. 5.1.5.2). Any uncertainty in  $B(T)$  translates directly into a relative uncertainty in  $z - 1$ , where  $z$  is the compressibility factor  $p / \rho RT$ . A conservative estimate of a 10 % expanded uncertainty in  $B(T)$ , taken at the maximum pressure  $p_v$  where the nonideality is greatest, produces the uncertainty estimates shown in Figure 5.10. Between 350 K and 425 K, this estimate conveniently matches the uncertainty estimated based on the two lowest isotherms measured by Kell *et al.*<sup>102</sup> Thus, the estimate of a 0.5 % uncertainty of calculated vapor densities is extended to the temperature range from 350 K to 450 K. At lower temperatures down to 300 K, the uncertainty is within 0.1 %; and at temperatures below 300 K it does not exceed 0.03 %. In fact, the real uncertainties in density are even smaller at the lowest pressures shown in Figure 5.10, because in the low-pressure limit the density approaches that of the ideal gas, which is known almost exactly. In Figure 5.11, selected experimental data including the vapor-phase data of Kell *et al.*<sup>102</sup> are shown along various

(quasi-)isotherms. Solid lines represent results of the previous standard EOS of Hill *et al.*<sup>1</sup> Comparing the representation of the vapor-phase data of Kell *et al.*<sup>102</sup> with the new EOS and the EOS of Hill *et al.*<sup>1</sup> shows that the previous standard EOS enables a comparably accurate description of the data for the lowest three isotherms (423 K to 473 K). At higher temperatures, values calculated from the EOS of Hill *et al.*<sup>1</sup> exhibit higher deviations from this data set. Especially at elevated pressures and densities, the new EOS yields considerably more accurate results (see also Figure 5.8). It should consequently be noted that the description of densities in the homogenous vapor phase is improved by the EOS presented here.

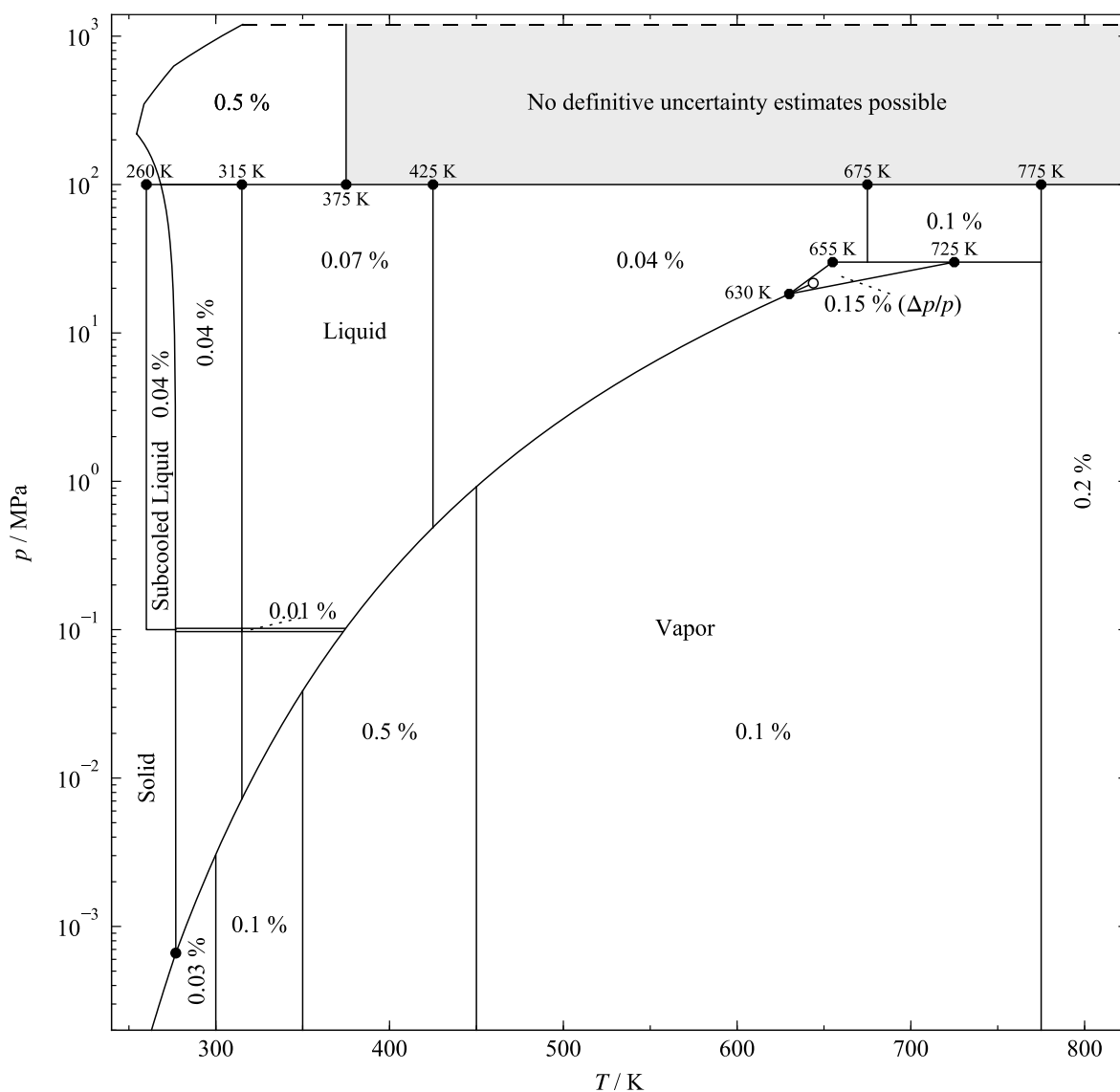


**Figure 5.10** Expanded relative uncertainties in density,  $\Delta\rho/\rho$ , estimated for the new EOS. In the enlarged critical region (triangle), the uncertainty is given as percentage uncertainty in pressure,  $\Delta p/p$ . This region is bordered by the two isochores  $8 \text{ mol dm}^{-3}$  and  $29 \text{ mol dm}^{-3}$  and by the 30 MPa isobar. The positions of the lines separating the uncertainty regions are approximate. At low pressures for the vapor, the uncertainties become much smaller than indicated because the vapor is nearly an ideal gas.



Highly accurate densities of liquid heavy water from its melting line up to 315 K and at pressures up to 100 MPa were recently measured by Duška *et al.*<sup>107</sup> at the Institute of Thermomechanics in Prague. The data set also includes measurements in the metastable subcooled-liquid region that are discussed in Sec. 5.1.7. In personal communications, the experimentalists estimated the so far unpublished data to be accurate within an expanded ( $k = 2$ ) uncertainty of 0.04 %. As is apparent from Figure 5.11, this uncertainty is confirmed by the accurate data sets of Emmet and Millero<sup>108</sup> and Aleksandrov *et al.*<sup>109</sup>

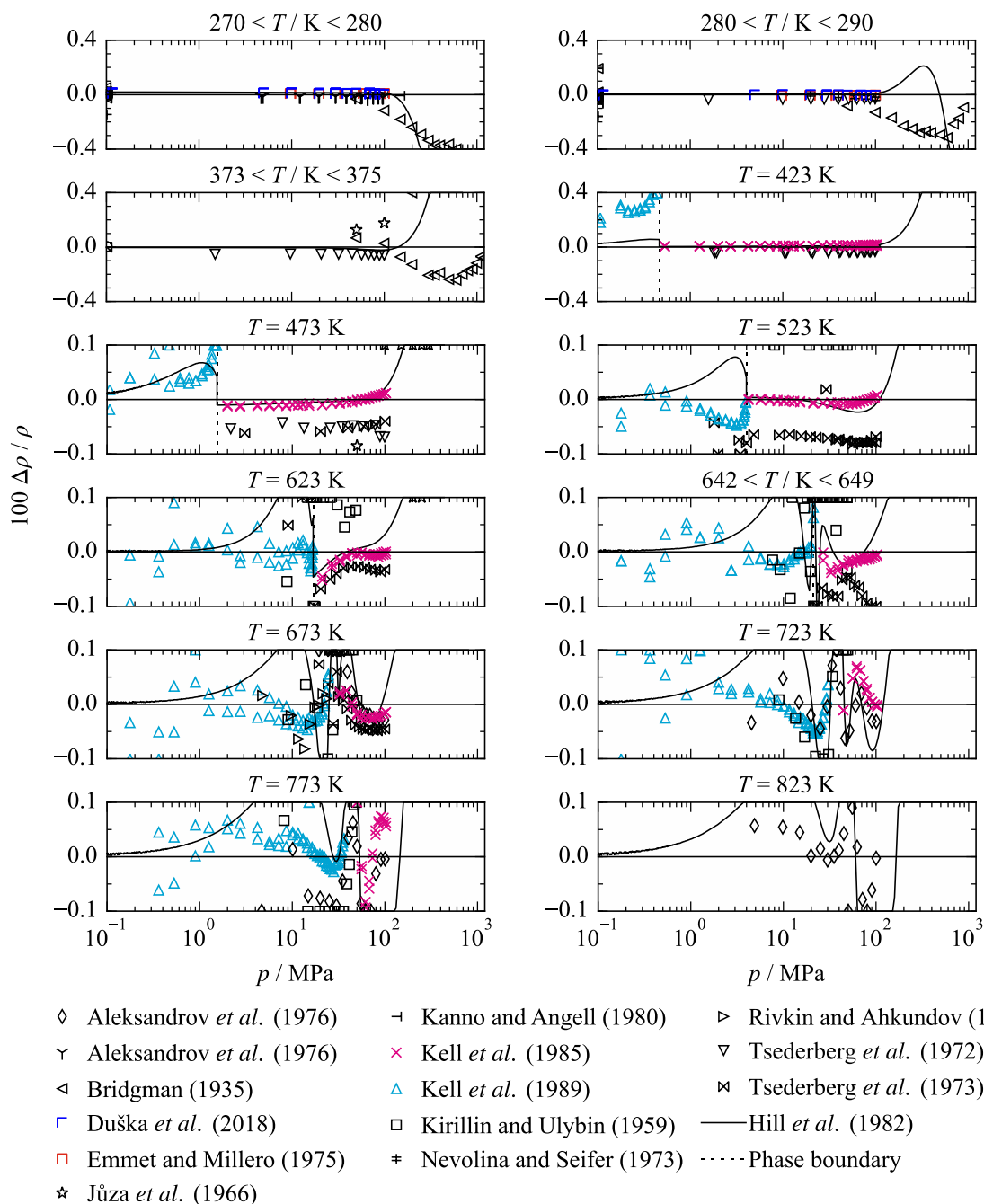


**Figure 5.11** Relative deviations  $\Delta\rho/\rho = (\rho_{\text{exp}} - \rho_{\text{calc}})/\rho_{\text{exp}}$  of selected experimental density data along (quasi-)isotherms from the new EOS. The EOS of Hill *et al.*<sup>1</sup> is plotted for comparison. For plots showing a temperature range, the EOS of Hill *et al.*<sup>1</sup> was calculated at the average temperature. The first four diagrams have a larger deviation scale than the other diagrams.

Since the EOS describes all the data of Duška *et al.*<sup>107</sup> within their experimental uncertainty, the estimated uncertainty of liquid densities calculated from the present EOS is 0.04 % at temperatures up to 315 K and pressures up to 100 MPa. At temperatures between 315 K and 423 K, the most reliable liquid densities at pressures exceeding 1 atm (0.101 325 MPa) were published by Tseederberg *et al.*<sup>110</sup> The authors state an accuracy of  $0.0015 \text{ cm}^3 \text{ g}^{-1}$ , which was interpreted as the standard uncertainty of their results. The corresponding relative uncertainties are between 0.05 % and 0.06 %, which would be equivalent to an expanded uncertainty of about 0.1 %. However, although the EOS was not fitted to these data, all data points between 315 K and 423 K are represented within deviations of 0.06 %. Thus, the uncertainty of calculated liquid densities between 315 K and 425 K at pressures up to 100 MPa is estimated to be 0.07 %. As is apparent from Figure 5.11, liquid densities calculated from the present EOS and the previous standard EOS are in quite good agreement within the region from the melting line up to 425 K and pressures up 100 MPa and higher than 1 atm. In fact, deviations between the two EOS are within the uncertainties of the data.

A particularly detailed evaluation of the EOS should be made for liquid densities at atmospheric pressure, and thus at temperatures between the normal-melting-point temperature  $T_m \approx 276.961 \text{ K}$  as calculated from Eq. (5.4) and the normal-boiling-point temperature  $T_{\text{nbp}} \approx 374.549 \text{ K}$ . For  $\text{H}_2\text{O}$ , there are extremely accurate experimental data at these conditions. In fact, the relative uncertainty of these metrological measurements is within  $10^{-6}$  (1 ppm).<sup>29,111</sup> For  $\text{D}_2\text{O}$ , the available data are of clearly lower quality but there are still some very accurate data sets. Deviations of the most reliable data from the new EOS and the EOS of Hill *et al.*<sup>1</sup> are shown in Figure 5.12.

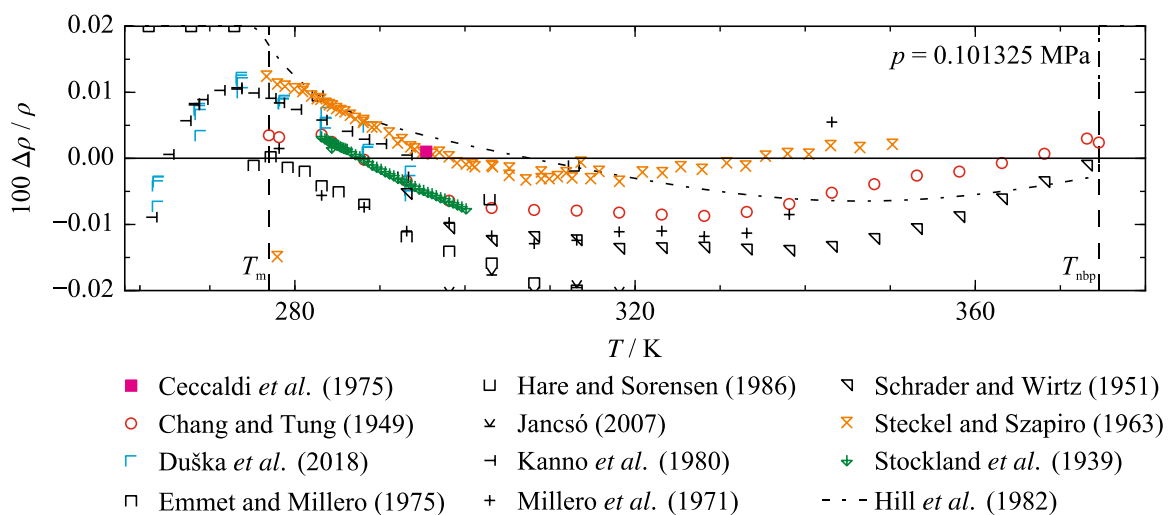


**Figure 5.12** Relative deviations  $\Delta\rho / \rho = (\rho_{\text{exp}} - \rho_{\text{calc}}) / \rho_{\text{exp}}$  of the most accurate experimental density data in the liquid phase at atmospheric pressure from the new EOS. The EOS of Hill *et al.*<sup>1</sup> is plotted for comparison.

The only data set covering the entire temperature range from the freezing to the boiling point was published by Chang and Tung<sup>112</sup> in 1949. Despite the age of this work, the data are of remarkably high quality. Over the complete temperature range, the data exhibit deviations

below 85 ppm. The authors corrected their data to 100 % D<sub>2</sub>O and provide an experimental uncertainty of 0.05 g dm<sup>-3</sup>, which corresponds to about 2.5 mmol dm<sup>-3</sup>. The resulting relative expanded uncertainties are within 94 ppm. Accordingly, the EOS represents every state point within its experimental uncertainty. The publication additionally includes measurements of H<sub>2</sub>O at identical temperatures. In this state region, liquid densities calculated from IAPWS-95 are accurate to 1 ppm. The H<sub>2</sub>O densities of Chang and Tung<sup>112</sup> deviate from IAPWS-95 by less than 31 ppm, which confirms the high quality of the data. In addition, their D<sub>2</sub>O data are in remarkably good agreement with the measurements of Stokland *et al.*<sup>113</sup> The experimentalists involved in this work were among the pioneers of heavy water research. Nevertheless, the claimed experimental uncertainty of 10<sup>-5</sup> kg dm<sup>-3</sup>, which is equivalent to an expanded relative uncertainty of about 18 ppm, seems somewhat underestimated, although the data are obviously quite accurate with deviations below 76 ppm. Aside from these data sets, the most accurate measurements covering a range of temperature were published by Steckel and Szapiro.<sup>114</sup> The reliability of the data was verified by comparing their measurements of H<sub>2</sub>O with IAPWS-95. The calculated deviations are nowhere larger than 18 ppm. The D<sub>2</sub>O data set includes a result for the maximum density of heavy water that is reported with an uncertainty of 3 × 10<sup>-5</sup> g ml<sup>-1</sup> (1.5 mmol dm<sup>-3</sup>). Adopting this value as the experimental uncertainty of the density measurement over the entire range of the data, and adding the uncertainty contribution of the D<sub>2</sub>O purity of the sample in quadrature, yields a relative expanded uncertainty of approximately 60 ppm. The uncertainty contribution of the D<sub>2</sub>O purity can be estimated by calculating the deviation of the reported density  $\rho_{\text{sample}}$  (for 99.78 mol% D<sub>2</sub>O, meaning that 99.78 % of the hydrogen atoms are D) from the value corrected to 100 % D<sub>2</sub>O. The corrected density  $\rho_{\text{D}_2\text{O}}$  is defined as:

$$\rho_{\text{D}_2\text{O}} = \frac{x_{\text{D}_2\text{O}}}{\left(\rho_{\text{sample}}^{-1} - (1 - x_{\text{D}_2\text{O}})\rho_{\text{H}_2\text{O}}^{-1}\right)}, \quad (5.11)$$

where  $x_{\text{D}_2\text{O}}$  is the molar D fraction of the investigated sample and  $\rho_{\text{H}_2\text{O}}$  is the density of ordinary water as calculated from IAPWS-95 at the given temperature and pressure. At temperatures above 287 K, the EOS represents all data points of Steckel and Szapiro<sup>114</sup> within their uncertainty. At lower temperatures, the deviations are within 0.01 %, except for the last two data points that exhibit slightly higher deviations. More intensive fitting of the EOS to the data at temperatures below 287 K led to lower deviations, but worsened the representation of the data in the metastable subcooled liquid region (see Sec. 5.1.7). The already discussed experimental work of Duška *et al.*<sup>107</sup> includes some measurements at atmospheric pressure and temperatures up to 294 K. The investigated sample contained 99.993 mol% D. The uncertainty contribution of the remaining H<sub>2</sub>O content is below 1 ppm as estimated from Eq. 5.11, and thus negligible. Since the main focus of this experimental investigation was metastable subcooled heavy water, the provided expanded uncertainty of

0.04 % is a conservative estimate for the densities of the stable liquid phase. In fact, above the freezing point all data are represented within a maximum deviation of 85 ppm. The data confirm the measurements of Steckel and Szapiro<sup>114</sup> and Chang and Tung,<sup>115</sup> with slightly better agreement with the latter data set. Considering the deviations of these accurate data sets, the uncertainty of liquid densities at atmospheric pressure is estimated to be within 0.01 % at temperatures from the freezing point to the normal boiling point. From Figure 5.12, it can be seen that the EOS agrees with the previous standard EOS within this estimated uncertainty except in a small temperature range from the melting-point temperature to 282 K. There, the EOS of Hill *et al.*<sup>1</sup> provides a more accurate description of the data of Steckel and Szapiro.<sup>114</sup>

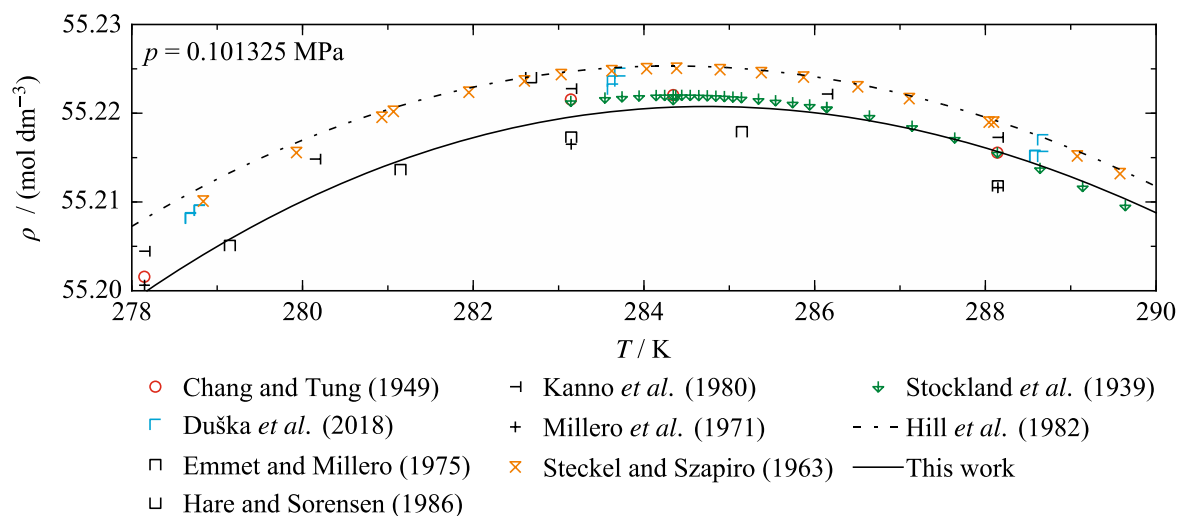
Some additional comments should be made about the experiments of Ceccaldi *et al.*<sup>116</sup> carried out at the Bureau International des Poids et Mesures (BIPM), Paris, and published in 1975. This extremely thorough work presents the density of D<sub>2</sub>O at 22.3 °C and 1 atm with metrological accuracy. The authors claim a precision on the order of 10<sup>-3</sup> kg m<sup>-3</sup>, which corresponds to 0.05 mmol dm<sup>-3</sup>. This precision is equivalent to a relative expanded ( $k = 2$ ) uncertainty of approximately 2 ppm. The exact isotopic composition of the sample was carefully studied (with regard to both hydrogen and oxygen isotopes) and the density was then corrected to isotopically pure D<sub>2</sub>O with all oxygen atoms being ordinary oxygen <sup>16</sup>O. Since “standard” heavy water also contains certain proportions of the heavier oxygen isotopes <sup>17</sup>O and <sup>18</sup>O (see Sec. 2.1), the mass-based density of Ceccaldi *et al.*<sup>116</sup> must be converted to a molar value not by means of the molar mass given in Figure 5.5 but instead by  $M = 20.023\ 118\ \text{g mol}^{-1}$ , which is the molar mass of isotopically pure D<sub>2</sub><sup>16</sup>O. The so-obtained molar density deviates from the new EOS by 10 ppm (and by about 25 ppm from the previous standard EOS) Thus, it is not represented within its experimental uncertainty. Nevertheless, its small deviation underscores the high accuracy of both the new EOS and of the other accurate experimental data at atmospheric pressures (see Figure 5.12).

When discussing the representation of liquid densities, the description of the maximum density of heavy water is of special interest. For ordinary water, the maximum density at atmospheric pressure is widely known to occur at approximately 4 °C, or to more digits 3.983 °C, as recommended by Tanaka *et al.*<sup>111</sup> The physical behavior of heavy water exhibits the same anomalous negative isothermal expansion, but the resulting maximum density and its corresponding temperature are less accurately investigated. An overview of parameters taken from the literature and calculated from the new EOS as well as from the EOS of Hill *et al.*<sup>1</sup> is given in Table 5.4. All temperatures were converted to ITS-90. The temperature of the maximum density at 1 atm is reported in various references, but only two of them also present the corresponding density. The new EOS deviates from the maximum density of Stokland *et al.*<sup>113</sup> by about 18 ppm, which is within the claimed (but questioned) experimental uncertainty of this value. The result of Steckel and Szapiro<sup>114</sup> is represented within 73 ppm and thus not within the estimated experimental uncertainty of 60 ppm.

**Table 5.4** Maximum density of D<sub>2</sub>O at atmospheric pressure and its corresponding temperature as taken from the literature and calculated from the new EOS and the EOS of Hill *et al.*<sup>1</sup>

Reference	Year	$T_{\rho_{\max, \text{atm}}} / \text{K}$	$\rho_{\max, \text{atm}} / (\text{mol dm}^{-3})$
Lewis and MacDonald <sup>117</sup>	1933	284.742	-
Takéuchi and Inai <sup>118</sup>	1936	284.542	-
Stokland <i>et al.</i> <sup>113</sup>	1939	284.373	55.222
Steckel and Szapiro <sup>114</sup>	1963	284.383	55.225
Aleksandrov <i>et al.</i> <sup>119</sup>	1977	284.329	-
Kanno and Angell <sup>120</sup>	1980	284.417	-
Hill <i>et al.</i> <sup>1</sup>	1982	284.321	55.225
This work	2018	284.748	55.221

The calculated value agrees with the experimental results of Stokland *et al.*<sup>113</sup> and Steckel and Szapiro<sup>114</sup> within the estimated uncertainty of the EOS, which is 0.01 % as discussed above. The temperature of the maximum density calculated from the EOS is 284.748 K (about 11.6 °C), which is slightly higher than all experimentally based results and not within the temperature uncertainty given by Stokland *et al.*<sup>113</sup> (0.02 K) and Steckel and Szapiro<sup>114</sup> (0.03 K). This shift in temperature can be seen in Figure 5.13, which shows the shape of the 1 atm isobar in the vicinity of the maximum density as calculated from the new EOS and the EOS of Hill *et al.*<sup>1</sup> together with the most accurate experimental data.

**Figure 5.13** Liquid density calculated from the new EOS and the EOS of Hill *et al.*<sup>1</sup> versus temperature at atmospheric pressure. The diagram is focused on the vicinity of the maximum density resulting from the anomalous negative isothermal expansion of (heavy) water. Selected experimental data are shown for comparisons.

In the vicinity of the maximum density, neither EOS performs obviously better than the other; the difference between the two formulations is within the estimated uncertainty of the new EOS. Additionally, it should be noted that the maximum density at 1 atm is not only defined by the experimental data that were fitted in this region, but also by other liquid-phase data at higher pressures, where the maximum density occurs at lower temperatures. Also, the maximum in density is correlated with other characteristics of water such as the

maximum in speed of sound. Thus, the representation of the maximum density is additionally influenced by the speed-of-sound data used to fit the EOS.

The high-pressure liquid phase was investigated by Bridgman.<sup>73</sup> His data cover temperatures from the melting curve up to 373 K at pressures to approximately 1200 MPa, which defines the upper pressure limit of the new EOS ( $p_{\max} = 1200$  MPa). As already discussed in Sec. 5.1.2, all pressures specified within this data set were corrected by a factor of 1.0102 in order to compensate for an obsolete calibration. Because Bridgman's publication does not provide any clear information about uncertainties, his data were not used to fit the EOS. However, their representation was continuously evaluated during fitting. Except for one outlier, all data points are clearly represented within 0.4 %. Thus, the expanded uncertainty of calculated liquid densities is estimated to be 0.5 % in the high-pressure range from 100 MPa to 1200 MPa and at temperatures from the melting curve to 375 K. Apart from Bridgman's data, the only high-pressure data set available was published by Jůza *et al.*<sup>121</sup> While fitting the EOS, these data were found to be less reliable, and thus are not considered to estimate the uncertainty of calculated values. Therefore, no definitive uncertainty estimates are possible in the high-pressure region at temperatures above 375 K. The EOS of Hill *et al.*<sup>1</sup> is not valid at pressures above 100 MPa. The results illustrated in Figure 5.8 and Figure 5.11 were calculated by extrapolating the EOS to higher pressures. These calculated densities deviate considerably from Bridgman's data.

At pressures up to 100 MPa and temperatures higher than investigated by Tsederberg *et al.*,<sup>110</sup> the EOS was fitted to the very accurate liquid-phase data of Kell *et al.*<sup>103</sup> that range from 423 K to 773 K. As "a good approximation," the authors estimated the error of their measurements to be within 0.01 %, which at least needs to be expanded ( $k = 2$ ) to 0.02 %. In fact, for temperatures up to 673 K the EOS represents more than 95 % of the data within 0.02 %. Some higher deviations occur at moderate pressures and thus lower densities. Because all of the data up to 673 K are represented within 0.04 % (see Figure 5.11), the expanded uncertainty of calculated liquid densities is conservatively estimated to be 0.04 % at temperatures between 425 K and 675 K and pressures up to 100 MPa. This uncertainty estimate is not valid in the critical region, which is discussed later in this section. The two highest isotherms measured by Kell *et al.*<sup>122</sup> (723 K and 773 K) exhibit maximum deviations of 0.07 % and 0.09 %, respectively. Hence, the uncertainty of calculated supercritical liquid-like densities is estimated to be 0.1 % in the temperature range from 675 K to 775 K. More intensive fitting of the EOS to the data at these isotherms did not significantly improve these deviations, but led to an unreasonable description of the physical behavior of the fluid. Thus, it can be assumed that at these temperatures the experimental uncertainty of the data is considerably higher than stated in the publication. This assumption is supported by reviewing the H<sub>2</sub>O measurements by Kell *et al.*<sup>122</sup> that were published in the same year as the D<sub>2</sub>O data. At 723 K and 773 K, the H<sub>2</sub>O densities deviate by up to 0.1 % from IAPWS-95.<sup>29</sup> As already noted in the discussion of vapor densities, the EOS of Hill *et al.*<sup>1</sup> enables a

remarkably accurate description of the experimental data of Kell and co-workers, although the data were published in 1985 and 1989, and thus some years after the publication of the previous reference EOS. However, the publication of Hill *et al.*<sup>1</sup> refers to some then-unpublished data provided by Kell. The later published article of Kell *et al.*<sup>122</sup> states that preliminary values of the liquid density up to 400 °C were contributed to the correlating work of Hill and co-workers. This explains why the previous standard EOS is in very good agreement with these data for temperatures up to 673 K (see Figure 5.11), but exhibits larger deviations from the data at higher temperatures. The measurements at 723 K and 773 K correspond to the lowest densities in the data set. As is apparent from Figure 5.8, within this state region, at densities below approximately 35 mol dm<sup>-3</sup>, the new EOS enables a clearly more accurate description of the data.

The upper temperature limit of the new EOS ( $T_{\max} = 825$  K) is defined by the data of Aleksandrov *et al.*<sup>123</sup> ranging from 673 K up to 823 K. The data set is a correction and extension of the high-temperature study carried out by the same group of experimentalists and published by Tseiderberg *et al.*<sup>124</sup> Considering the given information about the uncertainties in temperature, pressure, and volume, combined expanded ( $k = 2$ ) uncertainties for every presented state point were calculated. At the two highest isotherms, which exceed the temperature range experimentally investigated by Kell *et al.*,<sup>103</sup> these uncertainties range from about 0.1 % to 0.16 %. It can be seen from Figure 5.8 that, except for some outliers, the new EOS represents these data clearly within 0.2 %, which is consequently a reasonable estimate for the expanded uncertainty of calculated supercritical densities between 775 K and 825 K. Like all other estimated uncertainties in densities calculated from the new EOS, this estimate is illustrated in Figure 5.10. Since the discussion of the experimental data that lead to the uncertainty estimates in the liquid and supercritical state region has been quite comprehensive, the representation of these data sets is additionally summarized in Figure 5.14.

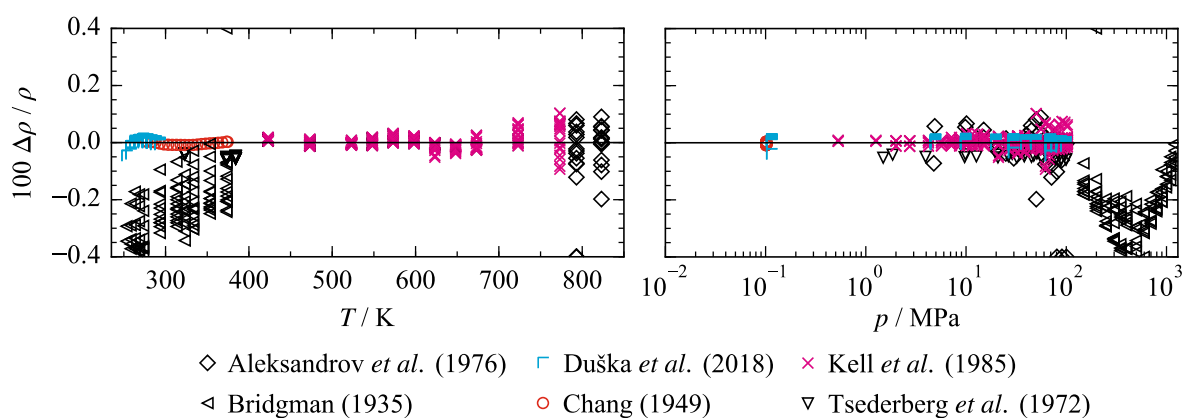


**Figure 5.14** Left: Relative deviations  $\Delta\rho/\rho = (\rho_{\text{exp}} - \rho_{\text{calc}})/\rho_{\text{exp}}$  of selected experimental liquid and supercritical density data from the new EOS versus temperature. Right: Relative deviations of the selected experimental data from the new EOS versus pressure. Depicted are the data sets that lead to the uncertainty estimates for calculated density data in the liquid and supercritical state region as summarized in Figure 5.10. Only selected points of the data sets of Bridgman,<sup>73</sup> Tseiderberg *et al.*,<sup>110</sup> and Aleksandrov *et al.*<sup>123</sup> are depicted.

For a complete discussion of the description of homogeneous  $pVT$  data, some statements should be made about the accuracy of the EOS in the critical region. Within the IAPWS-95 release for the thermodynamic properties of  $H_2O$ , the critical region is bordered by the two isochores  $144 \text{ kg m}^{-3}$  and  $527 \text{ kg dm}^{-3}$  and by the 30 MPa isobar.<sup>88</sup> In order to define the critical region of heavy water, the 30 MPa isobar was adopted as the upper pressure limit and the density limits were transferred by means of the corresponding-states principle. Thereby, the critical region is bordered by the two isochores  $8 \text{ mol dm}^{-3}$  and  $29 \text{ mol dm}^{-3}$ , which yields the triangular temperature and pressure range shown in Figure 5.10. The experimental database in this state region is quite limited. The available data and their representation by means of the new EOS and the previous standard EOS of Hill *et al.*<sup>1</sup> are illustrated in Figure 5.15. Within the critical region, very large values of  $(\partial\rho/\partial p)_T$  lead to less meaningful deviations in density. Therefore, the deviations shown in Figure 5.15 are calculated in pressure at the given temperature and density.

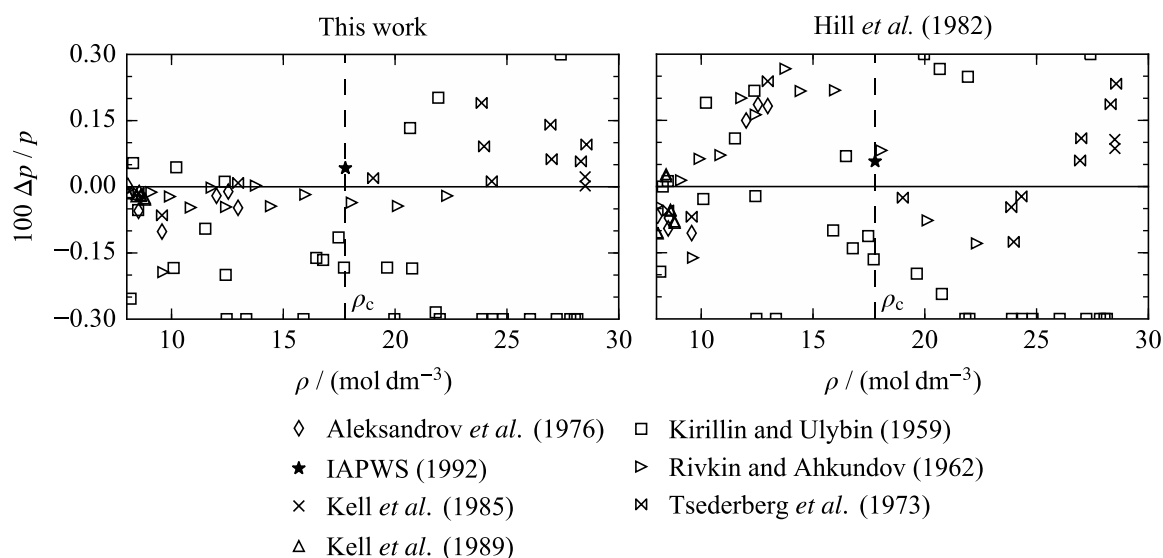


**Figure 5.15** Left: Relative deviations  $\Delta p / p = (p_{\text{exp}} - p_{\text{calc}}) / p_{\text{exp}}$  of experimental  $pVT$  data in the critical region from the new EOS versus density. The temperature and pressure range of the depicted data is  $633 < T / \text{K} < 724$  and  $18.8 < p / \text{MPa} < 29.7$ . Right: Relative deviations of experimental data from the EOS of Hill *et al.*<sup>1</sup>

In the critical region, the data of Rivkin and Akhundov<sup>64</sup> and Kell *et al.*<sup>102,103</sup> are considered to be the most reliable experimental studies, but only the data set of Rivkin and Akhundov<sup>64</sup> covers densities close to the critical value. Except for one clear outlier, the entire data set deviates from the new EOS by less than 0.05 % in pressure. The two “high-density” measurements and the few more “low-density” data points of Kell *et al.*<sup>102,103</sup> are represented within 0.03 %. As discussed in Sec. 5.1.4.1, the new EOS represents the critical pressure recommended by IAPWS<sup>60</sup> within its given uncertainty of about 0.05 %. Since this uncertainty is the same order of magnitude as the deviations discussed above, it emphasizes the reliability of these data sets. Based on these deviations, and because the experimental uncertainty of the data is not clearly stated, the expanded uncertainty of calculated  $pVT$  data is very conservatively estimated to be 0.15 % in pressure. In addition to the three data sets



discussed above, this estimate also includes the results of Aleksandrov *et al.*<sup>123</sup> that deviate by up to 0.1 % from the new EOS. As mentioned in Sec. 2.1 and Sec. 5.1.4.1, IAPWS does not recommend using the previous standard EOS in the vicinity of the critical point.<sup>15</sup> In fact, the data of Rivkin and Akhundov<sup>64</sup> deviate by up to 0.27 % from the EOS of Hill *et al.*<sup>1</sup> (see in Figure 5.15). Therefore, it can be concluded that the EOS presented here enables far more reliable calculations of critical region  $pvT$  data than the previous standard EOS.

### 5.1.5.2 Virial Coefficient Data

In most cases, EOS that enable an accurate description of  $pvT$  data and particularly of homogeneous vapor densities also provide reliable values for the virial coefficients. This is logical, since most virial coefficient data are determined from gas-phase  $pvT$  measurements that are subsequently described by means of a virial expansion truncated after the third coefficient. Therefore, most virial coefficient data are redundant with the underlying  $pvT$  data, and thus not independently valuable for fitting EOS. For D<sub>2</sub>O, experimentally based data for the second and third virial coefficients,  $B$  and  $C$ , were published by Kell *et al.*<sup>102</sup> The data were determined from the corresponding vapor densities discussed in Sec. 5.1.5.1. Because the EOS was intensively fitted to these densities, the virial coefficient data were not considered additionally in the fit. Instead, the EOS was fitted to the theoretically obtained second virial coefficient data of Garberoglio *et al.*<sup>125</sup> These  $B(T)$  were calculated from a high-quality flexible pair potential<sup>126</sup> with full accounting for quantum effects, agreeing with available experimental data for both D<sub>2</sub>O and H<sub>2</sub>O but covering a much wider temperature range. The  $B(T)$  data are depicted in the top panel of Figure 5.16, which also shows the second virial coefficient calculated from the new EOS and the previous standard EOS as a function of temperature. At high temperatures, the second virial coefficient should become positive and eventually exhibit a maximum before gradually decreasing while remaining positive. At low temperatures, the EOS should yield large negative values of the virial coefficients, which corresponds to an attraction-dominated interaction between the molecules. Both the new and the previous standard EOS exhibit qualitatively correct low-temperature behavior, but the EOS of Hill *et al.*<sup>1</sup> incorrectly produces negative  $B(T)$  at very high temperatures. The new EOS is in excellent agreement with the recently established theoretical data of Garberoglio *et al.*<sup>125</sup> throughout the temperature range, meaning that its vapor densities can be trusted even at temperatures where no experimental data exist. At low temperatures (heavy) water exhibits a considerably steeper slope of  $B$  versus temperature than most other fluids; Figure 5.16 shows that the new EOS describes this specific behavior quite accurately.

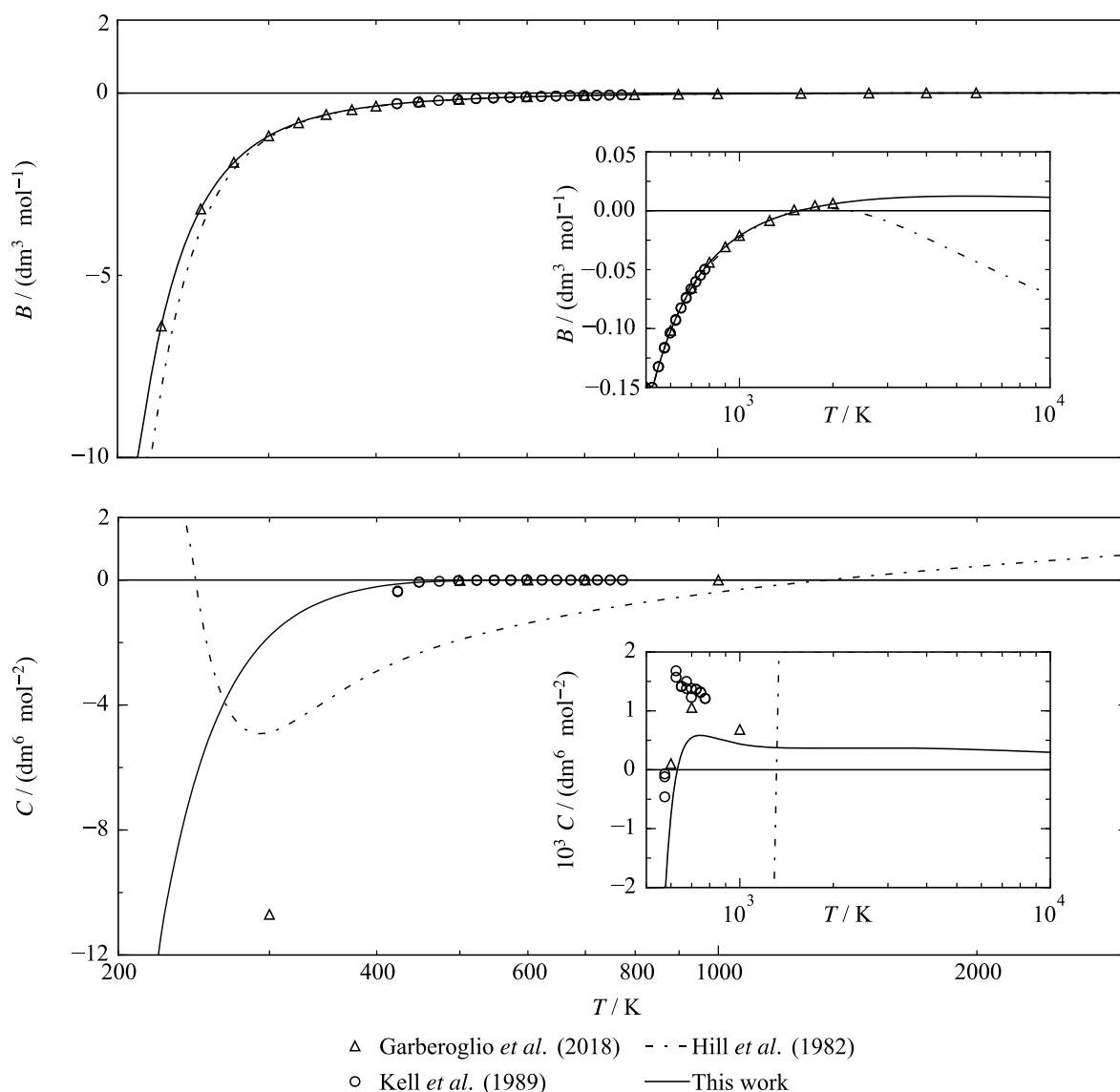


**Figure 5.16** Top: Second virial coefficient  $B$  as a function of temperature as calculated from the new EOS and the EOS of Hill *et al.*<sup>1</sup> The available data are plotted for comparison. Bottom: Third virial coefficient  $C$  as a function of temperature as calculated from both EOS; the available data are included for comparison.

For the third virial coefficient, values for real fluids become increasingly negative at low temperatures. At higher temperatures,  $C(T)$  becomes positive and goes through a maximum before declining but remaining positive. The bottom panel of Figure 5.16 shows that the new EOS exhibits the correct qualitative behavior, but that the EOS of Hill *et al.*<sup>1</sup> exhibits qualitatively wrong behavior at both low and high temperatures. The only experimental  $C(T)$  data for heavy water again come from Kell *et al.*,<sup>102</sup> but their uncertainty was not stated. In addition, five points given by Garberoglio *et al.*<sup>125</sup> are plotted which were based on high-quality pair<sup>126</sup> and three-body<sup>127</sup> potentials. Unlike with  $B(T)$ , these theoretical  $C(T)$  values are not considered to be highly accurate; Garberoglio *et al.*<sup>125</sup> concluded that the available three-body potentials were inadequate to produce quantitatively accurate  $C(T)$ . From the bottom panel of Figure 5.16, it is apparent that the new EOS is in qualitative agreement with the available data, but there are systematic differences. Since no uncertainty information are available about either data source, it is not possible to say if these differences are significant.

The accurate representation of the second virial coefficient data, including its steep slope at low temperatures, and the qualitatively correct description of  $C$ , underscore the exceptionally good extrapolation behavior of the new EOS, which is strongly connected to the representation of the so-called “ideal curves” as discussed in Sec. 5.1.8.

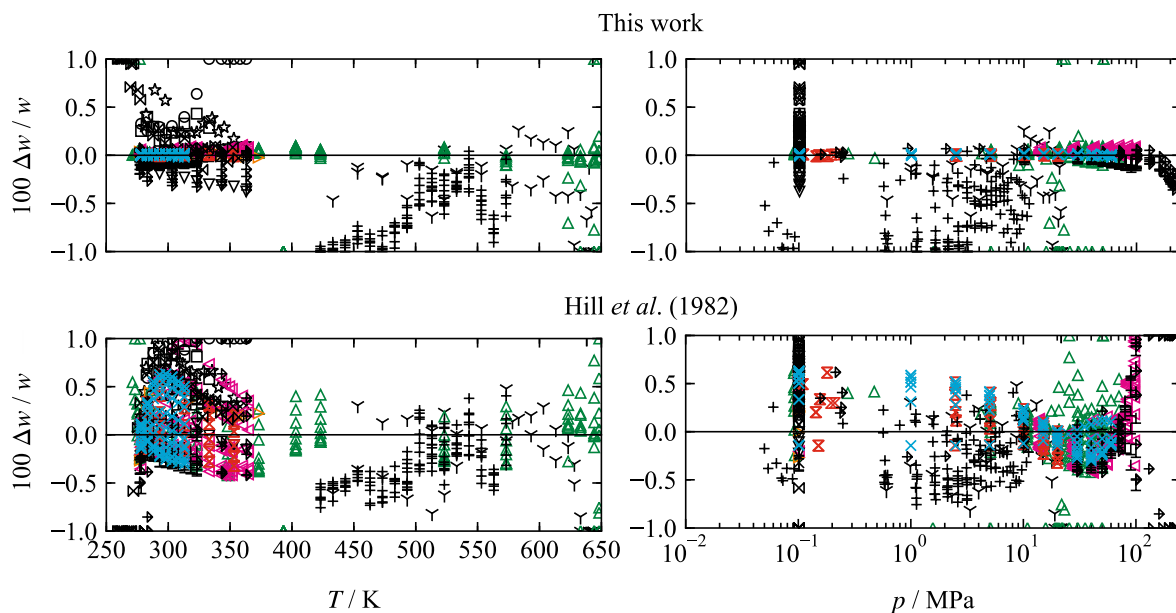
### 5.1.6 Caloric Property Data

Caloric property data on, for example, speed of sound or isobaric heat capacity are of special interest during the development and validation of fundamental equations of state. Whereas  $pvT$  data only depend on the first derivative of the residual Helmholtz energy with respect to density, caloric properties depend on higher-order derivatives, including temperature derivatives, of both the ideal and residual parts of the Helmholtz energy (see Sec. 3.3). Thus, fitting the EOS to such data is essential for the overall functional form including the ideal-gas correlation (see Sec. 5.1.3). This aspect is particularly interesting with regard to speed-of-sound data, which can be measured with quite low experimental uncertainties. The complete caloric property data for heavy water are summarized in Table B.6 in Appendix B. The  $AAD$  given in this table are reported following the conventions presented in Sec. 5.1.5.

#### 5.1.6.1 Speed-of-Sound Data

When comparing the new equation with the previous standard EOS of Hill *et al.*,<sup>1</sup> by far the greatest improvement can be noted in the representation of speed-of-sound data. This aspect is highlighted in Figure 5.17, which shows deviations of values calculated by means of both equations from the available experimental data.

Considering the most accurate data sets by Wegge *et al.*,<sup>128</sup> Fehres and Rudtsch,<sup>129</sup> Aleksandrov and Larkin,<sup>130</sup> and Wilson,<sup>131</sup> the previous standard equation deviates from the data by up to 1 %, whereas the new EOS describes all relevant data within 0.1 % or better. Because the description of the available data by means of the new EOS is so much better than with the EOS of Hill *et al.*,<sup>1</sup> no further discussion of the old EOS is given in this section. Nevertheless, results of the old EOS are included in Figure 5.18.



- |                                 |                                 |                                |
|---------------------------------|---------------------------------|--------------------------------|
| △ Aleksandrov and Larkin (1977) | × Fehres and Rudtsch (2018)     | > Marczak (1999)               |
| ▷ Aleksandrov and Larkin (1978) | ⊗ Fine and Millero (1975)       | □ McMillan and Lagemann (1947) |
| ⊥ Chen and Millero (1977)       | ☆ Gupta <i>et al.</i> (1976)    | ○ Pancholy (1953)              |
| ⊗ Conde <i>et al.</i> (1982)    | ∇ Heusinger (1949)              | ⊗ Wege <i>et al.</i> (2016)    |
| ∇ Erokhin and Kompaniets (1980) | ◇ Ivanov <i>et al.</i> (2009)   | ◁ Wilson (1961)                |
| + Evsteev <i>et al.</i> (1979)  | ‡ Lago and Giuliano Albo (2019) |                                |

**Figure 5.17** Top: Relative deviations  $\Delta w / w = (w_{\text{exp}} - w_{\text{calc}}) / w_{\text{exp}}$  of experimental speed-of-sound data from the new EOS versus temperature (left) and pressure (right). Bottom: Relative deviations of experimental speed-of-sound data from the equation of Hill *et al.*<sup>1</sup>

An accurate experimental study of the speed of sound in liquid heavy water was carried out by Wege *et al.*<sup>128</sup> at RUB. The data were specifically obtained to enhance the fitting process of the new EOS. The experimentalists applied the double-path-length pulse-echo technique with a relative combined expanded ( $k = 2$ ) uncertainty of 0.011 %. The data range from 278 K to 354 K at pressures up to approximately 20 MPa. The new EOS describes all data points within the given uncertainty. Based on these data, the combined expanded ( $k = 2$ ) uncertainty of speeds of sound calculated from the new EOS is conservatively estimated to be 0.015 % at temperatures from the melting line up to 355 K and pressures up to 20 MPa. Selected isotherms of the data of Wege *et al.*<sup>128</sup> are included in Figure 5.18, whereas the complete data set is shown on a more suitable deviation scale in Figure 5.19. Both figures emphasize that the data from RUB are in very good agreement with the most recent and so far unpublished results of Fehres and Rudtsch.<sup>129</sup> This work was performed at Physikalisch-Technische Bundesanstalt (PTB), Berlin, also applying the pulse-echo technique. The data cover pressures up to about 60 MPa, which exceeds the pressure range investigated by Wege *et al.*,<sup>128</sup> and temperatures up to 314 K, which is lower than the upper temperature limit of Wege's investigations.

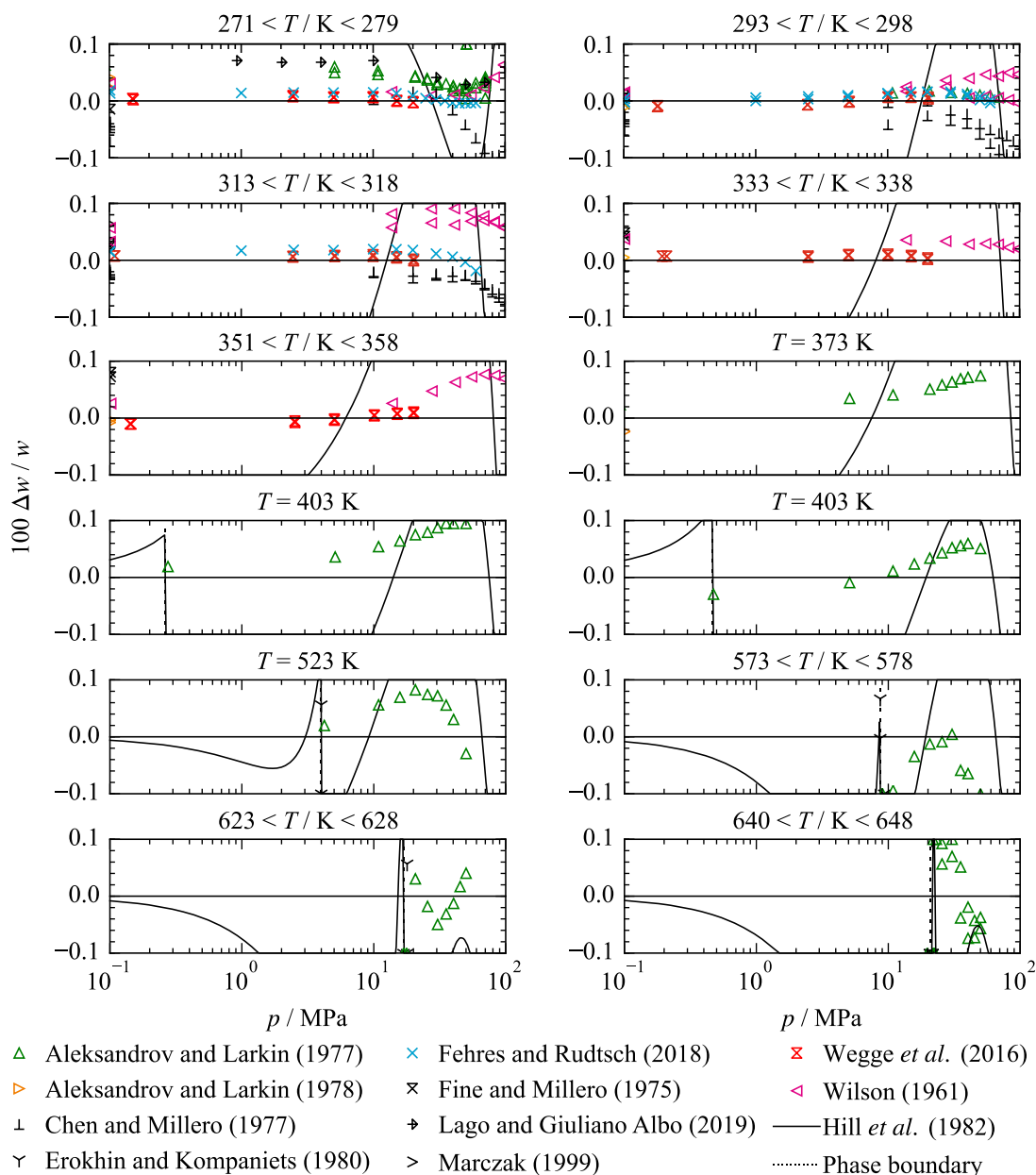


**Figure 5.18** Relative deviations  $\Delta w / w = (w_{\text{exp}} - w_{\text{calc}}) / w_{\text{exp}}$  of selected experimental speed-of-sound data along (quasi-)isotherms from the new EOS. The EOS of Hill *et al.*<sup>1</sup> is plotted for comparisons. For plots showing a temperature range, the EOS of Hill *et al.*<sup>1</sup> was calculated at the average temperature.

The new EOS describes all data points of Fehres and Rudtsch within 0.02 %. Because the data are unpublished, no concrete results of an uncertainty analysis are available. With regard to their deviations from the EOS, the uncertainty estimate for calculated speeds of sound is 0.02 % for temperatures up to 315 K and pressures between 20 MPa and 60 MPa.

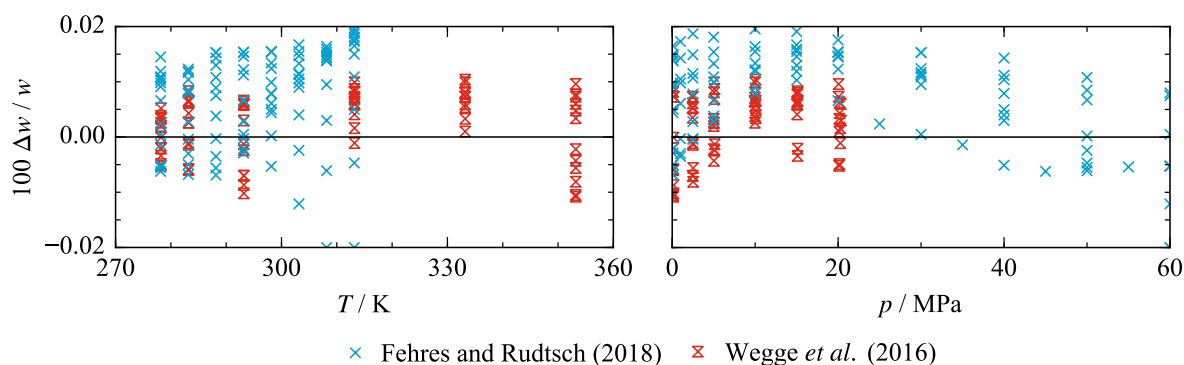


**Figure 5.19** Top: Relative deviations  $\Delta w / w = (w_{\text{exp}} - w_{\text{calc}}) / w_{\text{exp}}$  of the experimental speed-of-sound data of Wegge *et al.*<sup>128</sup> and Fehres and Rudtsch<sup>129</sup> from the new EOS versus temperature. Bottom: Relative deviations of the experimental data from the new EOS versus pressure.

At higher pressure, the uncertainty estimate is based on the data of Wilson<sup>131</sup> that cover temperatures and pressures up to 365 K and 97 MPa. The maximum deviation of these data is 0.1 % (see Figure 5.18). Within the corresponding publication, no detailed statement about the uncertainty of the data is given. In an earlier work, Wilson studied the speed of sound in ordinary water.<sup>132</sup> In the IAPWS-95 publication, the uncertainty of the data was estimated to be within 0.05 %.<sup>29</sup> The D<sub>2</sub>O data exhibit a maximum offset of about 0.08 % from the very accurate data of Fehres and Rudtsch.<sup>129</sup> Therefore, it is assumed that an uncertainty estimate of 0.1 % is reasonable for Wilson's data, and this is adopted as the estimated uncertainty of sound speeds calculated from the new EOS at temperatures from the melting line up to 365 K and pressures between 60 MPa and 100 MPa. All estimated uncertainties in calculated sound speeds are summarized in Figure 5.20.

After the work on the heavy-water EOS was completed, new sound-speed measurements at temperatures from 277 K to 363 K and pressures up to 210 MPa were carried out by Lago and Giuliano Albo.<sup>133</sup> Comparisons to these data are shown in Figure 5.17 and for one isotherm also in Figure 5.18. At and below 100 MPa, these data confirm the estimates for the uncertainties in calculated values given in Figure 5.20 and consequently also the data sources on which those estimates were based. At higher pressures, where there were previously no experimental data that could be used in fitting, there is a small systematic deviation between the EOS and these new data, with the EOS sound speeds higher than the data by amounts up to 0.36% at the highest pressure.

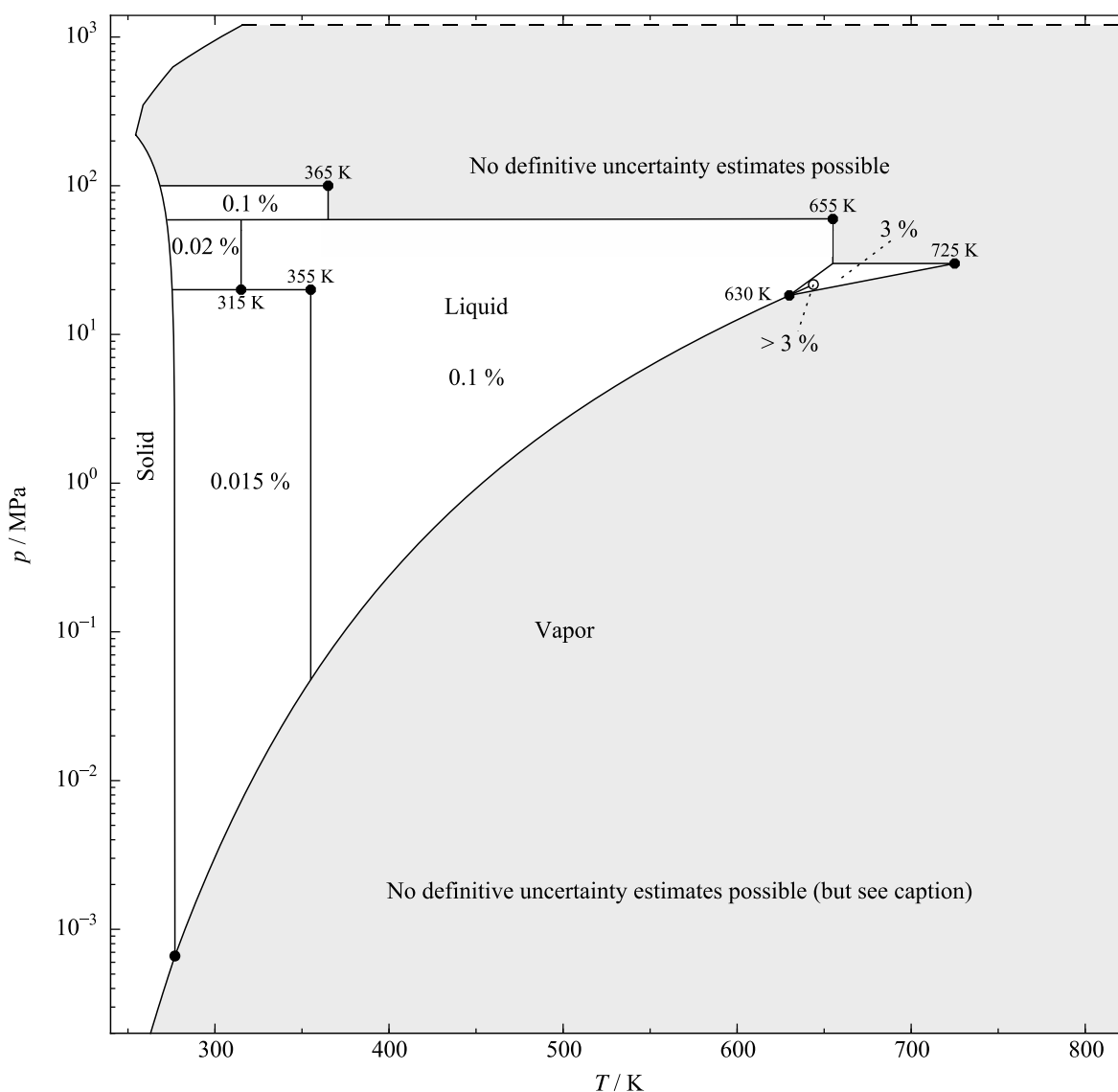


**Figure 5.20** Expanded relative uncertainties in speed of sound,  $\Delta w / w$ , estimated for the new EOS. For the definition of the triangle around the critical point, see the Figure 5.10 caption. The positions of the lines separating the uncertainty regions are approximate. At low pressures for the vapor, the uncertainty becomes small because the vapor approaches the ideal-gas limit.

As is apparent from Figure 5.20, for the rest of the liquid phase, excluding the critical region, the uncertainty estimate is 0.1 %. This estimate is based on the representation of the data of Aleksandrov and Larkin<sup>130</sup> published in 1977. The data range from the melting line up to 649 K at pressures up to 72 MPa. Deviations between the EOS and almost all data points are below 0.1 %, except for some measurements close to the phase boundary, where the experiment might have been carried out in the two-phase region, and a few data points within the critical region. The data are shown in Figures 5.17 and 5.18; the critical-region data are also depicted separately in Figure 5.21.

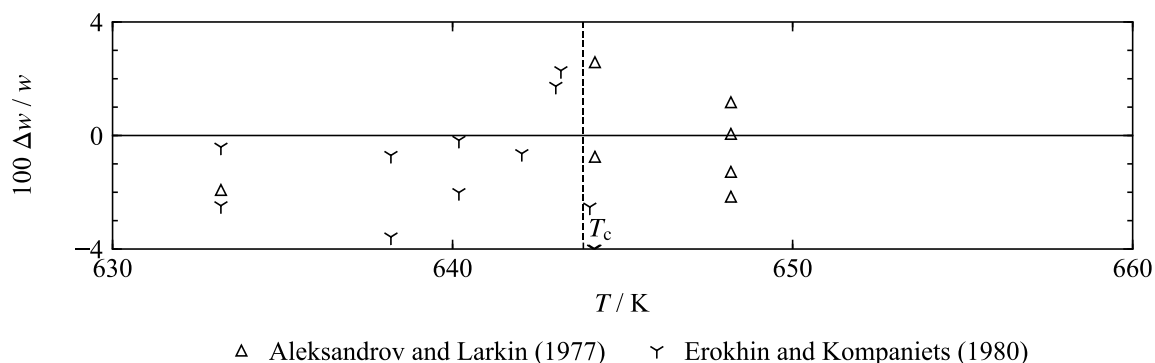


**Figure 5.21** Relative deviations  $\Delta w / w = (w_{\text{exp}} - w_{\text{calc}}) / w_{\text{exp}}$  of the available experimental speed-of-sound data in the critical region from the new EOS versus temperature. The density and pressure range of the depicted data is  $8.5 < \rho / (\text{mol dm}^{-3}) < 28.4$  and  $p < 26$  MPa.

As is evident from Figure 5.21, the critical-region data of Aleksandrov and Larkin are represented within 3 %, which is adopted as the uncertainty of calculated sound speeds within the critical region (as defined in Sec. 5.1.5.1). However, in the vicinity of the critical point the speed of sound decreases steeply and should, in theory, be zero at the critical point. Since the new EOS does not allow for the description of this phenomenon, it should be noted that the uncertainty of calculated sound speeds is larger than 3 % in the vicinity of the critical point (see Figure 5.20). The description of the physical behavior in the critical region is discussed in more detail in Sec. 5.1.8. Figure 5.21 also includes the data of Erokhin and Kompaniets<sup>134</sup> that were measured along the dew and bubble curves. This data set is the only experimental investigation of the speed of sound at saturation. It can be seen that, in the critical region, the data deviate by about 4 % from the EOS, whereas Figure 5.17 illustrates that the majority of the data down to 433 K is represented within 0.5 %, which is also equivalent to the approximate scatter of the data. However, due to the lack of comparative data from other sources, no definitive uncertainty estimate for calculated sound speeds at saturation is possible. However, as discussed for density in Sec. 5.1.2, the uncertainty in sound speed for the saturated liquid should be similar to that in the adjacent one-phase liquid region. No experimental data for the speed of sound in heavy water vapor are available, and therefore Figure 5.20 shows that no definitive estimate of uncertainty can be made in this region. However, it should be noted that, at low pressures, the uncertainty of calculated values is small, since the vapor approaches the ideal-gas state which is described accurately (see Sec. 5.1.3).

### 5.1.6.2 Heat-Capacity Data

The experimental database for other caloric properties is much less satisfactory than for the speed of sound. Aside from one data set with Joule-Thomson coefficients, which is not accurate enough to contribute to the fitting process, some data on the isochoric and isobaric heat capacity are available. Since the isochoric heat-capacity data exhibit relatively large uncertainties and inconsistencies, only the isobaric heat-capacity data were relevant during the fitting of the present EOS. Nevertheless, these data also cannot be considered very



accurate. Consequently, the equation was fitted only to a careful selection of low-weighted data points in order to reach at least a representation of the data within their estimated experimental uncertainties.

### Isobaric Heat-Capacity Data

An overview of the experimental isobaric heat capacities and their deviations from values calculated from the new EOS and the previous standard EOS is shown in Figure 5.22.

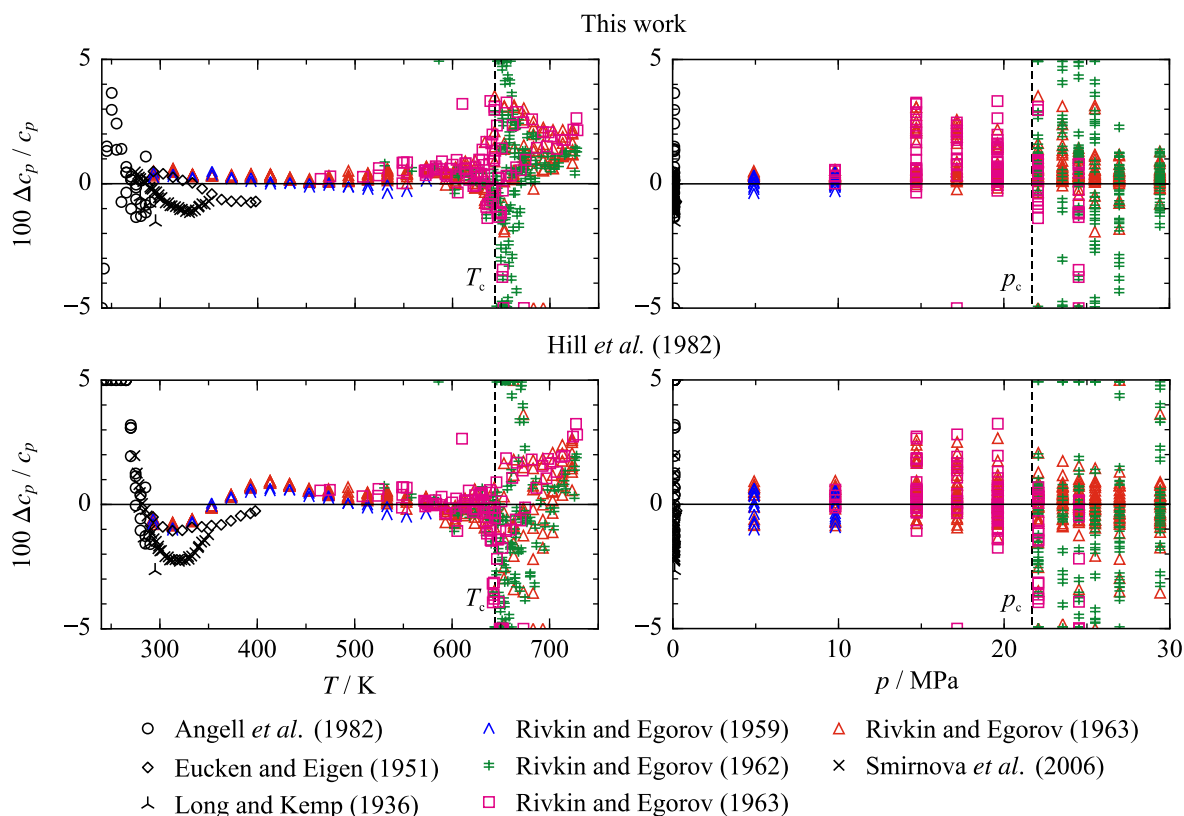


**Figure 5.22** Top: Relative deviations  $\Delta c_p / c_p = (c_{p,\text{exp}} - c_{p,\text{calc}}) / c_{p,\text{exp}}$  of experimental isobaric heat-capacity data from the new EOS versus temperature (left) and pressure (right). Bottom: Relative deviations of experimental isobaric heat-capacity data from the equation of Hill *et al.*<sup>1</sup>

With respect to temperature, the data cover almost the entire range of validity of the EOS. The high-temperature data range up to approximately 730 K. The lowest isotherms were investigated below the triple point, and thus within the metastable subcooled liquid region (see Sec. 5.1.7). Most of the measurements were carried out in the liquid phase at pressures up to 30 MPa. The vapor phase was only investigated at pressures above 15 MPa and temperatures higher than 620 K. The large majority of the experimental data were obtained by Rivkin and Egorov between 1959 and 1963.<sup>135–138</sup> The first data set published in 1959 contains measurements of the liquid phase at temperatures between 293 K and 574 K and at pressures up to 10 MPa,<sup>135</sup> whereas the publication from 1962 presents measurements of the critical and supercritical regions between 530 K and 728 K and higher pressures between 22.1 MPa and 30 MPa.<sup>136</sup> In 1963, Rivkin and Egorov published two further articles: one presenting new data at temperatures between 464 K and 729 K and pressures between

9.8 MPa and 25 MPa,<sup>137</sup> and another one that seems to supersede all prior publications.<sup>138</sup> The second study presents data at temperatures ranging from 293 K to 723 K at pressures between 4.9 MPa and 30 MPa, and also includes a few vapor-phase data points at pressures starting at approximately 15 MPa. It should be noted that the chronological order of the two publications from 1963 could not be clarified, since neither of them is cited within the other. However, it was assumed that the data of the more comprehensive study, can be considered as Rivkin's and Egorov's final values of the isobaric heat capacity of heavy water. Within this publication, the authors claim that the maximum error of their measurements is 0.35 % for the liquid and vapor at a certain distance from the saturation line and within 1 % or 2 % close to saturation or near the maximum heat capacity along the supercritical isobars. It can be assumed that these error estimates are underestimated and also not equivalent to combined expanded uncertainties. The new EOS clearly represents all liquid-phase data within 1 % excluding the critical region. This deviation is adopted as the estimated uncertainty of calculated isobaric heat capacities in the liquid phase at pressures up to 30 MPa. Although this uncertainty estimate might be conservative with regard to the deviations of the data, it is reasonable because no experimental data from other sources are available. The 1 % uncertainty estimate can be extended to temperatures lower than 293 K as investigated by Rivkin and Egorov, since the EOS was fitted to extremely accurate speed-of-sound data in this state region (see Sec. 5.1.6.1). The available experimental heat-capacity data at temperatures below 293 K are of lower accuracy and limited to atmospheric pressure.<sup>77,139,140</sup>

The EOS represents the few vapor-phase measurements of Rivkin and Egorov<sup>137,138</sup> within maximum deviations of approximately 3 % (AAD of 1.1 %), which is adopted as the estimated uncertainty of calculated isobaric heat capacities of the vapor phase at pressures above 15 MPa and temperatures between  $T_{\text{sat}}(15 \text{ MPa}) \approx 614 \text{ K}$  and 730 K. At lower pressures and temperatures, no definitive uncertainty estimates for calculated isobaric heat capacities are possible, because no experimental data are available. Nevertheless, it should be noted that with decreasing pressures the uncertainty approaches the uncertainty of the ideal-gas heat capacity, which is less than 0.02 % as discussed in Sec. 5.1.3.

The critical-region data of Rivkin and Egorov<sup>136-138</sup> are shown in Figure 5.23. It can be seen that the EOS describes the majority of the data within about 5 %. In fact, the two newer data sets from 1963 are mainly represented within about 3 %. However, 5 % seems as a reasonable uncertainty estimate for calculated isobaric heat capacities within the critical region. The uncertainty will be larger in the immediate vicinity of the critical point, where the values of  $c_p$  diverge.

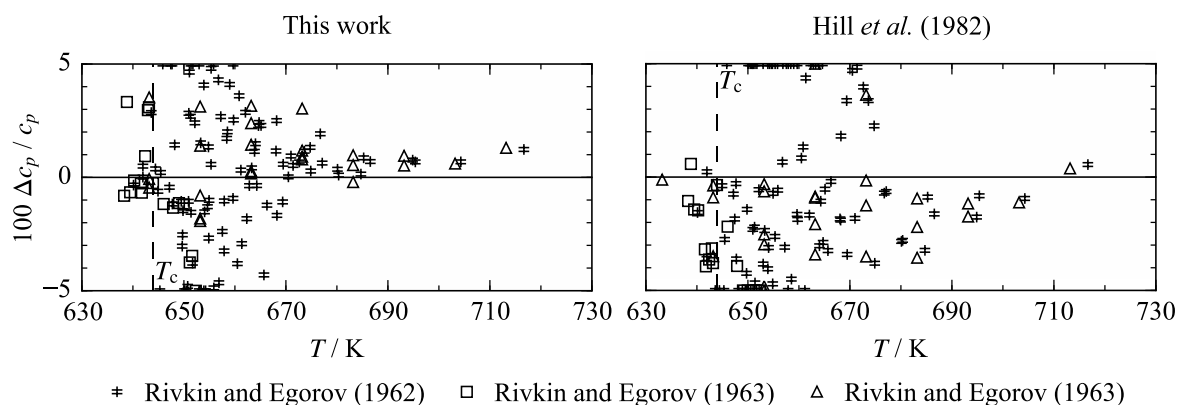


**Figure 5.23** Left: Relative deviations  $\Delta c_p / c_p = (c_{p,\text{exp}} - c_{p,\text{calc}}) / c_{p,\text{exp}}$  of experimental isobaric heat-capacity data in the critical region from the new EOS versus temperature. Right: Relative deviations of experimental isobaric heat-capacity data from the equation of Hill *et al.*<sup>1</sup>

Isobaric heat capacities of the saturated liquid were published by Eucken and Eigen,<sup>141</sup> who claim a relative experimental uncertainty of 0.15 %. However, this uncertainty seems to be underestimated. The EOS describes the data within a maximum deviation of 0.76 %. Further fitting of the data lead to a worse description of some homogeneous liquid-phase data such as the highly accurate speed-of-sound data (see Sec. 5.1.6.1) or the density data at atmospheric pressure. Since no comparative data are available, a concrete uncertainty estimate for isobaric heat capacities at saturation cannot be provided, but the uncertainties should be similar to that in the adjacent one-phase region. All other results of the uncertainty analysis discussed within this section are illustrated in Figure 5.24.

Some comments should be made on comparisons between isobaric heat capacities calculated from the new EOS and the previous standard EOS of Hill *et al.*<sup>1</sup> From Figure 5.22, it can be seen that the new EOS represents the stable liquid-phase data at temperatures up to about 500 K more consistently than the old EOS. However, the differences between calculated values are mostly within the 1 % uncertainty estimate. The same applies for the gas phase, where calculated values agree within the uncertainty estimate of 3 %. In the critical region, as shown in Figure 5.23, the new EOS represents a better compromise between all available data points. In addition, considerably more data points exhibit deviations above 5 % from the old EOS than from the one presented in this work.

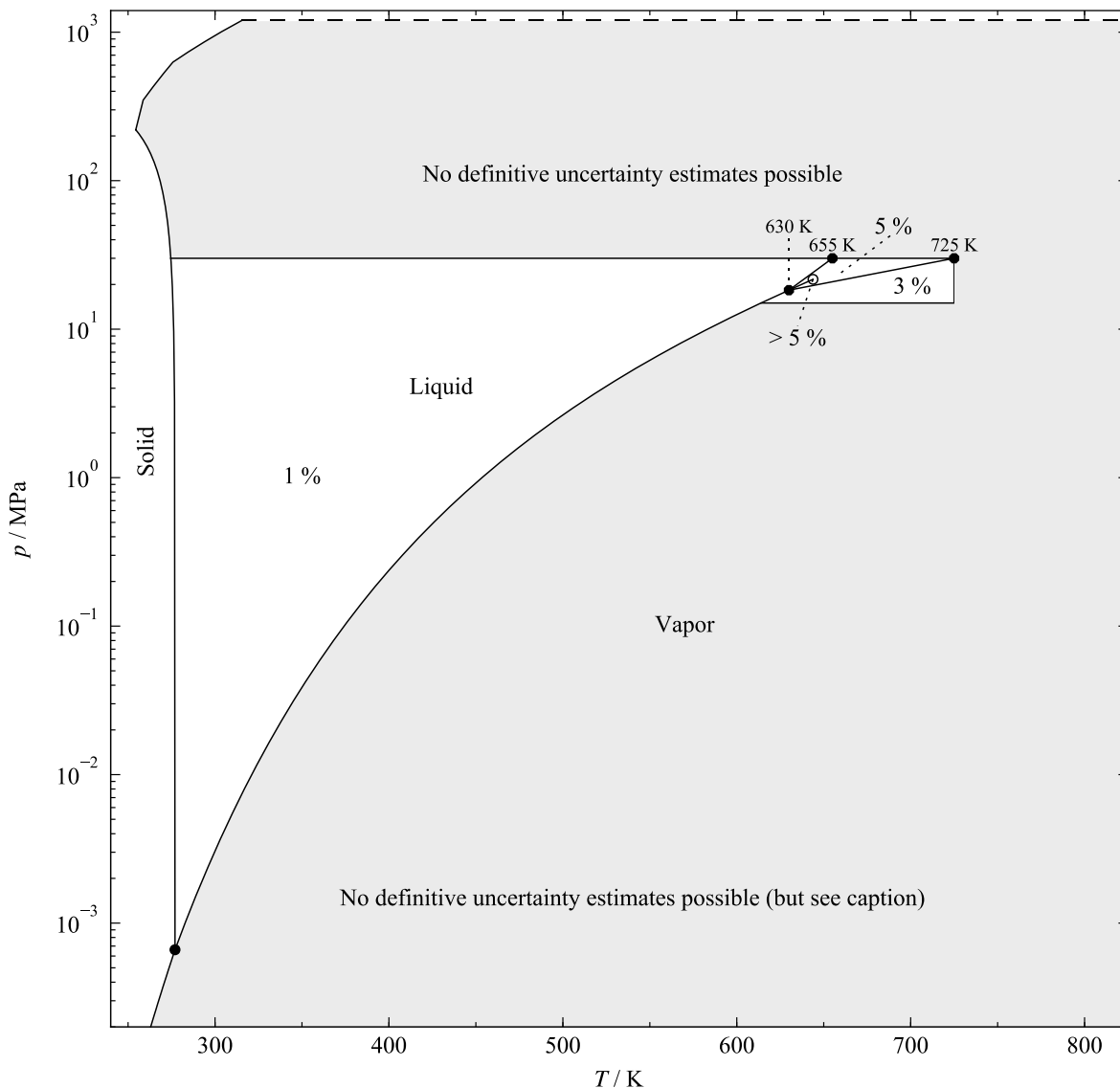


**Figure 5.24** Expanded relative uncertainties in isobaric heat capacity,  $\Delta c_p / c_p$ , estimated for the new EOS. For the definition of the triangle around the critical point, see the Figure 5.10 caption. The positions of the lines separating the uncertainty regions are approximate. The uncertainty in the vapor phase at low pressures approaches the uncertainty of the ideal-gas heat capacity, which is less than 0.02 % as discussed in Sec. 5.1.3.

### ***Isochoric Heat-Capacity Data***

Figure 5.25 shows that there is a considerable amount of experimental data on the isochoric heat capacity covering the liquid phase as well as the critical and supercritical regions. The complete database was measured at the Dagestan Scientific Center of the Russian Academy of Science. The earliest study of Amirkhanov *et al.*<sup>142</sup> was superseded and extended by the work of Mursalov *et al.*<sup>97</sup> Subsequently, Polikhronidi *et al.*<sup>143</sup> investigated the critical region more intensively. As is evident from Figure 5.25, the work of Polikhronidi and co-workers also includes some data points in the vapor-liquid equilibrium region. These are results for the overall heat capacity of the two-phase system in the measuring cell instead of separate results for the coexisting saturated liquid and vapor. During the fitting process, these data always exhibited quite large deviations from the EOS. Therefore, relatively high experimental uncertainties were assumed, and thus these data were omitted. Deviations of

the single-phase isochoric heat-capacity data are shown in Figure 5.26 and the two-phase data are shown in Figure 5.27.

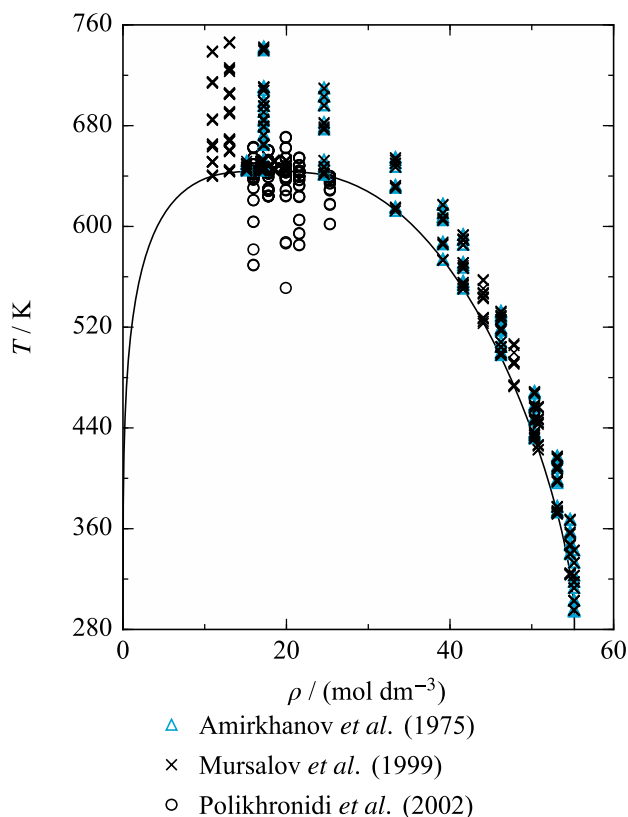


**Figure 5.25** Distribution of the available experimental data on the isochoric heat capacity in a  $T, \rho$  diagram.

The left panel of Figure 5.26 shows that the available experimental data exhibit fairly large deviations from the new EOS, which could never be significantly reduced during the fitting process. In order to get an impression of the quality of the available data, the experimental results of Amirkhanov *et al.*<sup>144</sup> for ordinary water were compared with the IAPWS-95 formulation. The results are shown in the right panel of Figure 5.26. It can be seen that at temperatures up to about 525 K the data agree with IAPWS-95 within about 5 %. With increasing temperatures, these deviations increase to about 10 % or even higher in the critical region. In the IAPWS-95 publication of Wagner and Pruß,<sup>29</sup> it is noted that due to the relatively large uncertainties and inconsistencies in the data measured at the Dagestan Scientific Center, none of these points was used to develop the IAPWS-95 formulation. Instead, the EOS was fitted to limited data from other sources. This statement agrees with the findings of this work. The new EOS for D<sub>2</sub>O was therefore only fitted with low weight to a small number of data points taken from Mursalov *et al.*<sup>97</sup> and Polikhronidi *et al.*<sup>143</sup>

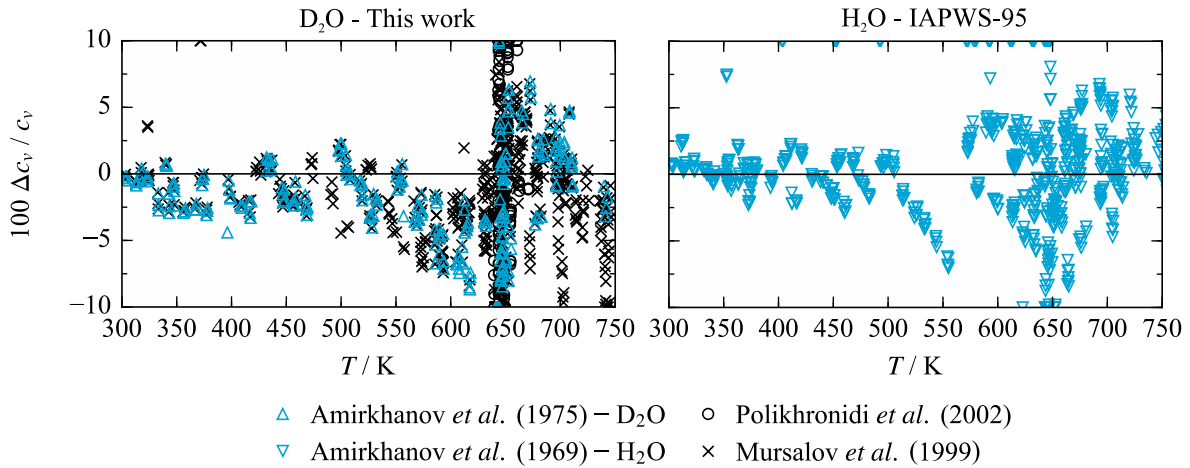


**Figure 5.26** Left: Relative deviations  $\Delta c_v / c_v = (c_{v,\text{exp}} - c_{v,\text{calc}}) / c_{v,\text{exp}}$  of experimental isochoric heat-capacity data for  $\text{D}_2\text{O}$  from the new EOS versus temperature. Right: Relative deviations of experimental isochoric heat-capacity data for  $\text{H}_2\text{O}$  from the IAPWS-95 formulation.<sup>29,88</sup>

At temperatures up to about 550 K, the new EOS represents the available liquid-phase data mostly within 5 %. As shown in Secs. 5.1.6.1 and 5.1.6.2, the EOS enables a clearly more accurate description of the available speed-of-sound and isobaric heat-capacity data in this region. Therefore, it can be assumed that the uncertainty of calculated isochoric heat capacities in the liquid phase is less than 5 % at temperatures up to 550 K. Over the rest of the fluid surface, the quality of the experimental data does not allow any uncertainty estimates. Nevertheless, it should once again be noted that in the vapor phase and at low pressures the uncertainty becomes small, since the accuracy of the EOS is essentially defined by the ideal-gas part  $\alpha^0$  (see Sec. 5.1.3).

As previously mentioned, the two-phase data of Polikhronidi *et al.*<sup>143</sup> deviate considerably from the new EOS (see Figure 5.27), which can be explained by potentially higher uncertainties of these data. Thus, an uncertainty estimate for calculated overall isochoric heat capacities of the two-phase system is not provided.

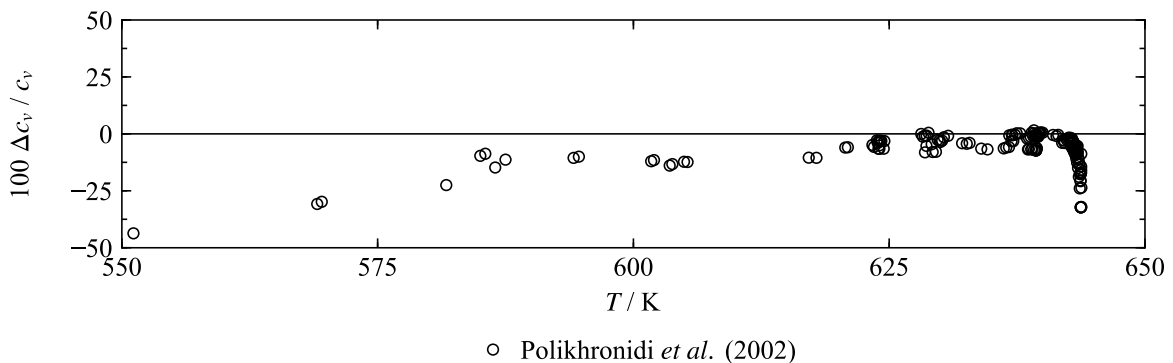


**Figure 5.27** Relative deviations  $\Delta c_v / c_v = (c_{v,\text{exp}} - c_{v,\text{calc}}) / c_{v,\text{exp}}$  of the experimental isochoric heat-capacity data of Polikhronidi *et al.*<sup>143</sup> in the two-phase from the new EOS versus temperature.

Deviations of the isochoric heat capacity of the saturated liquid and vapor as measured by Mursalov *et al.*<sup>97</sup> from the EOS are shown in Figure 5.28. The saturated-vapor data exhibit maximum deviations of about 5 % at temperatures below 640 K, whereas the

saturated-liquid data are represented within about 1.8 % for temperatures up to 612 K. At higher temperatures, the deviations for the saturated-liquid data increase to almost 40 %. These extremely large deviations result from critical phenomena that are only qualitatively described by the new EOS. In theory, the isochoric heat capacity should become infinite at the critical point. Because the functional form of the EOS does not include special provisions for incorporating nonclassical critical phenomena, it does not enable the description of such non-analytic effects at the critical point (see Sec. 5.1.8).

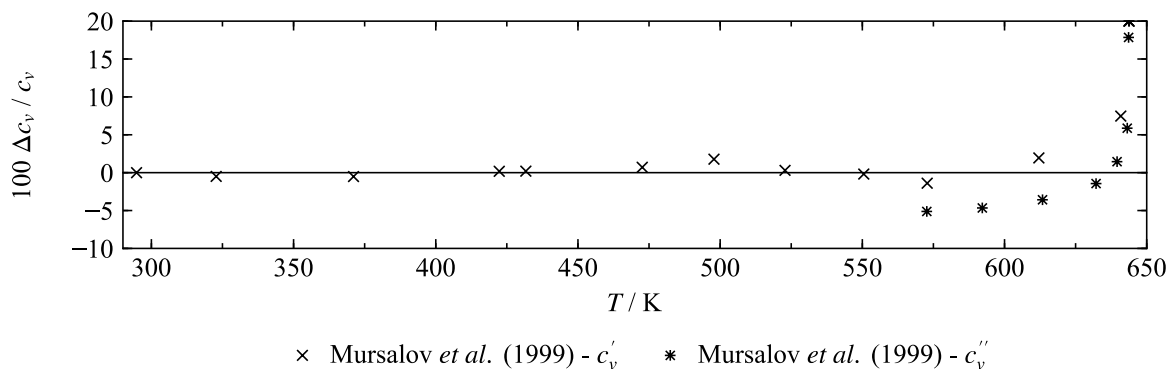


**Figure 5.28** Relative deviations  $\Delta c_v / c_v = (c_{v,\text{exp}} - c_{v,\text{calc}}) / c_{v,\text{exp}}$  of the experimental isochoric heat-capacity data of Mursalov *et al.*<sup>97</sup> at saturation from the new EOS versus temperature.

Due to the large deviations between the experimental isochoric heat capacities and calculated values, comparisons between the new EOS and the previous standard EOS of Hill *et al.*<sup>1</sup> are less meaningful and are consequently not presented in this section. In general, the deviations of the data from the old EOS are comparable to those presented here. Within their publication, Hill *et al.* discuss the same limitations of describing critical phenomena by means of an analytical functional form as mentioned here.

### 5.1.7 Data at Metastable States

The fluid surface includes three metastable regions: the subcooled liquid (metastable with respect to the solid), the superheated liquid (metastable with respect to the vapor), and the subcooled vapor (metastable with respect to the liquid or solid). Except for one data set for the speed of sound in the superheated liquid,<sup>145</sup> all experimental studies are focused on the subcooled liquid. No experimental data on the subcooled vapor were found. However, at low and moderate pressures it should be described accurately if the second and third virial coefficients (see Sec. 5.1.5.2) are accurate.

The speed of sound in superheated liquid was investigated by Evstefeev *et al.*<sup>145</sup> in the temperature range from 423 K to 573 K. Unfortunately, these data are only graphically given in the corresponding publication and the underlying experimental results are no longer available. Thus, the data were extracted from the figure presented in the article. Comparisons between the experimental uncertainty of these data and their deviations from the EOS are consequently of limited value because a considerable additional uncertainty was added by

the graphical determination. Nevertheless, the authors state a “total error” of approximately 0.2 %, which should probably not be equated with the combined expanded uncertainty of the data. Deviations of the data from the new EOS are shown in Figure 5.17. The EOS represents the majority of the graphically determined data within 1 %. The data at temperatures above 493 K are in better agreement with the EOS than the results along the lower isotherms. The distribution of the data in relation to the saturation curve is illustrated in Figure 5.29. Since the measurements were carried out along isotherms, the degree of superheating is not obvious. The largest difference between the saturation pressure and the pressure investigated occurs at 503 K, and is equivalent to a superheating of approximately 130 K.

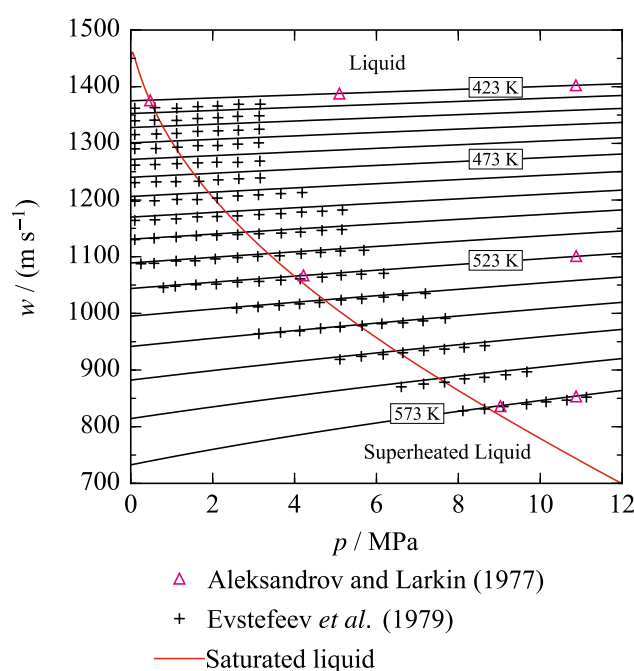


**Figure 5.29** Speed of sound along isotherms as a function of pressure in the metastable superheated and stable liquid region as calculated from the new EOS. The experimental data of Evstefeev *et al.*<sup>145</sup> and Aleksandrov and Larkin<sup>130</sup> are plotted for comparisons.

Along the lower isotherms, the offset between the data of Evstefeev *et al.*<sup>145</sup> and sound speeds calculated from the EOS is quite evident. In the stable liquid region at temperatures between 423 K and 523 K, the EOS was fitted to the accurate data of Aleksandrov and Larkin,<sup>130</sup> which are represented within 0.1 % (see Sec. 5.1.6.1). For comparison, some of these data points are included in Figure 5.29. At 423 K it is apparent that they deviate considerably from the results of Evstefeev *et al.*<sup>145</sup> It could not be clarified whether the results presented by Evstefeev are of significantly less accuracy or whether these deviations are a result of the graphical determination of the data. Nevertheless, Figure 5.29 indicates that the EOS allows for a qualitatively and, to a certain extent, also quantitatively correct description of the metastable superheated liquid region. Figure 5.17 shows that the previous reference EOS of Hill *et al.*<sup>1</sup> is in surprisingly good agreement with Evstefeev’s data. The data deviate by less than 0.8 % from values calculated from Hill’s EOS. However, Hill did



not discuss or cite the data of Evstefeev *et al.*<sup>145</sup> within his publication. In addition to this, and as discussed in Sec. 5.1.6.1, the new EOS enables a significantly more accurate description of the speed-of-sound data in the stable liquid. Thus, it is reasonable to assume that the good agreement between the old EOS and the superheated-liquid data is coincidental.

In recent years, the thermodynamics of metastable subcooled (also referred to as “supercooled”) water has been a very active scientific subject. Aside from its relevance for the understanding of meteorological phenomena such as cloud formation, its thermodynamic properties are important for the modelling of seawater and other aqueous mixtures, where the employed models for water are often evaluated below the pure-water freezing temperature. The most important IAPWS-associated work in this field is the EOS for supercooled water published by Holten *et al.*,<sup>146</sup> which also led to an IAPWS guideline on this topic.<sup>147</sup> This guideline is for the thermodynamic properties of H<sub>2</sub>O and does not include any information on D<sub>2</sub>O. Nevertheless, an EOS for subcooled heavy water was published by Holten *et al.*<sup>148</sup> within the supplement of an article presenting a preliminary version of the EOS for ordinary water. Because the range of validity of the present EOS is officially limited to stable states at temperatures above the minimum temperature along the melting line, detailed comparisons with the EOS of Holten *et al.*,<sup>148</sup> which was exclusively developed for the small temperature range of the subcooled liquid, are not presented here. Nevertheless, their work was carefully studied in order to identify the most reliable data sets that enabled a reasonable extrapolation of the new EOS below its lower temperature limit.

In addition to the theoretical work of Holten and collaborators, there are some experimental activities on subcooled light and heavy water within IAPWS. In Sec. 5.1.5.1 the highly accurate density measurements of Duška *et al.*,<sup>107</sup> which comprise both the stable liquid at low temperatures and the metastable subcooled liquid at pressures up to 100 MPa, were discussed. Measurements of the vapor pressure of subcooled heavy water are currently carried out at the Italian National Institute of Metrological Research (INRiM), Turin, that could not be completed prior to the development of the present EOS. Thus, the most recent and (with an expanded ( $k = 2$ ) uncertainty of 0.04 %) also most accurate experimental data are the densities of Duška *et al.*<sup>107</sup> Deviations of these data from values calculated from the new EOS are shown in Figure 5.30, which additionally presents data from other sources. In order to get a better impression of the accuracy of these experimental works, Figure 5.30 not only presents the data in the metastable but, if investigated, also in the stable liquid region. Due to the negative slope of the melting-pressure curve of (heavy) water (see Sec. 5.1.2), it can be difficult to see the magnitude of subcooling of the data when plotted versus absolute temperature. Therefore, the corresponding melting temperature was calculated for every data point at its investigated pressure by means of Eq. (5.4). This allows plotting the deviations in Figure 5.30 against the difference between the measured temperature and the melting temperature.

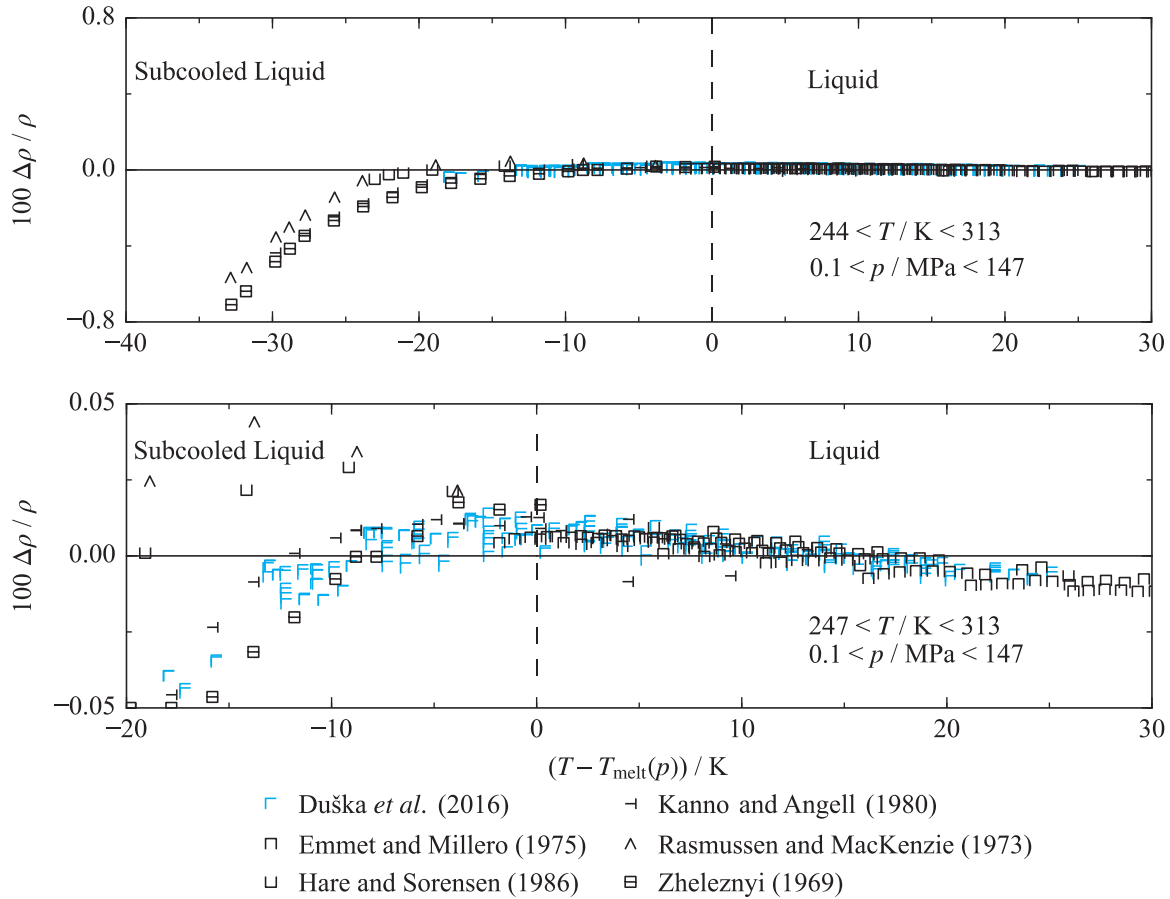


**Figure 5.30** Top: Relative deviations  $\Delta \rho / \rho = (\rho_{\text{exp}} - \rho_{\text{calc}}) / \rho_{\text{exp}}$  of the experimental density data in the liquid phase and in the metastable subcooled liquid region of the new EOS. The deviations are plotted versus the difference between the measured temperature and the melting temperature at given pressure calculated from Eq. (5.4). Bottom: Relative deviations of the most accurate experimental data from the new EOS.

It can be seen that, except for two data points at a subcooling of about 17 K (absolute temperature of 255 K), the EOS represents the complete data set of Duška *et al.*<sup>107</sup> within its experimental uncertainty of 0.04 %. Thus, the uncertainty of calculated densities of the subcooled liquid at temperatures from the melting line down to 260 K and at pressures up to 100 MPa is estimated to be 0.04 %. This temperature range is equivalent to a maximum subcooling of about 18 K. Due to the high reliability of Duška's data, the 0.04 % uncertainty estimate is included in Figure 5.30, although the data are beyond the official range of validity of the new EOS. As is evident from the left panel of Figure 5.30, three experimental studies investigated even deeper states of subcooling. Kanno and Angell<sup>120</sup> measured densities down to 247 K (subcooling of 30 K), whereas Zheleznyi<sup>149</sup> and Rasmussen and MacKenzie<sup>150</sup> realized measurements at about 244 K (subcooling of 33 K), which is stated to be close to the homogeneous nucleation temperature, which is the natural limit of subcooling. All these experiments were carried out at atmospheric pressure. The corresponding publications do not provide any useful information about experimental uncertainties. Thus, it can only be stated that the new EOS describes all these data within 0.8 %, which is not necessarily equivalent to the uncertainty of calculated densities in this temperature range. The EOS of Hill *et al.*<sup>1</sup> is not valid at temperatures below the triple point. Nevertheless, the EOS can be

reasonably extrapolated to calculate densities of the subcooled liquid. At 260 K, these calculated densities deviate by about 0.25 % from the data of Duška *et al.*;<sup>107</sup> the data at deeper states of subcooling exhibit deviations of up 2.2 %.

The vapor pressure of the subcooled liquid is reported in two experimental studies published by Bottomley<sup>80</sup> and Kraus and Greer.<sup>89</sup> The data were already mentioned briefly in Sec. 5.1.4.1 and are included in Figure 5.5, which shows deviations of all available vapor-pressure data from the new EOS. A more detailed presentation of these two specific data sets is given in Figure 5.31.

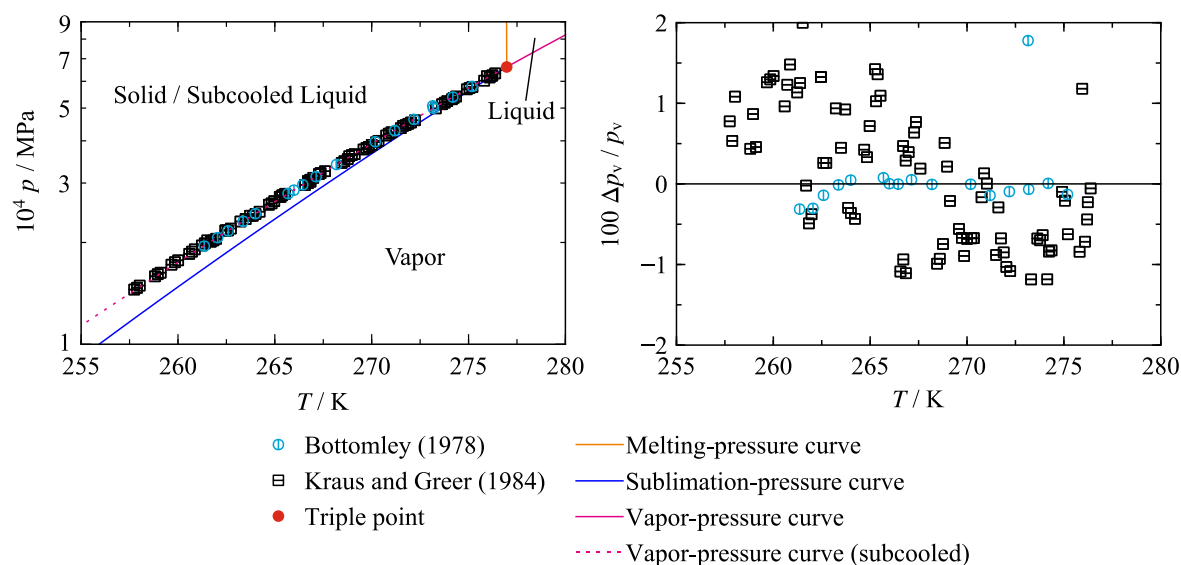


**Figure 5.31** Left: Available experimental data for the vapor pressure of the metastable subcooled liquid in a  $p, T$  diagram. The vapor-pressure curve is calculated by means of the new EOS. The sublimation- and melting-pressure curves are obtained from Eqs. (5.9) and (5.4), respectively. Right: Relative deviations  $\Delta p_v / p_v = (p_{v,\text{exp}} - p_{v,\text{calc}}) / p_{v,\text{exp}}$  of the experimental data from the new EOS.

The left panel of Figure 5.31 shows the distribution of the experimental vapor pressures of the subcooled liquid in relation to the phase boundaries that separate liquid, vapor, and solid states. It might be difficult to imagine the vapor pressure of a subcooled liquid. Thus, the experimental procedure for measuring this property is worth summarizing. A measuring cell is filled with an extremely pure water sample and then repeatedly frozen, degassed in vacuum, and re-liquefied. After this preparation, the water sample is in vapor-liquid equilibrium, and thus at its saturation pressure. The sample is cooled and can be subcooled below the triple-point temperature while the corresponding pressure is always equivalent to the vapor pressure. The so-obtained pressures follow the vapor-pressure curve extended to temperatures below the triple-point temperature. As is apparent from the left panel of Figure 5.31, this “extrapolation” of the vapor-pressure curve exhibits a considerable difference from the sublimation-pressure curve; the difference in slope is related to the difference between the enthalpy of vaporization of the liquid and the enthalpy of sublimation of the solid. Bottomley<sup>80</sup> reported experimental results for this difference between vapor and sublimation pressure. The corresponding sublimation pressures were obtained from Eq. (5.9). Because

the data determined in this way are dependent on the new sublimation-pressure correlation, they were not used for fitting the new EOS. Nevertheless, all deviations between the data and calculated values are below 0.15 % at temperatures down to about 263 K except for one outlier; at the two lowest temperatures (261 K and 262 K), the deviations increase up to 0.32 %. The data of Kraus and Greer<sup>89</sup> range to slightly lower temperatures, down to 257 K, but they also exhibit considerably larger deviations of up to 1.5 % and a scatter of at least 1 %. Thus, they do not allow for a reasonable uncertainty analysis of the new EOS. The uncertainty estimate for calculated vapor pressures of the subcooled liquid is consequently based on comparisons to the data of Bottomley. From the triple-point temperature down to 260 K, this uncertainty estimate is 0.5 %. This estimate is conservative with regard to the deviations, but reasonable considering that the experimental uncertainty of Bottomley's data is not clearly specified and that no comparative data are available. Comparisons between subcooled-liquid  $p_v$  data calculated from the new EOS and the EOS of Hill *et al.*<sup>1</sup> were not carried out, since numerical issues did not allow for evaluating the old EOS at temperatures below the triple point.

The isobaric heat capacity of the subcooled liquid was comprehensively investigated by Angell *et al.*<sup>139</sup> The work of Smirnova *et al.*<sup>140</sup> only includes two data points at a maximum subcooling of about 2.5 K, and is thus of little relevance for the present discussion. Both data sets are limited to atmospheric pressure. In Figure 5.32, it can be seen that Angell's data range to extremely low temperatures, down to 240 K (about 37 K of subcooling). The authors of the corresponding publication state a reproducibility of 1 %, which is not equivalent to the experimental uncertainty of the data. Within the IAPWS-95 publication,<sup>29</sup> the uncertainty of the light-water data from the same reference is estimated to be 3 %, which is consistent with the deviations between the D<sub>2</sub>O data and the new EOS (see right panel of Figure 5.32). In fact, down to 242 K the maximum deviation between the data and the EOS is 3.65 %. It can consequently be concluded that the EOS represents the majority of the data within their estimated experimental uncertainty. Only the data point at the lowest temperature exhibits a quite large deviation of 13.8 %. The reason for this is evident in the left panel of Figure 5.32: the EOS overestimates the anomalous increase of  $c_p$  with decreasing temperature. The EOS of Holten *et al.*<sup>148</sup> is shown for comparison. Since this model is based on the existence of a liquid-liquid critical point in subcooled water, the calculated isobaric heat capacity exhibits a maximum that comes along with a change in curvature allowing for a more accurate description of Angell's data. During the development of the present EOS, no critical-like phenomena in the subcooled liquid region were considered. However, the EOS provides a qualitatively and at temperatures above 242 K also quantitatively correct description of  $c_p$  in the subcooled liquid. It should be noted that so far no experimental evidence for the peak of  $c_p$  at lower temperatures has been published, either for H<sub>2</sub>O or D<sub>2</sub>O. Extrapolating the EOS of Hill *et al.*<sup>1</sup> to temperatures below its lower temperature limit yields quantitatively reasonable results for the isobaric heat capacity down

to 265 K (deviations from Angell's data within 6.3 %). At lower temperatures, the deviations from Angell's data increase significantly with decreasing temperature. The maximum deviation is almost 62 % at 240 K. Furthermore, the left panel of Figure 5.32 shows that Hill's EOS does not reproduce the anomalous increase of  $c_p$  with decreasing temperature, instead  $c_p$  becomes smaller at higher magnitudes of subcooling.

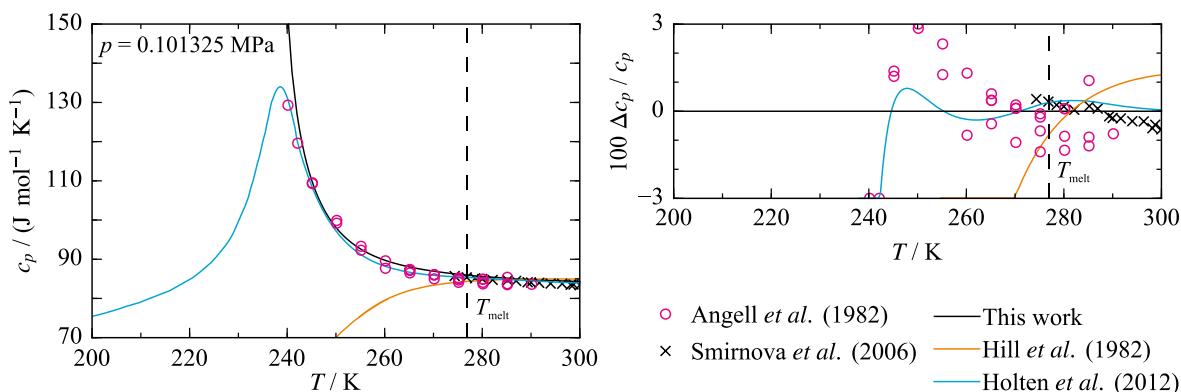


**Figure 5.32** Left: Isobaric heat capacity at atmospheric pressure as a function of temperature in the metastable subcooled and stable liquid region as calculated from the new EOS, the EOS of Hill *et al.*,<sup>1</sup> and the EOS of Holten *et al.*<sup>148</sup> The available experimental data are plotted for comparisons. Right: Relative deviations  $\Delta c_p / c_p = (c_{p,\text{exp}} - c_{p,\text{calc}}) / c_{p,\text{exp}}$  of the experimental data from the new EOS. The EOS of Hill *et al.*<sup>1</sup> and of Holten *et al.*<sup>148</sup> are shown for comparisons.

For the sake of completeness, the speed-of-sound data of Conde *et al.*<sup>151</sup> should be mentioned. The measurements were carried out at atmospheric pressure at temperatures ranging down to 259 K. The data are only graphically presented in the corresponding publication. Personal communications with Conde clarified that the experimental raw data are no longer available. In the stable liquid region, the graphically determined data agree with the most accurate data within 0.5 % (see Figure 5.17). In the subcooled liquid region, the deviations increase with decreasing temperatures and reach a maximum of 3.2 % at 259 K. Because no comparative data are available, the accuracy of both the graphical determination of the data and of the underlying experiments in the subcooled liquid could not be clarified. Consequently, an uncertainty estimate for calculated sound speeds in this state region is not provided.

### 5.1.8 Representation of Physical Behavior and Extrapolation

One of the main targets in the development of EOS is that the final solution should not only exhibit the lowest possible deviations from the available experimental data, but also provide a correct representation of the physical behavior of the fluid. The physical behavior of (heavy) water includes some characteristic features such as the density maximum, the sharp increase of the second virial coefficient with decreasing temperature, and the anomalous steep slope of the isobaric heat capacity over temperature in the subcooled liquid. It was already shown that the EOS enables an accurate description of these characteristics (see

Secs. 5.1.5.1, 5.1.5.2, and 5.1.7). As mentioned in Sec. 5.1.5.1, the density maximum also leads to a maximum speed of sound in the liquid phase. In Figure 5.33, it can be seen that the EOS excellently reproduces this characteristic behavior. The most accurate experimental data are included in order to highlight that the maximum sound speed in liquid (heavy) water is experimentally proven.

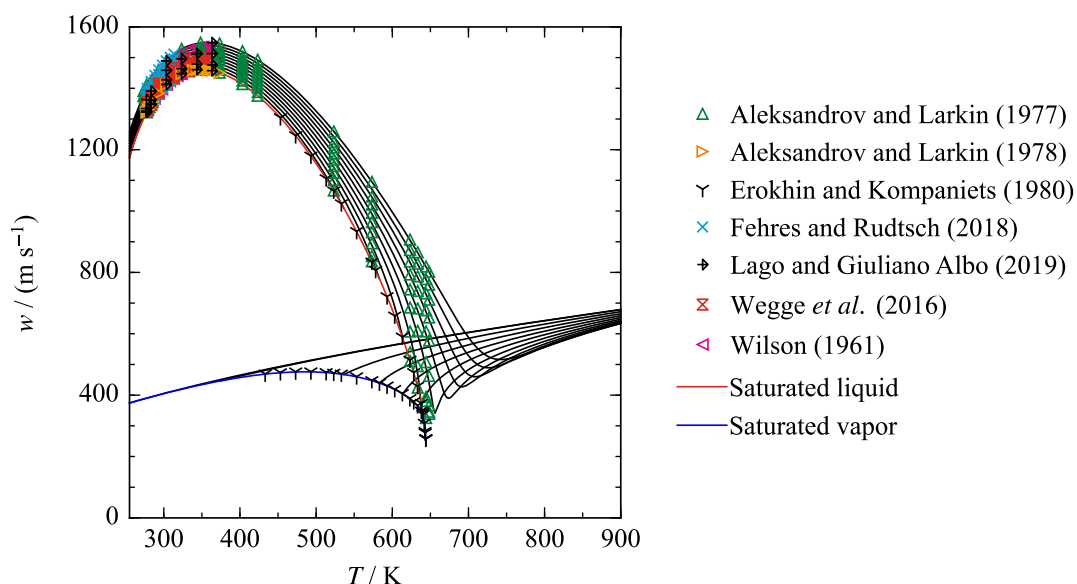


**Figure 5.33** Speed of sound along isobars up to 50 MPa as a function of temperature as calculated from the new EOS. The most accurate experimental data are plotted for comparisons.

Figure 5.33 also shows the distinct minimum of the speed of sound at the critical point. As already discussed in Sec. 5.1.6.1, in theory, the speed of sound should be zero at the critical point, which cannot be reproduced by the functional form of the present EOS. As is evident from Figure 5.33, there are no experimental data close enough to the critical point to give such extremely low values of the speed of sound. However, Figure 5.33 shows that the EOS yields a steep decrease of the sound speed in the critical region.

Comparisons between the new EOS and the available  $p, \rho$  data in the critical region were discussed in Sec. 5.1.5.1 (see also Figure 5.15). An absolute  $p, \rho$  diagram showing the behavior of the EOS in the critical region is presented in the right panel of Figure 5.34. The diagram includes the phase boundaries, the rectilinear diameter, and the critical isotherm as calculated from the EOS. As required, the critical isotherm shows a distinct horizontal inflection point at the critical point. Moreover, the rectilinear diameter (the average between saturated-liquid and -vapor density) exhibits a smooth behavior up to the critical point without any unphysical bends.

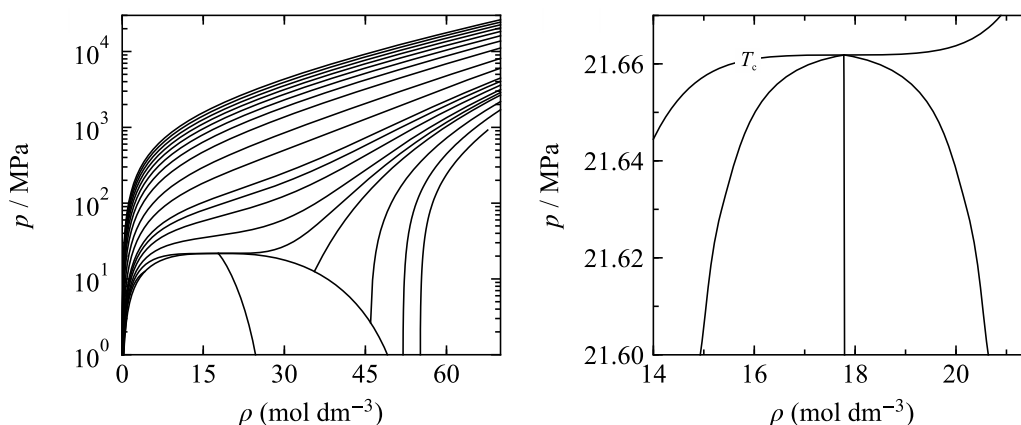


**Figure 5.34** Left:  $p, \rho$  diagram along isotherms up to 10 000 K as calculated from the new EOS. Right: Critical region in a  $p, \rho$  diagram showing the phase boundaries, the rectilinear diameter, and the critical isotherm as calculated from the new EOS.

As important as the validation of the EOS within its range of validity is the evaluation of its extrapolation behavior into regions beyond the experimental data. In general, this aspect is particularly important for the employment of EOS in mixture models that can often access regions outside the range of validity of its pure components. However, since mixtures with heavy water are probably of low technical interest, it is more important to consider that a correct extrapolation behavior also leads to a more accurate description of state points in technically relevant regions.<sup>31</sup> A standard procedure to validate the extrapolation behavior of an EOS is the calculation and discussion of various diagrams showing the behavior of properties at extreme values of temperature and pressure. The left panel of Figure 5.34 illustrates a  $p, \rho$  diagram along isotherms up to 10 000 K, which leads to pressures up to about 30 GPa. It can be seen that the isotherms exhibit the desired converging behavior without crossing each other.

Another important criterion to judge the extrapolation behavior is the shape of the “ideal curves”. These are curves along which one specific property of the real fluid is equivalent to the corresponding property of the hypothetical ideal gas at the same temperature and density.<sup>26</sup> The ideal curves are usually defined for the compressibility factor  $z$  and its derivatives. The most commonly discussed ideal curves are the ideal curve (where  $z = 1$ ), the Boyle curve (where  $(\partial z / \partial \rho)_T = 0$ ), the Joule-Thomson inversion curve (where  $(\partial z / \partial T)_p = 0$ ), and the Joule inversion curve (where  $(\partial z / \partial T)_\rho = 0$ ). In Figure 5.35, these curves are shown in a  $(p / p_c)$  versus  $(T / T_c)$  diagram as calculated from the new EOS and the previous reference EOS of Hill *et al.*<sup>1</sup>

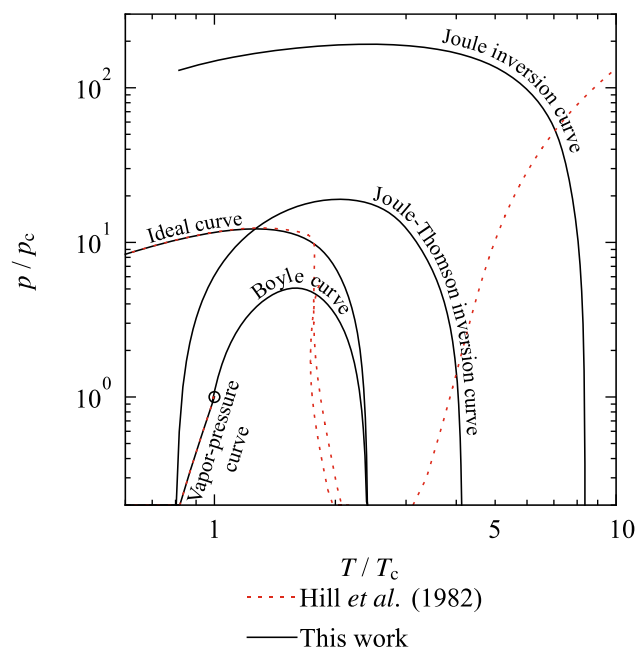


**Figure 5.35** Ideal curves as calculated from the new EOS and the EOS of Hill *et al.*<sup>1</sup>.

As is apparent from Figure 5.35, the ideal curves calculated from the present EOS are smooth over the entire plotted temperature and pressure range and do not exhibit any unreasonable bumps or overhangs. The gap between the y-axis and the Joule inversion curve occurs where this curve would theoretically intersect with the melting-pressure curve of the ice structure VII that could not be correlated for heavy water (see Sec. 5.1.2). The EOS of Hill *et al.*<sup>1</sup> does not allow for reasonable calculations of the ideal curves; they are not even qualitatively correct except for the ideal curve at low reduced temperature. This emphasizes the numerical problems of this EOS, which are among the main reasons to develop the new EOS for heavy water.

Aside from the examples shown in this section, a large number of other property plots were carefully evaluated at technically relevant conditions as well as at extreme values of temperature, pressure, and density. It can be concluded that the new EOS enables a correct description of the physical behavior of heavy water and that it can be extrapolated reasonably into regions beyond the experimentally investigated states.



## 5.2 Equation of State for Chlorine

Chlorine is a halogen that rarely occurs in nature as a chemical element. Due to its high binding propensity, it is mainly found in its diatomic molecular form or in chemical compounds such as sodium chloride (NaCl). Molecular chlorine (Cl<sub>2</sub>, CAS no. 7782-50-5) is a pale yellow-green gas at ambient conditions. Whereas elemental chlorine is extremely reactive, the molecular form is not flammable and only explosive at special conditions and through reactions with other fluids; nevertheless, chlorine is extremely hazardous for all living organism. Inhaling gaseous chlorine harms the respiratory system. For this reason, it was misused by the German army as a chemical weapon during World War I. In addition to its toxicity, it can react to corrosive acid compounds when exposed to moisture. These two aspects pose exceptional challenges to experimental studies of its thermodynamic properties. The available experimental data are therefore limited. Nevertheless, reliable thermodynamic property data are needed due to the significant importance of chlorine for many chemical applications, such as water purification, bleaching, paper manufacturing, or the production of pharmaceuticals.

In the present work, chlorine is considered as a minor impurity in CO<sub>2</sub>-rich mixtures as relevant to CCS. In these mixtures, chlorine usually occurs as a residue of the burned fossil fuels. The implementation of chlorine into the extended CCS-mixture model presented in this work required the development of a new pure-fluid EOS. The current standard formulation of the International Union of Pure and Applied Chemistry (IUPAC) was presented by Angus *et al.*<sup>152</sup> in 1985. The functional form of that EOS is not suitable for the use in Helmholtz-energy explicit multi-component mixture models; thus, a new fundamental EOS was developed in this work. Table 5.5 features various physical constants and characteristic properties of chlorine that were important to the development of the EOS, as well as further quantities that were calculated using this EOS.

**Table 5.5** Physical constants and characteristic properties of chlorine (Cl<sub>2</sub>).

Quantity	Symbol	Value	Reference
Molar gas constant	$R$	8.314 459 8 J mol <sup>-1</sup> K <sup>-1</sup>	Mohr <i>et al.</i> <sup>59</sup>
Molar mass	$M$	70.906 g mol <sup>-1</sup>	Angus <i>et al.</i> <sup>152</sup>
Critical temperature	$T_c$	416.8654 K	Ambrose <i>et al.</i> <sup>153</sup>
Critical pressure	$p_c$	7.6424 MPa	This work
Critical density	$\rho_c$	8.06 mol dm <sup>-3</sup>	This work
Triple-point temperature	$T_{tp}$	172.17 K	Angus <i>et al.</i> <sup>152</sup>
Triple-point pressure	$p_{tp}$	1.3808 kPa	This work
Vapor density at triple point	$\rho_{pv}$	0.000 966 mol dm <sup>-3</sup>	This work
Liquid density at triple point	$\rho_{pl}$	24.602 mol dm <sup>-3</sup>	This work
Normal-boiling-point temperature	$T_{nbp}$	239.198 K	This work
Vapor density at the normal boiling point	$\rho_{nbpv}$	0.052 336 mol dm <sup>-3</sup>	This work
Liquid density at the normal boiling point	$\rho_{nbpl}$	22.052 mol dm <sup>-3</sup>	This work
Acentric factor	$\omega$	0.070	This work

The EOS for chlorine is based on the reduced Helmholtz-energy explicit functional form discussed in Sec. 3.3 (see Eqs. (3.33) to (3.38)). Thus, it is a function of the reduced density and reciprocal reduced temperature, which are calculated by using the critical-point parameters given in Table 5.5 as reducing quantities. According to Eq. (3.33), the reduced Helmholtz energy is split into an ideal-gas and a residual part. The ideal-gas part of the Helmholtz energy of chlorine is described by:

$$\alpha^o(\tau, \delta) = a_1 + a_2\tau + \ln \delta + (c_0 - 1)\ln \tau + \sum_{k=1}^3 v_k \ln [1 - \exp(-u_k \tau/T_c)]. \quad (5.12)$$

All parameters including the constants  $a_1$ ,  $a_2$ ,  $c_0$ , and the adjustable parameters  $v_1$  to  $v_3$ , and  $u_1$  to  $u_3$  are given in Table C.1 in Appendix C. The reference state of the EOS is the normal boiling point ( $T_{\text{nbp}} = 239.198$  K). The integration constants  $a_1$  and  $a_2$  were consequently adjusted to yield zero enthalpy and entropy for the saturated liquid at this reference state.

The residual part of the EOS includes a total of 15 terms. It consists of five polynomial(-like) terms, five exponential terms, and five Gaussian bell-shaped terms. The complete equation can be written as:

$$\begin{aligned} \alpha^r(\delta, \tau) = & \sum_{k=1}^5 n_k \delta^{d_k} \tau^{t_k} + \sum_{k=6}^{10} n_k \delta^{d_k} \tau^{t_k} \exp(-\delta^{l_k}) \\ & + \sum_{k=11}^{15} n_k \delta^{d_k} \tau^{t_k} \exp\left[-\eta_k (\delta - \varepsilon_k)^2 - \beta_k (\tau - \gamma_k)^2\right]. \end{aligned} \quad (5.13)$$

All parameters of this function (coefficients  $n_k$ , temperature exponents  $t_k$ , density exponents  $d_k$  and  $l_k$ , and the parameters of the Gaussian bell-shaped terms  $\eta_k$ ,  $\varepsilon_k$ ,  $\beta_k$ , and  $\gamma_k$ ) are listed in Table C.2 in Appendix C.

The EOS is valid for all stable fluid states from the triple-point temperature  $T_{\text{tp}} = 172.17$  K to  $T_{\text{max}} = 440$  K and at pressures up to  $p_{\text{max}} = 20$  MPa.

Deviations between ideal-gas isobaric heat-capacity data from the literature and results calculated from the ideal-gas part of the new EOS are shown in Figure 5.36. The EOS was fitted to a selection of data points up to a temperature of 2000 K, which is far above the temperature range of technical applications. At low temperatures, it was fitted to the data of Hurly *et al.*,<sup>154</sup> which were derived from very accurate speed-of-sound measurements in the temperature range from 260 K to 440 K. Excluding the two lowest-temperature data points, the average value of the given standard uncertainties of the data is 0.06 %, which corresponds to an expanded ( $k = 2$ ) uncertainty of 0.12 %. As apparent from Figure 5.36, the EOS represents the complete data set within this uncertainty. The data of Hurly *et al.*<sup>154</sup> are consistent with the values published by Evans *et al.*<sup>155</sup> that range to high temperatures of up to 3000 K. The data result from a correlation of spectroscopical results. The authors provide no uncertainty of the data. Conservatively estimated, the expanded ( $k = 2$ ) uncertainty in ideal-gas isobaric heat capacities calculated from Eq. (5.12) is 0.15 %.

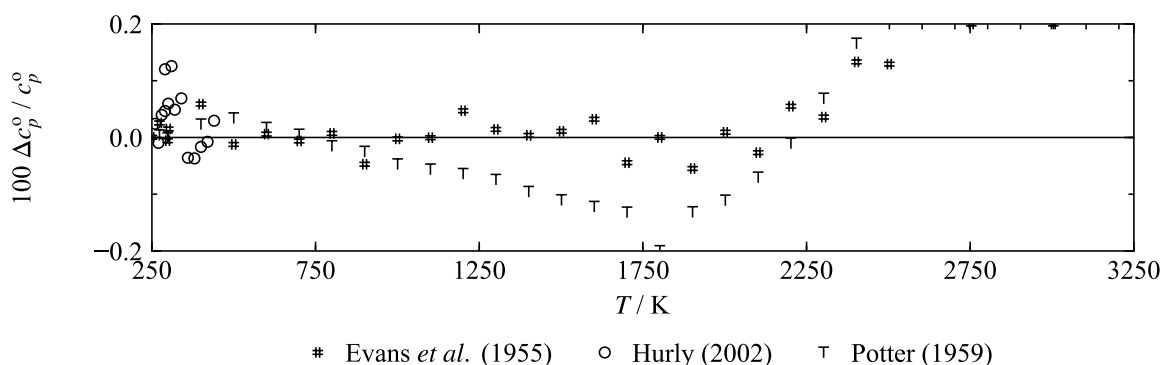


**Figure 5.36** Relative deviations  $\Delta c_p^o / c_p^o = (c_{p,\text{data}}^o - c_{p,\text{calc}}^o) / c_{p,\text{data}}^o$  of ideal-gas isobaric heat-capacity data calculated from Eq. (5.12) versus temperature.

For the real fluid state of chlorine, reliable experimental data are available for vapor pressure, saturated and homogeneous density, speed of sound, and isobaric heat capacity. The available thermal saturation data including vapor pressure, saturated-liquid and saturated-vapor density are shown in Figure 5.37. It presents deviations between the experimental data and values calculated from the new EOS and the EOS of Angus *et al.*<sup>152</sup>

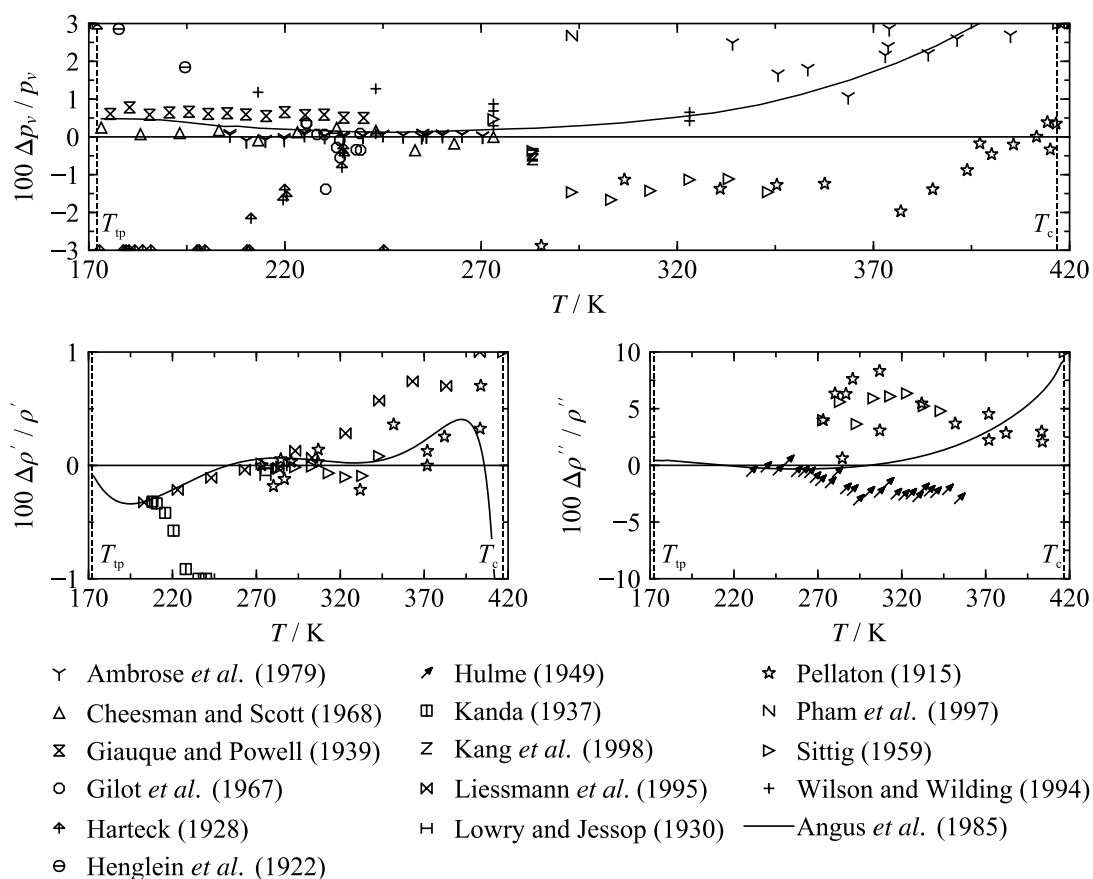


**Figure 5.37** Top: Relative deviations  $\Delta p_v / p_v = (p_{v,\text{exp}} - p_{v,\text{calc}}) / p_{v,\text{exp}}$  of the experimental vapor-pressure data from the new EOS versus temperature. Bottom: Relative deviations  $\Delta \rho / \rho = (\rho_{\text{exp}} - \rho_{\text{calc}}) / \rho_{\text{exp}}$  of the experimental density data for the saturated-liquid (left) and saturated-vapor (right) versus temperature. In all plots, the EOS of Angus *et al.*<sup>152</sup> is included for comparison.

An important set of experimental vapor pressures was published by Ambrose *et al.*<sup>153</sup> The authors investigated two temperature regions with two different apparatuses. The

temperature range from 205 K to 270 K was investigated in a vapor-pressure glass bulb. For the measurements at higher temperatures between approximately 335 K and 405 K a mercury filled U-tube was used as introduced in an earlier work of the same group.<sup>156</sup> Ambrose *et al.*<sup>153</sup> provide some uncertainty information about the low-temperature measurements. The uncertainty in saturation temperature is stated to be 0.02 K; whereas a repeatability of 1 Pa is reported for the pressure measurements. Considering these specifications and additionally calculating the sensitivity coefficient  $(\partial p / \partial T)_{\text{sat}}$  from the present EOS, leads to expanded ( $k = 2$ ) experimental uncertainties between 0.14 % and 0.25 %. The EOS represents the complete low-temperature data set up to 270 K with deviations below 0.11 %, and thus within their estimated experimental uncertainty. Ambrose *et al.*<sup>153</sup> reported no uncertainty information for the high-temperature measurements between 335 K and 405 K. It is only stated that the data are believed to be more reliable than the previous measurements by Pellaton.<sup>157</sup> During the fitting of the EOS, any attempt to reduce the deviations to Ambrose's high-temperature data, worsened the description of the accurate speed-of-sound data of Hurly *et al.*<sup>154</sup> This leads to the conclusion, that the experimental uncertainty in the data of Ambrose *et al.*<sup>153</sup> corresponds to the deviations shown in Figure 5.37. Fitting only a few low weighted data points from that data set, lead to a good compromise between the representation of those data and the measurements of Pellaton.<sup>157</sup> Both data sets are represented with deviations below 3 %. For the latter data set, no experimental uncertainties are available.

At temperatures lower than investigated by Ambrose *et al.*,<sup>153</sup> the only reliable data were published by Giauque and Powell<sup>158</sup> and Cheesman and Scott.<sup>159</sup> In the latter reference, no experimental data are presented. Instead, the data were correlated based on the measurements of Giauque and Powell.<sup>158</sup> The underlying method of this correlation is not specified. It is surprising that the calculated data are in better agreement with the present EOS than the original data by Giauque and Powell.<sup>158</sup> Those data result from a calorimetric investigation. The uncertainty in saturation pressure is given with 0.002 cmHg (about 2.67 Pa), whereas the uncertainty in temperature is stated to be 0.05 K in an earlier work.<sup>160</sup> Based on these uncertainties and the calculated sensitivity coefficient  $(\partial p / \partial T)_{\text{sat}}$ , combined expanded ( $k = 2$ ) uncertainties of the data were estimated. These range from 0.93 % at a temperature of 175 K to 0.44 % at 240 K. The deviations between the data and the EOS are in good agreement ( $AAD = 0.61$  %) with these experimental uncertainties.

Based on the present discussion of the available data and the deviations shown in the top panel of Figure 5.37, the estimated uncertainties in vapor pressures calculated from the present EOS are 1 % at  $T < 205$  K, 0.5 % at  $205 \leq T / \text{K} \leq 270$ , and 3 % at higher temperatures. At temperatures up to 270 K, the agreement between the present EOS and that of Angus *et al.*<sup>152</sup> is within the estimated uncertainty of the data. The deviations between both EOS increase with increasing temperature. Angus *et al.*<sup>152</sup> apparently fitted their EOS

to the high-temperature data of Ambrose *et al.*,<sup>153</sup> which are not consistent with the accurate gaseous sound-speed data of Hurly *et al.*<sup>154</sup>

In the bottom panels of Figure 5.37, deviations between calculated saturated-liquid and -vapor densities are presented. The quality of the data for these two properties differs considerably. Whereas almost all saturated-liquid densities are represented with deviations below 1 %, the saturated-vapor data deviate from the EOS by up to 10 %. No experimental uncertainties are specified in the corresponding publications. The good representation of the saturated-liquid data has been achieved by exclusively fitting the EOS to the homogeneous liquid densities of Wagenbreth.<sup>161</sup> It can be assumed that the thus obtained deviations of the saturated-liquid data correspond to their experimental uncertainties. None of the data for saturated-vapor densities were used in the fitting process. The data of Hulme,<sup>162</sup> which are in comparably good agreement with the EOS, were not obtained experimentally but result from calculations that are not further specified in the corresponding publication.

Because the experimental uncertainties of the saturated-liquid data are unknown and the saturated-vapor data are not sufficiently accurate, no uncertainties of calculated data can be estimated from the deviation plots in Figure 5.37. Instead, the uncertainties are estimated following the approach discussed for heavy water and given by Eq. (5.10). According to this correlation, the uncertainty in calculated saturated densities can be derived from the uncertainties in calculated vapor pressures and homogeneous densities. The uncertainties in vapor pressures were given in the previous paragraph. As discussed later in this section, the uncertainty in calculated homogeneous densities is 0.2 % in the liquid phase and 0.25 % in the gas phase. Considering these uncertainties in density and vapor pressure and additionally calculating the sensitivity coefficient  $(\partial\rho/\partial p)_{\text{sat}}$  from the present EOS, leads to the following uncertainties in calculated saturated densities: The uncertainty in saturated-liquid densities is 0.5 % for temperatures up to 375 K. At higher temperatures, the uncertainty increases considerably with increasing temperature. The uncertainties in saturated-vapor densities are 2 % for temperature up to 205 K and 1 % for higher temperatures up to 270 K. At higher temperatures, the high uncertainty in vapor pressure is dominating and the uncertainty increases to more than 6 %.

Deviations between calculated homogeneous densities and the experimental data are shown in Figure 5.38. The EOS was fitted to the gas densities of Ross and Maass<sup>163</sup> and the liquid densities of Wagenbreth.<sup>161</sup> The correlated data of Hulme<sup>162</sup> additionally cover the supercritical gas-like state region; nevertheless, fitting the EOS to these data worsened the representation of other data such as the liquid densities of Wagenbreth.<sup>161</sup> or the speed-of-sound data of Hurly *et al.*<sup>162</sup> The data of Ross and Maass<sup>163</sup> mostly supersede those of Jaquerod and Tourpaian;<sup>164</sup> however, it should be noted that the measurements of Jaquerod and Tourpaian are remarkably accurate despite their age. Neither Wagenbreth<sup>161</sup> nor Ross and Maass<sup>163</sup> report useful information about experimental uncertainties. The EOS

represents most of the liquid-phase data of Wagenbreth with deviations below 0.1 % except for some points close to the phase boundary or at supercritical temperatures. The calculated  $AAD$  for the liquid-phase data is 0.046 % and the  $AAD$  of high-density supercritical state data is 0.125 % (see Table C.4 in Appendix C). Based on these deviations, the estimated uncertainty of calculated liquid and supercritical liquid-like density data is 0.2 %. This estimate is valid for temperatures between 265 K to 425 K and at pressures up to 20 MPa. Excluding one outlier, the gas-phase data of Ross and Maass<sup>163</sup> are represented with deviations below 0.25 % and an  $AAD$  of 0.098 %. The maximum deviation of 0.25 % is adopted as the uncertainty of calculated gas-phase densities at temperatures between 290 K and 350 K and at pressures up to  $p_{v,max}(T) \approx 0.2$  MPa. At lower temperatures between 273 K and 290 K, the data of Jaquerod and Tourpaian<sup>164</sup> are represented within a maximum deviation of 0.5 %, which is a reasonable uncertainty estimate for calculated gas densities in this temperature range.

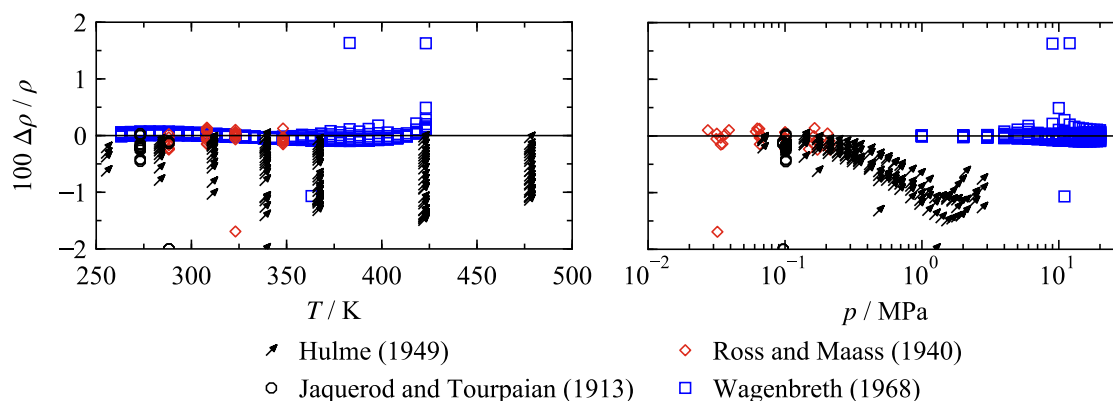


**Figure 5.38** Relative deviations  $\Delta\rho/\rho = (\rho_{exp} - \rho_{calc})/\rho_{exp}$  of experimental density data from the EOS versus temperature (left) and pressure (right).

Comparisons between  $p\rho T$  results of the new EOS and that of Angus *et al.*<sup>152</sup> are only possible by plots in which one property is kept constant. In Figure 5.39, deviations between both models and experimental data are shown for selected isotherms. It can be seen that the EOS mostly agree within the uncertainties estimated in the previous paragraph. Significant deviations are only noted for the supercritical isotherm (423 K), for which the EOS of Angus *et al.*<sup>152</sup> exhibits considerable deviations from the data of Wagenbreth.<sup>161</sup> The good agreement of both EOS is not surprising because no additional  $p\rho T$  data have become available since the development of the previous standard EOS.

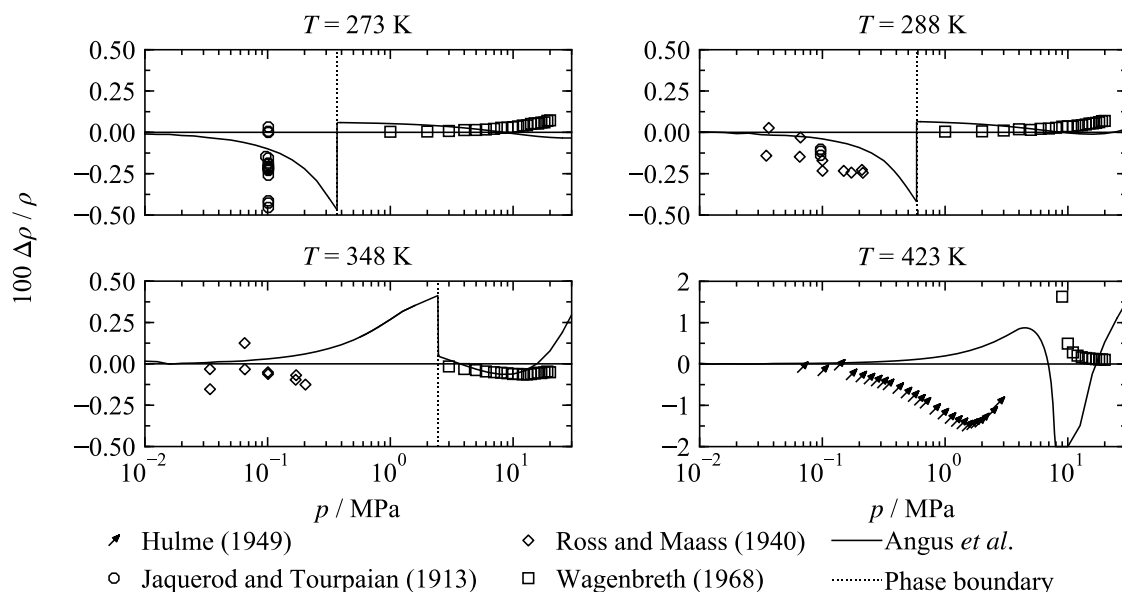


**Figure 5.39** Relative deviations  $\Delta\rho / \rho = (\rho_{\text{exp}} - \rho_{\text{calc}}) / \rho_{\text{exp}}$  of selected experimental density data along isotherms from the new EOS. The EOS of Angus *et al.*<sup>152</sup> is plotted for comparison.

In fact, the only significantly important data published after the development of Angus' EOS are the speed-of-sound measurements of Hurly *et al.*<sup>154</sup> The data cover the gas phase and the supercritical gas-like fluid at temperatures between 260 K and 440 K and pressures up to 1.5 MPa. The reported standard uncertainty of the data is 0.01 %. The EOS represents the complete data set with a maximum deviation of 0.02 % ( $AAD = 0.005 \%$ ), and thus within the expanded ( $k = 2$ ) experimental uncertainty. Hence, the estimated uncertainty of calculated sound speeds in gaseous chlorine is 0.02 % at temperatures between 260 K and 440 K and pressures up to 1.5 MPa. The data of Hurley and colleagues supersede the older measurements of Schulze,<sup>165</sup> Sittig,<sup>166</sup> and Strecker.<sup>167</sup>  $AAD$  between these data, those of Hurly *et al.*,<sup>154</sup> and the present EOS are given in Table C.5 in Appendix C.

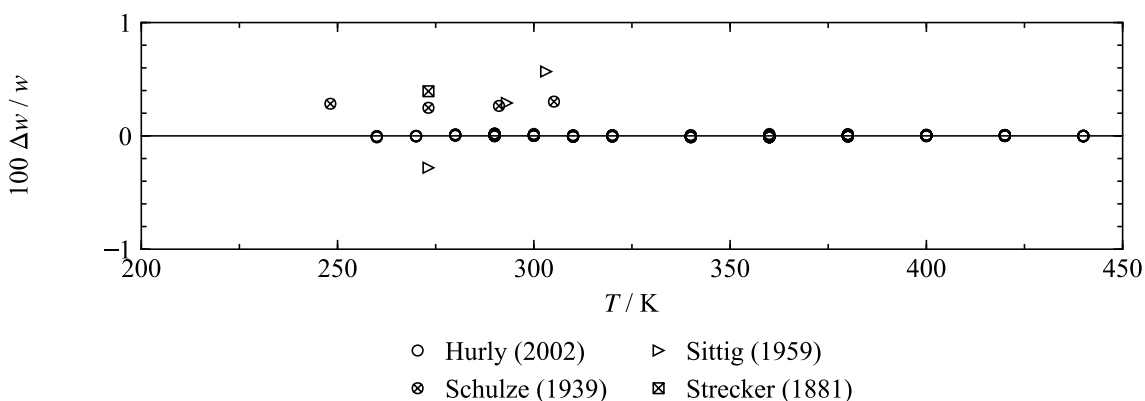


**Figure 5.40** Relative deviations  $\Delta w / w = (w_{\text{exp}} - w_{\text{calc}}) / w_{\text{exp}}$  of experimental speed-of-sound data from the EOS versus temperature.

Comparisons between sound speeds calculated from the new and the previous standard EOS are shown in Figure 5.41. Since no accurate experimental speed-of-sound data were available for the development of the EOS of Angus *et al.*,<sup>152</sup> it exhibits large deviations from

the data. It can therefore be noted that the description of sound speeds in gaseous chlorine has been significantly improved with the new EOS.

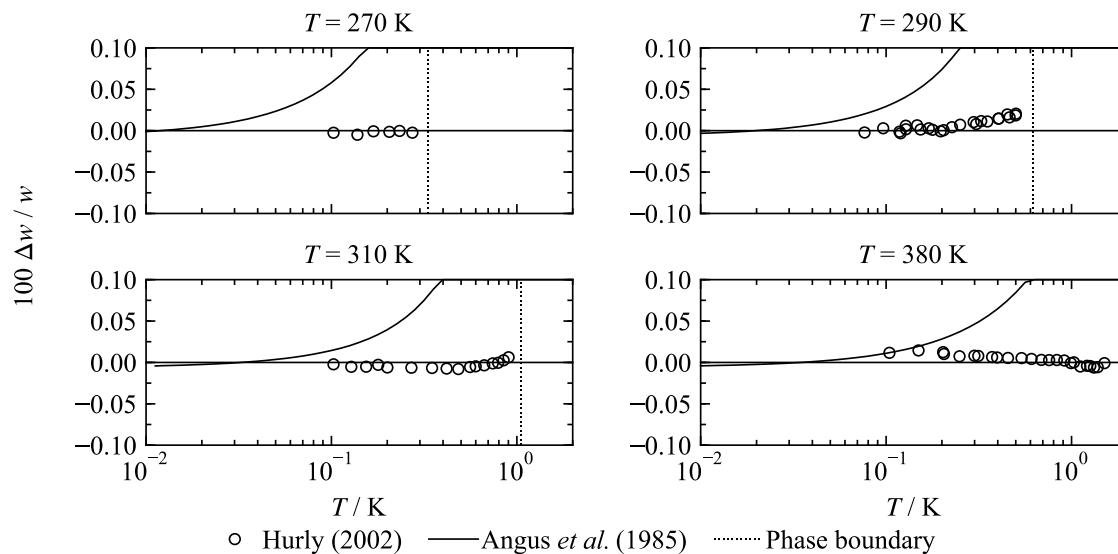


**Figure 5.41** Relative deviations  $\Delta w / w = (w_{\text{exp}} - w_{\text{calc}}) / w_{\text{exp}}$  of selected experimental speed-of-sound data along isotherms from the new EOS. The EOS of Angus *et al.*<sup>152</sup> is plotted for comparison.

Two data sets with experimental isobaric heat capacities of liquid chlorine at ambient pressure were found in the literature. Only the data of Giauque and Powell<sup>158</sup> cover a sufficiently wide temperature range and are accurate enough to validate the present EOS. The EOS represents the data between 179 K and 237 K with an AAD of 0.349 %. Since the authors did not discuss the uncertainty of their measurements, and since the only comparative data of Eucken and Karwat<sup>168</sup> are considered to be less accurate, no uncertainty of heat capacities calculated for the EOS is given here. For the sake of completeness, it should be noted that the EOS of Angus *et al.*<sup>152</sup> exhibits higher deviations from the data.

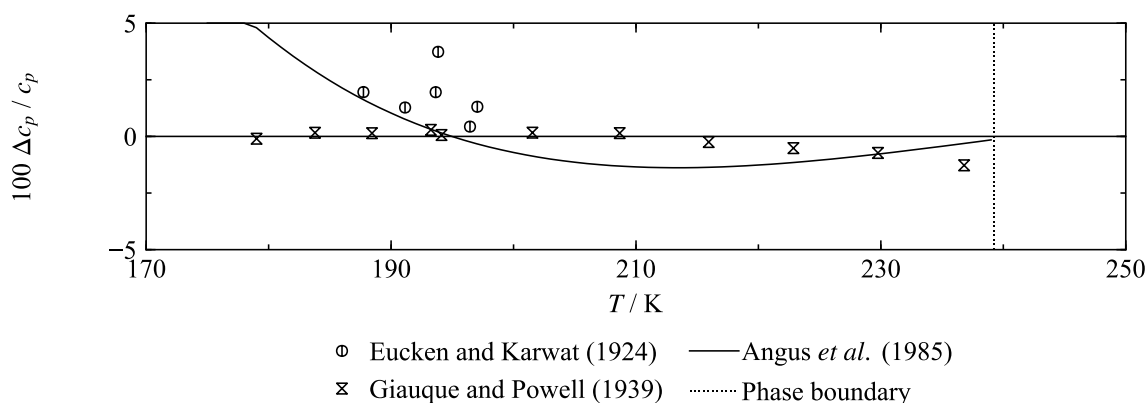


**Figure 5.42** Relative deviations  $\Delta c_p / c_p = (c_{p,\text{exp}} - c_{p,\text{calc}}) / c_{p,\text{exp}}$  of experimental isobaric heat-capacity data at ambient pressure from the new EOS versus temperature. The EOS of Angus *et al.*<sup>152</sup> is plotted for comparison.

In order to complete the validation of the new EOS for chlorine, it is essential to briefly discuss the representation of the physical behavior as well as the extrapolation behavior of the equation. Two property plots that were continuously validated while fitting the EOS are



shown in Figure 5.43. The residual part of the isochoric heat capacity as well as the speed of sound are both depicted along isobars as a function of temperature. The saturated-vapor curve in the  $c_v^r, T$  diagram must have a positive slope and curvature over the entire temperature range. It has to reach a maximum at the critical point, where it meets the saturated-liquid curve. Along the saturated-liquid curve the slope with respect to temperature has to be negative at low temperatures, exhibit a minimum, and increase to its maximum at the critical point. It can be seen in Figure 5.43 that the present EOS is in excellent agreement with these physical constraints. In the  $w, T$  diagram, the saturated-liquid curve should exhibit a negative slope over the entire temperature range. It should furthermore meet the saturated-vapor curve in a local minimum. The slope of the saturated-vapor curve should be positive at low temperatures, reach a maximum, and then decrease to the minimum at the critical point. Again, Figure 5.43 shows that the EOS matches all these constraints.

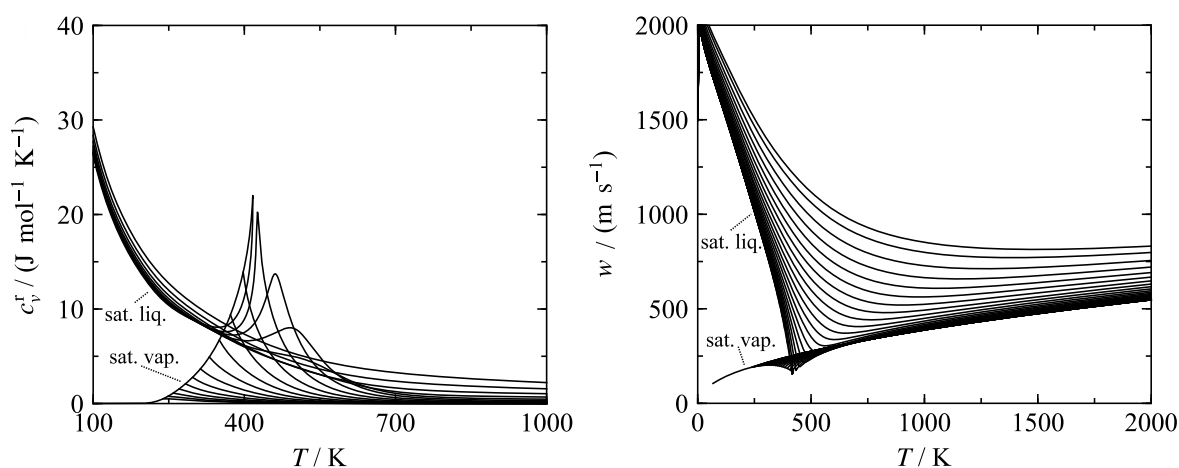


**Figure 5.43** Residual isochoric heat capacity (left) and speed of sound (right) versus temperature calculated from the EOS along isobars up to 200 MPa.

In addition to the qualitatively correct shape of the saturation lines, the property plots exhibit a smooth shape of the isobars up to 200 MPa without any unphysical discontinuities. Despite the importance of chlorine for the chemical industry, the new equation was mainly developed to be implemented into the multi-component mixture model. In order to ensure the numerical stability of mixture calculations, it is important to also evaluate the EOS at extreme values of temperature and pressure. In the left panel of Figure 5.44, a  $T, \rho$  diagram for temperatures up to 1000 K along isobars up to 750 MPa is shown. In the right panel, a  $p, \rho$  diagram covering pressures up to  $10^6$  MPa is presented along isotherms up to 500 000 K. The isobars and isotherms exhibit the desired converging behavior without crossing each other.

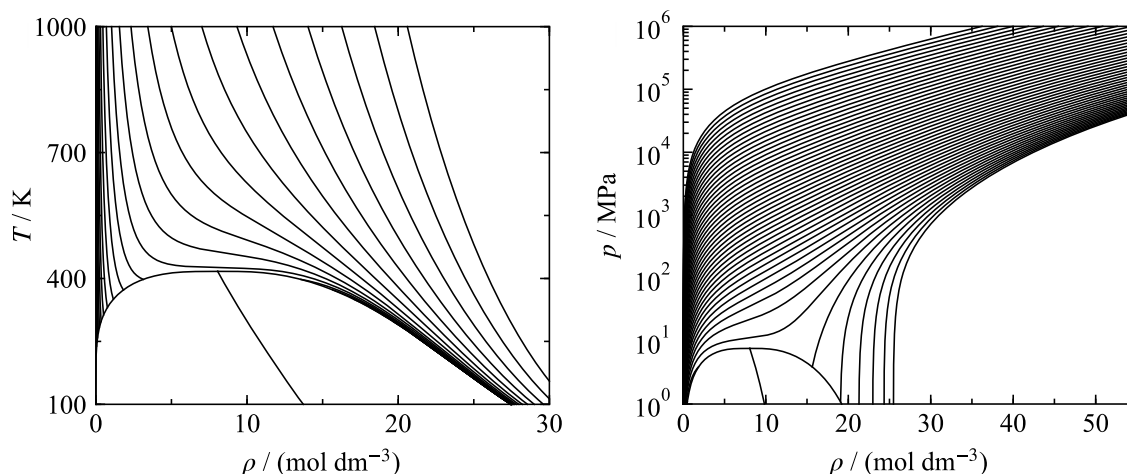


**Figure 5.44** Left:  $T, \rho$  diagram along isobars up to 750 MPa as calculated from the EOS. Right:  $p, \rho$  diagram along isotherms up to 500 000 K. The rectilinear diameter (the average between saturated-liquid and -vapor density) is included in both diagrams.

Both diagrams in Figure 5.44 additionally present the rectilinear diameter, which corresponds to the average between the saturated-liquid and -vapor density. As discussed for heavy water in Sec. 5.1.8, this characteristic curve should exhibit a smooth behavior up to the critical point. For a comparably simple fluid like chlorine, the rectilinear diameter should actually be an almost straight line. As shown in both diagrams, the rectilinear diameter calculated from the present EOS meets this requirement.

In Sec. 5.1.8, the importance of the ideal curves for the validation of the extrapolation behavior was explained. Constraints for these characteristic curves were also essential for the fitting process of the present EOS. The final curves are presented in the right panel of Figure 5.45. They are smoothly shaped over the entire temperature and pressure range of the diagram, which emphasizes that the extrapolation behavior of EOS is excellent.

Similar important as the description of the ideal curves is a proper representation of the thermal virial coefficients. In the left panels of Figure 5.45, the second and third virial coefficient  $B$  and  $C$  are presented as a function of temperature. Unfortunately, no useful virial-coefficient data for chlorine were found in the literature; thus, a quantitatively correct validation (as done for  $D_2O$  in Sec. 5.1.5.2) is not possible for this fluid. Nevertheless, the course of the plots qualitatively meets all theoretical requirements. Both coefficients are negative at low temperatures and increase with increasing temperature. After crossing the zero line, they reach a maximum, and converge to zero while remaining positive. The maximum in  $C$  is distinct and occurs almost at the critical temperature, which has been reported for various other EOS.<sup>33,169</sup>

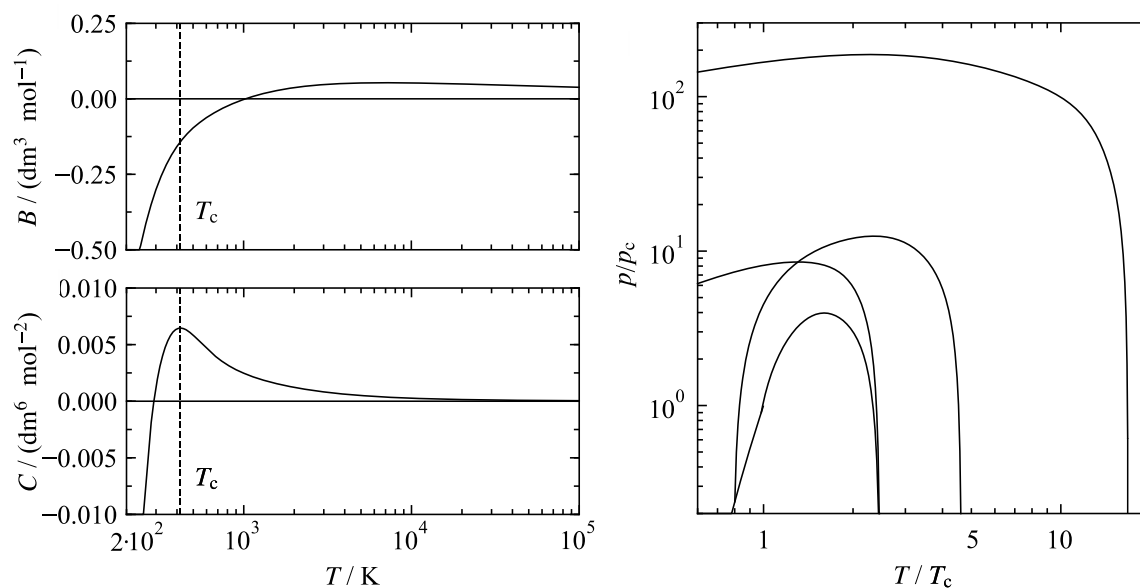


**Figure 5.45** Left: Second and third virial coefficients  $B$  and  $C$  calculated from the EOS as a function of temperature. Right: Ideal curves as calculated from the EOS.

Based on the present validation, it is believed that the new EOS for chlorine also provides reliable results beyond the range of the experimental data. It is therefore suitable for the implementation in mixture models. As discussed later in this thesis (see Secs. 6.3.1.5 and 6.3.3), this has already successfully been done. Despite the limited experimental database, the EOS is sufficiently accurate to be used in the multi-component mixture model developed in this work but also accurate enough for most chemical applications. In order to provide thermodynamic properties of chlorine with reference quality, additional experimental values especially for thermal saturation data are needed to further improve the EOS. However, with regard to the hazardous nature of this fluid, it is unlikely that such data will become available in the future.

### 5.3 Equation of State for Monoethanolamine

Monoethanolamine (CAS no. 141-43-5) is a colorless and viscous liquid at ambient conditions. It is an organic substance and, as the name implies, belongs to the family of the amines. These substances are derivatives of ammonia ( $\text{NH}_3$ ) with one or more hydrogen atoms being replaced by another functional group. Monoethanolamine is a “primary” amine with only one hydrogen atom replaced by a  $\text{CH}_2\text{CH}_2\text{OH}$  group. Hence, the molecular formula of monoethanolamine is  $\text{C}_2\text{H}_7\text{NO}$ . It is often referred to as “MEA”; an abbreviation that is also frequently used in this work. Besides, many other names are common, for example 2-aminoethanol, 2-ethanolamine, 2-hydroxyethylamine,  $\beta$ -aminoethanol, ethanolamine, or ethylolamine. MEA is a highly polar fluid which makes it an important solvent in many chemical applications; however, the most important application is “amine gas treating” or also called “amine scrubbing”. The aim of these processes is to remove, mostly,  $\text{H}_2\text{S}$  or  $\text{CO}_2$  from combustion gases or natural gases by using aqueous amine solutions as solvents. Amine gas treating with MEA is the most widely used  $\text{CO}_2$ -separation technique in CCS. MEA therefore needs to be considered as minor impurity in typical  $\text{CO}_2$ -rich mixtures relevant to CCS. Because no accurate fundamental EOS for pure MEA was available, a new formulation was developed within the present work in order to implement this important substance into the multi-component mixture EOS presented in Sec. 6. A preliminary EOS was proposed in the Master thesis of Kortmann.<sup>55</sup> It turned out that all density data in that work were converted to molar quantities with an incorrect value for the molar mass. The EOS presented here consequently replaces the one of Kortmann. Comparisons between both EOS are not meaningful and not discussed within this section. Nevertheless, the work of Kortmann is an exceptionally useful source of literature and information on the thermodynamic properties of MEA. It provided essential input to the development of the present EOS. An overview of the most important physical constants and characteristic properties of MEA as relevant for the new EOS is given in Table 5.6.

**Table 5.6** Physical constants and characteristic properties of monoethanolamine (MEA).

Quantity	Symbol	Value	Reference
Molar gas constant	$R$	8.314 459 8 J mol <sup>-1</sup> K <sup>-1</sup>	Mohr <i>et al.</i> <sup>59</sup>
Molar mass	$M$	61.0831 g mol <sup>-1</sup>	NIST TDE 103b <sup>170</sup>
Critical temperature	$T_c$	671.4 K	Teja and Rosenthal <sup>171</sup>
Critical pressure	$p_c$	8.125 MPa	This work
Critical density	$\rho_c$	5.39 mol dm <sup>-3</sup>	This work
Triple-point temperature	$T_{tp}$	283.7 K	Lafontaine <sup>172</sup>
Triple-point pressure	$p_{tp}$	0.015 907 kPa	This work
Vapor density at triple point	$\rho_{tpv}$	0.000 007 mol dm <sup>-3</sup>	This work
Liquid density at triple point	$\rho_{tpl}$	16.758 mol dm <sup>-3</sup>	This work
Normal-boiling-point temperature	$T_{nbp}$	443.564 K	This work
Vapor density at the normal boiling point	$\rho_{nbpv}$	0.027 982 mol dm <sup>-3</sup>	This work
Liquid density at the normal boiling point	$\rho_{nbpl}$	14.499 mol dm <sup>-3</sup>	This work
Acentric factor	$\omega$	0.573	This work

The new EOS follows the general functional form presented in Sec. 3.3 (see Eqs. (3.33) to (3.38)). It is explicit in the reduced Helmholtz energy as a function of reduced density and reciprocal reduced temperature. The reducing quantities are the critical-point parameters given in Table 5.6. According to Eq. (3.33), the functional form consists of an ideal-gas and a residual part. The ideal-gas part of the Helmholtz energy of MEA can be written as:

$$\alpha^o(\tau, \delta) = a_1 + a_2\tau + \ln \delta + (c_0 - 1)\ln \tau + \sum_{k=1}^2 v_k \ln[1 - \exp(-u_k \tau/T_c)]. \quad (5.14)$$

The integration constants  $a_1$ ,  $a_2$ , the low-temperature limit of the isobaric ideal-gas heat capacity  $c_0$ , and the adjustable parameters  $v_1$ ,  $v_2$ ,  $u_1$  and  $u_2$  are given in Table D.1 in Appendix D. The integration constants  $a_1$  and  $a_2$  were adjusted to yield zero enthalpy and entropy for the saturated liquid at the normal boiling point ( $T_{\text{nbp}} = 443.564$  K), which is consequently the reference state of the present EOS.

The residual part of the EOS contains a total of 14 terms including five polynomial(-like) terms, five exponential terms, and four Gaussian bell-shaped terms. The complete equation reads:

$$\begin{aligned} \alpha^r(\delta, \tau) = & \sum_{k=1}^5 n_k \delta^{d_k} \tau^{t_k} + \sum_{k=6}^{10} n_k \delta^{d_k} \tau^{t_k} \exp(-\delta^{l_k}) \\ & + \sum_{k=11}^{14} n_k \delta^{d_k} \tau^{t_k} \exp\left[-\eta_k (\delta - \varepsilon_k)^2 - \beta_k (\tau - \gamma_k)^2\right]. \end{aligned} \quad (5.15)$$

All parameters (coefficients  $n_k$ , temperature exponents  $t_k$ , density exponents  $d_k$  and  $l_k$ , and the parameters of the Gaussian bell-shaped terms  $\eta_k$ ,  $\varepsilon_k$ ,  $\beta_k$ , and  $\gamma_k$ ) are listed in Table D.2 in Appendix D.

The present EOS is valid for all stable fluid states from the triple-point temperature  $T_{\text{tp}} = 283.7$  K to  $T_{\text{max}} = 675$  K and at pressures up to  $p_{\text{max}} = 9$  MPa. The upper limits for temperature and pressure are defined to be only slightly higher than the critical parameters. The reason for this is that no experimental data are available above the critical point ( $T_c = 671.4$  K and  $p_c = 8.125$  MPa). In fact, measuring the critical-point parameters is already exceptionally challenging since MEA often decomposes at high temperatures. This phenomenon is described in various sources, for example in Anselme and Teja,<sup>173</sup> Daubert *et al.*,<sup>174</sup> Danov *et al.*,<sup>175</sup> Lyons,<sup>176</sup> Noll *et al.*,<sup>177</sup> Teja and Rosenthal,<sup>171</sup> and Wilding *et al.*<sup>178</sup> The decomposition does not happen abruptly; thus, defining a decomposition temperature is difficult. Only Daubert *et al.*<sup>174</sup> provide a more or less concrete temperature value of  $\approx 623$  K. Nevertheless, measurements at high temperatures are possible by rapidly heating the sample. The critical-point temperature reported by Teja and Rosenthal<sup>171</sup> and used for the development of the present EOS was obtained through this technique. It is by far the data point at the highest temperature and pressure; thus, the range of validity was limited just above it. Since the EOS for MEA was exclusively developed to be used in mixture

calculations, its extrapolation behavior was carefully constrained during the fitting process as discussed later in this section.

Deviations between the available data for the ideal-gas isobaric heat capacity and values calculated from the ideal-gas part of the present EOS are shown in Figure 5.46.

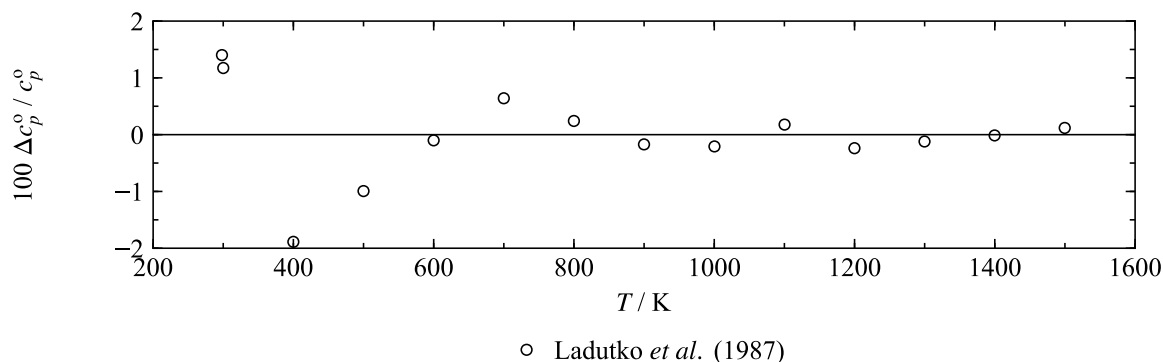
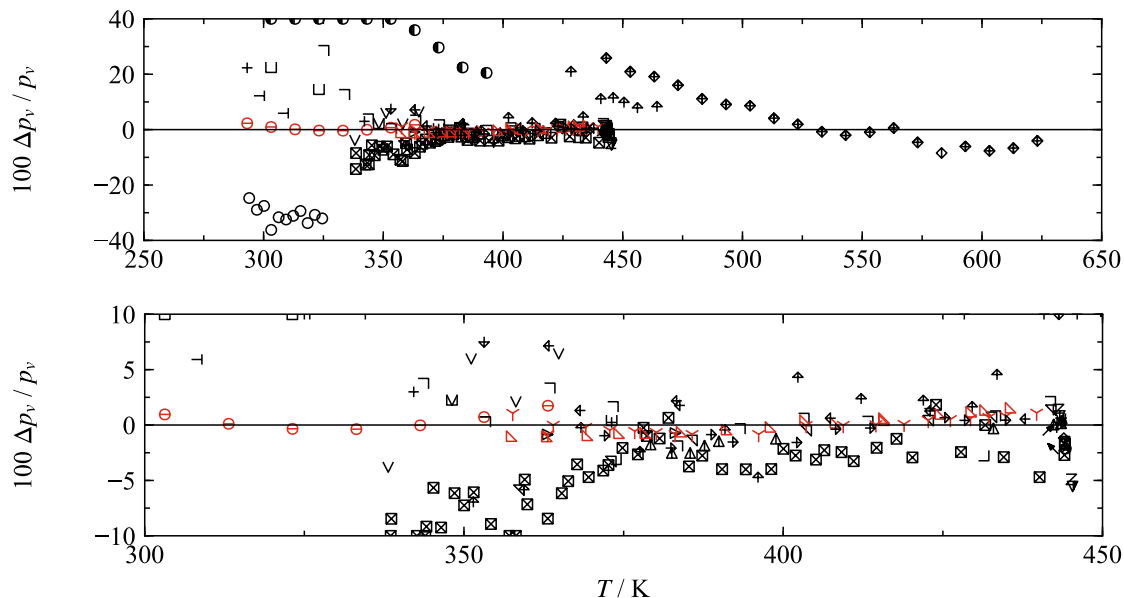


**Figure 5.46** Relative deviations  $\Delta c_p^o / c_p^o = (c_{p^o, \text{data}} - c_{p^o, \text{calc}}) / c_{p^o, \text{data}}$  of ideal-gas isobaric heat-capacity data calculated from Eq. (5.14) versus temperature.

The only available data set was published by Ladutko *et al.*<sup>179</sup> covering temperatures between approximately 300 K and 1500 K. The data were obtained through spectroscopic measurements. No concrete uncertainty information is given in the publication, but in personal communications Frenkel, one of the co-authors, estimated the data to be accurate within 1 %. The EOS represents the data within this uncertainty estimate at temperatures between 500 K and 1500 K; however, at lower temperatures the deviations increase to about 2 %. The ideal-gas part of the EOS was also fitted to caloric property data of the real fluid. The final formulation represents a compromise between the best representation of the ideal-gas data of Ladutko *et al.*<sup>179</sup> and the representation of the available speed-of-sound and isobaric heat-capacity data of the real fluid. Based on the deviations shown in Figure 5.46. The uncertainty of calculated ideal-gas isobaric heat capacities is 2 % at temperatures between 300 K and 500 K and 1 % at higher temperatures up to 1500 K.

The only thermal saturation data available for MEA are measurements of the vapor pressure. Results of such measurements were published in a large number of references. All these data are significantly less accurate than the discussed vapor-pressure data for heavy water (see Sec. 5.1.4.1) and chlorine (see Sec. 5.2). A complete overview of all references providing vapor pressures of MEA is given in Table D.3 in Appendix D. The table additionally provides the *AAD* for each data set as defined by Eq. (5.1). Aside from the overall *AAD*, separate *AAD* for the low and medium temperature range are given following the conventions discussed in Sec. 5.1.4.1 (low temperature range  $T / T_c < 0.6$ , medium temperature range  $0.6 \leq T / T_c \leq 0.98$ ). No experimental data were found for the high-temperature range ( $T / T_c > 0.98$ ) of the vapor-pressure curve. If given in the respective reference, Table D.3 additionally provides the MEA purity of the investigated sample. Since MEA is a highly hygroscopic fluid, water is often present as an impurity, which might lead

to large experimental uncertainties. Deviations between all experimental data and vapor pressures calculated from the EOS are shown in Figure 5.47. The top panel shows the data over the complete temperature range from about 285 K up to 625 K. In the bottom panel, the more accurately investigated temperature region between 300 K and 450 K is plotted.



- |                                   |                                  |                                  |
|-----------------------------------|----------------------------------|----------------------------------|
| ○ Anderson and Shimanskaya (1969) | ➔ Hahn and Freydank (1983)       | △ McDonald <i>et al.</i> (1959)  |
| + Anonymous (1956)                | ○ Kapteina <i>et al.</i> (2005)  | ∇ Nath and Bender (1983)         |
| ⊖ Belabbaci <i>et al.</i> (2009)  | ▴ Kim <i>et al.</i> (2008)       | ∇ Park and Lee (1997)            |
| × Bergman and Shulyak (1972)      | ∇ Klepacova <i>et al.</i> (2011) | ▷ Pividal and Sandler (1990)     |
| ∇ Bogacheva <i>et al.</i> (1980)  | ∇ Kogan <i>et al.</i> (1970)     | ↘ Reddy <i>et al.</i> (2012)     |
| ⊐ Cadle <i>et al.</i> (1949)      | ∋ Lafontaine (1958)              | ⊗ Reitmeier <i>et al.</i> (1940) |
| ⊐ Cai <i>et al.</i> (1996)        | △ Landauer <i>et al.</i> (1974)  | ↗ Sunder and Prasad (2007)       |
| ⊐ Danov <i>et al.</i> (1969)      | ◇ Lecat (1947)                   | × Tanaka <i>et al.</i> (2001)    |
| ⊕ Daubert <i>et al.</i> (1987)    | ⊐ Leibush and Shorina (1947)     | ↘ Tochigi <i>et al.</i> (1999)   |
| ● Gas Research Institute (1981)   | ◇ Lyons (1985)                   | ⊐ Touhara <i>et al.</i> (1982)   |
| ⊕ Graubner (2010)                 | ⊗ Matthews <i>et al.</i> (1950)  | z Zaretskii <i>et al.</i> (1970) |
| ⊕ Hahn <i>et al.</i> (1989)       |                                  |                                  |

**Figure 5.47** Top: Relative deviations  $\Delta p_v / p_v = (p_{v,\text{exp}} - p_{v,\text{calc}}) / p_{v,\text{exp}}$  of the available experimental vapor-pressure data from the EOS versus temperature. Bottom: Relative deviations of selected experimental data in the temperature range from 300 K to 450 K from the EOS.

In the low temperature region between 283 K and 364 K, the EOS was fitted to the data of Belabbaci *et al.*<sup>180</sup> The purity of the sample is stated to be higher than 99 mol% MEA. The experimental uncertainties in pressure and temperature are given as 3 % and 0.02 K. Combining the uncertainties in pressure and temperature (with the sensitivity coefficient  $(\partial p / \partial T)_{\text{sat}}$  calculated from the EOS), leads to an expanded ( $k = 2$ ) uncertainty in vapor pressure of about 6 %. The EOS represents the complete data set with deviations below 4.4 %, and thus within the experimental uncertainty. The estimated uncertainty of vapor pressures calculated from the EOS for temperatures between 285 K and 360 K is therefore estimated to be 6 %.

At elevated temperatures, the fitted data of Belabbaci *et al.*<sup>180</sup> are in good agreement with the data of Tochigi *et al.*<sup>181</sup> and Kim *et al.*<sup>182</sup> The EOS was fitted to the data of Tochigi *et al.*,<sup>181</sup> which range from 363 K (excluding two outliers at lower temperatures) to 440 K. The investigated sample has a high purity of more than 99.6 mol% MEA. The data are described with a maximum deviation of 1.1 % and an *AAD* of 0.531 %. The authors provide experimental uncertainties of 0.01 K in temperature and 0.03 kPa in pressure. Considering these specifications and  $(\partial p / \partial T)_{\text{sat}}$  calculated from the EOS, the maximum combined expanded ( $k = 2$ ) uncertainty of the data is about 1.5 %. Since the deviations of the data from the EOS agree with this experimental uncertainty, the estimated uncertainty of calculated vapor pressures between 360 K and 440 K is 1.5 %.

At higher temperatures, the available data of Daubert *et al.*<sup>174</sup> and Lyons<sup>176</sup> exhibit a large offset from all data at lower temperatures. It is believed that these deviations result from higher experimental uncertainties caused by a decomposition of the sample. Hence, no uncertainty estimate for calculated vapor pressures is possible at temperatures above 440 K. It can only be noted that the uncertainty is expected to be higher than at lower temperatures.

Homogeneous densities of MEA were found in a large number of references; however, almost the complete database is limited to measurements in the liquid phase at ambient pressure. This is not surprising with regard to the motivation of the experimental works. All measurements were focused on properties of amines under conditions relevant to amine gas treating, which is only performed under ambient pressure. Furthermore, this explains the large number of references providing only one single data point. Amine gas treating is realized with aqueous amine solutions; thus, almost all the experimental studies present data for aqueous MEA mixtures with different compositions including only one measurement of pure MEA. All references and their *AAD* from the present EOS are listed in Table D.4 in Appendix D. Again, the table additionally includes the purity of the investigated sample, if stated in the corresponding publication. Deviations between the experimental data and liquid densities calculated from the EOS are presented in Figure 5.48. The data range from 273 K to 432 K. The EOS represents most of them with deviations below 0.5 %. It was fitted to a selection of data points taken from Han *et al.*<sup>183</sup> and Valtz *et al.*<sup>184</sup> Han and colleagues carried out measurements at temperatures between 298 K and 424 K with two different Anton Paar vibrating-tube densimeters. The sample purity is stated to be 99.5 mol% MEA. The measurements below 373 K were carried out at ambient pressure with a combined expanded ( $k = 2$ ) uncertainty of  $0.68 \text{ kg m}^{-3}$ , whereas at temperatures above 373 K a pressure of 0.7 MPa was applied. These data are thus the only values at pressures higher than ambient pressure. The expanded ( $k = 2$ ) uncertainty of these values is  $0.70 \text{ kg m}^{-3}$ . The specified uncertainties correspond to a maximum relative uncertainty of 0.08 %. The data are represented with a maximum deviation of 0.05 % (*AAD* = 0.035 %) and consequently within the experimental uncertainty. Valtz *et al.*<sup>184</sup> provide no experimental uncertainty, but their data are in excellent agreement with the data Han *et al.*<sup>183</sup> They also used an Anton Paar



vibrating-tube densimeter. They purchased a MEA sample with a purity higher than 99 mol% and additionally degassed it for further purification. Due to the good agreement between the data of Han *et al.*<sup>183</sup> and Valtz *et al.*,<sup>184</sup> these data sets are considered to be the most reliable ones. Based on the discussed experimental uncertainty of Han *et al.*<sup>183</sup>, it could be justified to define a 0.1 % uncertainty estimate for results calculated from the new EOS; however, with regard to the overall deviations plotted in Figure 5.48 a more conservative uncertainty estimate seems reasonable. The estimated uncertainty of calculated liquid phase densities at ambient pressure and temperatures up to 430 K is 0.3 %.

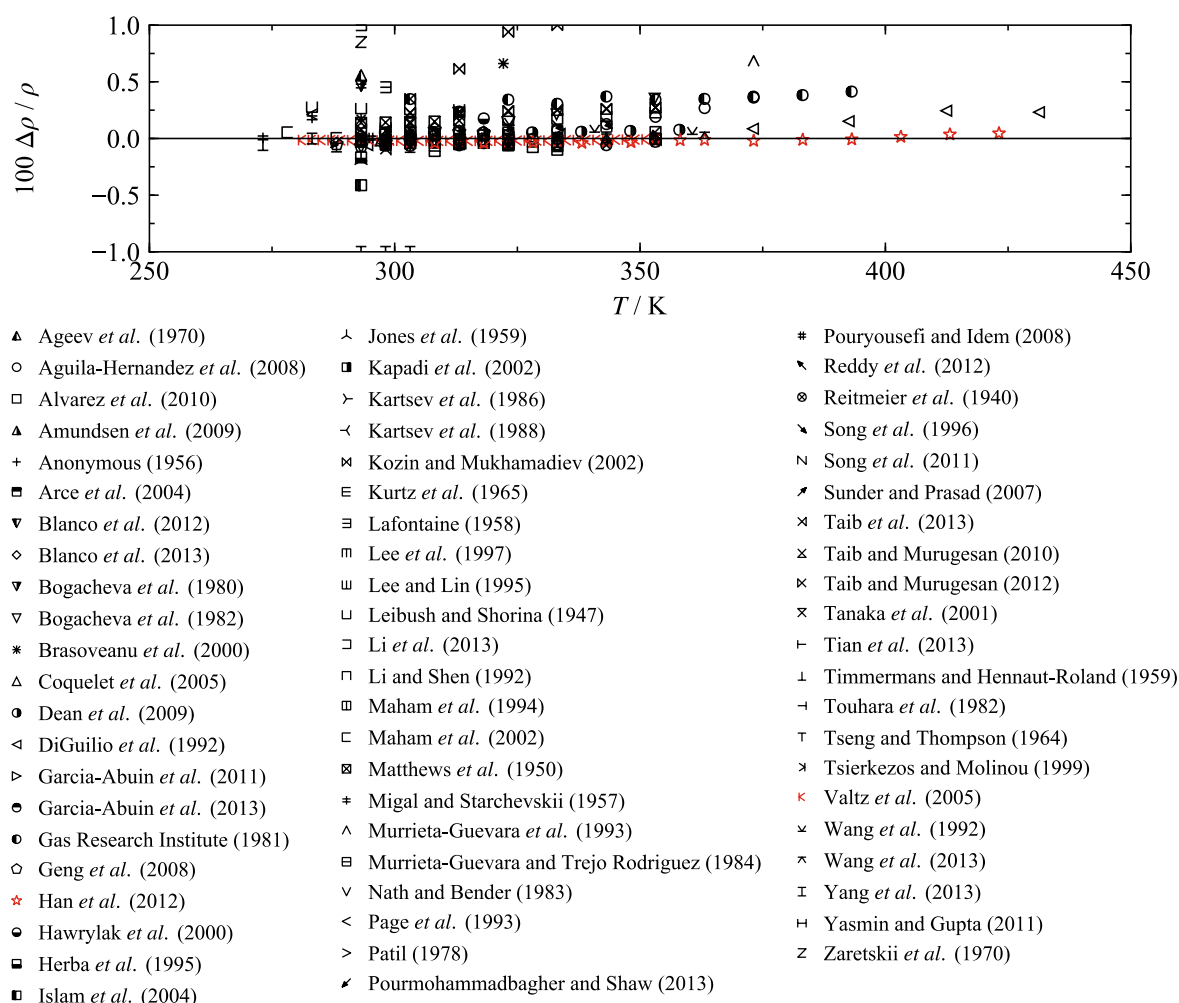


**Figure 5.48** Relative deviations  $\Delta\rho / \rho = (\rho_{\text{exp}} - \rho_{\text{calc}}) / \rho_{\text{exp}}$  of experimental density data from the EOS versus temperature.

The available speed-of-sound data are much more limited than the vapor-pressure or density data. Only a few references covering temperatures between 293 K and 324 K were found in the literature. Again, all data are restricted to the liquid phase at ambient pressure. Deviations between the data and the present EOS are shown in Figure 5.49. In addition, all data sets and their AAD from the EOS as well as sample purities are listed in Table D.5 in Appendix D. The EOS was fitted to the experimental results of Blanco *et al.*<sup>185</sup> The authors claim a sample purity higher than 99 mol% MEA and an experimental uncertainty of  $1.3 \text{ m s}^{-1}$ , which is

interpreted as a standard uncertainty. The maximum value of the relative expanded ( $k = 2$ ) uncertainty is 0.15 %. The EOS represent the complete data set with deviations below 0.05 %, and thus within its experimental uncertainty. Excluding the measurements of Patil<sup>186</sup> and Willard,<sup>187</sup> the complete database is consistent within 0.1 %. Considering a possible additional uncertainty contribution resulting from sample impurities, the conservatively estimated uncertainty of calculated liquid-phase speed-of-sound data at ambient pressure and temperatures between 295 K and 325 K is 0.2 %.

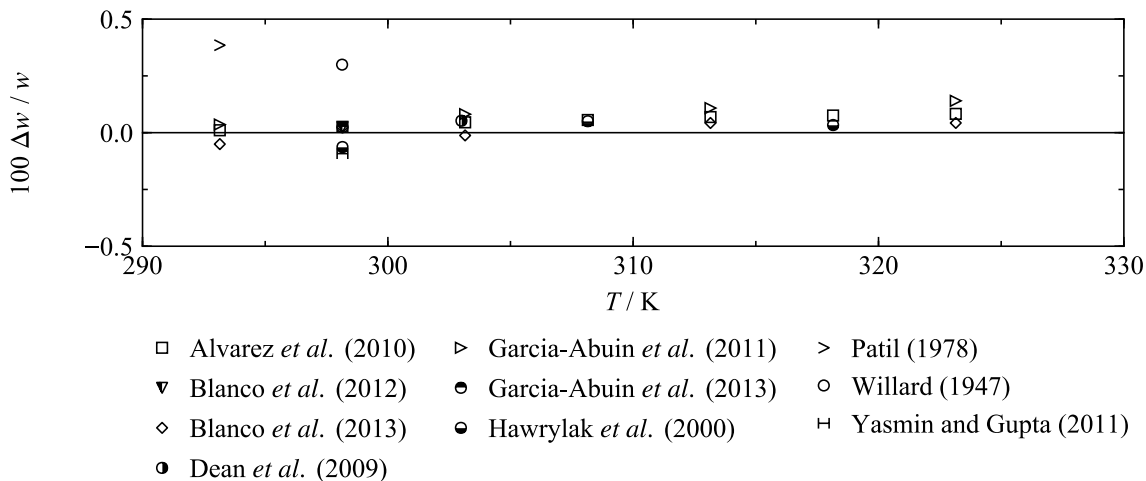


**Figure 5.49** Relative deviations  $\Delta w / w = (w_{\text{exp}} - w_{\text{calc}}) / w_{\text{exp}}$  of experimental speed-of-sound data from the EOS versus temperature.

A few references were found that present results of isobaric heat-capacity measurements. Like for density and speed of sound, all measurements were carried out in the liquid phase at ambient pressure. As shown in Figure 5.50, the EOS represents most of the data with deviations below 5 %.

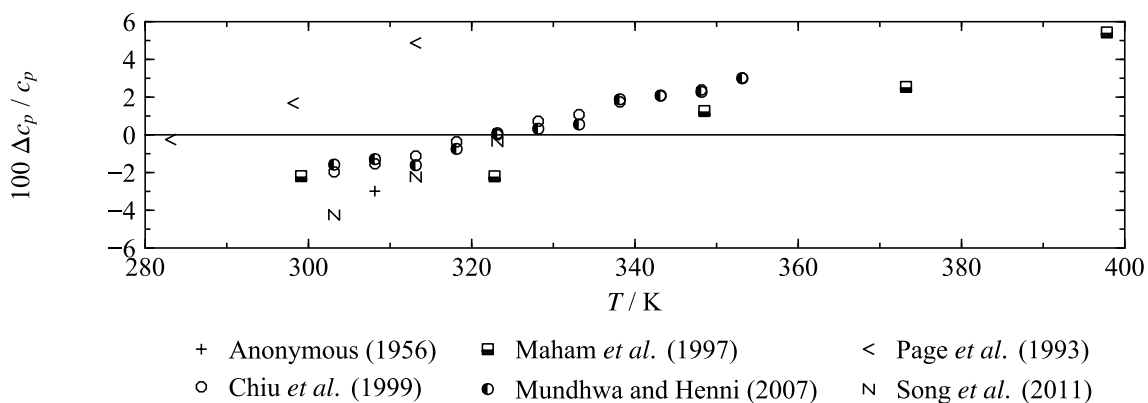


**Figure 5.50** Relative deviations  $\Delta c_p / c_p = (c_{p,\text{exp}} - c_{p,\text{calc}}) / c_{p,\text{exp}}$  of experimental isobaric heat-capacity data from the EOS versus temperature.

The EOS was fitted to the data of Chiu *et al.*,<sup>188</sup> who estimated the experimental uncertainty of their data to be 3 %. The authors further state that results of verification measurements in pure water deviate from the reference values by about 2 %. The sample purity is given as over 99 mol% MEA. The EOS represents the data within a maximum deviation of 3 %,

which corresponds to the specified experimental uncertainty. The data of Chiu *et al.*<sup>188</sup> cover a temperature range between 303 K and 353 K. In order to fit the EOS in the elevated temperature region, the data of Maham *et al.*<sup>189</sup> were considered with low weights. The data are found to be less accurate because they exhibit an offset from the data of Chiu *et al.*,<sup>188</sup> which are confirmed by measurements of the Mundhwa and Henni.<sup>190</sup> In their publication, Maham *et al.*<sup>189</sup> claim an estimated experimental uncertainty of 0.9 %. During the fitting process it was repeatedly tried to minimize the deviations of these data below 2 % in order to match the expanded ( $k = 2$ ) uncertainty specification. However, the result of this effort was a significant increase of all deviations between the model and the speed-of-sound data shown in Figure 5.49. It is therefore reasonable to assume that the experimental uncertainty given by Maham *et al.*<sup>189</sup> is considerably underestimated. The deviations presented in Figure 5.50 represent the best compromise among all available data. Based on these deviations, the estimated uncertainty of calculated isobaric heat capacities in the liquid phase at ambient pressure and temperatures between 300 K and 400 K is 5 %. An overview of the experimental isobaric heat-capacity data and their AAD from the EOS is given in Table D.5 in Appendix D.

Because the experimental database for MEA is so limited, the representation of its physical behavior predicted by the EOS as well as the qualitative reliability of results obtained from extrapolations were validated carefully. These validations are exceptionally important in order to ensure that the EOS for MEA yields reasonable results when evaluated in mixture calculations. In Figure 5.51, two property plots are shown that are typically validated during the fitting process. In the left panel, the residual part of the isochoric heat capacity is plotted along isobars as a function of temperature. The speed of sound as a function of temperature and also plotted along isobar is presented in the right panel.

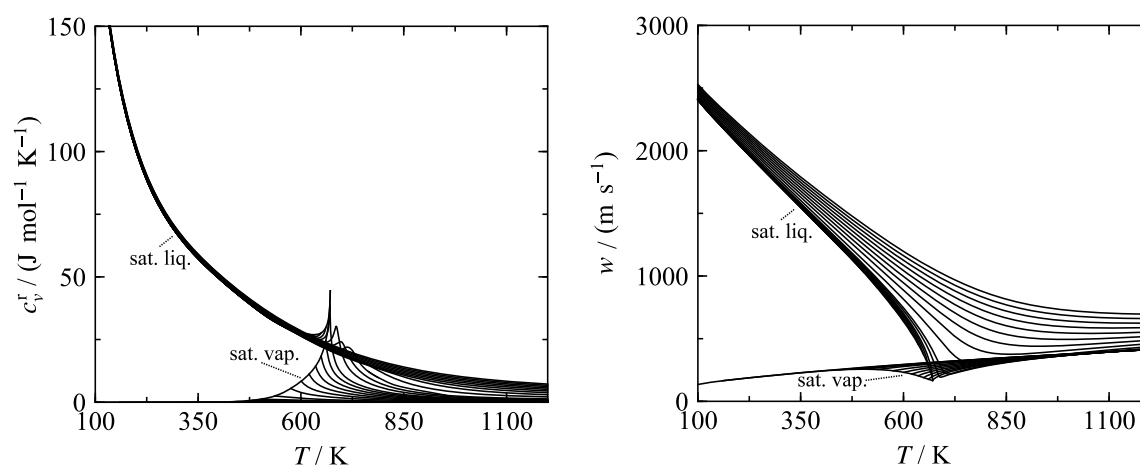


**Figure 5.51** Residual isochoric heat capacity (left) and speed of sound (right) versus temperature calculated from the EOS along isobars up to 12 MPa.

Both property plots emphasize an excellent qualitative behavior of the calculated properties following the conventions briefly explained for the EOS of pure chlorine (see Sec. 5.2). The

isobars are smoothly shaped over the whole depicted part of the fluid surface including temperatures considerably below the triple point ( $T_{\text{tp}} = 283.7 \text{ K}$ ) and above the critical point ( $T_c = 671.4 \text{ K}$ ). Furthermore, the required distinct peak of the isochoric heat capacity as well as the minimum in speed of sound both occur at the critical point. Both plots include isobars up to 12 MPa, and thus already much higher pressures than the experimentally investigated ( $p_{\text{exp}} \approx 1 \text{ atm}$ ). Nevertheless, the EOS was additionally validated at higher pressures and temperatures. A  $T, \rho$  diagram for temperatures up to 1000 K along isobars up to 200 MPa is shown in the left panel of Figure 5.52. The right panel of this figure presents a  $p, \rho$  diagram calculated for extreme values of temperature and pressure. The pressure is calculated up to  $10^6 \text{ MPa}$  along isotherms up to 900 000 K. It can be seen that the isolines in both diagrams exhibit an excellent converging behavior without any unreasonable crossing of each other. The plots additionally include the rectilinear diameter introduced in Sec. 5.1.8. As requested, it is almost a straight line up to the critical point.

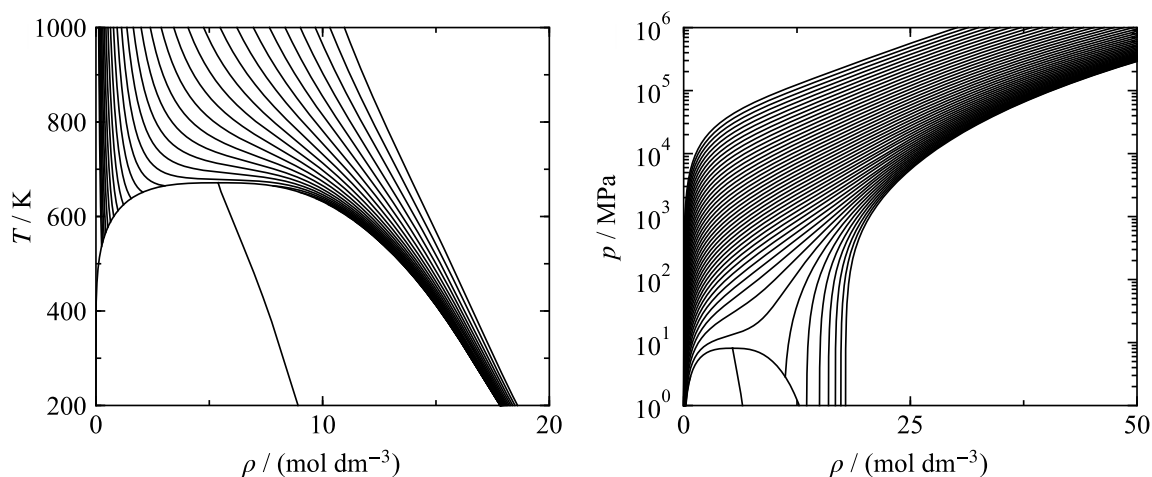


**Figure 5.52** Left:  $T, \rho$  diagram along isobars up to 200 MPa as calculated from the EOS. Right:  $p, \rho$  diagram along isotherms up to 900 000 K. The rectilinear diameter (the average between saturated-liquid and -vapor density) is included in both diagrams.

The extrapolation behavior of the EOS was decisively shaped by fitting constraints for the ideal curves presented in the right panel of Figure 5.53. The importance of these characteristic curves has already been explained by the example of heavy water (see Sec. 5.1.8). As can be seen from Figure 5.53, the ideal curves calculated from the EOS for MEA are smooth over the entire depicted temperature and pressure range. This demonstrates that the EOS can be reasonably extrapolated into regions beyond the limited range of the experimental data.

A qualitatively correct behavior of the ideal curves is often correlated with a good representation of the virial coefficients. The second and third virial coefficients  $B(T)$  and  $C(T)$  calculated from the new EOS are presented in the left panels of Figure 5.53. At low temperatures, the EOS should yield negative values for  $B(T)$  and  $C(T)$ . With increasing temperature, the coefficients should increase, become positive, exhibit a maximum, and then

decrease gradually while approaching zero (and thus the ideal-gas state). Many reference Helmholtz-energy explicit EOS predict a distinct peak of  $C(T)$  near the critical temperature. It can be seen that this also applies to MEA. In general, both virial coefficients are in good agreement with the explained theoretical constraints. The good representation of the virial coefficients is particularly notable because it indicates a qualitatively reasonable description of gaseous MEA, which could not be validated by comparisons with experimental data.

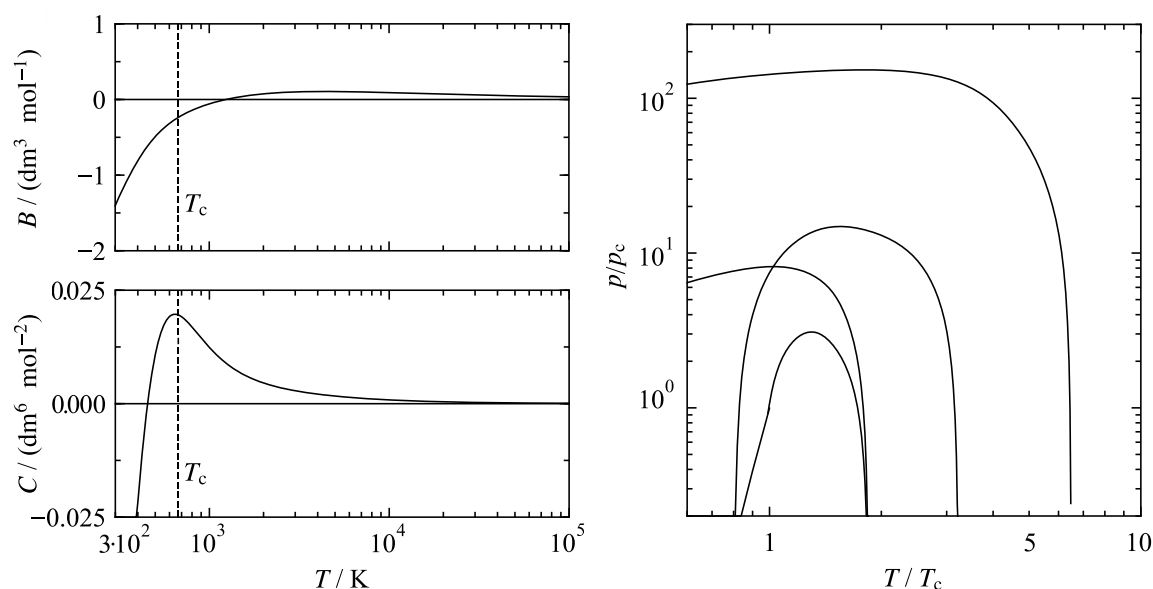


**Figure 5.53** Left: Second and third virial coefficients  $B$  and  $C$  calculated from the EOS as a function of temperature. Right: Ideal curves as calculated from the EOS.

Despite the excellent extrapolation behavior of the new EOS, it is not expected that it provides quantitatively accurate results outside the experimentally investigated state region. Comprehensive measurement campaigns on MEA should consequently be considered in future research on thermodynamic properties for CCS applications. Such measurements should most importantly provide homogeneous gaseous and liquid densities over a wide temperature and pressure range, accurate thermal saturation data, and in the best case additional speed-of-sound data. The EOS presented here should be considered as a preliminary EOS representing the best possible fit to the currently available data but it should be revised as soon as comprehensive experimental data are available. Nevertheless, the present EOS has already been successfully used to describe binary mixtures with MEA as discussed in detail in Secs. 6.3.1.7, 6.3.2.1, and 6.3.2.2.



## 6 Extended Equation of State for CCS-Mixtures

As already discussed, two main projects were carried out within the scope of this doctoral thesis: (1) the development of a new reference EOS for pure heavy water (as discussed in Sec. 5.1) and (2) of an extended mixture model for CO<sub>2</sub>-rich mixtures relevant to CCS applications. A first model for CO<sub>2</sub>-rich mixtures was presented by Gernert and Span<sup>2</sup> (“EOS-CG”, “Equation of State for Combustion Gases and Combustion-Gas-Like Mixtures”) covering the major CCS-relevant components. The aim of the present work was to extend that model to additional components. Because for each component a reliable pure-fluid EOS is mandatory, extending the mixture model required the development of additional pure fluid EOS that were discussed in Secs. 5.2 and 5.3. Within this section, the results of the mixture-modelling work are presented.

As pointed out in Secs. 3.3 and 4, depending on the quantity and quality of the available experimental (or simulated) data, there are different options of fitting the model to the data. This results in a certain “hierarchy of fitting”: The most accurate models are obtained by fitting a binary specific departure function; but typically, only the reducing parameters are fitted; and if no data are available, simple combining rules are applied to the reducing functions. The structure of this section follows this “hierarchy of fitting”. The following Sec. 6.1 gives an overview of the components and the resulting binary mixtures covered by the CCS-mixture model. It is specified which of these systems are described with departure functions, only with adjusted reducing functions, or with simple combining rules. Systems modelled with new departure functions are discussed in detail in Sec. 6.2. The quality of the description of binary mixtures with new adjusted reducing functions (and no departure function) is presented in Sec. 6.3. A detailed discussion of the remaining systems that could only be described with simple combining rules is not meaningful, since there are no reliable data for comparisons. However, some explanations of the procedure of selecting the proper combining rule and its challenges are given in Sec. 6.4. Some more general aspects relevant to the mixture model and its development are discussed in Sec. 6.5.

The validation of the developed binary mixtures models is mainly based on comparisons with the available experimental (or simulated) data. In addition, some comparative calculations with other EOS were carried out; however, for the sake of concision it is not reasonable to discuss comparisons with all types of models introduced in Sec. 3. For the mixtures covered by a new binary specific departure function, comparisons with results calculated from the GERG-2008 model for natural gases and similar mixtures of Kunz and Wagner<sup>36</sup> and from EOS-CG of Gernert and Span<sup>2</sup> were carried out. Comparisons with SRK (Soave-Redlich-Kwong EOS)<sup>18</sup> or LKP (Lee-Kesler-Plöcker EOS)<sup>19</sup> are only shown, for systems covered by a comparably comprehensive experimental database. For a few systems,

comparisons with the more predictive approaches PSRK of Holderbaum and Gmehling,<sup>41</sup> PC-SAFT of Gross and Sadowski,<sup>44</sup> and PCP-SAFT (for mixtures containing polar components) of Gross<sup>45</sup> and Gross and Vrabec<sup>46</sup> are included in the discussion.

An overview of the complete database used to develop the new binary mixture models is provided in Appendix E of this work that additionally includes average absolute relative deviations (*AAD*) between the data sets and the binary models.

## 6.1 Overview of the Mixture Model

The Helmholtz-energy explicit functional form of the CCS-mixture model introduced in Sec. 3.3 allows for a description of multi-component mixtures based on formulations developed for every possible binary mixture of the components. An overview of the 91 binary combinations that result from 14 components relevant to CCS is given in Figure 6.1.

		chlorine	hydrogen chloride	diethanolamine	monoethanolamine	sulfur dioxide	hydrogen sulfide	methane	hydrogen	carbon monoxide	argon	oxygen	nitrogen	water
major components	carbon dioxide	●	●	●	●	●	KW	KW	KW	●	●	GS	GS	GS
	water	●	●	●	●	●	●	●	KW	GS	GS	GS	GS	
	nitrogen	●	●	●	●	●	●	KW	KW	GS	GS	GS		
	oxygen	●	●	●	●	●	●	KW	KW	GS	GS			
	argon	●	●	●	●	●	●	KW	KW	GS				
↕	carbon monoxide	●	●	●	●	●	KW	KW	KW					
	hydrogen	●	●	●	●	●	KW	KW						
	methane	●	●	●	●	●	KW							
minor components	hydrogen sulfide	●	●	●	●	●								
	sulfur dioxide	●	●	●	●									
	monoethanolamine	●	●	●										
	diethanolamine	●	●											
	hydrogen chloride	●												

Specific departure function

Generalized departure function

Adjusted reducing functions

Lorentz-Berthelot combining rules

Linear combining rules

● Model developed in this work

GS EOS-CG model of Gernert and Span

KW GERG model of Kunz and Wagner

**Figure 6.1** Overview of the 91 binary combinations that result from the 14 components considered for the development of the new EOS for CCS-relevant mixtures. The initial mixture model EOS-CG of Gernert and Span<sup>2</sup> was extended by adopting binary models from GERG-2008 of Kunz and Wagner<sup>36</sup> and by the models developed in this work. According to their mole fraction in typical CCS-mixtures, the components are classified as major or minor components. Carbon monoxide, hydrogen, and methane occur as major or minor components depending on the CCS process design.



The complete multi-component model includes 13 binary formulations of the initial mixture model EOS-CG of Gernert and Span,<sup>2</sup> 19 binary formulations adopted from the GERG-2008 mixture model of Kunz and Wagner,<sup>36</sup> and 59 binary formulations developed within the scope of this work. Out of these 59 new formulations, four contain a new binary specific departure function and 13 are based on adjusted reducing functions without a departure function. The remaining systems were described by simple combining rules because no or far from sufficient data were available to fit the parameters of the reducing functions.

The departure function for CO<sub>2</sub> + Ar as well as the parameters of the reducing functions for SO<sub>2</sub> + CO<sub>2</sub>, SO<sub>2</sub> + N<sub>2</sub>, SO<sub>2</sub> + O<sub>2</sub> were mainly developed by Neumann,<sup>49</sup> whose master thesis was supervised within the context of this doctoral thesis. The same applies for the reducing functions for SO<sub>2</sub> + CH<sub>4</sub>, SO<sub>2</sub> + Cl<sub>2</sub>, SO<sub>2</sub> + HCl, Cl<sub>2</sub> + HCl, SO<sub>2</sub> + DEA, and DEA + H<sub>2</sub>O that were mainly developed by Zosimenko<sup>191</sup> within the scope of her master thesis. These binary models are discussed in the present work, because their development was meant to contribute to this project and because the validations presented in this work differ from the ones in those master theses.

The parameters of all reducing functions and binary specific departure functions of the binary formulations developed within this PhD project are listed in Tables E.1 and E.2 in Appendix E of this thesis.

As pointed out in Sec. 3.3, the multi-component Helmholtz-energy explicit mixture model requires accurate EOS for the pure components. An overview of the EOS used in the mixture model is presented in Table 6.1. The table additionally shows the range of validity and critical-point parameters of each EOS. These specifications are important when using the EOS in mixture calculations. For binary mixtures, the difference in their critical-point parameters is a good indicator for the mixing behavior. The range of validity of the pure-fluid EOS is of special interest because mixture calculations often require evaluations beyond these temperature and pressure limits.

**Table 6.1** Pure-fluid Helmholtz-explicit EOS used in the model for CCS-relevant mixtures.

Component	Pure-fluid EOS	Year	Range of validity	Critical parameters
Carbon dioxide	Reference EOS of Span and Wagner <sup>28</sup>	1996	$216.592 \leq T / \text{K} \leq 1100$ ; $p \leq 800 \text{ MPa}$	$T_c = 304.128 \text{ K}$ ; $\rho_c = 10.625 \text{ mol dm}^{-3}$
Water	Reference EOS of Wagner and Pruß <sup>29</sup> (IAPWS-95)	2002	$T_m(p) \leq T / \text{K} \leq 2000$ ; $p \leq 1000 \text{ MPa}$	$T_c = 647.096 \text{ K}$ ; $\rho_c = 17.874 \text{ mol dm}^{-3}$
Nitrogen	Reference EOS of Span <i>et al.</i> <sup>48</sup>	2000	$63.151 \leq T / \text{K} \leq 2000$ ; $p \leq 2200 \text{ MPa}$	$T_c = 126.192 \text{ K}$ ; $\rho_c = 11.184 \text{ mol dm}^{-3}$
Oxygen	Reference EOS of Schmidt and Wagner <sup>192</sup>	1985	$54.361 \leq T / \text{K} \leq 2000$ ; $p \leq 82 \text{ MPa}$	$T_c = 154.581 \text{ K}$ ; $\rho_c = 13.63 \text{ mol dm}^{-3}$
Argon	Reference EOS of Tegeler <i>et al.</i> <sup>193</sup>	1999	$83.806 \leq T / \text{K} \leq 2000$ ; $p \leq 1000 \text{ MPa}$	$T_c = 150.687 \text{ K}$ ; $\rho_c = 13.407 \text{ mol dm}^{-3}$

*continued...*

**Table 6.1** ...continued

Component	Pure-fluid EOS	Year	Range of validity	Critical parameters
Carbon monoxide	Short industrial EOS of Lemmon and Span <sup>194</sup>	2006	$68.16 \leq T / \text{K} \leq 500$ ; $p \leq 100 \text{ MPa}$	$T_c = 132.86 \text{ K}$ ; $\rho_c = 10.85 \text{ mol dm}^{-3}$
Hydrogen	Reference EOS of Leachman <i>et al.</i> <sup>195</sup>	2009	$13.957 \leq T / \text{K} \leq 1000$ ; $p \leq 2000 \text{ MPa}$	$T_c = 33.145 \text{ K}$ ; $\rho_c = 15.508 \text{ mol dm}^{-3}$
Methane	Reference EOS of Setzmann and Wagner <sup>196</sup>	1991	$90.694 \leq T / \text{K} \leq 625$ ; $p \leq 1000 \text{ MPa}$	$T_c = 190.564 \text{ K}$ ; $\rho_c = 10.139 \text{ mol dm}^{-3}$
Hydrogen sulfide	Short industrial EOS of Lemmon and Span <sup>194</sup>	2006	$187.7 \leq T / \text{K} \leq 760$ ; $p \leq 170 \text{ MPa}$	$T_c = 373.1 \text{ K}$ ; $\rho_c = 10.19 \text{ mol dm}^{-3}$
Sulfur dioxide	EOS of Gao <i>et al.</i> <sup>33</sup>	2016	$197.7 \leq T / \text{K} \leq 525$ ; $p \leq 35 \text{ MPa}$	$T_c = 430.64 \text{ K}$ ; $\rho_c = 8.078 \text{ mol dm}^{-3}$
Monoethanolamine	EOS developed in this work (see Sec. 5.3)	2018	$283.7 \leq T / \text{K} \leq 675$ ; $p \leq 9 \text{ MPa}$	$T_c = 671.4 \text{ K}$ ; $\rho_c = 5.39 \text{ mol dm}^{-3}$
Diethanolamine	EOS of Kortmann <sup>55</sup>	2016	$301.7 \leq T / \text{K} \leq 740$ ; $p \leq 5 \text{ MPa}$	$T_c = 736.5 \text{ K}$ ; $\rho_c = 3.3 \text{ mol dm}^{-3}$
Chlorine	EOS developed in this work (see Sec. 5.2)	2015	$172.17 \leq T / \text{K} \leq 440$ ; $p \leq 20 \text{ MPa}$	$T_c = 416.865 \text{ K}$ ; $\rho_c = 8.06 \text{ mol dm}^{-3}$
Hydrogen chloride	EOS of Thol <i>et al.</i> <sup>50</sup>	2018	$159.07 \leq T / \text{K} \leq 670$ ; $p \leq 200 \text{ MPa}$	$T_c = 324.68 \text{ K}$ ; $\rho_c = 11.87 \text{ mol dm}^{-3}$

In principle, other EOS for the pure components can be applied; however, it should be noted that, depending on the mixture, the results obtained might deviate considerably from those shown in this work. This is particularly important for the binary mixtures  $\text{CH}_4 + \text{H}_2\text{O}$  and  $\text{H}_2\text{S} + \text{H}_2\text{O}$  for which new binary specific departure functions were developed (see Secs. 6.2.3 and 6.2.4) because for mixtures with water, the departure functions often correct some numerical deficiencies of the complex functional form of the EOS for pure  $\text{H}_2\text{O}$ .

The complete multi-component mixture model including the pure-fluid EOS developed in this work will be implemented in the upcoming version 4.0 of the software package TREND<sup>22</sup> developed at RUB and will be made available in REFPROP<sup>39</sup> of NIST and the open source software CoolProp.<sup>40</sup>

## 6.2 Binary Mixtures Described with Specific Departure Functions

As explained before, the highest level of accuracy in describing fluid mixtures with Helmholtz-energy explicit EOS is achieved by fitting a binary specific departure function to the available experimental data. Within the scope of this work, such functions were developed for four binary systems:  $\text{CO}_2 + \text{Ar}$ ,  $\text{CO}_2 + \text{CO}$ ,  $\text{H}_2\text{O} + \text{CH}_4$ , and  $\text{H}_2\text{O} + \text{H}_2\text{S}$ . The following subsections present these departure functions and show comparisons to the experimental data.

### 6.2.1 Carbon Dioxide + Argon

Prior to the development of the present binary formulation for the system CO<sub>2</sub> + Ar, two Helmholtz-energy explicit formulations were already available, one developed for the EOS-CG model of Gernert and Span<sup>2</sup> and another presented as a part of the GERG-2008 model by Kunz and Wagner.<sup>36</sup> Because the GERG-2008 was developed for the description of natural-gas mixtures, CO<sub>2</sub> + Ar was a binary system of minor relevance. The GERG-2008 model for this system does not include a binary specific departure function and is therefore significantly less accurate than the one included in the EOS-CG, which was explicitly developed for the description of CO<sub>2</sub>-rich mixtures. The work of Gernert and Span was published in 2016, but the development of the EOS-CG was already completed in 2013.<sup>17</sup> Since then, additional accurate data for CO<sub>2</sub> + Ar became available that allowed an improved binary mixture formulation. The new data include accurate density, speed-of-sound, and dew-point measurements carried out at RUB (partly in collaboration with NIST and The University of Western Australia, UWA, in Perth), as well as vapor-liquid-equilibrium (VLE) data measured at SINTEF Energy Research, Trondheim. The improved binary formulation developed within the scope of the present work was published together with those VLE data in a collaborative article of RUB and SINTEF. The experimental section of that article was contributed by Løvseth, Austegard, Westman, and Stang and the EOS section by Herrig, Neumann, and Span. The following subsection of this work is to a large extent based on that article by Løvseth *et al.*<sup>197</sup>

The improved departure function for CO<sub>2</sub> + Ar consists of two polynomial(-like) terms and four so-called “special” exponential terms. After developing and rejecting many other preliminary models with other functional forms, the present structure was adopted from the EOS-CG model, but all parameters were refitted to the enhanced experimental database. The complete equation with a total of six terms reads:

$$\alpha_{\text{CO}_2+\text{Ar}}^r(\delta, \tau) = \sum_{k=1}^2 n_k \delta^{d_k} \tau^{t_k} + \sum_{k=3}^6 n_k \delta^{d_k} \tau^{t_k} \exp\left[-\eta_k (\delta - \varepsilon_k)^2 - \beta_k (\delta - \gamma_k)\right]. \quad (6.1)$$

All parameters (coefficients  $n_k$ , temperature exponents  $t_k$ , density exponent  $d_k$ , and parameters of the “special” exponential terms  $\eta_k$ ,  $\varepsilon_k$ ,  $\beta_k$ , and  $\gamma_k$ ) are listed in Table E.2 in Appendix E. The parameters of the reducing functions for temperature and density according to Eqs. (3.42) and (3.43) are given in Table E.1.

With regard to the quantity of the experimental data, CO<sub>2</sub> + Ar is aside from H<sub>2</sub>O + CH<sub>4</sub> the best investigated system considered in this work; furthermore, the quality of the most important data sets is outstanding within the entire database used to develop the multi-component model for CCS-mixtures. The database includes homogeneous density data over a wide range of compositions for pressures up to about 100 MPa and within a temperature range of 253 K to 573 K. The available VLE measurements cover temperatures

from 213 K to about 300 K; thus, from below the triple point of pure CO<sub>2</sub> ( $T_{\text{tp,CO}_2} = 216.592$  K) to almost its critical point ( $T_{\text{c,CO}_2} = 304.128$  K). In addition, accurate speed-of-sound data at equimolar composition and at 75 mol% CO<sub>2</sub> were used to fit the new model. The data range from 275 K to 500 K in temperature and cover pressures up to 8 MPa. Some data on the second virial coefficient and the Joule-Thomson coefficient can be found in the literature. Those data were of less importance during the fitting process and will not be discussed here.

Selected experimental VLE data along exemplary isotherms are shown in Figure 6.2. Phase boundaries calculated from the new binary model are plotted for comparisons. Results of the previous reference formulation included in the EOS-CG of Gernert and Span<sup>2</sup> and results of the GERG-2008 model of Kunz and Wagner<sup>36</sup> are shown too. The figure additionally includes phase boundaries calculated from SRK, LKP, PSRK, and PCP-SAFT. The SRK EOS of Soave<sup>18</sup> was used with the binary interaction coefficient of Li and Yan<sup>198</sup> ( $k_{\text{CO}_2+\text{Ar}} = 0.180$ ). Because no interaction parameter for the LKP EOS of Plöcker *et al.*<sup>19</sup> was found in the literature, the standard value was used ( $k_{\text{CO}_2+\text{Ar}} = 1$ ); thus, the plotted results give an impression of the quality of that EOS without fitting it to experimental data. For the PSRK EOS of Holderbaum and Gmehling<sup>41</sup> two (out of six adjustable) binary parameters given by Gmehling *et al.*<sup>199</sup> were implemented. No interaction parameter was used in the calculations with the PCP-SAFT approach of Gross;<sup>45</sup> nevertheless; the results are interesting because the approach is (to a certain degree) considered to be physically based.

Particularly highlighted are the VLE data by Løvseth *et al.*,<sup>197</sup> which provide information on both coexisting phases, and the dew-point measurements carried out at RUB by Tsankova *et al.*<sup>200,201</sup> Those three experimental studies became available after the finalization of the EOS-CG model of Gernert and Span<sup>2</sup> and are among the most important data sets for the refitting of this binary formulation.

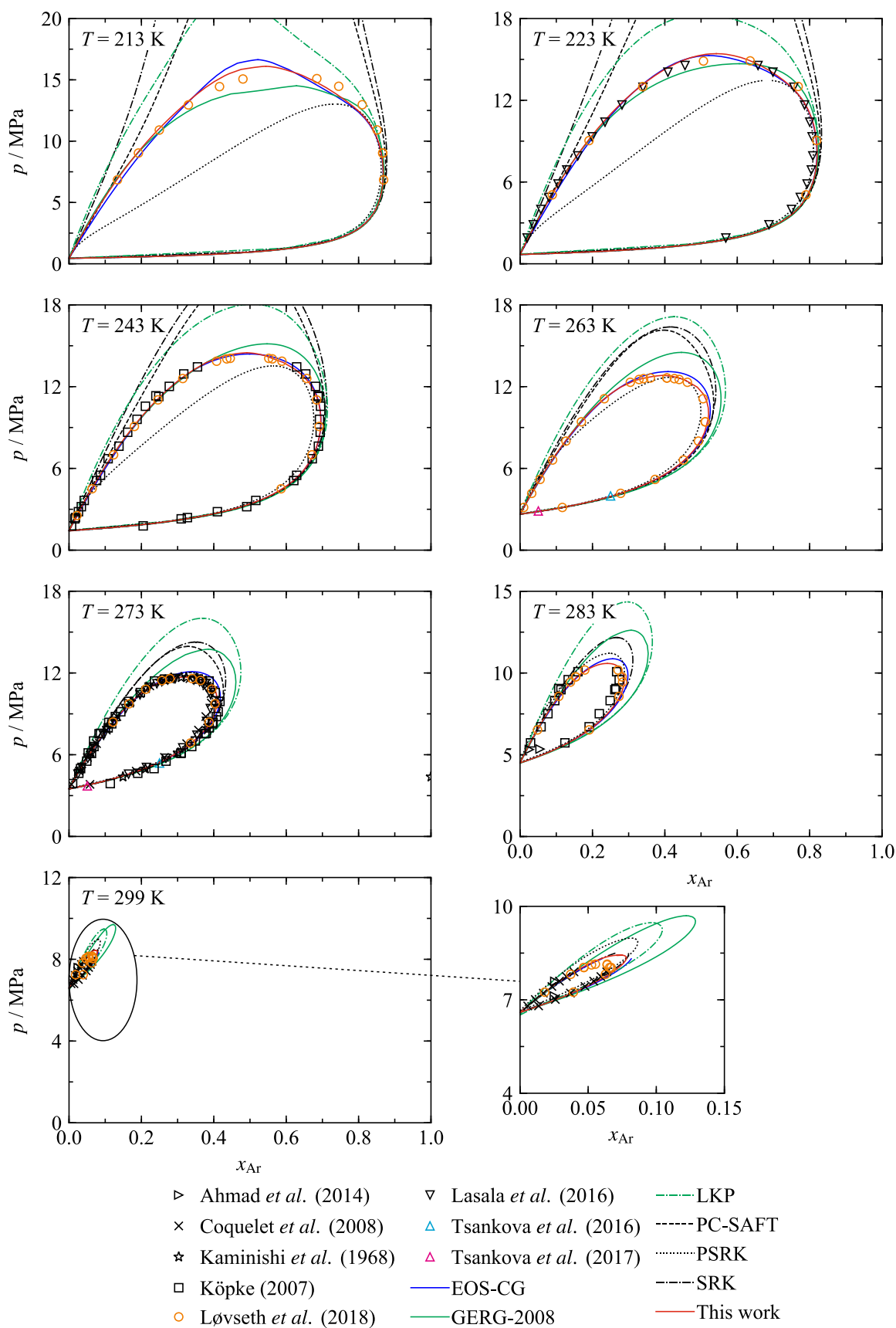


**Figure 6.2** Phase boundaries of the system  $\text{CO}_2 + \text{Ar}$  in  $p, x$  diagrams at temperatures of 213 K, 223 K, 243 K, 263 K, 273 K, 283 K, and 299 K as calculated from the new EOS. The available experimental data and results calculated from EOS-CG, GERG-2008, PSRK, PCP-SAFT, SRK, and LKP are shown for comparisons.

In general, the new model provides significantly more accurate results than all other models shown in Figure 6.2. The largest improvements compared to the EOS-CG model were achieved for temperatures above 243 K, where the EOS-CG overestimates the maximum saturation pressures. Between temperatures of 213 K and 243 K, the GERG-2008 is in quite good agreement with the experimental data, but the deviations between the model and the data increase significantly with increasing temperature. None of the other models enables a representation of the data as accurate as with the present model (or with the EOS-CG). Among the other models, the best results can be obtained from PSRK. For the three lowest isotherms ( $213 \leq T / \text{K} \leq 243$ ), PSRK enables a comparably good representation of the dew line but exhibits large deviations from the available data along the bubble line. The best agreement between PSRK and the data is at 273 K. This isotherm is covered by the experimental data of Kaminishi *et al.*,<sup>202</sup> which is the only data set that was already available, when Holderbaum and Gmehling<sup>41</sup> fitted interaction parameters for this system. Because CO<sub>2</sub> and argon are individual molecular groups within the group-contribution approach, the pool of experimental data used to fit the interaction parameters for CO<sub>2</sub> + Ar in PSRK is limited. The results shown in Figure 6.2 emphasize that in this case the predictive potential of this model is quite limited too.

To reasonably quantify deviations between calculated and experimental VLE data for a system like CO<sub>2</sub> + Ar is a more challenging task than could be expected. Because argon is a super-critical fluid at all investigated conditions, the VLE region of the mixture does not cover the entire composition range. The shape of the dew line at “lower” CO<sub>2</sub>-fractions is consequently defined by retrograde-condensation effects. At these conditions, small changes in composition lead to comparably large differences in saturation pressure. Thus, the discussion of deviations in pressure is not meaningful over the entire range of the VLE region. Nevertheless, the accuracy with regard to this property is of special interest during the development of the mixture model, because the standard method of fitting its parameters to VLE information is a minimization of deviations between calculated saturation pressures (at given  $T$  and  $\bar{x}$ ) and the experimental data. In order to provide a more meaningful impression of the modelling accuracy, deviations in composition (at given  $T$  and  $p$ ) should be considered too.

As mentioned before, the description of VLE by means of the new model was defined by fitting its adjustable parameters to the most recent VLE data of Løvseth *et al.*<sup>197</sup> and to the dew-point data of Tsankova *et al.*<sup>200,201</sup> Deviations between these data and calculated values are shown in Figure 6.3. Following the considerations discussed in the previous paragraph, deviations in saturation pressure as well as in composition are presented. The data points are plotted versus temperature and pressure to get a clearer impression of their location along the phase boundary. The isotherms investigated by Løvseth *et al.* are shown in different colors in order to make a link between the plotted deviations and the  $p,x$  diagrams presented

in Figure 6.2. The deviations of the dew points measured by Tsankova *et al.*<sup>200,201</sup> are so consistent that a special coloring is not needed.

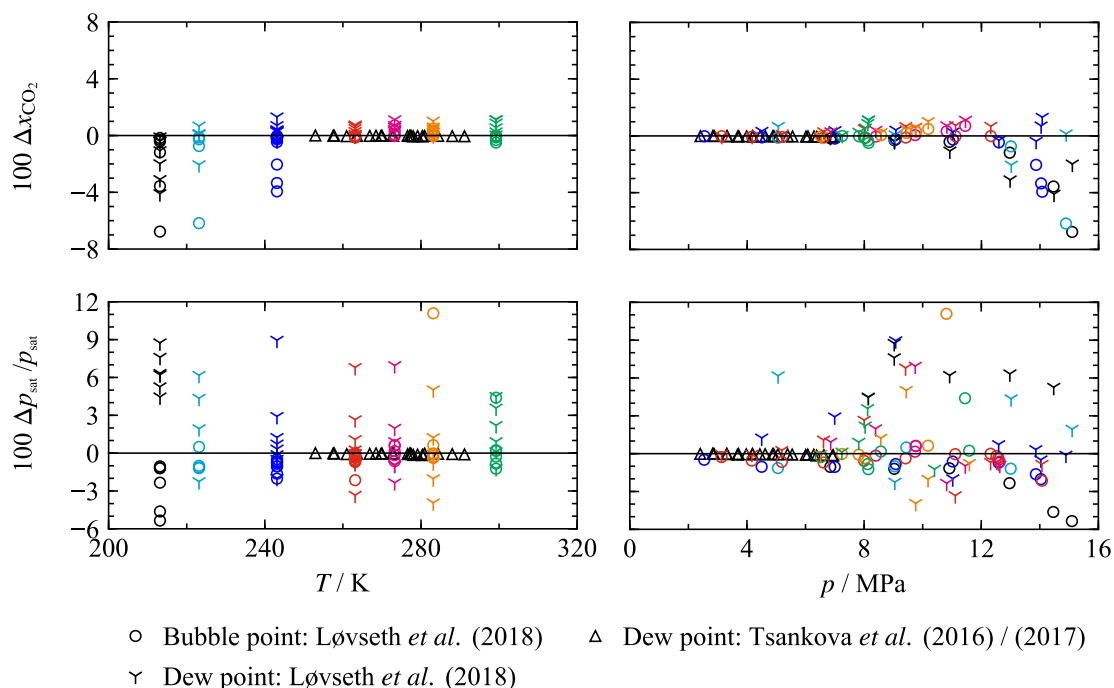


**Figure 6.3** Deviations between the experimental VLE data of Løvseth *et al.*,<sup>197</sup> the dew-point measurements of Tsankova *et al.*<sup>200,201</sup> and values calculated from the new EOS. Depending on the location of a state point along the dew or bubble line, the deviation in composition might be more meaningful than in saturation pressure, or vice versa. Deviations in pressure are given as  $\Delta p_{\text{sat}} / p_{\text{sat}} = (p_{\text{sat,exp}} - p_{\text{sat,calc}}) / p_{\text{sat,exp}}$  and deviations in composition as  $\Delta x_{\text{CO}_2} = (x_{\text{CO}_2,\text{exp}} - x_{\text{CO}_2,\text{calc}})$ . For the data of Løvseth *et al.*<sup>197</sup> different colors are used for the different isotherms.

For the data of Løvseth *et al.*,<sup>197</sup> deviations in composition are particularly meaningful because the data were measured using an analytical technique, in which samples from the coexisting phases are withdrawn and analyzed in a gas chromatograph. The mixture model represents the majority of these data within deviations of 1 mol%. Higher deviations occur along the 213 K isotherm and in the critical region at 223 K and 243 K. During the fitting process, the representation of the data at 213 K could not be improved without worsening the description of accurate data on homogeneous density and speed of sound at higher temperatures. This behavior is probably not caused by a contradiction between these different data sets but by numerical problems that occur when evaluating the reference EOS for pure CO<sub>2</sub> below the triple-point temperature ( $T_{\text{tp,CO}_2} = 216.59$  K). With regard to the critical region data, it has to be noted that a quantitatively accurate description of this region is always particularly challenging not only for mixtures but also for pure fluids (see Sec. 5). For quite asymmetric mixtures, it requires strong and thus mathematically complex departure terms, which are in most cases not compatible with a reasonable extrapolation behavior of the EOS beyond the experimentally covered region. In addition, deviations in terms of composition are less meaningful in the critical region due to the flat shape of the

phase boundaries. In this region, relatively small uncertainties in pressure lead to large deviations in composition (large  $dx_i / dp$ ).

Based on the deviations shown in Figure 6.3, the uncertainty in phase-equilibrium compositions calculated from the new mixture model for  $\text{CO}_2 + \text{Ar}$  is estimated to be 1 mol%, except for temperatures below the triple point of pure  $\text{CO}_2$  and in the critical region at low temperatures ( $T \leq 243 \text{ K}$ ). This uncertainty does not match the experimental uncertainties of the data. Løvseth *et al.*<sup>197</sup> provide combined expanded ( $k = 2$ ) uncertainties in composition of 0.030 mol% for bubble points and 0.028 mol% in dew points; in the critical region the uncertainty increases to 0.2 mol%. During the fitting process, it was never possible to reduce the deviations to these very low values without increasing deviations between the model and the most accurate density or speed-of-sound data. Similar conclusions were obtained for many other models fitted within the scope of this work. Most likely even small inconsistencies in the reported compositions of the multi-property data make it impossible to fit all data within the uncertainties claimed by the experimentalists.

The deviations in saturation pressure shown in Figure 6.3 are relatively consistent along the bubble line (with higher deviations in the critical region of each isotherm) but exhibit significant scatter along the dew line. The reason for this is the already explained change of  $dp / dx_i$  along the dew line. The highest deviations occur at medium pressures for each isotherm, hence in the region defined by retrograde-condensation effects. The wide range of deviations makes it difficult to estimate an uncertainty in saturation pressures calculated from the model. To make a reasonable estimate, comparisons with data obtained from synthetic experiments are more meaningful. Synthetic measurement techniques allow for the identification of the dew or bubble point of a prepared mixture with known composition at a specified temperature or pressure. Accurate dew-point measurements were performed by Tsankova and co-workers at RUB in collaboration with UWA.<sup>200,201</sup> Two mixtures containing 75 mol% and 95 mol%  $\text{CO}_2$  were investigated utilizing a microwave re-entrant cavity resonator. This apparatus is designed for the experimental determination of the dielectric permittivity. In order to obtain dew points, the investigated sample is cooled at quasi-isochoric conditions, while the permittivity is continuously detected. A sudden change in the derivative of this property with respect to temperature occurs when the dew line is crossed. Thoroughly analyzing the collected data leads to quite accurate dew-point data. The combined expanded ( $k = 2$ ) uncertainties in terms of pressure range from 0.15 % to 0.31 % for the mixture containing 75 mol%  $\text{CO}_2$  and from 0.24 % to 0.40 % for 95 mol%  $\text{CO}_2$ . Deviations between these data and values calculated from the new binary formulation are included in Figure 6.2. In addition, the pressure deviations are again shown on a more suitable scale in Figure 6.4, which additionally present deviations from the EOS-CG model. Because Tsankova *et al.*<sup>200,201</sup> report all data points with the corresponding uncertainties, these are indicated as error bars.



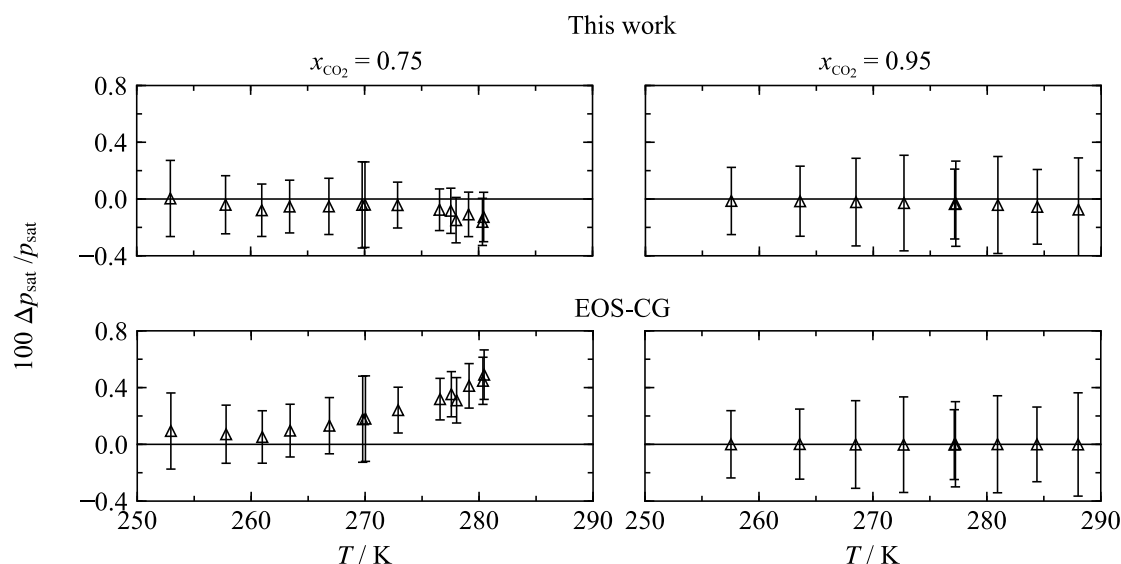


**Figure 6.4** Relative deviations  $\Delta p_{\text{sat}} = (p_{\text{sat,exp}} - p_{\text{sat,calc}}) / p_{\text{sat,exp}}$  between the experimental dew-point data of Tsankova *et al.*<sup>200,201</sup> for the system  $\text{CO}_2 + \text{Ar}$  and results calculated from the new EOS (top) and from EOS-CG (bottom) as a function of temperature.

Although these data were not available for the development of the EOS-CG model, the binary formulation represents all dew points of the 95 mol% mixture within their uncertainty. Thus, only the representation of the 75 mol% mixture needed to be improved in the refit. The new model enables a description of all data points within their experimental uncertainty. This aspect is particularly important, because it allows for a reliable statement on the pressure uncertainty of calculated dew points. Conservatively estimated, this uncertainty is 0.4 % for the two experimentally investigated compositions (75 mol% and 95 mol%  $\text{CO}_2$ ) and for temperatures between 255 K to 290 K.

Because the new model was exclusively fitted to the most recent and most accurate VLE data of Løvseth *et al.*<sup>197</sup> and Tsankova *et al.*,<sup>200,201</sup> the representation of the other data sets by Coquelet *et al.*,<sup>203</sup> Lasala *et al.*,<sup>204</sup> Ahmad *et al.*,<sup>205</sup> Sarashina *et al.*,<sup>206</sup> Kaminishi *et al.*,<sup>202</sup> and Köpke and Eggers<sup>207,208</sup> are not discussed here. A brief discussion of these data sets can be found in the journal article on the present mixture model.<sup>197</sup>

Accurate density data in the homogeneous gas phase were measured at RUB and published by Ben Souissi *et al.*<sup>209</sup> in the temperature range from 273 K to 323 K and for pressures up to about 9 MPa. The authors investigated two different mixtures with 50 mol% and 75 mol%  $\text{CO}_2$ . The measurements were performed with a two-sinker magnetic suspension densimeter. The relative combined expanded ( $k = 2$ ) uncertainty is stated to be within 0.033 %. The same apparatus was used to obtain the data published by Yang *et al.*<sup>210</sup> These data cover the same temperature and pressure range for a mixture containing 95 mol%  $\text{CO}_2$ . The relative combined expanded ( $k = 2$ ) uncertainty of the data for this mixture is 0.043 %. Comparisons between both data sets and the mixture model are given in Figure 6.5 for all three compositions along selected isotherms.

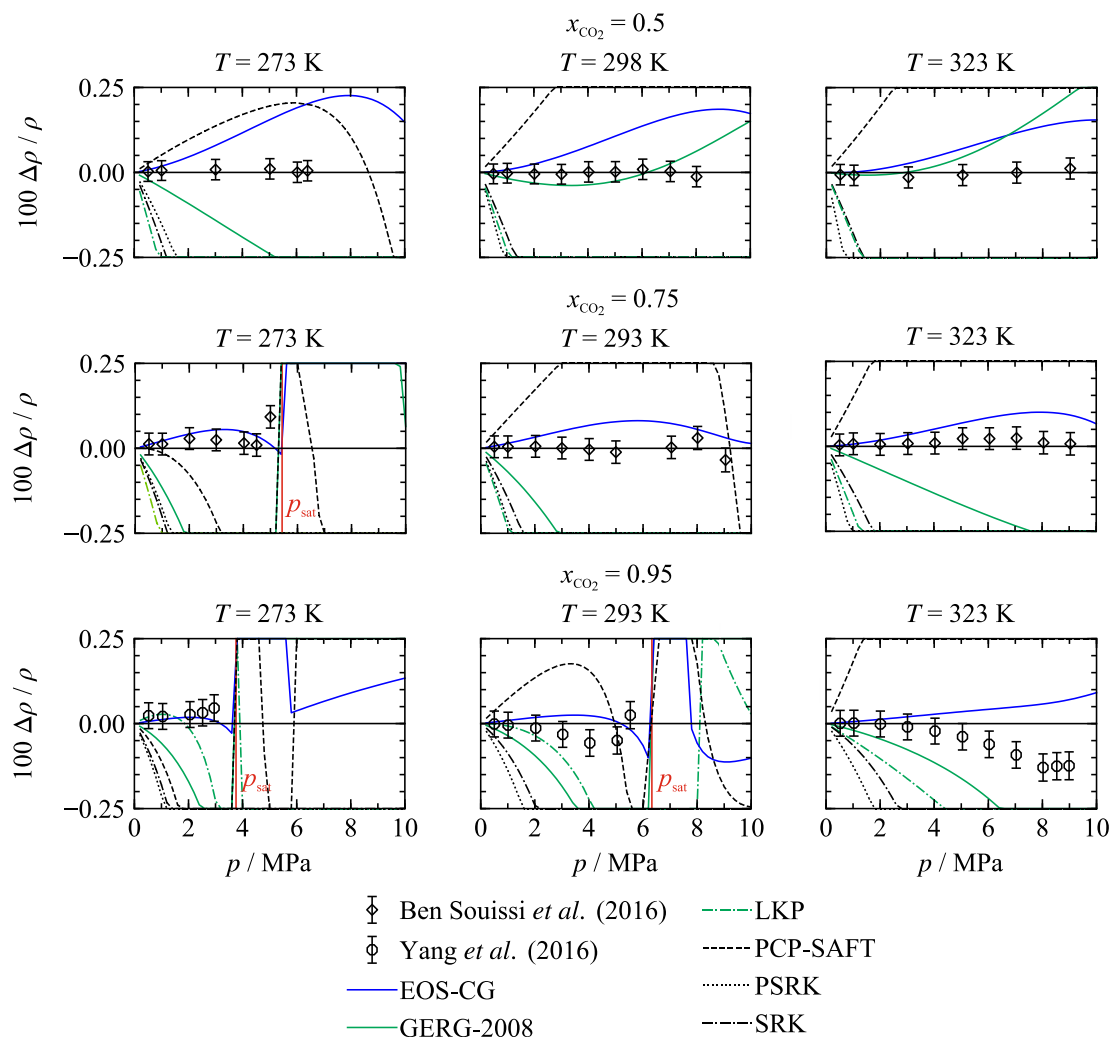


**Figure 6.5** Relative deviations  $\Delta\rho/\rho = (\rho_{\text{exp}} - \rho_{\text{calc}})/\rho_{\text{exp}}$  of accurate density data for the system  $\text{CO}_2 + \text{Ar}$  at three different compositions and selected isotherms from the new EOS as a function of pressure. Results calculated from EOS-CG, GERG-2008, PSRK, PCP-SAFT, SRK, and LKP are shown for comparisons.

The new model represents most of these data within their experimental uncertainties. However, for some points, especially at elevated pressures, the deviations are somewhat higher. Further fitting of the model to the data reduced these deviations, but led to a less accurate description of other properties. Thus, minor concessions had to be made in order to enable a description that represents the best compromise along all types of data. Still the AAD between the new model and the data of Ben Souissi *et al.*<sup>209</sup> is 0.016 %, and thus exceptionally small. The data of Yang *et al.*<sup>210</sup> are represented with an AAD of 0.037 %. The new mixture model provides a significantly more accurate description than the EOS-CG model for both data sets. It can consequently be noted that the accuracy of the model presented here was significantly enhanced by the experimental work carried out after the development of the EOS-CG model. None of the other models is able to represent these accurate data within their uncertainties. For the equimolar mixture, the GERG-2008 is in acceptable agreement with the data, but it exhibits quite large deviations for the other mixtures. All other EOS exhibit comparably small deviations at low pressures, where the mixing behavior is still relatively ideal, but the deviations increase drastically with

increasing pressure. At equimolar composition, a temperature of 298 K and pressures up to 10 MPa, the maximum deviation between the new model and the other EOS is about 4 % for SRK, 5.5 % for PSRK, 2.6 % for LKP, and 0.9 % for PCP-SAFT.

Prior to the already discussed measurements with a two-sinker densimeter at RUB, Yang *et al.*<sup>211</sup> measured the gas density of two CO<sub>2</sub>-rich mixtures with a single-sinker densimeter at Tsinghua University, Beijing. Selected isotherms investigated in that work are shown in Figure 6.6, which provides a rough overview of the data situation for homogeneous densities. Yang *et al.*<sup>211</sup> reported a relative combined expanded ( $k = 2$ ) uncertainty of 0.12 %. In this uncertainty analysis, the composition was found to be the main contributor to the combined uncertainty. During the fitting process it was not possible to set up a functional form that would reproduce the data within their experimental uncertainty. As shown for the 298 K, 323 K, and 373 K isotherms in Figure 6.6, the data exhibit a systematic offset. Since the corresponding publication contains density measurements in pure carbon dioxide, which are in good agreement with the reference equation of state, it seems unlikely that the offset is caused by an error in the apparatus. Discussions with the authors lead to the result that the reported composition might not agree with the one of the investigated sample, because of adsorption effects in the measuring cell or insufficient purging of the system. A more detailed analysis of this data set including a suggestion for a corrected composition can be found in the journal publication on the present mixture model.<sup>197</sup>

The single-sinker densimeter technique was also employed at RUB by Wegge.<sup>212</sup> The author carried out measurements in two gaseous mixtures containing 50 mol% and 75 mol% CO<sub>2</sub>. The data cover temperatures from 253 K to 453 K and pressures up to 20 MPa. Selected isotherms from this study are included in Figure 6.6. The author provides combined expanded ( $k = 2$ ) uncertainties for every state point that range from 0.047 % to 0.123 % for the equimolar mixture and from 0.032 % to 0.130 % for the sample containing 75 mol% CO<sub>2</sub>. As apparent from the deviation plots in Figure 6.6, the present model does not represent all the data within their uncertainties. Especially at lower temperatures and elevated pressures the model deviates considerably from the data. Personal communication with the author revealed that filling the utilized densimeter is challenging and that the mixture might have decomposed during this process. However, while the resulting shift in composition would be a satisfying explanation for large deviations of a single isotherm, it contradicts the good reproducibility of the results of the different, independent measurement runs performed for every isotherm. Since the data are currently being further evaluated by the author and no other experimental data were available to prove the trend of the data, they were not included in the final fit of the present mixture model. Nevertheless, it should be noted that more intensive fitting of the data at supercritical temperatures probably would have led to a description that matches the experimental uncertainty at these conditions.

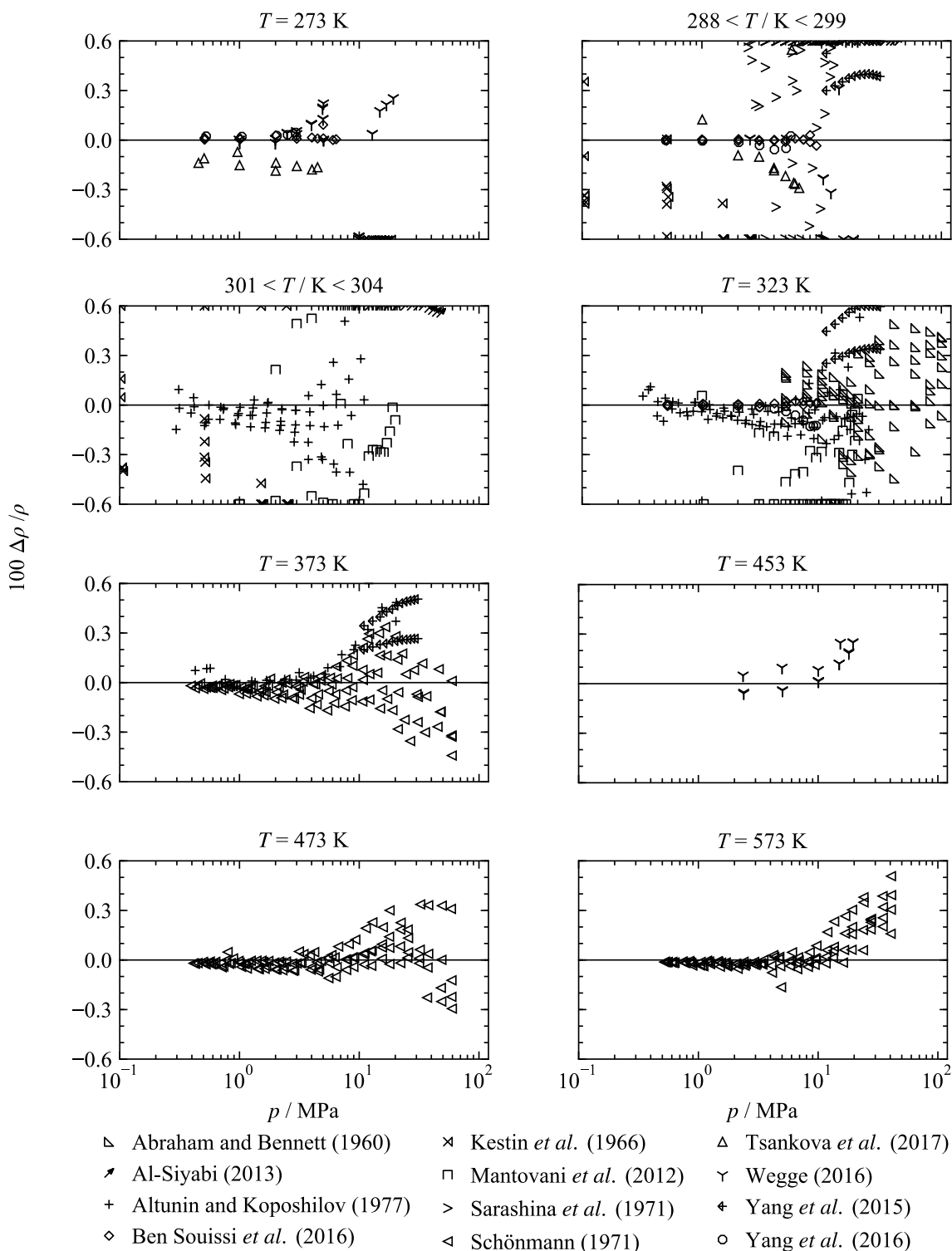


**Figure 6.6** Relative deviations  $\Delta\rho/\rho = (\rho_{\text{exp}} - \rho_{\text{calc}})/\rho_{\text{exp}}$  of experimental density data for the system  $\text{CO}_2 + \text{Ar}$  at selected isotherms from the new EOS as a function of pressure. The data cover a composition range of  $0.01 < x_{\text{CO}_2} < 0.97$ .

The two-sinker densimeter measurements by Ben Souissi *et al.*<sup>209</sup> and Yang *et al.*<sup>210</sup> provide by far the most accurate density data for the system  $\text{CO}_2 + \text{Ar}$ . Nevertheless, some other sources of data were used to fit the mixture model or were at least of interest for the validation of the model. One of the deviation plots included in Figure 6.6 presents the data situation at around 300 K. With regard to this isotherm, it becomes evident that the

overlapping data of Kestin *et al.*,<sup>213</sup> Mantovani *et al.*,<sup>214</sup> and Al-Siyabi<sup>215</sup> are of low accuracy. Thus, these data were not included in the fitting process and will not be discussed here. The work of Altunin and Koposhilov<sup>216</sup> is one of the most comprehensive experimental studies of the thermophysical properties of CO<sub>2</sub> + Ar. A detailed analysis of their data revealed inconsistencies at pressures higher than about 5 MPa and other references were found to be more reliable. Their data were consequently not used to fit the mixture model.

Abraham and Bennett<sup>217</sup> published compressibility factors over a wide range of compositions and for pressures up to 100 MPa. These values were converted into gas densities and were partly included in the fitting process to shape the functional form at high pressures. In the corresponding publication, no details about the experimental apparatus are provided, but some information regarding uncertainties is given. The temperature and pressure measurements are accurate within 0.01 K and 0.01 %, respectively. The investigated samples contained impurities of up to 0.1 mass%, which means a relatively high level of contamination. The compressibility factors are given as smoothed values with four digits resulting in a rounding error of 0.1 % to 0.3 %. Thus, the given uncertainty of 0.14 % is quite questionable. Calculating a combined expanded ( $k = 2$ ) uncertainty leads to a more realistic average value of 0.24 % and a maximum uncertainty of 0.65 %. These results are in line with the minimum deviations obtained during the fitting process and shown for selected isotherms in Figure 6.6. The *AAD* between the data and the mixture model is 0.184 %. Thus, the model overall agrees with the data within their experimental uncertainty.

A comprehensive experimental data set was published by Schönmann.<sup>218</sup> This study includes gaseous mixtures with eight different compositions at temperatures up to 573 K and pressures up to 60 MPa. The data was obtained with the Burnett method. The author estimates the overall uncertainty for the compressibility factor to be within a range of 0.04 % to 0.3 %. Since the corresponding publication provides relatively detailed information on the accuracy of the employed experimental set-up this total combined uncertainty was recalculated in order to avoid “overfitting” the data. The uncertainty with respect to pressure is stated to be 0.0002 bar, whereas the uncertainty in temperature is stated to be 0.06 K for temperatures up to 100 °C and 0.16 K up to 300 °C. The estimated uncertainty in composition is 0.5 mol%. Considering all given uncertainties, the recalculated combined expanded ( $k = 2$ ) uncertainties range from 0.06 % to 0.72 %. As shown in Figure 6.6, the mixture model represents the data with a deviation of 0.08 % for pressures up to 3 MPa and 0.3 % for pressure up to 30 MPa. At higher pressures, the offset increases to 0.5 %. The *AAD* between this data set and the mixture model is 0.079 % and thus clearly within the experimental uncertainty.

Some comments should be made on the density measurements of Tsankova and colleagues.<sup>201</sup> That work was already discussed within the discussion of the VLE database. The microwave re-entrant cavity resonator employed to obtain the presented dew-point

measurements also allows for the determination of homogenous gas densities. In fact, these densities are not directly measured but calculated from dielectric permittivity values. For these data, no exact uncertainty analysis was carried out, but the accuracy was estimated by means of the overlapping and very accurate measurements of Ben Souissi *et al.*<sup>209</sup> The total combined expanded ( $k = 1.73$ ) uncertainty was thereby estimated to be within 0.3 %. With regard to the deviations shown in Figure 6.6 (see the two lowest isotherms), this estimation seems to be reasonable. The new mixture model agrees with these data with an *AAD* of 0.177 %. Unsurprisingly, this *AAD* agrees with the estimated uncertainty because the model was fitted to the experimental data of Ben Souissi *et al.*<sup>209</sup> Although the data of Tsankova *et al.* are not the most accurate values, they are mentioned here for completeness. In addition, their work demonstrates that the technique leads to reliable mixture densities, that can be obtained comparably quickly, namely within one day per isotherm.

Considering the deviations shown in Figure 6.6 and the discussed experimental uncertainties, some estimates for uncertainties in homogeneous densities calculated from the new model can be made. Over most of the composition range and for temperatures up to 570 K, densities in the gas phase and in supercritical states can be calculated with an uncertainty of 0.3 % for pressures up to 30 MPa and 0.6 % for pressures up to 100 MPa. For the molar compositions of 50 mol%, 75 mol%, and 95 mol% CO<sub>2</sub>, highly accurate homogeneous gas densities were used to fit the mixture model within a temperature range from 273 K to 323 K and for pressures up to 9 MPa. Thus, the maximum uncertainty of calculated gas densities in this temperature and pressure region is within 0.035 % for the 50 mol% and 75 mol% CO<sub>2</sub> mixture and within 0.045 % for the mixture containing 95 mol% CO<sub>2</sub>. The uncertainty of calculated liquid densities cannot be estimated, since no reliable data are available in this state region.

Speed-of-sound data are always of high interest during the fitting process of EOS for mixtures and pure fluids because calculating this property requires the combination of different derivatives of the functional form (see also Sec. 5.1.6). Consequently, fitting such data has a strong impact on the final EOS. In addition, by thorough experimental work quite low uncertainties can be achieved, which makes this type of data very valuable for fitting. The database for the speed of sound in CO<sub>2</sub> + Ar, and in general in mixtures, is unfortunately very limited. Two sources of experimental results are available, namely the dissertation of Al-Siyabi<sup>215</sup> and the work of Wegge *et al.*,<sup>219</sup> which was carried out as a collaboration between RUB and NIST.

During the fitting process, the data of Al-Siyabi<sup>215</sup> were found to be of low accuracy, which is most likely caused by the method of filling the apparatus with the sample. During the filling process, the author had no technical capability to heat the mixture above its critical temperature. Consequently, the almost isenthalpic expansion when filling the mixture from the gas cylinder into the measuring cell results in crossing the two-phase region, which leads

to a shift in the composition of the investigated sample. With regard to the systematic offset of the data, as evident in Figure 6.7, this explanation seems plausible. The measurements of Al-Siyabi<sup>215</sup> were therefore not used to fit the present mixture model.

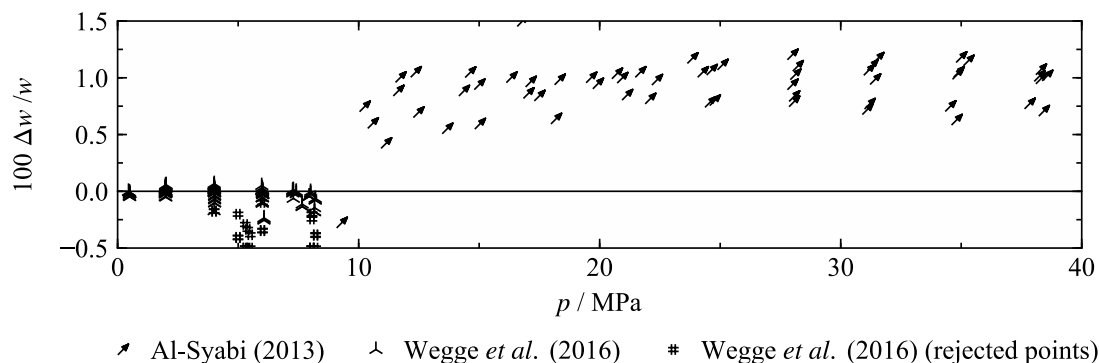


**Figure 6.7** Relative deviations  $\Delta w / w = (w_{\text{exp}} - w_{\text{calc}}) / w_{\text{exp}}$  of the available experimental speed-of-sound data for the system  $\text{CO}_2 + \text{Ar}$  from the new EOS as a function of pressure.

In contrast, Wegge *et al.*<sup>219</sup> describe a supercritical filling procedure. Due to the use of this method and the overall thoroughness of their experimental work, the presented data are deemed to be of quite high quality. Deviations between the data and the present mixture model are shown in Figure 6.8.

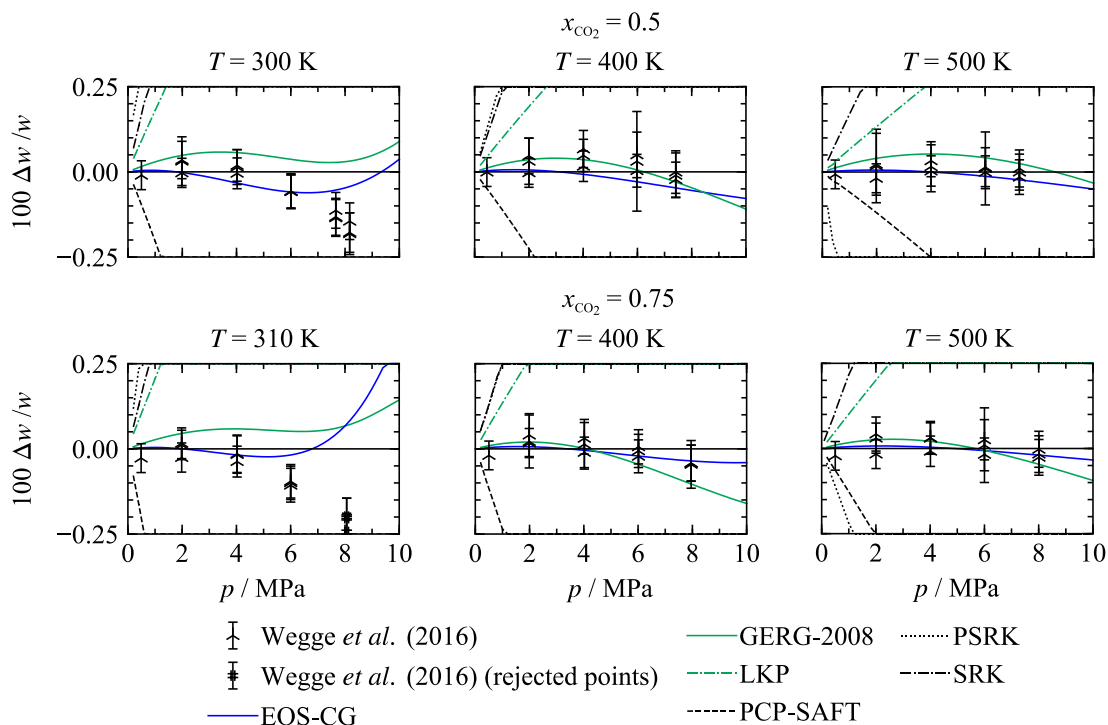


**Figure 6.8** Relative deviations  $\Delta w / w = (w_{\text{exp}} - w_{\text{calc}}) / w_{\text{exp}}$  of the available experimental speed-of-sound data for the system  $\text{CO}_2 + \text{Ar}$  from the new EOS as a function of pressure. Results calculated from EOS-CG, GERG-2008, PSRK, PCP-SAFT, SRK, and LKP are shown for comparisons.

The measurements were carried out with a spherical acoustic resonator at temperatures between 275 K and 500 K and pressures up to 8 MPa. The fluid was investigated at two different compositions with 50 mol% and 75 mol%  $\text{CO}_2$ . The authors state combined

expanded ( $k = 2$ ) uncertainties in speed of sound ranging from 0.042 % to 0.056 %. The mixture model represents most of the data within their experimental uncertainties, except for some points at low temperatures and higher pressures (see 300 K and 310 K in Figure 6.8). The GERG-2008 and the EOS-CG are in acceptable agreement with the data. None of the other models allows for a representation of the data within their experimental uncertainties. It should be noted that the thermal EOS SRK, LKP, and PSRK were combined with simple correlations for the ideal-gas state,<sup>27</sup> which is mandatory to calculate caloric properties. The EOS-CG model of Gernert and Span<sup>2</sup> was developed prior to the publication of these experimental results, and is thus in surprisingly good agreement with the data. In fact, the points that cannot be reproduced within their experimental uncertainties with the new model, also significantly deviate from EOS-CG. Since Wegge and co-workers carried out comparisons between the data and EOS-CG, these higher deviations are discussed within the corresponding publication. The authors identified some data points for which they assume pre-condensation effects caused by sound-induced pressure waves. In Figures 6.7 to 6.9, these points are depicted with different symbols and indicated as “rejected points”. Pre-condensation effects seem to be possible in the vicinity of the phase boundary; however, with regard to Figure 6.9, only some of the measurements for the CO<sub>2</sub>-rich mixture were carried out very close to the saturation line.

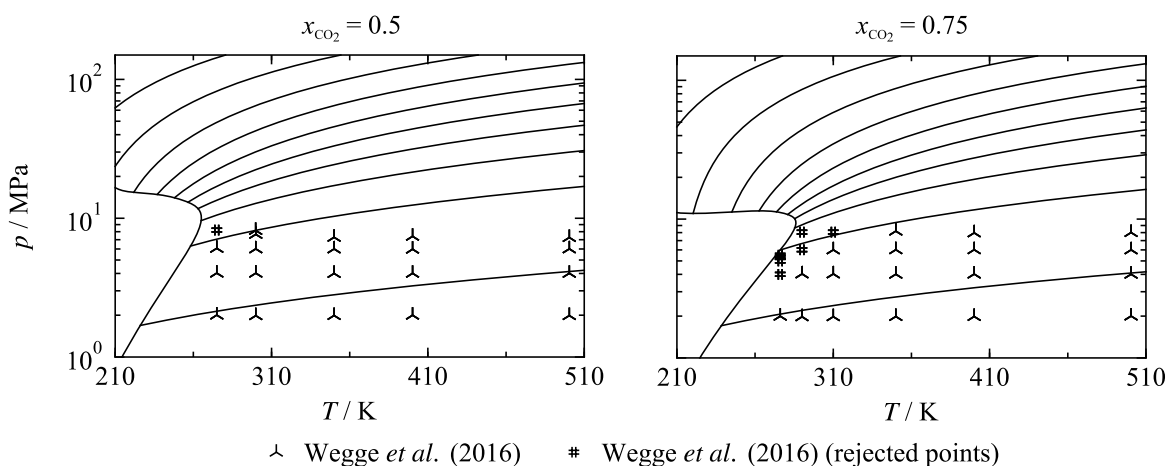


**Figure 6.9**  $p, T$  diagrams along isochores calculated with the new EOS for the two compositions investigated by Wegge *et al.*<sup>219</sup> The location of these speed-of-sound data is presented with regard to the phase boundary.

For the other rejected state points, other factors must have contributed to higher uncertainties and thus larger deviations from the mixture models. Including all data points, the AAD from the new model is 0.106 %, whereas rejecting the less reliable points leads to an AAD of 0.04 %.

Based on the deviations of the reliable speed-of-sound data, the estimated uncertainty of calculated sound speeds in the gas phase at 50 mol% and 75 mol% CO<sub>2</sub> for temperatures up to 500 K and pressures up to 8 MPa is 0.06 %. For compositions between 50 mol% and



75 mol% CO<sub>2</sub>, the uncertainty of calculated data is assumed to be at the same order of magnitude, though additional data are needed to validate the model for these mixtures.

The assumption that the present model also yields high-quality results in regions that are not experimentally covered is based on a continuous careful validation of its extrapolation behavior during the fitting process. As briefly discussed in Sec. 4, the development of empirical mixture models based on experimental data is particularly challenging, since the Helmholtz-energy function has to be shaped within a multidimensional surface defined by temperature, density, and composition. Thus, only parts of this large surface are defined by experimental data. In order to ensure that the final model also yields reasonable results in state regions where it was not fitted to experimental data, diagrams of various properties were continuously calculated from preliminary models during the fitting process. The validation of these diagrams is of special interest in state regions defined by extreme values of temperature, pressure, or density. A smooth extrapolation behavior of the model is crucial not only to ensure reasonable results at extreme conditions, but also in technically relevant state regions that are not sufficiently covered by the experimental database. In Figure 6.10, the pressure is plotted versus enthalpy, density, and temperature. Within these property plots, the mixing behavior is shown for pressures up to 1 GPa and temperatures up to 3000 K in the  $p,h$  diagram and 10 000 K in the  $p,\rho$  diagram. Even at high temperatures and pressures the isolines are smoothly shaped and no bumps or crossings are found.

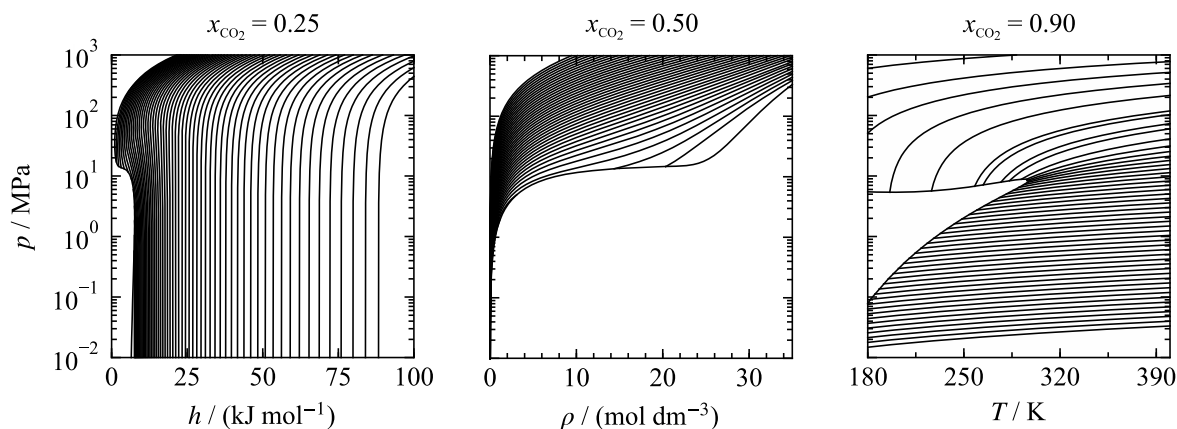


**Figure 6.10** Left to right:  $p,h$ ,  $p,\rho$ , and  $p,T$  diagrams calculated with the new EOS for three different compositions (25 mol%, 50 mol%, and 90 mol% CO<sub>2</sub>) at extreme conditions. The mixing behavior is shown for pressures up to 1 GPa and along isotherms up to 3000 K in the  $p,h$  diagram and 10 000 K in the  $p,\rho$  diagram. The  $p,T$  diagram includes isochores up to 33 mol dm<sup>-3</sup>.

In addition to these plots, a variety of other diagrams was calculated and validated including a selection of derivatives of the Helmholtz-energy function. Based on these validations, the overall extrapolation behavior of this binary mixture model was found to be excellent. However, it has to be noted that especially at very high pressures or temperatures below the triple point of pure CO<sub>2</sub> ( $T_{\text{tp,CO}_2} = 216.59$  K), the formation of solid structures has to be considered. Since the present model enables only the description of fluid phases, additional models and algorithms as implemented in TREND<sup>22</sup> are required to predict solidification.

### 6.2.2 Carbon Dioxide + Carbon Monoxide

With regard to Helmholtz-energy explicit EOS as developed in this work, the model situation for the system CO<sub>2</sub> + CO is similar to that of CO<sub>2</sub> + Ar: The system is considered in the EOS-CG model of Gernert and Span<sup>2</sup> and in the GERG-2008 of Kunz and Wagner.<sup>35</sup> Both binary formulations cannot be considered as very accurate. Within the GERG-2008 framework, the system CO<sub>2</sub> + CO is of little relevance; thus, the binary model was not fitted to experimental data but the parameters of the reducing functions for temperature and density were adjusted following the Lorentz-Berthelot combining rules. In EOS-CG, all four reducing parameters were fitted to experimental data that were available at the time of its development. As mentioned before, the development of EOS-CG was completed in 2013.<sup>17</sup> Since then, three comprehensive data sets became available that allowed the present improved binary formulation including a binary specific departure function. VLE data covering a wide temperature range were recently published by Westman *et al.*<sup>220</sup> and Souza *et al.*<sup>221</sup> Subsequent to the already published VLE experiments, Souza also carried out comprehensive homogeneous density measurements in the gas and liquid phases. These data will be published together with the present mixture model, which was developed as a collaboration between Imperial College London and RUB.<sup>222</sup> Additional homogeneous densities were measured by Tsankova *et al.*<sup>223</sup> and Blanco *et al.*<sup>224</sup> These measurements are of lower accuracy than the data of Souza *et al.*;<sup>222</sup> nevertheless, the data of Tsankova *et al.*<sup>223</sup> were valuable for the validation of the present model.

The new departure function for CO<sub>2</sub> + CO contains two polynomial(-like) terms, two exponential terms, and two Gaussian bell-shaped terms. The complete function reads:

$$\alpha_{\text{CO}_2+\text{CO}}^r(\delta, \tau) = \sum_{k=1}^2 n_k \delta^{d_k} \tau^{t_k} + \sum_{k=3}^4 n_k \delta^{d_k} \tau^{t_k} \exp(-\delta^{l_k}) + \sum_{k=5}^6 n_i \delta^{d_k} \tau^{t_k} \exp\left[-\eta_k (\delta - \varepsilon_k)^2 - \beta_k (\tau - \gamma_k)^2\right]. \quad (6.2)$$

All parameters of this function are given in Table E.2 in Appendix E of this thesis; the reducing parameters of Eqs. (3.42) and (3.43) are given in Table E.1. Gaussian bell-shaped terms have been used for decades in the functional forms of pure-fluid EOS, but their use in mixture models is comparably new (see Sec. 3.3). In fact, Eq. (6.2) is the first departure function using the “classic” combination of polynomial(-like) terms, exponential terms and Gaussian bell-shaped terms that was used in a large number of pure-fluid EOS.

Figure 6.11 shows phase boundaries at selected isotherms as calculated from the mixture model together with experimental VLE data from Kaminishi *et al.*,<sup>202</sup> Christiansen *et al.*,<sup>225</sup> Huamin,<sup>226</sup> Blanco *et al.*,<sup>224</sup> and from the very accurate studies of Westman *et al.*<sup>220</sup> and Souza *et al.*<sup>221</sup> Results calculated from other EOS are included for comparisons.

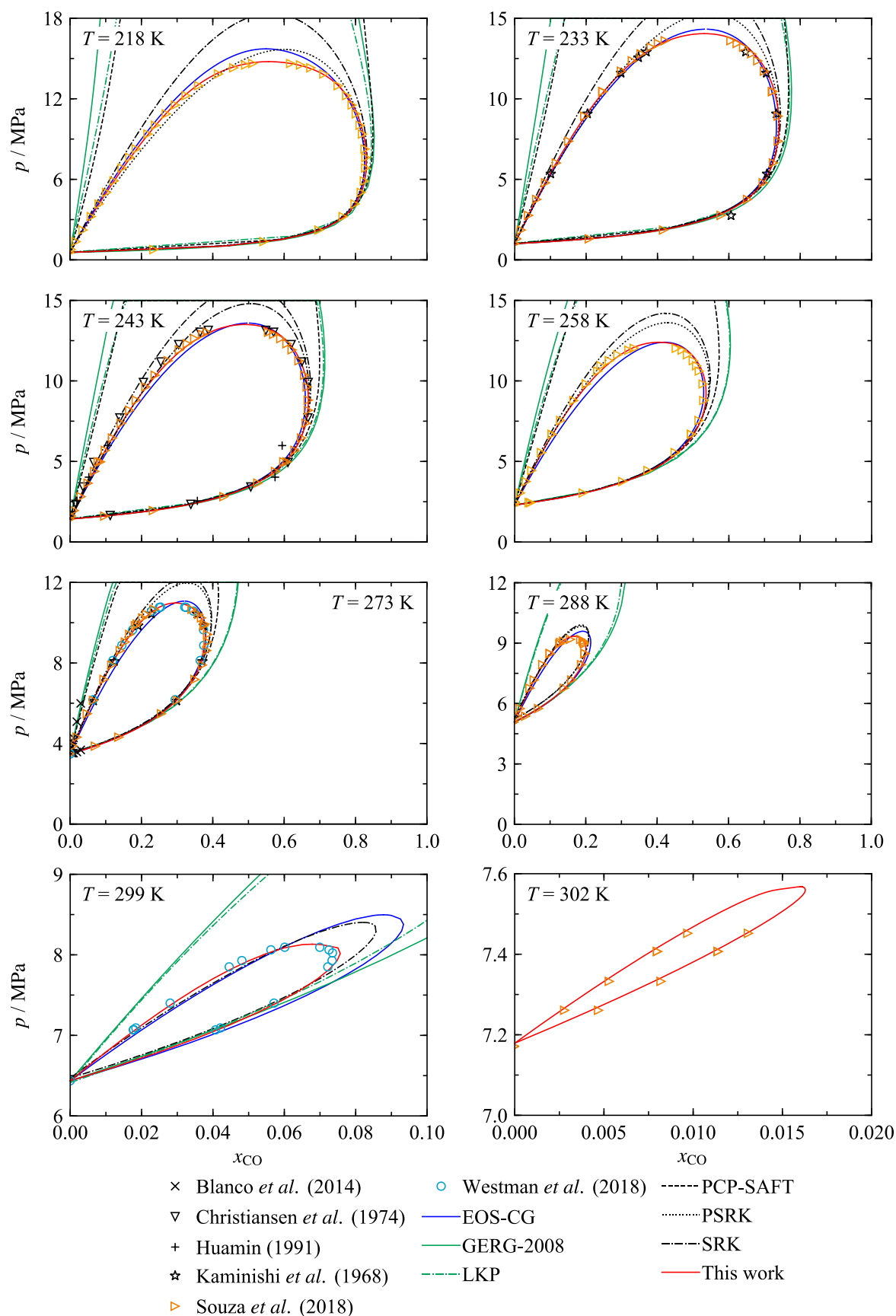


**Figure 6.11** Phase boundaries of the system  $\text{CO}_2 + \text{CO}$  in  $p, x$  diagrams at 218 K, 233 K, 243 K, 258 K, 273 K, 288 K, 299 K, and 302 K as calculated from the new EOS. The available experimental data and results calculated from EOS-CG, GERG-2008, PSRK, PCP-SAFT, SRK, and LKP are shown for comparisons.

The LKP EOS of Plöcker *et al.*<sup>19</sup> was used with the standard binary interaction parameter ( $k_{\text{CO}_2+\text{CO}} = 1$ ). For the SRK EOS of Soave,<sup>18</sup> the interaction coefficient of Jana<sup>227</sup> ( $k_{\text{CO}_2+\text{CO}} = -0.04$ ) was applied. The calculations with the PSRK EOS of Holderbaum and Gmehling<sup>41</sup> were carried out with two (out of six adjustable) binary parameters published by Fischer and Gmehling.<sup>228</sup> No interaction parameter was used to obtain the results of the PCP-SAFT approach of Gross.<sup>45</sup>

The  $p,x$  diagrams emphasize that the experimental database is qualitatively consistent, except for the data of Blanco *et al.*<sup>224</sup> that deviate considerably from all other sources. Surprisingly, those data are in very close agreement with the GERG-2008 model, which was not fitted to any experimental data but which is based on simple combining rules for the pure-fluid EOS. The GERG-2008 model, does not agree with any data sets other than the one of Blanco and co-workers. Regarding the 273 K isotherm in Figure 6.11, the agreement between those data and the model is so good that Blanco *et al.*<sup>224</sup> might have accidentally reported calculated values instead of the experimental data. The corresponding publication provides very limited information on how the VLE data were obtained. It is only stated that the data were determined from density measurements carried out in the same study.

The results calculated from LKP and PCP-SAFT exhibit large deviations from the reliable data and all other models, which is expected, because no interaction parameters were used in these calculations. With regard to PCP-SAFT, this underlines that the predictive potential of this approach is limited without fitting it to any experimental data. The accuracy of the VLE data obtained from SRK and PSRK is comparable. Both models yield qualitatively reasonable results but considerably overestimate saturation pressures in the critical region.

As expected, the new model provides the most accurate description of the available data. Due to the new departure function, which was fitted to the experimental data of Souza *et al.*,<sup>221</sup> the results are significantly more accurate than the ones obtained from EOS-CG. The calculated phase boundaries are in close agreement with the data from just above the triple-point temperature of pure CO<sub>2</sub> ( $T_{\text{tp,CO}_2} = 216.592$  K) to almost its critical temperature ( $T_{\text{c,CO}_2} = 304.128$  K). Especially the representation of the highest isotherm underlines the high accuracy of the model. At this temperature, the pressure and composition range of the VLE is exceptionally small, which makes it numerically challenging to achieve good modelling results. None of the other models allows for a reliable description of the data at this temperature. The overall description of the phase boundaries shown in Figure 6.11 can be considered as the best description of VLE data achieved within this work. Deviations between calculated values and the two most recent and accurate data sets by Westman *et al.*<sup>220</sup> and Souza *et al.*<sup>221</sup> are presented in Figure 6.12. The data by Kaminishi *et al.*,<sup>202</sup> Christiansen *et al.*,<sup>225</sup> and Huamin<sup>226</sup> are of considerably lower accuracy and were not relevant for the fitting process; thus, they are not further discussed here and are also not shown in Figure 6.12.

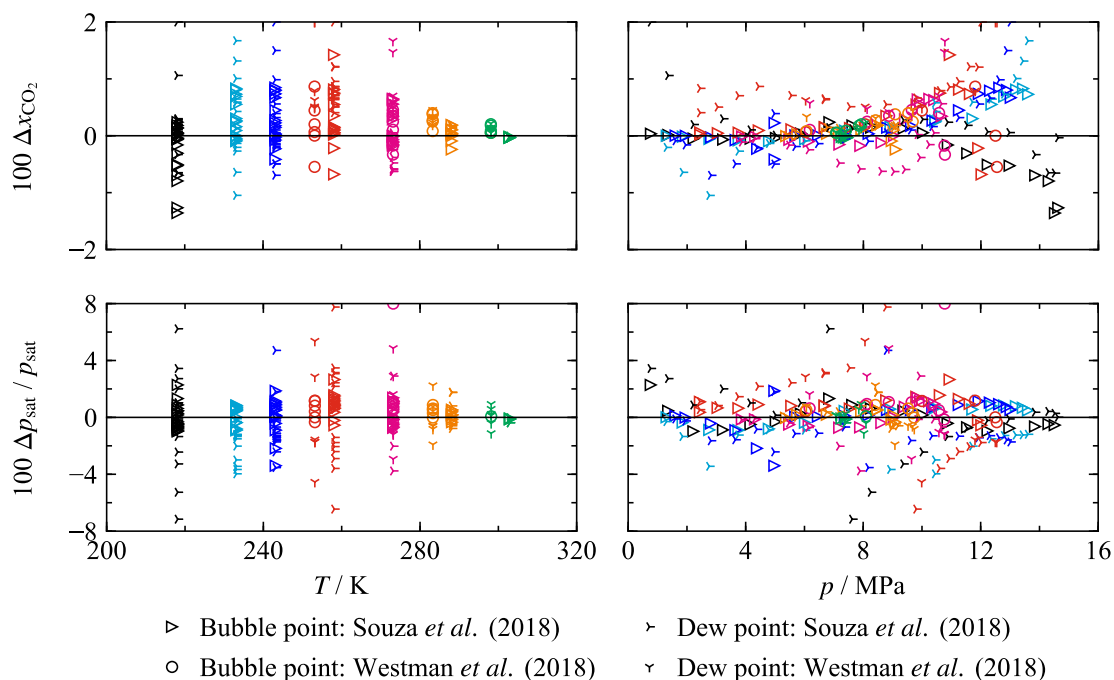


**Figure 6.12** Deviations between the experimental VLE data of Souza *et al.*<sup>221</sup> and Westman *et al.*<sup>220</sup> and values calculated from the new EOS versus temperature (left) and pressure (right). The top panels show deviations in saturation pressure given as  $\Delta p_{\text{sat}} / p_{\text{sat}} = (p_{\text{sat,exp}} - p_{\text{sat,calc}}) / p_{\text{sat,exp}}$  and the bottom panels show deviations in composition given as  $\Delta x_{\text{CO}_2} = (x_{\text{CO}_2,\text{exp}} - x_{\text{CO}_2,\text{calc}})$ . Depending on the temperature, the data are depicted in different colors. If temperatures investigated by Souza *et al.*<sup>221</sup> and Westman *et al.*<sup>220</sup> are not identical but similar, the same color is used.

The majority of the data is represented within deviations of 1 mol%, which is adopted as the expanded ( $k = 2$ ) uncertainty of calculated phase-equilibrium compositions. As also discussed for the system  $\text{CO}_2 + \text{Ar}$ , this uncertainty does not match the very low experimental uncertainties. The data of Souza *et al.*<sup>221</sup> were obtained through the use of the “static-analytic method” with online sampling from the phase equilibrium and composition measurement in a gas chromatograph. The average values of the combined expanded ( $k = 2$ ) uncertainties in composition are 0.06 mol% for the bubble points and 0.12 mol% for the dew points. The measurements of Westman *et al.*<sup>220</sup> were carried out with a similar experimental set-up, which was also used for the measurements in  $\text{CO}_2 + \text{Ar}$  published by Løvseth *et al.*<sup>197</sup> (see Sec. 6.2.1). The average values for the combined expanded ( $k = 2$ ) uncertainties are 0.07 mol% for the bubble points and 0.05 mol% for the dew points.

Based on the pressure deviations plotted in Figure 6.12, it is challenging to estimate an uncertainty in calculated saturation pressures. Most of the data are represented within 2 % in pressure. Higher deviations occur along the dew line in the sections characterized by retrograde condensation effects. As discussed Sec. 6.2.1, pressure deviations are less meaningful in this state region.

Compared to many other mixtures considered in this work, the database for homogeneous densities is quite comprehensive for  $\text{CO}_2 + \text{CO}$ . The complete data cover temperatures from 253 K to 423 K at pressures up to 50 MPa. The compositions range from almost pure  $\text{CO}_2$  to about 75 mol%  $\text{CO}$ . Deviations between calculated values and selected experimental data

are shown in Figure 6.13. The deviations are plotted as a function of density, which spreads the data and enables a better overview.

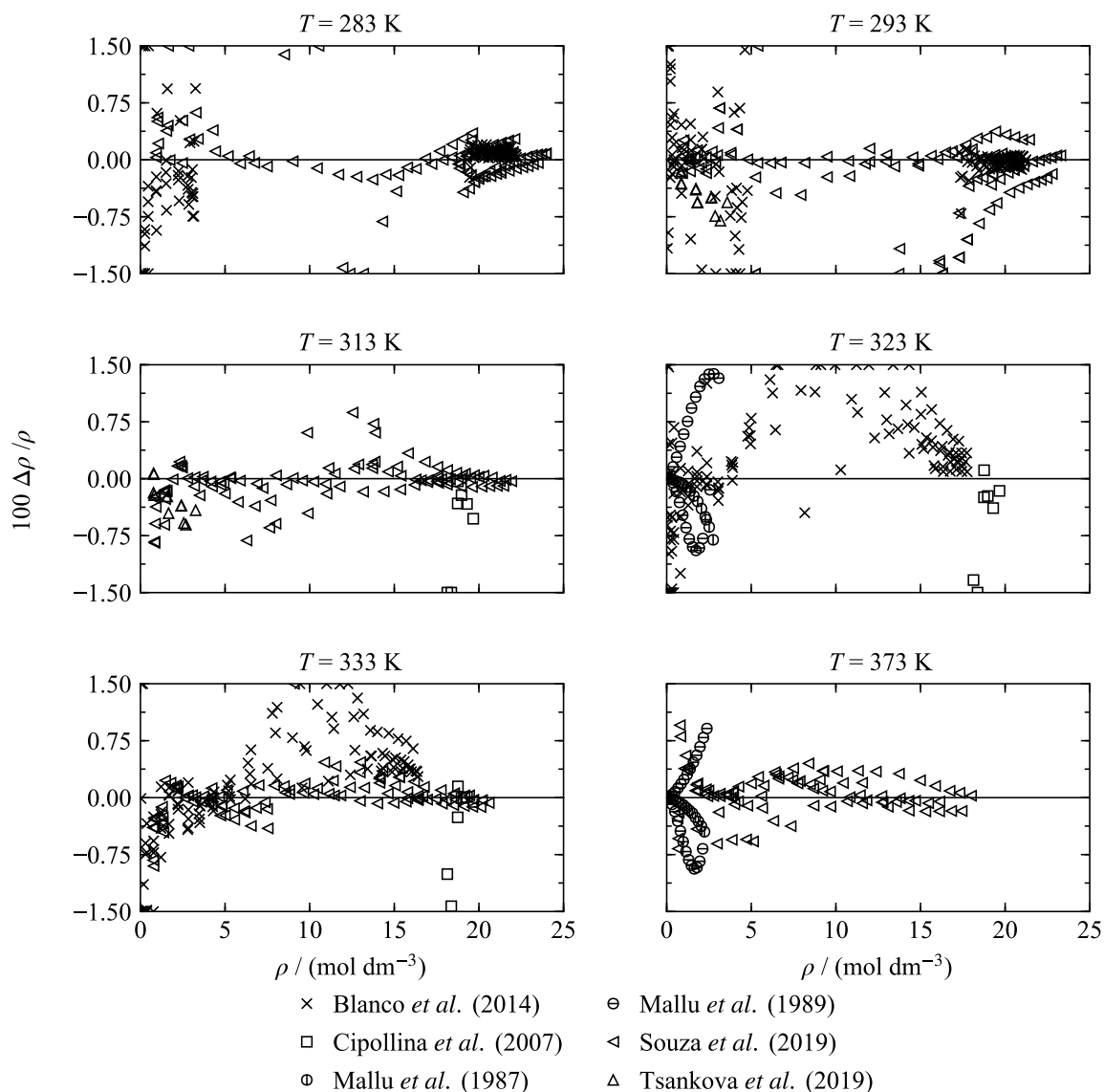


**Figure 6.13** Relative deviations  $\Delta\rho/\rho = (\rho_{\text{exp}} - \rho_{\text{calc}}) / \rho_{\text{exp}}$  of experimental density data for the system  $\text{CO}_2 + \text{CO}$  at selected isotherms from the new EOS as a function of density. The data cover a composition range of  $0.004 < x_{\text{CO}} < 0.75$ .

The most comprehensive data set was published by Blanco *et al.*<sup>224</sup> The complete study includes more than 40 000 points. Apparently, the data were automatically measured with a vibrating-tube densimeter and the raw data were published without making a meaningful selection. Because considering all points would have been impracticable for both fitting and validating the EOS, the data set was reduced to about 1000 representative points. The data cover the liquid and gas phase in a temperature range from 253 K to 343 K at pressures up to 20 MPa; however, the investigated samples contain only between 0.4 mol% and 3.0 mol% CO. Due to this limited composition range and because the data exhibit quite large scatter (up to about 2 %), the data set was omitted from the fitting process.

Cipollina *et al.*<sup>229</sup> measured densities of seven CO<sub>2</sub>-rich mixtures with a CO content between 4.6 mol% and 13.8 mol% at supercritical liquid-like conditions covering temperatures between 308 K and 343 K at pressures between 22 MPa and 47 MPa. The EOS represents this data set with an AAD of 0.56 % with a maximum deviation of about 2 %. Because the data are partly overlapping with the accurate measurements of Souza *et al.*,<sup>222</sup> which were used to fit the EOS and which exhibit significantly lower deviations, the experimental uncertainties of Cipollina's data are estimated to be equivalent to their deviations from the EOS.

The two data sets by Mallu *et al.*<sup>230,231</sup> provide densities of the supercritical gas-like fluid at temperatures between 323 K and 423 K at pressures up to 6.5 MPa. The experimentalists investigated three different mixtures with a comparably wide composition range (20.2 mol%, 42.7 mol%, and 70.1 mol% CO). The data are represented with a maximum deviation of about 1.5 %, which is comparable to the deviations from EOS-CG as presented by Gernert.<sup>17</sup> During the fitting process, these deviations could never be significantly reduced without worsening the representation of the most reliable density data by Souza *et al.*<sup>222</sup>

The measurements of Souza *et al.*<sup>222</sup> were carried out with a vibrating-tube densimeter and cover the gas, liquid, and supercritical state region of four different mixtures (5.0 mol%, 10.1 mol%, 25.3 mol%, and 50.2 mol% CO). The data range from 283 K to 373 K in temperature and up to 48 MPa in pressure. Combined expanded ( $k = 2$ ) experimental uncertainties are given for every state point. These uncertainties range from 0.2 % to 1.8 %, with values below 1 % for most points. The present mixture model was intensively fitted to these data. The fitting process benefitted from the high consistency between this data set and the VLE data of Souza *et al.*<sup>221</sup> This consistency was experimentally ensured by analyzing the compositions of the samples for the density measurements with the same set-up that was used (and calibrated) for the measurements of the VLE compositions. In the development of EOS for mixtures, consistent VLE and homogeneous density data are quite rare. For many other binary systems considered in this work, the EOS represents a compromise between the representation of the VLE and density data because the experimental data are not consistent enough. The present model for CO<sub>2</sub> + CO accurately represents the most reliable VLE data (see Figure 6.11) and additionally describes almost all the density data of Souza *et al.*<sup>221</sup> within their experimental uncertainties. Deviations between the complete data set and values calculated from the EOS are shown in Figure 6.14. The experimental uncertainties are illustrated with error bars.

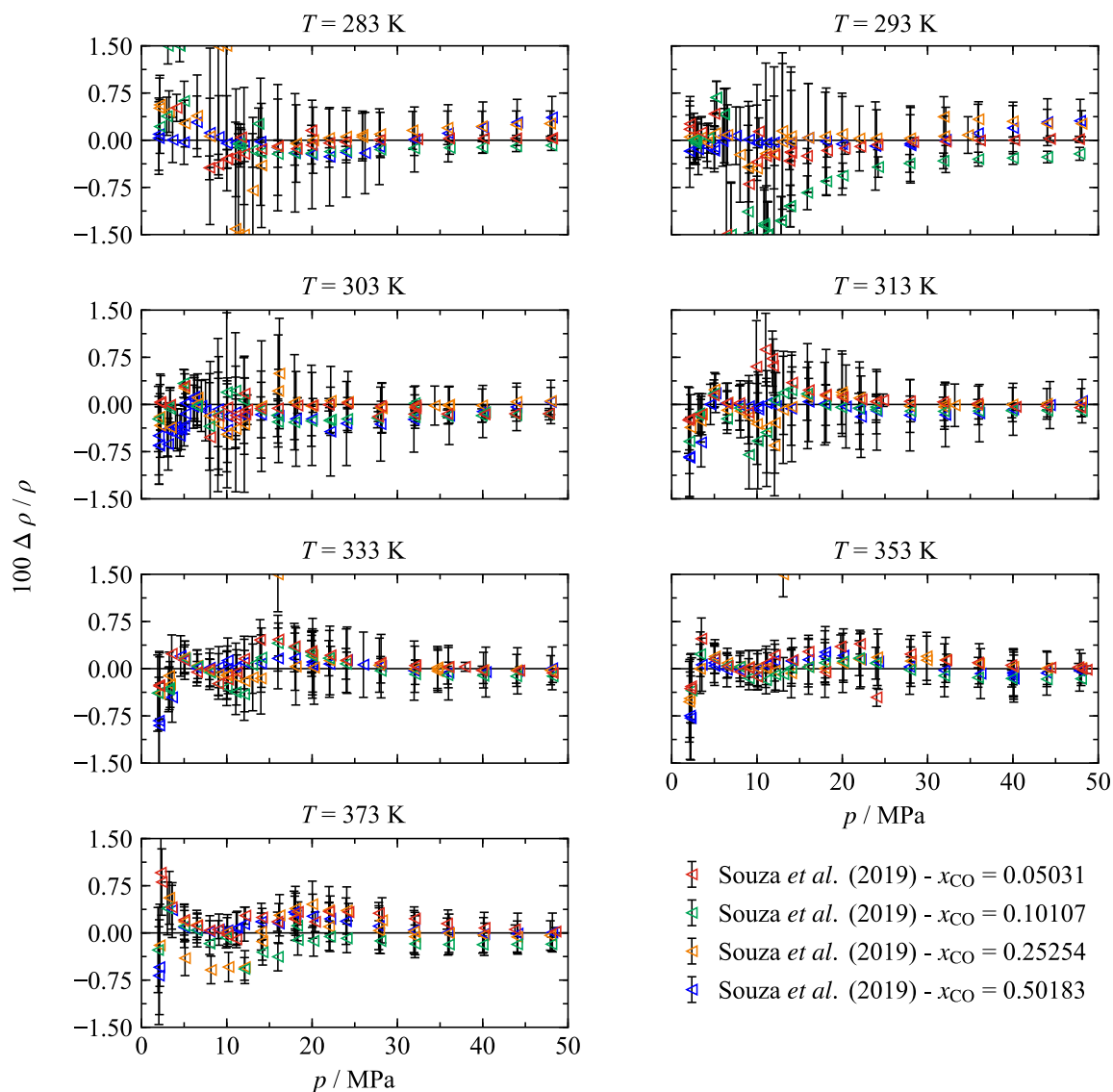


**Figure 6.14** Relative deviations  $\Delta\rho / \rho = (\rho_{\text{exp}} - \rho_{\text{calc}}) / \rho_{\text{exp}}$  of the experimental density data of Souza *et al.*<sup>222</sup> for the system  $\text{CO}_2 + \text{CO}$  from the new EOS as a function of pressure.

In Sec. 6.2.1, the density measurements of Tsankova *et al.*<sup>201</sup> for  $\text{CO}_2 + \text{Ar}$  carried out with a microwave re-entrant cavity resonator were discussed. Recently, the authors also published results for the system  $\text{CO}_2 + \text{CO}$ .<sup>223</sup> That work had not been published, when the fitting process of the present model was completed; however, some preliminary data were kindly provided. Because at that point the reported compositions were still evaluated and slightly corrected, the data were only used for validation. Gas-phase densities of an equimolar mixture and a mixture with 75 mol% CO were measured at temperatures between 255 K and 313 K and at pressures up to 8 MPa. Since the data were determined from measurements of the dielectric permittivity and are based on mixing rules from the literature, no full uncertainty analysis for the densities is yet possible, but will be addressed in future research. Nevertheless, the combined expanded ( $k = 2$ ) uncertainty in density is estimated to be 0.53 % for the equimolar mixture and 0.46 % for the mixture containing 75 mol% CO.<sup>223</sup> The model represents the data at equimolar composition with an AAD of 0.45 % and a maximum deviation of 0.83 %. The AAD of the data set for the CO-rich mixture is 0.36 % with a



maximum deviation of 0.77 %. The data are thus mostly represented within their estimated experimental uncertainties. Deviations between the complete data set and the mixture model are shown in Figure 6.15.

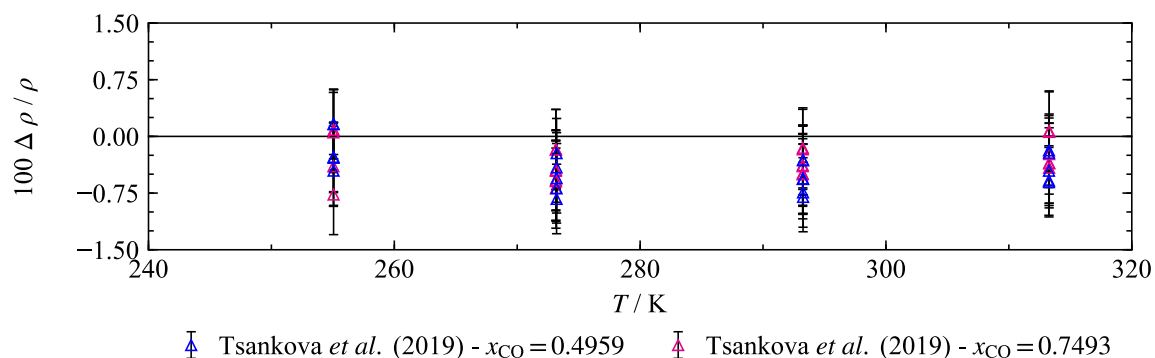


**Figure 6.15** Relative deviations  $\Delta\rho / \rho = (\rho_{\text{exp}} - \rho_{\text{calc}}) / \rho_{\text{exp}}$  of the experimental density data of Tsankova *et al.*<sup>223</sup> for the system  $\text{CO}_2 + \text{CO}$  from the new EOS as a function of temperature. The data cover pressures up to 8 MPa.

Considering the deviations discussed before, some rough uncertainty estimates for calculated homogeneous densities are possible. For mixtures with compositions between 5 mol% and 50 mol% CO (as investigated by Souza *et al.*<sup>222</sup>), the conservatively estimated uncertainty in gas and liquid-phase densities at temperatures between 315 K and 370 K is 0.75 % at pressures up to 50 MPa. At lower temperatures between 285 K and 315 K, the 0.75 % uncertainty estimate is only valid at pressures above 15 MPa; at lower pressures, the uncertainty is 1 %. Gas-phase densities of the equimolar mixture at pressures up to 8 MPa and temperatures between 255 K and 285 K can be calculated with an estimated uncertainty of 1 %. This uncertainty estimate is also valid for gas-phase densities of mixtures with around 75 mol% CO at pressures up to 8 MPa and temperatures between 255 K and 310 K; both estimates are based on the data of Tsankova *et al.*<sup>223</sup> At other conditions of temperature, pressure, and composition, homogeneous densities are expected to have an uncertainty below 2 %; however, the available experimental data should be considered for more precise uncertainty estimates.

Some brief comments should be made on comparisons between the present EOS and the other models considered in the discussion of the available VLE data. Figure 6.16 shows results of comparative density calculations for an equimolar mixture.

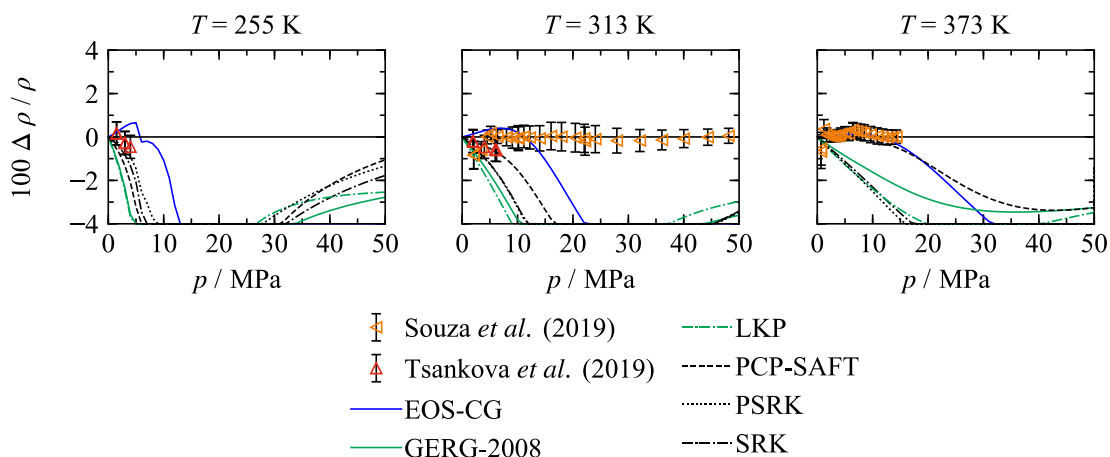


**Figure 6.16** Relative deviations  $\Delta\rho/\rho = (\rho_{\text{exp}} - \rho_{\text{calc}}) / \rho_{\text{exp}}$  of the selected density data for the system  $\text{CO}_2 + \text{CO}$  at equimolar composition and three different isotherms from the new EOS as a function of pressure. Results calculated from EOS-CG, GERG-2008, PSRK, PCP-SAFT, SRK, and LKP are shown for comparisons.

Only the present model represents the selected accurate density data by Souza *et al.*<sup>222</sup> and Tsankova *et al.*<sup>223</sup> within their experimental uncertainties. EOS-CG and PCP-SAFT provide at least a reliable description of the gas-phase data, but also exhibit increasing deviations with increasing pressures. The results calculated from GERG-2008, SRK, PSRK, and LKP deviate considerably from the data and the present model. Of course, these results do not allow for a quantification of the accuracies of the other models at other conditions of temperature, pressure, and composition. Because none of the models was intensively fitted to experimental data, it cannot be expected that they yield much better results at other conditions, except at high temperatures and low pressures, where the mixing behavior is comparable to the ideal gas, or at a composition close to one of the pure fluids.

As discussed for  $\text{CO}_2 + \text{Ar}$  in Sec. 6.2.1, the extrapolation behavior of the mixture model should be validated carefully to ensure that the model does not only describe the available experimental data, but also represents a qualitatively correct physical behavior of the fluid. In Figure 6.17, the pressure is plotted versus enthalpy, density, and temperature. The mixing behavior is shown for pressures up to 1 GPa and temperatures up to 6000 K in the  $p, h$  diagram and 10 000 K in the  $p, \rho$  diagram. The shape of the isolines emphasizes excellent extrapolation behavior.

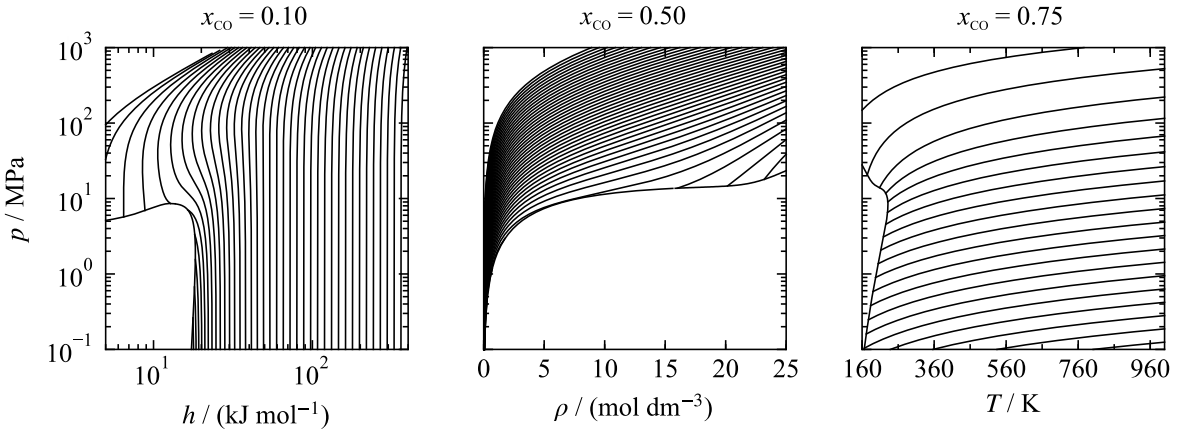


**Figure 6.17** Left to right:  $p,h$ ,  $p,\rho$ , and  $p,T$  diagrams calculated with the new EOS for  $\text{CO}_2 + \text{CO}$  for three different compositions (10 mol%, 50 mol%, and 75 mol% CO) at extreme conditions. The mixing behavior is shown along isotherms up to 6000 K in the  $p,h$  diagram and along isotherms up to 10 000 K in the  $p,\rho$  diagram. The  $p,T$  diagram includes isochores up to 30 mol  $\text{dm}^{-3}$ .

### 6.2.3 Water + Methane

A reduced Helmholtz-energy explicit formulation for the binary system  $\text{H}_2\text{O} + \text{CH}_4$  is included in the GERG-2008 model of Kunz and Wagner.<sup>36</sup> Since  $\text{CH}_4$  is the most relevant component in that mixture model, the binary formulation for  $\text{H}_2\text{O} + \text{CH}_4$  is considered to yield reliable results, although binary mixtures with water are normally not accurately described within GERG-2008. For the binary model in GERG-2008, all four reducing parameters were fitted but no binary specific departure function. Because  $\text{CH}_4$  is not considered in the EOS-CG model of Gernert and Span,<sup>2</sup> no binary formulation for  $\text{H}_2\text{O} + \text{CH}_4$  is included in that model.

Compared to many other binary mixtures, the experimental database for  $\text{H}_2\text{O} + \text{CH}_4$  is comprehensive. VLE data are presented in many publications but also data for homogeneous densities and some values for isobaric heat capacities, virial coefficients, and excess enthalpies are available. Although none of the data sets published after the development of the GERG-2008 model is regarded as very accurate, it was attempted in this work to improve the description of this system by developing a binary specific departure function. This new departure function reads:

$$\alpha_{\text{H}_2\text{O}+\text{CH}_4}^r(\delta, \tau) = \sum_{k=1}^2 n_k \delta^{d_k} \tau^{t_k} + \sum_{k=3}^6 n_k \delta^{d_k} \tau^{t_k} \exp(-\delta^{l_k}). \quad (6.3)$$

The function contains a total of six terms including two polynomial(-like) terms and four exponential terms. All parameters (coefficients  $n_k$ , temperature exponents  $t_k$ , density exponents  $d_k$  and  $l_k$ ) are listed in Table E.2 in Appendix E. It is notable that neither the use of “special” exponential terms (as used for  $\text{CO}_2 + \text{Ar}$ ) nor the use of Gaussian bell-shaped terms (as used for  $\text{CO}_2 + \text{CO}$ ) was found to be suitable for this mixture. Gernert and Span<sup>2</sup> proposed similar functional forms, which only contain polynomial(-like) and exponential

terms, for the system  $\text{CO}_2 + \text{H}_2\text{O}$  and for a generalized description of the aqueous systems  $\text{H}_2\text{O} + \text{N}_2$ ,  $\text{H}_2\text{O} + \text{O}_2$ , and  $\text{H}_2\text{O} + \text{CO}$ . This leads to the conclusion that this set of terms is recommended for a proper description of these special mixtures, which are all characterized by a very low solubility of the gaseous component in liquid water. Nevertheless, even with the “appropriate” set of terms it is still an exceptional numerical challenge to fit a departure function for  $\text{H}_2\text{O} + \text{CH}_4$ . In the VLE region, the coexisting phases are almost pure fluids. The result of this is that even small composition uncertainties of the data lead to extreme deviations in pressure. In Figure 6.18  $p,x$  diagrams for four isotherms illustrate this special mixing behavior. The phase boundaries were calculated from the new model and the one included in GERG-2008. Selected experimental data are shown for comparisons.

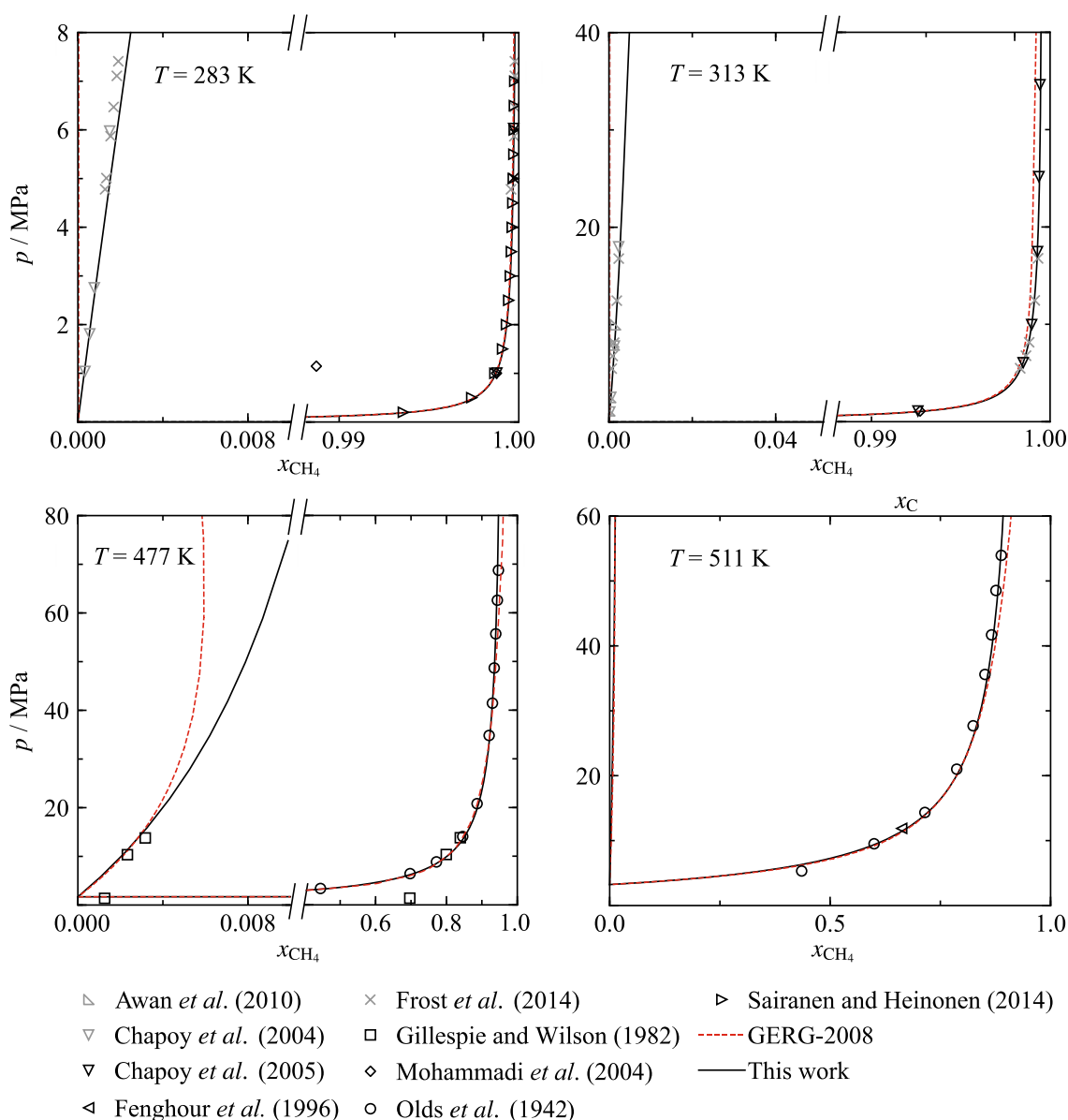


**Figure 6.18** Phase boundaries of the system  $\text{H}_2\text{O} + \text{CH}_4$  in  $p,x$  diagrams for selected isotherms as calculated from the new EOS and GERG-2008. Selected experimental data are shown for comparisons.

Due to the almost pure coexisting phases, absolute differences in composition between the new model and GERG-2008 are quite small. Nevertheless, the new model provides a more accurate description of the data. Especially along the bubble lines of the two lower isotherms, results calculated from GERG-2008 do not follow the trend of the data. For these isotherms, the GERG-2008 model underestimates the solubility of CH<sub>4</sub> in H<sub>2</sub>O and yields a saturated liquid that is almost pure H<sub>2</sub>O. Deviations between values calculated from both models and experimental VLE data from different sources are shown in Figure 6.19. It has to be noted that additional data were found in the literature; however, those data exhibit extremely large deviations from GERG-2008, the present model, and all its preliminary versions. These large deviations are presumably caused by high composition uncertainties; thus, only the data sets found to be reliable are included in Figure 6.19. The plots present deviations in composition that give a good impression of the accuracy of both models. As mentioned before, deviations in pressure are not meaningful for a system with such steep  $p,x$  phase boundaries.

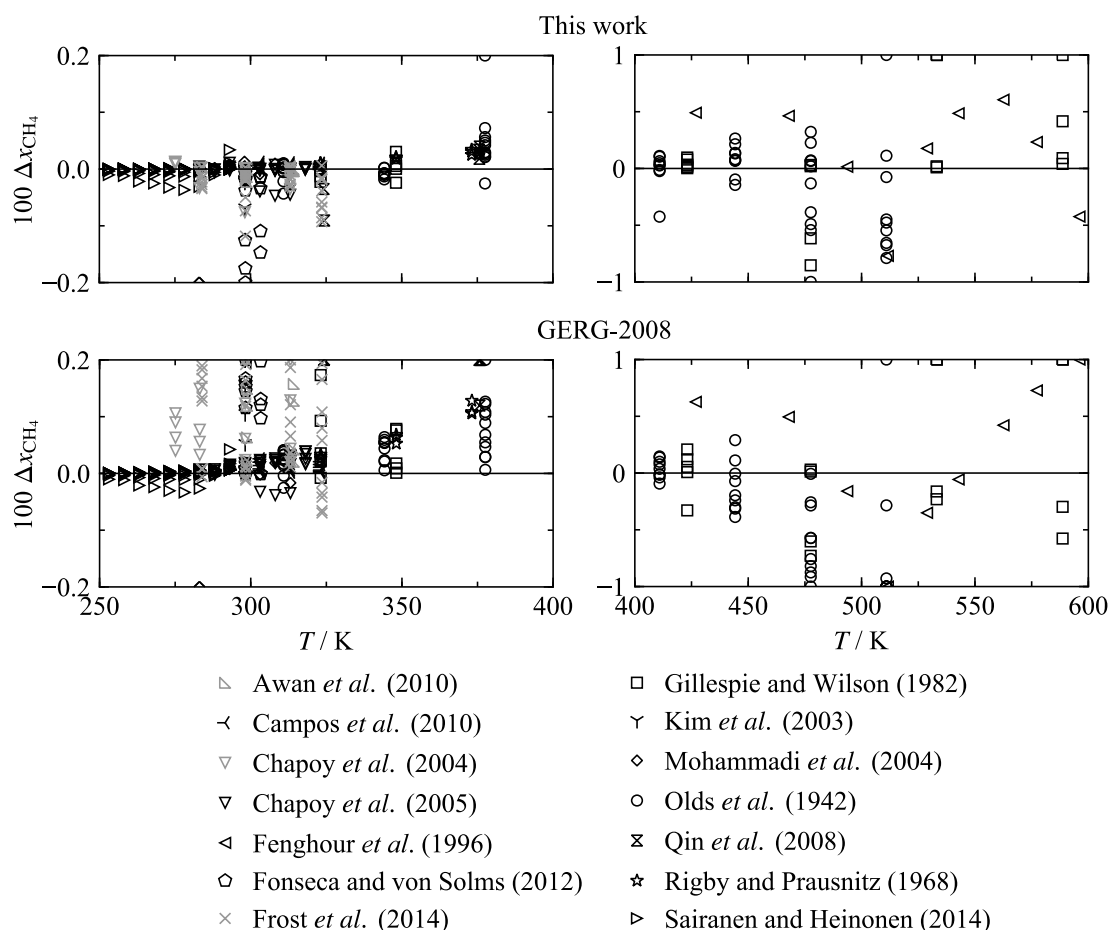


**Figure 6.19** Deviations  $\Delta x_{\text{CH}_4} = (x_{\text{CH}_4, \text{data}} - x_{\text{CH}_4, \text{calc}})$  between available VLE data for the system H<sub>2</sub>O + CH<sub>4</sub> and results calculated from the new EOS (top) and the GERG-2008 (bottom) as a function of temperature for the temperature range  $250 \leq T/\text{K} \leq 400$  (left) and  $400 \leq T/\text{K} \leq 600$  (right).

At temperatures between 255 K and 400 K, the present model represents the majority of the data with deviations below 0.15 mol%. The overall representation of the data in this temperature range is clearly more consistent than with the GERG-2008, especially with

regard to the accurate saturated-liquid data of Awan *et al.*,<sup>232</sup> Chapoy *et al.*,<sup>233</sup> and Frost *et al.*<sup>234</sup> At elevated temperatures between 400 K and 600 K, the data are mostly described within 1 mol%. In this region, the accuracy of both models is comparable, although the GERG-2008 exhibits some higher deviations.

In the previous sections, deviations between calculated and experimental data were compared with given or estimated experimental uncertainties of the data. For this mixture, such a discussion is only partly possible. None of the references included in Figure 6.19 provides combined uncertainties in composition. In fact, many references do not state any composition uncertainties at all. Instead, some less meaningful information on the reproducibility or the calibration precision of the used gas chromatograph are given. These inadequate uncertainty specifications are unfortunate for the validation of the present model but not surprising with regard to the shape of phase boundaries, which are characterized by extremely small mole fractions of one component. Nevertheless, some further comments on the experimental database are useful for a better assessment of the present model.

Complete VLE data sets including the compositions of both phases are only given by Gillespie and Wilson,<sup>235</sup> Fonseca and von Solms,<sup>236</sup> Qin *et al.*,<sup>237</sup> and Frost *et al.*<sup>234</sup> All these data sets were obtained by withdrawing samples from the coexisting phases and analyzing them in a gas chromatograph. The experimental set-up of Frost *et al.*<sup>234</sup> was developed in the work of Fonseca and von Solms,<sup>236</sup> whose data result from the first measurements with that apparatus. The measurements of Frost and co-workers consequently supersede those data. They cover a temperature range from 284 K to 324 K and are among the most valuable data sets for the development of the present model. The data of Gillespie and Wilson<sup>235</sup> were useful to fit the model at elevated temperatures up to 589 K; nevertheless, they exhibit some scatter and cannot be considered as highly accurate.

The solubility of CH<sub>4</sub> in H<sub>2</sub>O, which is equivalent to the saturated-liquid phase in VLE, was measured at temperatures above 275 K by Awan *et al.*,<sup>232</sup> Campos *et al.*,<sup>238</sup> Chapoy *et al.*,<sup>233</sup> and Kim *et al.*<sup>239</sup> In all those works, the mole fractions of CH<sub>4</sub> in the saturated-liquid were measured instead of the bubble point of a mixture with known composition. All data sets are in good agreement with the full VLE data of Frost *et al.*<sup>234</sup> The deviations of the data of Chapoy *et al.*<sup>233</sup> correspond to the representation of their data for H<sub>2</sub>O + CO<sub>2</sub> by the EOS-CG model of Gernert and Span, who report a maximum deviation of 0.2 mol%.<sup>2</sup>

Solubilities of H<sub>2</sub>O in CH<sub>4</sub>, and thus the saturated-vapor states of the VLE were again investigated by Chapoy *et al.*<sup>240</sup> but also by Fenghour *et al.*,<sup>241</sup> Sairanen and Heinonen,<sup>242</sup> Mohammadi *et al.*,<sup>243</sup> Olds *et al.*,<sup>244</sup> and Rigby and Prausnitz.<sup>245</sup> In the latter work, the water mole fractions are estimated to be accurate within 1 %. Considering the highest measured water concentration  $x_{\text{H}_2\text{O}} = 0.01992$ , this uncertainty estimate is equivalent to an expanded ( $k = 2$ ) uncertainty of about 0.04 mol%. The maximum deviation between those data and the present model is 0.034 mol% (AAD = 0.016 mol%). The data are consequently represented

within their experimental uncertainty. The measurements of Olds *et al.*<sup>244</sup> were published in 1942 and are the oldest reliable experimental data found in the literature. Although they are not considered as highly accurate, they were important for the fitting process because they cover a relatively wide temperature range from 310 K to 510 K. According to the authors, the mole fractions of water are accurate within 2 %. At temperatures below 400 K, this corresponds to a maximum expanded ( $k = 2$ ) uncertainty of 0.17 mol%. This maximum uncertainty increases up to 2.2 mol% at higher temperatures. These uncertainties mostly agree with the deviations shown in Figure 6.19. Fenghour *et al.*<sup>241</sup> investigated the high-temperature region up to almost 600 K. Dew points were obtained from isochoric  $p\rho T$  measurements. The pressure of a mixture with known composition was continuously measured while varying the temperature. Discontinuities in the obtained pressure versus temperature diagram indicated that the dew point of the mixture was reached. No uncertainties are given for those dew points; however, it is expected that this approach is not as accurate as a “real” dew-point experiment. Neglecting one clear outlier, the data are represented with a maximum deviation of 0.6 mol%. At low temperatures between 283 K and 318 K, very accurate dew points were published by Chapoy *et al.*<sup>240</sup> as a correction of an earlier work by the same authors.<sup>246</sup> The data are represented with an AAD of 0.006 mol% and a maximum deviation of 0.05 mol%. The authors provide a maximum uncertainty in the mole fraction of water of 0.2 %. Interpreting this value as the standard uncertainty of every state point leads to an average expanded ( $k = 2$ ) uncertainty of 0.006 mol% and maximum uncertainty of 0.04 mol%, which is both in close agreement with the deviations from the present model. The most recent saturated-vapor data were published by Sairanen and Heinonen<sup>242</sup> covering low temperatures between 253 K, which is close the hydrate-formation temperature, and 293 K. The data were used to fit the model in the low temperature region but are not considered as highly accurate. At 283 K and 293 K, they are in close agreement with the measurements of Chapoy *et al.*<sup>240</sup> but exhibit some scatter with decreasing temperatures.

Estimating uncertainties in calculated VLE compositions is difficult because none of the discussed references provides a complete and reliable uncertainty analysis. The uncertainty of the present model is therefore conservatively estimated based on the deviations plotted in Figure 6.19. At temperatures between 255 K and 400 K, the uncertainty of dew-point compositions is expected to be below 0.15 mol%. For bubble-point compositions, the 0.15 mol% uncertainty estimate is valid at temperatures between 275 K and 400 K. In the high-temperature region between 400 K and approximately 600 K, the uncertainty in both dew- and bubble-point compositions is estimated to be 1 mol%.

The development of the present model for  $\text{H}_2\text{O} + \text{CH}_4$  was enhanced by a comprehensive database of homogenous densities. Deviations between the available experimental data, the present model, and the binary formulation included in GERG-2008 are shown in

Figure 6.20. The database is restricted to the gas and supercritical state region. No liquid-phase data were found in the literature.

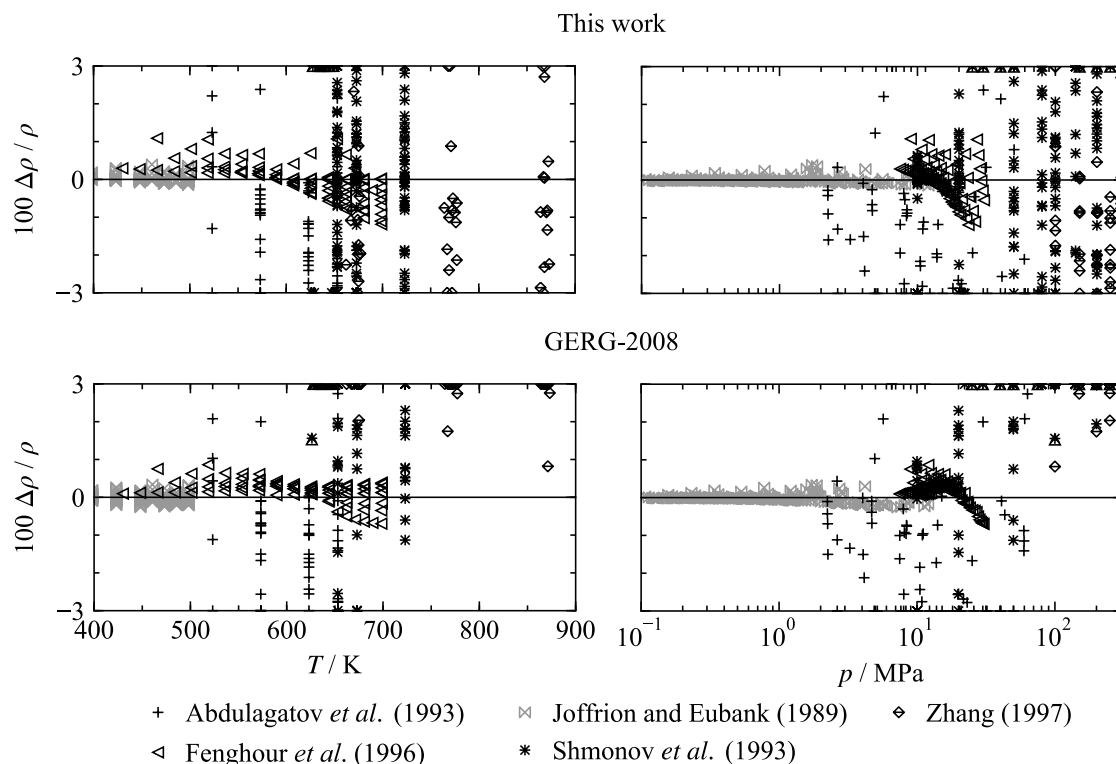


**Figure 6.20** Relative deviations  $\Delta\rho/\rho = (\rho_{\text{exp}} - \rho_{\text{calc}})/\rho_{\text{exp}}$  of available experimental density data for the system  $\text{H}_2\text{O} + \text{CH}_4$  from the new EOS (top) and GERG-2008 (bottom) as a function of temperature (left) and pressure (right). The data cover the entire composition range from almost pure  $\text{H}_2\text{O}$  to almost pure  $\text{CH}_4$ .

The most accurate data for homogeneous gas-phase densities were published by Joffrion and Eubank.<sup>247</sup> The authors investigated three mixtures with 50 mol%, 25 mol%, and 10 mol%  $\text{H}_2\text{O}$  in a temperature range from 398 K to 498 K and at pressures up to 12 MPa. The combined standard uncertainty is stated to be 0.08 %. The present model describes more than 95 % of the data within deviations of 0.16 %, which corresponds to the expanded ( $k = 2$ ) uncertainty of the data. The GERG-2008 model represents the data mostly with comparable deviations; however, the deviations increase with increasing pressure. Above 3 MPa, deviations between the data and GERG-2008 are higher than the experimental uncertainty. Another important data set was measured by Fenghour *et al.*,<sup>241</sup> which also lead to the dew-point data discussed before. That work provides gas-phase densities for nine mixtures covering  $\text{H}_2\text{O}$  contents between 7.6 mol% and 67.6 mol% at temperatures between 430 K and 700 K and pressures ranging from 7.5 MPa to 30 MPa. The given standard uncertainty of the data is 0.08 % for the mixture with the lowest  $\text{H}_2\text{O}$  content and 0.014 % for the mixture with the highest  $\text{H}_2\text{O}$  content. The expanded ( $k = 2$ ) uncertainties consequently range from 0.16 % to 0.28 %, which does not agree with the deviations of up to 1.2 % from the present model. The GERG-2008 enables a more consistent description of the data but also exhibits deviations up to 0.84 %. During the development of the present model, many different functional forms for the departure function were applied and then rejected, before the final



set of terms according to Eq. (6.3) was obtained. None of these preliminary models provided both a more accurate description of the data of Fenghour *et al.*<sup>241</sup> and an accurate description of the VLE data. It is consequently assumed that the experimental uncertainty of Fenghour *et al.*<sup>241</sup> is underestimated.

The high-temperature and high-pressure region of H<sub>2</sub>O + CH<sub>4</sub> was investigated by Abdulagatov *et al.*<sup>248</sup> and Shmonov *et al.*<sup>249</sup> The work of Abdulagatov and co-workers presents data for various different mixtures covering the complete composition range at temperatures between 525 K and 653 K and at pressures between 2 MPa and 64 MPa. The claimed expanded ( $k = 2$ ) uncertainty of the data is 0.4 %, which seems to be significantly underestimated. The data exhibit scatter of at least 6 %. The work of Shmonov *et al.*<sup>249</sup> provides no clear information on experimental uncertainties. It includes measurements of four mixtures with 20 mol%, 40 mol%, 60 mol%, and 80 mol% H<sub>2</sub>O as well as results for both pure components. The measurements were carried out at temperatures between 653 K and 723 K and at pressures between 10 MPa and 200 MPa. The data deviate by more than 8 % from the model. In order to check the reliability of the data, comparisons between the pure-fluid measurements and results calculated from the reference EOS of Setzmann and Wagner<sup>196</sup> (for CH<sub>4</sub>) and Wagner and Pruß<sup>29</sup> (for H<sub>2</sub>O) were made. The data exhibits deviations up to 9 % for pure CH<sub>4</sub> and 2 % for pure H<sub>2</sub>O. It is not believed that the results for the binary mixtures are more accurate than the pure-fluid data. Another high-pressure data set was published by Zhang.<sup>250</sup> It provides densities of the supercritical fluid at temperatures between 675 K and 873 K and pressures ranging from 100 MPa to 300 MPa. The data were not experimentally obtained but result from calculations. The underlying method is only vaguely described as being based on “synthetic fluid inclusion data” and an equation fitted to CH<sub>4</sub> clathrate melting temperatures and pressures.<sup>250</sup> No uncertainties are given in the corresponding publication. The data were not used to fit the present binary mixture model; nevertheless, they are mostly represented with deviations below 4 %. As apparent from this paragraph, none of high-temperature and high-pressure data sets is sufficiently accurate to allow for a quantitative validation of the present model. Nevertheless, the deviations shown in Figure 6.20 emphasize that the model yields qualitatively reasonable results in that state region, whereas GERG-2008 exhibits much higher deviations from the data.

Estimated uncertainties of homogeneous densities calculated from the present binary model can only be provided for gas-phase data. The uncertainties are based on the discussed comparisons with the two reliable experimental data sets of Joffrion and Eubank<sup>247</sup> and Fenghour *et al.*<sup>241</sup> For mixtures containing between 10 mol% and 50 mol% H<sub>2</sub>O, gas-phase densities for temperatures between 400 K and 495 K and at pressures up to 12 MPa can be calculated with an uncertainty of 0.16 %. At higher temperatures up 700 K and pressures between 7.5 MPa and 30 MPa, the uncertainty of calculated data is expected to be below

1.5 %. This uncertainty estimate is also valid for mixtures containing higher fractions of water of up to 67 mol%.

Validating the extrapolation behavior of models for binary mixtures with water is much more complicated than, for example, for the systems  $\text{CO}_2 + \text{Ar}$  and  $\text{CO}_2 + \text{CO}$ . As apparent from the  $p, x$  diagrams shown in Figure 6.18, the mixture is unstable over most of the composition range and splits into two almost pure phases. Nevertheless, various state diagrams were continuously validated during the fitting process. Two examples are shown in Figure 6.21. The smooth isochores in the  $p, T$  diagrams emphasize a reliable representation of the physical behavior of the fluid. Besides, the left panel of Figure 6.21 highlights the special mixing behavior of these fluids. Even a mole fraction of 1 %  $\text{CH}_4$  causes a two-phase split over a large temperature and pressure range, which represents a significant deviation from the vapor-pressure curve of pure  $\text{H}_2\text{O}$ .

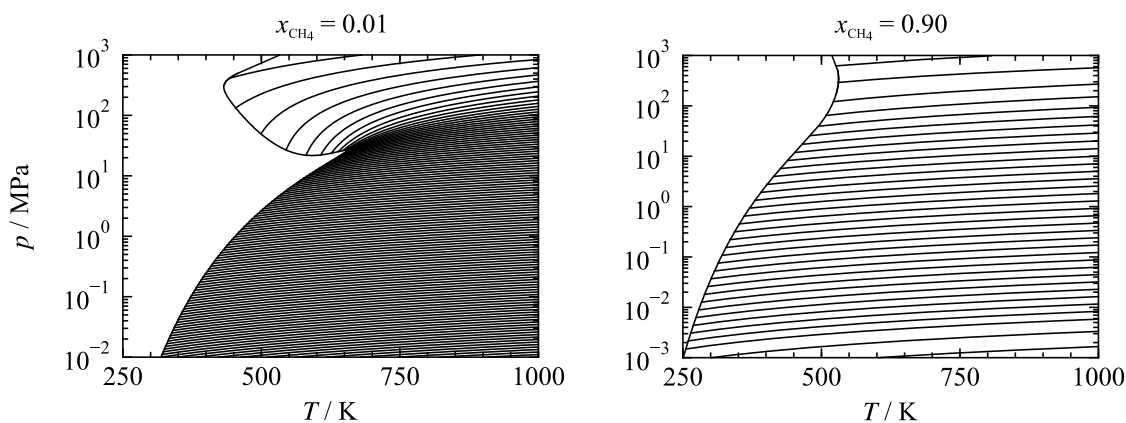


**Figure 6.21**  $p, T$  diagrams calculated with the new EOS for  $\text{H}_2\text{O} + \text{CH}_4$  for a mixture with 1 mol%  $\text{CH}_4$  (left) and a mixture with 90 mol%  $\text{CH}_4$  (right). The mixing behavior is shown along isochores up to  $65 \text{ mol dm}^{-3}$  (left) and  $30 \text{ mol dm}^{-3}$  (right).

Overall, the development of the departure function for  $\text{H}_2\text{O} + \text{CH}_4$  lead to a more accurate description of this mixture compared to the GERG-2008 model. Especially, the representation of the low-temperature VLE region has been improved. Nevertheless, the model for this important binary mixture could still be improved, if additional accurate experimental data would become available. Homogeneous liquid densities, high-temperature VLE data and caloric data such as speed of sound would be beneficial for a refit of the present model. In this context, some additional comments should be made on other types of experimental data than discussed in this section. Excess enthalpies were published by Smith *et al.*<sup>251</sup> and Wormald and Colling,<sup>252</sup> isobaric heat capacities by Hnědkovský and Wood,<sup>253</sup> and virial coefficients by Smith *et al.*,<sup>251</sup> Welsch<sup>254</sup> and Abdulagatov *et al.*<sup>248,255</sup> None of these data sets was used for fitting because all of them exhibit large deviation from GERG-2008 and all preliminary versions of the present model. For completeness, the data are listed in Table E.3 in Appendix E. Very accurate cross virial coefficient data were published by Akin-Ojo *et al.*;<sup>256</sup> however, as discussed by Gernert<sup>2</sup> and Kunz *et al.*<sup>35</sup> the mathematical approach of the mixture model does not allow for a proper description of such data.

Calculated values of the second cross-virial coefficient  $B_{12}$  vary with composition, although  $B_{12}$  is per definition independent on composition. Comparisons with such data are consequently not meaningful for the validation of the model.

#### 6.2.4 Water + Hydrogen Sulfide

The binary specific departure function for the mixture  $\text{H}_2\text{O} + \text{H}_2\text{S}$  is the result of an attempt to develop such a function based on a relatively limited experimental database. The previously proposed departure functions for the systems  $\text{CO}_2 + \text{Ar}$ ,  $\text{CO}_2 + \text{CO}$ , and  $\text{H}_2\text{O} + \text{CH}_4$  were not only fitted to VLE data but also to some homogeneous-property data. This is normally recommended to set up a reasonably constrained departure function. For  $\text{H}_2\text{O} + \text{H}_2\text{S}$ , accurate experimental values are restricted to VLE data, although some saturated-liquid densities and isobaric heat capacities are available too. The densities are briefly discussed within this section. The heat-capacity measurements of Hnědkovský and Wood<sup>253</sup> were carried out in almost pure water ( $x_{\text{H}_2\text{S}} = 0.0067$ ) and are thus not relevant to the present validation of the mixture model. The system  $\text{H}_2\text{O} + \text{H}_2\text{S}$  is also considered in the GERG-2008 model of Kunz and Wagner.<sup>36</sup> In that model, no binary specific departure function was developed. Instead, only two reducing parameters were fitted. The EOS-CG model of Gernert and Span<sup>2</sup> does not allow for the description of any mixture with  $\text{H}_2\text{S}$ .

The binary specific departure function developed in this work reads:

$$\alpha_{\text{H}_2\text{O}+\text{H}_2\text{S}}^r(\delta, \tau) = \sum_{k=1}^2 n_k \delta^{d_k} \tau^{t_k} + \sum_{k=3}^6 n_k \delta^{d_k} \tau^{t_k} \exp(-\delta^{l_k}). \quad (6.4)$$

The set of terms corresponds to the one used in the functional form for  $\text{H}_2\text{O} + \text{CH}_4$ . It contains a total of six terms and includes only the simplest types of terms: two polynomial(-like) terms and four exponential terms. This corresponds to the experience that “special” exponential or Gaussian bell-shaped terms are less suitable for mixtures of  $\text{H}_2\text{O}$  with a gaseous component (see Sec. 6.2.3). As for all other departure functions developed in this work, all parameters (coefficients  $n_k$ , temperature exponents  $t_k$ , density exponents  $d_k$  and  $l_k$ ) are given in Table E.2 in Appendix E.

As typical for binary mixtures with water, the phase-equilibrium behavior of  $\text{H}_2\text{O} + \text{H}_2\text{S}$  is complex. This is not only due to the fact that solid water or hydrates might form, but also to the possible split into both vapor-liquid and liquid-liquid-equilibria (LLE). The solubility of  $\text{H}_2\text{S}$  in water is higher than that of  $\text{CH}_4$  (see Sec. 6.2.3) but still so limited that phase equilibria mostly consist of two phases very rich in one of the components. At temperatures below the critical temperature of  $\text{H}_2\text{S}$  ( $T_{c,\text{H}_2\text{S}} = 373.1 \text{ K}$ ), the  $\text{H}_2\text{S}$ -rich phase in equilibrium may be liquid or gaseous depending on the pressure of the system. The resulting VLE and LLE regions are separated by a three-phase line along which a  $\text{H}_2\text{S}$ -rich vapor, a  $\text{H}_2\text{O}$ -rich liquid, and a  $\text{H}_2\text{S}$ -rich liquid are in a phase equilibrium (VLLE). This behavior is illustrated

in Figure 6.22. The phase boundaries for two isotherms ( $T < T_{c,H_2S}$ ) were calculated from the new model and the one included in GERG-2008. Selected literature data are shown for comparisons. The VLE data found in the literature cover many other isotherms than those shown in Figure 6.22. The limitation to two  $p,x$  diagrams is due to the high complexity of their calculation. Tracing the different saturation lines is numerically challenging and no algorithms are so far available that enable the complete calculation of all these lines. Instead, the results for VLE, LLE, and VLLE need to be calculated separately and are then combined to obtain the full  $p,x$  diagrams.

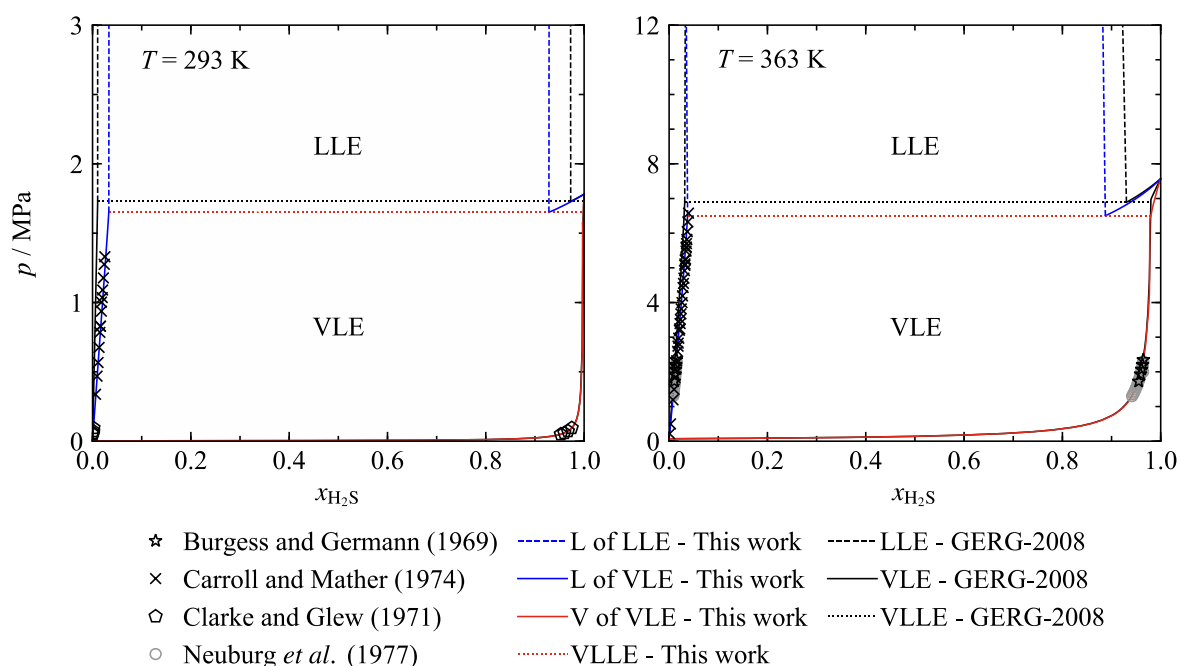


**Figure 6.22** Phase boundaries of the system  $H_2O + H_2S$  in  $p,x$  diagrams for two isotherms as calculated from the new EOS and the GERG-2008. Selected data from the literature are shown for comparisons.

For the two presented isotherms, both models yield qualitatively comparable results. In fact, the saturated-vapor lines calculated from the present model and GERG-2008 are almost congruent. Nevertheless, the left panel of Figure 6.22 indicates that the GERG-2008 model underestimates the solubility of  $H_2S$  in the liquid, whereas the new model is in excellent agreement with experimental data. The most distinct differences between the models are found in the prediction of the LLE region and VLLE line; however, no experimental data are available to validate these predictions. The representation of the VLE data is presented in more detail in Figure 6.23. Deviations between literature data and bubble- and dew-point compositions calculated from the new model and GERG-2008 are shown over the complete temperature range of the data.

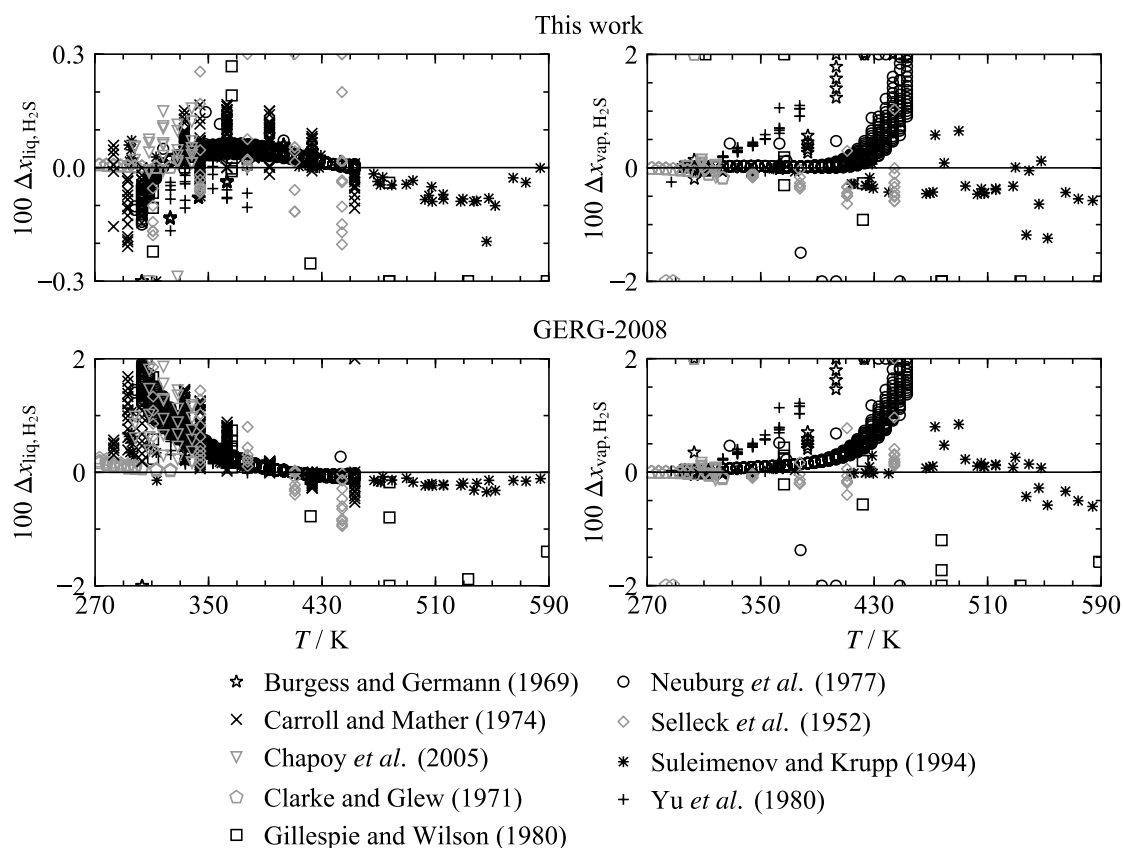


**Figure 6.23** Deviations  $\Delta x_{H_2S} = (x_{H_2S, data} - x_{H_2S, calc})$  between available bubble-point (left) and dew-point (right) data for the system  $H_2O + H_2S$  and results calculated from the new EOS (top) and the GERG-2008 (bottom) as a function of temperature.

The deviation plots confirm the impression obtained from the  $p, x$  diagrams: The new model enables a significantly more accurate description of the available bubble-point data and thus of the  $H_2S$ -solubility in the liquid than the GERG-2008. Most of the data are represented with deviations below 0.2 mol%, whereas the same data deviate by up to 2 mol% from the GERG-2008. The representation of the dew-point data is comparable for both models, although the new model provides more consistent results at temperatures below approximately 430 K.

The available data should briefly be discussed in order to further quantify the accuracy of the present model. Complete VLE values were published by Burgess and Germann,<sup>257</sup> Chapoy *et al.*,<sup>258,259</sup> Clarke and Glew,<sup>260</sup> Gillespie and Wilson,<sup>261</sup> Neuburg *et al.*,<sup>262</sup> Selleck *et al.*,<sup>263</sup> Suleimenov and Krupp,<sup>264</sup> and Yu *et al.*<sup>265</sup> The work of Carroll and Mather<sup>266</sup> is restricted to bubble-point data. The most comprehensive data set was published by Neuburg *et al.*<sup>262</sup> The data were not obtained experimentally but correlated based on data from various other sources. No uncertainty of these correlated values is given in the corresponding publication. The same applies to the data of Burgess and Germann<sup>257</sup> and Carroll and Mather,<sup>266</sup> who also calculated data without providing uncertainties. Those three data sets therefore do not allow a quantitative validation of the present mixture model. The data of Gillespie and Wilson<sup>261</sup> and Yu *et al.*<sup>265</sup> cannot be used for validation either. The results of Gillespie and Wilson<sup>261</sup> exhibit unreasonable large scatter, whereas the deviations of the

dew-point data of Yu *et al.*<sup>265</sup> increase significantly with increasing pressure. Furthermore, both works do not include any useful uncertainty information.

Clarke and Glew<sup>260</sup> carried out thorough measurements of the solubility of H<sub>2</sub>S in water in a temperature range from 273 K to 323 K. The presented mole fractions are claimed to be accurate within 0.1 %. Due to the very small mole fractions of H<sub>2</sub>S in the liquid phase, this leads to an extremely low expanded ( $k = 2$ ) uncertainty of 0.0006 mol%. The model represents the data with an AAD of 0.004 mol%, which is about two orders of magnitude higher than the claimed experimental uncertainty. The uncertainty is thus believed to be underestimated. Nevertheless, the good agreement between the bubble-point data of Clarke and Glew<sup>260</sup> emphasize the accuracy of the new model. Dew-points from the same reference are also accurately represented; however, Clarke and Glew<sup>260</sup> obtained these values from phase-equilibrium calculations based on their bubble-point data without providing uncertainties.

Chapoy *et al.*<sup>258,259</sup> measured the composition of both coexisting phases at temperatures between 298 K and 338 K. The measurements are based on a static-analytic method with fluid phase sampling. The corresponding publication does not provide combined uncertainties in composition; nevertheless, the data are in very good agreement with the present model. The bubble points are represented with a maximum deviation of 0.3 mol% and an AAD of 0.07 mol%, whereas the maximum deviation of the dew points is 0.17 mol% and the AAD 0.07 mol%. These deviations are comparable with those of Chapoy's data for H<sub>2</sub>O + CO<sub>2</sub> and H<sub>2</sub>O + CH<sub>4</sub> from the EOS-CG<sup>2</sup> and from the model presented in Sec. 6.2.3.

Selleck *et al.*<sup>263</sup> carried out measurements along five isotherms between 311 K and 444 K. The authors estimated the uncertainty in H<sub>2</sub>S mole fractions of the gas phase to be 0.02 %, which leads to an expanded ( $k = 2$ ) uncertainty of 0.4 mol%. The model describes the dew-point data below the VLLE pressure with a maximum deviation of 0.63 mol% and an AAD of 0.25 mol% (excluding one clear outlier), which is in good agreement with the experimental uncertainty. Unfortunately, no experimental uncertainty is given for the bubble-point data. The publication also provides VLE data at pressures higher than the VLLE pressures calculated from the present model. The data are presented as extrapolation results.<sup>263</sup> Since they are equivalent with LLE data, these extrapolations are found to be unreasonable and they exhibit large deviations from the present and the GERG-2008 model.

The high-temperature VLE region up to 584 K was investigated by Suleimenov and Krupp,<sup>264</sup> whose data also include lower temperatures (down to 293 K). The authors give no useful information about the experimental uncertainty. The data are sufficiently consistent with comparative measurements at lower temperatures to use them for a validation of the present model at temperatures between 445 K and 585 K. In this temperature range, the model represents most of the bubble- and dew-point data within 0.1 mol% and 1 mol%, respectively.

Based on the deviations shown in Figure 6.23 and considering the discussed quality of the underlying data, rough uncertainty estimates for calculated VLE compositions can be made. The uncertainty in calculated bubble-point compositions is 0.2 mol% at temperatures from the normal melting point of water to 340 K and 0.3 mol% at temperatures up to 585 K. For dew points, the uncertainty in composition is conservatively estimated to be approximately 1 mol% at temperatures up to 445 K and 2 mol% at temperatures up to 585 K.

The only density data found in the literature are included in the VLE study of Selleck *et al.*<sup>263</sup> The data were consequently not measured at homogeneous but at saturated-liquid states between 310 K and 445 K. Deviations between the data, the present mixture model, and GERG-2008 are presented in Figure 6.24.

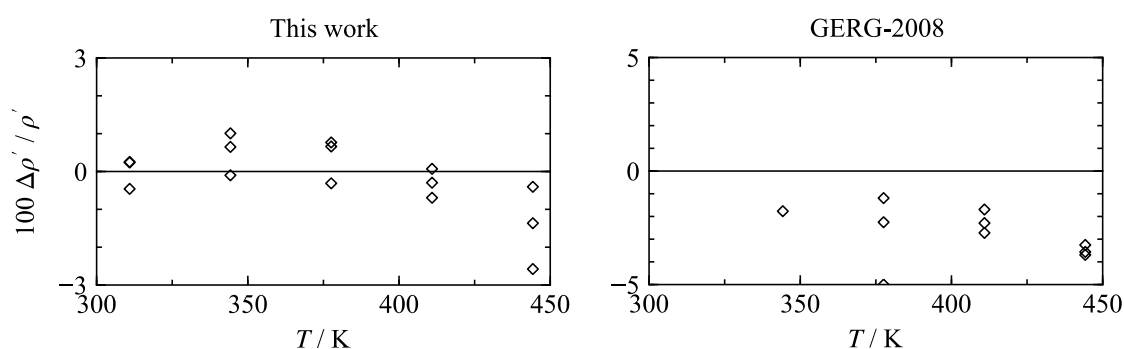


**Figure 6.24** Relative deviations  $\Delta\rho/\rho = (\rho_{\text{exp}} - \rho_{\text{calc}})/\rho_{\text{exp}}$  of experimental saturated-liquid density data for the system  $\text{H}_2\text{O} + \text{H}_2\text{S}$  from the new EOS (left) and GERG-2008 (right) as a function of temperature. The data cover a composition range of  $0.02 < x_{\text{H}_2\text{S}} < 0.06$ .

The data deviate by approximately 3 % from the new model and by about 5 % from GERG-2008. Selleck *et al.*<sup>263</sup> estimated the uncertainty of their data to be within 3 %, which is interpreted as a standard uncertainty. An expanded ( $k = 2$ ) uncertainty of 6 % agrees with the deviations from both models. Nevertheless, this uncertainty is so high that it does not allow for a reasonable uncertainty estimate for calculated saturated-liquid densities.

A validation of the physical behavior predicted by the present model is particularly interesting in order to clarify whether the developed departure function provides reasonable results, although it is based on limited experimental data. Figure 6.25 shows  $p, T$  phase envelopes (also referred to as “isopleths”, lines of constant composition) for a  $\text{H}_2\text{O}$ -rich and a  $\text{H}_2\text{S}$ -rich mixture. The saturation lines are shaped smoothly up to pressures of 1000 MPa and no unreasonable behavior of the isochores is found. Many other property diagrams were evaluated while fitting the present model. From these evaluations and the comparisons with experimental data discussed in this section it follows that the development of a binary specific departure function is also possible with limited experimental data. However, in order to further improve the present model for  $\text{H}_2\text{O} + \text{H}_2\text{S}$  at least some experimental data for homogeneous densities should be contributed.

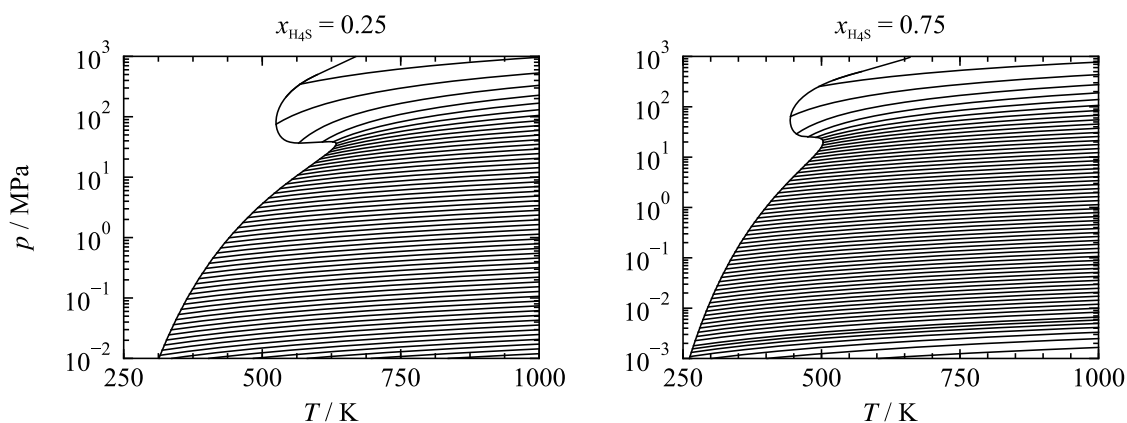


**Figure 6.25**  $p, T$  diagrams calculated with the new EOS for  $\text{H}_2\text{O} + \text{H}_2\text{S}$  for a mixture with 25 mol%  $\text{H}_2\text{S}$  (left) and a mixture with 75 mol%  $\text{H}_2\text{S}$  (right). The mixing behavior is shown along isochores up to  $40 \text{ mol dm}^{-3}$  (left) and  $30 \text{ mol dm}^{-3}$  (right).

### 6.3 Binary Mixtures Described with Adjusted Reducing Parameters

The following subsections present the mixture models that were developed by adjusting the parameters of the reducing functions of the Helmholtz-explicit EOS (see. Sec. 3.3, Eqs. (3.42) and (3.43)) but no binary specific departure function. Most of these binary mixtures contain either  $\text{SO}_2$  or one of the amines (MEA or DEA). Binary mixture with  $\text{SO}_2$  are discussed in Sec. 6.3.1, whereas the amine mixtures are the subject of Sec. 6.3.2. The system  $\text{Cl}_2 + \text{HCl}$  is separately presented in Sec. 6.3.3.

The values of the reducing parameters are not given in the corresponding subsections but are listed completely in Table E.1 in Appendix E of this thesis.

#### 6.3.1 Binary Mixtures with Sulfur Dioxide

Of the components defined as minor impurities in  $\text{CO}_2$ -rich mixtures,  $\text{SO}_2$  is one of the technically most relevant. In particular, it needs to be considered in post-combustion separation processes but also in coal-fired oxyfuel processes. As described by Nazeri *et al.*,<sup>267</sup> post-combustion separation with amines can be impeded by higher mole fractions of  $\text{SO}_2$  that might lead to foaming, increased viscosities, formation of heat-stable salt structures, and most importantly to a reduced  $\text{CO}_2$ -absorption rate. The additional presence of water poses a particular challenge for the transportation process because  $\text{SO}_2$  dissolved in water forms sulfurous acid which is an intermediate species in the formation of highly corrosive sulfuric acid.

Over the last years, the scientific interest in the thermodynamic properties of  $\text{SO}_2$ -mixtures increased and a number of experimental studies were published in the literature. This allowed for the development of new binary models for mixtures containing  $\text{SO}_2$  and  $\text{CO}_2$ ,  $\text{N}_2$ ,  $\text{O}_2$ ,  $\text{CH}_4$ ,  $\text{Cl}_2$ ,  $\text{HCl}$ , DEA, MEA and  $\text{H}_2\text{O}$ . Nevertheless, the data situation could still be



improved, especially since almost all experimental studies are focused on VLE and rarely provide any reliable data for homogeneous states.

### 6.3.1.1 Sulfur Dioxide + Carbon Dioxide

With regard to the quantity of the available data, the binary system  $\text{SO}_2 + \text{CO}_2$  is, aside from the system  $\text{SO}_2 + \text{H}_2\text{O}$  (see Sec. 6.3.1.8), the experimentally best investigated system of the binary mixtures with  $\text{SO}_2$  considered in this work. The development of the mixture model for this system was completed in mid-2017. The experimental database available at this point allowed and required to fit all four adjustable parameters of the binary reducing functions. Two comprehensive  $pVT$  data sets were published later in 2017 and recently in 2018 by Nazeri *et al.*<sup>267</sup> and Gimeno *et al.*<sup>268</sup> These two data sets did consequently not contribute to the fitting process, but comparisons to the mixture model are discussed in this section.

The most recent and probably also most accurate and consistent VLE data set was published by Coquelet *et al.*<sup>269</sup> It covers two isotherms of the VLE region, 263 K and 333 K. The data result from the static-analytical method that is based on the extraction of the liquid and vapor phases from the two-phase equilibrium. The extracted samples are analyzed in a gas chromatograph in order to obtain the phase-equilibrium compositions. The equilibrium cell that was part of the experimental set-up of Coquelet *et al.*<sup>269</sup> was used before in the work of Lachet *et al.*<sup>270</sup> Unfortunately, Lachet's data were only graphically reported in the corresponding publication. Coquelet and co-workers re-measured the isotherms investigated by Lachet. Graphically obtained points of Lachet *et al.*<sup>270</sup> are included in the  $p,x$  diagrams shown in Figure 6.26.

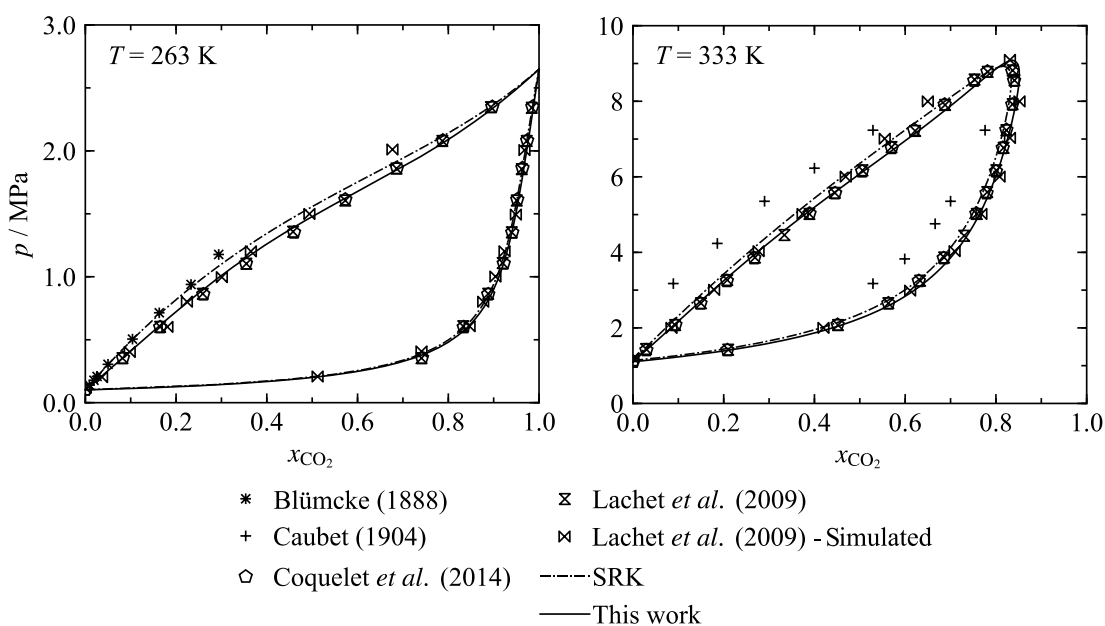


**Figure 6.26** Phase boundaries of the system  $\text{SO}_2 + \text{CO}_2$  in  $p,x$  diagrams for two isotherms as calculated from the new EOS. The available experimental data and results calculated from SRK are shown for comparisons.

In addition to data of Lachet *et al.*<sup>270</sup> and the data from Coquelet's group, Figure 6.26 also shows molecular-simulation data of Lachet as well as very old experimental data of Blümcke<sup>271</sup> and Caubet.<sup>272</sup> The  $p,x$  diagrams do not include the data of Thiel and Schulte,<sup>273</sup> who only reported two equilibrium points at atmospheric pressure and with very low accuracy. Not surprisingly, the bubble and dew points of Coquelet *et al.*<sup>269</sup> and Lachet *et al.*<sup>270</sup> are in very close agreement because Coquelet and co-workers repeated Lachet's measurements with a slightly modified apparatus. The mixture model was fitted to the data of Coquelet. Thus, it quite accurately represents these data including the characteristic changes in curvature along the bubble line at 263 K. The simulated data of Lachet *et al.*<sup>270</sup> overall agree with the reliable experimental works, but the bubble points exhibit increasing offsets with increasing pressure. The very old data of Blümcke<sup>271</sup> and Caubet<sup>272</sup> have systematic offsets to the other studies.

Figure 6.26. additionally shows the phase boundaries calculated from the cubic SRK EOS of Soave<sup>18</sup> with the binary interaction parameter of Li and Yan<sup>198</sup> ( $k_{\text{CO}_2+\text{SO}_2} = 0.048$ ). Except for the dew line at 263 K, which is in close agreement with the Helmholtz-explicit EOS, the results calculated from SRK exhibit an offset from the new model and the reliable data. The present Helmholtz-explicit EOS yields more accurate results especially for bubble points.

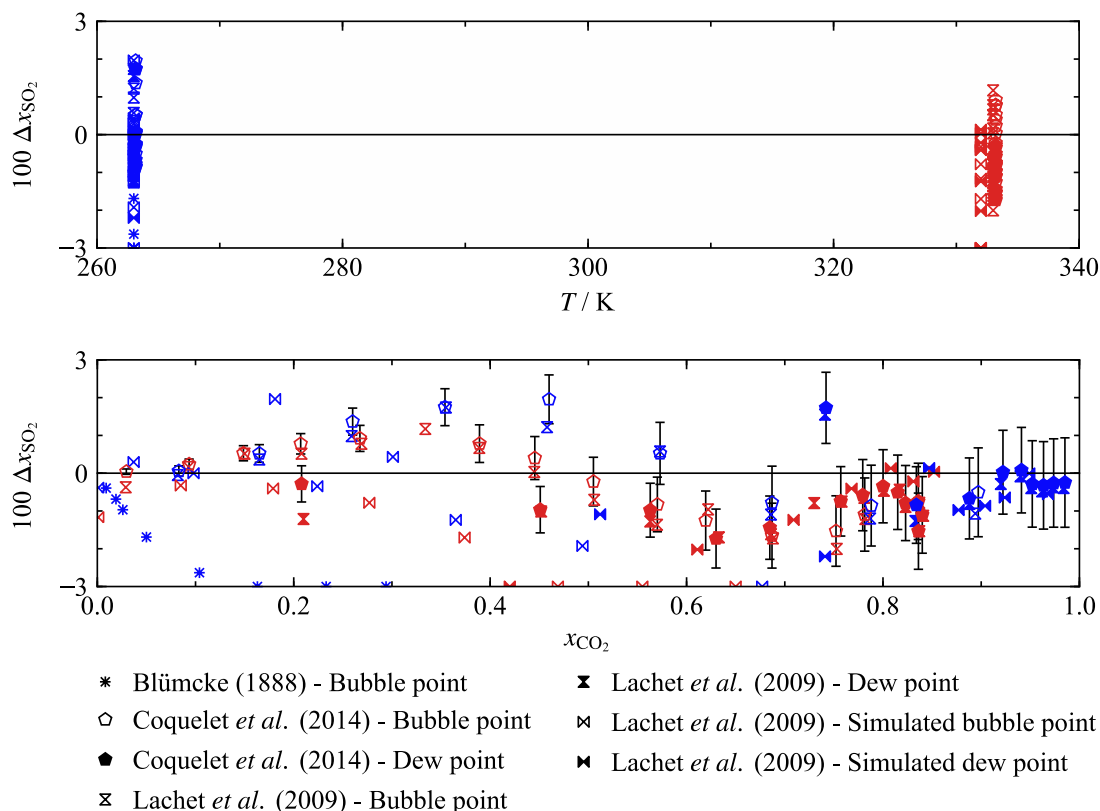


**Figure 6.27** Top: Deviations  $\Delta x_{\text{SO}_2} = (x_{\text{SO}_2,\text{data}} - x_{\text{SO}_2,\text{calc}})$  between the available VLE data for the system  $\text{SO}_2 + \text{CO}_2$  and results calculated from the new EOS as a function of temperature. Bottom: Deviations of the data as a function of  $\text{CO}_2$  content. Error bars showing the (estimated) experimental uncertainty are just added to the data of Coquelet *et al.*<sup>269</sup> The other references do not provide reliable information on the uncertainty of the data.

Deviations between the present model and the available data are shown in Figure 6.27. Due to their very large deviations the data of Caubet<sup>272</sup> are not included in the deviation plots. The figure shows deviations between phase-equilibrium compositions calculated from the present mixture model and the available VLE data. It can be seen that the model describes the most accurate data by Coquelet *et al.*<sup>269</sup> within a maximum deviation of 2 mol%. The corresponding publication states expanded ( $k = 2$ ) uncertainties of 0.0002 MPa (at  $p \leq 1.6$  MPa) and 0.002 MPa (at  $p > 1.6$  MPa) in pressure and of 0.02 K in temperature. The uncertainty in composition of both phases is stated to be 0.6 %. Because no  $k$ -factor is given, this value is interpreted as a standard uncertainty. The publication does not provide combined uncertainties in composition; thus, these uncertainties were calculated based on the given individual uncertainties in temperature, pressure, and composition. The thus obtained combined expanded uncertainties range from 0.14 mol% to 1.2 mol% for the bubble points and from 0.4 mol% to 1.2 mol% for the dew points. They are included as error bars in the bottom panel of Figure 6.27. The model represents the data within their experimental uncertainties for  $x_{\text{CO}_2} > 0.65$ . At lower  $\text{CO}_2$  contents, most deviations do not match the quite low uncertainties. Even intensive fitting of the data, did not lead to significantly lower deviations. It can therefore be assumed that the experimental uncertainties are to some extent underestimated. The uncertainty of calculated values is consequently estimated based on the deviations between the mixture model and the data. The uncertainty in both dew- and bubble-point compositions calculated from the new mixture model is 2 mol% at temperatures between 260 K and 335 K. This uncertainty is estimated on the assumption that the model can be reasonably interpolated between the two isotherms investigated in the literature.

As mentioned at the beginning of this section, two  $pVT$  data sets were published after the development of this binary mixture model. The only homogeneous density data available during the fitting process were the measurements of Wang *et al.*<sup>274</sup> That study presents 12 data points along one single isotherm, 328 K, but no uncertainty analysis. Because no uncertainties of the instruments are given in the publication, no combined uncertainty in density could be estimated. Fitting the model to the data, worsened the representation of the VLE data. The data were therefore not included in the fitting process; and thus, the model was not adjusted to any density data. The deviations between calculated densities and Wang's data, and the new data sets of Nazeri *et al.*<sup>267</sup> and Gimeno *et al.*<sup>268</sup> result from the extended corresponding states principle enabled by exclusively fitting the reducing parameters to the reliable VLE data. These deviations are shown in Figure 6.28.

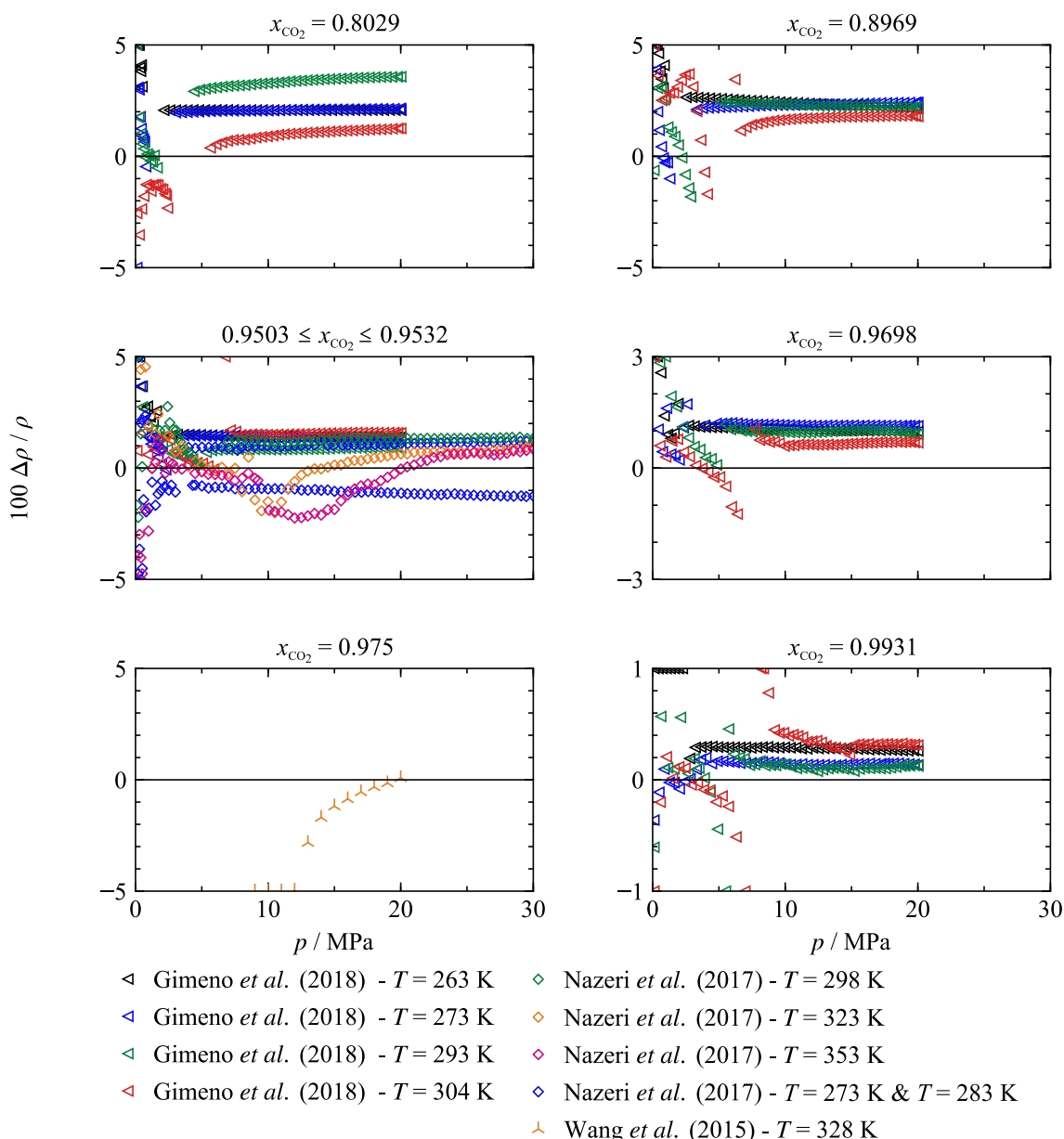


**Figure 6.28** Relative deviations  $\Delta\rho / \rho = (\rho_{\text{exp}} - \rho_{\text{calc}}) / \rho_{\text{exp}}$  of available experimental density data for the system  $\text{SO}_2 + \text{CO}_2$  from the new EOS as a function of pressure.

The most recent work of Gimeno *et al.*<sup>268</sup> includes liquid and gas-phase densities for five  $\text{CO}_2$ -rich compositions ( $0.8029 \leq x_{\text{CO}_2} \leq 0.9931$ ) and along four isotherms ( $263 \leq T / \text{K} \leq 304$  K). Nazeri *et al.*<sup>267</sup> investigated the gas and liquid for only one composition ( $x_{\text{CO}_2} \leq 0.9503$ ) along five isotherms ( $273 \leq T / \text{K} \leq 353$  K). Both data sets were measured with vibrating-tube densimeters; thus, comparisons between the overlapping data for the mixture with 95 mol%  $\text{CO}_2$  at 273 K are of special interest. In Figure 6.29 it can be seen that, in the liquid phase at 20 MPa, both data sets agree within 0.26 %, which is the closest agreement of the data. With decreasing pressure, the deviations between the two data sets increase up to 0.68 % at 4 MPa. The maximum expanded ( $k = 2$ ) uncertainty of the liquid-phase data between 4 MPa and 20 MPa stated by Gimeno *et al.*<sup>268</sup> and Nazeri *et al.*<sup>267</sup> is 0.08 % and 0.1 %, respectively. In Figure 6.29 error bars illustrate the uncertainty of every state point. It is apparent that in the liquid-phase the deviations between the two data sets are

considerably higher than the reported uncertainties. Because the deviation plot is at constant temperature and (quasi-)constant composition, it is possible to additionally include results calculated from SRK. The results deviate considerably from the experimental data and the present EOS.

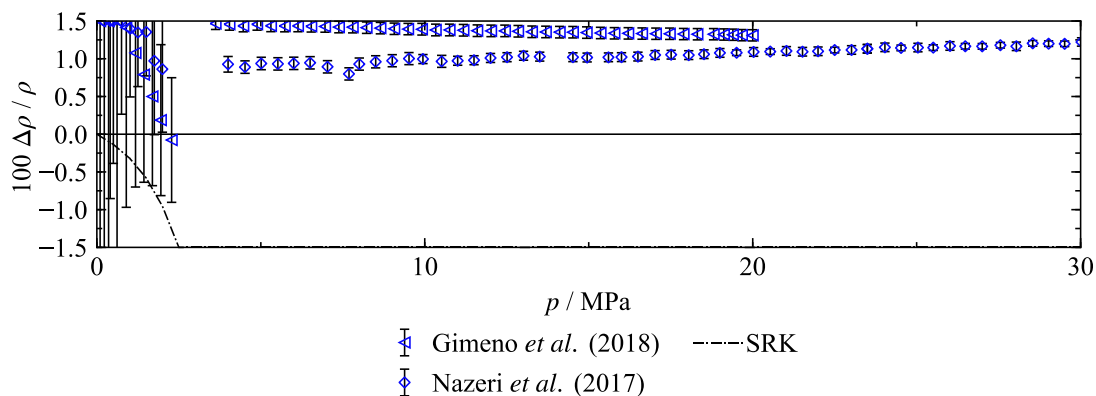


**Figure 6.29** Relative deviations  $\Delta\rho/\rho = (\rho_{\text{exp}} - \rho_{\text{calc}})/\rho_{\text{exp}}$  of the experimental density data of Gimeno *et al.*<sup>268</sup> ( $x_{\text{CO}_2} = 0.9532$ ) and Nazeri *et al.*<sup>267</sup> ( $x_{\text{CO}_2} = 0.9503$ ) for the system  $\text{SO}_2 + \text{CO}_2$  at 273 K from the new EOS as a function of pressure; results calculated from SRK are included for comparisons.

Although the experimental uncertainties of the data seem to be underestimated, they are certainly lower than their deviations from the present binary mixture model. Uncertainties of calculated densities are consequently equivalent to these deviations. Thus, the uncertainty in liquid-phase densities for  $x_{\text{CO}_2} \geq 0.95$  is 1.5 % at temperatures up to 305 K. For lower  $\text{CO}_2$  contents of  $0.80 \leq x_{\text{CO}_2} < 0.95$ , the uncertainty is conservatively estimated to be 3.5 %. In the gas phase, densities decrease with decreasing pressure; thus, the relative uncertainties of the experimental data get larger. Figure 6.30 shows deviations of the gas-phase densities of Gimeno *et al.*<sup>268</sup> from the mixture model. The experimental uncertainties are again indicated by error bars.

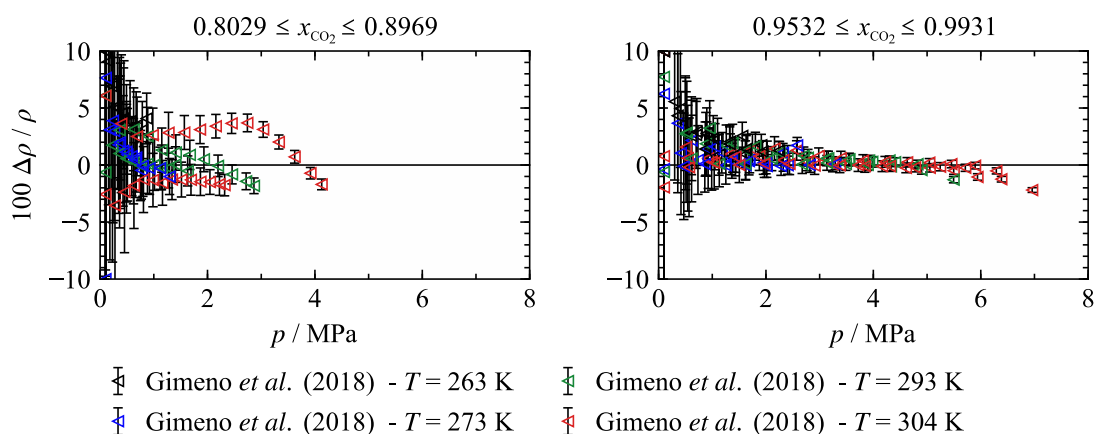


**Figure 6.30** Relative deviations  $\Delta\rho/\rho = (\rho_{\text{exp}} - \rho_{\text{calc}})/\rho_{\text{exp}}$  of the experimental gas-density data of Gimeno *et al.*<sup>268</sup> for the system  $\text{SO}_2 + \text{CO}_2$  from the new EOS as a function of pressure.

Excluding the 304 K isotherm of the mixture with  $x_{\text{CO}_2} = 0.8969$ , the majority of the data is represented within their experimental uncertainties. This is remarkable because the data were

not included in the fit. However, it is difficult to deduce relative uncertainties of calculated values from the deviations because, as evident in Figure 6.30, the experimental uncertainties exhibit a significant pressure dependency. Conservatively estimated, it can be said that the uncertainty of calculated gas-phase densities at temperatures up to 305 K and pressures above 2 MPa is 3 % for  $0.80 \leq x_{\text{CO}_2} < 0.95$  and 2 % for  $x_{\text{CO}_2} \geq 0.95$ . Based on the deviations of the experimental data, the uncertainty of the EOS seems to increase significantly with decreasing pressure; however, it has to be noted that at very low pressures, the uncertainty becomes small because the gas approaches the ideal-gas limit.

To conclude, it should be noted that the model for  $\text{SO}_2 + \text{CO}_2$  allows for a quantitatively correct description of the available VLE data and homogeneous density data in the gas phase, but that it does not match the uncertainties of the experimental liquid-densities. The accuracy of the model could be improved by fitting it to the recently published  $pVT$  data sets. Describing these data within their experimental uncertainties might require the development of a short binary specific departure function, although it would remain to be seen whether the composition range of these data is large enough to allow for a numerically stable fit of such a complex functional form.

### 6.3.1.2 Sulfur Dioxide + Nitrogen

The experimental database for the binary system  $\text{SO}_2 + \text{N}_2$  is much more limited than for the previously discussed system  $\text{SO}_2 + \text{CO}_2$ . Nevertheless, the data were still found to be sufficient to fit all four parameters of the binary reducing functions. The only data set providing information about both phases in equilibrium was published by El Ahmar *et al.*,<sup>275</sup> who measured 49 VLE points along four isotherms. The data are based on an analytical measurement technique, where the compositions of the coexisting phases at given conditions of temperature and pressure are analyzed in a gas chromatograph. The data are shown in Figure 6.31 together with the phase boundaries calculated from the new mixture model.

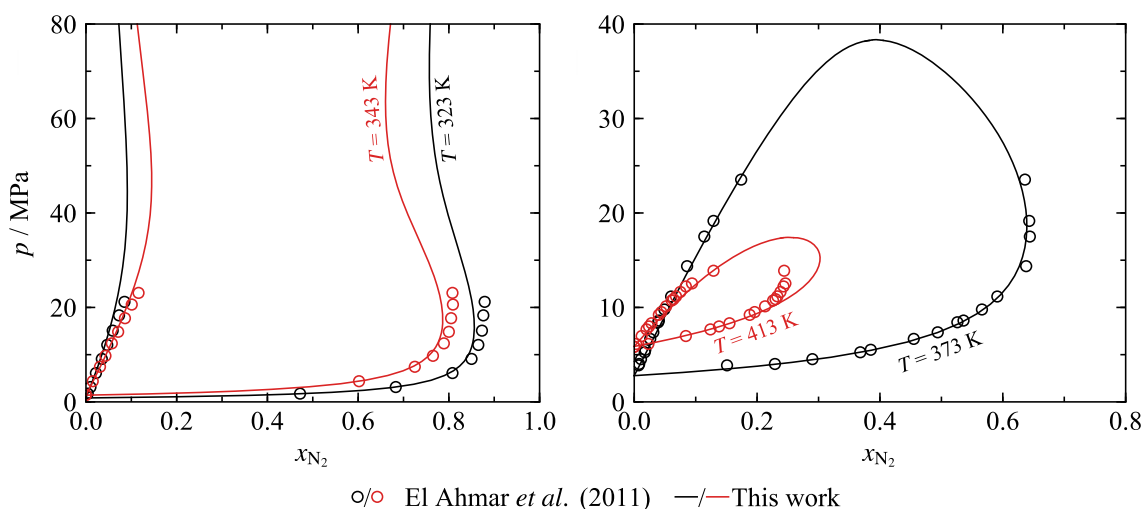


**Figure 6.31** Phase boundaries of the system  $\text{SO}_2 + \text{N}_2$  in  $p,x$  diagrams for four isotherms as calculated from the new EOS. The experimental data of El Ahmar *et al.*<sup>275</sup> are shown for comparisons.

The  $p,x$  diagrams show that, especially along the SO<sub>2</sub>-rich bubble line, the model is in good agreement with the experimental data. Along the dew line the data exhibit an increasing offset with increasing pressure and N<sub>2</sub> content. This is plausible with regard to the shape of the phase boundaries calculated from the new mixture model. Based on the underlying extended corresponding states principle the model predicts a miscibility gap for the two lower temperatures investigated by El Ahmar *et al.*<sup>275</sup> but at pressures higher than measured (see left panel of Figure 6.31). The phase boundaries do not match the trend of the dew-point data at pressures above 10 MPa. With increasing temperature, the calculated demixing curves that limit the high-pressure miscibility gap get closer and closer to each other until a closed VLE region is predicted (see right panel of Figure 6.31). It might be challenging to imagine that the shape of the phase boundaries shifts from open to closed with increasing temperature. For easier understanding, the three dimensional  $p,T,x$  surface of the mixture is shown Figure 6.32.

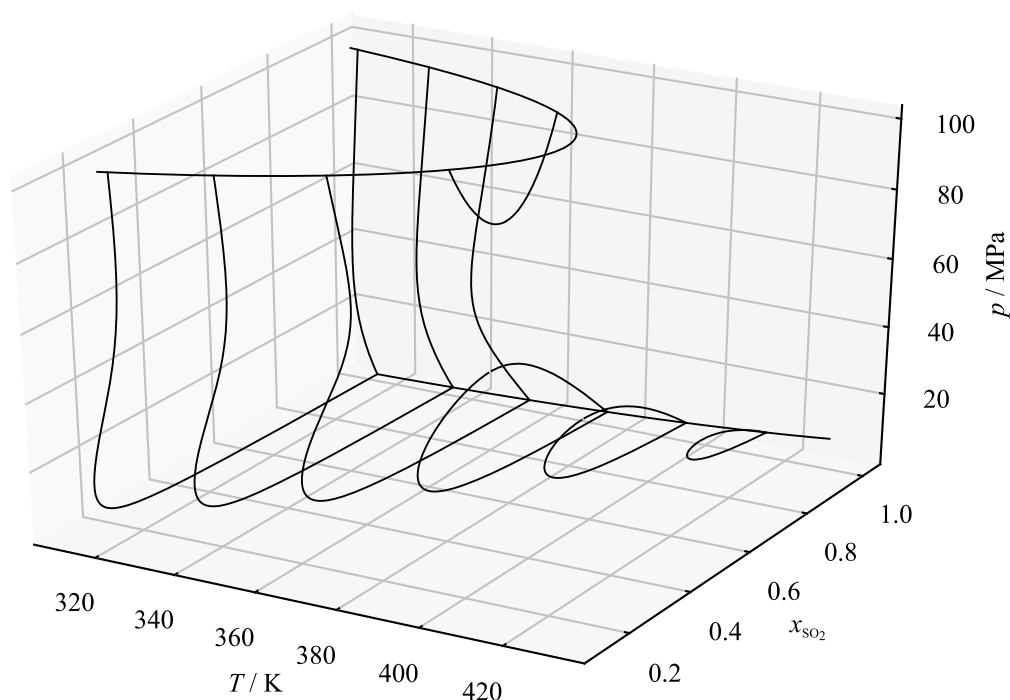


**Figure 6.32** Isothermal phase boundaries of the system SO<sub>2</sub> + N<sub>2</sub> in a  $p,T,x$  diagram as calculated from the new EOS. The  $p,x$  projections of the  $p,T,x$  surface were calculated at 315 K, 335 K, 355 K, 375 K, 395 K, and 415 K. The plot was kindly provided by Ian Bell of NIST using algorithms presented by Bell and Deiters.<sup>276</sup>

The special mixing behavior of this system are not an artifact of the model. It was already reported by Tsiklis<sup>277</sup> in 1947. Unfortunately, his publication does not provide any useful data, but some  $p,x$  diagrams which qualitatively confirm the shape of the calculated phase boundaries. Over a certain temperature range, Tsiklis<sup>277</sup> also reports the existence of a second high-pressure two-phase region. The same behavior can be seen for the 355 K isotherm shown in Figure 6.32.

As mentioned above, the predicted mixing behavior seems only partly compatible with the representation of the experimental data of El Ahmar *et al.*<sup>275</sup> Even intensive fitting of these

data did not considerably reduce the deviations from the model. In principle, by fitting all four adjustable parameters of the reducing functions the mathematical flexibility of the model should be sufficient to allow for a quite accurate description of the data, if these are sufficiently accurate and consistent. The publication of El Ahmar *et al.*<sup>275</sup> does not provide combined experimental uncertainties of the VLE data, but individual uncertainties in temperature (0.1 K), pressure (0.4 kPa), and mole fraction (3.2 %). Unfortunately, the uncertainty in composition is not further specified; thus, it is not clear whether this is a “real” relative uncertainty ( $100 \Delta x/x$ ) or a difference given in mol% ( $100 \Delta x$ ). Interpreting the value as a relative uncertainty and carrying out a propagation of uncertainties, leads to a maximum combined expanded ( $k=2$ ) uncertainty in both bubble- and dew-point compositions of 0.65 mol%. As evident from Figure 6.33, this uncertainty does clearly not match the deviations between the data and calculated results from the present mixture model. The deviation plots show absolute deviations in composition given in mol% as a function of temperature and composition ( $x_{N_2}$ ).

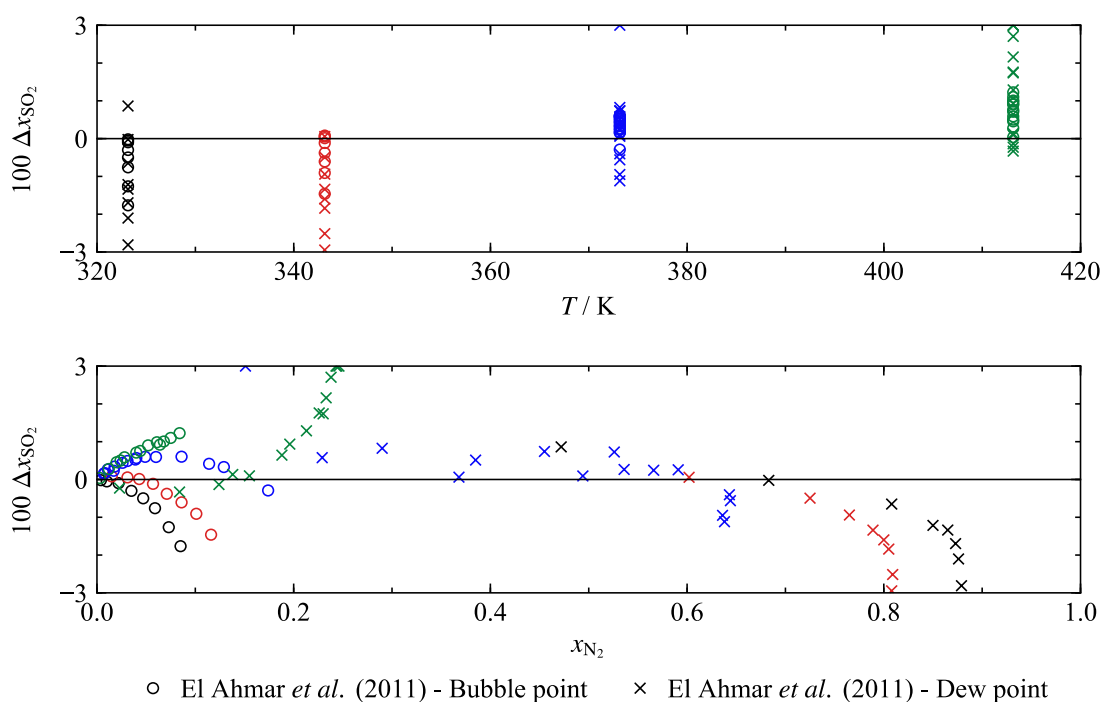


**Figure 6.33** Top: Deviations  $\Delta x_{SO_2} = (x_{SO_2,exp} - x_{SO_2,calc})$  between the experimental VLE data of El Ahmar *et al.*<sup>275</sup> for the system  $SO_2 + N_2$  and results calculated from the new EOS as a function of temperature. Bottom: Deviations of the experimental data as a function of  $N_2$  content.

The bubble-point data are represented with a maximum deviation of 2 mol%. The deviations between calculated dew points and the experimental data are mostly within 1.5 mol% for  $N_2$  contents lower than in the retrograde regions of the phase boundaries. For higher mole fractions of  $N_2$ , the deviations increase up to about 3 % for the 323 K and 343 K isotherms and up to about 5.5 % at 413 K. The best agreement between the data and the model was reached at 373 K. At this temperature, the model predicts a closed shape of the phase boundaries which matches the trend of the data (see right panel of Figure 6.31) and which



leads to the comparably low deviations. At 423 K, the data and the new model again qualitatively agree about the shape of the VLE region, but the model predicts a wider composition range of the two-phase region. Unfortunately, no reliable comparative data from other source are available. Dean and Walls<sup>278</sup> and Dornte and Ferguson<sup>279</sup> also measured some VLE points, but both groups did not state any uncertainties and their data exhibit extremely large deviations from both the model and the data of El Ahmar *et al.*<sup>275</sup> Both data sets were consequently omitted from the fitting process; thus, it cannot be clarified whether the experimental uncertainties of El Ahmar's data are underestimated or not. Considering the discussed deviations of these data, the uncertainty of calculated phase-equilibrium compositions between 320 K and 415 K is conservatively estimated to be within 2 mol% for bubble points and 5 mol% for dew points.

For this mixture no experimental densities are available in the literature; however, the discussed publication by El Ahmar *et al.*<sup>275</sup> includes some molecular-simulation data obtained from Monte-Carlo calculations. The data supplement the experimental VLE data with additional saturation densities. Köster and Vrabec<sup>280</sup> contributed additional simulated homogeneous densities (gas and liquid phase) over a wide composition range to the development of the present mixture model. Deviations of both data sets from the EOS are shown in Figure 6.34.

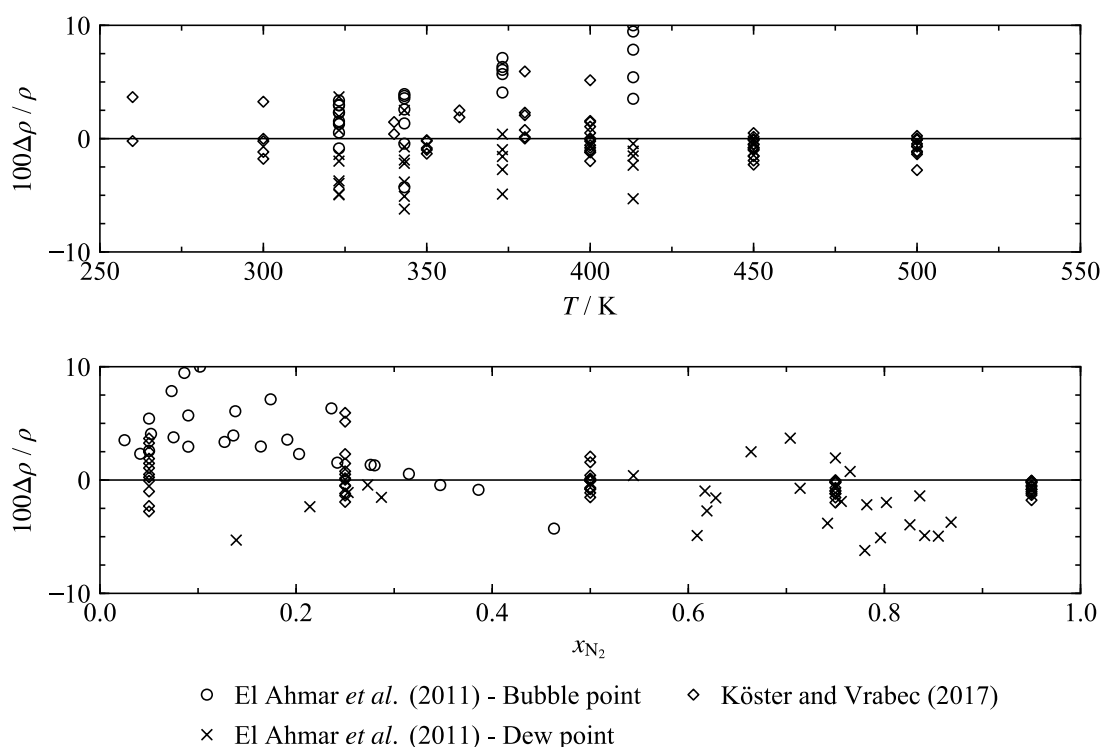


**Figure 6.34** Top: Relative deviations  $\Delta\rho/\rho = (\rho_{\text{data}} - \rho_{\text{calc}}) / \rho_{\text{data}}$  of simulated density data for the system  $\text{SO}_2 + \text{N}_2$  from the new EOS as a function of temperature. The molecular-simulation data of El Ahmar *et al.*<sup>275</sup> describe phase equilibria, whereas Köster and Vrabec<sup>280</sup> simulated homogeneous densities in the gas and liquid phase. Bottom: Deviations of the data as a function of  $\text{N}_2$  content.

The homogeneous density data obtained by Köster and Vrabec<sup>280</sup> are represented within a maximum deviation of approximately 6 %. The approach of their molecular simulations is based on a force field that describes the interactions between the molecules in the fluid. Thereby, it is required to distinguish between like and unlike molecular interactions. The like interactions were modeled with pure-substance force fields. For the unlike interactions, a binary interaction parameter needs to be adjusted to at least one experimental data point of the binary mixture. For this mixture Köster and Vrabec<sup>280</sup> could only use the VLE data of El Ahmar *et al.*<sup>275</sup> to adjust this binary interaction parameter; thus, deviations of up to 6 % are considered to be reasonable. It is interesting that for  $x_{N_2} \geq 0.5$  the data are mostly represented within 2.5 %, whereas the higher deviations occur with increasing SO<sub>2</sub> content. Because the pure-fluid EOS for SO<sub>2</sub> of Gao *et al.*<sup>33</sup>, whose influence increases with increasing SO<sub>2</sub> content, yields very reliable results for calculated densities (uncertainties within 0.1 % in the liquid and 0.25 % in the vapor phase), these higher deviations indicate shortcomings in the molecular model for pure SO<sub>2</sub>. The saturated-vapor densities simulated by El Ahmar's group mostly deviate within 5 % from the present mixture model whereas the saturated-liquid points exhibit higher deviations of up to 10 %. Since the present mixture model was essentially fitted to the VLE data from the same group, the density data and the VLE data seem to be slightly inconsistent. Summarizing the data situation, it can be said that neither the simulated data of Köster and Vrabec<sup>280</sup> nor of El Ahmar *et al.*<sup>275</sup> are accurate enough to allow for a reasonable estimate of uncertainties in densities calculated from the binary model.

### 6.3.1.3 Sulfur Dioxide + Oxygen

The data situation for the binary system SO<sub>2</sub> + O<sub>2</sub> corresponds to the previously discussed situation for SO<sub>2</sub> + N<sub>2</sub>; experimental VLE data and simulated homogeneous densities were published by El Ahmar *et al.*<sup>275</sup> Again, all four reducing parameters were adjusted to those data. The experimental set-up used by El Ahmar *et al.*<sup>275</sup> to measure the VLE data was the same as for SO<sub>2</sub> + N<sub>2</sub>. The 27 points along the four investigated isotherms are shown in Figure 6.35 together with the phase boundaries calculated from the binary mixture model.

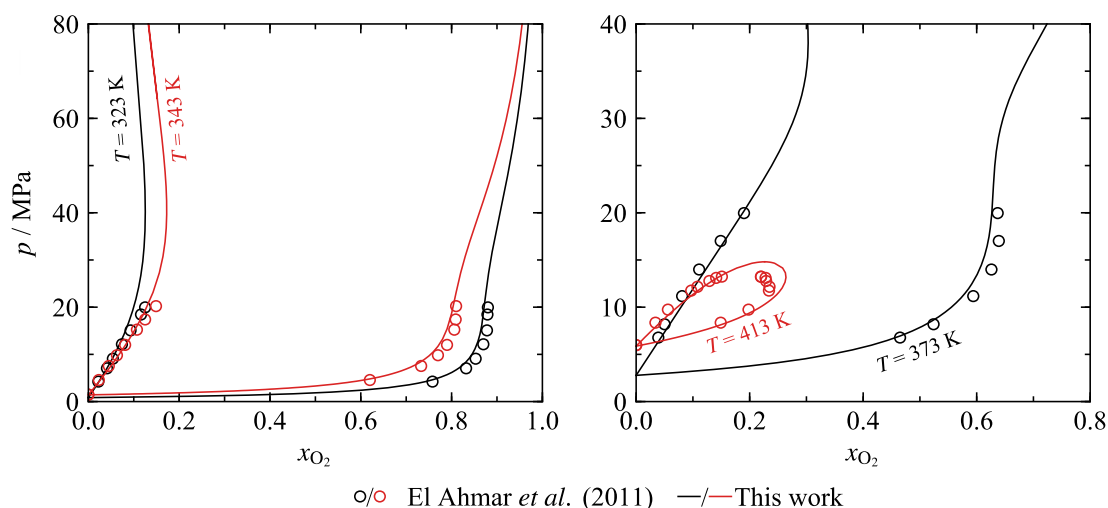


**Figure 6.35** Phase boundaries of the system  $\text{SO}_2 + \text{O}_2$  in  $p, x$  diagrams for four isotherms as calculated from the new EOS. The experimental data of El Ahmar *et al.*<sup>275</sup> are shown for comparisons.

As for  $\text{SO}_2 + \text{N}_2$ , the mixture model predicts a high-pressure miscibility gap, whose composition range decreases with increasing temperature. At 413 K, the highest investigated temperature, the phase boundaries are closed, which is unquestionably confirmed by the experimental data. The deviations between experimental and calculated data with respect to composition are comparable to the previously discussed results for  $\text{SO}_2 + \text{N}_2$  and are presented in Figure 6.36.

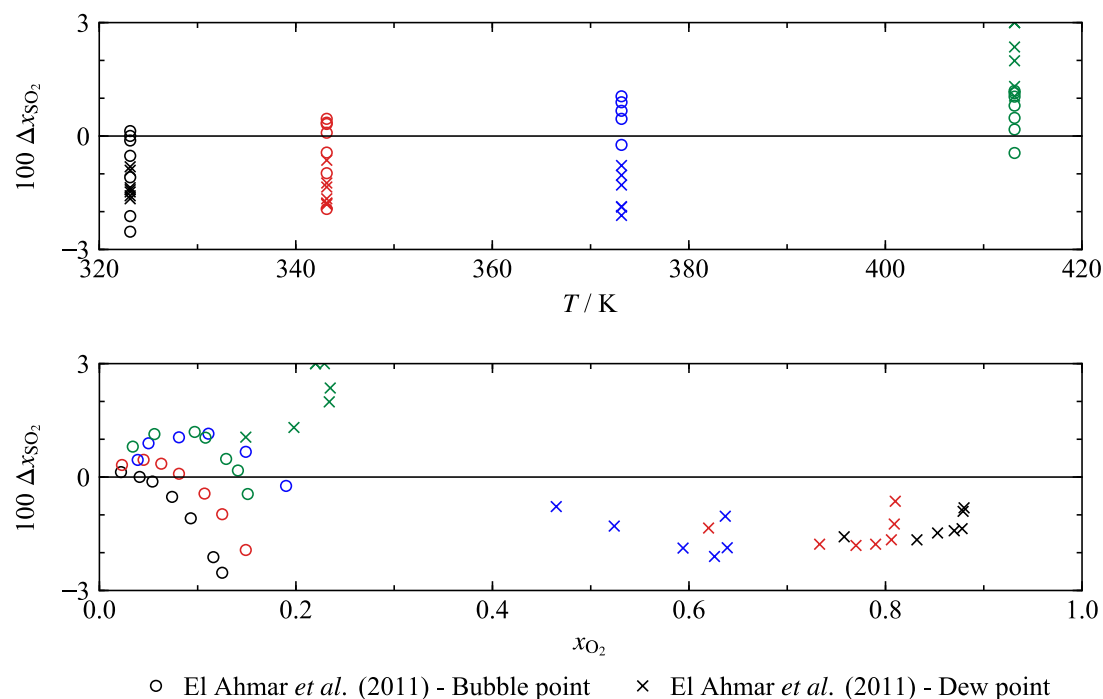


**Figure 6.36** Top: Deviations  $\Delta x_{\text{SO}_2} = (x_{\text{SO}_2, \text{exp}} - x_{\text{SO}_2, \text{calc}})$  between the experimental VLE data of El Ahmar *et al.*<sup>275</sup> for the system  $\text{SO}_2 + \text{O}_2$  and results calculated from the new EOS as a function of temperature. Bottom: Deviations of the experimental data as a function of  $\text{O}_2$  content.

Except for two dew points in the critical region at 413 K, the model represents all the data within 3 mol%, which is reasonably adopted as the estimated uncertainty of calculated VLE compositions between 320 K and 415 K. The combined expanded ( $k = 2$ ) uncertainties of

the data were calculated considering the individual uncertainties in temperature, pressure, and composition as already discussed for  $\text{SO}_2 + \text{N}_2$  (see Sec. 6.3.1.2). As for  $\text{SO}_2 + \text{N}_2$  the experimental uncertainties for  $\text{SO}_2 + \text{O}_2$  do not match the deviations shown in Figure 6.36. The calculated maximum uncertainty is 0.63 mol%. Again, no comparative data are available to clarify whether the experimental uncertainties are underestimated or whether the EOS needs to be improved.

The available database for densities is limited to the simulations of El Ahmar *et al.*<sup>275</sup> that provide densities of the saturated liquid and vapor. Deviations of these data from the new model are shown in Figure 6.37

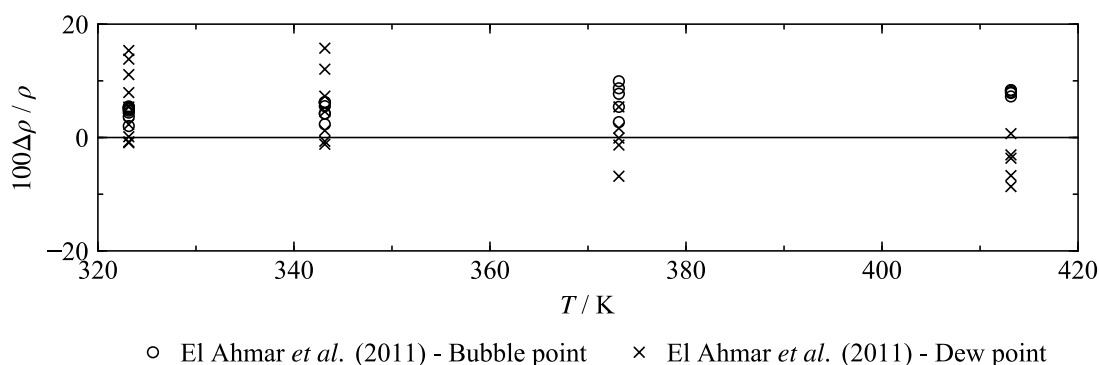


**Figure 6.37** Relative deviations  $\Delta\rho / \rho = (\rho_{\text{data}} - \rho_{\text{calc}}) / \rho_{\text{data}}$  of simulated saturated-liquid and saturated-vapor density data of El Ahmar *et al.*<sup>275</sup> for the system  $\text{SO}_2 + \text{O}_2$  from the new EOS as a function of temperature.

Comparing the results with the ones for  $\text{SO}_2 + \text{N}_2$  (see Figure 6.34) shows that the deviations are even slightly higher, especially for the dew-point densities that deviate by up to 16%. It can only be noted that the present mixture model is probably much more accurate than these deviations indicate. Especially saturated-liquid densities at low temperatures, where the mixture is comparably rich in  $\text{SO}_2$ , are expected to benefit from the reliable description of liquid densities of pure  $\text{SO}_2$  enabled by the EOS of Gao *et al.*<sup>33</sup>

#### 6.3.1.4 Sulfur Dioxide + Methane

Aside from  $\text{SO}_2 + \text{MEA}$  and  $\text{SO}_2 + \text{DEA}$  (see Sec. 6.3.1.7), the experimental database for the binary system  $\text{SO}_2 + \text{CH}_4$  is the most limited one of the mixtures with  $\text{SO}_2$  considered in this work. Only two references presenting VLE data were found in the literature. These data sets by Dean and Walls<sup>278</sup> and Sayegh *et al.*<sup>281</sup> include a total of not more than six points. Considering this poor data situation, it might seem surprising that all four parameters of the binary reducing functions were fitted; however, this mathematical flexibility was needed in order to reasonably shape the phase-boundaries of this system.

Dean and Walls<sup>278</sup> investigated the solubility of  $\text{CH}_4$  in  $\text{SO}_2$  at two different temperatures, 241 K and 302 K, using an analytical measuring technique. Their data are shown in Figure 6.38 together with the data of Sayegh *et al.*<sup>281</sup> that are limited to a single VLE measurement at 318 K.

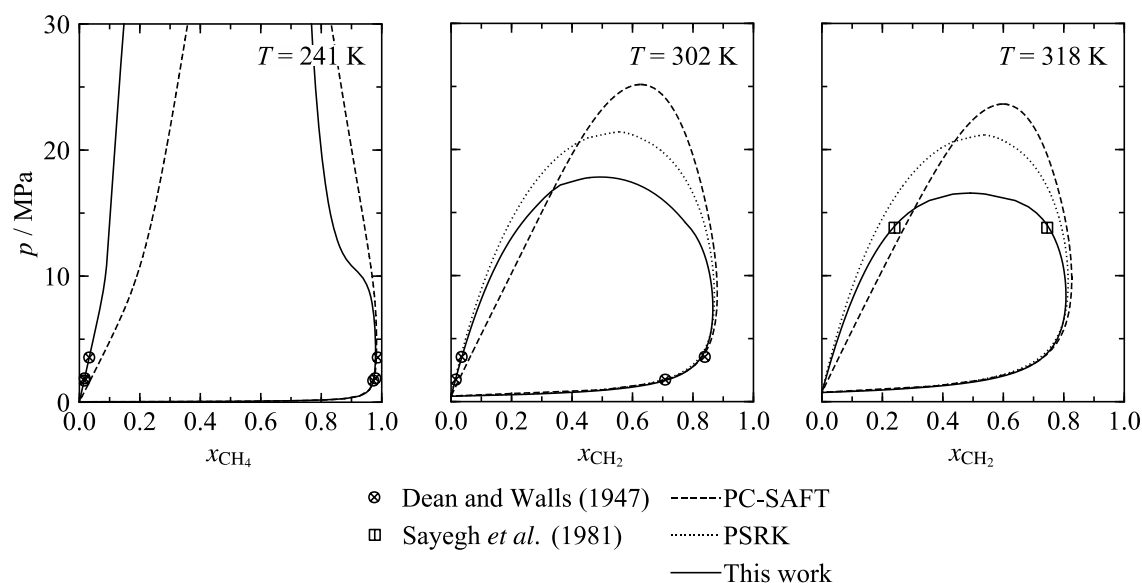


**Figure 6.38** Phase boundaries of the system  $\text{SO}_2 + \text{CH}_4$  in  $p,x$  diagrams for three isotherms as calculated from the new EOS, PC-SAFT and PSRK. The available experimental data are shown for comparisons.

The  $p,x$  diagrams shown in Figure 6.38 and the deviation plot presented in Figure 6.39 emphasize that the present model provides a good representation of both experimental works. The available dew and bubble points are represented within 1.5 mol% and 0.5 mol%, respectively. When fitting a model to such a small number of data points, achieving relatively small deviations is usually not very challenging; thus, the experimental uncertainty of the data is much more meaningful than their deviations. Unfortunately, in the publication of Dean and Walls,<sup>278</sup> no concrete information about experimental uncertainties is given except for some vague statements about the purity of the pure components. The authors expect the  $\text{CH}_4$  to be contaminated by approximately 0.5 vol% of  $\text{C}_2\text{H}_6$  and state the purity of the  $\text{SO}_2$  as 99.6 vol%. Sayegh *et al.*<sup>281</sup> do not provide any uncertainties of their data. Due to this lack of information about the uncertainty of the data and the very small number of points for each investigated isotherm, no uncertainty of VLE data calculated from the model can be provided.

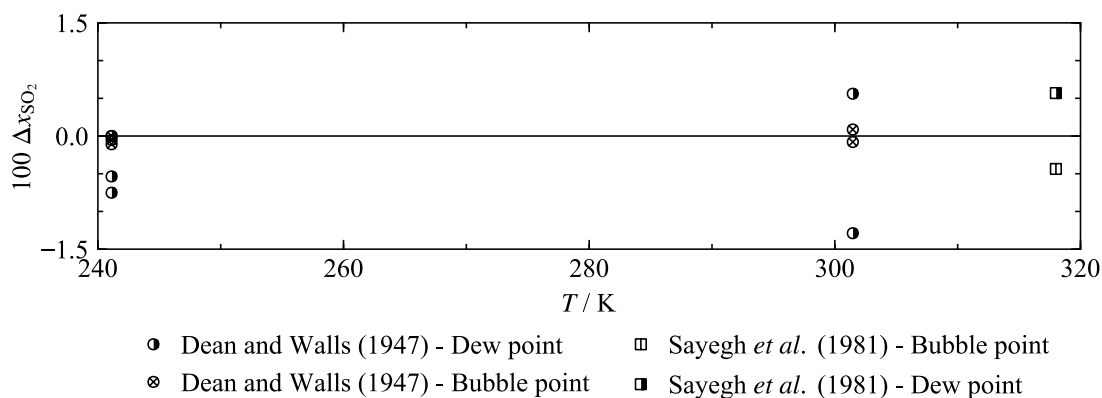


**Figure 6.39** Deviations  $\Delta x_{\text{SO}_2} = (x_{\text{SO}_2,\text{exp}} - x_{\text{SO}_2,\text{calc}})$  between the available experimental VLE data for the system  $\text{SO}_2 + \text{CH}_4$  and results calculated from the new EOS as a function of temperature.

Another challenge of fitting the model to such a small number of experimental data is that the available points only define a quite small part of the phase boundaries (see Figure 6.38), whereas the rest depends on the extrapolation behavior of the model based on the extended corresponding states principle. This aspect is especially relevant for two isotherms investigated by Dean and Walls.<sup>278</sup> At a temperature of 241 K, the extrapolation behavior of the model predicts open phase boundaries at elevated pressures, whereas a closed VLE region is predicted for 302 K. This special mixing behavior was already discussed in detail for  $\text{SO}_2 + \text{N}_2$  (see especially Figure 6.32) and also for  $\text{SO}_2 + \text{O}_2$ . During the fitting process for  $\text{SO}_2 + \text{CH}_4$ , the shape of the phase boundaries calculated from the model turned out to be extremely sensitive to slight changes in the reducing parameters. Depending on the values of the parameters, the phase boundaries at 241 K and 301 K repeatedly changed from a closed to an open form. In order to validate the phase-equilibrium behavior, comparisons with the more predictive models PSRK of Holderbaum and Gmehling<sup>41</sup> and PC-SAFT of Gross and Sadowski<sup>44</sup> (see Sec. 3.4 for more information about these EOS) were carried out. Both models qualitatively confirm the shape of the phase boundaries, but yield considerably higher critical pressures at 302 K and 318 K; however, the predictive potential of both models is limited for this mixture. For PC-SAFT, no binary interaction parameter was found for this fluid combination; whereas for PSRK, two (out of six adjustable) interaction parameters from Gmehling *et al.*<sup>199</sup> were implemented. Nevertheless, since both equations consider the molecular structure of the mixture components and are thus to a certain degree physically based (though still empirical), the phase-equilibrium behavior predicted by these models was taken into account while constraining the present mixture model. However, the model was not fitted to calculated values from PC-SAFT or PSRK because it is not clear which model is more accurate; thus, new experimental data are crucial to further validate and improve the present model for  $\text{SO}_2 + \text{CH}_4$ .

#### 6.3.1.5 Sulfur Dioxide + Chlorine

For the binary-mixture model for  $\text{SO}_2 + \text{Cl}_2$  all four reducing parameters were fitted to the available experimental data. Considering the noxiousness of both pure components, it is surprising that at least two experimental studies were found in the literature. Both of these report VLE data and thus the most essential data for fitting mixture correlations. The data of Wilson and Wilding<sup>282</sup> cover three isotherms 243 K, 273 K, and 323 K; whereas the measurements of Gilot *et al.*<sup>283</sup> were carried out along four isobars 53 kPa, 67 kPa, 80 kPa and 101.325 kPa. The isothermal data of Wilson and Wilding<sup>282</sup> are plotted in  $p,x$  diagrams shown in Figure 6.40. Gilot's isobaric results are depicted in  $T,x$  diagrams presented in Figure 6.41. Both figures additionally include phase boundaries calculated from the present mixture model.

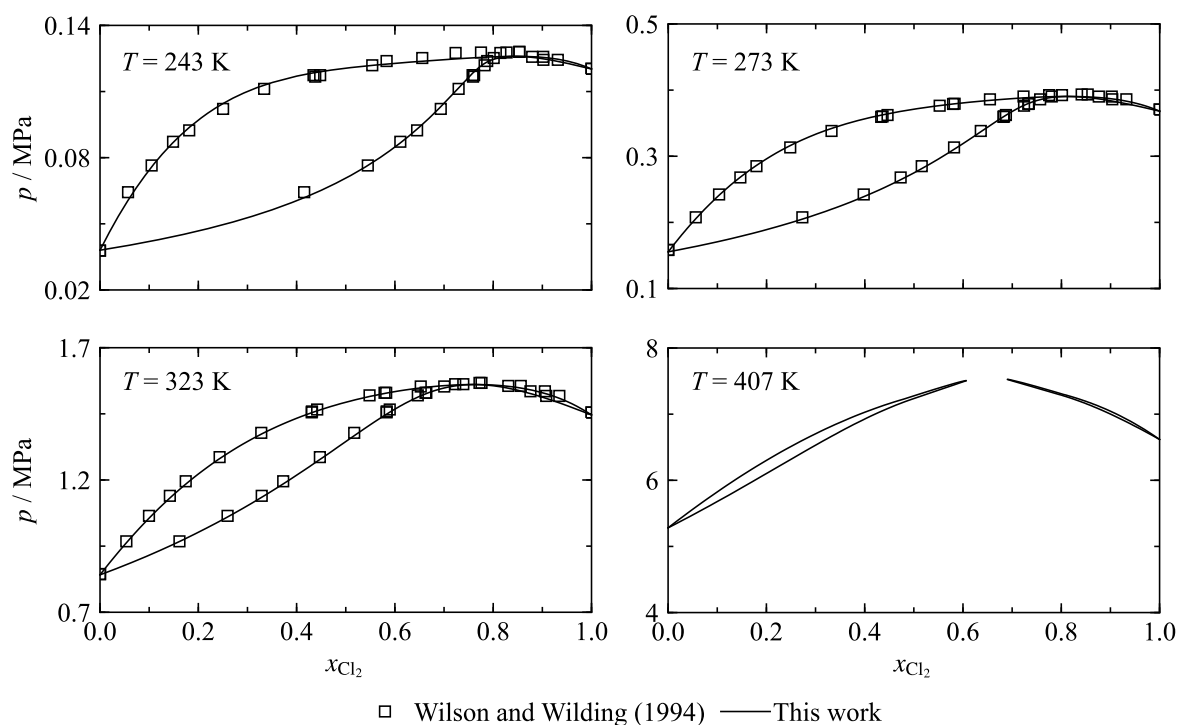


**Figure 6.40** Phase boundaries of the system  $\text{SO}_2 + \text{Cl}_2$  in  $p, x$  diagrams for four isotherms as calculated from the new EOS. For comparisons, the experimental data of Wilson and Wilding<sup>282</sup> are shown, except for the 407 K isotherm that is not experimentally investigated.

It can be seen that the data show an azeotropic mixing behavior, which is often the case for two components with such similar critical parameters ( $T_{c,\text{SO}_2} = 430.64 \text{ K}$ ,  $\rho_{c,\text{SO}_2} = 8.078 \text{ mol dm}^{-3}$ ,  $p_{c,\text{SO}_2} = 7.887 \text{ MPa}$ ;  $T_{c,\text{Cl}_2} = 416.865 \text{ K}$ ,  $\rho_{c,\text{Cl}_2} = 8.06 \text{ mol dm}^{-3}$ ,  $p_{c,\text{Cl}_2} = 7.642 \text{ MPa}$ ), and for which one compound is polar ( $\text{SO}_2$ ) and the other ( $\text{Cl}_2$ ) is not. It is remarkable that the extended corresponding states principle allows for a description of such a complex mixing behavior by fitting only the reducing parameters but no binary specific departure function. The model is in excellent agreement with the experimental data. Extrapolated to temperatures higher than experimentally investigated, it even predicts the split of the azeotropic phase boundaries into two separated VLE regions, which is reported in the literature for chemically similar mixtures such as  $\text{CO}_2 + \text{C}_2\text{H}_6$  (see for instance the experimental study of Ohgaki and Katayama<sup>284</sup>).

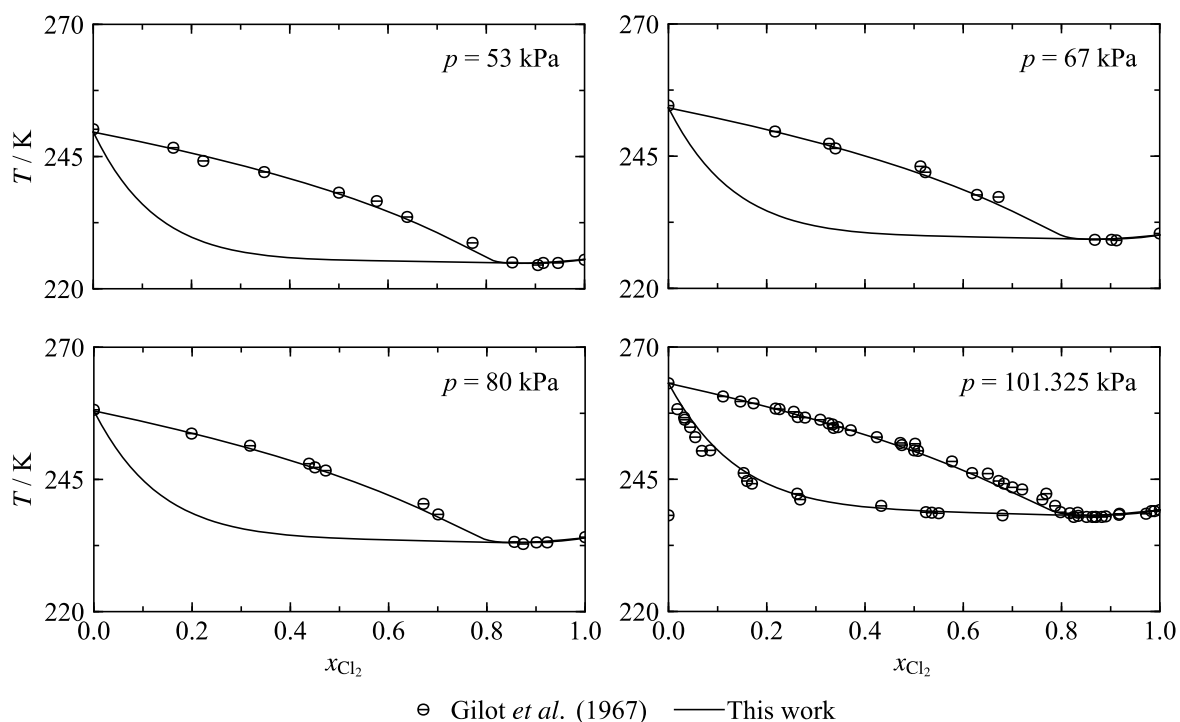


**Figure 6.41** Phase boundaries of the system  $\text{SO}_2 + \text{Cl}_2$  in  $T,x$  diagrams for four isobars as calculated from the new EOS. The experimental data of Gilot *et al.*<sup>283</sup> are shown for comparisons.

Unfortunately, both publications are quite limited with regard to information about experimental uncertainties. Gilot *et al.*<sup>283</sup> do not provide any uncertainties but explain that the dew points at pressures lower than ambient pressure were optically detected through the use of a hygrometer; the dew- and bubble-points measurements at ambient pressure (101.325 kPa) were carried out with an ebulliometer. The analysis of the phase compositions is vaguely described to have been done with chemical analysis and gas chromatography. Wilson and Wilding<sup>282</sup> state some uncertainties in temperature (0.112 K) and pressure (0.67 kPa at  $p \leq 150$  kPa, 1 kPa at  $150 < p / \text{kPa} \leq 400$  kPa, and 0.25 % at  $p > 400$  kPa) but provide no uncertainties in the compositions of the coexisting phases. In the description of the experimental procedure, the authors explain that they filled the measuring cell with a known amount of the first component (most likely  $\text{SO}_2$ ) and measured its vapor pressure. Then, increments of the second component were filled in, the mixture was homogenized, and the pressure of the equilibrium state was measured. The measurements at saturation pressures below 150 kPa (at 243 K) were performed in a glass cell with a magnetic stirrer. The pressure was measured with a mercury manometer. The other measurements were carried out in a stainless steel cell whose content had to be stirred manually to “ensure” homogeneous mixing. In this set-up, saturation pressures were measured using pressure gauges that were calibrated with a dead-weight piston gauge. Both experimental procedures seem to be subject to quite large uncertainties in composition. Especially the manual stirring procedure for the measurements at higher pressures, probably did not ensure a proper mixing of the two components. In addition, the authors write about a degassing process after filling the cell with both components. If the sample was not carefully homogenized, this must have





represented within 0.25 % ( $\Delta T < 0.8$  K), which underlines the overall impression that this work is more reliable.

For the sake of completeness, deviations between the experimentally investigated mixture compositions and calculated phase-equilibrium compositions at given temperature and pressure are presented in Figure 6.44.

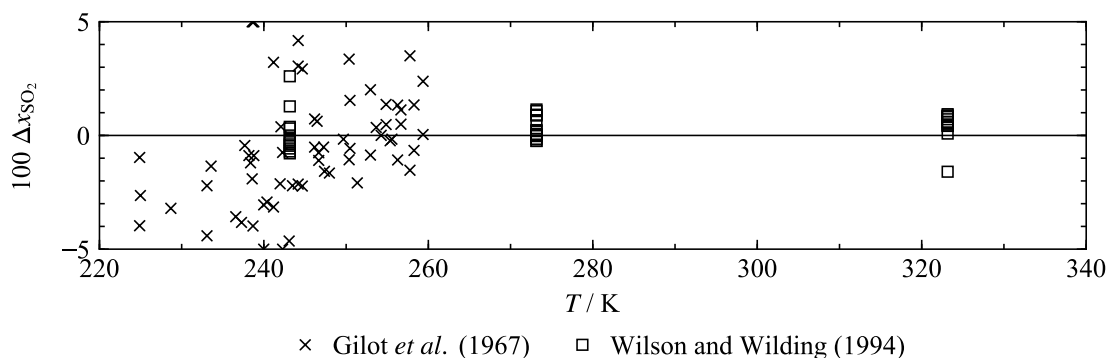


**Figure 6.44** Relative deviations  $\Delta x_{\text{SO}_2} = (x_{\text{SO}_2, \text{exp}} - x_{\text{SO}_2, \text{calc}})$  between the available experimental VLE data for the system  $\text{SO}_2 + \text{Cl}_2$  and results calculated from the new EOS as a function of temperature.

It is challenging to determine uncertainties of calculated VLE data from the deviations plotted in Figures 6.42 to 6.44, because both experimental works do not provide combined experimental uncertainties. As mentioned above, Wilson and Wilding<sup>282</sup> at least state uncertainties of their temperature and pressure measurements. Considering these uncertainties and ignoring a potentially large additional uncertainty in the composition measurement, expanded combined uncertainties were calculated following the law of uncertainty propagation. Because the sensitivity of the composition with respect to temperature and pressure changes significantly along the phase boundary, the calculated uncertainties vary depending on the location of the VLE points. The average of the experimental uncertainties in bubble and dew points is about 1.2 mol% and 0.7 mol%, respectively. Taking into account an unknown additional uncertainty in composition and the deviations plotted in Figure 6.44, the conservatively estimated uncertainty of VLE data calculated from the EOS with respect to composition is 2 mol% between 240 K and 325 K. At lower temperatures, between 225 K and 240 K, the uncertainty increases to 5 mol% as estimated based on comparisons with the data of Gilot *et al.*<sup>283</sup>

Considering the deviations in saturation temperature and pressure, the uncertainty in saturation temperature is estimated to be 0.75 % ( $\Delta T < 2.4$  K) at pressures up to 1.6 MPa and temperatures between 225 K and 325 K; saturation pressures in the same temperature range are expected to have a maximum uncertainty of 5 %.

### 6.3.1.6 Sulfur Dioxide + Hydrogen Chloride

To represent the available data for the system  $\text{SO}_2 + \text{HCl}$  it was sufficient to fit two out of four reducing parameters,  $\beta_T$  and  $\gamma_T$ ; thus, only the temperature-reducing function was fitted.

For the density-reducing function, the quadratic combining rule of Lorentz-Berthelot was applied by setting  $\beta_v$  and  $\gamma_v$  to unity. The experimental database is limited to the VLE measurements of Wilson and Wilding<sup>282</sup> that were already discussed in the previous section. For this system, their work consists of results for two isotherms, 203 K and 273 K. The data situation has been improved by molecular-simulation data of Köster and Vrabec<sup>280</sup> including VLE data and homogeneous densities. Köster and Vrabec<sup>280</sup> used the experimental data of Wilson and Wilding<sup>282</sup> to adjust the binary mixing parameter that considers interactions between unlike molecules. The molecular-simulation data, consequently, have to be interpreted as an extension of the experimental data and not as an independent comparative source of data. The experimental and simulated VLE data are shown in Figure 6.45 together with the phase boundaries calculated from the mixture model.

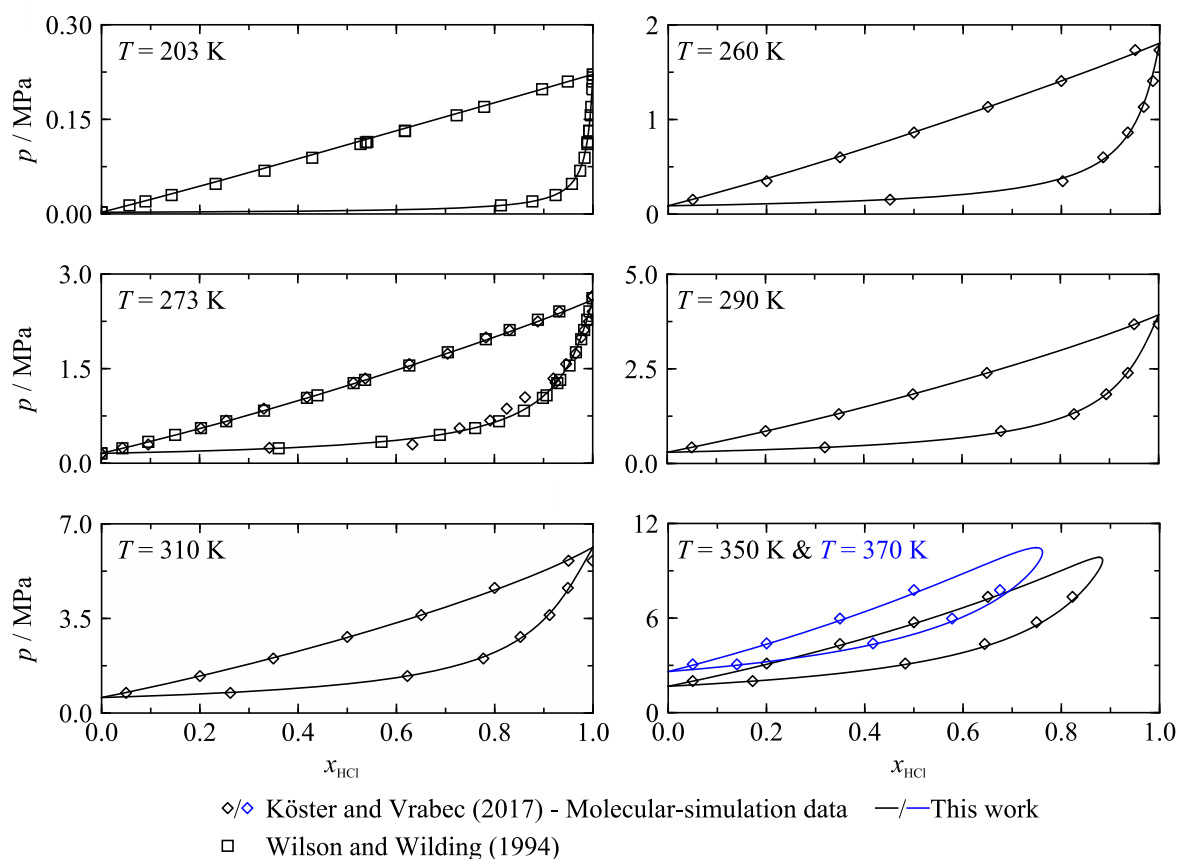


**Figure 6.45** Phase boundaries of the system  $\text{SO}_2 + \text{HCl}$  in  $p,x$  diagrams for six isotherms as calculated from the new EOS. The experimental data of Wilson and Wilding<sup>282</sup> and the molecular-simulation data of Köster and Vrabec<sup>280</sup> are shown for comparisons.

During the fitting process, it was prioritized to describe the experimental data at 203 K and 273 K. After this was ensured, the fitted data were carefully extended to higher temperatures by additionally fitting the molecular-simulation data. At a temperature of 273 K, these simulated values can be validated with the experimental data. The  $p,x$  diagram given in Figure 6.45 emphasizes a close agreement between both data sets, except for a section of the dew line between about 65 mol% and 90 mol% HCl. The mixture model accurately describes

the dew and bubble points over the whole temperature range of the data. Some higher deviations occur at 370 K and elevated saturation pressures. Deviations of the data from calculated values are shown in Figure 6.46 (with respect to saturation pressure) and Figure 6.47 (with respect to composition).

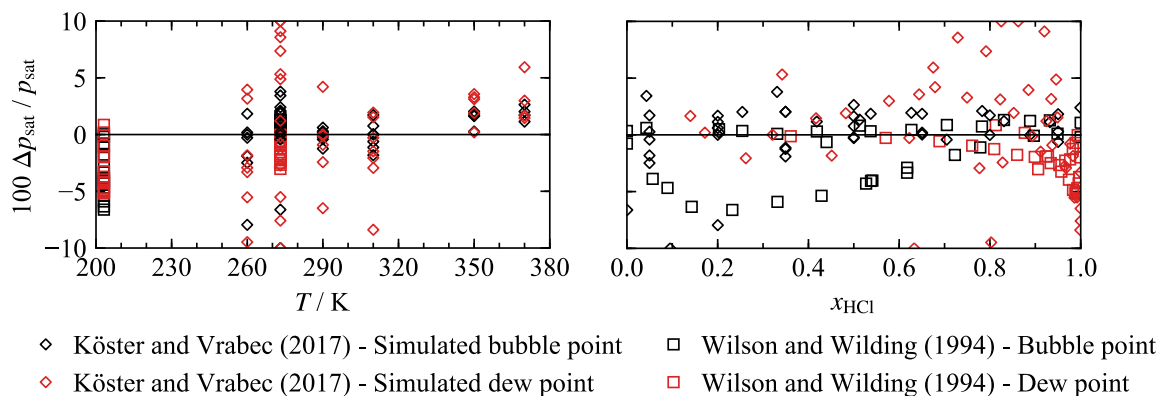


**Figure 6.46** Relative deviations  $\Delta p_{\text{sat}} = (p_{\text{sat,data}} - p_{\text{sat,calc}}) / p_{\text{sat,data}}$  between the available VLE data for the system  $\text{SO}_2 + \text{HCl}$  and results calculated from the new EOS as a function of temperature (left) and composition (right).

Figure 6.46 shows that the mixture model describes most of the experimental data of Wilson and Wilding<sup>282</sup> within 5 %, except for a few (mostly bubble) points at 203 K. The deviations of the molecular-simulation data of Köster and Vrabec<sup>280</sup> are of the same order of magnitude, which is expected, since they are partly based on the experimental data. Most of the higher deviations occur along the above mentioned section of the dew line at 273 K. Based on these deviations (and by ignoring a few higher deviations) the estimated uncertainty of calculated saturation pressures between 200 K and 370 K is 5 %.

As usual the deviations in compositions are lower than in saturation pressure. As illustrated in Figure 6.46, the majority of the data are represented within 3 mol%. The maximum of the calculated combined uncertainty of the experimental data of Wilson and Wilding<sup>282</sup> is 1.3 mol%. This value considers the given experimental uncertainties in temperature and pressure (see Sec. 6.3.1.5) but no uncertainty in composition. The estimated uncertainty of calculated phase-equilibrium compositions between 200 K and 370 K is consequently 3 mol%. Deviations higher than this uncertainty estimate occur for the simulated dew points at 273 K, where the model was fitted to the experimental data that exhibits a slight offset from the simulated values.

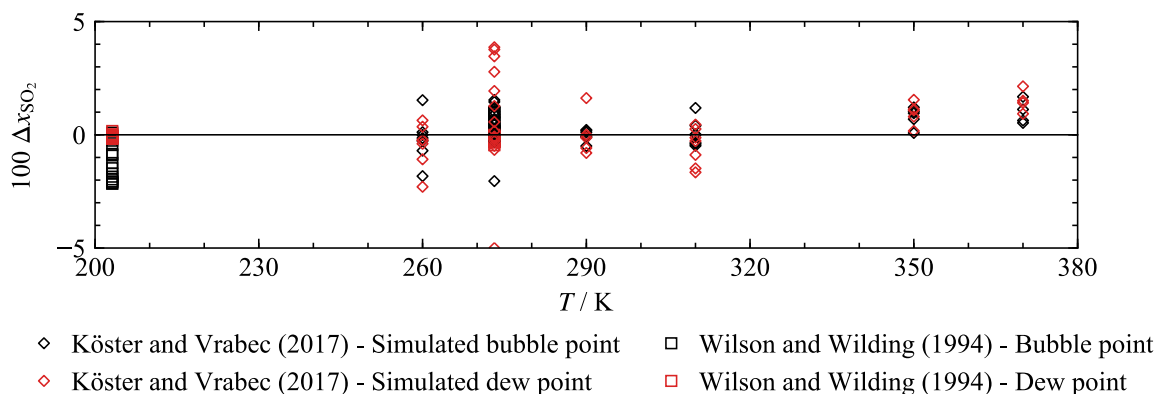


**Figure 6.47** Deviations  $\Delta x_{\text{SO}_2} = (x_{\text{SO}_2, \text{data}} - x_{\text{SO}_2, \text{calc}})$  between the available VLE data for the system  $\text{SO}_2 + \text{HCl}$  and results calculated from the new EOS as a function of temperature.

No experimental data for homogeneous densities are available in the literature, but again Köster and Vrabec<sup>280</sup> simulated liquid and gas-phase data over comparably wide ranges in temperature, pressure and composition. Deviations of these data from calculated values are shown in Figure 6.48.

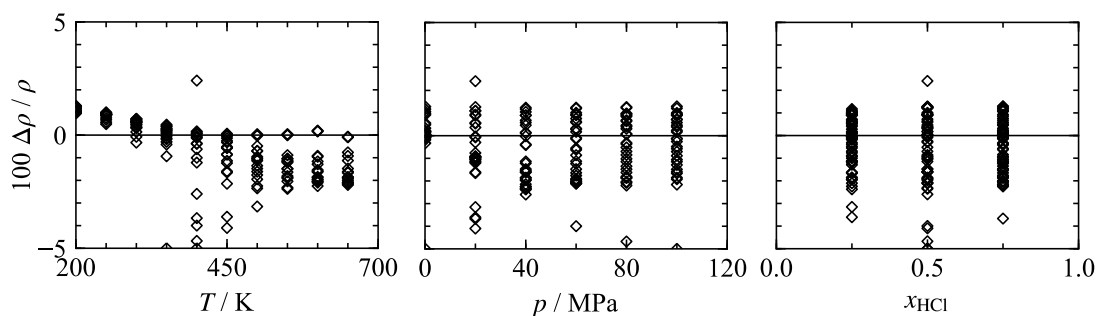


**Figure 6.48** Relative deviations  $\Delta \rho / \rho = (\rho_{\text{data}} - \rho_{\text{calc}}) / \rho_{\text{data}}$  of the simulated density data of Köster and Vrabec<sup>280</sup> for the system  $\text{SO}_2 + \text{HCl}$  from the new EOS as a function of temperature (left), pressure (middle), and composition (right).

Except for very few points, the mixture model describes the data within deviations of 3 %. This is consequently a reasonable estimate for calculated homogeneous densities at temperature between 200 K and 650 K, pressures up 100 MPa, and HCl contents between  $0.25 \leq x_{\text{HCl}} < 0.75$ . In conclusion, it can be said that the quality of the model for  $\text{SO}_2 + \text{HCl}$  was significantly improved by the molecular-simulation data.

### 6.3.1.7 Sulfur Dioxide + DEA and Sulfur Dioxide + MEA

For the system  $\text{SO}_2 + \text{DEA}$ , the two parameters  $\beta_T$  and  $\gamma_T$  of the temperature-reducing function were fitted to the very few experimental data. The parameters of the density-reducing function  $\beta_v$  and  $\gamma_v$  were not adjusted but set to unity. This set of parameters was adopted for the system  $\text{SO}_2 + \text{MEA}$  for which no experimental data are available.

The only data set available for  $\text{SO}_2 + \text{DEA}$  was published by Li *et al.*<sup>285</sup> This study reports six bubble points at ambient pressure (0.101 325 MPa). The compositions of the coexisting dew points are not given. The data of Li *et al.*<sup>285</sup> were obtained through a synthetic measurement technique in which bubble-point temperatures of prepared mixtures (with

known compositions) are identified. The few measured points are plotted in a  $T,x$  diagram shown in the left panel of Figure 6.49. Deviations with respect to the saturation temperature and bubble-point composition between the data and values calculated from the mixture model are shown in the right panels. The model accurately describes the data. All deviations with respect to temperature are within 0.4 % ( $0.2 < \Delta T / \text{K} < 1$ ); the deviations with respect to composition are within 0.6 mol%. The data are so limited that these deviations do not enable a reliable uncertainty estimate for calculated VLE data. Nevertheless, the comparisons presented here highlight that the model allows for a reasonable description of the phase-boundaries which is considered sufficient for the description of CCS-relevant mixture that usually contain only few ppm of the amines used in the capturing process.

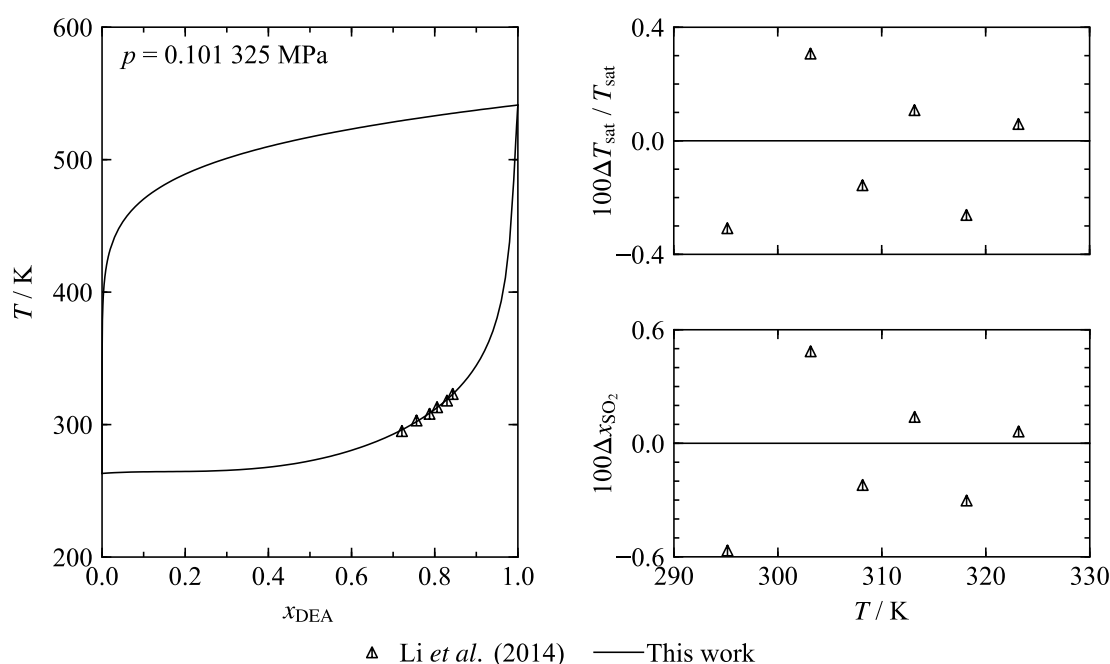


**Figure 6.49** Left: Phase boundaries of the system  $\text{SO}_2 + \text{DEA}$  in  $T,x$  diagrams at 101.325 kPa as calculated from the new EOS. The experimental data of Li *et al.*<sup>285</sup> are shown for comparisons. Right: Relative deviations  $\Delta T_{\text{sat}} = (T_{\text{sat,exp}} - T_{\text{sat,calc}}) / T_{\text{sat,exp}}$  (top) and deviations  $\Delta x_{\text{SO}_2} = (x_{\text{SO}_2,\text{exp}} - x_{\text{SO}_2,\text{calc}})$  (right) between the data of Li *et al.*<sup>285</sup> and results calculated from the new EOS as a function of temperature.

Because no experimental data for the binary system  $\text{SO}_2 + \text{MEA}$  were found in literature, the systems was first described with the simple linear or quadratic combining rules. Test calculations with the resulting mixture models revealed considerable numerical problems. The fitting processes of the models for  $\text{MEA} + \text{H}_2\text{O}$  and  $\text{DEA} + \text{H}_2\text{O}$  suggested that parameter sets for one of these amines with another component are good starting points for fitting the other amine with the same second component (see Sec. 6.3.2.1). Since no further fitting of the parameters for  $\text{SO}_2 + \text{MEA}$  was possible, the parameters for  $\text{SO}_2 + \text{DEA}$  were completely adopted. The resulting model for  $\text{SO}_2 + \text{MEA}$  cannot be quantitatively validated, but at least allows for numerically stable equilibrium calculations over a relatively large temperature range. Calculated  $p,x$  diagrams for some exemplary isotherms are shown in Figure 6.50.

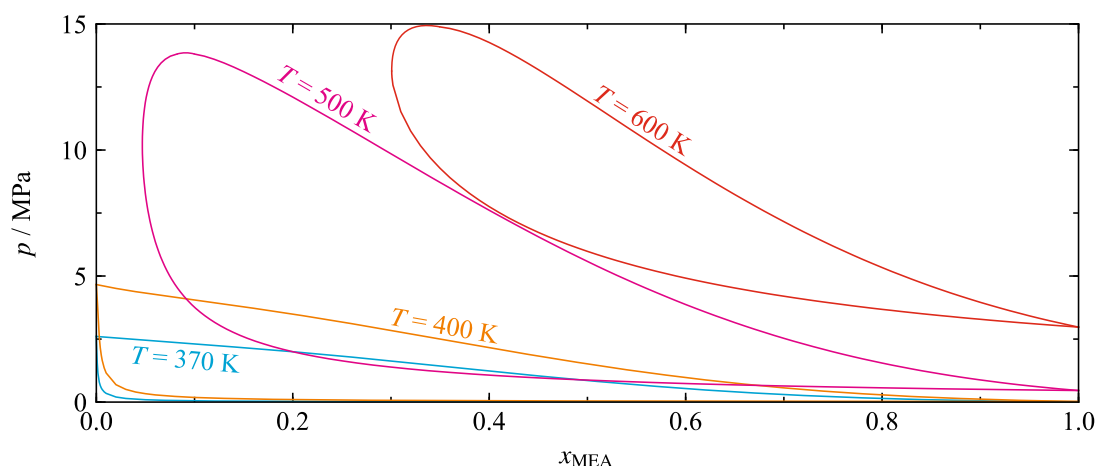


**Figure 6.50** Phase boundaries of the system  $\text{SO}_2 + \text{MEA}$  in a  $p,x$  diagram for four isotherms as calculated from the new EOS.

### 6.3.1.8 Sulfur Dioxide + Water

The relevance of the system  $\text{SO}_2 + \text{H}_2\text{O}$  was already pointed out in the introduction to Sec. 6.3.1. Aside from  $\text{H}_2\text{O} + \text{CH}_4$  and  $\text{H}_2\text{O} + \text{H}_2\text{S}$ , it is the binary system with the most complex mixing behavior considered in this work. Although the solubility of  $\text{SO}_2$  in water is higher than for many other gases, it is still limited. Phase equilibria mostly consist of one phase very rich in  $\text{SO}_2$  and another phase very rich in  $\text{H}_2\text{O}$ . Below the critical temperature of  $\text{SO}_2$  ( $T_{c,\text{SO}_2} = 430.64 \text{ K}$ ) and above the normal-melting-point temperature of water, the  $\text{SO}_2$ -rich phase might undergo a phase transition from vapor to liquid with increasing pressure. This means that for temperatures above the normal-melting-point temperature of water and below the critical temperature of  $\text{SO}_2$ , the binary system can split into a vapor-liquid equilibrium or at higher pressures into a liquid-liquid equilibrium (LLE). These two equilibrium states are separated by a three-phase line along which a  $\text{SO}_2$ -rich vapor, a  $\text{H}_2\text{O}$ -rich liquid, and a  $\text{SO}_2$ -rich liquid are in equilibrium (VLLE). The complexity of the phase equilibria is further increased by the possible formation of solid phases at low temperatures. First of all, at temperatures below the normal melting point of water, the existence of ice has to be considered. In addition,  $\text{SO}_2$  can form a hydrate phase in water as reported in the work of van Berkum and Diepen.<sup>286</sup> Because Helmholtz-explicit mixture models as developed in this work are restricted to the description of fluid phases, the binary model for  $\text{SO}_2 + \text{H}_2\text{O}$  does not allow the calculation of solid-phase properties. However, the algorithms implemented in the software package TREND<sup>22</sup> enable to predict the formation of ice and hydrates. The software additionally includes special EOS for these solid phases; however,  $\text{SO}_2$ -hydrates are currently not implemented in TREND.

The limited but compared to other gaseous components relatively good solubility of  $\text{SO}_2$  in water is influenced by a chemical reaction between both components, the formation of sulfurous acid ( $\text{H}_2\text{SO}_3$ ) an intermediate species in the formation of sulfuric acid ( $\text{H}_2\text{SO}_4$ ). This reaction increases the solubility of  $\text{SO}_2$  and water. So far, the functional form of the Helmholtz-explicit EOS is restricted to the description of the physical mixing behavior. It

does not include special terms that take chemical reactions into account. As discussed in Sec. 6.5.2, future improvements of the model for CCS-relevant mixtures will require such modifications of the functional form. Nevertheless, it is not entirely correct to say that chemical reactions are not considered in the mixture model, because the parameters are fitted to data that were influenced by chemical reactions during the experiment. For  $\text{SO}_2 + \text{H}_2\text{O}$ , it should further be noted that the composition of the chemical equilibrium state is clearly on the side of the educts; thus, only a small amount of sulfurous acid is formed.<sup>287</sup>

Because the available experimental data for  $\text{SO}_2 + \text{H}_2\text{O}$  did not allow for the development of a binary specific departure function, only the four parameters of the reducing functions were adjusted to the data. The validation of the binary model is therefore particularly interesting, since the mixing behavior is expected to deviate considerably from the corresponding states principle (see Sec. 4). Larger deviations from corresponding states normally require a strong departure function in order to describe the experimental data.

Quantitatively, the system  $\text{SO}_2 + \text{H}_2\text{O}$  is the experimentally best investigated system to be discussed in Sec. 6.3. There is a large number of references providing VLE data. In addition, one data set for LLE and two data sets with saturated-liquid densities were found. However, none of the experimental studies of the VLE region present results for both coexisting phases. All data sets only give information on the  $\text{SO}_2$ -solubility in water, which is equivalent to the composition of the saturated-liquid phase in VLE. In addition, most of the data are expected to have quite large experimental uncertainties. In many works, it is also not clearly specified whether the reported values correspond to the amount of  $\text{SO}_2$  in the mixture or in pure water, which leads to different compositions of the saturated liquid. Finally, many publications present solubilities in terms of partial pressures of  $\text{SO}_2$  without further specifications of the total pressure or composition. The experimental data shown in this section are only a selection of the data found in the literature. Many additional publications were omitted because they do not provide any data useful for fitting.

Selected experimental solubility data along exemplary isotherms are shown in Figure 6.51. VLE and LLE phase boundaries calculated from the mixture model are plotted for comparisons. The pressure and the compositions along the three-phase lines (VLLE) were calculated from the model with the three-phase-flash algorithms implemented in TREND.<sup>22</sup> No reliable literature data were found for these three-phase equilibria. The available LLE data are not depicted, because for the selected isotherms the data are at much higher pressures than shown. Besides, the LLE experiments were carried out at constant composition; thus, there are rarely more than two or three points at the same temperature.



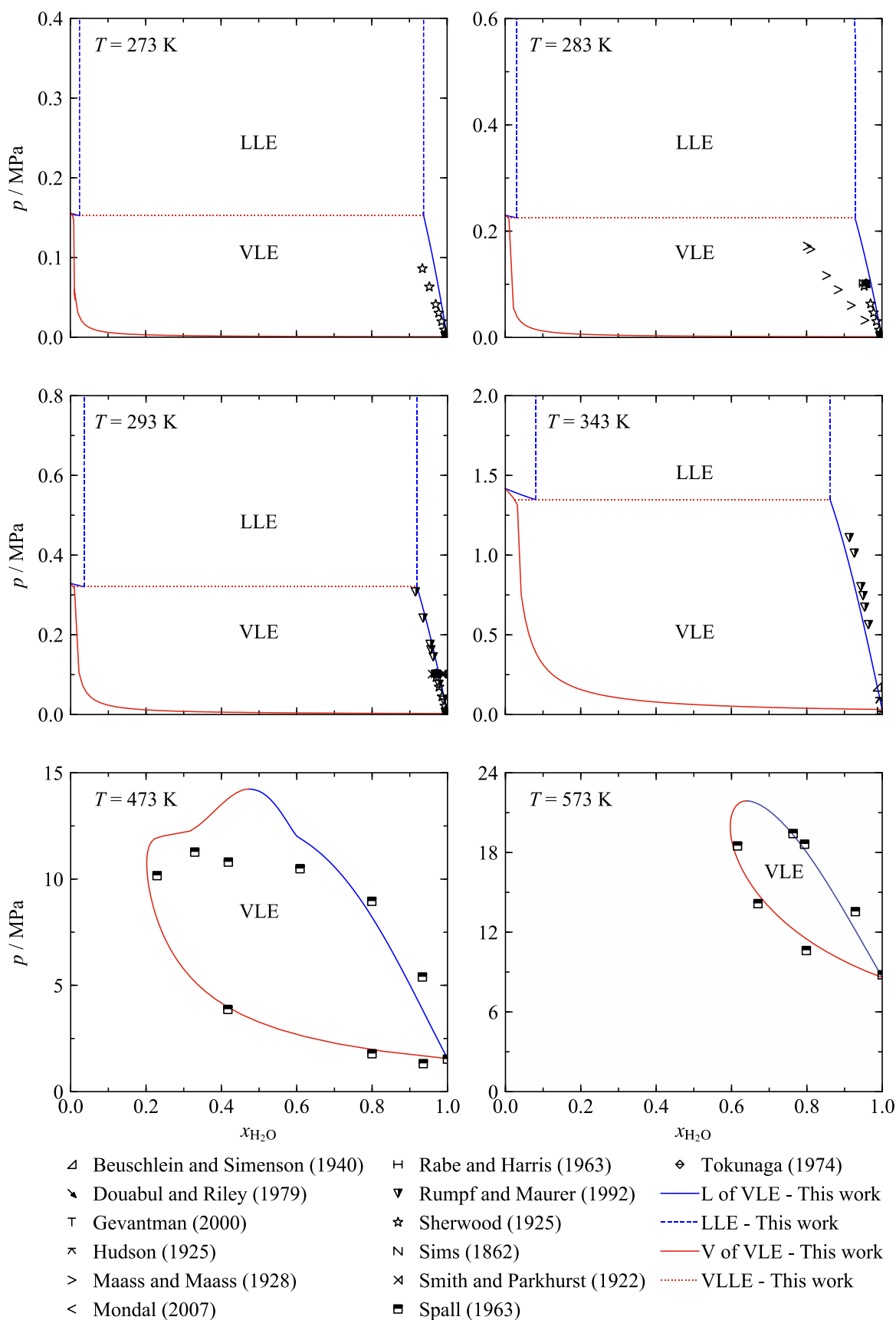


**Figure 6.51** Phase boundaries of the system  $\text{SO}_2 + \text{H}_2\text{O}$  in  $p, x$  diagrams for selected isotherms as calculated from the new EOS. Selected experimental data are shown for comparisons.

The complex mixing behavior of this system is evident in Figure 6.51. For the four lowest isotherms ( $T \leq 343$  K), the model predicts the characteristic wide composition range of the two-phase region with a shift from VLE to LLE at increasing pressures. As already mentioned, only the shape of the VLE bubble line can be validated by comparisons with experimental results. Nevertheless, the mixing behavior is qualitatively confirmed by phase diagrams shown in the work of van Berkum and Diepen,<sup>286</sup> who also provide experimental results that prove the existence of the LLE region and VLLE line. The two highest isotherms presented in Figure 6.51 are above the critical temperature of pure  $\text{SO}_2$  ( $T_{c,\text{SO}_2} = 430.64$  K). For these isotherms, the model predicts only a VLE region; however, some additional comments should be made on  $p,x$  diagram at 473 K. For this temperature, the model predicts extreme changes in slope and curvature of both phase boundaries in the critical region. There is no experimental evidence for this behavior, but it is discussed in various publications on mixtures of  $\text{CO}_2$  with alcohols, for example in the work of Hsieh *et al.*<sup>288</sup> The behavior is considered to be a “relic” of the LLE at lower temperatures. In fact, Hsieh *et al.*<sup>288</sup> label similar areas of the two-phase region as “LLE”. This labeling is based on the evaluation of the curvature of the isotherm:  $(\partial p / \partial \rho)_{T,x} < 0$  for a gas phase,  $(\partial p / \partial \rho)_{T,x} > 0$  for a liquid phase. If one component is supercritical, this distinction seems arguable because no three-phase line can be calculated between the VLE and the so-called LLE.

The present mixture model used to calculate the phase boundaries shown in Figure 6.51 is a compromise between an accurate description of the available data at  $T < T_{c,\text{SO}_2}$  and a qualitatively correct description at higher temperatures. If the model was more intensively fitted to the high-temperature data, the representation of the phase boundaries at low temperatures was worsened, and vice versa. This issue was also discussed by Gernert and Span<sup>2</sup> for the similarly complex system  $\text{CO}_2 + \text{H}_2\text{O}$ . It should also be mentioned that the high-temperature data for  $\text{SO}_2 + \text{H}_2\text{O}$  by Spall<sup>289</sup> cannot be considered very accurate. In addition, the experimental values are not available any more. The depicted data were graphically extracted from low-quality phase diagrams shown in the publication. At low temperatures, the most valuable data sets were measured by Sherwood<sup>290</sup> and Rumpf and Maurer.<sup>291</sup> But also these data sets are not entirely consistent. At a temperature of 273 K (approximately the normal melting point of water), the data of Sherwood indicate a higher  $\text{SO}_2$ -solubility than calculated from the model. Further fitting of the model lead to larger deviations from the data of Rumpf and Maurer<sup>291</sup> and other references at higher temperature (see for example 293 K and 343 K).

Deviations between calculated phase-equilibrium compositions and selected experimental data are shown in Figure 6.52.

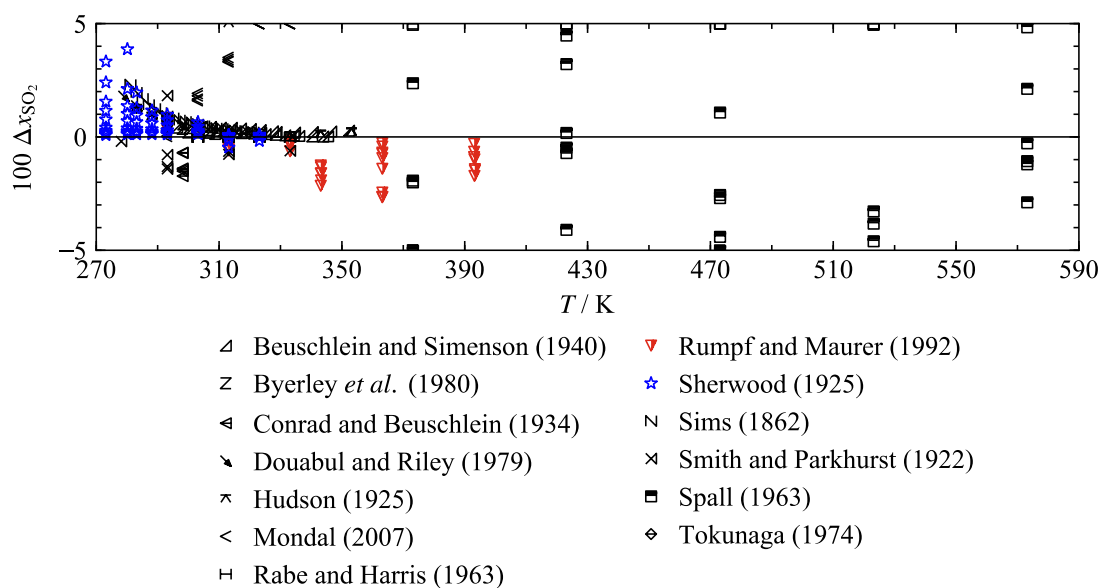


**Figure 6.52** Deviations  $\Delta x_{\text{SO}_2} = (x_{\text{SO}_2, \text{exp}} - x_{\text{SO}_2, \text{calc}})$  between selected experimental VLE data for the system  $\text{SO}_2 + \text{H}_2\text{O}$  and results calculated from the new EOS as a function of temperature.

Most of the data at temperatures between 273 K and 393 K are represented with deviations below 3 mol%. At higher temperatures, the model deviates by up to 5 mol% from the data of Spall.<sup>289</sup> Unfortunately, none of the data sets presented in Figure 6.52 were published with reliable information on the experimental uncertainties. The oldest works, published between 1862 and 1940, do not provide any uncertainties, whereas some of the newer works, at least, state uncertainties in saturation pressure. Comparisons in saturation pressure are not discussed here and are in general not meaningful with regard to the mixing behavior shown in Figure 6.51. The steep slope of the saturated-liquid line at given temperature and composition leads to extremely large deviations in pressure, if the calculated VLE composition only slightly deviates from the experimental result. The uncertainties of VLE compositions calculated from the mixture model are therefore based on the deviations shown above. The uncertainty in saturated-liquid compositions at temperatures from the normal-melting point of water to 390 K is 3 mol%. Between 390 K and 570 K, the uncertainty increases to 5 mol%. The uncertainty in calculated dew-point compositions cannot be estimated because no experimental data were found in the literature.

Densities of the saturated liquid were measured by Campbell and Maass<sup>292</sup> and Beuschlein and Simenson.<sup>293</sup> The work of Beuschlein and Simenson is limited to one single isotherm, 296 K, whereas the data of Campbell and Maass cover temperatures from 293 K to 383 K. The compositions of the investigated solutions range from approximately 95 mol% to almost 99.9 mol%  $\text{H}_2\text{O}$ . Deviations between the data and results obtained from the mixture model are plotted in Figure 6.53.

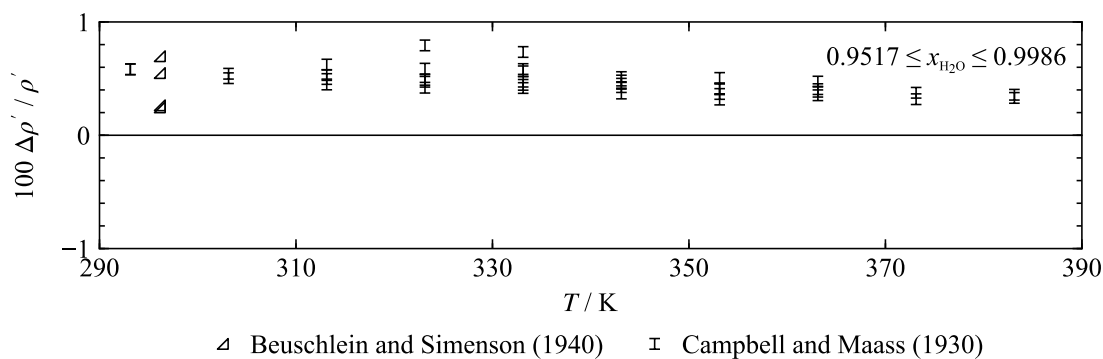


**Figure 6.53** Relative deviations  $\Delta\rho/\rho = (\rho_{\text{exp}} - \rho_{\text{calc}}) / \rho_{\text{exp}}$  of experimental saturated-liquid density data for the system  $\text{SO}_2 + \text{H}_2\text{O}$  from the new EOS as a function of temperature.

The maximum deviation between the model and the data is 0.8 %. Both publications do not provide any useful information about experimental uncertainties. Because the investigated samples are almost pure water, the uncertainty of saturated-liquid densities calculated from the reference EOS for water (IAPWS-95) by Wagner and Pruss<sup>29</sup> can be considered to estimate the experimental uncertainty of the data shown in Figure 6.53. The maximum uncertainty stated by IAPWS<sup>88</sup> is 0.003 %, which is far below the plotted deviations. The deviations of up to 0.8 % are consequently not caused by inaccuracies of the dominating pure-fluid EOS for water; thus, it can be assumed that the experimental uncertainty of the data is similar to the deviations. The uncertainty of calculated saturated-liquid densities between 295 K and 380 K is consequently estimated to be 1 %.

The phase equilibria of  $\text{SO}_2 + \text{H}_2\text{O}$  were thoroughly investigated by van Berkum and Diepen.<sup>286</sup> Aside from different equilibria including hydrates, the authors also measured saturation pressures along a “demixing curve” at given temperature and composition. This “demixing curve” is equivalent to the  $\text{H}_2\text{O}$ -rich saturated liquid of the LLE. The data range from just above the normal melting point of water to 390 K at pressures up to 345 MPa. Because the data only provide information on one phase of the LLE, they could not directly be used to fit the mixture model. The non-linear fitting algorithm (see Sec. 4) only allows fitting the model to complete LLE data sets. In order to enable, at least, a qualitatively correct representation of the LLE region, the missing phase composition was iteratively calculated from preliminary fits of the mixture model. These calculations were carried out with the phase-equilibrium algorithms implemented in TREND.<sup>22</sup> This method allowed for a numerically stable fit and improved the description of the liquid phase measured by van Berkum and Diepen.<sup>286</sup> Deviations between these data and values calculated from the mixture model are shown in Figure 6.54.

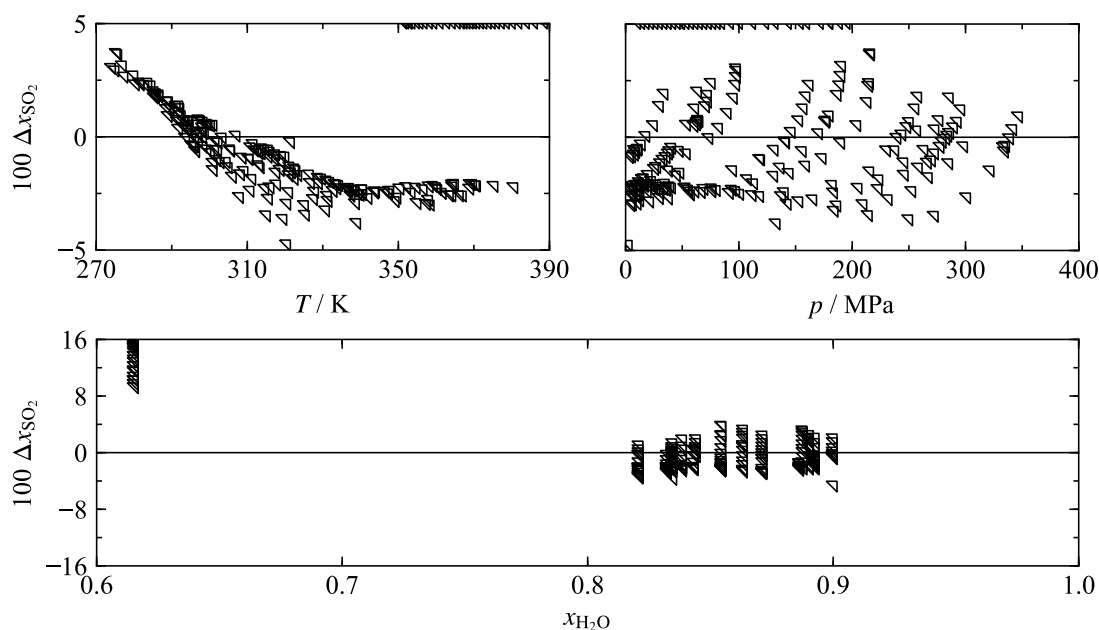


**Figure 6.54** Deviations  $\Delta x_{\text{SO}_2} = (x_{\text{SO}_2,\text{exp}} - x_{\text{SO}_2,\text{calc}})$  between the experimental LLE data of van Berkum and Diepen<sup>286</sup> for the system  $\text{SO}_2 + \text{H}_2\text{O}$  and results calculated from the new EOS as a function of temperature (top left), pressure (top right), and composition (bottom). The measurements were carried out at constant composition.

The model represents the data with a maximum deviation of 5 mol%, except for the saturated liquid with the highest  $\text{SO}_2$  content ( $x_{\text{H}_2\text{O}} = 0.6147$ ). Because no comparative data are available and because the fitting process was complicated due to the missing information on the coexisting phase, the deviations shown in Figure 6.54 should not be used to estimate the uncertainty of calculated LLE data. Nevertheless, the deviations indicate that the model enables a reliable description of the  $\text{H}_2\text{O}$ -rich liquid in LLE.

Calculating the  $p,x$  diagrams shown in Figure 6.51 yielded some interesting insights, which justify an additional brief excursus on the complex phase equilibria of this mixture. Tracing the phase boundaries at  $T < T_{c,\text{SO}_2}$  with the VLE algorithms in TREND<sup>22</sup> yields results that seem to be unreasonable. Comparative calculations were therefore made with PSRK and PC-SAFT. For PC-SAFT, no binary interaction parameter was implemented.; whereas for PSRK, four (out of six adjustable) interaction parameters of Gmehling *et al.*<sup>199</sup> were used. In addition, the parameters for  $\text{SO}_2 + \text{H}_2\text{O}$  were adopted for  $\text{SO}_2 + \text{D}_2\text{O}$ . Then, an analogous  $p,x$  diagram was calculated for  $\text{SO}_2 + \text{D}_2\text{O}$  using the pure-fluid EOS presented in Sec. 5.1. This calculation should clarify whether the shape of the phase boundaries for  $\text{SO}_2 + \text{H}_2\text{O}$  is negatively influenced by the numerically complex functional form of the IAPWS-95 formulation for  $\text{H}_2\text{O}$ . The calculated phase boundaries at 373 K are shown in a  $p,x$  diagram in Figure 6.55.

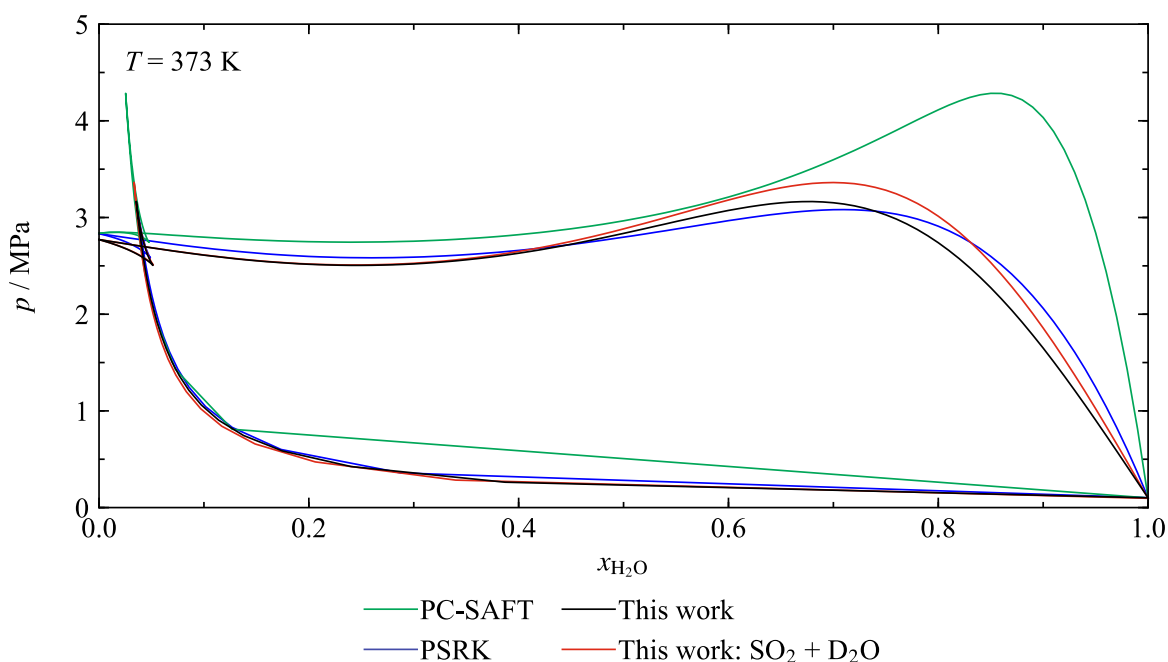


**Figure 6.55** Phase boundaries of the system  $\text{SO}_2 + \text{H}_2\text{O}$  in a  $p, x$  diagram at 373 K as calculated from the new EOS, PC-SAFT, PSRK. Additionally, phase boundaries for the system  $\text{SO}_2 + \text{D}_2\text{O}$  (with reducing parameters adopted from the model for  $\text{SO}_2 + \text{H}_2\text{O}$ ) are shown for comparisons. The phase boundaries were calculated by algorithms tracing the VLE region. In some areas of the pressure and composition range, the system is expected to split in a LLE instead of the shown VLE. The shape of dew line calculated from PC-SAFT at low saturation pressures is not physically correct but results from numerical problems during the calculation.

All models exhibit qualitatively the same behavior: a maximum along the bubble line as well as a sharp peak and a self-crossing of the dew line. Apparently, this behavior is not a result of bad fitting, because it is confirmed by all models. The calculated phase boundaries correspond to mathematically correct VLE solutions, even though they might not be experimentally accessible. In order to further investigate these phase equilibria, the three-phase line (VLLE) that separates the VLE from LLE region was calculated in TREND.<sup>22</sup> Additional flash calculations were carried out at two saturation pressures above the VLLE line (2.65 MPa and 3 MPa) and one saturation pressure below (2.515 MPa). Out of the two calculations above the VLE line, one was carried out below the saturation pressure of pure  $\text{SO}_2$  ( $p_{\text{sat}, \text{SO}_2}(373 \text{ K}) = 2.77 \text{ MPa}$ ) and one above. At a pressure of 3 MPa, only a LLE solution is thermodynamically “stable”; however, depending on the bulk composition and the used composition estimates for the coexisting phases, the phase-equilibrium routines yield two additional VLE solutions. At 2.65 MPa, both a VLE and a LLE solution are thermodynamically “stable” depending on the bulk composition. Again, the algorithms find two additional VLE solutions. Below the VLLE line, at 2.515 MPa, only the VLE solution consisting of a  $\text{SO}_2$ -rich vapor phase and a  $\text{H}_2\text{O}$ -rich liquid phase is thermodynamically “stable”; nevertheless, two other VLE solutions are found. Both of these solutions exhibit a comparably high concentration of  $\text{SO}_2$  in the liquid phase. The results of these phase-equilibrium calculations are illustrated in Figure 6.56.

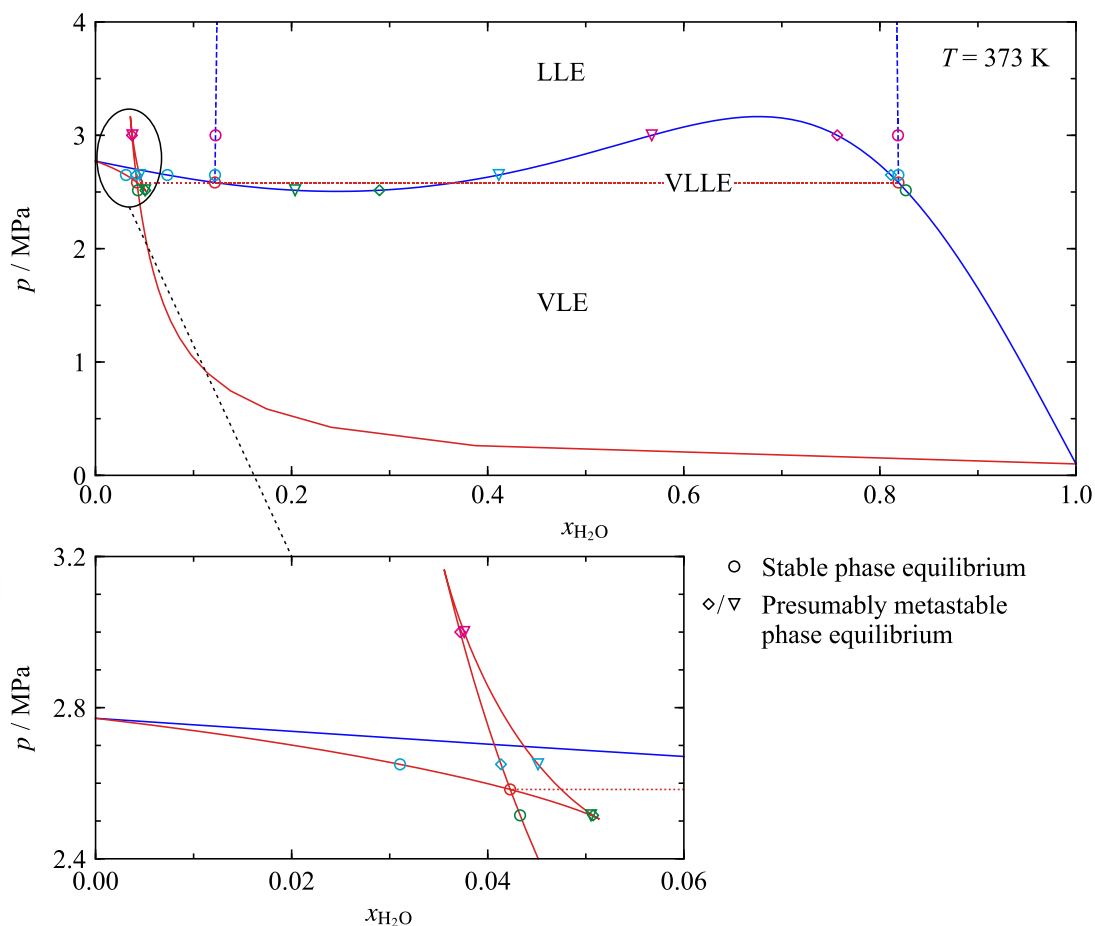


**Figure 6.56** Phase boundaries of the system  $\text{SO}_2 + \text{H}_2\text{O}$  in a  $p,x$  diagram at 373 K as calculated from the new EOS. The three-phase line (VLLE) separating the LLE and the VLE region was also calculated from the EOS. Additional phase-equilibrium calculations were carried out at two saturation pressures above the VLLE pressure and one saturation pressure below the VLLE pressure; both stable and presumably metastable phase-equilibrium solutions are shown.

For all not expected phase-equilibrium solutions, the derivative  $(\partial p / \partial \rho)_{T,x}$  was calculated to ensure that the solutions are mechanically stable. The results of all derivatives are positive, which confirms mechanical stability. The not expected phase-equilibria are presumably (thermodynamically) metastable. In this case, “metastable” does not mean that the fluid is at a homogeneous state, although it should split into two phases, but that it is in another phase-equilibrium than expected. In order to completely ensure that some of the solutions are not unstable for other reasons, more advanced VLE tracing routines as presented by Bell and Deiters<sup>276</sup> should be used; however, such algorithms are currently not implemented in TREND.<sup>22</sup> No experimental results were found that could proof the discussed behavior; thus, it is exceptionally interesting whether the discussed phase-equilibria can be realized in highly accurate experiments. In general, additional experimental data are crucial to improve the present formulation for this important binary system.

### 6.3.2 Binary Mixtures with Amines

As explained in Sec. 2.2, the thermodynamic properties of amines are of particular relevance for CCS applications since they are widely used as solvents in post-combustion separation processes. In this work, mixtures with monoethanolamine (MEA) and diethanolamine (DEA) were considered. Unfortunately, experimental data for binary mixtures with MEA or DEA are rare and could only be found for DEA + H<sub>2</sub>O, MEA + H<sub>2</sub>O, MEA + DEA, and SO<sub>2</sub> + DEA. It is particularly unfortunate that no experimental data were found for the important systems MEA + CO<sub>2</sub> and DEA + CO<sub>2</sub>.

The system SO<sub>2</sub> + DEA was already discussed in the section on binary mixtures with SO<sub>2</sub> (see Sec. 6.3.1.7). In the following section, validations based on the experimental data for the remaining three systems are discussed. The validation process turned out to be a challenging task because the experimental uncertainties of the available VLE data were almost always found to be significantly underestimated. This problem was already discussed for other binary systems, but the discrepancies of the stated uncertainties and the deviations from the models are exceptionally large for the following systems.

A possible reason for this was discussed by Kim *et al.*<sup>182</sup> The authors describe the analysis of amine solutions by gas chromatography as a complex task. This is explained by the high reactivity of the amines and their strong adsorption affinity for the gas chromatograph column. Furthermore, Kim *et al.*<sup>182</sup> mention the potential problem of thermal degradation of the amines at high column temperatures that would significantly falsify the results of the gas chromatography. A widely known challenge of experimental work on amine system is posed by their high saturation temperatures and consequently very low saturation pressures. Both require very accurate instruments in order to obtain reliable experimental data.

#### 6.3.2.1 DEA + Water and MEA + Water

The available experimental data for the two binary systems DEA + H<sub>2</sub>O and MEA + H<sub>2</sub>O show that both systems have a qualitatively quite similar mixing behavior; thus, their description with the mixture models developed in this project is discussed in one section. The model for DEA + H<sub>2</sub>O was developed first, because the work on the pure-fluid EOS for DEA by Kortmann<sup>55</sup> was completed prior to the development of the EOS for MEA (see Sec. 5.3). The final set of parameters for DEA + H<sub>2</sub>O was used as a starting point for fitting MEA + H<sub>2</sub>O. Both models were obtained by adjusting all four parameters of the binary reducing functions.

The experimental data for DEA + H<sub>2</sub>O found in the literature consists of five VLE data sets published by Wilding *et al.*,<sup>294</sup> Horstmann *et al.*,<sup>295</sup> Abdi and Meisen,<sup>296</sup> Cai *et al.*,<sup>297</sup> and Sidi-Boumedine *et al.*<sup>298</sup> The latter publication only includes two points for the binary system DEA + H<sub>2</sub>O; thus, the data were not relevant for the fitting process. Wilding's and Horstmann's experimental groups carried out measurements along isotherms. Their data are



consequently shown in  $p,x$  diagrams given in Figure 6.57. The other two relevant data sets were obtained under isobaric conditions, and are thus depicted in  $T,x$  diagrams presented in Figure 6.58.

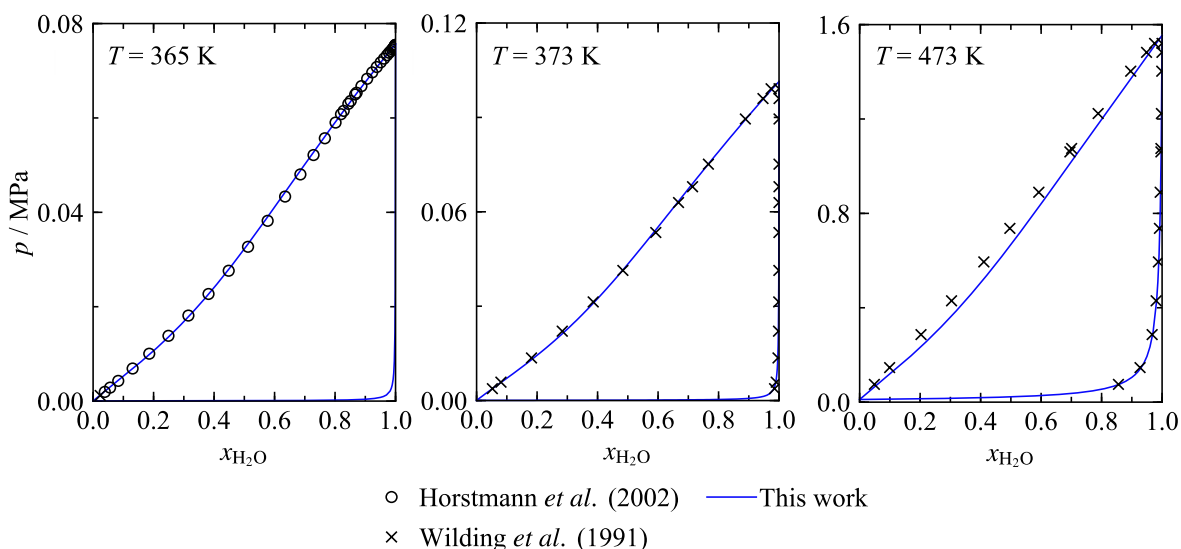


**Figure 6.57** Phase boundaries of the system DEA + H<sub>2</sub>O in  $p,x$  diagrams for selected isotherms as calculated from the new EOS. The available experimental data are shown for comparisons.

The diagrams illustrate some characteristic behavior of this mixture: The shape of the phase boundaries exhibits a negative deviation from Raoult's law<sup>299</sup> and quite low saturation pressures. In fact, even the phase diagram at 373 K is almost completely at pressures below 1 atm. The VLE region ranges over a comparably wide composition range. These characteristics are not artifacts of the model, but are confirmed by the data of Wilding *et al.*<sup>294</sup> that include both dew- and bubble-point compositions. Unfortunately, there is almost no overlap of the available data sets in temperature or pressure. Only Wilding's data include one point at a temperature comparable to Horstmann's work. The isobaric studies of Abdi and Meisen<sup>296</sup> and Cai *et al.*<sup>297</sup> are carried out at different saturation pressures (see Figure 6.58). Because the available data are not at completely comparable conditions, their reliability was not easily assessed during the fitting process. However, the  $p,x$  and  $T,x$  diagrams show no major offsets or inconsistencies; thus, the different data sets are considered to be sufficiently consistent.

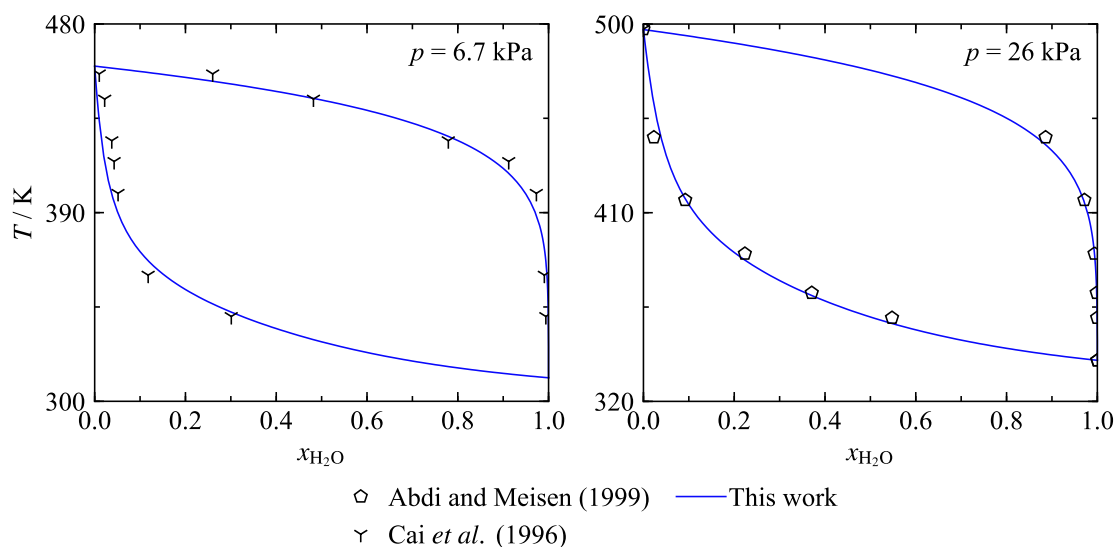


**Figure 6.58** Phase boundaries of the system DEA + H<sub>2</sub>O in  $T,x$  diagrams for two isobars as calculated from the new EOS. The experimental data are shown for comparisons.

Deviations between calculated phase-equilibrium compositions and the experimental data are shown in Figure 6.59. Due to the low saturation pressures, relative deviations in pressure are quite large; thus, they are less meaningful and not discussed for this mixture.

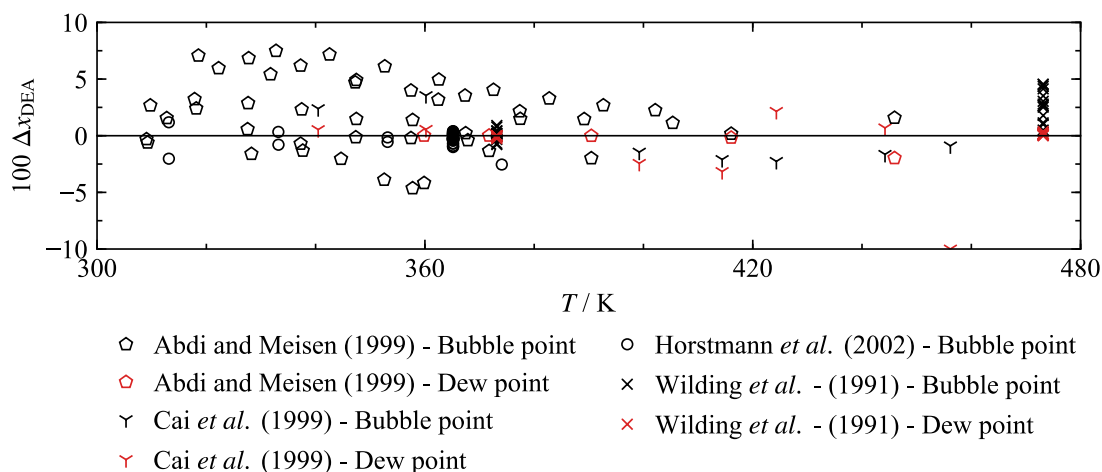


**Figure 6.59** Relative deviations  $\Delta x_{\text{DEA}} = (x_{\text{DEA,exp}} - x_{\text{DEA,calc}})$  between the available experimental VLE data for the system DEA + H<sub>2</sub>O and results calculated from the new EOS as a function of temperature.

Excluding the bubble-point data of Wilding *et al.*<sup>294</sup> at 473 K, almost all coupled data points, which means dew and bubble points that belong to one phase equilibrium, are represented within 2.5 mol%.

The data of Abdi and Meisen<sup>296</sup> also includes a considerable number of bubble points for which the composition of the coexisting saturated vapor is unknown. The “complete” VLE data points are results of a different experimental procedure than their bubble-point measurements. The bubble points were obtained through a synthetic measuring technique in which a thermostatted cell is almost completely filled with a liquid mixture of known composition. The content of the cell is agitated with a magnetic stirrer until a stable equilibrium is obtained. Then, the pressure of the thermostatted system is measured. Since

the liquid-phase fraction is much larger than the phase fraction of the vapor, the composition of the saturated liquid is considered to be almost identical to the composition of the initial liquid filling. This procedure is probably subject to a considerably large uncertainty in composition that is not stated in the paper but that explains the large deviations shown in Figure 6.59. The “complete” VLE data points were measured with a so-called “dynamic” measurement in which the coexisting phases are analyzed in a gas chromatograph. The compositions thus obtained should be considerably more accurate than the bubble-point compositions resulting from the static experiment.

The experimental procedure of Wilding *et al.*<sup>294</sup> is the same as for the data of Wilson and Wilding<sup>282</sup> that are also discussed for the systems  $\text{SO}_2 + \text{Cl}_2$  (see Sec. 6.3.1.5),  $\text{SO}_2 + \text{HCl}$  (Sec. 6.3.1.6), and  $\text{Cl}_2 + \text{HCl}$  (Sec. 6.3.3). The uncertainty in composition is not specified for any of these data sets. For  $\text{DEA} + \text{H}_2\text{O}$ , the authors state experimental uncertainties in pressure (0.05 kPa at 373 K and 0.25 % at 473 K) and temperature (0.05 K). Considering these specifications in order to calculate combined expanded ( $k = 2$ ) uncertainties leads to a maximum uncertainty in composition of 0.46 mol%. This value is clearly not confirmed by the deviations shown in Figure 6.59.

Horstmann *et al.*<sup>295</sup> applied a measuring technique in which the pressure of a thermostated mixture with a known overall composition in a phase-equilibrium state is obtained. The overall compositions are determined from the known quantities of liquids injected into the equilibrium cell, whereas the composition of the saturated liquid results from solving mass and volume balance equations considering the VLE. This procedure is not further explained but should be influenced by higher uncertainties than other methods that include an analysis of the coexisting phases. The experimental uncertainties given in the corresponding publication are 0.02 kPa in pressure, 0.03 K, and 0.01 mol% in composition. Taking that information into account, the calculated combined uncertainties range from 0.08 mol% to 0.56 mol% which is between five to ten times smaller than the deviations from the EOS.

The publication of Cai *et al.*<sup>297</sup> also includes some statements about the experimental uncertainties (133 Pa in pressure, 0.1 K in temperature, 0.001 in mole fraction). Combining these uncertainties for every state points leads to averaged expanded ( $k = 2$ ) uncertainties in phase-equilibrium compositions of about 0.4 mol% for the liquid phase and 1.1 mol% for the vapor phase. Again, these uncertainties do not agree with the deviations discussed above and shown in Figure 6.59. However, a further investigation of the applied experimental technique indicates that the given uncertainties might be underestimated. First of all, the uncertainty in temperature is equivalent to the thermometer graduation; thus, it should be considered as the resolution of the measurement and not its uncertainty. More significant is a closer look at the composition measurement. The data were obtained at isobaric conditions (6.7 kPa) in a (modified Rose-Williams) equilibrium still in which the mixture is repeatedly evaporated and condensed. The process is conducted in a cycle that includes a liquid and

vapor sampler. The specified uncertainty in composition should be interpreted as the uncertainty of the subsequent analysis device. It does not consider that the equilibrium vapor is most likely not fully condensed; thus, the composition of the withdrawn sample is not equivalent to the one of the saturated vapor. Aside from this shift in the saturated-vapor composition, this procedure also leads to a change of the overall composition which then again also yields a shift in the saturated-liquid composition. Considering these aspects, it seems realistic that the deviations between the data of Cai *et al.*<sup>297</sup> and the mixture model are within the real experimental uncertainty.

Based on the deviations shown in Figure 6.59, the uncertainty of calculated VLE data is conservatively estimated to be 5 mol% in composition for temperatures between 315 K and 475 K.

The experimental database for MEA + H<sub>2</sub>O is more comprehensive than for DEA + H<sub>2</sub>O. There are several publications presenting VLE data that exhibit overall a quite satisfying degree of consistency. As briefly mentioned at the beginning of this section, the parameters for MEA + H<sub>2</sub>O were fitted by using the ones for DEA + H<sub>2</sub>O as starting values. Using the parameters of a chemically comparable mixture as starting values instead of simple combining rules is a common procedure; however, in this case, it is worth discussing since the results obtained with these adopted parameters are remarkably accurate. Figure 6.60 shows the available experimental VLE data at 333 K together with the phase boundaries calculated from the final model MEA + H<sub>2</sub>O and from the model containing the reducing parameters adopted from the system DEA + H<sub>2</sub>O. The phase boundaries calculated with the adopted parameters are in very good agreement with the data. In fact, fitting the final parameter set only required a careful fine-tuning of the starting values.

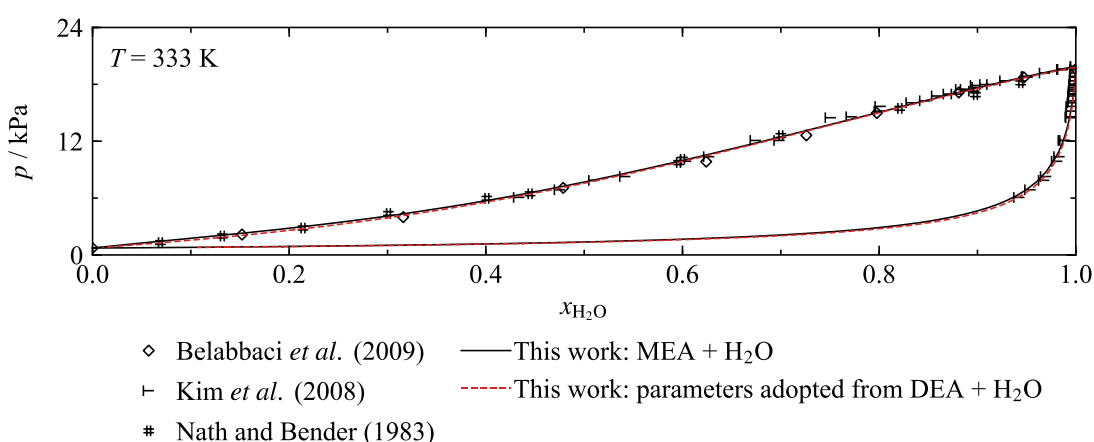


**Figure 6.60** Phase boundaries of the system MEA + H<sub>2</sub>O in a  $p, x$  diagram at 333 K as calculated from the new EOS and a preliminary model for which the reducing parameters were directly adopted from the model for DEA + H<sub>2</sub>O. The available experimental data are shown for comparisons.

Phase boundaries calculated from the final parameter set are shown in Figure 6.61. The  $p, x$  diagrams presented in that figure only include the experimental data obtained under isothermal conditions. The depicted data cover a temperature range from 283 K to 373 K;

thus, from just above the triple point of MEA ( $T_{tp,MEA} = 283.7$  K) to approximately the normal boiling point of H<sub>2</sub>O. In contrast to the previously discussed data situation for DEA + H<sub>2</sub>O, the available data sets exhibit some overlaps that indicate a good consistency of the data. Overall, the calculated phase boundaries are in good agreement with the data. It should be noted that there are considerably more data along the bubble line than along the dew line. The isothermal data shown in Figure 6.61 only allow for a validation of calculated dew points for H<sub>2</sub>O-rich mixtures at  $T \geq 333$  K. The dew-point data at these conditions were measured by Lenard *et al.*,<sup>300</sup> Tochigi *et al.*,<sup>181</sup> and Kim *et al.*<sup>182</sup> The data confirm the shape of the dew lines calculated from the mixture model.

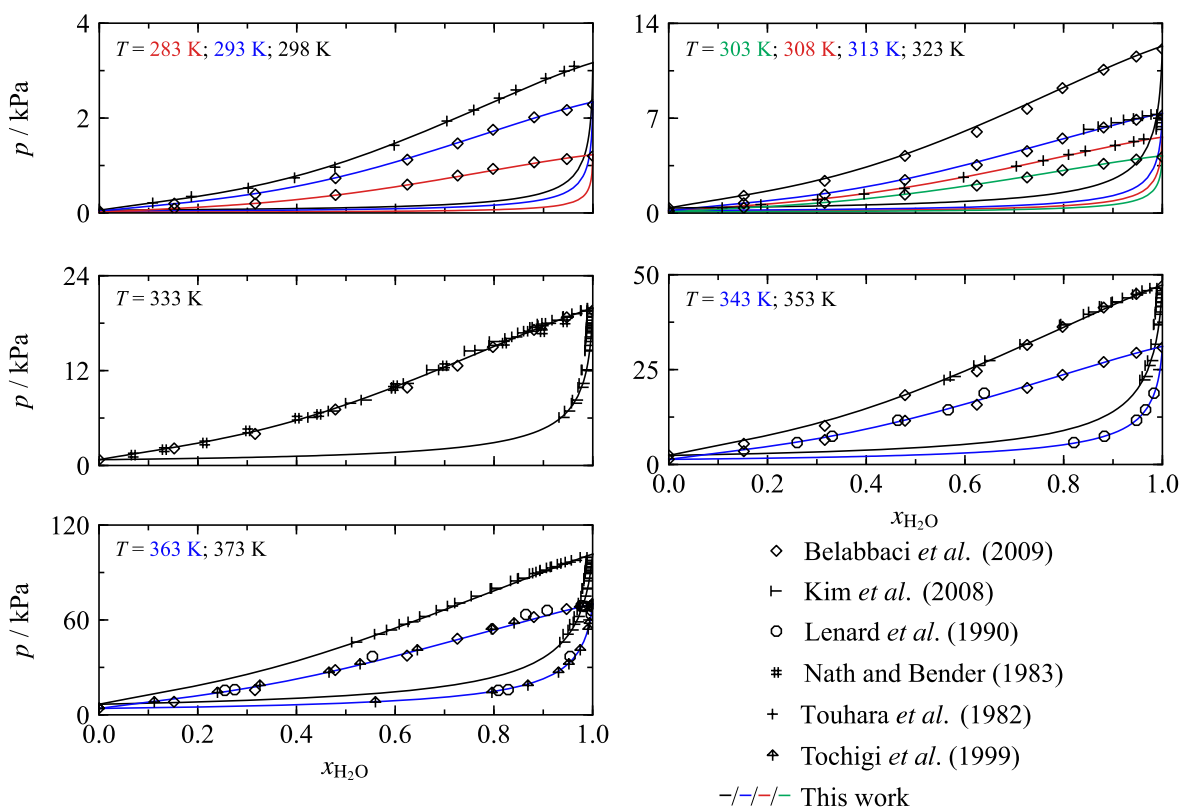


**Figure 6.61** Phase boundaries of the system MEA + H<sub>2</sub>O in  $p,x$  diagrams for selected isotherms as calculated from the new EOS. The available experimental data are shown for comparisons.

Deviations between calculate compositions of the coexisting phases and the experimental VLE data are shown in Figure 6.62. The deviation plot includes some additional data sets that were not presented in the  $p,x$  diagrams given in Figure 6.61. These data sets by Cai *et al.*,<sup>297</sup> Park *et al.*,<sup>301</sup> Park and Lee<sup>302</sup> and Tanaka *et al.*<sup>303</sup> result from isobaric experiments that extend the experimentally investigated temperature up to 440 K.

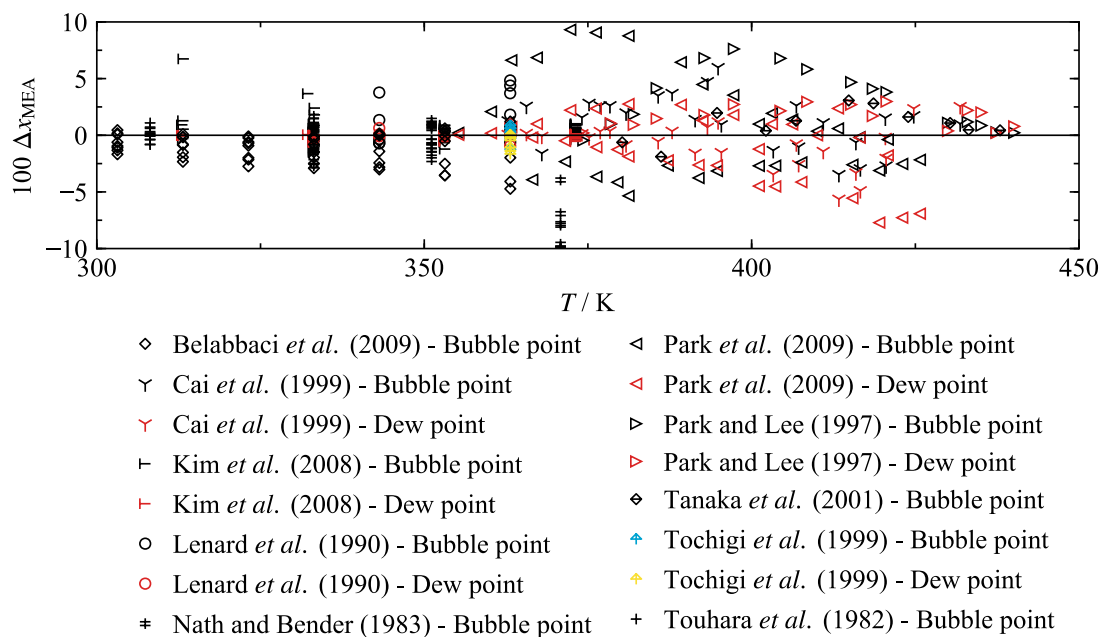


**Figure 6.62** Relative deviations  $\Delta x_{\text{MEA}} = (x_{\text{MEA,exp}} - x_{\text{MEA,calc}})$  between the available experimental VLE data for the system MEA + H<sub>2</sub>O and results calculated from the new EOS as a function of temperature.

The mixture model represents the majority of the data within deviations of 5 mol%. The data of Cai *et al.*,<sup>297</sup> Park *et al.*,<sup>301</sup> and Park and Lee<sup>302</sup> exhibit some higher deviations. The same applies for the data of Nath and Bender<sup>304</sup> at about 370 K that should probably be considered as an incorrect measurement series because the other data from this reference are in good agreement with values from comparative sources. Possible problems of the experimental method used by Cai *et al.*<sup>297</sup> were already discussed for DEA + H<sub>2</sub>O. The results of Park *et al.*<sup>301</sup> and Park and Lee<sup>302</sup> were obtained with a comparable equilibrium still. However, a detailed discussion of these studies is not meaningful. Using the given experimental uncertainties in temperature, pressure, and compositions to calculate combined uncertainties showed that these specifications are clearly underestimated. Unfortunately, the same applies to the uncertainties given by Belabbaci *et al.*,<sup>180</sup> Kim *et al.*,<sup>182</sup> Lenard *et al.*,<sup>300</sup> and Tanaka *et al.*<sup>303</sup> Nath and Bender<sup>304</sup> and Touhara *et al.*<sup>305</sup> do not provide any uncertainties of their experiments.

Realistic uncertainty estimates can be taken from the publications of Tochigi *et al.*<sup>181</sup> The study was carried out with a (Rogalski-Malanoski) equilibrium still. The authors specify uncertainties in temperature (0.01 K), pressure (0.03 kPa), and most importantly also in composition (0.7 mol%). Using these specifications yields combined expanded ( $k = 2$ ) uncertainties ranging from 1.4 mol% to 2 mol%, which agrees with the deviations from the EOS. Since this data set is limited to one single isotherm, 363 K, it only enables a good validation of the EOS, but does not define its uncertainty over a wide temperature range. With regard to the overall level of consistency between the data sets shown in Figure 6.3, the composition uncertainty of calculated VLE data is estimated to be 3 mol% at temperatures below 360 K and 5 mol% at higher temperatures.

### 6.3.2.2 DEA + MEA

Compared to the other binary systems containing amines discussed in this thesis, DEA + MEA exhibits a less complex mixing behavior as expected because both components are chemically quite similar. Nevertheless, an accurate description of the limited available VLE data required to fit all four adjustable parameters of the binary reducing functions. Only two useful data sets were found in the literature, namely the work by Cai *et al.*,<sup>297</sup> which was already discussed for the systems MEA + H<sub>2</sub>O and DEA + H<sub>2</sub>O, and Tsintsarska *et al.*<sup>306</sup> Each of these data sets includes only results along one single isobar, 6.7 kPa and 1.8 kPa. The data and phase boundaries calculated from the mixture model are shown in  $T,x$  diagrams given in Figure 6.63.

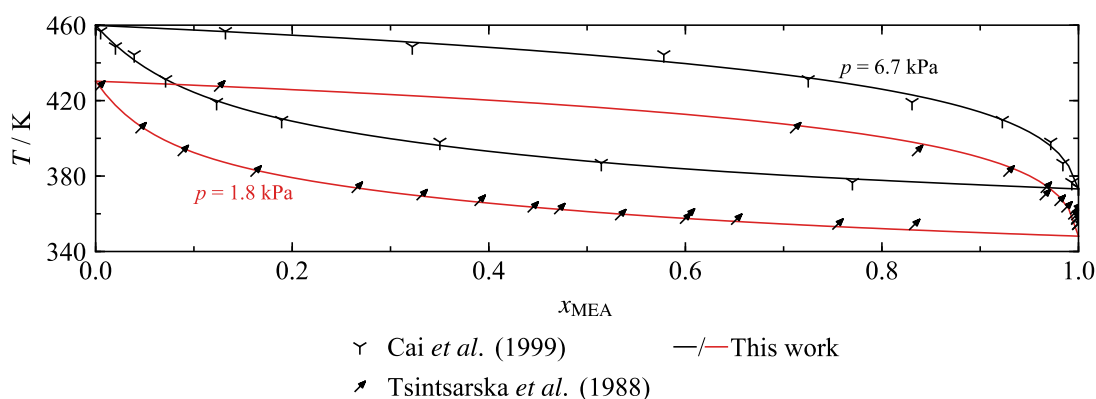


**Figure 6.63** Phase boundaries of the system DEA + MEA in a  $T,x$  diagram for two isobars as calculated from the new EOS. The experimental data are shown for comparisons.

The  $T,x$  diagram emphasizes a good agreement between calculated VLE data and the experimental results, especially when considering the quite low saturation pressures that are also very sensitive to small deviations in temperature and composition. The resulting deviations between calculated phase-equilibrium compositions and the data are presented in Figure 6.64.

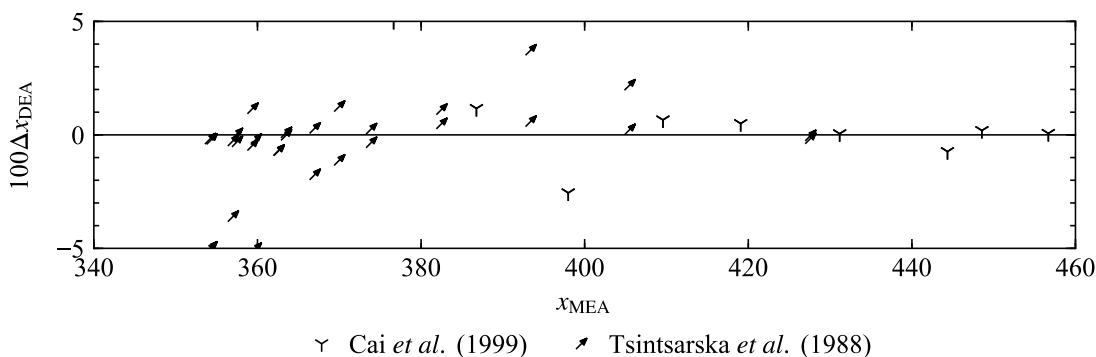


**Figure 6.64** Relative deviations  $\Delta x_{\text{MEA}} = (x_{\text{MEA,exp}} - x_{\text{MEA,calc}})$  between the available experimental VLE data for the system DEA + MEA and results calculated from the new EOS as a function of temperature.

Except for one outlier at 377 K, the model represents all the data of Cai *et al.*<sup>297</sup> within a maximum deviation of 2.6 mol%. The deviations between the model and the measurements

of Tsintsarska *et al.*<sup>306</sup> are mostly within 2 mol%. As previously discussed, in the publication of Cai *et al.*<sup>297</sup> the experimental uncertainties seem to be underestimated, whereas Tsintsarska *et al.*<sup>306</sup> do not provide any uncertainties. Based on the deviations shown in Figure 6.64, the uncertainty of calculated VLE data is conservatively estimated to be 5 mol% at temperatures between 355 K and 460 K.

### 6.3.3 Chlorine + Hydrogen Chloride

As for most binary systems presented in this section, the mixing behavior of Cl<sub>2</sub> + HCl is described by four adjusted reducing parameters. The database consists of the experimental VLE data of Wilson and Wilding<sup>282</sup> (that was already discussed for the systems SO<sub>2</sub> + Cl<sub>2</sub> and SO<sub>2</sub> + HCl) and of an industrial study carried out at Höchst AG.<sup>307</sup> Molecular-simulation data for both VLE and homogeneous densities were contributed by Köster and Vrabec.<sup>280</sup>

The VLE data of Wilson and Wilding<sup>282</sup> cover two isotherms, 213 K and 273 K. At 273 K the data overlap with the measurements of Höchst AG,<sup>307</sup> whose study includes three isotherms, 253 K, 273 K, and 293 K. These measurements were performed through a static-analytic method, in which the coexisting phases were sampled and analyzed. The report from which the data were obtained does not state any uncertainties. As apparent from Figure 6.65, there is a considerable offset between the data of Höchst AG and Wilson's and Wilding's data. Fitting the mixture model to the latter data set led to a more consistent and numerically stable description of the VLE region. The results obtained at Höchst AG were consequently omitted from the fitting process. Köster and Vrabec<sup>280</sup> used the VLE data of Wilson and Wilding<sup>282</sup> to adjust the unlike interaction parameter in the molecular simulations. They thereby extended the available data up to 370 K. Their simulations were validated by Wilson's and Wilding's data at 273 K that are in close agreement.



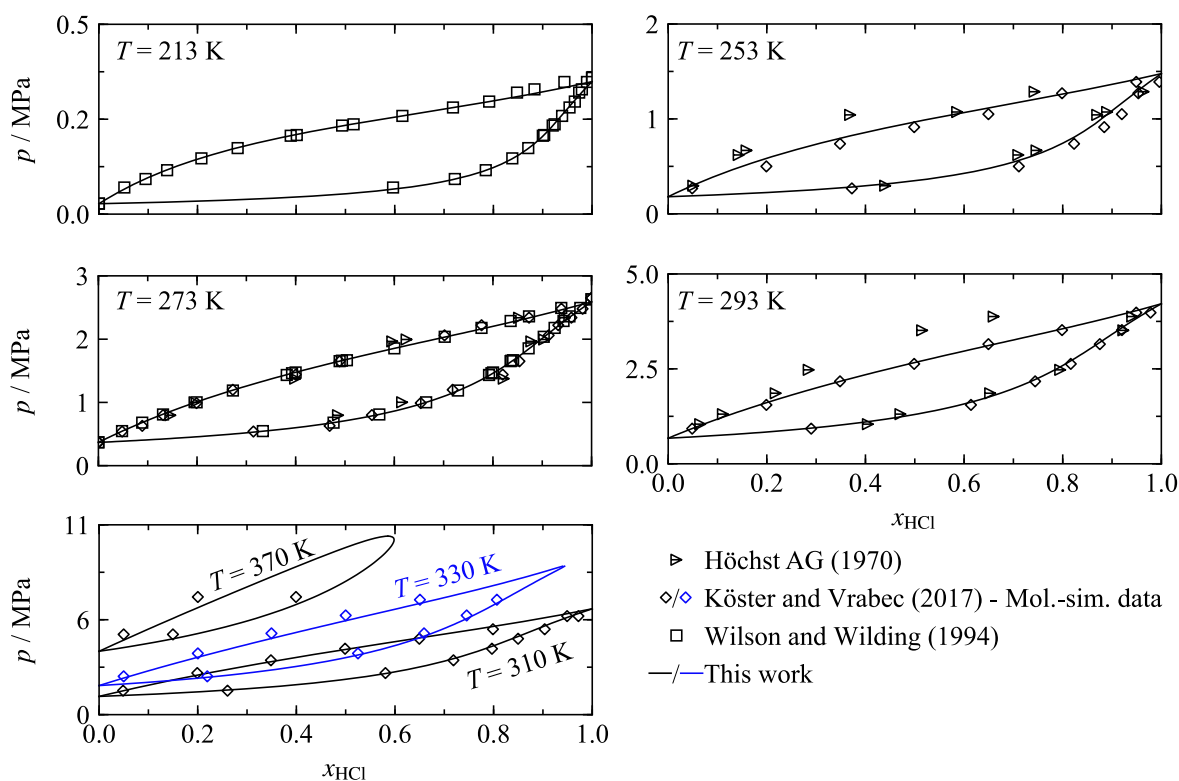


**Figure 6.65** Phase boundaries of the system  $\text{Cl}_2 + \text{HCl}$  in  $p, x$  diagrams for seven isotherms as calculated from the new EOS. The available experimental and molecular-simulation data are shown for comparisons.

Deviations between calculated VLE data and the experimental and simulated data are shown in Figure 6.66. The figure presents deviations in both saturation pressure and phase-equilibrium composition. The deviations in pressure are especially of interest for the data of Wilson and Wilding<sup>282</sup> who measured pressures instead of analyzing the compositions of the phases in equilibrium.

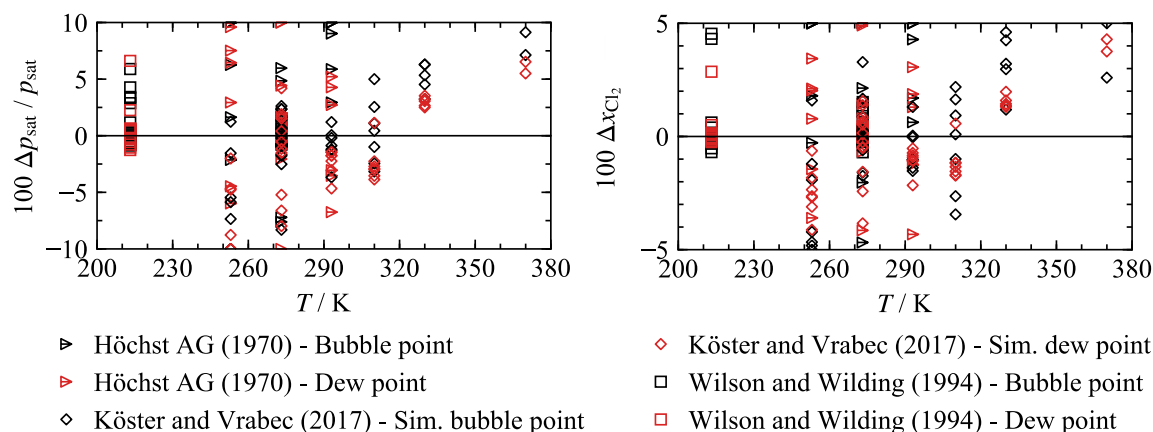


**Figure 6.66** Left: Relative deviations  $p_{\text{sat}} = (p_{\text{sat,data}} - p_{\text{sat,calc}}) / p_{\text{sat,data}}$  between the available VLE data for the system  $\text{Cl}_2 + \text{HCl}$  and results calculated from the new EOS as a function of temperature. Right: Deviations  $\Delta x_{\text{Cl}_2} = (x_{\text{Cl}_2,\text{data}} - x_{\text{Cl}_2,\text{calc}})$  of the available data and results calculated from the new EOS as a function of temperature.

Figure 6.66 shows that the deviations of the data are comparable for dew and bubble points. Neglecting the measurements of Höchst AG,<sup>307</sup> most of the data are described within 10 % in saturation pressure and 5 mol% in composition. These should also be realistic estimates

for the uncertainty of VLE data calculated from the model. Compared with other systems, these uncertainties are relatively large, which is not surprising with regard to the quality of the available data. The reliable experimental data are limited to the two isotherms investigated by Wilson and Wilding.<sup>282</sup> The combined experimental uncertainties of these data were calculated considering the given uncertainties in temperature and pressure (see Sec. 6.3.1.5); the maximum value is 1.5 mol%. At a temperature of 213 K most of the data is, in fact, represented within this uncertainty; however, the measurements at 273 K exhibit clearly higher deviations. It consequently seems like the experimental uncertainties are considerably underestimated. The molecular simulation data are based on these experimental results, and thus are not independent comparative data.

As mentioned before, Köster and Vrabec<sup>280</sup> additionally contributed molecular-simulation results for homogeneous densities in the gas and liquid phase. Their simulations cover three mixture compositions (25 mol%, 50 mol%, 75 mol% HCl) at temperatures ranging from 180 K to 630 K and pressures up to 100 MPa. Due to the lack of any comparative data and the questionable accuracy of the experimental VLE data that contributed to the molecular simulations, the simulated densities are not considered to be very accurate. The mixture model was consequently only fitted with low weights to a small number of these data points. Deviations between the data and calculated values are shown in Figure 6.67.

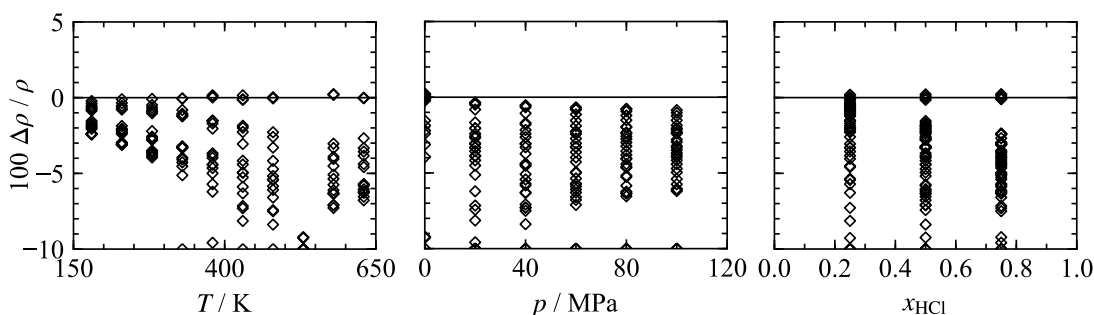


**Figure 6.67** Relative deviations  $\Delta\rho/\rho = (\rho_{\text{data}} - \rho_{\text{calc}})/\rho_{\text{data}}$  of the simulated density data of Köster and Vrabec<sup>280</sup> for the system  $\text{Cl}_2 + \text{HCl}$  from the new EOS as a function of temperature (left), pressure (middle), and composition (right).

The deviations increase with increasing temperature but show no clear trends with respect to pressure and composition. Especially the latter aspect is interesting to note, because it indicates that the molecular-simulation results are not more accurate for one of the pure components. In general, the plotted deviations are within 10 % which is clearly higher than expected for the description of homogeneous densities with a Helmholtz-explicit EOS. As a side note, both pure-fluid EOS allow for a quite accurate description of homogeneous densities (see Sec. 5.2 about the EOS for  $\text{Cl}_2$  and the work of Thol *et al.*<sup>50</sup> on HCl). It can therefore be assumed that the underlying extended corresponding states principle allows for the calculation of more accurate homogeneous densities than indicated by the deviations in Figure 6.67. Nevertheless, no concrete uncertainty estimate for calculated values can be provided without additional experimental or comparative molecular-simulation data.

### 6.4 Binary Mixtures Described with Simple Combining Rules

During the development of the present EOS for multi-component CCS-mixtures, one of the most demanding tasks was the description of the large number of binary systems for which no reliable experimental data or no data at all are available. With regard to the list of components shown in Figure 6.1, the scarce data situation for many systems is not surprising because several components are toxic, corrosive, highly reactive, or explosive. Without sufficient input data it is not possible to fit the parameters of the binary reducing functions. Since the mathematical structure of the multi-component mixture EOS requires models for every possible binary combination of the components, other ways of describing systems without reliable experimental data must be found.

In the recent past, some interesting work on automated fitting but also on the estimation of reducing parameters has been done at NIST, Boulder. Bell and Lemmon<sup>54</sup> showed that for some groups of binary mixtures the parameters of the temperature-reducing function are correlated with the ratio of the molar masses of the components. In the top panels of Figure 6.68, this dependency is shown for the example of binary mixtures of CH<sub>4</sub> with other alkanes (including branched alkanes and cycloalkanes), H<sub>2</sub>O, CO, O<sub>2</sub>, H<sub>2</sub>S, and Ar. The underlying reducing parameters were fitted with the automatic evolutionary optimization algorithm presented in the same publication.<sup>54</sup> Neglecting some outliers, both reducing parameters follow a sufficiently distinct trend. Bell and Lemmon provide a linear regression function that can be used to estimate  $\beta_{T,ij}$  and  $\gamma_{T,ij}$  for other binary mixtures with CH<sub>4</sub>.

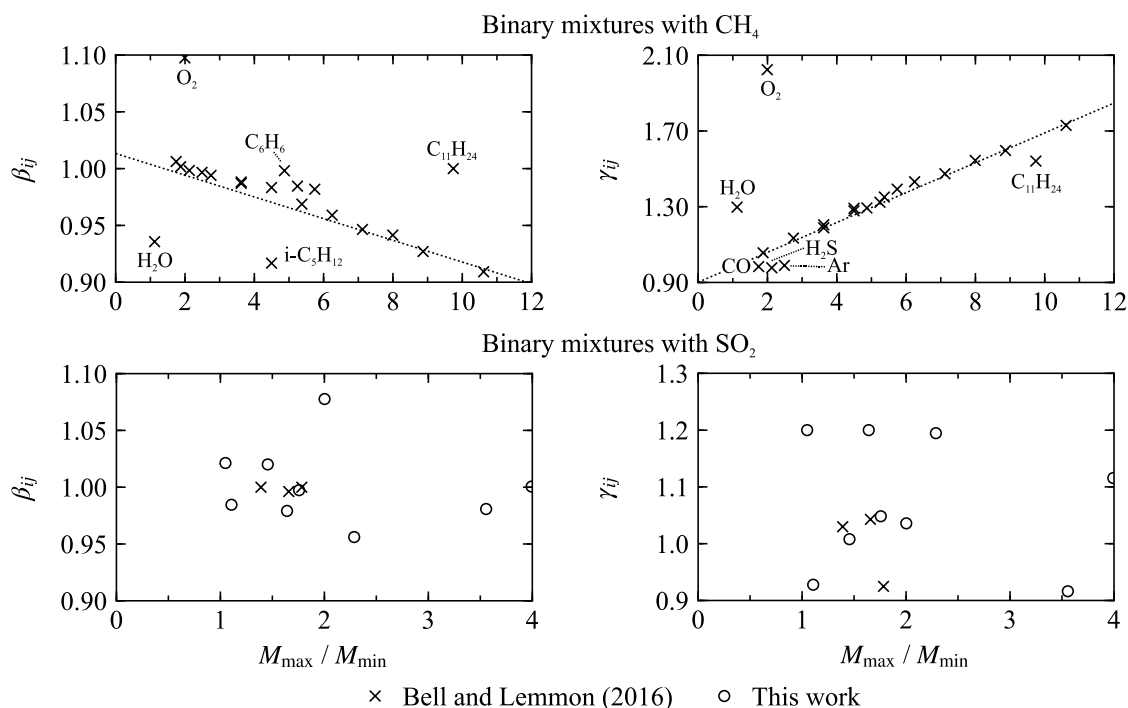


**Figure 6.68** Top: Binary reducing parameters  $\beta_{T,ij}$  (left) and  $\gamma_{T,ij}$  (right) for various mixtures with CH<sub>4</sub> plotted versus the ratio of the molar mass of CH<sub>4</sub> and the second component ( $M_{\max} / M_{\min}$ ). The approach and parameters were adopted from Bell and Lemmon.<sup>54</sup> Bottom: Binary reducing parameters  $\beta_{T,ij}$  (left) and  $\gamma_{T,ij}$  (right) for mixtures with SO<sub>2</sub> plotted versus the ratio of the molar mass of SO<sub>2</sub> and the second component. The parameters were taken from this work and Bell and Lemmon.<sup>54</sup>

For this work, the estimation scheme suggested by Bell and Lemmon<sup>54</sup> was applied to mixtures with SO<sub>2</sub>. Reducing parameters for the corresponding binary mixtures were taken from this work (see 6.3.1) and for three additional mixtures (SO<sub>2</sub> plus ethanol, cyclohexane, and isooctane) from Bell and Lemmon<sup>54</sup> and plotted versus the ratio of the molar masses. The results are shown in the bottom panels of Figure 6.68. As apparent, the fitted reducing parameters for binary mixtures with SO<sub>2</sub> do not follow any clear trend. Because this is partly caused by the small number of available parameters sets, the same approach was also applied to, for example, binary mixtures with CO<sub>2</sub> or Cl<sub>2</sub>. Unfortunately, none of these efforts yielded a useful estimation scheme. Changing the independent variable from the ratio of the molar masses to the ratio of the acentric factors, the differences in the critical parameters, or other combinations of characteristic properties does not lead to any reliable results either. The binary systems that cannot be described by reducing parameters obtained from conventional fitting were consequently not obtained from estimations based on the parameters for other binary mixtures.

Many of the binary mixtures not sufficiently covered with experimental data include components that are only present in CCS-mixtures on a parts-per-million level. Therefore, generalized approaches to describe such binary systems might be sufficiently accurate within the multi-component mixture model. In Sec. 4, the linear and quadratic (Lorentz-Berthelot) combining rules were introduced. In case of a relatively “ideal”, symmetric mixing behavior, indicated by a closed  $p, T$  phase envelope, both rules yield qualitatively comparable results (see CH<sub>4</sub> + HCl in the left panel of Figure 6.69). However, the matrix of CCS-relevant fluids includes various binary combinations of components with very different characteristic properties such as critical or triple-point parameters, molecular weight, or polarity. These chemical differences can lead to a highly asymmetric mixing behavior. With regard to the right panel of Figure 6.69 (CH<sub>4</sub> + Cl<sub>2</sub>), it becomes apparent that for those systems the two simple combining rules might lead to completely different results.

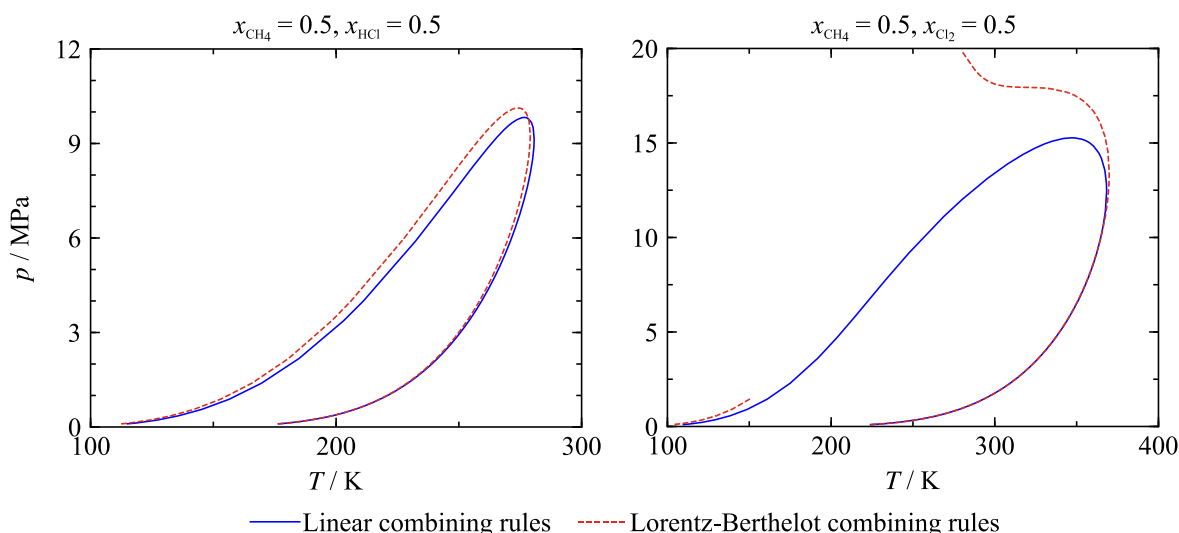


**Figure 6.69** Calculated  $p,T$  diagrams for a relatively ideal, symmetric ( $\text{CH}_4 + \text{HCl}$ ) and a non-ideal, asymmetric binary mixture ( $\text{CH}_4 + \text{Cl}_2$ ) with equimolar composition. The phase envelopes are obtained by the linear and Lorentz-Berthelot combining rules.

While the Lorentz-Berthelot combining rules yield an open  $p,T$  phase envelope for  $\text{CH}_4 + \text{Cl}_2$ , a linear combination of the pure fluids results in a relatively “ideal”, closed phase envelope. Since open phase envelopes often indicate a non-ideal mixing behavior, it is probably more reasonable to choose the Lorentz-Berthelot combining rules for this example system. Nevertheless, in other comparable cases the linear combining rules were found to give more reasonable results. It is obvious that without sufficient experimental information choosing the appropriate rules is difficult.

It would therefore be of special interest to classify binary mixtures into groups based on convenient criteria such as differences in polarity, molecular mass, acentric factor, critical temperature or “length” of the vapor-pressure curve ( $\Delta T_{c, \text{tp}, i} = T_{c,i} - T_{\text{tp}, i}$ ). The aim of this effort is to define which combining rules are more suitable for each of these groups. Unfortunately, no completely satisfying method was found within the scope of the present work. Every group of binary systems should show a quite similar symmetric or asymmetric and ideal or non-ideal mixing behavior. But in every group, exceptions were found that yield completely different types of phase envelopes, when described by the same combining rules as the other binary mixtures in this group. Nevertheless, the listed criteria were still considered in order to choose the most appropriate combining rules as possible. Systems for which the two combining rules lead to a different description of the phase boundaries were compared to other systems that were considered to be comparable and ideally covered by some experimental VLE information. However, the final selection of the combining rules was also based on a subjective estimation of which phase-equilibrium behavior was found to be more reasonable. If both combination rules yield a closed phase envelope, the Lorentz-Berthelot combining rules were chosen, since the corresponding parameters are easier to implement (all parameters are set to unity). The final selection of combining rules is presented in the component matrix shown in Figure 6.1 in Sec. 6.1.

The description of a comparably large number of binary systems only with combining rules of limited accuracy, is an unsatisfying aspect of the present work. Approaches to overcome this unsolved problem should be the focus of future research in the field of thermodynamic property data for multi-component mixtures. Of course, comprehensive experimental campaigns would yield the most valuable input; however, this would first of all require a larger collective understanding of the importance of experiments on binary systems of impurities. Nowadays, most of the experimental work on binary mixtures useful for fitting EOS is still focused on major components of typical multi-component mixtures. Besides, data gaps will still remain for binary mixtures with hazardous components that pose unreasonable risks to the experimentalists. Such gaps could potentially be closed by molecular simulations. For pure fluids, the approach of combining experimental data with molecular-simulation data was successfully used for a considerable number of EOS (see, for example, Thol<sup>169</sup>). In the present work, molecular-simulation data also contributed to the development of some binary mixture models (see, for example, Secs. 6.3.1.6 and 6.3.3). However, the quality of these data varies largely and still depends on some reliable experimental data in order to tune parameters used in the simulation. With regard to EOS, two promising works were recently published by Jäger *et al.*<sup>308,309</sup> that present a combination of the Helmholtz-energy explicit structure of the present mixture model and the  $g^E$ -models UNIFAC<sup>42</sup> and COSMO-SAC.<sup>310,311</sup> It is expected that further developments in this field will allow for more accurate results than the simple combining rules; however, the more physically based  $g^E$ -models still require some fitting to experimental data in order to yield reliable results.

## 6.5 Additional Information on the Multi-Component Mixture EOS

In the following section, some additional information relevant to the EOS for multi-component CCS-mixtures is given. Some of these aspects were already mentioned in preceding sections; nevertheless, they are important enough to be discussed in a more summarized manner.

### 6.5.1 Range of Validity and Estimated Uncertainties

In general, the present multi-component mixture model is valid over the whole stable fluid region. Solid states of water and CO<sub>2</sub> or hydrates are not considered. At low temperatures, where solid states might become relevant, it is recommended to use complex phase-equilibrium algorithms as implemented in TREND<sup>22</sup> to predict the formation of such phases.

Estimating uncertainties of calculated properties is only possible for binary mixtures in state regions that are covered by reliable experimental data or at least by data of known accuracy. Such uncertainty estimates for calculated properties of binary mixtures were discussed in

detail in Sec. 6.2 and 6.3. A summary of the uncertainty estimates for the models developed in this work is given in Table 6.2. The table only presents uncertainties in VLE and homogeneous density data because other types of data are not available for most systems. Binary mixtures that could only be described by combining rules are not included in this summary because no experimental data for fitting and validating the models are available. As discussed in Sec. 6.1, the binary models developed in this work only allow for a description of CCS-relevant mixtures when adopting most of the binary formulations included in EOS-CG and some additional formulations from GERG-2008. Uncertainty estimates for the adopted models are given in the corresponding publications by Gernert and Span<sup>2</sup> and Kunz and Wagner,<sup>36</sup> respectively. The uncertainties in Table 6.2 correspond to the maximum uncertainties estimated based on comparisons with all reliable data collected from the literature. In some cases, these estimates might be very conservative; thus, the corresponding subsections of this thesis should be considered for a more detailed impression of the accuracy of models. The complete overview of the available database including average absolute relative deviations from the binary models is given in Appendix E.

For multi-component mixtures, the estimated uncertainties of calculated data for binary mixtures give an impression of the quality of the included binary models. This enables at least some qualitative conclusions about the accuracy of multi-component mixture calculations; however, a quantitative assessment is only possible based on accurate experimental multi-component mixture data. For natural-gas mixtures, a large amount of multi-component data was published over the years, which allowed for a quite detailed validation of the GERG-2008 model.<sup>36</sup> For CCS-mixtures, experimental multi-component data are scarce. Gernert and Span discussed some comparisons with data for mixtures of some of the major CCS-components considered in EOS-CG.<sup>2,36</sup> Experimental thermodynamic property data for CCS-mixtures with a larger number of components including minor impurities as mostly considered in this work are not available in the literature. Future research in the field of thermodynamic property data for the CCS community should include experimental work on multi-component mixture data to enable a validation of the model developed in this work and other models available in the literature.

**Table 6.2** Summary of estimated uncertainties in VLE data and homogeneous densities calculated from the binary models developed within this work. Only systems described with binary specific departure functions and / or adjusted reducing parameters are considered. The given uncertainties correspond to the maximum uncertainties estimated through comparisons with reliable data. For some binary mixtures, the model might be significantly more accurate in certain areas of the fluid surface. For more detailed information about the accuracy of the models, see the corresponding subsections of the present work.

Binary system	Data coverage		VLE results <sup>a</sup>		<i>pvT</i> results	
	VLE	<i>pvT</i>	Dew points	Bubble points	Gas	Liquid
CO <sub>2</sub> + Ar	213 < <i>T</i> / K < 300	213 < <i>T</i> / K < 570, <i>p</i> < 100 MPa, 0.03 < <i>x</i> <sub>Ar</sub> < 0.99	< 1 mol%	< 1 mol%	< 0.6 % <sup>b</sup>	-
CO <sub>2</sub> + CO	218 < <i>T</i> / K < 303	253 < <i>T</i> / K < 423, <i>p</i> < 50 MPa, 0.004 < <i>x</i> <sub>CO</sub> < 0.75	< 1 mol%	< 1 mol%	< 1.0 % <sup>b</sup>	< 0.75 % <sup>b</sup>
H <sub>2</sub> O + CH <sub>4</sub>	253 < <i>T</i> / K < 596	398 < <i>T</i> / K < 873, <i>p</i> < 300 MPa, 0 < <i>x</i> <sub>CO</sub> < 1	< 1 mol% <sup>b</sup>	< 1 mol% <sup>b</sup>	< 1.5 % <sup>b</sup>	-
H <sub>2</sub> O + H <sub>2</sub> S	273 < <i>T</i> / K < 588	-	< 2 mol% <sup>b</sup>	< 0.3 mol%	-	-
SO <sub>2</sub> + CO <sub>2</sub>	263 < <i>T</i> / K < 334	263 < <i>T</i> / K < 354, <i>p</i> < 30 MPa, 0.80 < <i>x</i> <sub>CO<sub>2</sub></sub> < 0.993	< 2 mol%	< 2 mol%	< 3.0 %	< 3.5 %
SO <sub>2</sub> + N <sub>2</sub>	323 < <i>T</i> / K < 414	-	< 5 mol%	< 2 mol%	-	-
SO <sub>2</sub> + O <sub>2</sub>	323 < <i>T</i> / K < 414	-	< 3 mol%	< 3 mol%	-	-
SO <sub>2</sub> + CH <sub>4</sub>	241 < <i>T</i> / K < 302	-	≈ 2 mol% <sup>c</sup>	≈ 2 mol% <sup>c</sup>	-	-
SO <sub>2</sub> + Cl <sub>2</sub>	224 < <i>T</i> / K < 324	-	< 2 mol%	< 2 mol%	-	-
SO <sub>2</sub> + HCl <sub>2</sub>	203 < <i>T</i> / K < 370	200 < <i>T</i> / K < 650, <i>p</i> < 100 MPa, 0.25 < <i>x</i> <sub>CO<sub>2</sub></sub> < 0.75	< 3 mol%	< 3 mol%	< 3 %	< 3 %
SO <sub>2</sub> + DEA	295 < <i>T</i> / K < 324	-	-	≈ 2 mol% <sup>c</sup>	-	-
SO <sub>2</sub> + H <sub>2</sub> O	293 < <i>T</i> / K < 574	-	-	< 5 mol%	-	-
MEA + H <sub>2</sub> O	283 < <i>T</i> / K < 374	-	< 5 mol%	< 5 mol%	-	-
DEA + H <sub>2</sub> O	298 < <i>T</i> / K < 474	-	< 5 mol%	< 5 mol%	-	-
DEA + MEA	354 < <i>T</i> / K < 459	-	< 5 mol%	< 5 mol%	-	-
Cl <sub>2</sub> + HCl	253 < <i>T</i> / K < 370	-	< 5 mol%	< 5 mol%	<sup>d</sup>	<sup>d</sup>

<sup>a</sup>Uncertainties in VLE data are given in mol%  $\pm 100 u_c(x_i)$ .

<sup>b</sup>The experimental database for this binary mixture and property contains some more accurate data, which are (mostly) represented within their experimental uncertainties.

<sup>c</sup>Uncertainty estimate based on extremely limited experimental data.

<sup>d</sup>No concrete uncertainty estimate possible, but see Sec. 6.3.3 for some considerations based on molecular simulations.

## 6.5.2 Chemically Reactive Mixtures

For some binary systems of the component matrix shown in Figure 6.1, the mixing behavior is probably not only defined by thermodynamic mixing effects but also by chemical reactions. This applies, for example, to some systems with water, acid-forming components (such as SO<sub>2</sub> or H<sub>2</sub>S), carbon dioxide, the amines, or oxygen. So far, the mathematical structure of the multi-component mixture model does not include any terms to specifically describe chemical reactions. Besides, considering chemical reactions within the mixture model will require considerably more efforts than simply adding special terms to its functional form. Assuming that the binary mixture of the components A and B is in a chemical equilibrium state with a new component C ( $A + B \rightleftharpoons C$ ), this reaction product needs to be described by a pure-fluid EOS. In addition, implementing this new component



in the multi-component mixture model requires a list of new correlations, namely for all possible binary combinations of the reaction product C and the other components. Because the experimental database will in most cases be insufficient to describe the pure component C and all resulting binary mixtures with Helmholtz-energy EOS, other ways of implementing these fluids, for example, by means of cubic equations, should be considered.

Aside from these aspects, an additional challenge is posed by preparing the experimental data for the fitting process. In most cases, the corresponding references will not provide any information on the equilibrium composition of the experimentally investigated state points. Thus, additional algorithms have to be developed to calculate the chemical-equilibrium composition during the fitting process but also to calculate properties from the final mixture model. With regard to this, it should be noted that assumptions made for the chemical equilibrium of one binary system are probably not valid in the multi-component mixture. For example, the additional presence of oxygen changes many chemical reactions. Furthermore, second or higher order “generations” of reactions might be relevant to consider. The product of one chemically reactive binary system might again react with other components of the multi-component mixture, which would then lead to the formation of new species.

In this work as well as in the multi-component mixture models EOS-CG<sup>2</sup> and GERG-2008,<sup>36,36</sup> binary systems for which chemical reactions are expected to be relevant are just fitted conventionally without any special considerations of reactive effects. As briefly explained for the system H<sub>2</sub>O + SO<sub>2</sub> (see Sec. 6.3.1.8), chemical reactions are nevertheless indirectly considered by fitting the adjustable parameters of the EOS to experimental data influenced by such effects. However, the multi-component mixture model neither allows for the calculation of the chemical-equilibrium composition nor does it allow for the prediction of the formation of new species. To further improve the quality of the description of CCS-relevant mixtures, especially with regard to amine or ammonia-separation processes, addressing the problem of chemically reactive systems is the most consequent next step. Corresponding research activities have already started as a collaboration between RUB and NTNU, Trondheim.



## 7 Impact of Impurities on Thermodynamic Properties of CCS-Mixtures

In the motivation of this thesis (see Sec. 2.2), it was explained that the thermodynamic properties required for CCS-processes should not be calculated for pure CO<sub>2</sub> but for CO<sub>2</sub>-rich mixtures with various components. It is expected that some of these impurities have a significant impact on the fluid behavior. This section is a brief analysis of this impurity impact on the thermodynamic properties of the working fluid in CCS processes. With regard to the number of components included in the multi-component mixture model (see Sec. 6.1), it is apparent that a comprehensive analysis requires an extensive parameter study, in which the mixture composition is varied systematically and the change of various properties is quantified. Since this would go beyond the scope of this work, the following analysis is only focused on four possible CCS-mixtures given in Table 7.1. The compositions of these mixtures loosely follow specifications given by García *et al.*<sup>312</sup> and Eickhoff *et al.*<sup>313</sup> as well as given in the “IMPACTS Toolbox” compiled by Koornneef and Neele.<sup>314</sup> The four CO<sub>2</sub>-rich mixtures include one mixture captured from an oxyfuel-combustion process, one resulting from post-combustion amine-based separation, one from natural gas processing with subsequent amine-based separation, and one from pre-combustion synthesis gas processing.

**Table 7.1** Compositions of four CCS mixtures loosely based on specifications of García *et al.*,<sup>312</sup> Eickhoff *et al.*,<sup>313</sup> and Koornneef and Neele.<sup>314</sup>

Component	Oxyfuel-combustion	Post-combustion amine-based separation	Natural gas processing, amine-based separation	Synthesis gas processing, pre-combustion separation
	Mole fractions in the mixture			
CO <sub>2</sub>	92.6295 %	99.5973 %	95.3298 %	96.8465 %
H <sub>2</sub> O	1500 ppm	1500 ppm	1500 ppm	1500 ppm
N <sub>2</sub>	2 %	2000 ppm	5000 ppm	300 ppm
O <sub>2</sub>	3 %	200 ppm	-	50 ppm
Ar	2 %	100 ppm	-	-
CO	1500 ppm	20 ppm	-	1000 ppm
H <sub>2</sub>	-	-	-	-
CH <sub>4</sub>	500 ppm	-	4 %	2 %
H <sub>2</sub> S	100 ppm	100 ppm	200 ppm	9000 ppm
SO <sub>2</sub>	100 ppm	100 ppm	-	-
MEA	-	2 ppm	2 ppm	-
DEA	-	-	-	-
HCl	4 ppm	4 ppm	-	-
Cl <sub>2</sub>	1 ppm	1 ppm	-	-

It has to be noted that the presence of NO<sub>x</sub> and higher order alkanes is neglected because these components are not yet considered in the present multi-component mixture model. Besides, the H<sub>2</sub>O content in all mixtures was increased to a comparably high value of

1500 ppm and  $H_2$  was omitted completely, although it should at least be considered for the mixture resulting from natural gas processing (with about 500 ppm).<sup>312</sup> However, both fluids frequently cause numerical problems when present in low concentrations. In case, of  $H_2$  this results from its extremely low solubility in the liquid phase of the mixture. In fact, such mole fractions can be smaller than the precision of the variables in the source code of the phase-equilibrium algorithms. With regard to  $H_2O$ , it is believed that the numerical problems are caused by the extremely complex mathematical structure of the pure-fluid reference EOS, IAPWS-95,<sup>29,88</sup> though this assumption needs to be evaluated more carefully. Phase envelopes for all four mixtures are shown in a  $p,T$  diagram in Figure 7.1. For comparison, the vapor-pressure curve of pure  $CO_2$  is included as well.

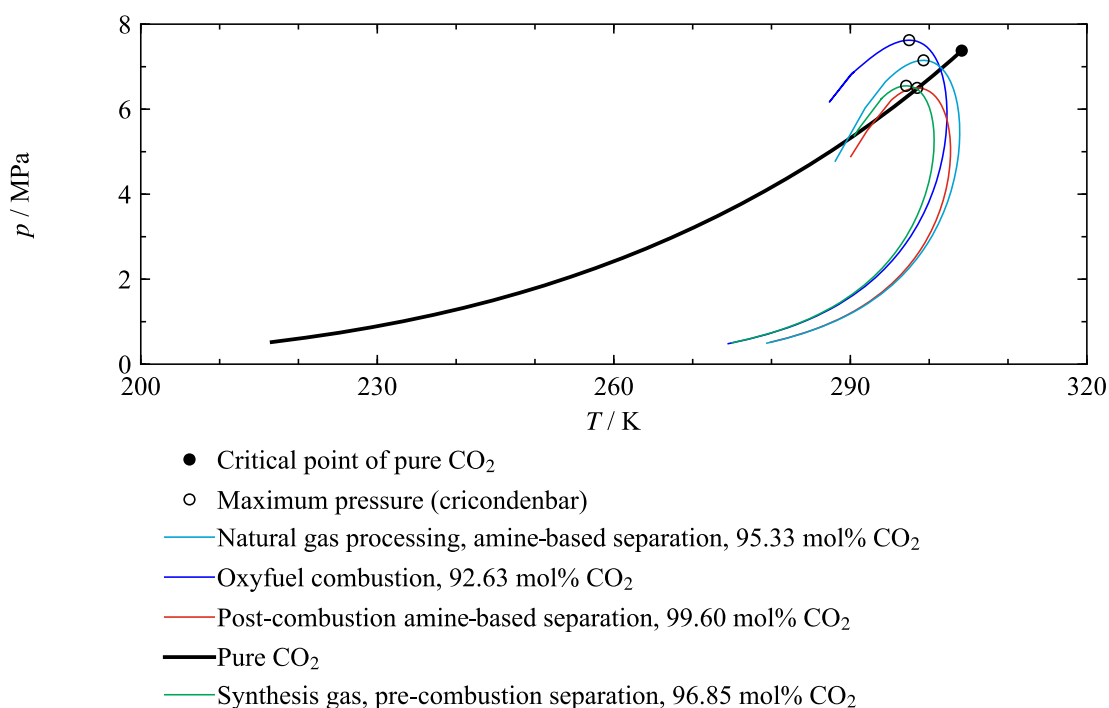


**Figure 7.1**  $p,T$  phase envelopes of four CCS mixtures calculated from the present multi-component mixture model. The vapor-pressure curve of pure  $CO_2$  calculated from the reference EOS of Span and Wagner<sup>28</sup> is shown for comparison.

One of the most important constraints to CCS-process design is that phase separation must be avoided during pipeline transportation; thus, the minimum operational pressure needs to be higher than the maximum pressure along the  $p,T$  phase envelope, also referred to as “cricondenbar”. For all exemplary mixtures shown in Figure 7.1, this maximum pressure is higher than the corresponding vapor pressure of pure  $CO_2$ . A two-phase system is consequently present at conditions where pure  $CO_2$  is expected to be liquid. However, the operational pressure would never be defined by the vapor pressure of pure  $CO_2$ , instead it is normally considerably higher than its critical pressure. Some references suggest a pipeline pressure above 8.6 MPa in order to always ensure single-phase conditions.<sup>315,316</sup> This suggestion can be confirmed by the present phase-envelope calculations. In fact, for three of the four mixtures, the calculated maximum pressure is lower than the critical pressure of

pure CO<sub>2</sub>. Only the mixture captured from oxyfuel combustion and containing the highest level of impurities exhibits a maximum pressure slightly above  $p_{c,\text{CO}_2}$ . In general, the presented phase envelopes suggest that the maximum pressure increases with increasing impurity content. Since this assumption is only based on four exemplary mixtures, a more systematic investigation is provided in Figure 7.2. Phase envelopes of eight binary mixtures of CO<sub>2</sub> and the most prominent impurities in the CCS mixtures specified in Table 7.1 are plotted in comparison to the vapor-pressure curve of pure CO<sub>2</sub>. For a better comparability, most of the mixtures contain 98 mol% CO<sub>2</sub> and 2 mol% of the respective impurity. Exceptions to this are the binary mixtures CO<sub>2</sub> + H<sub>2</sub>O and CO<sub>2</sub> + MEA that contain 1500 ppm H<sub>2</sub>O and 10 ppm MEA. Both components change the shape of the phase boundaries so drastically that including binary mixtures with 2 mol% would not lead to any meaningful conclusions. The systems CO<sub>2</sub> + CH<sub>4</sub> and CO<sub>2</sub> + H<sub>2</sub>S are not included, although they are relevant for the exemplary CCS mixtures. At 2 mol%, the impact of both components is so small that the corresponding phase envelopes are almost congruent with the vapor-pressure curve of CO<sub>2</sub>; thus, both systems were omitted for the sake of clarity. Although H<sub>2</sub> is not included in the multi-component mixtures shown in Figure 7.1, the system CO<sub>2</sub> + H<sub>2</sub> is presented too. The system CO<sub>2</sub> + SO<sub>2</sub> is included because various binary formulations for mixtures with SO<sub>2</sub> were developed within this work.

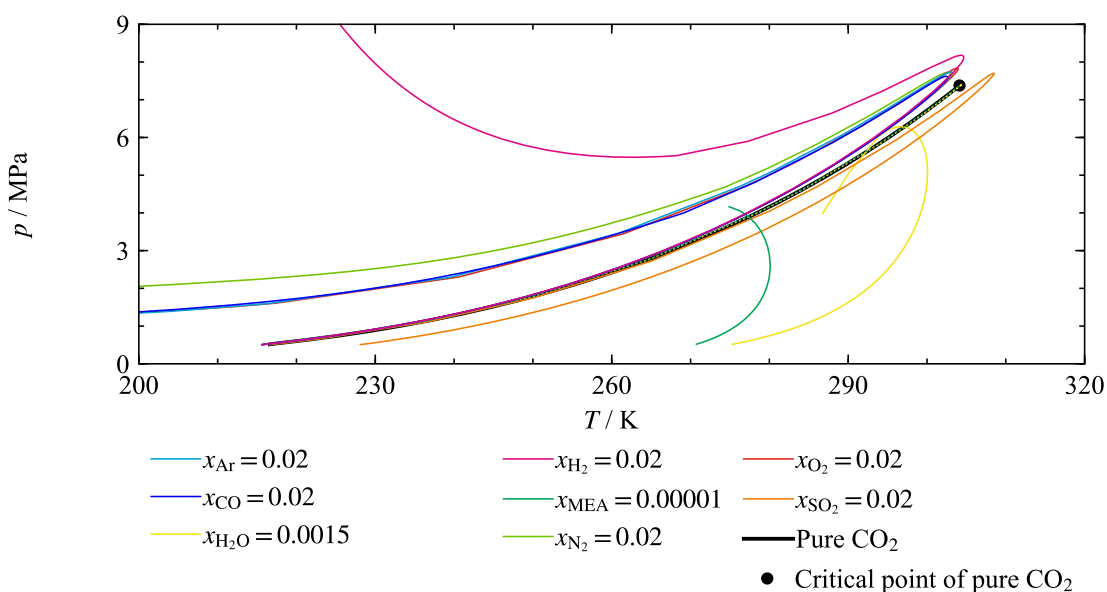


**Figure 7.2**  $p, T$  phase envelopes of selected binary mixtures with CO<sub>2</sub> calculated from the present multi-component mixture model including binary models from this work, EOS-CG,<sup>2</sup> and GERG-2008.<sup>36</sup> The vapor-pressure curve of pure CO<sub>2</sub> calculated from the reference EOS of Span and Wagner<sup>28</sup> is shown for comparison.

With regard to Figure 7.2, it can be noted that, except for SO<sub>2</sub>, H<sub>2</sub>O, and MEA, all other impurities shift the VLE region to higher saturation pressures. The presence of SO<sub>2</sub> leads to saturation pressure lower than the vapor pressure of CO<sub>2</sub>, which is notable with regard to CO<sub>2</sub> + SO<sub>2</sub> co-capturing processes (see Gimeno *et al.*<sup>268,317</sup> for a further discussion of this possibility). The most significant impact is noted for H<sub>2</sub>, H<sub>2</sub>O, and MEA. The systems

CO<sub>2</sub> + H<sub>2</sub>O and CO<sub>2</sub> + MEA exhibit particularly interesting phase envelopes consisting of one part almost congruent with the vapor-pressure curve of CO<sub>2</sub> and another part that mostly covers higher saturation temperatures. It has to be noted that the binary formulation for CO<sub>2</sub> + MEA is only based on Lorentz-Berthelot combining rules; thus, the results for this mixture are not validated by experimental data. However, considering the potentially high impact of MEA (and DEA) on the fluid behavior, comprehensive experimental data for pure amines and binary amine mixtures should be the focus of future research on thermodynamic property data for CCS. The same applies for binary mixtures with hydrogen: Within the scope of the present work, no binary system with H<sub>2</sub> was fitted to experimental data. In the multi-component mixture model GERG-2008, only CH<sub>4</sub> + H<sub>2</sub> is described with a binary specific departure function (see Secs. 3.3 and 4). For the remaining systems, the experimental data only allow for fitting reducing parameters or to apply simple combining rules. Considering the relevance of hydrogen also to energy-related topics other than CCS, new experimental data and improved models for binary systems with H<sub>2</sub> are needed.

The impact of impurities is not only interesting with regard to phase-equilibria but also to homogeneous properties. In Figure 7.3,  $\rho, p$  diagrams of pure CO<sub>2</sub> and the four CCS mixtures discussed before are shown for a subcritical and a supercritical isotherm.

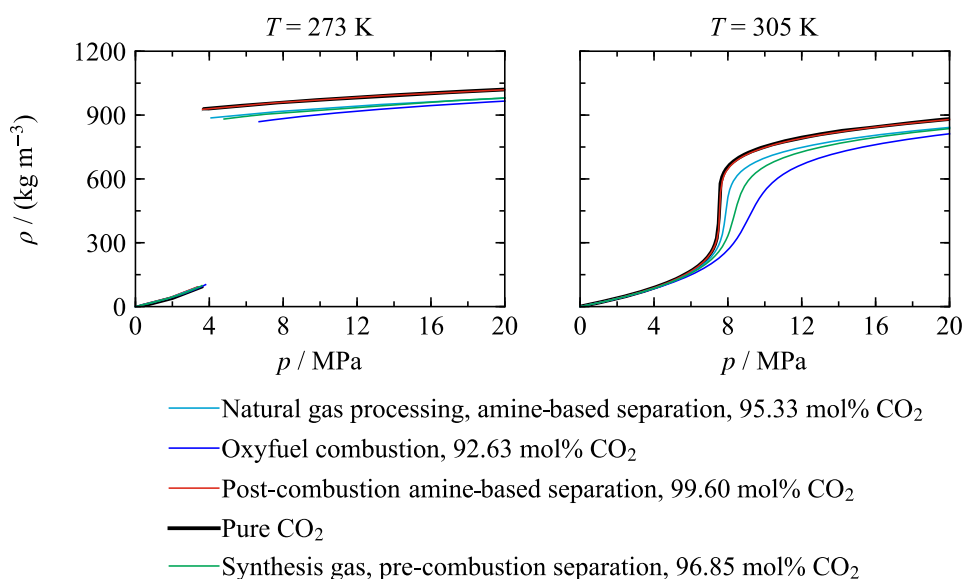


**Figure 7.3**  $\rho, p$  diagrams for four CCS mixtures calculated from the present multi-components mixture model at subcritical (left) and supercritical (right) temperature. The  $\rho, p$  diagram of pure CO<sub>2</sub> calculated from the reference EOS of Span and Wagner<sup>28</sup> is included for comparison.

As expected, the isotherms of the mixture with the highest CO<sub>2</sub> content are almost congruent with the ones of pure CO<sub>2</sub>. In the liquid phase, the densities of all other mixtures are considerably lower than the density of CO<sub>2</sub>. For the storage of CCS mixtures, this means that less fluid can be stored in a reservoir of given capacity. The impact of single impurities on the density is illustrated in Figure 7.4. All binary mixtures were calculated with an impurity mole fraction of 2 %.

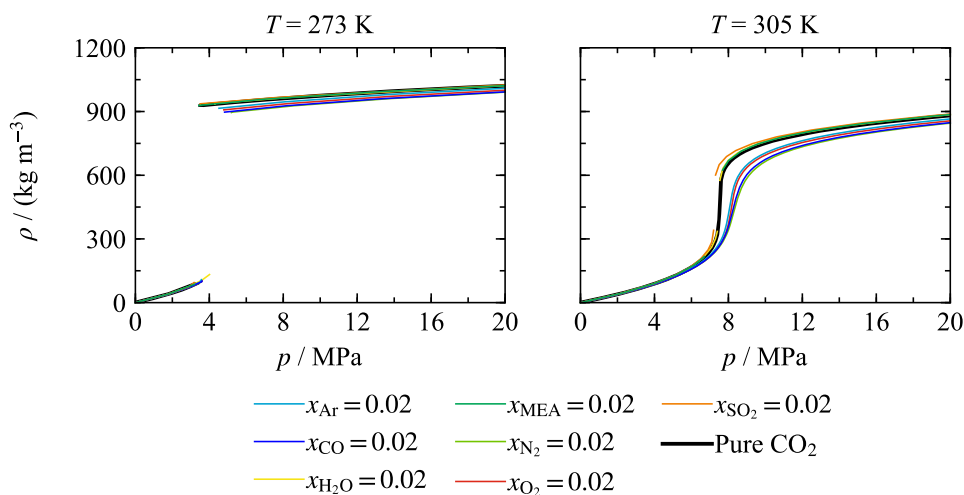


**Figure 7.4**  $\rho, p$  diagrams for selected binary mixtures calculated from the present multi-components mixture model including models from this work and EOS-CG<sup>2</sup> at subcritical (left) and, for some mixture, supercritical (right) temperature. The  $\rho, p$  diagram of pure CO<sub>2</sub> calculated from the reference EOS of Span and Wagner<sup>28</sup> is included for comparison.

Except for MEA, H<sub>2</sub>O, and SO<sub>2</sub>, all impurities cause a decrease in density compared to pure CO<sub>2</sub>. For various reasons higher contents of MEA and H<sub>2</sub>O should be avoided in CCS mixtures, but the fact that SO<sub>2</sub> increases the density of the mixture might be favorable and highlights again the concept of CO<sub>2</sub> + SO<sub>2</sub> co-capturing.<sup>268,317</sup>

The results presented in this section underline that the impact of impurities on the thermodynamic properties of CCS mixtures and thus on the CCS-process chain is considerable. Nevertheless, for a detailed analysis of this impact, a more comprehensive parameter study including additional properties such as speed of sound or Joule-Thomson coefficient should be carried out.





## 8 Conclusions and Recommendations

Within the scope of the present work, new empirical Helmholtz-explicit equations of state (EOS) for pure fluids and fluid mixtures were developed by non-linear fitting to mostly experimental data. The focus of these developments was on two main objectives: (1) a new reference EOS for pure heavy water and (2) an EOS for multi-component CO<sub>2</sub>-rich mixtures relevant to Carbon Capture and Storage (CCS). The work on CCS mixtures not only required the development of various mixture formulations but also the fitting of two additional pure-fluid EOS for chlorine and monoethanolamine (MEA).

The new EOS for heavy water will replace the previous standard formulation of the International Association for the Properties of Water and Steam (IAPWS) developed by Hill *et al.*<sup>1</sup> in 1982. The new EOS enables calculations of all thermodynamic properties over the whole fluid surface from the melting-pressure curve up to a temperature of 825 K and at pressures up to 1200 MPa. The development of the EOS was based on a comprehensive evaluation of the available experimental data, including the most recent studies. It was shown that the EOS describes the most accurate experimental results and almost all other available data within their uncertainties. Based on these comparisons with experimental data, detailed uncertainty estimates for calculated values of the most important thermodynamic properties were presented, namely thermal saturation data, density, speed of sound, and isobaric heat capacity. The most accurate experimental data were published for homogeneous liquid densities at atmospheric pressure from the triple-point to the normal-boiling-point temperature; the EOS represents these data within their uncertainty of 0.01 %. Compared to the previous EOS of Hill *et al.*, the new EOS allows for a significantly more accurate representation of sound speeds in the liquid phase (matching the most accurate data within their expanded uncertainty between 0.015 % and 0.02 %), liquid densities at pressures above 100 MPa, second and third virial coefficients, and also the available experimental data in the critical region and the metastable subcooled liquid. In fact, the description of the metastable subcooled liquid was carefully fitted, although the official range of validity of the EOS was limited to temperatures above the melting-pressure curve. Considering the entire fluid surface, it was shown that the EOS not only matches the experimental data, but also enables a correct representation of the physical behavior of the fluid including various specific characteristics of (heavy) water. Furthermore, the EOS has a more compact and numerically well-behaved functional form than its predecessor, and can be reasonably extrapolated to extreme values of temperature and pressure. For an explicit definition of the range of validity, auxiliary equations for the melting-pressure curves of the ice structures Ih, III, V, and VI, as well as the sublimation-pressure curve of ice Ih were developed that border the fluid region of heavy water described by the new reference EOS.

During the fitting process, some gaps in the available experimental database were revealed. If a further improved EOS were to be developed, accurate  $pvT$  data at pressures above 100 MPa and speed-of-sound data at pressures higher than 60 MPa would be extremely valuable. Between temperatures of 300 K and 350 K, the experimental database on vapor pressures was found to be less accurate than for lower and higher temperatures. New accurate data would improve the description of vapor-liquid equilibria, which would also benefit from accurate saturated-density data that are so far not available in the literature. In general, the homogeneous vapor phase is experimentally less investigated; densities are only available at temperatures above 423 K and no data have been published for vapor-phase sound speeds. Based on a thorough literature research, no reliable experimental data are available for metastable superheated-liquid and subcooled-vapor states, although these state regions are of significant relevance for energy applications. Since a further improvement of the present EOS through a refit is not planned or expected to become necessary in the next years, new data would primarily be used to improve uncertainty estimates for calculated properties. The new EOS for heavy water was recently published by Herrig *et al.*<sup>57</sup> and adopted as the new IAPWS standard at the 2018 IAPWS annual meeting in Prague. The IAPWS Release is expected to be available by the end of 2018 or early in 2019.

The second aim of this work, the multi-component mixture EOS for CCS applications, is considered as an expansion of the EOS-CG developed by Gernert<sup>17</sup> and published by Gernert and Span<sup>2</sup> that allows for a reliable description of mixtures containing the major components typically found in CCS processes (carbon dioxide, water, nitrogen, oxygen, argon, and carbon monoxide). Within the present work, that EOS was improved and extended to additional components typically present as minor impurities in CCS mixtures. The mathematical structure of the extended EOS consequently follows the one of EOS-CG, which was also adopted from the GERG-2008<sup>35,36</sup> model for natural gas mixtures. This framework of mixture modelling is based on the “extended corresponding states principle” and allows the description of multi-component mixtures by combining formulations for every possible binary combination of the components. Depending on the amount of experimental or, if available, also molecular-simulation data, these binary formulations can differ in their mathematical complexity and thus in their accuracy. The description of a binary mixture is essentially based on combining results of the respective pure-fluid EOS evaluated at “corresponding states”. This is enabled through the use of reduced input variables. If experimental data are scarce, the corresponding reducing functions for density and temperature are adjusted following simple combining rules. A more accurate description results from fitting the parameters of these reducing functions to experimental data. If comprehensive data are available that cover a wider range of the fluid surface, a binary specific departure function can be fitted. This function is a correction of the extended corresponding states principle and allows the most accurate description of a binary mixture.

In the present work, new formulations for 59 binary mixtures were developed. Out of these formulations, four contain a new binary specific departure function, and 13 are based on adjusted reducing functions without a departure function. The remaining systems were described by simple combining rules because the available database does not allow for fitting the parameters of the reducing functions. Together with 13 binary formulations adopted from EOS-CG and 19 formulations adopted from GERG-2008, the new binary models allow for a description of CCS mixtures with up to 14 components and thus 91 binary mixtures. The complete multi-component mixture model considers the presence of carbon dioxide, water, nitrogen, oxygen, argon, carbon monoxide, hydrogen, methane, hydrogen sulfide, monoethanolamine, diethanolamine, hydrogen chloride, and chlorine. Binary specific departure functions were developed for the systems  $\text{CO}_2 + \text{Ar}$ ,  $\text{CO}_2 + \text{CO}$ ,  $\text{H}_2\text{O} + \text{CH}_4$ , and  $\text{H}_2\text{O} + \text{H}_2\text{S}$  that replace previous formulations from EOS-CG and GERG-2008. Reducing parameters were adjusted for a number of binary systems with  $\text{SO}_2$ , namely  $\text{SO}_2$  plus  $\text{CO}_2$ ,  $\text{N}_2$ ,  $\text{O}_2$ ,  $\text{CH}_4$ ,  $\text{Cl}_2$ ,  $\text{HCl}$ ,  $\text{H}_2\text{O}$ , MEA and DEA (diethanolamine). Additional reducing parameters were fitted for MEA + DEA, MEA +  $\text{H}_2\text{O}$ , DEA +  $\text{H}_2\text{O}$ , and  $\text{Cl}_2 + \text{HCl}$ .

All new binary models were carefully validated through detailed comparisons with the available experimental data. Results for systems also considered in EOS-CG or GERG-2008 were additionally compared with values calculated from those models. Furthermore, results calculated from SRK,<sup>18</sup> LKP,<sup>19</sup> PSRK,<sup>41</sup> and PC(P)-SAFT<sup>44-46</sup> were considered for selected systems. The validation based on experimental data was mostly focused on vapor-liquid-equilibrium (VLE) data, which are the most important data for fitting and, in many cases, are the only data available. Overall, the new binary formulations provide a very accurate description of the available VLE data. Uncertainties in calculated VLE data were estimated for most binary formulations. These uncertainties vary considerably depending on the binary system and its phase-equilibrium behavior but mostly depending on the accuracy of the data used for fitting. The most accurate new formulations (for  $\text{CO}_2 + \text{Ar}$  and  $\text{CO}_2 + \text{CO}$ ) predict phase-boundaries mostly within uncertainties of about 1 mol% or smaller. For less well investigated systems such as MEA + DEA or  $\text{Cl}_2 + \text{HCl}$ , the uncertainties of calculated values might increase up to about 5 mol%. Estimated uncertainties in other calculated properties were given when comparative experimental data were available. Comparisons with the best data sets available, for example gas-phase densities for  $\text{CO}_2 + \text{Ar}$  (with experimental uncertainties between 0.033 % and 0.043 %), showed that these data can be represented within their experimental uncertainties.

The mathematical structure of the mixture model requires reliable pure-fluid EOS for every component. To implement the binary formulations discussed above, new Helmholtz-energy explicit EOS for pure chlorine and monoethanolamine (MEA) were developed.

The new EOS for chlorine replaces the current standard EOS of the International Union of Pure and Applied Chemistry (IUPAC) presented by Angus *et al.*<sup>152</sup> in 1985. The functional

form of that EOS is not suitable for the use in multi-component mixture models. The EOS developed in this work is valid from the triple point ( $T_{\text{tp,Cl}_2} = 172.17 \text{ K}$ ) up to 440 K and at pressures up to 20 MPa. Because it was exclusively developed for the application in the extended EOS for CCS mixtures, its extrapolation behavior beyond the experimentally investigated state regions was carefully constrained. The EOS consequently yields qualitatively reasonable results for state points outside its range of validity, which is important when evaluating it in mixture calculations. Due to its high toxicity, the quantity and quality of the experimental database for chlorine is much more limited than, for example, for heavy water. Nevertheless, sufficiently accurate data were available to fit the new EOS. These data are mostly represented within their experimental uncertainties.

Prior to the present work, no reliable EOS for MEA was available in the literature, which is not surprising with regard to the extremely limited experimental database. Nevertheless, a pure-fluid EOS was urgently needed due to the importance of MEA as a solvent in the  $\text{CO}_2$ -capturing process. The proposed EOS was fitted to the scarce data found in the literature, which only include measurements at saturation and in the liquid phase at atmospheric pressure. The limited data for homogeneous densities, vapor pressures, sound speeds, and isochoric heat capacities are accurately represented. The EOS is valid from the triple point ( $T_{\text{tp,MEA}} = 283.7 \text{ K}$ ) to at least 675 K and 9 MPa; thus, to slightly above its critical point ( $T_{\text{c,MEA}} = 671.4 \text{ K}$  and  $p_{\text{c,MEA}} = 8.125 \text{ MPa}$ ). Its extrapolation behavior was continuously validated to allow for reasonable results of mixture calculations as shown for the binary systems MEA + DEA, MEA +  $\text{H}_2\text{O}$ , DEA +  $\text{H}_2\text{O}$ , and  $\text{SO}_2$  + MEA.

The present extended version of the multi-component mixture model, also including the new pure-fluid EOS for chlorine and MEA, presents a significant improvement in the description of the thermodynamic properties of CCS mixtures. The importance of an EOS for these mixtures was underlined in this thesis by showing the impact of impurities on phase-equilibria and homogeneous densities based on comparisons with the respective properties of pure  $\text{CO}_2$ . For a more detailed impression of this impact and more importantly for a comprehensive validation of the multi-component mixture model, accurate experimental data for typical CCS mixtures with various components are mandatory and should be the focus of further research. Future measurement campaigns should also address the comparably large number of systems that are so scarcely covered by experimental data that no EOS parameters could be fitted in this work. In addition to extensive experimental work, a further improvement of the CCS-mixture model requires the development of new approaches to describe binary systems that will most likely never be covered by experimental data. Aside from this, the most important next step is a modification of the functional form that allows for the descriptions of chemically reactive systems, which are so far not considered but expected to be highly relevant to CCS. Finally, several other fluids such as ammonia, nitrogen oxides, methanol, or glycols are possible components of CCS-mixtures and should be considered for a further expansion of the multi-component EOS.

## References

- <sup>1</sup> P. G. Hill, R. D. C. MacMillan, and V. Lee, *J. Phys. Chem. Ref. Data* **11**, 1 (1982).
- <sup>2</sup> J. Gernert and R. Span, *J. Chem. Thermodyn.* **93**, 274 (2016).
- <sup>3</sup> C. Tietz, *Photograph of Heavy- and Ordinary-Water Ice Cubes in Ordinary Water*. (personal communication, 2018).
- <sup>4</sup> G. S. Kell, *J. Phys. Chem. Ref. Data* **6**, 1109 (1977).
- <sup>5</sup> International Association for the Properties of Water and Steam, IAPWS G5-01(2016), *Guideline on the Use of Fundamental Physical Constants and Basic Constants of Water* (2001).
- <sup>6</sup> H. C. Urey, F. G. Brickwedde, and G. M. Murphy, *Phys. Rev.* **40**, 1 (1932).
- <sup>7</sup> C. Waltham, arXiv:physics/0206076v2 [physics.hist-ph] (2011).
- <sup>8</sup> J. R. Dunning, G. B. Pegram, G. A. Fink, and D. P. Mitchell, *Phys. Rev.* **48**, 265 (1935).
- <sup>9</sup> N. Lifson, G. B. Gordon, and R. McClintock, *J. Appl. Phycol.* **7**, 704 (1955).
- <sup>10</sup> D. A. Schoeller and E. van Santen, *J. Appl. Phycol.* **53**, 955 (1982).
- <sup>11</sup> R. G. Fairchild, D. N. Slatkin, J. A. Coderre, P. L. Micca, B. H. Laster, S. B. Kahl, P. Som, I. Fand, and F. Wheeler, *Pigment Cell Res.* **2**, 309 (1989).
- <sup>12</sup> G. Czako, E. Mátyus, and A. G. Császár, *J. Phys. Chem. A* **113**, 11665 (2009).
- <sup>13</sup> M. Ceriotti, W. Fang, P. G. Kusalik, R. H. McKenzie, A. Michaelides, M. A. Morales, and T. E. Markland, *Chem. Rev.* **116**, 7529 (2016).
- <sup>14</sup> H. Preston-Thomas, *Metrologia* **27**, 3 (1990).
- <sup>15</sup> International Association for the Properties of Water and Steam, IAPWS R3-84(2005), *Revised Release on the IAPS Formulation 1984 for the Thermodynamic Properties of Heavy Water Substance* (2005).
- <sup>16</sup> Intergovernmental Panel on Climate Change, *IPCC Special Report on Carbon Capture and Storage* (2005).
- <sup>17</sup> J. Gernert, *A new Helmholtz Energy Model for Humid Gases and CCS Mixtures*, Ph.D. thesis, Ruhr-Universität Bochum.
- <sup>18</sup> G. Soave, *Chem. Eng. Sci.* **27**, 1197 (1972).
- <sup>19</sup> U. Plöcker, H. Knapp, and J. Prausnitz, *Ind. Eng. Chem. Proc. Des. Dev.* **17**, 324 (1978).

- <sup>20</sup> van der Waals, J. H., *Over de Continuïteit van den Gas- en Vloeistoestand*, Ph.D. thesis, University of Leiden (1873).
- <sup>21</sup> O. Redlich and J. N. S. Kwong, *Chem. Rev.* **44**, 233 (1949).
- <sup>22</sup> R. Span, R. Beckmüller, T. Eckermann, S. Herrig, S. Hielscher, A. Jäger, T. Neumann, S. Pohl, B. Semrau, and M. Thol, *TREND. Thermodynamic Reference and Engineering Data 4.0* (Lehrstuhl für Thermodynamik, Ruhr-Universität Bochum, Bochum, to be released, 2018).
- <sup>23</sup> I. H. Bell and A. Jäger, *J. Res. Natl. Inst. Stan.* **121**, 238 (2016).
- <sup>24</sup> M. Benedict, G. B. Webb, and L. C. Rubin, *J. Chem. Phys.* **8**, 334 (1940).
- <sup>25</sup> B. I. Lee and M. G. Kesler, *AIChE J.* **21**, 510 (1975).
- <sup>26</sup> R. Span, *Multiparameter Equations of State: An Accurate Source of Thermodynamic Property Data* (Springer, Berlin, 2000).
- <sup>27</sup> Verein Deutscher Ingenieure, *VDI-Wärmeatlas* (Springer Vieweg, Berlin, 2013).
- <sup>28</sup> R. Span and W. Wagner, *J. Phys. Chem. Ref. Data* **25**, 1509 (1996).
- <sup>29</sup> W. Wagner and A. Pruß, *J. Phys. Chem. Ref. Data* **31**, 387 (2002).
- <sup>30</sup> E. W. Lemmon and R. T. Jacobsen, *J. Phys. Chem. Ref. Data* **34**, 69 (2005).
- <sup>31</sup> E. W. Lemmon, M. O. McLinden, and W. Wagner, *J. Chem. Eng. Data* **54**, 3141 (2009).
- <sup>32</sup> M. Thol and E. W. Lemmon, *Int. J. Thermophys.* **37**, 28 (2016).
- <sup>33</sup> K. Gao, J. Wu, P. Zhang, and E. W. Lemmon, *J. Chem. Eng. Data* **61**, 2859 (2016).
- <sup>34</sup> E. W. Lemmon and R. Tillner-Roth, *Fluid Phase Equilib.* **165**, 1 (1999).
- <sup>35</sup> O. Kunz, R. Klimeck, W. Wagner, and M. Jaeschke, *The GERG-2004 Wide-Range Equation of State for Natural Gases and Other Mixtures* (VDI Verlag, Düsseldorf, 2007).
- <sup>36</sup> O. Kunz and W. Wagner, *J. Chem. Eng. Data* **57**, 3032 (2012).
- <sup>37</sup> I. H. Bell and A. Jäger, *Fluid Phase Equilib.* **433**, 159 (2017).
- <sup>38</sup> I. H. Bell, K. Gao, J. Wu, and E. W. Lemmon, *A Helmholtz-Energy Equation of State for Ammonia + Water* (to be published, 2019).
- <sup>39</sup> E. W. Lemmon, I. H. Bell, M. L. Huber, and M. O. McLinden, *NIST Standard Reference Database 23: Reference Fluid Thermodynamic and Transport Properties-REFPROP, Version 10.0* (National Institute of Standards and Technology, Standard Reference Data Program, Gaithersburg, 2018).

- <sup>40</sup> I. H. Bell, J. Wronski, S. Quoilin, and V. Lemort, *Ind. Eng. Chem. Res.* **53**, 2498 (2014).
- <sup>41</sup> T. Holderbaum and J. Gmehling, *Fluid Phase Equilib.* **70**, 251 (1991).
- <sup>42</sup> A. Fredenslund, R. L. Jones, and J. M. Prausnitz, *AIChE J.* **21**, 1086 (1975).
- <sup>43</sup> W. G. Chapman, K. E. Gubbins, G. Jackson, and M. Radosz, *Fluid Phase Equilib.* **52**, 31 (1989).
- <sup>44</sup> J. Gross and G. Sadowski, *Ind. Eng. Chem. Res.* **40**, 1244 (2001).
- <sup>45</sup> J. Gross, *AIChE J.* **51**, 2556 (2005).
- <sup>46</sup> J. Gross and J. Vrabec, *AIChE J.* **52**, 1194 (2006).
- <sup>47</sup> T. Eckermann, *Thermodynamic Property Models for Synthetic Lubricants and Their Mixtures with Working Fluids in ORCs*, Ph.D. thesis, Ruhr-Universität Bochum (2018).
- <sup>48</sup> R. Span, E. W. Lemmon, R. T. Jacobsen, W. Wagner, and A. Yokozeki, *J. Phys. Chem. Ref. Data* **29**, 1361 (2000).
- <sup>49</sup> T. Neumann, *Development of New Helmholtz Models for Binary Mixture Relevant for CCS*, Master thesis, Ruhr-Universität Bochum (2017).
- <sup>50</sup> M. Thol, F. H. Dubberke, E. Baumhögger, R. Span, and J. Vrabec, *J. Chem. Eng. Data* **63**, 2533 (2018).
- <sup>51</sup> K. Gao, J. Wu, I. H. Bell, and E. W. Lemmon, *J. Phys. Chem. Ref. Data* (to be published, 2019).
- <sup>52</sup> T. W. Leland, P. S. Chapplear, and B. W. Gamson, *AIChE J.* **8**, 482 (1962).
- <sup>53</sup> K. N. Marsh, *J. Chem. Eng. Data* **42**, 1 (1997).
- <sup>54</sup> I. H. Bell and E. W. Lemmon, *J. Chem. Eng. Data* **61**, 3752 (2016).
- <sup>55</sup> M. Kortmann, *Development of Empirical Multiparameter Equations of State for Monoethanolamine and Diethanolamine*, Master thesis, Ruhr-Universität Bochum (2016).
- <sup>56</sup> C. Tietz, *Development of Empirical Multiparameter Equations of State for Nitrogen Oxides*, Master thesis, Ruhr-Universität Bochum (2015).
- <sup>57</sup> S. Herrig, M. Thol, A. H. Harvey, and E. W. Lemmon, *J. Phys. Chem. Ref. Data* (accepted for publication, 2018).
- <sup>58</sup> International Association for the Properties of Water and Steam, IAPWS R16-17, *Release on the IAPWS Formulation 2017 for the Thermodynamic Properties of Heavy Water* (2017).

- <sup>59</sup> P. J. Mohr, D. B. Newell, and B. N. Taylor, *J. Phys. Chem. Ref. Data* **45**, 043102 (2016).
- <sup>60</sup> International Association for the Properties of Water and Steam, IAPWS R2-83(1992), *IAPWS Release on the Values of Temperature, Pressure and Density of Ordinary and Heavy Water Substances at their Respective Critical Points* (1992).
- <sup>61</sup> L. Markó, G. Jákli, and G. Jancsó, *J. Chem. Thermodyn.* **21**, 437 (1989).
- <sup>62</sup> G. Blank, *Wärme- und Stoffübertragung* **2**, 53 (1969).
- <sup>63</sup> J. M. H. Levelt Sengers, J. Straub, K. Watanabe, and P. G. Hill, *J. Phys. Chem. Ref. Data* **14**, 193 (1985).
- <sup>64</sup> S. L. Rivkin and T. S. Akhundov, *Teploenergetika* **9**(5), 62 (1962).
- <sup>65</sup> E. Bartholomé and K. Clusius, *Z. Phys. Chem.* **28** (1935).
- <sup>66</sup> W. M. Jones, *J. Am. Chem. Soc.* **74**, 6065 (1952).
- <sup>67</sup> E. H. Riesenfeld and T. L. Chang, *Z. Phys. Chem.* **30**, 61 (1935).
- <sup>68</sup> H. Eck, *Physik. Z.* **40**, 3 (1939).
- <sup>69</sup> G. D. Oliver and J. W. Grisard, *J. Am. Chem. Soc.* **78**, 561 (1956).
- <sup>70</sup> L. A. Guildner, D. P. Johnson, and F. E. Jones, *Science* **191**, 1261 (1976).
- <sup>71</sup> W. Wagner, A. Saul, and A. Pruß, *J. Phys. Chem. Ref. Data* **23**, 515 (1994).
- <sup>72</sup> W. Wagner, T. Riethmann, R. Feistel, and A. H. Harvey, *J. Phys. Chem. Ref. Data* **40**, 043103 (2011).
- <sup>73</sup> P. W. Bridgman, *J. Chem. Phys.* **3**, 597 (1935).
- <sup>74</sup> S. J. Henderson and R. J. Speedy, *J. Phys. Chem.* **91**, 3069 (1987).
- <sup>75</sup> P. W. Bridgman, *Proc. Amer. Acad. Arts Sci.* **47**, 347 (1911).
- <sup>76</sup> G. F. Molinar, V. Bean, J. Houck, and B. Welch, *Metrologia* **16**, 21 (1980).
- <sup>77</sup> E. A. Long and J. D. Kemp, *J. Am. Chem. Soc.* **58**, 1829 (1936).
- <sup>78</sup> J. Timmermans, M. Hennaut-Roland, and D. Rozental, *Comptes Rendus Acad. Sci.* **202**, 1061 (1936).
- <sup>79</sup> J. D. Pupezin, G. Jákli, G. Jancsó, and W. A. Van Hook, *J. Phys. Chem.* **76**, 743 (1972).
- <sup>80</sup> G. A. Bottomley, *Aust. J. Chem.* **31**, 1177 (1978).
- <sup>81</sup> K. Niwa and E. Shimazaki, *J. Chem. Soc. Japan* **60**, 985 (1939).
- <sup>82</sup> G. Jancsó, J. D. Pupezin, and W. A. Van Hook, *J. Phys. Chem.* **74**, 2984 (1970).



- <sup>83</sup> International Association for the Properties of Water and Steam, IAPWS R14-08(2011), *Revised Release on the Pressure along the Melting and Sublimation Curves of Ordinary Water Substance* (2011).
- <sup>84</sup> I. Simkó, T. Furtenbacher, J. Hrubý, N. F. Zobov, O. L. Polyansky, J. Tennyson, R. R. Gamache, T. Szidarovszky, N. Dénes, and A. G. Császár, *J. Phys. Chem. Ref. Data* **46**, 023104 (2017).
- <sup>85</sup> T. Furtenbacher, T. Szidarovszky, J. Hrubý, A. A. Kyuberis, N. F. Zobov, O. L. Polyansky, J. Tennyson, and A. G. Császár, *J. Phys. Chem. Ref. Data* **45**, 043104 (2016).
- <sup>86</sup> A. S. Friedman and L. Haar, *J. Chem. Phys.* **22**, 2051 (1954).
- <sup>87</sup> J. M. L. Martin, J. P. François, and R. Gijbels, *J. Chem. Phys.* **96**, 7633 (1992).
- <sup>88</sup> International Association for the Properties of Water and Steam, IAPWS R6-95(2016), *Revised Release on the IAPWS Formulation 1995 for the Thermodynamic Properties of Ordinary Water Substance for General and Scientific Use* (2016).
- <sup>89</sup> G. F. Kraus and S. C. Greer, *J. Phys. Chem.* **88**, 4781 (1984).
- <sup>90</sup> L. Besley and G. A. Bottomley, *J. Chem. Thermodyn.* **5**, 397 (1973).
- <sup>91</sup> G. Jákli and H. Illy, *Vapour Pressure Isotope Effect of the Equimolar H<sub>2</sub>O-D<sub>2</sub>O Mixture*, Hungarian Academy of Sciences, Budapest, Hungary (1980).
- <sup>92</sup> G. Jákli and W. A. Van Hook, *J. Chem. Eng. Data* **26**, 243 (1981).
- <sup>93</sup> G. Jákli and L. Markó, *ACH Models Chem.* **132**, 226 (1995).
- <sup>94</sup> K. Zieborak, *Z. Phys. Chem.* **231**, 248 (1966).
- <sup>95</sup> A. H. Harvey and E. W. Lemmon, *J. Phys. Chem. Ref. Data* **31**, 173 (2002).
- <sup>96</sup> N. S. Osborne and C. H. Meyers, *J. Res. Natl. Bur. Stand.* **13**, 1 (1934).
- <sup>97</sup> B. A. Mursalov, I. M. Abdulagatov, V. I. Dvoryanchikov, A. N. Kamalov, and S. B. Kiselev, *Int. J. Thermophys.* **20**, 1497 (1999).
- <sup>98</sup> U. Grossmann-Doerth, *Z. Naturforsch. A* **10**, 799 (1955).
- <sup>99</sup> U. Grossmann-Doerth, *Z. Naturforsch. A* **11**, 254 (1956).
- <sup>100</sup> G. M. Hebert, H. F. McDuffie, and C. H. Secoy, *J. Phys. Chem.* **62**, 431 (1958).
- <sup>101</sup> J. M. Costello and S. T. Bowden, *Recl. Trav. Chim. Pays-Bas* **77** (1958).
- <sup>102</sup> G. S. Kell, G. E. McLaurin, and E. Whalley, *Proc. R. Soc. London, Ser. A* **425**, 49 (1989).
- <sup>103</sup> G. S. Kell, G. E. McLaurin, and E. Whalley, *Phil. Trans. R. Soc. Lond. A* **315**, 247 (1985).

- <sup>104</sup> G. S. Kell and E. Whalley, *Phil. Trans. R. Soc. Lond. A* **258**, 565 (1965).
- <sup>105</sup> G. S. Kell, G. E. McLaurin, and E. Whalley, *Proc. R. Soc. London, Ser. A* **360** (1978).
- <sup>106</sup> G. S. Kell, G. E. McLaurin, and E. Whalley, *J. Chem. Phys.* **48**, 3805 (1968).
- <sup>107</sup> M. Duška, J. Hykl, P. Peukert, A. Blahut, V. Vinš, and J. Hrubý, *Relative Density and Isobaric Expansivity of Cold and Supercooled Heavy Water from 254 to 298 K and up to 100 MPa* (to be published, 2018).
- <sup>108</sup> R. T. Emmet and F. J. Millero, *J. Chem. Eng. Data* **20**, 351 (1975).
- <sup>109</sup> A. A. Aleksandrov, T. S. Khasanshin, and D. K. Larkin, *Zh. Fiz. Khim.* **50**, 394 (1976).
- <sup>110</sup> N. V. Tsederberg, A. A. Aleksandrov, and T. S. Khasanshin, *Therm. Eng.* **19**(10), 96 (1972).
- <sup>111</sup> M. Tanaka, G. Girard, R. S. Davis, A. Peuto, and N. Bignell, *Metrologia* **38**, 301 (2001).
- <sup>112</sup> C.-T. A. Chen and F. J. Millero, *J. Acoust. Soc. Am.* **62**, 553 (1977).
- <sup>113</sup> K. Stokland, E. Ronæss, and L. Tronstad, *Trans. Faraday Soc.* **35**, 312 (1939).
- <sup>114</sup> F. Steckel and S. Szapiro, *Trans. Faraday Soc.* **59**, 331 (1963).
- <sup>115</sup> T. L. Chang and L.-H. Tung, *Nature* **163**, 737 (1949).
- <sup>116</sup> M. Ceccaldi, G. Girard, M. Menaché, and M. Riedinger, *Metrologia* **11**, 53 (1975).
- <sup>117</sup> G. N. Lewis and R. T. MacDonald, *J. Am. Chem. Soc.* **55**, 3057 (1933).
- <sup>118</sup> T. Takéuchi and T. Inai, *Jpn. J. Physics* **11**, 67 (1936).
- <sup>119</sup> A. A. Aleksandrov, D. K. Larkin, A. B. Matveev, and Z. A. Ershova, *Izvestiia V. U. Z.* **11**, 84 (1977).
- <sup>120</sup> H. Kanno and C. A. Angell, *J. Chem. Phys.* **73**, 1940 (1980).
- <sup>121</sup> J. Jůza, V. Kmoníček, O. Šifner, and K. Schovanec, *Physica* **32**, 362 (1966).
- <sup>122</sup> G. S. Kell, G. E. McLaurin, and E. Whalley, *Phil. Trans. R. Soc. Lond. A* **315**, 235 (1985).
- <sup>123</sup> A. A. Aleksandrov, T. S. Khasanshin, and D. K. Larkin, *Specific Volumes of Ordinary and Heavy Water at High Pressures and Temperatures*, Report to Working Group I, IAPS (1976).
- <sup>124</sup> N. V. Tsederberg, A. A. Aleksandrov, T. S. Khasanshin, and D. K. Larkin, *Therm. Eng.* **20**(8), 17 (1973).
- <sup>125</sup> G. Garberoglio, P. Jankowski, K. Szalewicz, and A. H. Harvey, *Faraday Discuss.* (to be published 2018).

- <sup>126</sup> P. Jankowski, G. Murdachaew, R. Bukowski, O. Akin-Ojo, C. Leforestier, and K. Szalewicz, *J. Phys. Chem. A* **119**, 2940 (2015).
- <sup>127</sup> U. Góra, W. Cencek, R. Podeszwa, A. van der Avoird, and K. Szalewicz, *J. Chem. Phys.* **140**, 194101 (2014).
- <sup>128</sup> R. Wegge, M. Richter, and R. Span, *Fluid Phase Equilib.* **418**, 175 (2016).
- <sup>129</sup> F. Fehres and S. Rudtsch (personal communication, 2018).
- <sup>130</sup> A. A. Aleksandrov and D. K. Larkin, *Teploenergetika* **24**(1), 73 (1977).
- <sup>131</sup> W. D. Wilson, *J. Acoust. Soc. Am.* **33**, 314 (1961).
- <sup>132</sup> W. D. Wilson, *J. Acoust. Soc. Am.* **31**, 1067 (1959).
- <sup>133</sup> S. Lago and P. A. Giuliano Albo, *Speed of Sound Measurements in Deuterium Oxide (D<sub>2</sub>O) at Temperatures between (276.97 and 363.15) K and at Pressures up to 210 MPa* (to be published, 2019).
- <sup>134</sup> H. I. Erokhin and B. H. Kompaniets, *Teplofiz. Vys. Temp.* **18**, 1172 (1980).
- <sup>135</sup> S. L. Rivkin and B. N. Egorov, *At. Energ.* **7**, 462 (1959).
- <sup>136</sup> S. L. Rivkin and B. N. Egorov, *Teploenergetika* **9**(12), 60 (1962).
- <sup>137</sup> S. L. Rivkin and B. N. Egorov, *Teploenergetika* **10**(7), 75 (1963).
- <sup>138</sup> S. L. Rivkin and B. N. Egorov, *At. Energ.* **14**, 416 (1963).
- <sup>139</sup> C. A. Angell, W. J. Sichina, and M. Oguni, *J. Phys. Chem.* **86**, 998 (1982).
- <sup>140</sup> N. N. Smirnova, T. A. Bykova, K. van Durme, and B. van Mele, *J. Chem. Thermodyn.* **38**, 879 (2006).
- <sup>141</sup> A. Eucken and M. Eigen, *Z. Elektrochem. Angew. Physik. Chem.* **55**, 343 (1951).
- <sup>142</sup> K. I. Amirkhanov, G. V. Stepanov, B. A. Mursalov, and O. A. Bui, *Teploenergetika* **22**(4), 90 (1975).
- <sup>143</sup> N. G. Polikhronidi, I. M. Abdulagatov, J. W. Magee, and G. V. Stepanov, *Int. J. Thermophys.* **23**, 745 (2002).
- <sup>144</sup> K. I. Amirkhanov, G. V. Stepanov, and B. G. Alibekov, *Isochoric Heat Capacity of Water and Steam*, Akad. Nauk SSSR, Dagestanskii Filial (1969).
- <sup>145</sup> V. N. Evstefeev, V. P. Skripov, and V. N. Chukanov, *High Temperatures* **17**, 252 (1979).
- <sup>146</sup> V. Holten, J. V. Sengers, and M. A. Anisimov, *J. Phys. Chem. Ref. Data* **43**, 043101 (2014).

- <sup>147</sup> International Association for the Properties of Water and Steam, IAPWS G12-15, *Guideline on Thermodynamic Properties of Supercooled Water* (2015).
- <sup>148</sup> V. Holten, C. E. Bertrand, M. A. Anisimov, and J. V. Sengers, *J. Chem. Phys.* **136**, 094507 (2012).
- <sup>149</sup> B. V. Zheleznyi, *Russ. J. Phys. Chem.* **41**, 1311 (1969).
- <sup>150</sup> D. H. Rasmussen and A. P. MacKenzie, *J. Chem. Phys.* **59**, 5003 (1973).
- <sup>151</sup> O. Conde, J. Teixeira, and P. Papon, *J. Chem. Phys.* **76**, 3747 (1982).
- <sup>152</sup> S. Angus, B. Armstrong, and de Reuck, K. M., *International Thermodynamic Tables of the Fluid State - 8 - Chlorine: Tentative Tables*, IUPAC Chemical Data Series No. 31, London (1985).
- <sup>153</sup> D. Ambrose, D. J. Hall, D. A. Lee, G. B. Lewis, and C. J. Mash, *J. Chem. Thermodyn.* **11**, 1089 (1979).
- <sup>154</sup> J. J. Hurly, *Int. J. Thermophys.* **23**, 455 (2002).
- <sup>155</sup> W. H. Evans, T. R. Munson, and D. D. Wagman, *J. Res. Natl. Bur. Stand.* **55** (1955).
- <sup>156</sup> D. Ambrose, B. E. Broderick, and R. Townsend, *J. Chem. Soc., A*, 633 (1967).
- <sup>157</sup> M. Pellaton, *J. Chim. Phys.* **14**, 426 (1915).
- <sup>158</sup> W. F. Giauque and T. M. Powell, *J. Am. Chem. Soc.* **61**, 1970 (1939).
- <sup>159</sup> G. H. Cheesman and D. L. Scott, *Aust. J. Chem.* **21**, 287 (1968).
- <sup>160</sup> W. F. Giauque and C. J. Egan, *J. Chem. Phys.* **5**, 45 (1937).
- <sup>161</sup> H. Wagenbreth, *PTB-Mitteilung* **68**, 91 (1968).
- <sup>162</sup> R. E. Hulme, *Chem. Eng.* **56** (1949).
- <sup>163</sup> A. S. Ross and O. Maass, *Can. J. Res.* **18**, 55 (1940).
- <sup>164</sup> A. Jaquerod and M. Tourpaian, *J. Chim. Phys.* **11**, 3 (1913).
- <sup>165</sup> R. Schulze, *Ann. d. Phys.* **426**, 41 (1939).
- <sup>166</sup> E. Sittig, *Die Schwingungsrelaxation im flüssigen und gasförmigen Chlor*, Ph.D. thesis, Technische Hochschule Stuttgart (1959).
- <sup>167</sup> K. Strecker, *Wied. Annalen* **249** (1881).
- <sup>168</sup> A. Eucken and E. Karwat, *Z. Phys. Chem.* **112**, 467 (1924).
- <sup>169</sup> M. Thol, *Empirical Multiparameter Equations of State Based on Molecular Simulation and Hybrid Data Sets*, Ph.D. thesis, Ruhr-Universität Bochum (2015).
- <sup>170</sup> M. Frenkel, R. D. Chirico, V. Diky, K. Kroenlein, C. D. Muzny, A. F. Kazakov, J. W. Magge, I. M. Abdulagatov, and E. W. Lemmon, *NIST Standard Reference Database*

- 103b: NIST Thermo Data Engine - Pure Compounds, Binary Mixtures, Reactions, Version 8.0* (National Institute of Standards and Technology, Standard Reference Data Program, Gaithersburg, 2013).
- <sup>171</sup> A. S. Teja and D. J. Rosenthal, DIPPR Data Series **1**, 96 (1991).
- <sup>172</sup> I. Lafontaine, Bull. Soc. Chim. Belg. **67**, 153 (1958).
- <sup>173</sup> M. J. Anselme and A. S. Teja, AIChE Symp. Ser. **86**, 128 (1990).
- <sup>174</sup> T. E. Daubert, J. W. Jalowka, and V. Goren, AIChE Symp. Ser. **83**, 128 (1987).
- <sup>175</sup> S. M. Danov, N. B. Mashin, R. V. Efremov, and K. K. Slashchinina, Russ. J. Phys. Chem. **43**, 401 (1969).
- <sup>176</sup> R. L. Lyons, *The Determination of Critical Properties and Vapor Pressure of Thermally Stable and Unstable Compounds*, Master Thesis, Pennsylvania State University (1985).
- <sup>177</sup> O. Noll, A. Valtz, D. Richon, T. Getachew-Sawaya, I. Mokbel, and J. Jose, ELDATA: Int. Electron. J. Phys.-Chem. Data **4**, 105 (1998).
- <sup>178</sup> W. V. Wilding, L. C. Wilson, and G. M. Wilson, AIChE Symp. Ser. **83**, 49 (1987).
- <sup>179</sup> A. I. Ladutko, M. L. Frenkel, A. V. Pavlov, E. P. Petryaev, M. V. Korolevich, V. V. Civchik, V. A. Lastochkina, and R. G. Zhibankov, Ves. Akad. Navuk BSSR Ser. Khim. Navuk **0**, 52 (1987).
- <sup>180</sup> A. Belabbaci, A. Razzouk, I. Mokbel, J. Jose, and L. Negadi, J. Chem. Eng. Data **54**, 2312 (2009).
- <sup>181</sup> K. Tochigi, K. Akimoto, K. Ochi, F. Liu, and Y. Kawase, J. Chem. Eng. Data **44**, 588 (1999).
- <sup>182</sup> I. Kim, H. F. Svendsen, and E. Børresen, J. Chem. Eng. Data **53**, 2521 (2008).
- <sup>183</sup> J. Han, J. Jin, D. A. Eimer, and M. C. Melaaen, J. Chem. Eng. Data **57**, 1095 (2012).
- <sup>184</sup> A. Valtz, C. Coquelet, and D. Richon, Thermochim. Acta **428**, 185 (2005).
- <sup>185</sup> A. Blanco, A. García-Abuín, D. Gómez-Díaz, J. M. Navaza, and Ó. L. Villaverde, J. Chem. Eng. Data **58**, 653 (2013).
- <sup>186</sup> K. J. Patil, Indian J. Pure Appl. Phys. **16**, 608 (1978).
- <sup>187</sup> G. W. Willard, J. Acoust. Soc. Am. **19**, 235 (1947).
- <sup>188</sup> L.-F. Chiu, H.-F. Liu, and M.-H. Li, J. Chem. Eng. Data **44**, 631 (1999).
- <sup>189</sup> Y. Maham, L. G. Hepler, A. E. Mather, A. W. Hakin, and R. A. Marriott, J. Chem. Soc., Faraday Trans. **93**, 1747 (1997).
- <sup>190</sup> M. Mundhwa and A. Henni, J. Chem. Eng. Data **52**, 491 (2007).

- <sup>191</sup> V. Zosimenko, *New Helmholtz Energy Models for Minor Binary Mixtures Relevant for CCS*, Master thesis, Ruhr-Universität Bochum (2017).
- <sup>192</sup> R. Schmidt and W. Wagner, *Fluid Phase Equilib.* **19**, 175 (1985).
- <sup>193</sup> C. Tegeler, R. Span, and W. Wagner, *J. Phys. Chem. Ref. Data* **28**, 779 (1999).
- <sup>194</sup> E. W. Lemmon and R. Span, *J. Chem. Eng. Data* **51**, 785 (2006).
- <sup>195</sup> J. W. Leachman, R. T. Jacobsen, S. G. Penoncello, and E. W. Lemmon, *J. Phys. Chem. Ref. Data* **38**, 721 (2009).
- <sup>196</sup> U. Setzmann and W. Wagner, *J. Phys. Chem. Ref. Data* **20**, 1061 (1991).
- <sup>197</sup> S. W. Løvseth, A. Austegard, S. F. Westman, H. G. J. Stang, S. Herrig, T. Neumann, and R. Span, *Fluid Phase Equilib.* **466**, 48 (2018).
- <sup>198</sup> H. Li and J. Yan, *Appl. Energy* **86**, 826 (2009).
- <sup>199</sup> J. Gmehling, J. Li, and K. Fischer, *Fluid Phase Equilib.* **141**, 113 (1997).
- <sup>200</sup> G. Tsankova, M. Richter, A. Madigan, P. L. Stanwix, E. F. May, and R. Span, *J. Chem. Thermodyn.* **101**, 395 (2016).
- <sup>201</sup> G. Tsankova, P. L. Stanwix, E. F. May, and M. Richter, *J. Chem. Eng. Data* **62** (2017).
- <sup>202</sup> G.-I. Kaminishi, Y. Arai, S. Saito, and S. Maeda, *J. Chem. Eng. Jpn.* **1**, 109 (1968).
- <sup>203</sup> C. Coquelet, A. Valtz, F. Dieu, D. Richon, P. Arpentinier, and F. Lockwood, *Fluid Phase Equilib.* **273**, 38 (2008).
- <sup>204</sup> S. Lasala, P. Chiesa, R. Privat, and J.-N. Jaubert, *Fluid Phase Equilib.* **428**, 18 (2016).
- <sup>205</sup> M. Ahmad, J. Gernert, and E. Wilbers, *Fluid Phase Equilib.* **363**, 149 (2014).
- <sup>206</sup> E. Sarashina, Y. Arai, and S. Saito, *J. Chem. Eng. Jpn.* **4**, 379 (1971).
- <sup>207</sup> D. Köpke, *Verfahrenstechnik der CO<sub>2</sub>-Abscheidung aus CO<sub>2</sub>-reichen Oxyfuel-Rauchgasen*, Ph.D. thesis, Technische Universität Hamburg-Harburg (2007).
- <sup>208</sup> D. Köpke and R. Eggers, *Chem. Ing. Tech.* **79**, 1235 (2007).
- <sup>209</sup> M. A. Ben Souissi, M. Richter, X. Yang, R. Kleinrahm, and R. Span, *J. Chem. Eng. Data* **62**, 362 (2016).
- <sup>210</sup> X. Yang, M. Richter, M. A. Ben Souissi, R. Kleinrahm, and R. Span, *J. Chem. Eng. Data* **61**, 2676 (2016).
- <sup>211</sup> X. Yang, M. Richter, Z. Wang, and Z. Li, *J. Chem. Thermodyn.* **91**, 17 (2015).
- <sup>212</sup> R. Wegge, *Thermodynamic Properties of the (Argon + Carbon Dioxide) System: Instrument Development with Density and Speed-of-Sound Measurements*, Ph.D. thesis, Ruhr-Universität Bochum (2016).

- <sup>213</sup> J. Kestin, Y. Kobayashi, and R. T. Wood, *Physica* **32**, 1065 (1966).
- <sup>214</sup> M. Mantovani, P. Chiesa, G. Valenti, M. Gatti, and S. Consonni, *J. Supercrit. Fluids* **61**, 34 (2012).
- <sup>215</sup> I. Al-Siyabi, *Effects of Impurities on CO<sub>2</sub> Stream Properties*, Ph.D. thesis, Heriot-Watt University (2013).
- <sup>216</sup> V. V. Altunin and O. D. Koposhilov, *Therm. Eng.* **24**, 66 (1977).
- <sup>217</sup> W. H. Abraham and C. O. Bennett, *AIChE J.* **6**, 257 (1960).
- <sup>218</sup> W. Schönmann, *Messung der thermischen Eigenschaften und Aufstellung einer empirischen Zustandsgleichung gasförmiger Argon-Kohlendioxid-Gemische*, Ph.D. thesis, Universität Karlsruhe (1971).
- <sup>219</sup> R. Wegge, M. O. McLinden, R. A. Perkins, M. Richter, and R. Span, *J. Chem. Thermodyn.* **99**, 54 (2016).
- <sup>220</sup> S. F. Westman, A. Austegard, H. J. Stang, and S. W. Løvseth, *Fluid Phase Equilib.* **473**, 37 (2018).
- <sup>221</sup> L. F. S. Souza, Al Ghafri, Saif Z. S., and J. P. M. Trusler, *J. Chem. Thermodyn.* **126**, 63 (2018).
- <sup>222</sup> L. F. S. Souza, S. Herrig, R. Span, and J. P. M. Trusler, *Experimental Density and an Improved Helmholtz-Energy Explicit Mixture Model for (CO<sub>2</sub> + CO)* (to be published, 2019).
- <sup>223</sup> G. Tsankova, M. Richter, P. L. Stanwix, and E. F. May, *J. Chem. Thermodyn.* **129**, 114 (2019).
- <sup>224</sup> S. T. Blanco, C. Rivas, R. Bravo, J. Fernández, M. Artal, and I. Velasco, *Environ. Sci. Technol.* **48**, 10984 (2014).
- <sup>225</sup> L. J. Christiansen, A. Fredenslund, and N. Gardner in *Advances in Cryogenic Engineering*, edited by K. D. Timmerhaus (Springer US, Boston, MA, 1995), pp. 309–319.
- <sup>226</sup> S. Huamin, *Huaxue Gongcheng China* **19**, 61 (1991).
- <sup>227</sup> A. K. Jana, *Chemical Process Modelling and Computer Simulation* (PHI Learning, New Dehli, 2008).
- <sup>228</sup> K. Fischer and J. Gmehling, *Fluid Phase Equilib.* **121**, 185 (1996).
- <sup>229</sup> A. Cipollina, R. Anselmo, O. Scialdone, G. Filardo, and A. Galia, *J. Chem. Eng. Data* **52**, 2291 (2007).
- <sup>230</sup> B. V. Mallu, G. Natarajan, and D. S. Viswanath, *J. Chem. Thermodyn.* **21**, 989 (1989).

- <sup>231</sup> B.V. Mallu, G. Natarajan, and D.S. Viswanath, *J. Chem. Thermodyn.* **19**, 549 (1987).
- <sup>232</sup> J. A. Awan, K. Thomsen, C. Coquelet, P. L. Fosbøl, and D. Richon, *J. Chem. Eng. Data* **55**, 842 (2010).
- <sup>233</sup> A. Chapoy, A. H. Mohammadi, D. Richon, and B. Tohidi, *Fluid Phase Equilib.* **220**, 111 (2004).
- <sup>234</sup> M. Frost, E. Karakatsani, N. von Solms, D. Richon, and G. M. Kontogeorgis, *J. Chem. Eng. Data* **59**, 961 (2014).
- <sup>235</sup> P. C. Gillespie and G. M. Wilson, *Research Report RR-41: Vapor-Liquid Equilibrium Data on Water-Substitute Gas Components: N<sub>2</sub>-H<sub>2</sub>O, H<sub>2</sub>-H<sub>2</sub>O, CO-H<sub>2</sub>O, H<sub>2</sub>-CO-H<sub>2</sub>O, and H<sub>2</sub>S-H<sub>2</sub>O*, Project 758-B-79, Provo, Utah (1980).
- <sup>236</sup> J. M.S. Fonseca and N. von Solms, *Fluid Phase Equilib.* **329**, 55 (2012).
- <sup>237</sup> J. Qin, R. J. Rosenbauer, and Z. Duan, *J. Chem. Eng. Data* **53**, 1246 (2008).
- <sup>238</sup> C. E. P. Siqueira Campos, J. R. Penello, F. L. Pellegrini Pessoa, and A. M. Cohen Uller, *J. Chem. Eng. Data* **55**, 2576 (2010).
- <sup>239</sup> Y. S. Kim, S. K. Ryu, S. O. Yang, and C. S. Lee, *Ind. Eng. Chem. Res.* **42**, 2409 (2003).
- <sup>240</sup> A. Chapoy, C. Coquelet, and D. Richon, *Fluid Phase Equilib.* **230**, 210 (2005).
- <sup>241</sup> A. Fenghour, W. A. Wakeham, and J.T.R. Watson, *J. Chem. Thermodyn.* **28**, 447 (1996).
- <sup>242</sup> H. A. Sairanen and M. O. Heinonen, *Int. J. Thermophys.* **35**, 1280 (2014).
- <sup>243</sup> A. H. Mohammadi, A. Chapoy, D. Richon, and B. Tohidi, *Ind. Eng. Chem. Res.* **43**, 7148 (2004).
- <sup>244</sup> R. H. Olds, B. H. Sage, and W. N. Lacey, *Ind. Eng. Chem.* **34**, 1223 (1942).
- <sup>245</sup> M. Rigby and J. M. Prausnitz, *J. Phys. Chem.* **72**, 330 (1968).
- <sup>246</sup> A. Chapoy, C. Coquelet, and D. Richon, *Fluid Phase Equilib.* **214**, 101 (2003).
- <sup>247</sup> L. L. Joffrion and P. T. Eubank, *J. Chem. Eng. Data* **34**, 215 (1989).
- <sup>248</sup> I. M. Abdulagatov, A. R. Bazaev, and A. E. Ramazanov, *J. Chem. Thermodyn.* **25**, 249 (1993).
- <sup>249</sup> V. M. Shmonov, R. J. Sadus, and E. U. Franck, *J. Phys. Chem.* **97**, 9054 (1993).
- <sup>250</sup> Y. Zhang, *Chin. J. Geol.* **32**, 299 (1997).
- <sup>251</sup> G. Smith, A. Sellars, T.K. Yerlett, and C.J. Wormald, *J. Chem. Thermodyn.* **15**, 29 (1983).



- 252 C. J. Wormald and C. N. Colling, *AIChE J.* **30**, 386 (1984).
- 253 L. Hnědkovský and R. H. Wood, *J. Chem. Thermodyn.* **29**, 731 (1997).
- 254 H. Welsch, *Die Systeme Xenon-Wasser und Methan-Wasser bei hohen Drücken und Temperaturen*, Ph.D. thesis, Universität Karlsruhe (1973).
- 255 I. M. Abdulagatov, A. R. Bazaev, R. K. Gasanov, and A. E. Ramazanova, *J. Chem. Thermodyn.* **28**, 1037 (1996).
- 256 O. Akin-Ojo, A. H. Harvey, and K. Szalewicz, *J. Chem. Phys.* **125**, 14314 (2006).
- 257 M. P. Burgess and R. P. Germann, *AIChE J.* **15**, 272 (1969).
- 258 A. Chapoy, A. H. Mohammadi, B. Tohidi, A. Valtz, and D. Richon, *Ind. Eng. Chem. Res.* **44**, 7567 (2005).
- 259 A. Chapoy, A. H. Mohammadi, B. Tohidi, A. Valtz, and D. Richon, *Ind. Eng. Chem. Res.* **44**, 10021 (2005).
- 260 E. C. W. Clarke and D. N. Glew, *Can. J. Chem.* **49**, 691 (1971).
- 261 P. C. Gillespie and G. M. Wilson, *Research Report RR-48: Vapor-Liquid and Liquid-Liquid Equilibria: Water-Methane, Water-Carbon Dioxide, Water-Hydrogen Sulfide, Water-nPentane, Water-Methane-nPentane*, Project 758-B-77, Provo, Utah (1982).
- 262 H. J. Neuburg, J. F. Atherley, and L. G. Walker, *Girdler-Sulfide Process Physical Properties*, Atomic Energy of Canada Limited - Report 5702, Chalk River, Ontario (1977).
- 263 F. T. Selleck, L. T. Carmichael, and B. H. Sage, *Ind. Eng. Chem.* **44**, 2219 (1952).
- 264 O. M. Suleimenov and R. E. Krupp, *Geochim. Cosmochim. Acta* **58**, 2433 (1994).
- 265 Q. Yu, D. Liu, R. Liu, H. Zhou, M. Chen, and G. Chen, *Chem. Eng. (China)* **4**, 1 (1980).
- 266 J. J. Carroll and A. E. Mather, *Geochim. Cosmochim. Acta* **53**, 1163 (1989).
- 267 M. Nazeri, A. Chapoy, A. Valtz, C. Coquelet, and B. Tohidi, *Fluid Phase Equilib.* **454**, 64 (2017).
- 268 B. Gimeno, M. Artal, I. Velasco, J. Fernández, and S. T. Blanco, *Energy Fuels* (2018).
- 269 C. Coquelet, A. Valtz, and P. Arpentinier, *Fluid Phase Equilib.* **382**, 205 (2014).
- 270 V. Lachet, T. Bruin, P. Ungerer, C. Coquelet, A. Valtz, V. Hasanov, F. Lockwood, and D. Richon, *Energy Procedia* **1**, 1641 (2009).
- 271 A. Blümcke, *Ann. Phys. Chem.* **270**, 10 (1888).
- 272 F. Caubet, *Z. Phys. Chem.* **49**, 101 (1904).

- <sup>273</sup> A. Thiel and E. Schulte, *Z. Phys. Chem.* **96**, 312 (1920).
- <sup>274</sup> J. Wang, Z. Wang, D. Ryan, and C. Lan, *Int. J. Greenh. Gas Con.* **42**, 132 (2015).
- <sup>275</sup> E. El Ahmar, B. Creton, A. Valtz, C. Coquelet, V. Lachet, D. Richon, and P. Ungerer, *Fluid Phase Equilib.* **304**, 21 (2011).
- <sup>276</sup> I. H. Bell and U. K. Deiters, *AIChE J.* **64**, 2745 (2018).
- <sup>277</sup> D. S. Tsiklis, *Zh. Fiz. Khim.* **1947**, 349 (1947).
- <sup>278</sup> M. R. Dean and W. S. Walls, *Ind. Eng. Chem.* **39**, 1049 (1947).
- <sup>279</sup> R. W. Dornte and C. V. Ferguson, *Ind. Eng. Chem.* **31**, 112 (1939).
- <sup>280</sup> A. Köster and J. Vrabec (personal communication, 2017).
- <sup>281</sup> S. G. Sayegh, J. Najman, and B. Hlavacek, *J. Can. Petro. Tech.* **20**, 76 (1981).
- <sup>282</sup> H. L. Wilson and W. V. Wilding, *Vapor-Liquid and Liquid-Liquid Equilibrium Measurements on Twenty-two Binary Mixtures*, DIPPR Data Series No. 2, New York (1994).
- <sup>283</sup> B. Gilot, C. Guiglion, and M. Enjalbert, *Chimie & Industrie - Génie Chimique* **98**, 1052 (1967).
- <sup>284</sup> K. Ohgaki and T. Katayama, *Fluid Phase Equilib.* **1**, 27 (1977).
- <sup>285</sup> H. Li, X. Jiao, and W. Chen, *Phys. Chem. Liq.* **52**, 349 (2014).
- <sup>286</sup> J. G. van Berkum and G.A.M. Diepen, *J. Chem. Thermodyn.* **11**, 317 (1979).
- <sup>287</sup> A. F. Holleman, E. Wiberg, and N. Wiber, *Lehrbuch der Anorganischen Chemie* (de Gruyter, Berlin, 1995).
- <sup>288</sup> C.-M. Hsieh, T. Windmann, and J. Vrabec, *J. Chem. Eng. Data* **58**, 3420 (2013).
- <sup>289</sup> B. C. Spall, *Can. J. Chem. Eng.* **41**, 79 (1963).
- <sup>290</sup> T. K. Sherwood, *Ind. Eng. Chem.* **17** (1925).
- <sup>291</sup> B. Rumpf and G. Maurer, *Fluid Phase Equilib.* **81**, 241 (1992).
- <sup>292</sup> W. B. Campbell and O. Maass, *Can. J. Res.* **2**, 42 (1930).
- <sup>293</sup> W. L. Beuschlein and L. O. Simenson, *J. Am. Chem. Soc.* **62**, 610 (1940).
- <sup>294</sup> W. V. Wilding, L. C. Wilson, and G. M. Wilson, *Vapor-Liquid Equilibrium Measurements on Eight Binary Mixtures*, DIPPR Projects 805(A)/89 and 805(E)/89, New York (1991).
- <sup>295</sup> S. Horstmann, P. Mougin, F. Lecomte, K. Fischer, and J. Gmehling, *J. Chem. Eng. Data* **47**, 1496 (2002).
- <sup>296</sup> M. A. Abdi and A. Meisen, *Ind. Eng. Chem. Res.* **38**, 3096 (1999).

- <sup>297</sup> Z. Cai, R. Xie, and Z. Wu, *J. Chem. Eng. Data* **41**, 1101 (1996).
- <sup>298</sup> R. Sidi-Boumedine, S. Horstmann, K. Fischer, E. Provost, W. Fürst, and J. Gmehling, *Fluid Phase Equilib.* **218**, 85 (2004).
- <sup>299</sup> F. M. Raoult, *Comptes Rendus Acad. Sci.* **104** (1887).
- <sup>300</sup> J. L. Lenard, R. W. Rousseau, and A. S. Teja, *AIChE Symp. Ser.* **86**, 1 (1990).
- <sup>301</sup> S. J. Park, H. Y. Shin, B.-M. Min, A. Cho, and J.-S. Lee, *Korean J. Chem. Eng.* **26**, 189 (2009).
- <sup>302</sup> S.-B. Park and H. Lee, *Korean J. Chem. Eng.* **14**, 146 (1997).
- <sup>303</sup> H. Tanaka, D. Kodama, R. Yaginuma, Kato, and Masahiro, *Jpn. J. Thermophys. Prop.* **15**, 182 (2001).
- <sup>304</sup> A. Nath and E. Bender, *J. Chem. Eng. Data* **28**, 370 (1983).
- <sup>305</sup> H. Touhara, S. Okazaki, F. Okino, H. Tanaka, K. Ikari, and K. Nakanishi, *J. Chem. Thermodyn.* **14**, 145 (1982).
- <sup>306</sup> L. Tsintsarska, S. Dralcheva, P. Petrov, and M. Tsvetkova, *Khim. Ind. (Sofia)* **60** (1988).
- <sup>307</sup> Höchst AG, *Flüssigkeits-Dampf-Gleichgewicht des Systems Cl<sub>2</sub>-HCl*, Dr.Z/Ho-3484-III.1 (1970).
- <sup>308</sup> A. Jäger, I. H. Bell, and C. Breitkopf, *Fluid Phase Equilib.* **469**, 56 (2018).
- <sup>309</sup> A. Jäger, E. Mickoleit, and C. Breitkopf, *Fluid Phase Equilib.* **476**, 147 (2018).
- <sup>310</sup> S.-T. Lin and S. I. Sandler, *Ind. Eng. Chem. Res.* **41**, 899 (2002).
- <sup>311</sup> E. Mullins, R. Oldland, Y. A. Liu, S. Wang, S. I. Sandler, C.-C. Chen, M. Zwolak, and K. C. Seavey, *Ind. Eng. Chem. Res.* **45**, 4389 (2006).
- <sup>312</sup> D. A. García, S. Perez, M. A. Delgado, de Dios, J. C., A. Liebscher, K. Zemke, Fischer, S., Koenen, M., C. Hofstee, D. Loeve, and F. Neele, *D 1.5.5 - The Role of Impurities in the CO<sub>2</sub> Stream for Storage Systems*, IMPACTS - The Impact of the Quality of CO<sub>2</sub> on Transport and Storage Behaviour (2016).
- <sup>313</sup> C. Eickhoff, F. Neele, A. Brown, and F. Gisart, *D 2.2.2 & D2.2.3 - CCS Chain Element Parameters and Performance Variations due to the Impact of Impurities in the CO<sub>2</sub> Stream*, IMPACTS - The Impact of the Quality of CO<sub>2</sub> on Transport and Storage Behaviour (2015).
- <sup>314</sup> J. Koornneef and F. Neele, *EU FP7 IMPACTS: Toolbox of Effects of CO<sub>2</sub> Impurities on CO<sub>2</sub> Transport and Storage Systems* (Netherlands Organisation for Applied Scientific Research (TNO), Utrecht, 2015).

- <sup>315</sup> C. B. Farris, *Energy Prog.* **3**, 150 (1983).
- <sup>316</sup> N. I. Diamantonis, G. C. Boulougouris, D. M. Tsangaris, M. J. E. Kadi, H. Saadawi, S. Negahban, and I. G. Economou, *Chem. Eng. Res. Des.* **91**, 1793 (2013).
- <sup>317</sup> B. Gimeno, M. Artal, I. Velasco, S. T. Blanco, and J. Fernández, *Appl. Energy* **206**, 172 (2017).
- <sup>318</sup> W. M. Jones, *J. Chem. Phys.* **48**, 207 (1968).
- <sup>319</sup> V. A. Kirillin and S. A. Ulybin, *Teploenergetika* **8**(4), 67 (1959).
- <sup>320</sup> C.-T. Liu and W. T. Lindsay, *J. Chem. Eng. Data* **15**, 510 (1970).
- <sup>321</sup> F. T. Miles and A. W. C. Menzies, *J. Am. Chem. Soc.* **58**, 1067 (1936).
- <sup>322</sup> K. Quitzsch, R. Hüttig, H.-G. Vogel, H.-J. Gesemann, and G. Geiseler, *Z. Phys. Chem.* **223**, 225 (1963).
- <sup>323</sup> D. E. Hare and C. M. Sorensen, *J. Chem. Phys.* **84**, 5085 (1986).
- <sup>324</sup> E. V. Ivanov and E. Y. Lebedeva, *J. Mol. Liq.* **159**, 124 (2011).
- <sup>325</sup> E. V. Ivanov, E. Y. Lebedeva, and V. K. Abrosimov, *Thermochim. Acta* **500**, 38 (2010).
- <sup>326</sup> E. V. Ivanov, E. Y. Lebedeva, and V. K. Abrosimov, *Thermochim. Acta* **513**, 26 (2011).
- <sup>327</sup> G. Jancsó, *J. Solution Chem.* **35**, 991 (2006).
- <sup>328</sup> S. G. Kudryavtsev, A. N. Strakhov, O. V. Ershova, and G. A. Krestov, *Zh. Fiz. Khim.* **60**, 2202 (1986).
- <sup>329</sup> W. Marczak, *J. Chem. Eng. Data* **44**, 621 (1999).
- <sup>330</sup> F. J. Millero, R. Dexter, and E. Hoff, *J. Chem. Eng. Data* **16**, 85 (1971).
- <sup>331</sup> N. A. Nevolina and A. L. Seifer, *J. Struct. Chem.* **14**, 501 (1973).
- <sup>332</sup> E. Reisler and H. Eisenberg, *J. Chem. Phys.* **43**, 3875 (1965).
- <sup>333</sup> P. Scharlin and K. Steinby, *J. Chem. Thermodyn.* **35**, 279 (2003).
- <sup>334</sup> R. Schrader and K. Wirtz, *Z. Naturforsch. A* **6** (1951).
- <sup>335</sup> T. L. Chang and J. Y. Chien, *J. Am. Chem. Soc.* **63**, 1709 (1941).
- <sup>336</sup> K. Wirtz, *Physik. Z.* **43**, 465 (1942).
- <sup>337</sup> G. S. Kell, G. E. McLaurin, and E. Whalley, *J. Chem. Phys.* **49**, 2839 (1968).
- <sup>338</sup> A. A. Aleksandrov and D. K. Larkin, *Inzh-Fiz. Zh.* **34**, 110 (1978).
- <sup>339</sup> R. A. Fine and F. J. Millero, *J. Chem. Phys.* **63**, 89 (1975).

- <sup>340</sup> R. N. Gupta, P. C. Jain, and V. S. Nanda, *J. Chem. Thermodyn.* **8**, 627 (1976).
- <sup>341</sup> P.-P. Heusinger, *Naturwissenschaften* **36**, 279 (1949).
- <sup>342</sup> E. V. Ivanov, E. Y. Lebedeva, and V. K. Abrosimov, *J. Chem. Eng. Data* **54**, 2777 (2009).
- <sup>343</sup> D. R. McMillan and R. T. Lagemann, *J. Acoust. Soc. Am.* **19**, 956 (1947).
- <sup>344</sup> M. Pancholy, *J. Acoust. Soc. Am.* **25**, 1003 (1953).
- <sup>345</sup> S. L. Rivkin and B. N. Egorov, *Sov. J. At. Energy* **7**, 928 (1961).
- <sup>346</sup> S. L. Rivkin and B. N. Egorov, *Sov. J. At. Energy* **14**, 430 (1964).
- <sup>347</sup> N. G. Polikhronidi, I. M. Abdulagatov, J. W. Magee, and G. V. Stepanov, *Int. J. Thermophys.* **22**, 189 (2001).
- <sup>348</sup> S. Ertle, *Messungen des Joule-Thomson-Koeffizienten und des isothermen Drosselkoeffizienten von Wasserdampf*, Ph.D. thesis, TU München (1979).
- <sup>349</sup> P. Harteck, *Z. Phys. Chem.* **134**, 21 (1928).
- <sup>350</sup> F. A. Henglein, G.v. Rosenberg, and A. Muchlinski, *Z. Phys.* **11**, 1 (1922).
- <sup>351</sup> Y. W. Kang, S. Y. Cho, and I. W. Nah, *J. Chem. Eng. Data* **43**, 611 (1998).
- <sup>352</sup> H. T. Pham, R. R. Singh, and R. H. Thomas, *Azeotrope-like Compositions of Difluormethane and Chlorine*. Patent C07C 19/08, C01B 7/01, WO 97/47574. USA (1997).
- <sup>353</sup> E. Kanda, *Bull. Chem. Soc. Jpn.* **12**, 473 (1937).
- <sup>354</sup> G. Liessmann, W. Schmidt, and S. Reiffarth, *Recommended Thermophysical Data, Data Compilation of the Saechsische Olefinwerke 1*, Böhlen (1995).
- <sup>355</sup> T. M. Lowry and G. Jessop, *J. Chem. Soc., Faraday Trans.*, 1005 (1930).
- <sup>356</sup> A. I. Ageev, A. I. Ezrileev, and Roskin E.S., *J. Appl. Chem. USSR* **43**(2), 2392 (1970).
- <sup>357</sup> A. A. Anderson and M. V. Shimanskaya, *Latv. PSR Zinat. Akad. Vestis, Kim. Ser.* **5**, 537 (1969).
- <sup>358</sup> R. Anonymous, *Labratory Data Sheets*, Union Carbide Corp. (1956).
- <sup>359</sup> A. G. Bergman and L. F. Shulyak, *Russ. J. Inorg. Chem.* **17**, 596 (1972).
- <sup>360</sup> S. D. Beskow, L. I. Kotschetkova, and V. Goren, *Uch. Zap. Mosk. Obl. Pedagog. Inst.* **99**, 147 (1957).
- <sup>361</sup> I. S. Bogacheva, K. B. Zemdikhanov, G. K. Mukhamedzyanov, A. K. Sadykov, and A. G. Usmanov, *Russ. J. Phys. Chem.* **54**, 838 (1980).
- <sup>362</sup> D. Brasoveanu, M. Mihai, and M. Belcu, *Rev. Chim.* **51**, 687 (2000).

- <sup>363</sup> R. D. Cadle, B. J. Robson, and R. W. Moshier, *J. Am. Chem. Soc.* **71**, 2928 (1949).
- <sup>364</sup> Gas Research Institute, *Chem. Eng. Oil Gas* **3**, 1 (1981).
- <sup>365</sup> G. Graubner, *Charakterisierung neuer Lösungsmittel für die CO<sub>2</sub>-Absorption*, Master thesis, Universität Oldenburg (2010).
- <sup>366</sup> J. Hahn and H. Freydank, *Leuna Protocol* **10251** (1983).
- <sup>367</sup> J. Hahn, G. Müller, and K. Mörke, *Leuna Protocol* **12111** (1989).
- <sup>368</sup> S. Kapteina, K. Slowik, S. P. Verevkin, and A. Heintz, *J. Chem. Eng. Data* **50**, 398 (2005).
- <sup>369</sup> K. Klepáčová, P. J. G. Huttenhuis, P. W. J. Derks, and G. F. Versteeg, *J. Chem. Eng. Data* **56**, 2242 (2011).
- <sup>370</sup> L. M. Kogan, A. I. Ezrielev, A. V. Lebedev, and A. B. Peizner, *Russ. J. Gen. Chem.* **40**, 2292 (1970).
- <sup>371</sup> O. Landauer, G. Costeanu, and C. Mateescu, *Rev. Roum. Chim.* **19**, 1429 (1974).
- <sup>372</sup> A. G. Leibush and E. D. Shorina, *Zh. Prikl. Khim.* **20**, 69 (1947).
- <sup>373</sup> M. Lecat, *Bull. Cl. Sci. Acad. R. Belg.* **33**, 160 (1947).
- <sup>374</sup> J. B. Matthews, J. F. Sumner, and E. A. Moelwyn-Hughes, *Trans. Faraday Soc.* **46**, 797 (1950).
- <sup>375</sup> R. A. McDonald, S. A. Shrader, and D. R. Stull, *J. Chem. Eng. Data* **4**, 311 (1959).
- <sup>376</sup> K. A. Pividal and S. I. Sandler, *J. Chem. Eng. Data* **35**, 53 (1990).
- <sup>377</sup> K. R. Reddy, D. B. K. Kumar, G. S. Rao, P. V. S. Sairam, P. Anila, and C. Rambabu, *J. Chem. Eng. Data* **57**, 1412 (2012).
- <sup>378</sup> R. E. Reitmeier, V. Sivertz, and H. V. Tartar, *J. Am. Chem. Soc.* **62**, 1943 (1940).
- <sup>379</sup> J. N. Street and H. Adkins, *J. Am. Chem. Soc.* **50**, 162 (1928).
- <sup>380</sup> M. S. Sunder and D. H. L. Prasad, *J. Chem. Eng. Data* **52**, 2050 (2007).
- <sup>381</sup> R. Wohland, *Leuna Protocol* **6231** (1976).
- <sup>382</sup> M. I. Zaretskii, V. B. Kogan, N. F. Kononov, V. G. Podolyak, and F. K. Tolchinskaya, *J. Appl. Chem. USSR* **43**, 1304 (1970).
- <sup>383</sup> J. Águila-Hernández, A. Trejo, B. E. García-Flores, and R. Molnar, *Fluid Phase Equilib.* **267**, 172 (2008).
- <sup>384</sup> E. Álvarez, F. Cerdeira, D. Gómez-Díaz, and J. M. Navaza, *J. Chem. Eng. Data* **55**, 994 (2010).
- <sup>385</sup> T. G. Amundsen, L. E. Øi, and D. A. Eimer, *J. Chem. Eng. Data* **54**, 3096 (2009).

- <sup>386</sup> A. Arce, A. Marchiaro, and A. Soto, *Fluid Phase Equilib.* **226**, 121 (2004).
- <sup>387</sup> A. Blanco, A. García-Abuín, D. Gómez-Díaz, and J. M. Navaza, *J. Chem. Eng. Data* **57**, 3136 (2012).
- <sup>388</sup> I. S. Bogacheva, K. B. Zemdikhanov, and A. G. Usmanov, *Izv. Vyssh. Uchebn. Zaved. Khim. Khim. Tekhnol.* **25**, 182 (1982).
- <sup>389</sup> C. Coquelet, A. Valtz, and D. Richon, *J. Chem. Eng. Data* **50**, 412 (2005).
- <sup>390</sup> R. Dean, J. Moullins, A. MacInnis, and R. M. Palepu, *Phys. Chem. Liq.* **47**, 302 (2009).
- <sup>391</sup> R. M. DiGuilio, R. J. Lee, S. T. Schaeffer, L. L. Brasher, and A. S. Teja, *J. Chem. Eng. Data* **37**, 239 (1992).
- <sup>392</sup> A. García-Abuín, D. Gómez-Díaz, M. D. La Rubia, and J. M. Navaza, *J. Chem. Eng. Data* **56**, 646 (2011).
- <sup>393</sup> A. García-Abuín, D. Gómez-Díaz, and J. M. Navaza, *J. Chem. Eng. Data* **58**, 3387 (2013).
- <sup>394</sup> Y. Geng, S. Chen, T. Wang, D. Yu, C. Peng, H. Liu, and Y. Hu, *J. Mol. Liq.* **143**, 100 (2008).
- <sup>395</sup> B. Hawrylak, S. E. Burke, and R. Palepu, *J. Solution Chem.* **29**, 575 (2000).
- <sup>396</sup> H. Herba, G. Czechowski, B. Zywuicki, M. Stockhausen, and J. Jadzyn, *J. Chem. Eng. Data* **40**, 214 (1995).
- <sup>397</sup> M. N. Islam, M. M. Islam, and M. N. Yeasmin, *J. Chem. Thermodyn.* **36**, 889 (2004).
- <sup>398</sup> J. H. Jones, H. R. Froning, and E. E. Claytor, *J. Chem. Eng. Data* **4**, 85 (1959).
- <sup>399</sup> U. R. Kapadi, D. G. Hundiwale, N. B. Patil, and M. K. Lande, *Fluid Phase Equilib.* **201**, 335 (2002).
- <sup>400</sup> V. N. Kartsev, M. N. Rodnikova, V. V. Tsepulin, K. T. Dudnikova, and V. G. Markova, *J. Struct. Chem.* **27**, 671 (1986).
- <sup>401</sup> V. N. Kartsev, M. N. Rodnikova, V. G. Tsepulin, and V. G. Markova, *Russ. J. Phys. Chem.* **62**, 1152 (1988).
- <sup>402</sup> V. G. Kozin and A. A. Mukhamadiev, *Russ. J. Appl. Chem.* **75**, 1061 (2002).
- <sup>403</sup> S. S. Kurtz, D. L. Camin, and A. R. Thompson, *J. Chem. Eng. Data* **10**, 335 (1965).
- <sup>404</sup> M.-J. Lee and T.-K. Lin, *J. Chem. Eng. Data* **40**, 336 (1995).
- <sup>405</sup> M.-J. Lee, T.-K. Lin, Y.-H. Pai, and K.-S. Lin, *J. Chem. Eng. Data* **42**, 854 (1997).
- <sup>406</sup> M. H. Li and K. P. Shen, *J. Chem. Eng. Data* **37**, 288 (1992).

- <sup>407</sup> X.-X. Li, G.-C. Fan, Z.-L. Zhang, Y.-W. Wang, and Y.-Q. Lu, *J. Chem. Eng. Data* **58**, 1229 (2013).
- <sup>408</sup> Y. Maham, T. T. Teng, L. G. Hepler, and A. E. Mather, *J. Solution Chem.* **23**, 195 (1994).
- <sup>409</sup> Y. Maham, T. T. Teng, L. G. Hepler, and A. E. Mather, *Thermochim. Acta* **386**, 111 (2002).
- <sup>410</sup> P. K. Migal and V. S. Starchevskii, *Uch. Zap. Kishin. Gos. Univ.* **27**, 135 (1957).
- <sup>411</sup> F. Murrieta-Guevara and A. T. Rodriguez, *J. Chem. Eng. Data* **29**, 204 (1984).
- <sup>412</sup> F. Murrieta-Guevara, E. Rebolledo-Libreros, and A. Trejo, *Fluid Phase Equilib.* **86**, 225 (1993).
- <sup>413</sup> M. Pagé, J.-Y. Huot, and C. Jolicoeur, *Can. J. Chem.* **71**, 1064 (1993).
- <sup>414</sup> A. Pourmohammadbagher and J. M. Shaw, *J. Chem. Eng. Data* **58**, 2202 (2013).
- <sup>415</sup> F. Pouryousefi and R. O. Idem, *Ind. Eng. Chem. Res.* **47**, 1268 (2008).
- <sup>416</sup> J.-H. Song, S.-B. Park, J.-H. Yoon, H. Lee, and K.-H. Lee, *J. Chem. Eng. Data* **41**, 1152 (1996).
- <sup>417</sup> H.-J. Song, M.-G. Lee, H. Kim, A. Gaur, and J.-W. Park, *J. Chem. Eng. Data* **56**, 1371 (2011).
- <sup>418</sup> M. M. Taib and T. Murugesan, *J. Chem. Eng. Data* **55**, 5910 (2010).
- <sup>419</sup> M. M. Taib and T. Murugesan, *J. Chem. Eng. Data* **57**, 120 (2012).
- <sup>420</sup> M. M. Taib, M. M. Akbar, and T. Murugesan, *J. Mol. Liq.* **181**, 121 (2013).
- <sup>421</sup> S. Tian, S. Ren, Y. Hou, W. Wu, and W. Peng, *J. Chem. Eng. Data* **58**, 1885 (2013).
- <sup>422</sup> M. J. Timmermans and M. Hennaut-Roland, *J. Chim. Phys. Phys.- Chim. Biol.* **56**, 984 (1959).
- <sup>423</sup> Y.-M. Tseng and A. R. Thompson, *J. Chem. Eng. Data* **9**, 264 (1964).
- <sup>424</sup> N. G. Tsierkezos and I. E. Molinou, *J. Chem. Eng. Data* **44**, 955 (1999).
- <sup>425</sup> Y. W. Wang, S. Xu, F. D. Otto, and A. E. Mather, *Chem. Eng. J.* **48**, 31 (1992).
- <sup>426</sup> X. Wang, F. Yang, Y. Gao, and Z. Liu, *J. Chem. Thermodyn.* **57**, 145 (2013).
- <sup>427</sup> F. Yang, X. Wang, W. Wang, and Z. Liu, *J. Chem. Eng. Data* **58**, 785 (2013).
- <sup>428</sup> M. Yasmin and M. Gupta, *J. Solution Chem.* **40**, 1458 (2011).
- <sup>429</sup> V. V. Altunin and O. D. Koposhilov, *Trudy Moskov. Energ. Inst.* **1976**, 20 (1976).
- <sup>430</sup> N. D. Kosov and I. S. Brovanov, *J. Phys. Eng.* **36**, 413 (1979).



- <sup>431</sup> J. P. Strakey, C. O. Bennett, and B. F. Dodge, *AIChE J.* **20**, 803 (1974).
- <sup>432</sup> T. K. Bose and R. H. Cole, *J. Phys. Chem.* **52**, 140 (1970).
- <sup>433</sup> T. L. Cottrell, R. A. Hamilton, and R. P. Taubinger, *Trans. Faraday Soc.*, 1310 (1956).
- <sup>434</sup> M. L. Martin, R. D. Trengove, K. R. Harris, and P. J. Dunlop, *Aust. J. Chem.* **35**, 1525 (1982).
- <sup>435</sup> H. Schmiedel, R. Gehrman, and B. Schramm, *Ber. Bunsenges. Phys. Chem.* **84**, 721 (1980).
- <sup>436</sup> B. Schramm and W. Müller, *Ber. Bunsenges. Phys. Chem.* **86**, 110 (1982).
- <sup>437</sup> F. Caubet, *Z. Phys. Chem.* **40**, 257 (1902).
- <sup>438</sup> J. J. Byerley, G. L. Rempel, and V. T. Le, *J. Chem. Eng. Data* **25**, 55 (1980).
- <sup>439</sup> F. H. Conrad and W. L. Beuschlein, *J. Am. Chem. Soc.* **56**, 2554 (1934).
- <sup>440</sup> A. Douabul and J. Riley, *J. Chem. Eng. Data* **24**, 274 (1979).
- <sup>441</sup> J. C. Hudson, *J. Chem. Soc., Trans.* **127**, 1332 (1925).
- <sup>442</sup> M. K. Mondal, *Fluid Phase Equilib.* **253**, 98 (2007).
- <sup>443</sup> A. E. Rabe and J. F. Harris, *J. Chem. Eng. Data* **8**, 333 (1963).
- <sup>444</sup> T. H. Sims, *Q. J. Chem. Soc.* **14**, 1 (1862).
- <sup>445</sup> W. T. Smith and R. B. Parkhurst, *J. Am. Chem. Soc.* **44**, 1918 (1922).
- <sup>446</sup> J. Tokunaga, *J. Chem. Eng. Data* **19**, 162 (1974).



## Appendix A - Supplement to the Lee-Kesler-Plöcker Equation of State

### A.1 Parameters used for Calculations with the LKP EOS

**Table A.1** Parameters of the LKP EOS used for the calculation of the compressibility factors  $Z^o$  of the „simple fluid“ and  $Z^{ef}$  for the „reference fluid“ according to Eqs. (3.14) to (3.17). The parameters correspond to the original values given by Plöcker *et al.*<sup>19</sup>

Parameter	Simple fluid	Reference fluid
$b_1$	0.118 119 3	0.202 657 9
$b_2$	0.265 728	0.331 511
$b_3$	0.154 790	$0.276 550 \times 10^{-1}$
$b_4$	$0.303 230 \times 10^{-1}$	0.203 488
$c_1$	$0.236 744 \times 10^{-1}$	$0.313 385 \times 10^{-1}$
$c_2$	$0.186 984 \times 10^{-1}$	$0.503 618 \times 10^{-1}$
$c_3$	0	$0.169 010 \times 10^{-1}$
$c_4$	$0.427 240 \times 10^{-1}$	$0.415 770 \times 10^{-1}$
$d_1$	$0.155 428 \times 10^{-4}$	$0.487 360 \times 10^{-4}$
$d_2$	$0.623 689 \times 10^{-4}$	$0.740 336 \times 10^{-5}$
$\beta$	0.653 920	1.226
$\gamma$	$0.601 670 \times 10^{-1}$	0.037 54
$\omega$	0	0.397 8

### A.2 Derivatives of the Helmholtz-Energy Transformation of the LKP EOS

According to Eq. (3.28) the residual part of the LKP EOS transformed into the reduced Helmholtz-energy explicit form can be written as:

$$\alpha^r = \frac{B}{Z_c} \delta + \frac{1}{2} \frac{C}{Z_c^2} \delta^2 + \frac{1}{5} \frac{D}{Z_c^5} \delta^5 - \frac{c_4 \tau^3}{2\gamma} \left( \frac{\gamma}{Z_c^2} \delta^2 + \beta + 1 \right) \exp \left( -\frac{\gamma}{Z_c^2} \delta^2 \right) + \frac{c_4 \tau^3}{2\gamma} (\beta + 1). \quad (\text{A2.1})$$

The first derivate of the residual part with respect to the reduced density  $\delta = 1 / \Psi$  directly results from combining Eqs. (3.14) and (3.25) and reads:

$$\alpha_\delta^r = \frac{B}{Z_c} + \frac{C}{Z_c^2} \delta + \frac{D}{Z_c^5} \delta^4 + \frac{c_4 \tau^3}{Z_c^2} \delta \left( \frac{\gamma}{Z_c^2} \delta^2 + \beta \right) \exp \left( -\frac{\gamma}{Z_c^2} \delta^2 \right). \quad (\text{A2.2})$$

The second derivate with respect to  $\delta$  can consequently be given as:

$$\alpha_{\delta\delta}^r = \frac{C}{Z_c^2} + 4 \frac{D}{Z_c^5} \delta^3 + \frac{c_4 \tau^3}{Z_c^2} \left[ -2 \frac{\gamma^2}{Z_c^4} \delta^4 + (3-2\beta) \frac{\gamma}{Z_c^2} \delta^2 + \beta \right] \exp\left(-\frac{\gamma}{Z_c^2} \delta^2\right). \quad (\text{A2.3})$$

The third derivative with respect to  $\delta$  reads:

$$\alpha_{\delta\delta\delta}^r = 12 \frac{D}{Z_c^5} \delta^2 + 2 \frac{c_4 \tau^3 \gamma}{Z_c^4} \delta \left[ 2 \frac{\gamma}{Z_c^2} \delta^4 - (7-2\beta) \frac{\gamma}{Z_c^2} \delta^2 - 3\beta + 3 \right] \exp\left(-\frac{\gamma}{Z_c^2} \delta^2\right). \quad (\text{A2.4})$$

Differentiating Eq. (A2.1) with respect to the reduced temperature  $\tau = 1 / \mathcal{G}$  yields

$$\alpha_{\tau}^r = \frac{\delta}{Z_c} \frac{\partial B}{\partial \tau} + \frac{1}{2} \frac{\delta^2}{Z_c^2} \frac{\partial C}{\partial \tau} + \frac{1}{5} \frac{\delta^5}{Z_c^5} \frac{\partial D}{\partial \tau} - \frac{3}{2} \frac{c_4 \tau^2}{\gamma} \left( \frac{\gamma}{Z_c^2} \delta^2 + \beta + 1 \right) \exp\left(-\frac{\gamma}{Z_c^2} \delta^2\right) + \frac{3}{2} \frac{c_4 \tau^2}{\gamma} (\beta + 1), \quad (\text{A2.5})$$

with

$$\frac{\partial B}{\partial \tau} = -b_2 - 2b_3 \tau - 3b_4 \tau^2, \quad \frac{\partial C}{\partial \tau} = -c_2 + 3c_3 \tau^2, \quad \text{and} \quad \frac{\partial D}{\partial \tau} = d_2. \quad (\text{A2.6})$$

The second derivative with respect to  $\tau$  can be written as

$$\alpha_{\tau\tau}^r = \frac{\delta}{Z_c} \frac{\partial^2 B}{\partial \tau^2} + \frac{1}{2} \frac{\delta^2}{Z_c^2} \frac{\partial^2 C}{\partial \tau^2} + \frac{1}{5} \frac{\delta^5}{Z_c^5} \frac{\partial^2 D}{\partial \tau^2} - 3 \frac{c_4 \tau}{\gamma} \left( \frac{\gamma}{Z_c^2} \delta^2 + \beta + 1 \right) \exp\left(-\frac{\gamma}{Z_c^2} \delta^2\right) + 3 \frac{c_4 \tau}{\gamma} (\beta + 1), \quad (\text{A2.7})$$

with

$$\frac{\partial^2 B}{\partial \tau^2} = 2b_3 - 6b_4 \tau, \quad \frac{\partial^2 C}{\partial \tau^2} = 6c_3 \tau, \quad \text{and} \quad \frac{\partial^2 D}{\partial \tau^2} = 0. \quad (\text{A2.8})$$

The third derivative with respect to  $\tau$  reads

$$\alpha_{\tau\tau\tau}^r = \frac{\delta}{Z_c} \frac{\partial^3 B}{\partial \tau^3} + \frac{1}{2} \frac{\delta^2}{Z_c^2} \frac{\partial^3 C}{\partial \tau^3} + \frac{1}{5} \frac{\delta^5}{Z_c^5} \frac{\partial^3 D}{\partial \tau^3} - 3 \frac{c_4}{\gamma} \left( \frac{\gamma}{Z_c^2} \delta^2 + \beta + 1 \right) \exp\left(-\frac{\gamma}{Z_c^2} \delta^2\right) + 3 \frac{c_4}{\gamma} (\beta + 1), \quad (\text{A2.9})$$

with

$$\frac{\partial^3 B}{\partial \tau^3} = -6b_4, \quad \frac{\partial^3 C}{\partial \tau^3} = 6c_3, \quad \text{and} \quad \frac{\partial^3 D}{\partial \tau^3} = 0. \quad (\text{A2.10})$$

## Appendix B - Supplement to the EOS for Heavy Water

### B.1 Equation-of-State Parameters

**Table B.1** Parameters of the ideal-gas part of the EOS for heavy water according to Eq. (5.2).

$k$	$c_k$	$a_k$	$v_k$	$u_k / \text{K}$
0	4.0	-	-	-
1	-	-8.670 994 022 646 00	$0.106\ 33 \times 10^{-1}$	308.0
2	-	6.960 335 784 587 78	0.997 87	1695.0
3	-	-	$0.214\ 83 \times 10^1$	3949.0
4	-	-	0.354 90	10 317.0

**Table B.2** Parameters of the residual part of the EOS for heavy water according to Eq. (5.3).

$k$	$n_k$	$t_k$	$d_k$	$l_k$	$\eta_k$	$\beta_k$	$\gamma_k$	$\varepsilon_k$
1	$0.122\ 082\ 060 \times 10^{-1}$	1.0000	4	-				
2	$0.296\ 956\ 870 \times 10^1$	0.6555	1	-				
3	$-0.379\ 004\ 540 \times 10^1$	0.9369	1	-				
4	0.941 089 600	0.5610	2	-				
5	-0.922 466 250	0.7017	2	-				
6	$-0.139\ 604\ 190 \times 10^{-1}$	1.0672	3	-				
7	-0.125 203 570	3.9515	1	1				
8	$-0.555\ 391\ 500 \times 10^1$	4.6000	1	2				
9	$-0.493\ 009\ 740 \times 10^1$	5.1590	3	2				
10	$-0.359\ 470\ 240 \times 10^{-1}$	0.2000	2	1				
11	$-0.936\ 172\ 870 \times 10^1$	5.4644	2	2				
12	-0.691 835 150	2.3660	1	2				
13	$-0.456\ 110\ 600 \times 10^{-1}$	3.4553	1	-	0.6014	0.4200	1.5414	1.8663
14	$-0.224\ 513\ 300 \times 10^1$	1.4150	3	-	1.4723	2.4318	1.3794	0.2895
15	$0.860\ 006\ 070 \times 10^1$	1.5745	1	-	1.5305	1.2888	1.7385	0.5803
16	$-0.248\ 410\ 420 \times 10^1$	3.4540	3	-	2.4297	8.2710	1.3045	0.2236
17	$0.164\ 476\ 900 \times 10^2$	3.8106	1	-	1.3086	0.3673	2.7242	0.6815
18	$0.270\ 393\ 360 \times 10^1$	4.8950	1	-	1.3528	0.9504	3.5321	0.9495
19	$0.375\ 637\ 470 \times 10^2$	1.4300	2	-	3.4456	7.8318	2.4552	1.1158
20	$-0.177\ 607\ 760 \times 10^1$	1.5870	2	-	1.2645	3.3281	0.8319	0.1607
21	$0.220\ 924\ 640 \times 10^1$	3.7900	2	-	2.5547	7.1753	1.3500	0.4144
22	$0.519\ 652\ 000 \times 10^1$	2.6200	1	-	1.2148	0.9465	2.5617	0.9683
23	0.421 097 400	1.9000	1	-	18.738	1177.0	1.0491	0.9488
24	-0.391 921 100	4.3200	1	-	18.677	1167.0	1.0486	0.9487

## B.2 Data Sets for Heavy Water and Statistical Analysis

**Table B.3** Average absolute relative deviations of experimental vapor pressure, saturated-liquid density, and saturated-vapor density data from the EOS for D<sub>2</sub>O. Sources preceded by \* were used for fitting the EOS.

Reference	Year	No. of data	Temperature range in K	Average absolute relative deviations in %			
				LT <sup>a</sup>	MT <sup>a</sup>	HT <sup>a</sup>	overall
Vapor pressure $p_v$							
*Besley and Bottomley <sup>90</sup>	1973	37	277 - 299	0.024	-	-	0.024
Bottomley <sup>80 b,c</sup>	1978	17	261 - 276	0.088	-	-	0.088
Erokhin and Kompaniets <sup>134</sup>	1980	22	433 - 644	-	0.074	0.083	0.076
Jákli and Illy <sup>91</sup>	1980	157	280 - 362	0.068	-	-	0.068
Jákli and Markó <sup>93 d</sup>	1995	101	281 - 353	0.075	-	-	0.075
Jákli and Van Hook <sup>92</sup>	1981	57	280 - 363	0.068	-	-	0.068
Jones <sup>318</sup>	1968	32	361 - 388	0.303	0.108	-	0.289
Kirillin and Ulybin <sup>319</sup>	1959	4	573 - 645	-	0.035	0.042	0.039
Kraus and Greer <sup>89 c</sup>	1984	162	257 - 277	0.732	-	-	0.732
Lewis and MacDonald <sup>117</sup>	1933	10	293 - 389	0.341	-	-	0.341
Liu and Lindsay <sup>320</sup>	1970	12	379 - 574	0.064	0.091	-	0.089
Miles and Menzies <sup>321</sup>	1936	10	298 - 502	0.314	0.104	-	0.188
Niwa and Shimazaki <sup>81</sup>	1939	6	277 - 287	0.785	-	-	0.785
*Oliver and Grisard <sup>69</sup>	1956	36	481 - 645	-	0.010	0.053	0.017
Pupezin <i>et al.</i> <sup>79</sup>	1972	96	273 - 372	0.163	-	-	0.163
Quitzsich <i>et al.</i> <sup>322</sup>	1963	4	293 - 324	0.267	-	-	0.267
*Rivkin and Ahkundov <sup>64</sup>	1962	8	548 - 639	-	0.015	0.027	0.019
*Zieborak <sup>94</sup>	1966	15	354 - 494	0.014	0.006	-	0.008
Saturated liquid density $\rho'$							
Costello and Bowden <sup>101</sup>	1958	10	293 - 474	0.072	0.241	-	0.157
Grossmann-Doerth <sup>98</sup>	1955	14	368 - 434	-	0.007	-	0.005
Grossmann-Doerth <sup>99</sup>	1956	9	333 - 373	0.001	-	-	0.001
Hebert <i>et al.</i> <sup>100</sup>	1958	21	448 - 645	-	0.230	3.183	0.511
Mursalov <i>et al.</i> <sup>97</sup>	1999	14	294 - 644	0.055	0.163	0.656	0.246
Saturated vapor density $\rho''$							
Hebert <i>et al.</i> <sup>100</sup>	1958	21	448 - 645	-	13.406	8.222	12.913
Mursalov <i>et al.</i> <sup>97</sup>	1999	9	572 - 644	-	1.019	2.948	2.305

<sup>a</sup>LT:  $T/T_c < 0.6$ ; MT:  $0.6 \leq T/T_c \leq 0.98$ ; HT:  $T/T_c > 0.98$

<sup>b</sup>The publication presents differences between the vapor pressure of the metastable subcooled liquid and the sublimation pressure. The vapor pressures were recalculated by means of Eq. (5.9).

<sup>c</sup>The reference provides vapor pressures of the metastable subcooled liquid. The deviations were calculated by calculating the vapor pressure with the EOS extrapolated to temperatures below the triple-point temperature.

<sup>d</sup>The original reference does not provide experimental values for pure D<sub>2</sub>O. These were given later by Harvey and Lemmon<sup>95</sup> within an article presenting a vapor-pressure correlation for D<sub>2</sub>O.

**Table B.4** Average absolute relative deviations of available experimental data for homogeneous densities from the EOS for D<sub>2</sub>O. Clear outliers were not considered within the AAD. Sources preceded by \* were used for fitting the EOS.

Reference	Year	No. of data	$T / \text{K}$	$p / \text{MPa}$	Average absolute relative deviations in %						
					Gas	Liq.	Crit. Reg.	Supercritical fluid LD <sup>a</sup>	MD <sup>a</sup>	HD <sup>a</sup>	over-all
<i>pVT</i> data											
Aleksandrov <i>et al.</i> <sup>123</sup>	1976	143	673 - 824	4.5 - 101	-	-	0.048 <sup>b</sup>	0.088	0.316	0.030	0.126
Aleksandrov <i>et al.</i> <sup>109</sup>	1976	65	270 - 286	3.7 - 101	-	0.019	-	-	-	-	0.019
Bridgman <sup>73 c</sup>	1935	130	253 - 374	0.1 - 1189	-	0.208	-	-	-	-	0.208
Ceccaldi <i>et al.</i> <sup>116</sup>	1975	1	295.4	0.1	-	0.021	-	-	-	-	0.021
*Chang and Tung <sup>115 d</sup>	1949	23	276 - 375	0.1	-	0.005	-	-	-	-	0.005
*Duška <i>et al.</i> <sup>107</sup>	2018	242	254 - 294	0.1 - 101	-	0.006	-	-	-	-	0.006
*Emmet and Millero <sup>108</sup>	1975	129	275 - 314	0.1 - 101	-	0.007	-	-	-	-	0.007
Hare and Sorensen <sup>323</sup>	1986	11	253 - 313	0.1	-	0.023	-	-	-	-	0.023
Ivanov and Lebedeva <sup>324</sup>	2011	5	278 - 319	0.1	-	0.007	-	-	-	-	0.007
Ivanov <i>et al.</i> <sup>325</sup>	2010	5	278 - 319	0.1	-	0.010	-	-	-	-	0.010
Ivanov <i>et al.</i> <sup>326</sup>	2011	6	278 - 319	0.1	-	0.005	-	-	-	-	0.005
Jancsó <sup>327</sup>	2007	5	298 - 319	0.1	-	0.045	-	-	-	-	0.045
Juza <i>et al.</i> <sup>121</sup>	1966	36	353 - 624	50 - 351	-	0.302	-	-	-	-	0.302
*Kanno and Angell <sup>120</sup>	1980	32	247 - 294	0.1 - 148	-	0.052	-	-	-	-	0.052
*Kell <i>et al.</i> <sup>103</sup>	1985	415	423 - 774	0.1 - 103	-	0.009	0.011 <sup>b</sup>	-	0.048	0.024	0.013
*Kell <i>et al.</i> <sup>102</sup>	1989	631	423 - 774	0.1 - 37	0.065	-	-	0.039	-	-	0.051
Kirillin and Ulybin <sup>319</sup>	1959	124	523 - 774	7.3 - 50	0.602	0.299	0.366 <sup>b</sup>	0.090	0.615	0.214	0.301
Kudryavtsev <i>et al.</i> <sup>328</sup>	1986	5	278 - 319	0.1	-	0.006	-	-	-	-	0.006
Lewis and MacDonald <sup>117</sup>	1933	9	277 - 314	0.1	-	0.264	-	-	-	-	0.264
Marczak <sup>329</sup>	1999	5	293 - 314	0.1	-	0.082	-	-	-	-	0.082
Millero <i>et al.</i> <sup>330 e</sup>	1971	14	278 - 344	0.1	-	0.009	-	-	-	-	0.009
Nevolina and Seifer <sup>331</sup>	1973	6	293.1	0.1 - 101	-	0.016	-	-	-	-	0.016
Rasmussen and MacKenzie <sup>150</sup>	1973	11	244 - 274	0.1	-	0.217	-	-	-	-	0.217
Reisler and Eisenberg <sup>332</sup>	1965	7	278 - 309	0.1	-	0.005	-	-	-	-	0.005
*Rivkin and Ahkundov <sup>64</sup>	1962	43	663 - 699	4.7 - 29	-	-	0.027 <sup>b</sup>	0.056	0.120	-	0.056
Scharlin and Steinby <sup>333</sup>	2003	6	277 - 319	0.1	-	0.017	-	-	-	-	0.017
Schrader and Wirtz <sup>334 f</sup>	1951	17	293 - 374	0.1	-	0.015	-	-	-	-	0.015
*Steckel and Szapiro <sup>114</sup>	1963	61	276 - 351	0.1	-	0.004	-	-	-	-	0.004
Stokland <i>et al.</i> <sup>113</sup>	1939	51	283 - 301	0.1	-	0.003	-	-	-	-	0.003
Tsederberg <i>et al.</i> <sup>110</sup>	1972	71	293 - 474	1.5 - 100	-	0.044	-	-	-	-	0.044
Tsederberg <i>et al.</i> <sup>124</sup>	1973	173	473 - 699	1.8 - 101	0.102	0.058	0.032 <sup>b</sup>	0.066	0.057	0.061	0.061
Zheleznyi <sup>149</sup>	1969	20	244 - 278	0.1	-	0.176	-	-	-	-	0.176

<sup>a</sup>LD:  $\rho / \rho_c < 0.6$ ; MD:  $0.6 \leq \rho / \rho_c \leq 1.5$ ; HD:  $\rho / \rho_c > 1.5$

<sup>b</sup>The AAD of *pVT* data in the critical region is given with respect to pressure instead of density.

<sup>c</sup>All pressures of Bridgman<sup>73</sup> were multiplied by 1.0102 (see Sec. 5.1.2).

<sup>d</sup>The data supersede the data of Chang and Chien,<sup>335</sup> which were consequently omitted.

<sup>e</sup>The article presents two data sets with a D<sub>2</sub>O purity of 99.88 mol% and 98.35 mol%. The latter data were omitted.

<sup>f</sup>The data supersede the data of Wirtz,<sup>336</sup> which were consequently omitted.

**Table B.5** Average absolute deviations of available data for the second and third virial coefficient from the EOS for D<sub>2</sub>O. The reference preceded by \* was used for fitting the EOS.

Reference	Year	No. of data	$T / K$	Average absolute deviations
Second virial coefficient $B / (\text{cm}^3 \text{mol}^{-1})$				
*Garberoglio <i>et al.</i> <sup>125 a</sup>	2018	19	250 - 2000	1.648
Kell <i>et al.</i> <sup>102 b</sup>	1989	31	423 - 774	1.162
Third virial coefficient $C / (\text{dm}^6 \text{mol}^{-2})$				
Garberoglio <i>et al.</i> <sup>125 c</sup>	2018	4	500 - 1000	0.002
Kell <i>et al.</i> <sup>102 b</sup>	1989	31	423 - 774	0.0169

<sup>a</sup>The AAD excludes two data points at 200 K and 225 K where the magnitude of  $B$  becomes large. The AAD for all 21 data points is  $3.629 \text{ cm}^3 \text{mol}^{-1}$ .

<sup>b</sup>The data supersede the data of Kell *et al.*,<sup>337</sup> which were consequently omitted.

<sup>c</sup>The AAD excludes one data point at 300 K where the magnitude of  $C$  is much larger than for other points. The AAD for all 5 data points is  $1.785 \text{ dm}^6 \text{mol}^{-2}$ .

**Table B.6** Average absolute relative deviations of available experimental data for caloric properties from the EOS for D<sub>2</sub>O. Clear outliers were not considered within the AAD. Sources preceded by \* were used for fitting the EOS.

Reference	Year	No. of data	$T / K$	$p / \text{MPa}$	Average absolute relative deviations in %						
					Gas	Liq.	Crit. Reg.	Supercritical LD <sup>a</sup>	fluid MD <sup>a</sup>	over- HD <sup>a</sup>	all
Speed of sound $w$											
*Aleksandrov and Larkin <sup>130</sup>	1977	176	271-649	0.1-72	-	0.057	1.878	1.281	1.453	0.041	0.091
Aleksandrov and Larkin <sup>338</sup>	1978	15	277-374	0.1	-	0.011	-	-	-	-	0.011
*Chen and Millero <sup>112</sup>	1977	132	277-334	0.1-100	-	0.024	-	-	-	0.051	0.041
Conde <i>et al.</i> <sup>151</sup>	1982	32	259-357	0.1	-	0.651	-	-	-	-	0.651
Erokhin and Kompaniets <sup>134</sup>	1980	38	433-644	sat.	0.290	1.048	-	-	-	-	0.689
Evsteeffev <i>et al.</i> <sup>145</sup>	1979	139	423-574	0.1-12	-	0.600	-	-	-	-	0.600
*Fehres and Rudtsch <sup>129</sup>	2017	100	278-314	0.1-60	-	0.011	-	-	-	0.008	0.010
Fine and Millero <sup>339</sup>	1975	18	277-364	0.1	-	0.037	-	-	-	-	0.037
Gupta <i>et al.</i> <sup>340</sup>	1976	15	280-354	0.1	-	0.307	-	-	-	-	0.307
Heusinger <sup>341</sup>	1949	10	278-364	0.1	-	0.236	-	-	-	-	0.236
Ivanov <i>et al.</i> <sup>342</sup>	2009	4	283-339	0.1	-	0.050	-	-	-	-	0.050
Lago and Giuliano Albo <sup>133</sup>	2018	72	276-364	0.2-211	-	0.036	-	-	-	0.112	0.097
Marczak <sup>329</sup>	1999	5	293-314	0.1	-	0.031	-	-	-	-	0.031
McMillan and Lagemann <sup>343</sup>	1947	9	278-334	0.1	-	0.282	-	-	-	-	0.282
Pancholy <sup>344</sup>	1953	14	278-364	0.1	-	0.716	-	-	-	-	0.716
*Wegge <i>et al.</i> <sup>128</sup>	2016	72	278-354	0.1-21	-	0.006	-	-	-	-	0.006
*Wilson <sup>131</sup>	1961	136	277-365	0.1-97	-	0.031	-	-	-	0.051	0.046
Isobaric heat capacity $c_p$											
*Angell <i>et al.</i> <sup>139</sup>	1982	30	240-291	0.1	-	1.484	-	-	-	-	1.484
*Eucken and Eigen <sup>141</sup>	1951	12	292-398	sat.	-	0.457	-	-	-	-	0.457
Long and Kemp <sup>77</sup>	1936	4	279-296	0.1	-	0.996	-	-	-	-	0.996
Rivkin and Egorov <sup>135 b</sup>	1959	28	293-574	4.9-10	-	0.184	-	-	-	-	0.184
Rivkin and Egorov <sup>136</sup>	1962	133	530-728	22.1-30	-	-	3.010	1.257	2.183	0.584	1.931
Rivkin and Egorov <sup>137</sup>	1963	100	464-729	9.8-25	1.106	0.539	3.993	1.741	1.894	0.708	1.194
*Rivkin and Egorov <sup>138 c</sup>	1963	293	293-724	4.9-30	1.086	0.348	2.425	1.484	2.046	0.353	0.668
*Smirnova <i>et al.</i> <sup>140</sup>	2006	34	274-351	0.1	-	0.649	-	-	-	-	0.649

*continued...*



**Table B.6** ...continued

Reference	Year	No. of data	$T / K$	$p / \text{MPa}$	Average absolute relative deviations in %						
					Gas	Liq.	Reg.	LD <sup>a</sup>	MD <sup>a</sup>	HD <sup>a</sup>	all
Isochoric heat capacity $c_v$											
Amirkhanov <i>et al.</i> <sup>142</sup>	1975	275	294- 743	0.002-77	-	2.474	4.731	-	1.813	5.274	3.261
*Mursalov <i>et al.</i> <sup>97</sup>	1999	636	294- 747	0.002-76	3.377	2.497	5.091	3.396	1.728	4.984	3.543
Mursalov <i>et al.</i> <sup>97</sup>	1999	23	294- 644	sat.	11.228	5.390	-	-	-	-	7.674
*Polikhronidi <i>et al.</i> <sup>143</sup> <sup>d</sup>	2002	115	639- 672	20.5-31	-	6.069	8.089	-	-	-	7.931
Joule-Thomson coefficient $\mu_{JT}$											
Jůza <i>et al.</i> <sup>121</sup> <sup>e</sup>	1966	27	423- 444	0.11-0.17	3.727	-	-	-	-	-	3.727

<sup>a</sup>LD:  $\rho / \rho_c < 0.6$ ; MD:  $0.6 \leq \rho / \rho_c \leq 1.5$ ; HD:  $\rho / \rho_c > 1.5$

<sup>b</sup>A translated version was published in 1961 by Rivkin and Egorov.<sup>345</sup>

<sup>c</sup>A translated version was published in 1964 by Rivkin and Egorov.<sup>346</sup>

<sup>d</sup>The data supersede the earlier data of Polikhronidi *et al.*<sup>347</sup>

<sup>e</sup>As shown by Ertle<sup>348</sup> for H<sub>2</sub>O, the data of Jůza *et al.*<sup>121</sup> are missing a correction considering a “heat leakage” of the experimental set-up. The data were not relevant for fitting the new EOS, and thus are not discussed within this article.

## Appendix C - Supplement to the EOS for Chlorine

### C.1 Equation-of-State Parameters

**Table C.1** Parameters of the ideal-gas part of the EOS for chlorine according to Eq. (5.12).

$k$	$c_k$	$a_k$	$v_k$	$u_k / \text{K}$
0	3.5	-	-	-
1	-	-3.953 901 364 055 381 5	$0.102 56 \times 10^1$	800.0
2	-	3.839 904 839 793 069 5	$0.677 56 \times 10^{-1}$	3000.0
3	-	-	0.140 68	8200.0

**Table C.2** Parameters of the residual part of the EOS for chlorine according to Eq. (5.13).

$k$	$n_k$	$t_k$	$d_k$	$l_k$	$\eta_k$	$\beta_k$	$\gamma_k$	$\varepsilon_k$
1	$0.245 017 0 \times 10^{-1}$	1.000	4	-				
2	0.913 290 4	0.196	1	-				
3	$-0.172 309 0 \times 10^1$	1.000	1	-				
4	-0.335 934 4	1.080	2	-				
5	0.120 049 5	0.390	3	-				
6	$-0.121 488 9 \times 10^1$	1.640	1	2				
7	-0.101 670 0	3.200	3	2				
8	0.619 681 9	1.320	2	1				
9	-0.657 851 2	2.163	2	2				
10	$-0.915 945 2 \times 10^{-2}$	0.930	7	1				
11	$0.190 941 8 \times 10^1$	0.872	1	-	0.969	1.220	1.142	0.880
12	$-0.716 341 2 \times 10^{-1}$	2.080	1	-	1.890	6.800	1.220	0.730
13	-0.189 334 5	1.600	3	-	1.320	3.500	1.552	0.280
14	-0.569 846 9	1.370	2	-	1.012	1.276	1.135	0.863
15	-0.896 449 6	1.050	2	-	0.980	1.600	0.754	0.554

## C.2 Data Sets for Chlorine and Statistical Analysis

**Table C.3** Average absolute relative deviations of experimental vapor pressure, saturated-liquid density, and saturated-vapor density data from the EOS for chlorine. Clear outliers were not considered within the AAD. Sources preceded by \* were used for fitting the EOS.

Reference	Year	No. of data	Temperature range in K	Average absolute relative deviations in %			
				LT <sup>a</sup>	MT <sup>a</sup>	HT <sup>a</sup>	overall
Vapor pressure $p_v$							
*Ambrose <i>et al.</i> <sup>153</sup>	1979	42	205 - 405	0.056	0.942	-	0.563
Cheesman and Scott <sup>159</sup>	1968	11	173 - 274	0.150	0.178	-	0.158
Giauque and Powell <sup>158</sup>	1939	15	172 - 241	0.629	-	-	0.629
*Gilot <i>et al.</i> <sup>283</sup>	1967	11	225 - 240	0.357	-	-	0.357
Harteck <sup>349</sup>	1928	19	178 - 236	3.248	-	-	3.248
Henglein <i>et al.</i> <sup>350</sup>	1922	1	194.54	1.842	-	-	1.842
Kang <i>et al.</i> <sup>351</sup>	1998	3	283 - 284	-	0.514	-	0.514
Pellaton <sup>157</sup>	1915	15	285 - 417	-	1.179	0.269	0.936
Pham <i>et al.</i> <sup>352</sup>	1997	1	293.15	-	2.680	-	2.680
Sittig <sup>166</sup>	1959	8	273 - 344	-	1.139	-	1.139
Wilson and Wilding <sup>282</sup>	1994	8	213 - 324	0.846	0.586	-	0.683
Saturated liquid density $\rho'$							
Kanda <sup>353</sup>	1937	7	208 - 240	0.832	-	-	0.832
*Liessmann <i>et al.</i> <sup>354</sup>	1995	12	203 - 404	0.217	0.420	-	0.369
Lowry and Jessop <sup>355</sup>	1930	4	275 - 285	-	0.036	-	0.036
Pellaton <sup>157</sup>	1915	14	273 - 404	-	0.182	-	0.182
Sittig <sup>166</sup>	1959	8	273 - 418	-	0.052	-	0.052
Saturated vapor density $\rho''$							
Hulme <sup>162</sup>	1949	26	230 - 355	0.364	0.364	-	1.677
Pellaton <sup>157</sup>	1915	14	273 - 404	-	-	-	4.294
Sittig <sup>166</sup>	1959	8	273 - 418	-	-	-	5.197

<sup>a</sup>LT:  $T/T_c < 0.6$ ; MT:  $0.6 \leq T/T_c \leq 0.98$ ; HT:  $T/T_c > 0.98$

**Table C.4** Average absolute relative deviations of available experimental data for homogeneous densities from the EOS for chlorine. Clear outliers were not considered within the AAD. Sources preceded by \* were used for fitting the EOS.

Reference	Year	No. of data	$T / K$	$p / \text{MPa}$	Average absolute relative deviations in %						
					Gas	Liq.	Reg.	LD <sup>a</sup>	MD <sup>a</sup>	HD <sup>a</sup>	all
$pVT$ data											
Hulme <sup>162</sup>	1949	132	255 - 478	0.1 - 3	0.535	-	-	0.760	-	-	0.624
Jaquerod and Tourpaian <sup>164</sup>	1913	21	273 - 289	0.1 - 1	0.197	-	-	-	-	-	0.197
*Ross and Maass <sup>163</sup>	1940	39	288 - 349	0.0 - 1.0	0.098	-	-	-	-	-	0.098
*Wagenbreth <sup>161</sup>	1968	576	263 - 424	1.0 - 21.0	-	0.046	-	-	-	-	0.125 0.049

<sup>a</sup>LD:  $\rho / \rho_c < 0.6$ ; MD:  $0.6 \leq \rho / \rho_c \leq 1.5$ ; HD:  $\rho / \rho_c > 1.5$

**Table C.5** Average absolute relative deviations of available experimental data for caloric properties from the new EOS for chlorine. Sources preceded by \* were used for fitting the EOS

Reference	Year	No. of data	$T / K$	$p / MPa$	Average absolute relative deviations in %						
					Gas	Liq.	Reg.	Crit. LD <sup>a</sup>	Supercritical MD <sup>a</sup>	fluid over- HD <sup>a</sup>	all
Speed of sound $w$											
*Hurly <sup>154</sup>	2002	222	260 - 441	0.1 - 2	0.006	-	-	0.003	-	-	0.005
Schulze <sup>165</sup>	1939	4	248 - 306	0.1	0.274	-	-	-	-	-	0.274
Sittig <sup>166</sup>	1959	3	273 - 304	0.1	-	0.380	-	-	-	-	0.380
Strecker <sup>167</sup>	1881	1	273.15	0.1	0.393	-	-	-	-	-	0.393
Isobaric heat capacity $c_p$											
Eucken and Karwat <sup>168</sup>	1924	6	187 - 198	0.1	1.777	-	-	-	-	-	1.777
*Giauque and Powell <sup>158</sup>	1939	11	179 - 237	0.1	0.349	-	-	-	-	-	0.349
Sittig <sup>166</sup>	1959	3	293 - 304	sat.	1.287	-	-	-	-	-	1.287

<sup>a</sup>LD:  $\rho / \rho_c < 0.6$ ; MD:  $0.6 \leq \rho / \rho_c \leq 1.5$ ; HD:  $\rho / \rho_c > 1.5$

## Appendix D - Supplement to the EOS for MEA

### D.1 Equation-of-State Parameters

**Table D.1** Parameters of the ideal-gas part of the EOS for MEA according to Eq. (5.14).

$k$	$c_k$	$a_k$	$v_k$	$u_k / \text{K}$
0	3.0	-	-	-
1	-	-1.037 113 046 226 409 1	$0.137 \times 10^2$	970.0
2	-	3.783 941 321 762 991 4	$0.111 \times 10^2$	3380.0

**Table D.2** Parameters of the residual part of the EOS for MEA according to Eq. (5.15).

$k$	$n_k$	$t_k$	$d_k$	$l_k$	$\eta_k$	$\beta_k$	$\gamma_k$	$\varepsilon_k$
1	$0.343\ 716\ 570 \times 10^{-1}$	1.000	4	-				
2	$0.280\ 481\ 500 \times 10^1$	0.530	1	-				
3	$-0.353\ 280\ 220 \times 10^1$	1.146	1	-				
4	-0.260 521 060	0.950	2	-				
5	$0.737\ 280\ 990 \times 10^{-1}$	0.350	3	-				
6	-0.923 286 400	1.470	1	2				
7	-0.152 436 360	2.800	3	2				
8	0.448 379 380	0.900	2	1				
9	-0.175 175 650	3.000	2	2				
10	$-0.129\ 363\ 620 \times 10^{-1}$	0.830	7	1				
11	$0.108\ 237\ 190 \times 10^1$	1.030	1	-	0.7100	1.8200	1.0400	0.8400
12	-0.567 555 230	0.760	1	-	1.1600	1.5000	1.0400	0.7700
13	-0.388 084 020	0.700	3	-	0.7330	1.7400	1.0400	0.6000
14	$-0.673\ 884\ 460 \times 10^1$	1.040	3	-	4.0800	57.000	1.3700	0.5900

## D.2 Data Sets for MEA and Statistical Analysis

**Table D.3** Average absolute relative deviations of experimental vapor-pressure data from the EOS for MEA. Sources preceded by \* were used for fitting the EOS

Reference	Year	No. of data	Temperature range in K	mol% MEA	AAD in %		
					LT <sup>a</sup>	MT <sup>a</sup>	overall
Vapor pressure $p_v$							
Ageev <i>et al.</i> <sup>356</sup>	1970	1	333.13		36.77	-	36.77
Anderson and Shimanskaya <sup>357</sup>	1969	1	444.11		-	1.714	1.714
Anonymous <sup>358</sup>	1956	4	293 - 445		8.518	1.805	6.84
Bergman and Shulyak <sup>359</sup>	1972	9	283 - 364		1.218	-	1.218
*Belabbaci <i>et al.</i> <sup>180</sup>	2009	1	444.11	> 99.0	-	1.714	1.714
Beskow <i>et al.</i> <sup>360</sup>	1957	3	293 - 302		56.95	-	56.95
Bogacheva <i>et al.</i> <sup>361</sup>	1980	1	445.31		-	5.551	5.551
Brasoveanu <i>et al.</i> <sup>362</sup>	2000	1	464.15		-	82.96	82.96
Cai <i>et al.</i> <sup>297</sup>	1996	1	443.64	> 99.9	-	0.242	0.242
Cadle <i>et al.</i> <sup>363</sup>	1949	3	373 - 444		3.089	1.665	2.140
Daubert <i>et al.</i> <sup>174</sup>	1987	14	325 - 444		6.536	0.905	4.123
Danov <i>et al.</i> <sup>175</sup>	1969	35	351 - 624		3.558	8.231	7.296
Gas Research Institute <sup>364</sup>	1981	10	303 - 394		50.21	-	50.21
Graubner <sup>365</sup>	2010	1	353.15		7.500	-	7.500
Hahn and Freydanck <sup>366</sup>	1983	7	363 - 438		3.106	0.813	2.123
Hahn <i>et al.</i> <sup>367</sup>	1989	12	372 - 444		1.402	0.386	0.810
Kapteina <i>et al.</i> <sup>368</sup>	2005	13	279 - 325	> 99.9	28.92	-	28.91
Kim <i>et al.</i> <sup>182</sup>	2008	16	357 - 436	> 99.0	0.698	0.853	0.776
Klepáčová <i>et al.</i> <sup>369</sup>	2011	7	358 - 442	> 99.5	3.526	0.734	1.931
Kogan <i>et al.</i> <sup>370</sup>	1970	1	443.11		-	1.395	1.395
Lafontaine <sup>172</sup>	1958	1	444.04		-	1.494	1.494
Landauer <i>et al.</i> <sup>371</sup>	1974	1	444.11		-	1.714	1.714
Leibush and Shorina <sup>372</sup>	1947	1	443.94		-	1.179	1.179
Lecat <sup>373</sup>	1947	4	303 - 374		9.961	-	9.961
Lyons <sup>176</sup>	1985	19	443 - 624	> 99.7	-	8.337	8.337
Matthews <i>et al.</i> <sup>374</sup>	1950	49	338 - 445	> 99.4	5.754	2.395	4.794
McDonald <i>et al.</i> <sup>375</sup>	1959	9	379 - 444	99.94	1.887	0.172	1.315
Nath and Bender <sup>304</sup>	1983	5	338 - 365		4.114	-	4.114
Park and Lee <sup>302</sup>	1997	1	443.30	> 99.0	-	0.817	0.817
Pividal and Sandler <sup>376</sup>	1990	2	363 - 384	> 99.0	0.790	-	0.790
Reddy <i>et al.</i> <sup>377</sup>	2012	1	442.28	> 99.5	-	2.151	2.151
Reitmeier <i>et al.</i> <sup>378</sup>	1940	1	444.24	99.96	-	2.124	2.124
Street and Adkins <sup>379</sup>	1928	1	394.13		82.73	-	82.73
Sunder and Prasad <sup>380</sup>	2007	1	441.45		-	0.475	0.475
Tanaka <i>et al.</i> <sup>303</sup>	2001	1	443.51		-	0.168	0.168
*Tochigi <i>et al.</i> <sup>181</sup>	1999	2	298 - 309	> 99.6 <sup>b</sup>	9.064	-	9.064
Touhara <i>et al.</i> <sup>305</sup>	1982	20	357 - 440	99.92 <sup>b</sup>	0.630	0.432	0.531
Wohland <sup>381</sup>	1976	11	389 - 524		108.3	59.84	64.24
Zaretskii <i>et al.</i> <sup>382</sup>	1970	1	445.11		-	4.903	4.903

<sup>a</sup>LT:  $T/T_c < 0.6$ ; MT:  $0.6 \leq T/T_c \leq 0.98$

<sup>b</sup>Sample purity in mass fraction m% MEA.

**Table D.4** Average absolute relative deviations of available experimental data for homogeneous densities from the EOS for MEA. The data are restricted to the liquid phase. Except for one indicated data set, all data were measured at ambient pressure. Sources preceded by \* were used for fitting the EOS.

Reference	Year	No. of data	Temperature range in K	mol% MEA	AAD in %
<i>pVT</i> data					
Ageev <i>et al.</i> <sup>356</sup>	1970	1	293.14		0.658
Águila-Hernández <i>et al.</i> <sup>383</sup>	2008	11	308 - 374	98.5	0.105
Álvarez <i>et al.</i> <sup>384</sup>	2010	7	293 - 324	> 99.0 <sup>a</sup>	0.049
Amundsen <i>et al.</i> <sup>385</sup>	2009	5	298 - 354	> 99.5	0.007
Anonymous <sup>358</sup>	1956	1	293.14		0.116
Arce <i>et al.</i> <sup>386</sup>	2004	1	298.15	> 99.0 <sup>a</sup>	0.115
Blanco <i>et al.</i> <sup>387</sup>	2012	1	298.15	> 99.0	0.132
Blanco <i>et al.</i> <sup>185</sup>	2013	5	293 - 324	> 99.0	0.054
Bogacheva <i>et al.</i> <sup>361</sup>	1980	1	293.14		0.560
Bogacheva <i>et al.</i> <sup>388</sup>	1982	3	312 - 353	99.95	0.263
Brasoveanu <i>et al.</i> <sup>362</sup>	2000	4	293 - 334		0.227
Coquelet <i>et al.</i> <sup>389</sup>	2005	1	297.15	> 99.0	0.116
Dean <i>et al.</i> <sup>390</sup>	2009	7	298 - 359		0.059
DiGuilio <i>et al.</i> <sup>391</sup>	1992	8	294 - 432	> 99.0	0.120
García-Abuín <i>et al.</i> <sup>392</sup>	2011	4	293 - 324	> 99.0	0.037
García-Abuín <i>et al.</i> <sup>393</sup>	2013	1	298.15	> 99.0	0.132
Gas Research Institute <sup>364</sup>	1981	10	303 - 394		0.346
Geng <i>et al.</i> <sup>394</sup>	2008	8	288 - 324	> 99.0	0.078
*Han <i>et al.</i> <sup>183 b</sup>	2012	20	298 - 424	99.5	0.035
Hawrylak <i>et al.</i> <sup>395</sup>	2000	3	298 - 319	> 99.0 <sup>a</sup>	0.118
Herba <i>et al.</i> <sup>396</sup>	1995	1	293.15		0.265
Islam <i>et al.</i> <sup>397</sup>	2004	1	293.15	> 99.98	0.510
Jones <i>et al.</i> <sup>398</sup>	1959	1	293.14		0.293
Kapadi <i>et al.</i> <sup>399</sup>	2002	4	303 - 319		0.032
Kartsev <i>et al.</i> <sup>400</sup>	1986	1	298.14		0.145
Kartsev <i>et al.</i> <sup>401</sup>	1988	1	298.15		0.144
Kozin and Mukhamadiev <sup>402</sup>	2002	5	293 - 334		0.662
Kurtz <i>et al.</i> <sup>403</sup>	1965	1	298.14		0.035
Lafontaine <sup>172</sup>	1958	2	293 - 299		0.883
Lee and Lin <sup>404</sup>	1995	3	303 - 324	99.0 <sup>a</sup>	0.057
Lee <i>et al.</i> <sup>405</sup>	1997	3	303 - 324	99.0 <sup>a</sup>	0.057
Leibush and Shorina <sup>372</sup>	1947	8	283 - 354		0.228
Li and Shen <sup>406</sup>	1992	8	303 - 354		0.067
Li <i>et al.</i> <sup>407</sup>	2013	6	293 - 334	> 99.0	0.048
Maham <i>et al.</i> <sup>408</sup>	1994	5	298 - 354	99.0	0.054
Maham <i>et al.</i> <sup>409</sup>	2002	2	278 - 289	99.0	0.029
Matthews <i>et al.</i> <sup>374</sup>	1950	5	293 - 314	99.4	0.146
Migal and Starchevskii <sup>410</sup>	1957	3	273 - 294		0.217
Murrieta-Guevara and Rodriguez <sup>411</sup>	1984	8	298 - 334		0.060
Murrieta-Guevara <i>et al.</i> <sup>412</sup>	1993	3	303 - 374	> 99.56	0.265
Nath and Bender <sup>304</sup>	1983	2	293 - 299		0.099
Pagé <i>et al.</i> <sup>413</sup>	1993	2	283 - 299	> 99.7	0.110

*continued...*

**Table D.4** ...continued

Reference	Year	No. of data	Temperature range in K	mol% MEA	AAD in %
<i>pvT</i> data					
Patil <sup>186</sup>	1978	1	293.14		0.042
Pourmohammadbagher and Shaw <sup>414</sup>	2013	3	288 - 354	99.9	0.070
Pouryousefi and Idem <sup>415</sup>	2008	4	295 - 334	99.0	0.008
Reddy <i>et al.</i> <sup>377</sup>	2012	2	303 - 309	> 99.5	0.095
Reitmeier <i>et al.</i> <sup>378</sup>	1940	7	298 - 354	99.96	0.071
Song <i>et al.</i> <sup>416</sup>	1996	5	303 - 344	99.0	0.103
Song <i>et al.</i> <sup>417</sup>	2011	3	303 - 324	> 99.8	0.015
Sunder and Prasad <sup>380</sup>	2007	1	298.15		0.066
Taib and Murugesan <sup>418</sup>	2010	6	303 - 354	99.0	0.249
Taib and Murugesan <sup>419</sup>	2012	8	293 - 354	99.0	0.181
Taib <i>et al.</i> <sup>420</sup>	2013	6	303 - 354	> 99.0	0.249
Tanaka <i>et al.</i> <sup>303</sup>	2001	1	298.15		0.190
Tian <i>et al.</i> <sup>421</sup>	2013	6	303 - 329	99.0 <sup>a</sup>	0.044
Timmermans and Hennaut-Roland <sup>422</sup>	1959	3	273 - 304		0.101
Touhara <i>et al.</i> <sup>305</sup>	1982	1	298.14	99.92 <sup>a</sup>	0.200
Tseng and Thompson <sup>423</sup>	1964	3	293 - 304	91.9	1.571
Tsierkezos and Molinou <sup>424</sup>	1999	1	293.15	> 99.0	0.009
*Valtz <i>et al.</i> <sup>184</sup>	2005	37	281 - 354	> 99.0	0.019
Wang <i>et al.</i> <sup>425</sup>	1992	5	293 - 361	99.0	0.070
Wang <i>et al.</i> <sup>426</sup>	2013	8	293 - 364	> 99.0 <sup>a</sup>	0.007
Yang <i>et al.</i> <sup>427</sup>	2013	7	283 - 344	99.0	0.004
Yasmin and Gupta <sup>428</sup>	2011	1	298.15	> 99.5	0.096
Zaretskii <i>et al.</i> <sup>382</sup>	1970	1	293.14		0.949

<sup>a</sup>Sample purity in mass fraction m% MEA.

<sup>b</sup>Pressure range of the of Han *et al.*:<sup>183</sup>  $0.1 \leq p / \text{MPa} \leq 0.7$

**Table D.5** Average absolute relative deviations of available experimental data for caloric properties from the EOS for MEA. The data are restricted to the liquid phase. Except for one indicated data set, all data were measured at ambient pressure. Sources preceded by \* were used for fitting the EOS.

Reference	Year	No. of data	Temperature range in K	mol% MEA	AAD in %
Speed of sound <i>w</i>					
Álvarez <i>et al.</i> <sup>384</sup>	2010	7	293-324	> 99.0 <sup>a</sup>	0.052
Blanco <i>et al.</i> <sup>387</sup>	2012	1	298.15	> 99.0	0.024
*Blanco <i>et al.</i> <sup>185</sup>	2013	5	293-324	> 99.0	0.034
Dean <i>et al.</i> <sup>390</sup>	2009	1	303	99.0	0.053
García-Abuín <i>et al.</i> <sup>392</sup>	2011	4	293-324	> 99.0	0.091
García-Abuín <i>et al.</i> <sup>393</sup>	2013	1	298.15	> 99.0	0.024
Hawrylak <i>et al.</i> <sup>395</sup>	2000	3	298-319	> 99.0 <sup>a</sup>	0.049
Patil <sup>186</sup>	1978	1	293.14		0.385
Willard <sup>187</sup>	1947	1	298.14		0.300
Yasmin and Gupta <sup>428</sup>	2011	1	298.15	> 99.5	0.092

continued...



**Table D.5** ...continued

Reference	Year	No. of data	Temperature range in K	mol% MEA	AAD in %
Isobaric heat capacity $c_p$					
Anonymous <sup>358</sup>	1956	1	308.13		2.986
*Chiu <i>et al.</i> <sup>188</sup>	1999	11	303 - 354	> 99.0	1.455
*Maham <i>et al.</i> <sup>189</sup>	1997	5	299 - 398	> 99.0	2.724
Mundhwa and Henni <sup>190</sup>	2007	11	303 - 354		1.403
Pagé <i>et al.</i> <sup>413</sup>	1993	3	283 - 314	> 99.7	2.268
Song <i>et al.</i> <sup>417</sup>	2011	3	303 - 324	> 99.8	2.273

<sup>a</sup>Sample purity in mass fraction m% MEA.

## Appendix E - Supplement to the CCS-Mixture Model

### E.1 Parameters of the Mixture Model

**Table E.1** Parameters of the reducing functions given in Eqs. (3.42) and (3.43) for the 59 binary formulations developed in this work.

Mixture $ij$	$\beta_{r,ij}$	$\gamma_{r,ij}$	$\beta_{v,ij}$	$\gamma_{v,ij}$	$F_{ij}$	<i>see</i>
Binary mixtures described with specific departure functions						
CO <sub>2</sub> + Ar	0.998 705 0	1.039 674 8	1.003 765 9	1.013 833 0	1	Sec. 6.2.1
CO <sub>2</sub> + CO	0.989 782 0	1.162 129 8	1.033 801 7	1.000 162 3	1	Sec. 6.2.2
H <sub>2</sub> O + CH <sub>4</sub>	0.791 766 0	0.748 000 0	0.850 340 1	1.038 000 0	1	Sec. 6.2.3
H <sub>2</sub> O + H <sub>2</sub> S	1.041 096 0	0.924 026 0	1.057 285 9	1.189 702 0	1	Sec. 6.2.4
Binary mixtures described with adjusted reducing function (and no departure function)						
SO <sub>2</sub> + CO <sub>2</sub>	0.980 331 6	1.007 975 3	1.123 766 0	1.005 778 3	0	Sec. 6.3.1.1
SO <sub>2</sub> + N <sub>2</sub>	1.045 874 0	1.194 658 8	0.903 624 5	1.215 580 8	0	Sec. 6.3.1.2
SO <sub>2</sub> + O <sub>2</sub>	0.927 961 0	1.035 878 2	1.219 246 3	1.660 631 7	0	Sec. 6.3.1.3
SO <sub>2</sub> + CH <sub>4</sub>	0.999 432 0	1.115 713 5	1.315 534 0	1.119 543 3	0	Sec. 6.3.1.4
SO <sub>2</sub> + Cl <sub>2</sub>	0.984 564 0	0.927 820 2	0.976 224 7	1.016 621 1	0	Sec. 6.3.1.5
SO <sub>2</sub> + HCl	1.002 605 0	1.048 380 2	1.000 000 0	1.000 000 0	0	Sec. 6.3.1.6
SO <sub>2</sub> + MEA	0.979 150 9	1.200 045 1	1.000 000 0	1.000 000 0	0	Sec. 6.3.1.7
SO <sub>2</sub> + DEA	0.979 150 9	1.200 045 1	1.000 000 0	1.000 000 0	0	Sec. 6.3.1.7
SO <sub>2</sub> + H <sub>2</sub> O	1.019 562 0	0.916 311 0	1.094 032 0	0.962 547 0	0	Sec. 6.3.1.8
MEA + H <sub>2</sub> O	1.025 500 0	1.052 467 0	1.236 603 0	0.482 099 0	0	Sec. 6.3.2.1
DEA + H <sub>2</sub> O	1.014 447 0	1.045 661 8	1.177 068 6	0.633 037 9	0	Sec. 6.3.2.1
DEA + MEA	1.015 703 0	1.020 484 0	0.766 762 0	0.852 448 0	0	Sec. 6.3.2.2
Cl <sub>2</sub> + HCl	1.007 373 0	0.968 864 5	0.928 100 0	0.917 288 3	0	Sec. 6.3.3
Binary mixtures described with linear combining rules						
SO <sub>2</sub> + Ar	1.000 000 0	1.141 020 2	1.000 000 0	1.021 291 1	0	Sec. 6.4
SO <sub>2</sub> + CO	1.000 000 0	1.177 903 2	1.000 000 0	1.007 241 4	0	Sec. 6.4
SO <sub>2</sub> + H <sub>2</sub>	1.000 000 0	1.940 852 1	1.000 000 0	1.035 171 0	0	Sec. 6.4
HCl + O <sub>2</sub>	1.000 000 0	1.069 637 9	1.000 000 0	1.001 592 4	0	Sec. 6.4
HCl + Ar	1.000 000 0	1.074 562 8	1.000 000 0	1.001 235 8	0	Sec. 6.4
HCl + H <sub>2</sub>	1.000 000 0	1.724 555 7	1.000 000 0	1.005 948 1	0	Sec. 6.4
Cl <sub>2</sub> + H <sub>2</sub>	1.000 000 0	1.914 078 4	1.000 000 0	1.035 410 1	0	Sec. 6.4
Binary mixtures described with Lorentz-Berthelot combining rules						
MEA + CO <sub>2</sub>	1.000 000 0	1.000 000 0	1.000 000 0	1.000 000 0	0	Sec. 6.4
MEA + N <sub>2</sub>	1.000 000 0	1.000 000 0	1.000 000 0	1.000 000 0	0	Sec. 6.4
MEA + O <sub>2</sub>	1.000 000 0	1.000 000 0	1.000 000 0	1.000 000 0	0	Sec. 6.4
MEA + Ar	1.000 000 0	1.000 000 0	1.000 000 0	1.000 000 0	0	Sec. 6.4
MEA + CO	1.000 000 0	1.000 000 0	1.000 000 0	1.000 000 0	0	Sec. 6.4
MEA + H <sub>2</sub>	1.000 000 0	1.000 000 0	1.000 000 0	1.000 000 0	0	Sec. 6.4
MEA + CH <sub>4</sub>	1.000 000 0	1.000 000 0	1.000 000 0	1.000 000 0	0	Sec. 6.4
MEA + H <sub>2</sub> S	1.000 000 0	1.000 000 0	1.000 000 0	1.000 000 0	0	Sec. 6.4
DEA + CO <sub>2</sub>	1.000 000 0	1.000 000 0	1.000 000 0	1.000 000 0	0	Sec. 6.4
DEA + N <sub>2</sub>	1.000 000 0	1.000 000 0	1.000 000 0	1.000 000 0	0	Sec. 6.4
DEA + O <sub>2</sub>	1.000 000 0	1.000 000 0	1.000 000 0	1.000 000 0	0	Sec. 6.4
DEA + Ar	1.000 000 0	1.000 000 0	1.000 000 0	1.000 000 0	0	Sec. 6.4
DEA + CO	1.000 000 0	1.000 000 0	1.000 000 0	1.000 000 0	0	Sec. 6.4

...continued

**Table E.1** ...continued

Mixture $ij$	$\beta_{T,ij}$	$\gamma_{T,ij}$	$\beta_{v,ij}$	$\gamma_{v,ij}$	$F_{ij}$	see
Binary mixtures described with Lorentz-Berthelot combining rules						
DEA + H <sub>2</sub>	1.000 000 0	1.000 000 0	1.000 000 0	1.000 000 0	0	Sec. 6.4
DEA + CH <sub>4</sub>	1.000 000 0	1.000 000 0	1.000 000 0	1.000 000 0	0	Sec. 6.4
DEA + H <sub>2</sub> S	1.000 000 0	1.000 000 0	1.000 000 0	1.000 000 0	0	Sec. 6.4
HCl + CO <sub>2</sub>	1.000 000 0	1.000 000 0	1.000 000 0	1.000 000 0	0	Sec. 6.4
HCl + H <sub>2</sub> O	1.000 000 0	1.000 000 0	1.000 000 0	1.000 000 0	0	Sec. 6.4
HCl + N <sub>2</sub>	1.000 000 0	1.000 000 0	1.000 000 0	1.000 000 0	0	Sec. 6.4
HCl + CO	1.000 000 0	1.000 000 0	1.000 000 0	1.000 000 0	0	Sec. 6.4
HCl + CH <sub>4</sub>	1.000 000 0	1.000 000 0	1.000 000 0	1.000 000 0	0	Sec. 6.4
HCl + H <sub>2</sub> S	1.000 000 0	1.000 000 0	1.000 000 0	1.000 000 0	0	Sec. 6.4
HCl + MEA	1.000 000 0	1.000 000 0	1.000 000 0	1.000 000 0	0	Sec. 6.4
HCl + DEA	1.000 000 0	1.000 000 0	1.000 000 0	1.000 000 0	0	Sec. 6.4
Cl <sub>2</sub> + CO <sub>2</sub>	1.000 000 0	1.000 000 0	1.000 000 0	1.000 000 0	0	Sec. 6.4
Cl <sub>2</sub> + H <sub>2</sub> O	1.000 000 0	1.000 000 0	1.000 000 0	1.000 000 0	0	Sec. 6.4
Cl <sub>2</sub> + N <sub>2</sub>	1.000 000 0	1.000 000 0	1.000 000 0	1.000 000 0	0	Sec. 6.4
Cl <sub>2</sub> + O <sub>2</sub>	1.000 000 0	1.000 000 0	1.000 000 0	1.000 000 0	0	Sec. 6.4
Cl <sub>2</sub> + Ar	1.000 000 0	1.000 000 0	1.000 000 0	1.000 000 0	0	Sec. 6.4
Cl <sub>2</sub> + CO	1.000 000 0	1.000 000 0	1.000 000 0	1.000 000 0	0	Sec. 6.4
Cl <sub>2</sub> + CH <sub>4</sub>	1.000 000 0	1.000 000 0	1.000 000 0	1.000 000 0	0	Sec. 6.4
Cl <sub>2</sub> + H <sub>2</sub> S	1.000 000 0	1.000 000 0	1.000 000 0	1.000 000 0	0	Sec. 6.4
Cl <sub>2</sub> + MEA	1.000 000 0	1.000 000 0	1.000 000 0	1.000 000 0	0	Sec. 6.4
Cl <sub>2</sub> + DEA	1.000 000 0	1.000 000 0	1.000 000 0	1.000 000 0	0	Sec. 6.4

**Table E.2** Parameters of the binary specific departure functions developed in this work.

$k$	$n_{ij,k}$	$t_{ij,k}$	$d_{ij,k}$	$l_{ij,k}$	$\eta_{ij,k}$	$\varepsilon_{ij,k}$	$\beta_{ij,k}$	$\gamma_{ij,k}$
CO <sub>2</sub> + Ar (see Eq. (6.1))								
1	$-0.656\ 00 \times 10^{-1}$	3.220	2	–	–	–	–	–
2	$0.237\ 00 \times 10^{-1}$	2.900	3	–	–	–	–	–
3	$0.352\ 17 \times 10^1$	1.900	1	–	1.243	0.650	1.208	0.5
4	$-0.283\ 10 \times 10^1$	1.570	1	–	1.072	0.727	0.820	0.5
5	$-0.140\ 60 \times 10^1$	2.730	1	–	1.465	0.648	1.527	0.5
6	0.864 00	1.080	2	–	0.946	0.706	0.860	0.5
CO <sub>2</sub> + CO (see Eq. (6.2))								
1	$0.186\ 10 \times 10^1$	2.820	1	–	–	–	–	–
2	$-0.401\ 70 \times 10^1$	3.260	1	–	–	–	–	–
3	0.273 40	0.940	2	–	–	–	–	–
4	$0.239\ 30 \times 10^1$	3.944	4	–	–	–	–	–
5	$0.264\ 60 \times 10^2$	2.530	1	–	0.385	0.144	5.100	0.109
6	$-0.121\ 30 \times 10^1$	4.380	1	–	0.295	0.310	1.661	2.596
H <sub>2</sub> O + CH <sub>4</sub> (see Eq. (6.3))								
1	$0.330\ 00 \times 10^1$	1.100	1	–	–	–	–	–
2	$-0.288\ 00 \times 10^1$	0.800	1	–	–	–	–	–
3	$0.960\ 00 \times 10^1$	0.800	1	1	–	–	–	–
4	$-0.117\ 00 \times 10^2$	1.000	1	1	–	–	–	–
5	$0.213\ 00 \times 10^1$	4.000	2	1	–	–	–	–
6	$-0.530\ 00$	3.400	4	1	–	–	–	–

continued...

**Table E.2** ...continued

$k$	$n_{ij,k}$	$t_{ij,k}$	$d_{ij,k}$	$l_{ij,k}$	$\eta_{ij,k}$	$\varepsilon_{ij,k}$	$\beta_{ij,k}$	$\gamma_{ij,k}$
H <sub>2</sub> O + H <sub>2</sub> S (see Eq. (6.4))								
1	0.170 00	0.900	1	–	–	–	–	–
2	–0.111 60	4.040	1	–	–	–	–	–
3	0.121 00	6.880	2	1	–	–	–	–
4	–0.235 20 × 10 <sup>–2</sup>	8.150	4	1	–	–	–	–
5	–0.431 00 × 10 <sup>–1</sup>	5.350	8	2	–	–	–	–
6	0.776 40	2.700	1	1	–	–	–	–

## E.2 Data Sets for the CCS-Mixture Model and Statistical Analysis

**Table E.3** Average absolute relative deviations of available experimental and molecular-simulation data for various thermodynamic properties from the binary mixture models developed in this work. Clear outliers were not considered within the *AAD*. Sources preceded by \* were used for fitting the EOS. The *AAD* for VLE data is given with respect to composition. No *AAD* is reported, if the calculated value is unreasonably high.

$x_1\text{CO}_2 + (1 - x_1)\text{Ar}$									
VLE data									
Reference	Year	$N_x$	$N_y$	$T / \text{K}$	$p / \text{MPa}$	$x_{1,\text{liq}}$	$x_{1,\text{vap}}$	$AAD_{\text{liq}}$	$AAD_{\text{vap}}$
Ahmad <i>et al.</i> <sup>205</sup>	2013	10	10	278.35 - 300.35	4.20 - 7.93	0.944 - 0.975	0.945 - 0.975	0.432	1.583
Coquelet <i>et al.</i> <sup>203</sup>	2008	62	62	233.32 - 299.21	1.52 - 14.03	0.423 - 0.993	0.292 - 0.986	1.068	1.680
Kaminishi <i>et al.</i> <sup>202</sup>	1968	13	19	233.18 - 273.15	2.57 - 13.20	0.650 - 0.967	0.246 - 0.851	0.509	1.250
Köpke and Eggers <sup>207,208</sup>	2007	63	63	244.30 - 283.30	1.78 - 13.45	0.645 - 0.990	0.305 - 0.886	0.602	1.458
Lasala <i>et al.</i> <sup>204</sup>	2016	66	71	223.07 - 293.07	0.70 - 14.55	0.544 - 0.989	0.012 - 1.000	1.820	3.270
*Løvseth <i>et al.</i> <sup>197</sup>	2018	46	54	213.14 - 299.22	2.54 - 15.01	0.492 - 0.990	0.131 - 1.000	1.035	0.688
Sarashina <i>et al.</i> <sup>206</sup>	1971	4	8	288.15	5.69 - 9.78	0.833 - 0.940	0.793 - 0.940	0.310	0.413
*Tsankova <i>et al.</i> <sup>200</sup>	2016	0	14	252.95 - 280.44	2.83 - 6.94	–	0.750	–	0.032
Tsankova <i>et al.</i> <sup>201</sup>	2017	0	10	257.54 - 291.13	2.41 - 6.01	–	0.950	–	0.024
Speed of sound $w$									
Reference	Year	$N$	$T / \text{K}$	$p / \text{MPa}$	$x_1$	<i>AAD</i>			
Al-Siyabi <sup>215</sup>	2013	59	268.15 - 301.15	9.31 - 41.75	0.955	0.906			
*Wegge <i>et al.</i> <sup>219</sup>	2016	67	274.99 - 500.50	0.45 - 8.22	0.501	0.065			
		82	276.09 - 500.49	0.49 - 8.20	0.750	0.140			
<i>Overall</i>		149	274.99 - 500.50	0.45 - 8.22	0.501 - 0.750	0.106			
$pVT$ data									
Reference	Year	$N$	$T / \text{K}$	$p / \text{MPa}$	$x_1$	<i>AAD</i>			
*Abraham and Bennett <sup>217</sup>	1960	13	323.13	5.07 - 101.33	0.831	0.255			
		13	323.13	5.07 - 101.33	0.751	0.276			
		13	323.13	5.07 - 101.33	0.642	0.295			
		13	323.13	5.07 - 101.33	0.464	0.120			
		13	323.13	5.07 - 101.33	0.371	0.162			
		13	323.13	5.07 - 101.33	0.238	0.135			
		13	323.13	5.07 - 101.33	0.129	0.046			
<i>Overall</i>		91	323.13	5.07 - 101.33	0.129 - 0.831	0.184			
Al-Siyabi <sup>215</sup>	2013	47	283.15 - 301.15	7.80 - 48.23	0.95	1.052			
Altunin and Koposhilov <sup>429</sup>	1976	15	313.14	0.32 - 15.33	0.351	0.182			
		15	313.14	0.66 - 18.71	0.811	0.221			
		14	313.14	0.66 - 20.91	0.501	0.234			
		16	313.14	0.30 - 14.81	0.661	0.216			
<i>Overall</i>		60	313.14	0.30 - 20.91	0.351 - 0.811	0.213			
Altunin and Koposhilov <sup>216</sup>	1977	14	303.14	0.30 - 10.76	0.362	0.212			
		12	303.14	0.51 - 10.98	0.481	0.104			
		14	303.14	0.31 - 10.30	0.534	0.052			
		10	303.14	1.01 - 9.29	0.647	0.208			
		12	303.14	0.31 - 10.30	0.665	0.134			
		13	313.14	0.56 - 14.83	0.351	0.290			
		14	313.14	0.66 - 20.91	0.501	0.233			
		15	313.14	0.32 - 13.24	0.575	0.172			

continued...

Table E.3 ...continued

Reference	Year	<i>N</i>	<i>T</i> / K	<i>p</i> / MPa	<i>x</i> <sub>1</sub>	AAD
		16	313.14	0.30 - 14.81	0.661	0.235
		15	313.14	0.66 - 18.71	0.811	0.224
		16	323.14	0.36 - 23.07	0.37	0.104
		13	323.14	0.88 - 21.95	0.486	0.094
		17	323.14	0.32 - 24.72	0.528	0.073
		16	323.14	0.42 - 23.71	0.559	0.172
		17	323.14	0.37 - 20.80	0.801	0.091
		14	343.14	0.53 - 20.07	0.435	0.054
		15	343.14	0.38 - 18.21	0.483	0.277
		15	343.14	0.48 - 18.63	0.608	0.268
		15	343.14	0.56 - 22.20	0.754	0.340
		14	373.14	0.53 - 20.40	0.526	0.128
		15	373.14	0.43 - 20.23	0.673	0.223
<i>Overall</i>		302	303.14 - 373.14	0.30 - 24.72	0.351 - 0.811	0.175
*Ben Souissi <i>et al.</i> <sup>209</sup>	2016	15	273.15 - 298.15	0.51 - 8.01	0.500	0.005
		6	323.15	0.52 - 9.02	0.500	0.008
		35	273.15 - 323.15	0.50 - 9.05	0.751	0.022
<i>Overall</i>		56	273.15 - 323.15	0.50 - 9.05	0.500 - 0.751	0.016
Kestin <i>et al.</i> <sup>213</sup>	1966	48	293.14 - 303.14	0.10 - 2.60	0.268 - 0.918	0.877
Kosov and Brovanov <sup>430</sup>	1979	31	313.03 - 353.12	6.46 - 58.80	0.714	3.297
		30	313.03 - 353.12	5.96 - 58.80	0.479	1.07
		30	313.03 - 353.12	5.87 - 58.81	0.204	0.533
<i>Overall</i>		91	313.03 - 353.12	5.87 - 58.81	0.204 - 0.714	1.652
Mantovani <i>et al.</i> <sup>214</sup>	2012	100	303.22 - 383.14	1.00 - 20.01	0.969	0.570
		94	303.22 - 383.14	1.00 - 20.00	0.831	1.676
<i>Overall</i>		194	303.22 - 383.14	1.00 - 20.01	0.831 - 0.969	1.106
Sarashina <i>et al.</i> <sup>206</sup>	1971	88	288.15	2.43 - 14.53	0.700 - 0.940	1.332
*Schönmann <sup>218</sup>	1971	28	373.01	0.50 - 59.02	0.188	0.103
		54	473.14 - 573.05	0.50 - 58.32	0.200	0.065
		29	373.01	0.42 - 59.23	0.398	0.094
		55	473.14 - 573.05	0.41 - 58.92	0.411	0.060
		30	373.01	0.39 - 59.27	0.598	0.090
		55	473.15 - 573.05	0.43 - 58.86	0.609	0.071
		29	373.00	0.47 - 58.88	0.802	0.086
		55	473.15 - 573.05	0.45 - 59.38	0.804	0.093
<i>Overall</i>		355	373.00 - 573.05	0.39 - 59.38	0.188 - 0.804	0.079
Tsankova <i>et al.</i> <sup>201</sup>	2017	30	273.20 - 293.28	0.45 - 6.50	0.751	0.170
		29	255.10 - 313.30	0.97 - 7.08	0.950	0.185
<i>Overall</i>		59	255.10 - 313.30	0.45 - 7.08	0.751 - 0.950	0.177
Wang <i>et al.</i> <sup>274</sup>	2015	18	308.15 - 358.15	7.00 - 23.00	0.858	12.54
*Wegge <sup>212</sup>	2016	121	253.15 - 453.15	2.39 - 18.79	0.500	0.947
		13	253.15	1.02 - 4.50	0.500	0.076
		58	253.15 - 453.15	2.30 - 20.01	0.750	0.213
		53	253.15 - 283.15	1.00 - 5.99	0.751	0.069
<i>Overall</i>		245	253.15 - 453.15	1.00 - 20.01	0.500 - 0.751	0.537
Yang <i>et al.</i> <sup>211</sup>	2015	66	298.17 - 423.36	10.97 - 30.96	0.010	0.274
		66	298.12 - 423.34	10.98 - 30.96	0.050	0.490
<i>Overall</i>		132	298.12 - 423.34	10.97 - 30.96	0.010 - 0.050	0.382
*Yang <i>et al.</i> <sup>210</sup>	2016	38	273.15 - 323.36	0.49 - 8.99	0.950	0.037

Joule-Thomson coefficient $\mu_{JT}$						
Reference		<i>N</i>	<i>T</i> / K	<i>p</i> / MPa	<i>x</i> <sub>1</sub>	AAD
*Strakey <i>et al.</i> <sup>431</sup>	1974	41	233.16 - 383.12	1.01 - 20.27	0.464	1.818
		32	233.16 - 383.12	1.01 - 20.27	0.754	5.185
<i>Overall</i>		73	233.16 - 383.12	1.01 - 20.27	0.464 - 0.754	3.294

Second virial coefficient $B(x_1)$ and cross-virial coefficient $B_{12}$ (AAD given in cm <sup>3</sup> mol <sup>-1</sup> )						
Reference	Year	<i>N</i>	<i>T</i> / K		<i>x</i> <sub>1</sub>	AAD
Bose and Cole <sup>432</sup>	1970	5	320.84 - 322.84		-	62.19
Cottrell <i>et al.</i> <sup>433</sup>	1956	3	303.13 - 363.12		-	6.308
*Martin <i>et al.</i> <sup>434</sup>	1982	3	290.00 - 319.99		-	0.359
Schmiedel <i>et al.</i> <sup>435</sup>	1980	12	213.01 - 474.96		-	6.615
*Schönmann <sup>218</sup>	1971	22	373.12 - 573.11		0.050 - 0.950	0.578

continued...

**Table E.3** ...continued

Reference	Year	$N$	$T / K$		$x_1$		AAD		
Schramm and Müller <sup>436</sup>	1982	1	296.14		-		1.418		
<b><math>x_1\text{CO}_2 + (1 - x_1)\text{CO}</math></b>									
VLE data									
Reference	Year	$N_x$	$N_y$	$T / K$	$p / \text{MPa}$	$x_{1,\text{liq}}$	$x_{1,\text{vap}}$	AAD <sub>liq</sub>	AAD <sub>vap</sub>
Blanco <i>et al.</i> <sup>224</sup>	2014	25	25	253.15 - 293.15	1.977 - 7.465	0.900 - 0.990	0.980 - 0.998	1.392	0.264
Christiansen <i>et al.</i> <sup>225</sup>	1974	34	34	223.16 - 283.16	0.827 - 14.15	0.537 - 0.997	0.200 - 0.985	1.649	0.362
Huamin <sup>226</sup>	1991	10	10	223.15 - 261.15	1.572 - 6.960	0.845 - 0.992	0.209 - 0.830	0.611	2.494
Kaminishi <i>et al.</i>	1968	19	19	223.16 - 283.15	2.360 - 12.91	0.631 - 0.957	0.213 - 0.827	0.353	0.590
*Souza <i>et al.</i> <sup>221</sup>	2018	103	103	218.15 - 302.94	0.766 - 14.63	0.488 - 0.997	0.523 - 0.995	0.283	0.451
Westman <i>et al.</i> <sup>220</sup>	2018	24	24	253.15 - 298.16	6.033 - 12.55	0.626 - 0.982	0.426 - 0.959	0.258	0.684
pvT data									
Reference	Year	$N$	$T / K$		$p / \text{MPa}$	$x_1$		AAD	
Blanco <i>et al.</i> <sup>224</sup>	2014	197	253.15 - 343.15		0.02 - 20.17	0.970		1.678	
		197	253.15 - 343.15		0.10 - 20.00	0.981		1.622	
		197	253.15 - 343.15		0.10 - 23.85	0.990		2.106	
		197	253.15 - 343.15		0.10 - 20.00	0.993		1.378	
		197	253.15 - 343.15		0.10 - 20.00	0.996		1.488	
<i>Overall</i>		985	253.15 - 343.15		0.02 - 23.85	0.970 - 0.996		1.654	
Cipollina <i>et al.</i> <sup>229</sup>	2007	8	308.00 - 343.00		26.00 - 42.30	0.862		1.350	
		8	308.00 - 343.00		26.60 - 44.10	0.866		1.549	
		8	308.00 - 343.00		25.50 - 44.40	0.883		0.228	
		8	308.00 - 343.00		25.40 - 43.30	0.885		0.130	
		8	308.00 - 343.00		24.70 - 43.00	0.911		0.252	
		8	308.00 - 343.00		26.50 - 47.00	0.935		0.195	
		8	308.00 - 343.00		22.50 - 42.20	0.954		0.215	
<i>Overall</i>		56	308.00 - 343.00		22.50 - 47.00	0.862 - 0.954		0.560	
*Mallu <i>et al.</i> <sup>231</sup>	1987	15	273.20-313.27		1.45 - 6.54	0.503		0.505	
		75	323.14-423.11		0.10 - 6.50	0.573		0.16	
<i>Overall</i>		90	273.20-423.11		0.10 - 6.54	0.504 - 0.573		0.333	
*Mallu <i>et al.</i> <sup>230</sup>	1989	75	323.15-423.15		0.10 - 6.50	0.299		0.498	
		75	323.15-423.15		0.10 - 6.50	0.798		0.275	
<i>Overall</i>		150	323.15-423.15		0.10 - 6.50	0.299 - 0.798		0.386	
*Souza <i>et al.</i> <sup>222</sup>		187	283.15 - 373.15		2.03 - 48.17	0.498		0.161	
		188	283.15 - 373.16		2.06 - 48.06	0.748		0.219	
		176	283.14 - 373.15		1.90 - 48.20	0.899		0.391	
		169	283.15 - 373.15		1.96 - 48.65	0.950		0.222	
		720	283.15 - 373.16		1.96 - 48.64	0.498 - 0.950		0.248	
Tsankova <i>et al.</i> <sup>223</sup>	2019	26	255.04 - 313.29		1.96 - 8.00	0.248		0.228	
		21	255.05 - 313.27		1.45 - 6.54	0.504		0.432	
<i>Overall</i>		47	255.04 - 313.29		1.45 - 8.00	0.248 - 0.504		0.323	
<b><math>x_1\text{H}_2\text{O} + (1 - x_1)\text{CH}_4</math></b>									
VLE data									
Reference	Year	$N_x$	$N_y$	$T / K$	$p / \text{MPa}$	$x_{1,\text{liq}}$	$x_{1,\text{vap}}$	AAD <sub>liq</sub>	AAD <sub>vap</sub>
Campos <i>et al.</i> <sup>238</sup>	2010	18	0	303.20-323.20	0.11 - 0.64	.9997 - .9999	-	0.005	-
*Chapoy <i>et al.</i> <sup>233</sup>	2004	10	0	275.11 - 313.11	0.97 - 18.00	.9975 - .9998	-	-	0.014
*Chapoy <i>et al.</i> <sup>240</sup>	2005	0	39	283.08 - 318.12	0.99 - 35.09	-	.0001 - .0099	-	0.005
*Fenghour and Wakeham <sup>241</sup>	1996	0	9	426.90-596.10	7.43 - 22.50	-	.0760 - .6761	-	0.407
Fonseca and von Solms <sup>236</sup>	2012	10	6	298.21-303.28	5.25 - 12.35	.9980 - .9990	.9992 - .9997	0.019	0.286
Frost <i>et al.</i> <sup>234</sup>	2014	22	22	283.89-323.56	4.78 - 19.49	.9974 - .9994	.0002 - .0039	0.028	0.16
*Gillespie and Wilson <sup>261</sup>	1982	13	16	323.14-588.67	1.38 - 16.89	.9932 - .9998	.0014 - .8322	0.019	0.015
*Kim <i>et al.</i> <sup>239</sup>	2003	5	0	298.15-298.15	2.30 - 16.60	.9974 - .9995	-	0.021	0.132
Mohammadi <i>et al.</i> <sup>243</sup>	2004	0	17	282.98-313.12	0.51 - 2.85	-	.0012 - .0124	-	-
*Olds <i>et al.</i> <sup>244</sup>	1942	0	78	310.91-510.94	2.67 - 68.88	-	.0004 - .5646	-	0.005
*Qin <i>et al.</i> <sup>237</sup>	2008	7	0	324.20-376.10	10.90 - 49.90	.9959 - .9986	-	0.039	-
Rigby and Prausnitz <sup>245</sup>	1968	0	12	298.14-373.12	2.35 - 9.35	-	.0009 - .0199	-	0.003
*Sairanen and Heinonen <sup>242</sup>	2014	0	135	253.15-293.15	0.20 - 7.00	-	.0000 - .0115	-	0.023
pvT data									
Reference	Year	$N$	$T / K$		$p / \text{MPa}$	$x_1$		AAD	
Abdulagatov <i>et al.</i> <sup>248</sup>	1993	64	523.11 - 653.10		2.24 - 63.24	0.045 - 0.847		3.126	

continued...

**Table E.3** ...continued

Reference	Year	$N$	$T / K$	$p / \text{MPa}$	$x_1$	AAD	
*Fenghour and Wakeham <sup>241</sup>	1996	16	429.90 - 698.43	7.49 - 12.66	0.076	0.124	
		14	465.95 - 698.45	8.96 - 14.07	0.174	0.210	
		12	501.13 - 698.60	10.72 - 15.66	0.265	0.263	
		11	518.58 - 698.60	12.09 - 17.24	0.338	0.377	
		9	554.25 - 698.53	14.18 - 18.84	0.402	0.44	
		8	571.56 - 698.66	15.84 - 20.52	0.457	0.552	
		6	607.66 - 698.75	19.32 - 23.47	0.539	0.669	
		5	625.21 - 698.23	22.13 - 26.18	0.602	0.623	
		6	652.70 - 698.31	27.03 - 30.38	0.676	0.477	
		<i>Overall</i>		87	429.90 - 698.75	7.49 - 30.38	0.076 - 0.676
*Joffrion and Eubank <sup>247</sup>	1989	48	398.12 - 498.11	0.20 - 12.03	0.100	0.038	
		61	398.12 - 498.11	0.15 - 8.67	0.250	0.055	
		60	398.12 - 498.11	0.07 - 4.20	0.500	0.050	
		<i>Overall</i>		16	398.12 - 498.11	0.07 - 12.03	0.100 - 0.500
		9					
Shmonov <i>et al.</i> <sup>249</sup>	1993	92	626.20 - 723.00	10.00-200.00	0.200 - 0.938	4.133	
Welsch <sup>254</sup>	1973	7	626.10 - 649.11	22.13 - 250.00	0.000 - 0.295	20.74	
Zhang <sup>250</sup>	1997	42	662.15 - 873.15	17.05 - 43.14	0.051 - 0.166	2.698	

Excess enthalpy $h^E$							
Reference	Year	$N$	$T / K$	$p / \text{MPa}$	$x_1$	AAD	
Smith <i>et al.</i> <sup>251</sup>	1983	69	373.17 - 423.16	0.30 - 0.65	0.304 - 0.650	-	
*Wormald and Colling <sup>252</sup>	1984	62	451.06 - 699.45	0.35 - 12.62	0.494 - 0.505	-	

Isobaric heat capacity $c_p$							
Reference	Year	$N$	$T / K$	$p / \text{MPa}$	$x_1$	AAD	
Hnědkovský and Wood <sup>253</sup>	1997	15	303.96 - 703.75	27.98 - 28.01	.99995	4.645	

Second virial coefficient $B(x_1)$ and cross-virial coefficient $B_{12}$ (AAD given in $\text{cm}^3 \text{mol}^{-1}$ )							
Reference	Year	$N$	$T / K$	$p / \text{MPa}$	$x_1$	AAD	
Abdulagatov <i>et al.</i> <sup>248</sup>	1993	25	298.14 - 373.12		0.000 - 1.000	3.896	
Abdulagatov <i>et al.</i> <sup>255</sup>	1996	24	521.15 - 653.15		0.000 - 1.000	7.611	
Akin-Ojo <i>et al.</i> <sup>256</sup>	2006	44	523.15 - 653.15		-	-	
Rigby and Prausnitz <sup>245</sup>	1968	4	373.17 - 423.16		-	-	
Smith <i>et al.</i> <sup>251</sup>	1983	6	233.16 - 653.15		-	-	

$x_1\text{H}_2\text{O} + (1 - x_1)\text{H}_2\text{S}$									
VLE data									
Reference	Year	$N_x$	$N_y$	$T / K$	$p / \text{MPa}$	$x_{1,\text{liq}}$	$x_{1,\text{vap}}$	AAD <sub>liq</sub>	AAD <sub>vap</sub>
*Burgess and Germann <sup>257</sup>	1969	39	39	303.13 - 443.14	1.72 - 2.34	.9702 - .9954	.0030 - .3208	0.064	2.423
*Chapoy <i>et al.</i> <sup>258,259</sup>	2005	31	15	298.16 - 338.14	0.50 - 3.96	.9649 - .9957	.0032 - .0213	0.065	0.069
*Clarke and Glew <sup>260</sup>	1971	36	36	273.15 - 323.12	0.05 - 0.10	.9970 - .9995	.0076 - .2250	0.003	0.799
Gillespie and Wilson <sup>235</sup>	1980	17	17	310.92 - 588.67	0.34 - 13.79	.9570 - .9956	.0038 - .8519	0.322	2.077
*Carroll and Mather <sup>266</sup>	1974	227	0	283.15 - 453.11	0.13 - 6.65	.9605 - .9997	-	0.070	-
*Neuburg <i>et al.</i> <sup>262</sup>	1977	651	651	298.14 - 453.11	1.30 - 2.30	.9682 - .9984	.0025 - .8953	0.033	0.269
*Selleck <i>et al.</i> <sup>263</sup>	1952	55	67	310.91 - 444.25	0.69 - 34.47	.8414 - .9971	.0004 - .6019	0.141	0.269
Suleimenov and Krupp <sup>264</sup>	1994	48	48	293.95 - 584.05	0.22 - 11.28	.9845 - .9999	.0039 - .9223	0.048	0.278
*Yu <i>et al.</i> <sup>265</sup>	1980	39	39	286.95 - 377.42	0.45 - 1.73	.9790 - .9970	.0033 - .1390	0.046	0.492

$pvT$ data							
Reference	Year	$N$	$T / K$	$p / \text{MPa}$	$x_1$	AAD	
*Selleck <i>et al.</i> <sup>263</sup>		15	310.91 - 444.25	sat.	0.023 - 0.057	0.657	

Isobaric heat capacity $c_p$							
Reference	Year	$N$	$T / K$	$p / \text{MPa}$	$x_1$	AAD	
*Hnědkovský and Wood <sup>253</sup>		15	304.01 - 703.75	27.97 - 28.04	.9933 - .9934	1.996	

$x_1\text{SO}_2 + (1 - x_1)\text{CO}_2$									
VLE data									
Reference	Year	$N_x$	$N_y$	$T / K$	$p / \text{MPa}$	$x_{1,\text{liq}}$	$x_{1,\text{vap}}$	AAD <sub>liq</sub>	AAD <sub>vap</sub>
Blümcke <sup>271</sup>	1988	8	0	263.00	0.14 - 1.18	0.706 - 0.991	-	2.676	-
Caubet <sup>437</sup>	1902	16	27	342.12 - 363.72	3.26 - 9.46	0.224 - 0.911	-	-	-

...continued

**Table E.3** ...continued

Reference	Year	$N_x$	$N_y$	$T / K$	$p / MPa$	$x_{1,liq}$	$x_{1,vap}$	$AAD_{liq}$	$AAD_{vap}$
Caubet <sup>272</sup>	1904	10	0	332.00	3.17 - 7.23	0.089 - 0.529	0.259 - 0.775	-	-
*Coquelet <i>et al.</i> <sup>269</sup>	2014	22	22	263.15 - 333.21	0.10 - 8.79	0.103 - 0.970	0.015 - 0.792	0.845	0.737
Lachet <i>et al.</i> <sup>270</sup>	2009	41	46	263.00 - 333.00	0.12 - 9.10	0.106 - 0.999	0.167 - 0.580	1.461	0.898
<i>pvT</i> data									
Reference	Year	$N$		$T / K$	$p / MPa$	$x_1$		$AAD$	
Gimeno <i>et al.</i> <sup>268</sup>	2018	200		263.15 - 304.21	0.10 - 20.00	0.007		0.395	
		200		263.15 - 304.21	0.10 - 20.00	0.030		1.197	
		200		263.15 - 304.21	0.10 - 20.00	0.047		1.525	
		200		263.15 - 304.21	0.10 - 20.00	0.103		2.321	
		200		263.15 - 304.21	0.10 - 20.00	0.197		2.368	
<i>Overall</i>		1000		263.15 - 304.21	0.10 - 20.00	0.007 - 0.197		1.561	
Nazeri <i>et al.</i> <sup>267</sup>	2017	443		273.15 - 353.15	0.10 - 30.00	0.050		1.168	
Wang <i>et al.</i> <sup>274</sup>	2015	12		328.15	9.00 - 20.00	0.025		3.855	
$x_1SO_2 + (1 - x_1)N_2$									
VLE data									
Reference	Year	$N_x$	$N_y$	$T / K$	$p / MPa$	$x_{1,liq}$	$x_{1,vap}$	$AAD_{liq}$	$AAD_{vap}$
Dean and Walls <sup>278</sup>	1947	6	2	241.12 - 301.47	1.55 - 3.55	0.986 - 0.996	0.011 - 0.307	-	-
Dornste and Ferguson <sup>279</sup>	1939	15	0	213.19 - 253.17	0.11 - 0.16	0.861 - 0.944	-	-	-
*El Ahmar <i>et al.</i> <sup>275</sup>	2011	44	46	323.15 - 413.15	1.48 - 23.53	0.826 - 1.000	0.121 - 1.000	0.542	1.311
<i>pvT</i> data									
Reference	Year	$N$		$T / K$	$p / MPa$	$x_1$		$AAD$	
*El Ahmar <i>et al.</i> <sup>275</sup>	2011	26		323.15 - 413.15	sat.	0.537 - 0.975		3.984	
Köster and Vrabec <sup>280</sup>	2017	63		260.00 - 500.00	1.50 - 40.00	0.050 - 0.950		1.107	
$x_1SO_2 + (1 - x_1)O_2$									
VLE data									
Reference	Year	$N_x$	$N_y$	$T / K$	$p / MPa$	$x_{1,liq}$	$x_{1,vap}$	$AAD_{liq}$	$AAD_{vap}$
*El Ahmar <i>et al.</i> <sup>275</sup>	2011	26	27	323.15 - 413.15	1.47 - 20.22	0.810 - 1.000	0.120 - 1.000	0.756	1.723
<i>pvT</i> data									
Reference	Year	$N$		$T / K$	$p / MPa$	$x_1$		$AAD$	
*El Ahmar <i>et al.</i> <sup>275</sup>	2011	26		323.15 - 413.15	sat.	0.627 - 0.979		5.781	
$x_1SO_2 + (1 - x_1)CH_4$									
VLE data									
Reference	Year	$N_x$	$N_y$	$T / K$	$p / MPa$	$x_{1,liq}$	$x_{1,vap}$	$AAD_{liq}$	$AAD_{vap}$
*Dean and Walls <sup>278</sup>	1947	5	5	241.12 - 301.47	1.72 - 3.55	0.965 - 0.985	0.013 - 0.292	0.066	0.627
*Sayegh <i>et al.</i> <sup>281</sup>	1981	1	1	318.00	13.80	0.760	0.255	0.436	0.570
$x_1SO_2 + (1 - x_1)Cl_2$									
VLE data									
Reference	Year	$N_x$	$N_y$	$T / K$	$p / MPa$	$x_{1,liq}$	$x_{1,vap}$	$AAD_{liq}$	$AAD_{vap}$
*Gilot <i>et al.</i> <sup>283</sup>	1967	18	48	224.89 - 259.36	0.05 - 0.10	0.450 - 0.982	0.167 - 0.827	3.346	1.779
*Wilson and Wilding <sup>282</sup>	1994	38	38	243.15 - 323.15	0.06 - 1.53	0.066 - 0.947	0.092 - 0.838	1.150	0.605
$x_1SO_2 + (1 - x_1)HCl$									
VLE data									
Reference	Year	$N_x$	$N_y$	$T / K$	$p / MPa$	$x_{1,liq}$	$x_{1,vap}$	$AAD_{liq}$	$AAD_{vap}$
*Köster and Vrabec <sup>280</sup>	2017	45	45	260.00 - 370.00	0.15 - 7.77	0.000 - 1.000	0.000 - 1.000	0.657	1.328
*Wilson and Wilding <sup>282</sup>	1994	35	35	203.15 - 273.15	0.00 - 2.62	0.000 - 1.000	0.000 - 1.000	0.713	0.165
<i>pvT</i> data									
Reference	Year	$N$		$T / K$	$p / MPa$	$x_1$		$AAD$	
*Köster and Vrabec <sup>280</sup>	2017	180		200.00 - 650.00	0.10 - 100	0.250 - 0.750		1.791	

continued...



Table E.3 ...continued

$x_1\text{SO}_2 + (1 - x_1)\text{DEA}$									
VLE data									
Reference	Year	$N_x$	$N_y$	$T / \text{K}$	$p / \text{MPa}$	$x_{1,\text{liq}}$	$x_{1,\text{vap}}$	$AAD_{\text{liq}}$	$AAD_{\text{vap}}$
*Li <i>et al.</i> <sup>285</sup>	2014	6	0	295.15 - 323.15	0.10	0.157 - 0.279	-	0.296	-
$x_1\text{SO}_2 + (1 - x_1)\text{H}_2\text{O}$									
VLE data									
Reference	Year	$N_x$	$N_y$	$T / \text{K}$	$p / \text{MPa}$	$x_{1,\text{liq}}$	$x_{1,\text{vap}}$	$AAD_{\text{liq}}$	$AAD_{\text{vap}}$
Beuschlein and Simenson <sup>293</sup>	1940	37	0	296.33 - 352.32	0.00 - 0.19	0.001 - 0.022	-	0.235	-
Byerley <i>et al.</i> <sup>438</sup>	1980	2	0	298.14 - 323.14	0.10	0.012 - 0.023	-	0.226	-
Conrad and Beuschlein <sup>439</sup>	1934	6	0	298.14	0.04 - 0.10	0.001 - 0.002	-	1.245	-
Douabul and Riley <sup>440</sup>	1979	6	0	278.97 - 303.24	0.10	0.021 - 0.051	-	0.972	-
Hudson <sup>441</sup>	1925	39	0	283.14 - 353.12	0.07 - 0.10	0.004 - 0.154	-	0.776	-
Mondal <sup>442</sup>	2007	19	0	293.00 - 333.00	0.10	0.023 - 0.091	-	3.801	-
Rabe and Harris <sup>443</sup>	1963	36	0	303.13 - 333.13	0.00 - 0.10	0.002 - 0.013	-	0.011	-
*Rumpf and Maurer <sup>291</sup>	1992	44	0	293.14 - 393.33	0.04 - 1.64	0.004 - 0.091	-	0.864	-
Sherwood <sup>290</sup>	1925	63	0	273.15 - 323.13	0.00 - 0.10	0.000 - 0.066	-	0.580	-
Sims <sup>444</sup>	1862	22	0	281.14 - 323.13	0.10	0.013 - 0.053	-	0.788	-
Smith and Parkhurst <sup>445</sup>	1922	8	0	278.15 - 333.12	0.10	0.002 - 0.031	-	0.942	-
Spall <sup>289</sup>	1963	19	17	373.12 - 573.18	0.18 - 21.85	0.064 - 0.951	0.032 - 0.975	3.125	4.784
Tokunaga <sup>446</sup>	1974	4	0	283.15 - 313.14	0.10	0.016 - 0.042	-	0.588	-
LLE data									
Reference	Year	$N_x$	$N_y$	$T / \text{K}$	$p / \text{MPa}$	$x_{1,\text{liq}}$	$x_{1,\text{vap}}$	$AAD_{\text{liq}}$	$AAD_{\text{vap}}$
van Berkum and Diepen <sup>286</sup>	1979	233	0	273.66 - 390.82	0.91 - 345.3	0.101 - 0.385	-	3.449	-
$pvT$ data									
Reference	Year	$N$	$T / \text{K}$	$p / \text{MPa}$	$x_1$	$AAD$			
Beuschlein and Simenson <sup>293</sup>	1949	4	296.14	0.00 - 0.11	0.001 - 0.022	0.440			
*Campbell and Maass <sup>292</sup>	1930	37	293.14 - 383.13	0.05 - 0.77	0.012 - 0.048	0.474			
$x_1\text{MEA} + (1 - x_1)\text{H}_2\text{O}$									
VLE data									
Reference	Year	$N_x$	$N_y$	$T / \text{K}$	$p / \text{MPa}$	$x_{1,\text{liq}}$	$x_{1,\text{vap}}$	$AAD_{\text{liq}}$	$AAD_{\text{vap}}$
*Belabbaci <i>et al.</i> <sup>180</sup>	2009	90	-	283.15 - 363.15	0.00 - 0.07	0.000 - 1.000	-	1.147	-
*Cai <i>et al.</i> <sup>297</sup>	1999	25	25	362.81 - 431.85	0.07 - 0.10	0.048 - 0.926	0.002 - 0.659	1.206	1.490
*Kim <i>et al.</i> <sup>182</sup>	2008	87	87	313.03 - 373.18	0.00 - 0.10	0.000 - 0.5663	0.000 - 0.058	0.685	0.101
*Lenard <i>et al.</i> <sup>300</sup>	1990	13	13	343.13 - 363.13	0.00 - 0.07	0.016 - 0.745	0.000 - 0.191	0.365	0.062
Nath and Bender <sup>304</sup>	1983	36	0	333.13 - 370.82	0.00 - 0.07	0.056 - 0.931	-	4.201	-
*Park <i>et al.</i> <sup>301</sup>	2009	33	33	355.2 - 430.3	0.05 - 0.07	0.030 - 0.988	0.001 - 0.927	3.450	2.362
*Park and Lee <sup>302</sup>	1997	16	16	374.30 - 443.30	0.10	0.035 - 1.000	0.003 - 1.000	3.168	1.641
Tanaka <sup>303</sup>	2001	13	13	373.15 - 443.51	0.10	0.000 - 1.000	0.000 - 1.000	1.424	1.077
Tochigi <i>et al.</i> <sup>181</sup>	1999	10	10	363.15	0.00 - 0.07	0.000 - 0.888	0.000 - 0.440	0.550	0.568
*Touhara <i>et al.</i> <sup>305</sup>	1982	26	0	298.14 - 308.14	0.00 - 0.005	0.038 - 0.892	-	0.628	-
$x_1\text{DEA} + (1 - x_1)\text{H}_2\text{O}$									
VLE data									
Reference	Year	$N_x$	$N_y$	$T / \text{K}$	$p / \text{MPa}$	$x_{1,\text{liq}}$	$x_{1,\text{vap}}$	$AAD_{\text{liq}}$	$AAD_{\text{vap}}$
Abdi and Meisen <sup>296</sup>	1999	48	5	309.05 - 445.95	0.00 - 0.03	0.339 - 0.977	0.000 - 0.114	2.913	0.436
Cai <i>et al.</i> <sup>297</sup>	1999	7	7	340.47 - 456.17	0.007	0.699 - 0.989	0.006 - 0.740	2.041	1.589
*Horstmann <i>et al.</i> <sup>295</sup>	2002	50	0	313.13 - 374.07	0.00 - 0.09	0.000 - 0.987	-	0.407	-
*Wilding <i>et al.</i> <sup>294</sup>	1991	26	23	373.15 - 473.15	0.00 - 1.52	0.025 - 0.951	0.000 - 0.145	1.600	0.097
$x_1\text{DEA} + (1 - x_1)\text{MEA}$									
VLE data									
Reference	Year	$N_x$	$N_y$	$T / \text{K}$	$p / \text{MPa}$	$x_{1,\text{liq}}$	$x_{1,\text{vap}}$	$AAD_{\text{liq}}$	$AAD_{\text{vap}}$
*Cai <i>et al.</i> <sup>297</sup>	1999	11	11	373.79 - 458.64	0.007	0.000 - 1.000	0.000 - 1.000	1.470	2.385
Tsintsarska <i>et al.</i> <sup>306</sup>	1988	15	15	354.23 - 427.61	0.002	0.167 - 0.996	0.001 - 0.874	2.259	0.760

continued...

**Table E.3** ...continued

$x_1\text{Cl}_2 + (1 - x_1)\text{HCl}$									
VLE data									
Reference	Year	$N_x$	$N_y$	$T / \text{K}$	$p / \text{MPa}$	$x_{1,\text{liq}}$	$x_{1,\text{vap}}$	$AAD_{\text{liq}}$	$AAD_{\text{vap}}$
Höchst AG <sup>307</sup>	1970	18	18	253.15 - 293.15	0.30 - 3.88	0.147 - 0.949	0.036 - 0.595	10.19	6.047
*Köster and Vrabec <sup>280</sup>	2017	42	42	253.00 - 369.97	0.27 - 6.82	0.000 - 0.999	0.000 - 1.000	3.330	3.814
*Wilson and Wilding <sup>282</sup>	1994	36	36	213.15 - 273.15	0.03 - 2.49	0.000 - 1.000	0.000 - 1.000	0.988	0.831
$pVT$ data									
Reference	Year	$N$	$T / \text{K}$	$p / \text{MPa}$	$x_1$	$AAD$			
*Köster and Vrabec <sup>280</sup>	2017	180	180.00 - 630.00	0.10 - 100	0.250 - 0.750	4.736			

## Lebenslauf

Name: Stefan Herrig  
Geburtsdatum und -ort: 08. April 1988, Essen  
Familienstand: ledig  
Staatsangehörigkeit: deutsch

---

## Ausbildung

Schule	08/1994 – 06/1998	Grundschule Dahlhausen, Bochum
	08/1998 – 06/2007	Theodor-Körner-Schule, Bochum Abschluss: Allgemeine Hochschulreife
Studium	10/2007 – 09/2011	Ruhr-Universität Bochum Maschinenbau Vertiefung: Energie- und Verfahrenstechnik Abschluss: Bachelor of Science
	10/2011 – 08/2013	Ruhr-Universität Bochum Maschinenbau Vertiefung: Energie- und Verfahrenstechnik Abschluss: Master of Science

## Berufliche Tätigkeit

Studentische Hilfskraft	11/2009 – 09/2013	Ruhr-Universität Bochum, Fakultät Maschinenbau Institut für Thermo- und Fluidodynamik, Lehrstuhl für Thermodynamik
Gastwissenschaftler	01/2013 – 06/2013, 06/2015 – 07/2015, 08/2017 – 10/2017	National Institute of Standards and Technology, Boulder, USA, Applied Chemicals and Materials Division, Thermophysical Properties of Fluids Group
Wissenschaftlicher Mitarbeiter	10/2013 – 09/2018	Ruhr-Universität Bochum, Fakultät Maschinenbau Institut für Thermo- und Fluidodynamik, Lehrstuhl für Thermodynamik